Flynn, Mary Frances (2003) *Dielectrophoretic characterisation and manipulation of sub-micron particles following surface modification.* PhD thesis.

http://theses.gla.ac.uk/1946/

Dielectrophoretic characterisation and manipulation of sub-micron particles following surface modification

Mary Frances Flynn

Thesis submitted for the degree of Doctor of Philosophy to the
Department of Electrical and Electronic Engineering
Faculty of Engineering
University of Glasgow

November, 2003

To my husband, Adam.

Acknowledgements

I wish to thank:

My supervisor, Professor Hywel Morgan, for having the bravery to let me carry out this research, for his helpful discussions and prompt corrections

Professor Antonio Castellanos for having a couch in his office and pointing out I didn't have to do astrophysics

Dr. Mike Hughes for early collaboration on surface conduction

Robert Harkins, for invaluable help and advice with e-beam lithography

Ronnie, Colin and Dave, for heroically catering to many dry-etch emergencies

Alex Ross and Nicholas Scott for all the rare and indispensable pieces of kit they let me twist their arms to borrow

Bill Monaghan and Mary Robertson for technical advice and assistance

Dave Bakewell, David Holmes, Irina Ermolina, Nic Green, Eric Johansen, Li Li Ciu and Dan Yanson for helpful discussions - and to all the other equally appreciable work comrades I have missed out, without whom the lab and coffee room would have been duller places

My Mum, for all the support she has given me in my studies

My friends and family, for putting up with all this nonsense for so long

My husband, Adam, without whose love and support this PhD would not have been possible – and to our baby, Jakub, for providing the ultimate deadline.

Abstract

Dielectrophoresis (DEP) is a force which acts on particles with a non-zero dipole moment in an inhomogeneous electric field. In an AC field the polarisability of real, dielectric particles in aqueous suspension is frequency dependent, therefore so also is the dielectrophoretically induced particle motion. Observation of this motion can thus be used to distinguish between particles with differing dielectric properties. With current trends in micro-scale analysis, DEP is presently and potentially a very powerful tool for particle characterisation, fractionation and manipulation.

The aim of this thesis is to dielectrophoretically characterise sub-micron particles on the basis of their surface properties and to devise a DEP technique suitable for the fractionation and manipulation of particles on this scale.

Polystyrene particles are modified by the attachment of biological ligands using various established localisation techniques and their DEP response observed using micro-electrodes with well defined high and low field regions, corresponding to a previously utilised design and modified in the course of this project for multiple sample handling. The results of these observations are modelled for the first time using a charge relaxation mechanism pertaining to a structured interfacial charge distribution and, through fitting the data to this model, fundamental parameters of the system - the surface conductance and electrokinetic charge – are predicted. The model viability is assessed with reference to both comparisons with alternative measurements and the technical limitations of the data fitting procedure, and corresponding surface charge transport mechanisms are discussed in the light of the DEP response following surface modification.

Investigations are made into the possibility of a DEP based device suitable for the transport/fractionation of sub-micron particles. Given the essentially dissipative nature of sub-micron particle ensembles, a Brownian ratchet principle is chosen. A Brownian ratchet is a generic system wherein a net directional drive is effected by biasing Brownian diffusion on a periodically activated anisotropic structure. Without need of thermal gradients or net macroscopic forces Brownian ratchet pumps could be an interesting alternative in many microfluidic applications. Simulated fields and corresponding particle transport rates are compared for two basic electrode structures in order to assess their viability for use as DEP Brownian ratchets and a new design proposed, based on the simultaneous juxtaposition of positive and negative DEP forces. This device is built on the necessary scale using multi-layer fabrication techniques with a silicon elastomer moulded channel. The existence of stochastic transport on the device is investigated experimentally by means of processed video sequences and resulting possibilities for particle separation on the basis of size and surface properties inferred.

Additional observed fluid flow is documented and discussed with reference to its compatibility with various physical mechanisms, which are modelled numerically and experimentally. A gallery of possibilities is presented for the manipulation of fluids and particles within the device.

Table of Contents

1 Introduction 8

1.1 Dielectrophoresis – Definition and background 8

1.2 Context and Motivation 8

1.3 Aims of thesis 9

1.4 Thesis outline 9

1.5 References 11

2 Dielectric Theory 15

2.1 Introduction 15

2.2 Dielectrics 15

2.3 Polarisation Mechanisms 15

2.4 Polarisation field and Maxwell-Wagner interfacial polarisation 16

2.5 Dipole Relaxation 17

2.6 Dipole of a spherical particle 20
- 2.6.1 Ideal case 20
- 2.6.2 Dielectric sphere with ohmic loss. 21

2.7 Surface Conductance and the Electrical Double Layer 22
- 2.7.1 Early Investigations 23
- 2.7.2 Double Layer Models 24
- 2.7.3 Gouy-Chapman Model 24
- 2.7.4 Gouy-Chapman-Graham-Stern Model 26

2.8 A closer look at surface conductance 28
- 2.8.1 Diffuse Layer Conductance 29
- 2.8.2 Stern Layer Conductance 30

2.9 Derivation of the Dielectrophoretic force 31

2.10 Summary 32

2.11 References 33

3 Separation methods and devices 35

3.1 Introduction 35

3.2 Travelling Wave Systems 35
3.2.1 Principle 36
3.2.2 Particle motion 36
3.2.3 Fluid motion 38
3.2.4 The electrothermal force 39
3.2.5 Electrorotation 40
3.2.6 Applications and recent work 40

3.3 Field Flow Fractionation 40
3.3.1 Example of DEP- FFF device design for sub-micron particles 41
3.3.2 Research in Dielectrophoretic Field-flow-fractionation 44

3.4 Brownian Ratchets 45
3.4.1 Brownian Motion 45
3.4.2 Principle of operation 46
3.4.3 Brownian ratchets in operation 49

3.5 Electro-osmosis 51
3.5.1 Electro-osmotic pumping 52

3.6 Summary 53

Appendix 3-1 Charge relaxation time 54

Appendix 3-2 Forces and the Maxwell Stress tensor 55

Appendix 3-3 Fabricated prototype of a μ-DEP-FFF device 57

Appendix 3-4 Generic concentration profile solution across a channel when DEP forces are balanced by diffusion 60

Appendix 3-5 1st order derivation of electro-osmotic flow velocity on parallel electrodes 60

3.7 References 63

4 DEP Characterisation – Materials and Methods 69

4.1 Introduction 69

4.2 Concept and Context 69

4.3 Definition of Crossover 70

4.4 Electrodes **71**

4.5 Experimental setup **75**

4.6 Surface Modification **75**

4.7 Coupling Mechanisms **76**
4.7.1 Adsorption 76
4.7.2 Covalent Attachment 77
4.7.3 Biotin-Avidin binding 77

4.8 Surface modification materials **78**
4.8.1 Substrate 78
4.8.2 Suspending medium 78
4.8.3 Immunoglobulin G Antibody 79
4.8.4 Biotin 80
4.8.5 Avidin 80
4.8.6 Streptavidin 81
4.8.7 Biotinylated oligonucleotide 81

4.9 BCA assay **82**
4.9.1 Method 82

4.10 Surface modification procedures **83**
4.10.1 Adsorption 83
4.10.2 Covalent attachment 86
4.10.3 Biotin-avidin binding 87

4.11 ζ-potential measurement techniques **87**

4.12 Summary **90**

Appendix 4-1 Resonance measurements on castellated electrodes **91**

4.13 References **92**

5 DEP Characterisation - Results **95**

5.1 Introduction **95**

5.2 Experimental Results **95**
5.2.1 Latex Beads 95
5.2.2 Beads with IgG 97
5.2.3 Beads with Streptavidin 98
5.2.4 Avidin Coupling 100
5.2.5 Beads with oligonucleotides 101

5.3 Relaxation mechanisms 102
5.3.1 Maxwell-Wagner-Gouy-Chapman 102
5.3.2 Summary of other investigated models 103
5.3.3 Gouy-Chapman-Graham-Stern surface conductance 104

5.4 Crossover predictions 105

5.5 Data fitting 108
5.5.1 Uncoated beads 108
5.5.2 IgG and complimentary antibody labeled 111
5.5.3 Streptavidin labeled 112
5.5.4 Avidin modified 114
5.5.5 Oligonucleotides 114

5.6 ζ-potential and surface modification 115

5.7 Electrophoretic Mobility Data 116

5.8 Discussion 121
5.8.1 Interpretation of ζ-potential 121
5.8.2 Experimentally measured ζ-potential 121
5.8.3 Mechanisms of surface conduction 123
5.8.4 Secondary layers 127
5.8.5 General Commentary on Data fits 128
5.8.6 Suggestions for data refinement 130

5.9 Conclusion 132

5.10 References 134

6 Fractionation device design 137

6.1 Introduction 137

6.2 Field Modelling 137

6.3 Design 1 – Asymmetric electrode pairs 137
6.3.1 Case 1 137
6.3.2 Potential schematic 141
6.3.3 Simulation of motion 142
6.3.4 Higher order approximation of potential 144
6.3.5 Case 2 145
6.3.6 System dimensions 145
6.3.7 Field modelling 146
6.3.8 Potential schematic 147

6.3.9 Simulation of Motion 148
6.3.10 Field decay 154

6.4 Design 2 – Interdigitated electrode clusters 157
6.4.1 Field Modelling 158
6.4.2 Field decay 164
6.4.3 Transport Simulation 165

6.5 Conclusion 168

6.6 References 169

7 Brownian ratchet Fabrication 170

7.1 WAM design 170

7.2 Electrode array fabrication 173
7.2.1 Layer 1 173
7.2.2 Layer 2 179
7.2.3 Layer 3 182

7.3 Channel 183
7.3.1 Materials 183
7.3.2 Methods 184
7.3.3 Preliminary constructions 185
7.3.4 Final channel construction 188

7.4 Printed Circuit boards 189

7.5 Final device construction 190

7.6 Conclusion 191

7.7 References 192

8 Particle transport and Separation 193

8.1 Introduction 193

8.2 Experimental set up 193

8.3 Simultaneous positive and negative DEP 196

8.4 3-electrode design 197

8.5 Channel requirement 198

8.6 Initial Collection 199

8.7 Image Processing 199
8.7.1 Matlab intensity analysis 199

8.8 Asymmetric Transport 201
8.8.1 A closer inspection 202

8.9 Diffusion 206
8.9.1 Spatial averaging 207
8.9.2 Intensity-concentration relationship 207
8.9.3 Electrode back-scattering 209
8.9.4 Diffusion rates 213
8.9.5 Theoretical comparison 215

8.10 Separation 216

8.11 Experimental/design refinement 218
8.11.1 Particle tracking 218
8.11.2 Fabrication 218

8.12 Conclusion 219

8.13 References 219

9 Fluid Flow 220

9.1 Non-stochastic pumping 220

9.2 Flow measurements 220
9.2.1 Experimental method 220

9.3 Results 222
9.3.1 Alternate electrodes 222
9.3.2 Variation with medium conductivity 222
9.3.3 Variation with voltage 223
9.3.4 Anomalous data 227
9.3.5 Potential mechanisms 228

9.4 Electro-osmotic flow experiments 228
9.4.1 Results 229

9.5 Electro-osmotic pumping 232

9.6 Numerical simulation of electrothermal pumping 233
9.6.1 Electrothermal field modelling 233

9.6.2 Simulated electrothermal flow pattern 235

9.7 Discussion 240

9.7.1 Compatibility with electro-osmosis 240

9.7.2 Compatibility with electrothermal motion 242

9.7.3 A combination of mechanisms 244

9.8 Pumping - a gallery of possibilities 245

9.9 Implications for Brownian ratchet functionality 251

9.10 Conclusion 251

9.11 References 253

10 Conclusion 254

10.1 DEP characterization 254

10.2 Fractionation device development 255

10.3 Microfluidic pumping 255

10.4 Fulfilment of aims 256

10.5 Future Work 257

10.5.1 DEP characterisation 257

10.5.2 Brownian ratchet fabrication/utilization 257

10.5.3 Fluid pumping 258

Publications and Presentations 259

1 Introduction

1.1 Dielectrophoresis – Definition and background

Dielectrophoresis (DEP) is the term given to the force on polarised particles under the action of a non-homogeneous electric field [1]. The dielectrophoretic force originates from the difference in field magnitude experienced at each end of the dipole and therefore the field must vary sufficiently on the scale of the particle for dielectrophoretically induced motion to be observable. The direction of the motion depends on the orientation of the dipole – aligned with or against the direction of field variation – which in turn depends on the relative polarisabilities of the particle and its suspending medium. Particles more polarisable than their suspending medium will be drawn towards higher field regions (positive DEP) and those less polarisable will experience a force in the direction of decreasing field gradient (negative DEP).

The name dielectrophoresis and early foundational work in the subject are attributed largely to Pohl who initially observed the movement of small synthetic particles suspended in dielectric fluid in response to an imposed AC or DC field [2]. Since then great strides have been made in elucidating the nature of the DEP force and transforming it into a useful tool for the characterisation and control of cells and micro-particles[1] [3-22], with recent applications ranging from the isolation of malaria [23] to sustaining boiling in space by using the DEP force as a replacement for terrestrial buoyancy [24, 25]! Improved miniaturisation of electrodes means, moreover, that sufficiently high, non-homogeneous fields can now be generated for the control of sub-micron particles, previously dominated by Brownian motion. This gives rise to exciting new possibilities concerning, for example, the manipulation of viral particles [26-29], DNA [30-34], protein macromolecules [35] and, since small particles are dominated by surface effects, prospects of new DEP diagnostic techniques based on colloidal surface modification [36-38].

1.2 Context and Motivation

The technology of miniaturised systems, with applications ranging from clinical diagnostics [39-43] and genetic analysis [44] to environmental monitoring [45] and drug screening [46], is in itself a rapidly developing field. This has led to the concept of multi-functional lab-on-a chip style arrangements – or micro-total analysis systems (μ-TAS)[2] – where the demand for integrable, microfluidic based components for sample fractionation,

---

[1] refer to papers cited in Chapters 3 and 4

[2] see references in Chapter 3

characterisation and manipulation is high. DEP and related techniques are prime candidates for this type of technology with the versatility so far displayed in diverse applications. Being an AC technique DEP has, in many cases, the advantage over related DC technology in a micro-scale fluidic environment and being responsive to the complex dielectric properties of analytes has the potential for higher selectivity and control.

From a more fundamental perspective, the dielectrophoretic study of colloids may help elucidate charge transport mechanisms at the solid liquid interface and thereby probe the physical structure of this enigmatic zone. This could provide better understanding of the polarisation processes involved in finitely conducting dielectrics in order to more accurately predict both their DEP response and assess other fundamental parameters such as the magnitude of the components of surface conductance and the electrokinetic charge.

It is against this background that I propose my aims.

1.3 Aims of thesis

1) To characterise colloidal latex spheres following biological surface modification so as to investigate the structure of the interfacial charge distribution (double-layer) and identify the scope for the utility of DEP as a discriminatory mechanism of sub-micron particles through their surface properties.

2) To investigate methods of DEP fractionation and build a device suitable for the manipulation/fractionation of submicron particles.

1.4 Thesis outline

- A basic framework of dielectric theory sufficient for the derivation of the DEP force on a lossy, dielectric sphere is outlined in Chapter Two. Emphasis is placed on the phenomenon of surface conductance with a review of background and current literature in this field.
- Chapter Three reviews current AC electrokinetic separation and transport methods and devices, with particular reference to those with relevance for sub-micron, dielectric particles.
- Chapter Four describes the materials and methods used in the DEP characterisation of surface modified colloids, outlining the basis and background literature of DEP characterisation with respect to crossover measurements and establishing a context for the utilised surface modification techniques and biological materials. Definitions of relevant parameters, measurement techniques and apparatus are included with experimental illustration.

- Experimental results of DEP crossover measurements on submicron polystyrene latex beads before and after surface modification are presented in Chapter Five. The influence of attached biological substances on the DEP response of the particles is observed and a data fitting method is proposed which allows the prediction of fundamental parameters of the system, based on an established model of charge distribution at the solid-liquid interface. The model viability is assessed with reference to both comparisons with alternative measurements and the technical limitations of the data fitting procedure, and corresponding surface charge transport mechanisms are discussed in the light of the DEP response following surface modification.
- In Chapter Six, the possibility of a DEP fractionation device based on a Brownian ratchet mechanism is investigated. Simulated fields and corresponding stochastic transport rates are compared for two basic electrode structures and a new design proposed.
- In Chapter Seven, fabrication techniques are investigated for the construction of this device and a multilayer structure is designed and built for use in a microfluidic context.
- An experimental set up is devised in Chapter Eight and the various components of the device are tested. Stochastic transport is investigated by means of processed video sequences and resulting possibilities for separation on the basis of size and surface properties inferred.
- In the final chapter, additional observed fluid flow is documented and discussed with reference to its compatibility with various physical mechanisms, which are modelled numerically and experimentally. A gallery of possibilities is presented for the manipulation of fluids and particles within the device.

1.5 References

[1] H. A. Pohl, *Dielectrophoresis*. Cambridge: Cambridge University Press, 1978.

[2] H. A. Pohl, "The Motion and Precipitation of Suspendoids in Divergent Electric Fields", *Journal of Applied Physics*, vol. 22, pp. 869-871, 1951.

[3] S. S. Dukhin, *Research on Surface Forces*, 1966.

[4] S. S. Dukhin and V. N. Shilov, *Dielectric phenomena and the Double Layer in Disperse Systems and Polyelectrolytes*. New York: Wiley-Interscience, 1974.

[5] R. Pethig, *Dielectric and Electronic Properties of Biological Materials*. Chichester: Wiley, 1979.

[6] E. Barnaby, G. Bryant, and J. Wolfe, "What is "dielectrophoresis"?", *Biochemistry and Bioenergetics*, vol. 19, pp. 347-352, 1988.

[7] R. Pethig, Y. Huang, X.-B. Wang, and J. P. H. Burt, "Positive and negative dielectrophoretic collection of colloidal particles using interdigitated castellated microelectrodes", *J. Phys. D: Appl. Phys.*, vol. 24, 1992.

[8] X. B. Wang, Y. Huang, F. F. Becker, and P. R. C. Gascoyne, "A Unified Theory of Dielectrophoresis and Traveling-Wave Dielectrophoresis", *Journal of Physics D-Applied Physics*, vol. 27, pp. 1571-1574, 1994.

[9] T. B. Jones and M. Washizu, "Equilibria and Dynamics of Dep-Levitated Particles - Multipolar Theory", *Journal of Electrostatics*, vol. 33, pp. 199-212, 1994.

[10] T. B. Jones, *Electromechanics of Particles*. New York: Cambridge University Press, 1995.

[11] M. P. Hughes, R. Pethig, and X. B. Wang, "Dielectrophoretic forces on particles in travelling electric fields", *Journal of Physics D-Applied Physics*, vol. 29, pp. 474-482, 1996.

[12] M. Washizu and T. B. Jones, "Generalized multipolar dielectrophoretic force and electrorotational torque calculation", *Journal of Electrostatics*, vol. 38, pp. 199-211, 1996.

[13] R. Pethig, "Dielectrophoresis: Using Inhomogeneous AC Electric Fields to Separate and Manipulate Cells", *Critical Reviews in Biotechnology*, vol. 16, pp. 331-348, 1996.

[14] N. G. Green and H. Morgan, "Dielectrophoretic investigations of sub-micrometre latex spheres", *J. Phys. D: Appl. Phys.*, vol. 30, pp. 2626-2633, 1997.

[15] N. G. Green, "Dielectrophoresis of sub-micron particles" in *Electrical and Electronic Engineering*: University of Glasgow, 1998, pp. 270.

[16] A. Ramos, H. Morgan, N. G. Green, and A. Castellanos, "Ac electrokinetics: a review of forces in microelectrode structures", *Journal of Physics D-Applied Physics*, vol. 31, pp. 2338-2353, 1998.

[17] J. Gimsa and D. Wachner, "A Polarization Model Overcoming the Geometric Restrictions of the Laplace Solution for Spheroidal Cells: Obtaining New Equations for Field-Induced Forces and Transmembrane Potential", *Biophysical Journal*, vol. 77, pp. 1316-1337, 1999.

[18] T. B. Jones, M. Gunji, M. Washizu, and M. J. Feldman, "Dielectrophoretic liquid actuation and nanodroplet formation", *Journal of Applied Physics*, vol. 89, pp. 1441-1448, 2001.

[19] H. Morgan, A. G. Izquierdo, D. Bakewell, N. G. Green, and A. Ramos, "The dielectrophoretic and travelling wave forces generated by interdigitated electrode arrays: analytical solution using Fourier series", *Journal of Physics D-Applied Physics*, vol. 34, pp. 1553-1561, 2001.

[20] N. G. Green, A. Ramos, and H. Morgan, "Numerical solution of the dielectrophoretic and travelling wave forces for interdigitated electrode arrays using the finite element method", *Journal of Electrostatics*, vol. 56, pp. 235-254, 2002.

[21] M. Washizu and T. B. Jones, "Dielectrophoretic interaction of two spherical particles calculated by equivalent multipole-moment method", *Ieee Transactions On Industry Applications*, vol. 32, pp. 233-242, 1996.

[22] T. B. Jones and M. Washizu, "Multipolar dielectrophoretic and electrorotation theory", *Journal of Electrostatics*, vol. 37, pp. 121-134, 1996.

[23] P. Gascoyne, C. Mahidol, M. Ruchirawat, J. Satayavivad, P. Watcharasit, and F. F. Becker, "Microsample preparation by dielectrophoresis: isolation of malaria", *Lab On a Chip*, vol. 2, pp. 70-75, 2002.

[24] T. J. Snyder, J. N. Chung, and J. B. Schneider, "Dielectrophoresis with application to boiling heat transfer in microgravity. II. Experimental investigation", *Journal of Applied Physics*, vol. 89, pp. 4084-4090, 2001.

[25] T. J. Snyder, J. B. Schneider, and J. N. Chung, "Dielectrophoresis with application to boiling heat transfer in microgravity. I. Numerical analysis", *Journal of Applied Physics*, vol. 89, pp. 4076-4083, 2001.

[26] M. P. Hughes, H. Morgan, and F. J. Rixon, "Dielectrophoretic manipulation and characterization of herpes simplex virus-1 capsids", *European Biophysics Journal With Biophysics Letters*, vol. 30, pp. 268-272, 2001.

[27] M. P. Hughes, H. Morgan, and F. J. Rixon, "Measuring the dielectric properties of herpes simplex virus type 1 virions with dielectrophoresis", *Biochimica Et Biophysica Acta-General Subjects*, vol. 1571, pp. 1-8, 2002.

[28] T. Muller, S. Fiedler, T. Schnelle, K. Ludwig, H. Jung, and G. Fuhr, "High frequency electric fields for trapping of viruses", *Biotechnology Techniques*, vol. 10, pp. 221-226, 1996.

[29] T. Schnelle, T. Muller, S. Fiedler, S. G. Shirley, K. Ludwig, A. Herrmann, G. Fuhr, B. Wagner, and U. Zimmermann, "Trapping of viruses in high-frequency electric field cages", *Naturwissenschaften*, vol. 83, pp. 172-176, 1996.

[30] C. L. Asbury and G. van den Engh, "Trapping of DNA in nonuniform oscillating electric fields", *Biophysical Journal*, vol. 74, pp. 1024-1030, 1998.

[31] C. L. Asbury, A. H. Diercks, and G. van den Engh, "Trapping of DNA by dielectrophoresis", *Electrophoresis*, vol. 23, pp. 2658-2666, 2002.

[32] S. Tsukahara, K. Yamanaka, and H. Watarai, "Dielectrophoretic behavior of single DNA in planar and capillary quadrupole microelectrodes", *Chemistry Letters*, pp. 250-251, 2001.

[33] M. Washizu and O. Kurosawa, "Electrostatic Manipulation of Dna in Microfabricated Structures", *Ieee Transactions On Industry Applications*, vol. 26, pp. 1165-1172, 1990.

[34] T. Yamamoto, O. Kurosawa, H. Kabata, N. Shimamoto, and M. Washizu, "Molecular surgery of DNA based on electrostatic micromanipulation", *Ieee Transactions On Industry Applications*, vol. 36, pp. 1010-1017, 2000.

[35] M. Washizu, S. Suzuki, O. Kurosawa, T. Nishizaka, and T. Shinohara, "Molecular Dielectrophoresis of Biopolymers", *Ieee Transactions On Industry Applications*, vol. 30, pp. 835-843, 1994.

[36] M. P. Hughes, M. F. Flynn, and H. Morgan, "Dielectrophoretic measurements of sub-micrometre latex particles following surface modification", in *Electrostatics 1999*, vol. 163, *Institute of Physics Conference Series*, 1999, pp. 81-84.

[37] M. F. Flynn and H. Morgan, "DEP Analysis of Oligonucleotide modified Latex Colloids", *6th Int. Conf. On dielectric and related phenomena, Spala, Poland*, 2000.

[38] M. P. Hughes, M. F. Flynn, and H. Morgan, "The dielectrophoretic behaviour of latex spheres: Influence of surface conductance", *Journal of Colloid and nerface Science*, vol. 220, pp. 454-457, 1999.

[39] J. Cheng, L. J. Kricka, E. L. Sheldon, and P. Wilding, "Sample preparation in microstructured devices", in *Microsystem Technology in Chemistry and Life Science*, vol. 194, *Topics in Current Chemistry*. Berlin 33: Springer-Verlag Berlin, 1998, pp. 215-231.

[40] C. L. Colyer, T. Tang, N. Chiem, and D. J. Harrison, "Clinical potential of microchip capillary electrophoresis systems", *Electrophoresis*, vol. 18, pp. 1733-1741, 1997.

[41] E. Dempsey, D. Diamond, M. R. Smyth, G. Urban, G. Jobst, I. Moser, E. M. J. Verpoorte, A. Manz, H. M. Widmer, K. Rabenstein, and R. Freaney, "Design and development of a miniaturised total chemical analysis system for on-line lactate and glucose monitoring in biological samples", *Analytica Chimica Acta*, vol. 346, pp. 341-349, 1997.

[42] I. R. Lauks, "Microfabricated biosensors and microanalytical systems for blood analysis", *Accounts of Chemical Research*, vol. 31, pp. 317-324, 1998.

[43] S. Shoji, M. Esashi, and T. Matsuo, "Prototype Miniature Blood-Gas Analyzer Fabricated On a Silicon- Wafer", *Sensors and Actuators*, vol. 14, pp. 101-107, 1988.

[44] L. J. Kricka, X. Y. Ji, O. Nozaki, S. Heyner, W. T. Garside, and P. Wilding, "Sperm Testing With Microfabricated Glass-Capped Silicon Microchannels", *Clinical Chemistry*, vol. 40, pp. 1823-1824, 1994.

[45] A. van den Berg, A. Grisel, E. Verneynorberg, B. H. Vanderschoot, M. Koudelkahep, and N. F. Derooij, "On-Wafer Fabricated Free-Chlorine Sensor With Ppb Detection Limit For Drinking-Water Monitoring", *Sensors and Actuators B-Chemical*, vol. 13, pp. 396-399, 1993.

[46] C. S. Effenhauser, G. J. M. Bruin, and A. Paulus, "Integrated chip-based capillary electrophoresis", *Electrophoresis*, vol. 18, pp. 2203-2213, 1997.

2 Dielectric Theory

2.1 Introduction

The study of the AC electrokinetics of dielectric particles requires a detailed knowledge of the main electromechanical processes which give rise to the governing forces. Investigation of how the particular parameters of a particle affect its electrokinetic behaviour can be used in characterisation and manipulation techniques as well as elucidating the underlying physical mechanisms of the polarisation process. The aim of this chapter is to outline sufficient dielectric theory in order to derive the dielectrophoretic force on a spherical, lossy dielectric particle and to provide the background for the theoretical assessment of the effect of surface conductance on the dielectrophoretic response.

2.2 Dielectrics

A dielectric is a material in which bound charges exist. These charges are not free to move long distances under the action of an applied external E-field, and so in the ideal case[3] there is no conduction. They may, however, move short distances or adjust in some way in order to minimise the energy of the applied E-field. This can result in the formation or reorientation of *dipoles* within the medium. A dipole is defined as two opposite charges , or centres of charge distributions $\pm q$, separated by a distance d, such that the *dipole moment*, $\underline{p}$, can be expressed as:

$$\underline{p} = q\underline{d} \qquad (2\text{-}1)$$

2.3 Polarisation Mechanisms

The three fundamental non macroscopic mechanisms by which an ideal dielectric adjusts in response to an external field are [1]:

i) **Orientational** - natural permanent molecular dipoles in the material align to cancel the field.

ii) **Electronic** – the cloud of charge around an atom shifts slightly in relation to the nucleus.

iii) **Atomic** – oppositely charged ions in an ionic crystal move slightly in opposing directions.

---

[3] Where only bound and no free charge is present.

2.4 Polarisation field and Maxwell-Wagner interfacial polarisation

The lowering of the stored energy in a dielectric can be expressed as a reduction in the magnitude of the field experienced within it by a factor ε_r, the relative permittivity of the dielectric. This is a result of a polarisation field in the opposite direction, the total source charge for which is effectively the positive and negative charges of the dipoles. For a block of dielectric material this can be quantified in terms of surface charge only, since, as shown schematically in Figure 2-1, due to symmetry the internal dipoles cancel. The total bound charge ρ_b in the volume, v, then, can be written in terms of the net dipole moment , $\underline{\boldsymbol{P}}$, in terms of a surface integral over the total bounding area, A, as:

$$\int_v \rho_b \, dv = -\int_A \underline{\boldsymbol{P}}.\underline{\boldsymbol{dA}} \tag{2-2}$$

where $\underline{\boldsymbol{dA}}$ is the area increment perpendicular to the applied field[4].

By the divergence theorem this implies:

$$\rho_b = \nabla.\underline{\boldsymbol{P}} \tag{2-3}$$

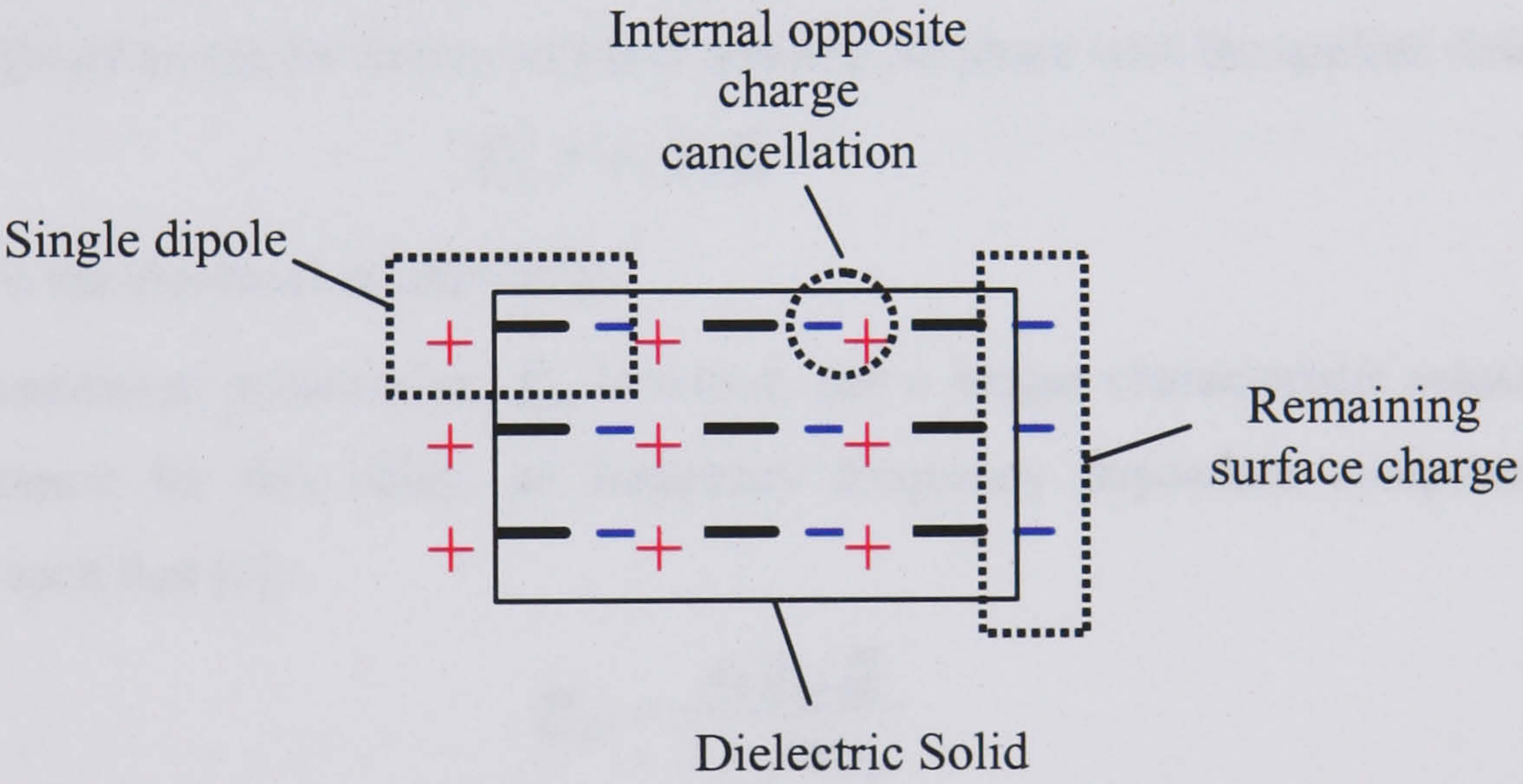

Figure 2-1

Effective charge distribution in a polarised dielectric

By Gauss' law, in a dielectric medium, a charge distribution of free and bound charge densities, ρ_f and ρ_b respectively, gives rise to an electric field, $\underline{\boldsymbol{E}}$, such that:

$$\nabla.\underline{\boldsymbol{E}} = \frac{\rho_b + \rho_f}{\varepsilon_0} \tag{2-4}$$

where ε_0 is the permittivity of free space.

---

[4] This volume does not, rigorously speaking, correspond to the physical dimensions of the dielectric but to a volume which encloses the centres of the superimposed positive and negative charge distributions.

Thus, from (2-3):

$$\nabla.(\varepsilon_0 \underline{\boldsymbol{E}} + \underline{\boldsymbol{P}}) = \rho_f \tag{2-5}$$

so that a quantity, $\underline{\boldsymbol{D}}$ - the electric flux density - can be defined as:

$$\underline{\boldsymbol{D}} = \varepsilon_0 \underline{\boldsymbol{E}} + \underline{\boldsymbol{P}} \tag{2-6}$$

where:

$$\nabla.\underline{\boldsymbol{D}} = \rho_f \tag{2-7}$$

and:

$$\underline{\boldsymbol{D}} = \varepsilon_0 \varepsilon_r \underline{\boldsymbol{E}} \tag{2-8}$$

where ε_r is defined as the relative permittivity of the medium.

2.5 Dipole Relaxation

The reorientation of the charge that is necessary for the polarisation field to reach a maximum requires a finite time. This is known as the *relaxation time*. This time will vary according to the particular polarisation mechanism. For atomic and electronic polarisation, dipole formation can be assumed to be almost instantaneous, (following the field up to ~10^{14}Hz [2]) and so can be written as a real quantity, in phase with the applied field as:

$$\underline{\boldsymbol{P}}_a = \varepsilon_0 \chi_a \underline{\boldsymbol{E}} \tag{2-9}$$

where χ_a is the electrical susceptibility.

The orientational polarisation, $\underline{\boldsymbol{P}}_{or}$, however, has a longer characteristic relaxation time, τ_{or}. To account for this delay, an imaginary frequency dependent component can be introduced such that [3]:

$$\underline{\boldsymbol{P}}_{or} = \frac{\varepsilon_0 \chi_{or} \underline{\boldsymbol{E}}}{1 + j\varpi\tau_{or}} \tag{2-10}$$

From equations (2-6), (2-8) and (2-9) it can be seen that $\chi = \varepsilon_r - 1$, so noting that in the high frequency limit the orientational polarisation can be neglected, the total polarisation can be expressed as:

$$\underline{\boldsymbol{P}}_{tot} = \varepsilon_0 (\varepsilon^* - 1) \underline{\boldsymbol{E}} \tag{2-11}$$

where the complex entity ε^* can be written in terms of the high and low frequency limits of permittivity, ε_∞ and ε_s respectively, as:

$$\varepsilon^* = \varepsilon_\infty + \frac{\varepsilon_s - \varepsilon_\infty}{1 + j\omega\tau_{or}} \tag{2-12}$$

Rationalising the denominator and writing this complex permittivity as:

$$\varepsilon^* = \varepsilon' + j\varepsilon'' \tag{2-13}$$

leads to the famous Debye equations [3]:

$$\varepsilon' = \varepsilon_{\infty} + \frac{\varepsilon_s - \varepsilon_{\infty}}{1+\omega^2\tau_{or}^2} \tag{2-14}$$

$$\varepsilon'' = \frac{\varpi\tau_{or}(\varepsilon_s - \varepsilon_{\infty})}{1+\omega^2\tau_{or}^2} \tag{2-15}$$

where the imaginary part, ε", represents the dielectric loss. In an ideal dielectric, this can be quantified as energy loss due to the polarisation current – i.e. the reorientation of bound charges - highest at the *relaxation frequency*. This frequency corresponds to the reciprocal of the relaxation time of the previously dominant polarisation mechanism, e.g. orientational polarisation, above which it can no longer respond to the increased rate of change of the field and so ceases to take part in the polarisation process. For water, which consists of polar molecules, this relaxation is ~18GHz. Increasing the frequency beyond this point results in a drop in permittivity. Depending on the medium, another mechanism, e.g. atomic, may then become the dominating polarisation process until the frequency reaches a range where this too becomes ineffective and so there is another relaxation. If ε_{∞} truly is the high frequency limit then no further relaxation will take place beyond this value. Figure 2-2 shows the Debye parameters as a function of frequency for a range corresponding to two dielectric relaxations of a generic, dispersive material.

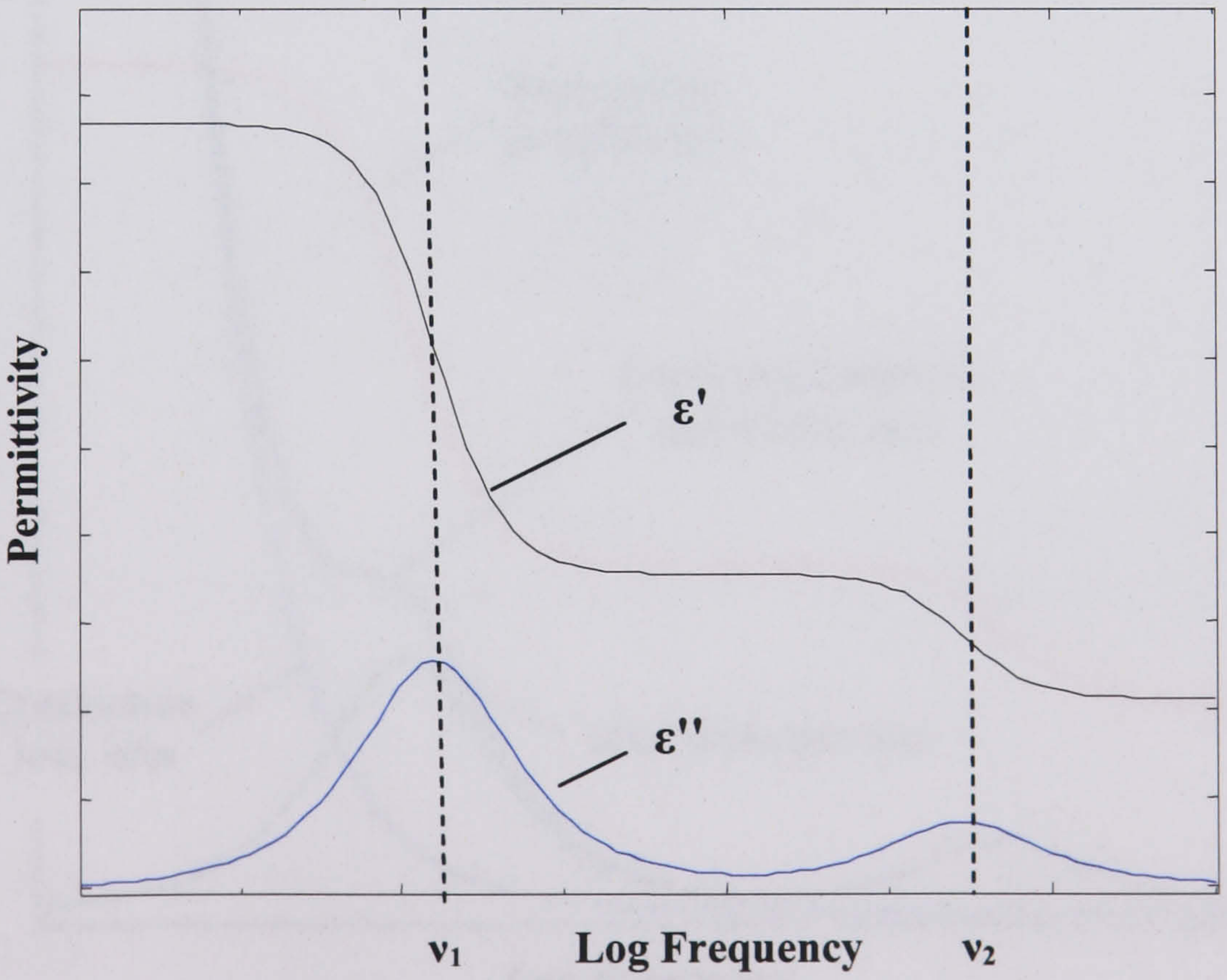

Figure 2-2

Real and imaginary parts of the Debye equation for an ideal, multi-dispersive dielectric. Dielectric loss, corresponding to the imaginary part, can be seen to peak at the relaxation frequencies ν_1 *and* ν_2*.*

It may be the case, however, that the dielectric in question is *non-dispersive* in the ideal sense – i.e. the real part of its permittivity is always the static value, ε_s, at least up to frequencies well outwith the range of experimental investigation. This is the case, for example, with many synthetic polymers such as latex, since the molecular structure is that of long entangled chains, with effectively no ordered dipoles. This need not be the case with other large molecules such as DNA or proteins since these possess a high degree of order which can result in the systematic alignment of internal dipoles such that real interfacial polarisation can take place. Real systems, however, generally also include loss due to an Ohmic conductivity component. This effect will obviously diminish with increasing frequency since the current will have less time to flow and therefore can be quantified as σ/ω, where σ represents the conductivity in the static limit. The net dielectric loss of a dispersive, non-ideal dielectric, then, can be expressed as:

$$\varepsilon'' = \frac{\varpi\tau_{or}(\varepsilon_s - \varepsilon_\infty)}{1+\omega^2\tau_{or}^2} + \frac{\sigma}{\varpi} \qquad (2\text{-}16)$$

This is shown in Figure 2-3 together with the individual conductivity loss and the imaginary part in the ideal case, compared with the real part, which is unchanged.

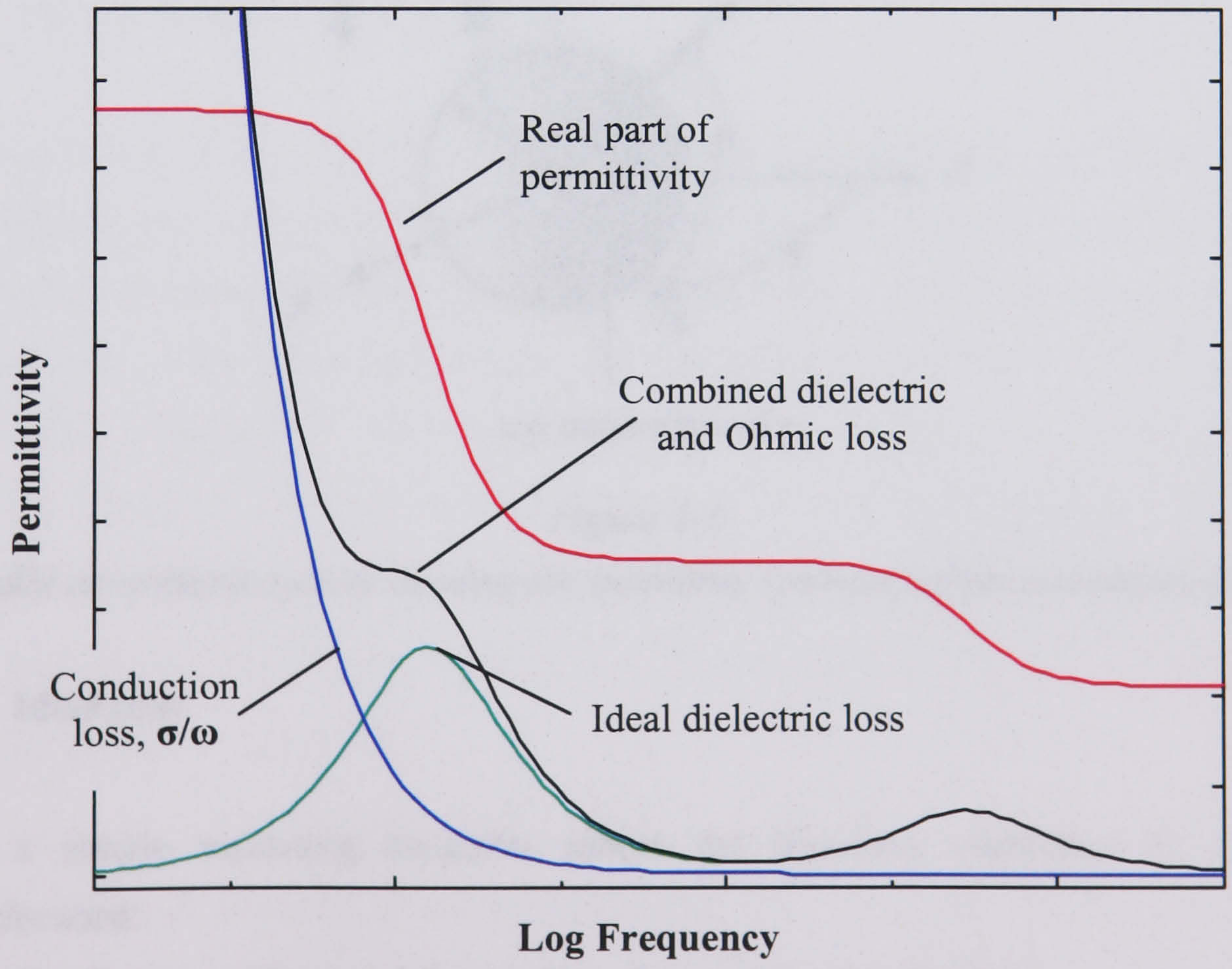

Figure 2-3
Dielectric dispersions comparing the real permittivity with losses due to dipole relaxation and free current.

2.6 Dipole of a spherical particle

The potential energy at distance r from a dipolar charge distribution is given by [1]:

$$V = \frac{\underline{p}.\hat{r}}{4\pi\varepsilon_0 r^2} \quad (2\text{-}17)$$

A comparison is necessary, then, between this and the potential of a polarised dielectric sphere. This can be found by solving Laplace's equation, which, with the azimuthal symmetry of a spherical particle in a uniform field, can be considered as two dimensional (Figure 2-4).

The general solution for all space is [1]:

$$V = \sum_{n=0}^{\infty}(A_n r^n + B_n r^{-(n+1)})P_n(\cos\theta) \quad (2\text{-}18)$$

where A and B are the co-efficients of the Legendre polynomials, P_n, functions of θ, the angle from the point of observation to the centre of the dipole. In the case of a particle suspended in a fluid, the effective dipole moment is determined by the electrical properties of both the dielectric and the suspending medium.

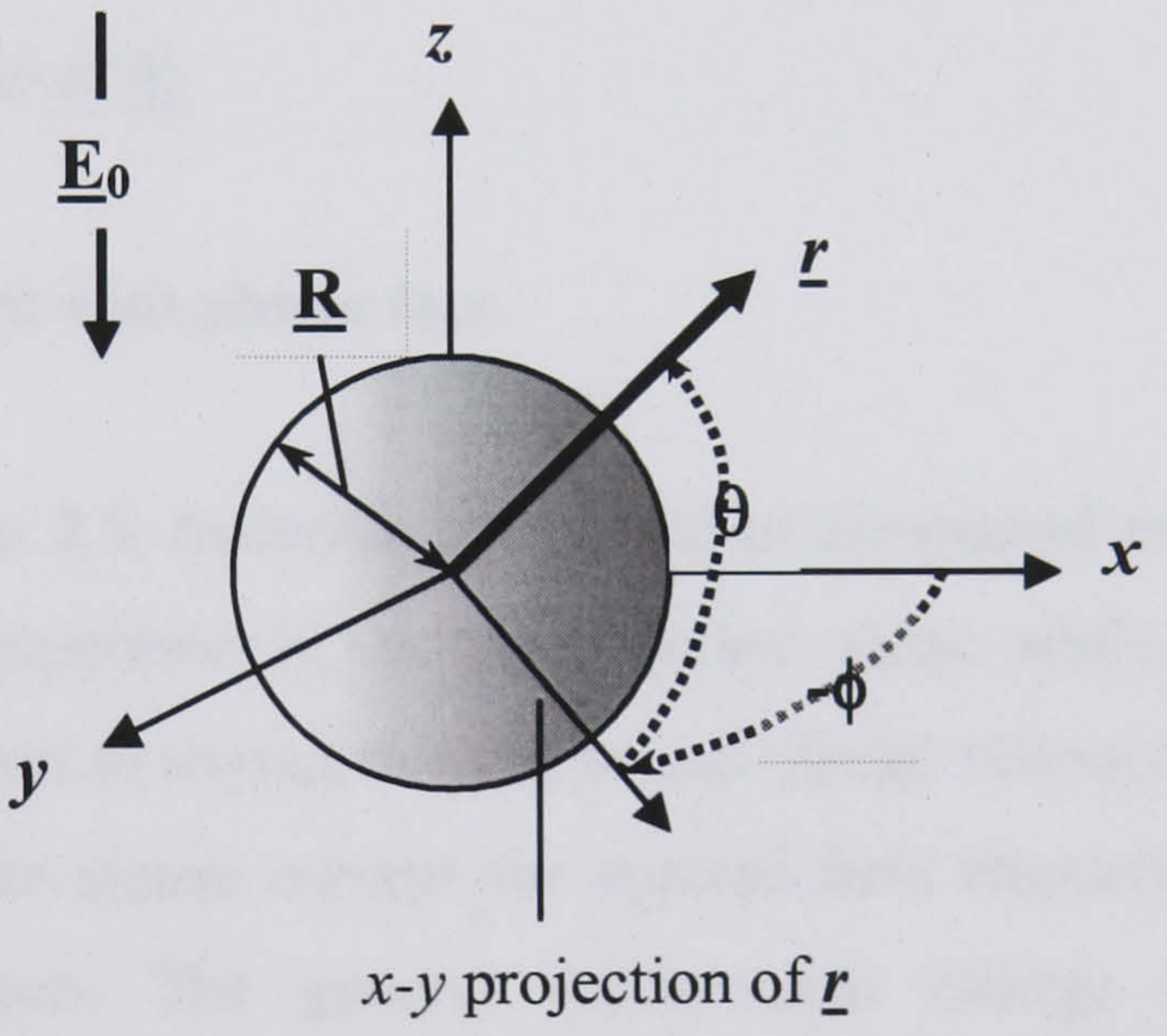

Figure 2-4

The radial co-ordinate system showing the azimuthal symmetry of the polarization direction, r

2.6.1 Ideal case

For a simple insulating dielectric sphere the boundary conditions at $r = R$ are straightforward:

i) The field is uniform and finite within the particle and at infinity.

ii) The electrostatic potential is continuous across the boundary to avoid having infinite field gradients.

iii) The normal component of the electric flux density, $\underline{\boldsymbol{D}}_{\mathbf{n}}$, is conserved since there is no free charge.

Condition (i) leads to the selection of the n=1 term of the general solution (2-18). Since all negative-index r terms are dropped, the potentials outside and inside the sphere can be written as:

$$V_1(r,\theta) = -\underline{\mathbf{E}}_0.\underline{\mathbf{r}}\cos\theta + \frac{A\cos\theta}{r^2}, \qquad r > R \tag{2-19}$$

$$\mathrm{V}_2(r,\theta) = -Br\cos\theta, \qquad r < R \tag{2-20}$$

where r and R are the magnitudes of $\underline{r}$ and $\underline{R}$ respectively.

Applying the remaining two boundary conditions:

$$\mathrm{V}_1(R,\theta) = \mathrm{V}_2(R,\theta) \tag{2-21}$$

$$\varepsilon_1 E_{r1} = \varepsilon_2 E_{r2} \tag{2-22}$$

where $E_{ri} = -\frac{\partial V_i}{\partial \underline{\boldsymbol{r}}}$, permits a solution for A and B giving:

$$A = \frac{\varepsilon_2 - \varepsilon_1}{\varepsilon_2 + 2\varepsilon_1} R^3 E_0 \quad \text{and} \quad B = \frac{3\varepsilon_1}{\varepsilon_2 + 2\varepsilon_1} \tag{2-23}$$

where E_0 is the magnitude of $\underline{\boldsymbol{E_0}}$

2.6.2 Dielectric sphere with ohmic loss.

As outlined in section 2.5, materials comprised of disordered macromolecules can often be considered as non-dispersive in the ideal, Debye sense while still possessing a finite conductance. This amounts to saying that the bound charge relaxation generates a negligible loss compared to the free ohmic current for applied field frequencies within the range of experimental investigation. The general fundamental change to the static boundary conditions, therefore, requires only the inclusion of finite conductivities, σ_1 and σ_2, defined outside and inside the particle respectively, the consequence of which is that there is now a time dependent accumulation of free charge, σ_{qf}, on the particle surface. Thus condition (iii) can be redefined as:

$$\sigma_{qf} = \varepsilon_1 E_{r1} - \varepsilon_2 E_{r2}, \qquad r = R \tag{2-24}$$

with the instantaneous charge conservation relation:

$$J_{r2} - J_{r1} + \frac{\partial \sigma_{qf}}{\partial t} = 0, \qquad r = R \tag{2-25}$$

where $J_{ri} = \sigma_i E_{ri}$ is the normal component of ohmic current in each of the two regions.

Since this energy loss is characterised by a time lag in the establishment of the polarisation field, the net dipole response is out of phase with the applied E-field. Thus, it is useful to write all the variables as complex phasors i.e. with $e^{j\omega t}$ dependence, whereupon equations (2-24) and (2-25) can be combined to give:

$$\varepsilon_1^* E_{n1} = \varepsilon_2^* E_{n2}, \qquad r = R \tag{2-26}$$

where now ε_i^* is a complex term given by:

$$\varepsilon_i^* = \varepsilon_i - j\frac{\sigma_i}{\omega} \tag{2-27}$$

This is equivalent to the Debye permittivity for a non-dispersive dielectric with finite conductivity, as required.

By analogy to (2-22), (2-26) gives the same A and B as before only now with complex permittivities. Thus, noting that the second term in (2-19) is in fact the potential originating from the dipole, this can be written as:

$$P_{eff} = 4\pi\varepsilon_1 A^* \tag{2-28}$$

The dipole by convention can be expressed in terms of the volume of the particle and a polarisability, α_p, as:

$$\underline{p} = \frac{4}{3}\pi R^3 \alpha_p \underline{E} \tag{2-29}$$

The effective polarisability of a dielectric sphere is therefore given by:

$$\alpha_p = 3\varepsilon_1 \left(\frac{\varepsilon_2^* - \varepsilon_1^*}{\varepsilon_2^* + 2\varepsilon_1^*} \right) \tag{2-30}$$

Note that here, the permittivity, ε_1, outwith parenthesis is real [4].

2.7 Surface Conductance and the Electrical Double Layer

Real particles, in addition to possessing homogenous free charge, generally have a fixed charge at the solid-liquid interface due, for example, to the presence of solvated molecular groups. In an aqueous solution, a layer of counter-ions therefore also forms around this charge, screening it from the bulk fluid. This is known as the **electrical double layer.** These charges may move under the influence of electric fields applied tangentially to the surface. Surface conduction, then, is the excess conduction that takes place as the result of the induced electric transport of charge carriers in the double layer. It can be quantified in terms of K_s, defined through Ohm's law as:

$$\underline{j}_s = K_s \, \underline{E} \tag{2-31}$$

where $\underline{j}_s$ is the surface current density.

Surface conductance is important from various perspectives. It governs, to a large extent:

i) colloid stability and interaction

ii) the electrokinetic response of the particle

and, through quantifying it, we can say something of :

iii) the structure of the double-layer.

2.7.1 Early Investigations

The intrinsic idea of surface conductance goes back some time. Inconsistencies in the measurements of ζ-potentials [5] computed from streaming potentials in glass capillaries were among the early indications of this phenomenon. The oldest theory of surface conduction goes back to Bikerman [6, 7] who analysed ionic transport and electro-osmosis in a simple diffuse layer. Miles and Robertson [8] first introduced the idea that the double layer would affect the dielectric properties of a particle and hence the dipole moment. Various theories of double layer distribution and their associated relaxation mechanisms have since been proposed. O'Konski, [9], through taking into account the radial charge flux due to interfacial polarisation as well as a postulated purely tangential conduction associated with a tightly bound layer of countercharge, defined the surface conductivity in terms of the specific conductance, K_s, as:

$$\sigma_s = \frac{2K_s}{R} \tag{2-32}$$

This theory was partially successful in predicting the higher than previously expected values of surface conductance. However, experimental evidence [10, 11] pointed to another lower frequency relaxation which seemed to imply that a Maxwell-Wagner interfacial based mechanism was not the only one in operation. Subsequent investigations by Schwarz [12] and Schurr [13] of purely tangential polarising currents where all ions were assumed to be confined in the plane of the bead – also did not succeed in explaining lower frequency relaxations reported in these experimental investigations. It became evident that in order to examine the surface conductance effectively the structure of the double layer had to be investigated - and vice versa.

2.7.2 Double Layer Models

It has been established that the relaxation time, τ_{rel}, is of fundamental importance in determining the degree of polarisation at a particular frequency. The dipole around a spherical particle can form in different ways depending on how much time is available. So far, the type of mechanism rigorously considered has been interfacial (Maxwell-Wagner) polarisation where the double layer polarises locally, with normal instead of tangential currents dominating. At lower frequencies, however, it is reasonable to assume that polarising currents due to surface conductance effects become increasingly significant. In order to quantify these effects then various models of the double layer have been proposed.

2.7.3 Gouy-Chapman Model

The first and simplest model of the charge distribution at a phase interface is that of Gouy and Chapman. This describes the double layer as essentially continuous with the density distribution governed by the requirement of balancing the Higgs chemical potential induced diffusion force with the electrostatic force due to the solvated ionic groups on the bead surface [14]. This leads to the Poisson-Boltzmann equation:

$$\nabla^2\psi = \frac{d^2\psi}{dx^2} = -\frac{1}{4\pi\varepsilon_0}\underbrace{\frac{4\pi}{\varepsilon_r}\sum_i n_i{}^0 z_i e \exp\left(\frac{-z_i e\psi}{kT}\right)}_{\text{Boltzmann Charge density}} \qquad (2\text{-}33)$$

where n_i^0 is the specific ion concentration when $\psi = 0$, z_i is the specific ion valency, e is the electronic charge, k is Boltzmann's constant and T is the temperature.
In the low ψ case[5] and assuming electroneutrality of the bulk, i.e:

$$\sum n_i^0 z_i e \qquad (2\text{-}34)$$

This can be written as:

$$\nabla^2\psi = \kappa^2\psi \qquad (2\text{-}35)$$

where κ, for a symmetrical electrolyte, is given by:

$$\kappa = \left(\frac{2z^2 e_0{}^2 n}{\varepsilon_m kT}\right)^{\frac{1}{2}} \qquad (2\text{-}36)$$

---

[5] using $e^{-x} = 1 - x$ as a first order approximation for small x

Assuming the particle surface to be locally flat, this reduces to the one-dimensional case and, since κ is not x-dependent, an exponential solution can be assumed:

$$\psi = \psi_0 e^{-\kappa x} \tag{2-37}$$

where the positive κ solution has been rejected as unphysical.

The significance of κ can be found by comparing the surface charge density σ_0 - defined by integrating Poisson's equation from zero to infinity - with the net potential drop ψ_0 from the charged interface to the bulk:

$$\sigma_0 = -\varepsilon \int_0^\infty \frac{d^2\psi}{dx^2} dx = -\varepsilon \left(\frac{d\psi}{dx} \right)_{x=0} \tag{2-38}$$

so that, from (2-37):

$$C_{DL} = \frac{\sigma_0}{\psi_0} = \varepsilon\kappa \tag{2-39}$$

This defines a local capacitance, C_{DL}, of the double layer which behaves like that of parallel plates with a separation $1/\kappa$ (see Figure 2-5). Thus, κ is known as the **inverse Debye length** and can be understood as the effective thickness of the double layer. Discrepancy remains, however, with experimentally measured conductivities generally higher than predicted by this homogenous diffuse layer [5, 15-19].

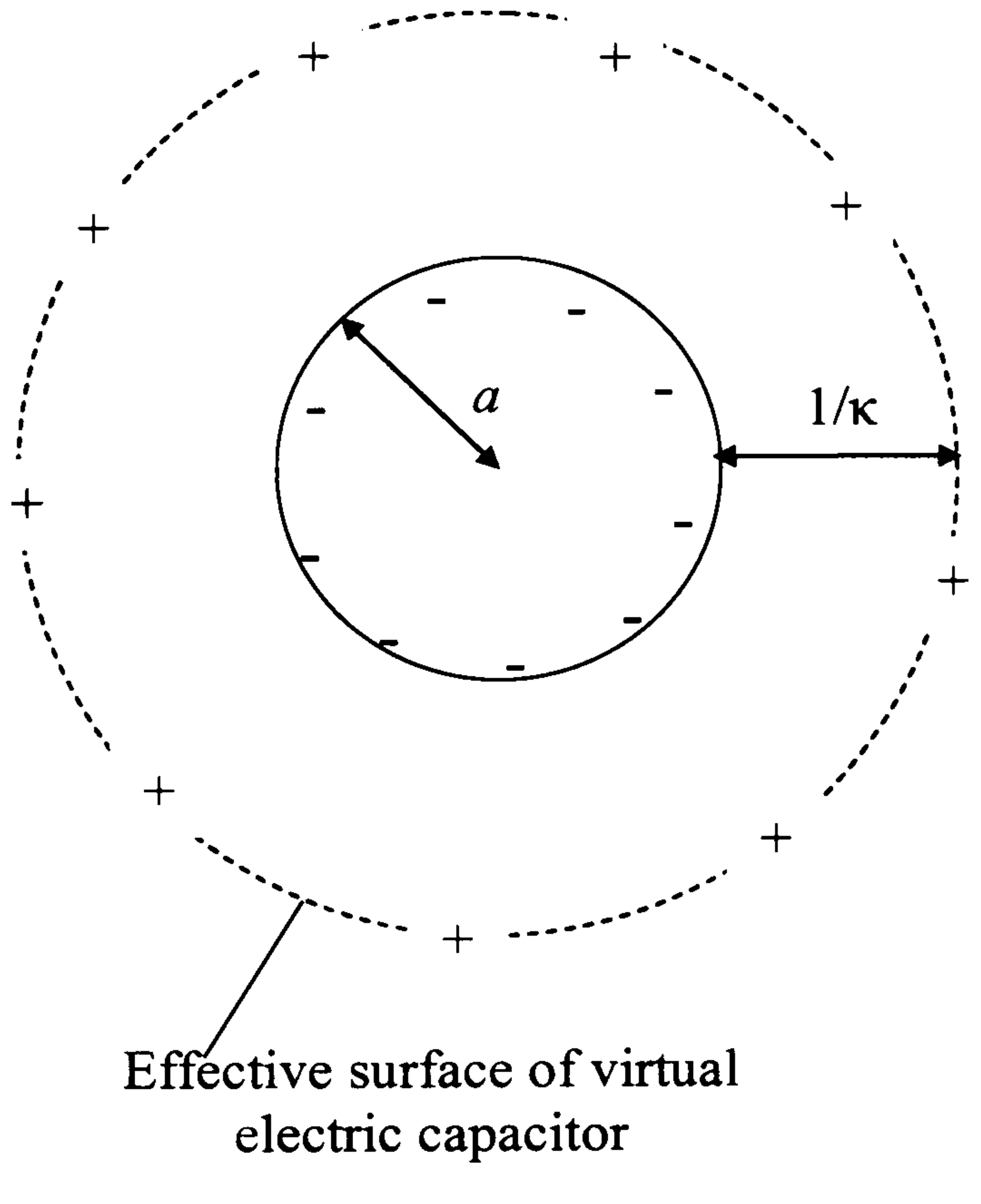

Figure 2-5

Interpretation of the inverse Debye length as a measure of the effective extent of the diffuse layer.

2.7.4 Gouy-Chapman-Graham-Stern Model

A more viable description of the double layer - termed the Gouy-Chapman-Graham-Stern model - is to divide the counter-charge distribution into two distinct regions (Figure 2-6):

- **The Stern layer**, where the counter charge, consisting of polarised water molecules and partially hydrated ions, is confined to move locally in the plane of the bead surface. This layer can be thought of as rigid, following the bead under induced motion - behaving essentially like fixed charge.

- **The diffuse layer** where the charges have an extra degree of freedom and move under diffusion, electro-osmosis and streaming as well as conduction

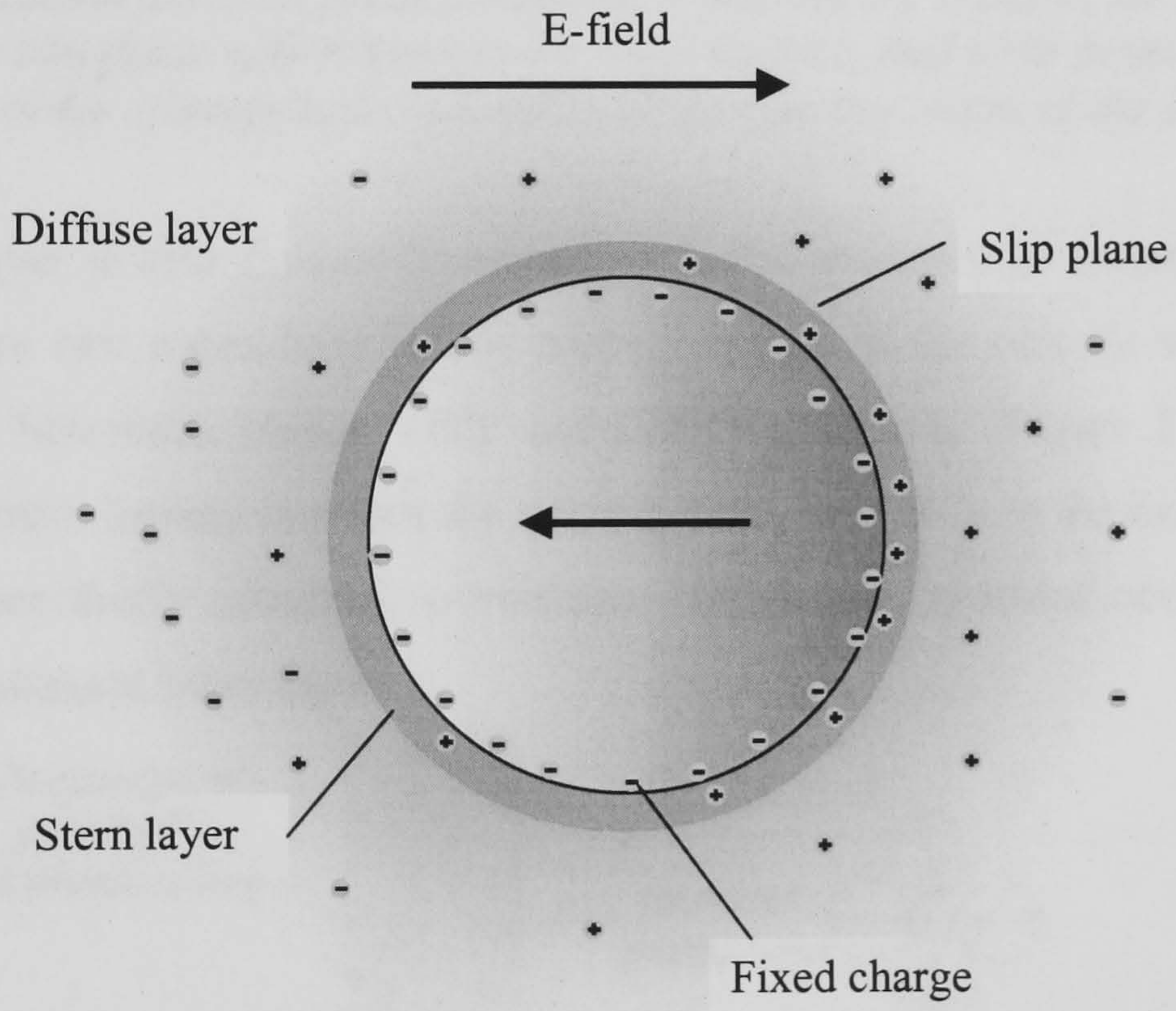

Figure 2-6
Schematic charge distribution of polarised sphere in the Gouy-Chapman-Graham-Stern model

The **ζ-potential** is here defined as the electrical potential at the boundary between the two layers[6] – or **slip plane.** Figure 2-7 shows the potential fall-off.

---

[6] Although this is a simplifying assumption which need not always be valid.

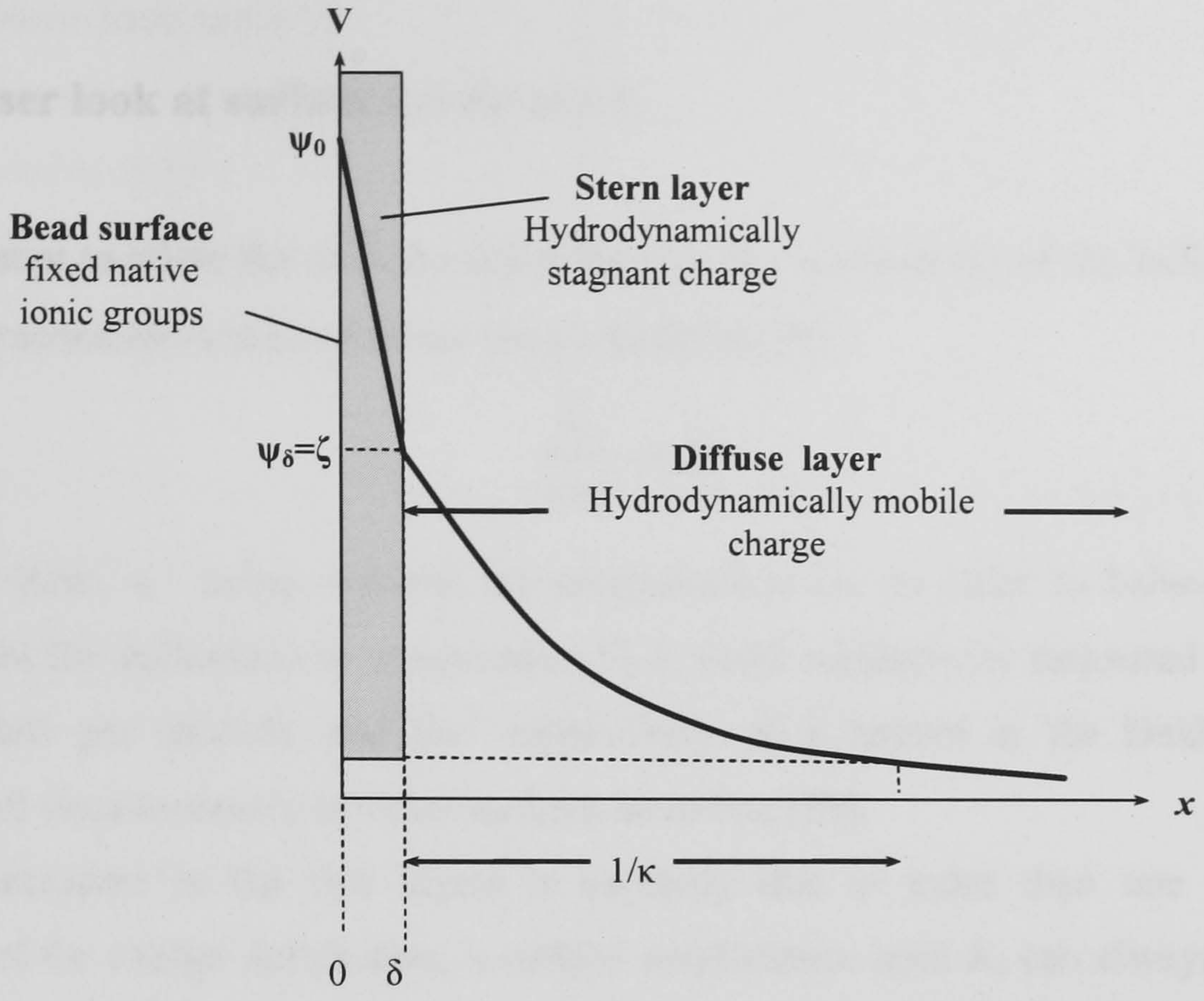

Figure 2-7

Potential distribution across a phase boundary. δ denotes the width of the stagnant layer or position of the slip plane with respect to the bead surface, and κ the inverse Debye length, giving an order of magnitude indication of the effective width of the diffuse layer.

The stagnant layer is also frequently presented in the literature as possessing a degree of stratification into two zones bounded by planes parallel to the particle surface termed the inner and outer Helmholtz planes – IHP and OHP respectively (Figure 2-8). This model is used to discriminate loosely between the strongly held ions close to the bead surface – small counter ions, specifically adsorbed co-ions etc. - and larger, hydrated counter charge in the less rigidly constrained outer layer.

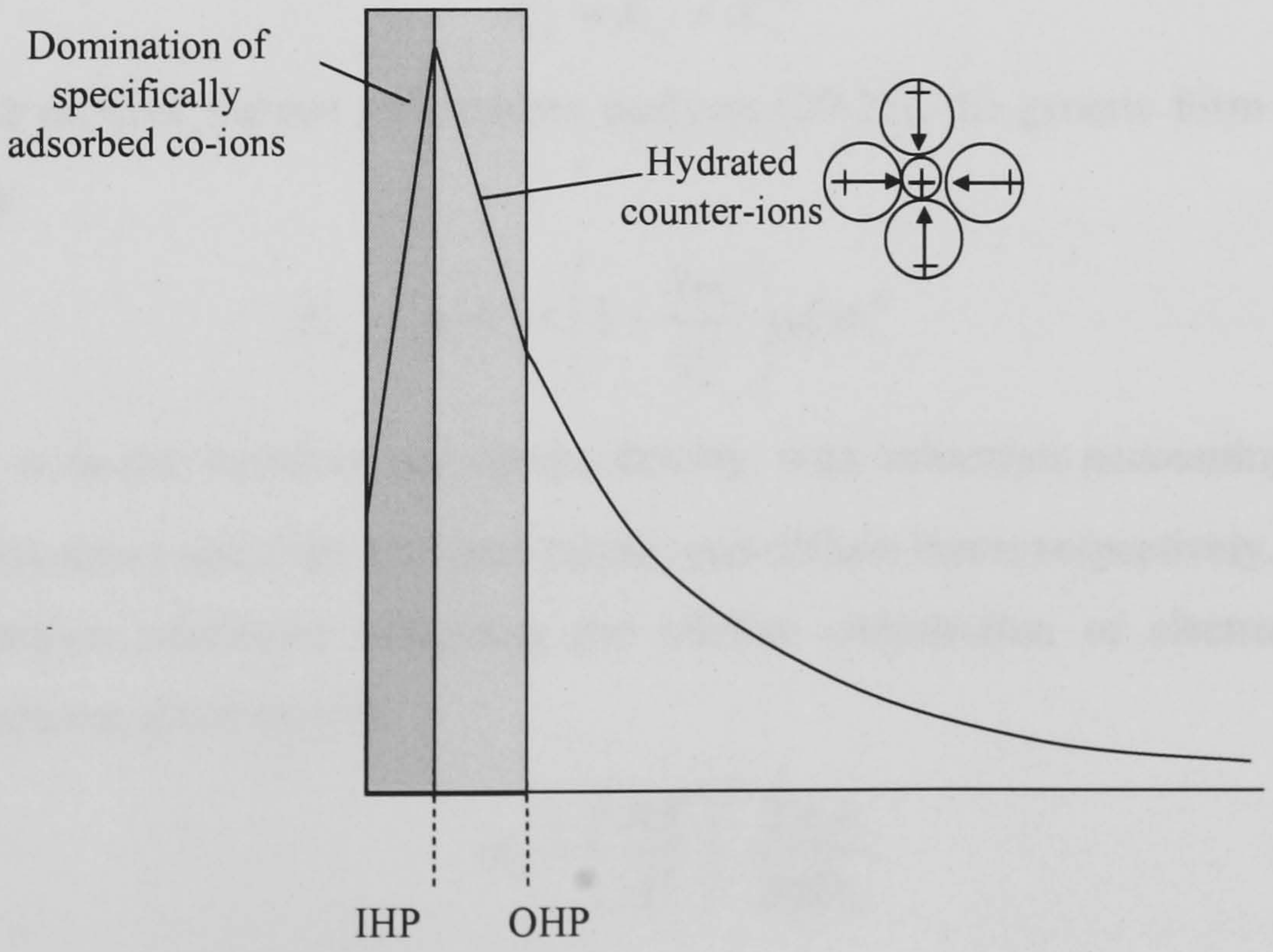

Figure 2-8

Alternative potential distribution involving specifically adsorbed ions showing the inner and outer Helmholtz planes (IHP and OHP respectively)

2.8 A closer look at surface conductance

In an attempt to relate the surface conductance to the conductivity of the bulk solution σ_l, a relative, dimensionless parameter has been introduced [5]:

$$\frac{K_s}{a\sigma_l} \equiv Du \tag{2-40}$$

- the radius term, *a,* being required for normalisation i.e. in order to balance the units resulting from the definitions of conductance (2-31) and conductivity measured in Siemens, *S* (charge flow per second), and Sm^{-1} respectively. It is known as the Dukhin number, although used simultaneously by other authors including [20].

Charge transport in the two layers is certainly due to more than one mechanism. Regardless of the charge distribution, a surface conductance term K_s can always be defined as previously through Ohm's law (2-31). However, the net current will have several contributions – as ions of different charges, mobilities and degrees of freedom are present in the different parts of the double layer. In the diffuse layer, both counter and co-ions are present in various proportions which may have transport components relating to both conduction and fluid effects [5]. Within the Stern layer it is assumed that there are only counter ions which are more rigidly bound, confined to move in the plane of the bead surface and not being subject to the hydrodynamics of the bulk and diffuse layers. In order to assess the net contribution of the whole double layer to dipole relaxation, therefore, it would seem natural to consider the surface conductance of each layer separately, dividing it into two distinct parts:

$$K_s = K_s^i + K_s^d \tag{2-41}$$

Taking into account various independent analyses [20-23], the generic form of each part can be written:

$$K_{si} = \mu_i^i \sigma_i^i + \left(1 + \frac{3m_i}{z_i^2}\right)\mu_i^d \sigma_i^d \tag{2-42}$$

where μ and σ denote mobility and charge density, with subscripts accounting for charge sign and superscripts *i* and *d* for the inner (Stern) and diffuse layers respectively. The term *m* is a dimensionless parameter indicating the relative contribution of electro-osmosis to surface conductance given by [6]:

$$m_\pm = \left(\frac{RT}{F}\right)^2 \frac{2\varepsilon_0\varepsilon}{3\eta D_\pm} \tag{2-43}$$

where η is the viscosity of the liquid medium.

This term appears in some shape or form in most recent theories involving a hydrodynamic as well as electrical quantification of charge transport. Theories in which such terms are absent have underestimated the conductivity to various levels depending on the nature of the system.

A comparative term[7] [17] has also been introduced for the ratio of Stern to diffuse layer conductances, K_{si} and K_{sd} respectively defined as:

$$\Theta = \frac{K_s^i}{K_s^d(q)} \tag{2-44}$$

where the *(q)* term denotes charge transport with respect to the liquid, excluding that induced by liquid volume flow.

With these basic definitions, it is possible to examine more effectively how experimental data translates into an indication of the relative contribution of the two layers.

2.8.1 Diffuse Layer Conductance

Bikerman's early analysis of double layer dynamics assumed essentially that the fixed charge on the interface was screened only by a Gouy-Chapman type diffuse double layer, where all the charges were free to move radially and tangentially in response to electroosmotic and conduction based transport mechanisms. Although a confined Stern layer was not considered, his arguments remain valid for the Gouy-Chapman-Graham-Stern diffuse layer [23].

For a symmetrical electrolyte i.e. one containing equal amounts of cations and anions Bikerman [6] quantified the mobilities and, based on a form similar to the second term in (2-42), derived the rather involved expression for the net ion flow in the diffuse layer:

$$K_s^d = \frac{\left(2F^2cz^2\right)}{RT\kappa}\left[D_+(\exp\left(\frac{zF\zeta}{2RT}\right)-1)\times\left(1+\frac{3m_+}{z^2}\right) + D_-(\exp\left(\frac{zF\zeta}{2RT}\right)-1)\times\left(1+\frac{3m_-}{z^2}\right)\right] \tag{2-45}$$

where *R, T* and *F* have their usual meanings, *c* is the ionic concentration, $D_{+/-}$ are the specific ionic diffusion constants, z is the ion valency and κ is the inverse Debye length .

If the mobilities of both ions are similar, (2-45) can be reduced to:

$$K_s^d = \frac{\left(4F^2cz^2D^d\,(1+3m/z^2)\right)}{RT\kappa}\left(\cosh\left[\frac{zF\zeta}{2RT}\right]-1\right) \tag{2-46}$$

where D^d is the general ionic diffusion constant in the double layer.

The immediate significance of this is the predicted ζ-potential dependency of the diffuse layer conductance. It can also be noted from (2-45) that in the incidence of high

---

[7] In a modification of the related quantity $\Theta_i = \sigma^i_i / \sigma^d_i$ introduced by Kijlstra [24]

ζ-potential the second term in the square brackets (co-ion contribution) becomes negligible. This model will be developed further in relation to dielectrophoretic crossover measurements.

2.8.2 Stern Layer Conductance

It has been debated for quite some time whether it is reasonable to assume that lateral ionic mobility is possible in the Stern layer. At first sight a finite mobility of ions confined in a hydrodynamically stagnant fluid may seem paradoxical. Now, however, convincing evidence exists that at least in a number of systems conduction behind the shear plane does take place [5, 23, 24]. This essentially results from the fact that again that anomalous ζ-potential measurements can be accounted for in this way – which otherwise would not fit with the predicted diffuse layer conduction. A number of different perspectives have been taken in this investigation. Ennis and White for example have produced a low ζ-potential analytic solution for a dynamic Stern layer contribution to colloidal mobility [25] and found it formally similar to those for thin double layers. From this, an approximation has been derived for the high ζ-potential case. Minor *et al* [17] have modified Bikerman's diffuse layer conductance (2-45) for large κa and one ionic type expressing the Dukhin number in terms of Θ as:

$$Du = \frac{1+\Theta+3m/z^2}{\kappa a}\left[exp\left(\frac{-zF\,|\,\zeta\,|}{2RT}\right)-1\right] \tag{2-47}$$

where Θ is used as an adjustable parameter to minimise the discrepancy between ζ-potentials measured using different techniques. It is generally found to be non-zero, thus implying a Stern-layer contribution. However, expression of the Dukhin number in this way this involves the elimination of D_i from (2-45) using the Nernst-Einstein equation [5]:

$$D^i = \frac{\mu_i RT}{|z_i|F} \tag{2-48}$$

and thus an estimation of μ, the ion mobility must be made.

Dukhin, Zimmerman and Werner have looked at the generalisation of the standard electrokinetic model [26] and Lyklema *et al* have performed molecular dynamics simulations to investigate the mobility of ions in this layer in order to elucidate the tangential transport mechanism [27]. The detailed nature of the transport mechanism however is far from clear. It is not known, for example, if charge carriers may move in the Stern layer itself, or are free to hop along via the diffuse layer. The recent work by Lyklema [27] seems to suggest that there is some interchange between ions in the two layers - that Stern layer ions can indeed leap into the diffuse layer for short periods with solvent particles also rebounding quite close to the particle surface.

The basis of all these analyses is that the fluid is assumed to be hydrodynamically stagnant and the ions monopopulational[8]. Their motion, then, is due entirely to conduction and so can be expressed in terms of the product of a charge density σ^i and corresponding ionic mobility μ^i:

$$K_s^i = \sigma^i \mu^i \qquad (2\text{-}49)$$

The question remains, however, as to how μ^i can be established.

Various approaches have been proposed to tackle this problem of an analytical, numerical and experimental nature [28-33]–including an interesting line of pursuit based on finding the isoelectric point[9] [15], effectively equal to having no diffuse layer, and then concluding that the entire measured surface conductance is due to ions in the stern layer. However, estimation of the number of these ions is also not straightforward and so as yet no convincing experimental verification of the exact nature of ion mobility in the Stern layer has been produced.

2.9 Derivation of the Dielectrophoretic force

The force arising as a result of the interaction of a dipole with a non-homogeneous E-field is known as the **dielectrophoretic force** or **dielectrophoresis (DEP)**. An expression for the force vector can be derived as follows. As previously alluded to, a dipole $\underline{p} = q\underline{d}$, is formally equivalent to two points of charge with opposite sign separated by a finite distance $\underline{d}$[10]. If the electric field strength varies across *d,* the net force on the dipole can be written as:

$$\underline{F} = q\underline{E}(\underline{r} + \underline{d}) - q\underline{E}(r) \qquad (2\text{-}50)$$

Taking a Taylor expansion about $\underline{r}$ gives:

$$\underline{E}(\underline{r} + \underline{d}) = \underline{E}(\underline{r}) + \underline{d}.\nabla\underline{E}(\underline{r}) + O(d^2)\ldots \qquad (2\text{-}51)$$

Assuming the field varies *linearly* across the extent of the dipole, higher order terms can be neglected. This reduces the force on the dipole to:

$$\underline{F} = \underline{p}.\nabla\underline{E} \qquad (2\text{-}52)$$

For a sinusoidally varying field of frequency ω, this force will consist of two components – an average, constant term and an oscillatory part which varies as *2ω* [34]. Thus, assuming the high frequency component to be damped at the working AC range, the average DEP force can be written as:

---

[8] dismissing the complication of ions hydrated to various degrees.

[9] see definition in Chapter 4

[10] This arises naturally from the uniqueness theorem and the method of images.

$$\langle \underline{F} \rangle = \frac{1}{2} \underline{p}.\nabla \underline{E} \tag{2-53}$$

Substituting in the expression for the dipole of a spherical particle given by (2-29) in terms of its volume, v, and polarisability, α_p, we have:

$$\langle \underline{\mathbf{F}} \rangle = \frac{1}{2} v \alpha_p \underline{\mathbf{E}}.\nabla \underline{\mathbf{E}} \tag{2-54}$$

which after some vector manipulation reads:

$$\langle \underline{\mathbf{F}} \rangle = \frac{1}{4} v \alpha_p \nabla |\underline{\mathbf{E}}|^2 \tag{2-55}$$

On substitution of the polarisability term, α_p, given by (2-30), the time averaged DEP force on a particle is conventionally expressed as:

$$\langle F_{DEP} \rangle = 2\pi a^3 \varepsilon_m \, Re(K(\omega)) \nabla E_{rms}^2 \tag{2-56}$$

where $K(\omega)$ is the **Claussius-Mossoti factor,** given by:

$$K(\omega) = \frac{\varepsilon_p^* - \varepsilon_m^*}{\varepsilon_p^* + 2\varepsilon_m^*} \tag{2-57}$$

Because these permittivities are expressed in the general, lossy form, the surface conductivity is also a factor through (2-27). In this way the DEP response of the particle is intimately linked to its surface conductance.

2.10 Summary

The polarisation of charged, spherical particles in an AC field considered in the real, lossy case is a complex phenomenon. The presence of a structured double layer of counter charge and adsorbed ions with both electro-osmotic and conductive transport component mechanisms gives rise to various discrepancies in predicting the parameters of the system in comparison with a simplified Maxwell-Wagner approach, where a multi-component surface conductance is ignored and only idealised interfacial polarisation considered. Since the experimental evidence to date has pointed to a definitive contribution from surface conductance related primarily to the electrical double layer this phenomenon cannot be ignored. The study of how this parameter affects DEP behaviour, then, is one approach to probing the nature of the charge distribution of dielectric particles and thereby refining the predictive power of experimental investigation of other parameters of the system, such as ζ-potential, as well as, ultimately, facilitating the separation/differentiation of particles based on their DEP response.

2.11 References

[1] P. Lorrain, D. R. Corson, and F. Lorrain, *Electromagnetic Fields and Waves*. New York: W.H. Freeman and Company, 1988.

[2] N. G. Green, "Dielectrophoresis of sub-micron particles" in *Electrical and Electronic Engineering*: University of Glasgow, 1998, pp. 270.

[3] P. Debye, *Polar Molecules*. New York: Lancaster Press, INC., 1929.

[4] F. A. Sauer, *Coherent Excitations in Biological systems*. Berlin: Springer-Verlag, 1983.

[5] J. Lyklema and M. Minor, "On surface conduction and its role in electrokinetics", *Colloids and Surfaces a-Physicochemical and Engineering Aspects*, vol. 140, pp. 33-41, 1998.

[6] J. J. Bikerman, *Kolloid Z.*, pp. 100, 1935.

[7] J. J. Bikerman, *Z. Phys. Chem.*, vol. A163, pp. 378, 1933.

[8] J.B. Miles and H. P. Robertson, *Physical Review*, vol. 40, pp. 583-591, 1932.

[9] C. T. O'Konski, "Electric properties of macromolecules v. theory of ionic polarisation in polyelectrolytes", *Journal of Physical Chemistry*, vol. 64, pp. 605-619, 1960.

[10] S. S. Dukhin and V. N. Shilov, *Dielectric phenomena and the Double Layer in Disperse Systems and Polyelectrolytes*. New York: Wiley-Interscience, 1974.

[11] H. P. Schwan, G. Schwarz, J. Maczuk, and H. Pauly, *J. Phys Chem.*, vol. 66, 1962.

[12] G. Schwarz, *Journal of Physical Chemistry*, vol. 66, pp. 2636-2642, 1962.

[13] J. M. Schurr, *Journal of Physical Chemistry*, vol. 68, pp. 2407-2413, 1964.

[14] Hunter, *Zeta Potential in Colloid Science*: Academic Press Inc., 1981.

[15] J. Lyklema, "Surface conduction", *Journal of Physics-Condensed Matter*, vol. 13, pp. 5027-5034, 2001.

[16] J. Lyklema, "Electrical double layers: Electrostatics and electrodynamics", *Chemie Ingenieur Technik*, vol. 71, pp. 1364-1369, 1999.

[17] M. Minor, H. P. van Leeuwen, and J. Lyklema, "Low-frequency dielectric response of polystyrene latex dispersions", *Journal of Colloid and Interface Science*, vol. 206, pp. 397-406, 1998.

[18] M. Minor, H. P. van Leeuwen, and J. Lyklema, "Low-frequency dielectric responses, static conductivities, and streaming potentials of polymer-coated latex dispersions and porous fluffs", *Langmuir*, vol. 15, pp. 6677-6685, 1999.

[19] R. W. Obrien, "The High-Frequency Dielectric-Dispersion of a Colloid", *Journal of Colloid and Interface Science*, vol. 113, pp. 81-93, 1986.

[20] P. H. Wiersema, A. L. Loeb, and J. T. G. Overbeek, *J. Colloid Sci.*, vol. 22, pp. 78, 1966.

[21] R. W. O'Brien and L. R. White, *J. ChemSoc. Faraday Transactions*, vol. 74, pp. 1607, 1978.

[22] M. Fixman, "Thin Double-Layer Approximation For Electrophoresis and Dielectric Response", *Journal of Chemical Physics*, vol. 78, pp. 1483-1491, 1983.

[23] J. Lyklema, *Fundamentals of Interface and Colloid Science*, vol. 2. New York: Academic Press, 1995.

[24] J. Kijlstra, H. P. Vanleeuwen, and J. Lyklema, "Effects of Surface Conduction On the Electrokinetic Properties of Colloids", *Journal of the Chemical Society-Faraday Transactions*, vol. 88, pp. 3441-3449, 1992.

[25] J. Ennis and L. R. White, "Dynamic Stern layer contribution to the frequency-dependent mobility of a spherical colloid particle: A low-zeta-potential analytic solution", *Journal of Colloid and Interface Science*, vol. 178, pp. 446-459, 1996.

[26] S. S. Dukhin, R. Zimmermann, and C. Werner, "A concept for the generalization of the standard electrokinetic model", *Colloids and Surfaces a-Physicochemical and Engineering Aspects*, vol. 195, pp. 103-112, 2001.

[27] J. Lyklema, S. Rovillard, and J. De Coninck, "Electrokinetics: The properties of the stagnant layer unraveled", *Langmuir*, vol. 14, pp. 5659-5663, 1998.

[28] C. S. Mangelsdorf and L. R. White, "Effects of Stern-Layer Conductance On Electrokinetic Transport- Properties of Colloidal Particles", *Journal of the Chemical Society-Faraday Transactions*, vol. 86, pp. 2859-2870, 1990.

[29] C. S. Mangelsdorf and L. R. White, "Effects of Surface Conduction On the Electrokinetic Transport- Properties", *Abstracts of Papers of the American Chemical Society*, vol. 208, pp. 212-COLL, 1994.

[30] C. S. Mangelsdorf and L. R. White, "The dynamic double layer - Part 1 - Theory of a mobile Stern layer", *Journal of the Chemical Society-Faraday Transactions*, vol. 94, pp. 2441-2452, 1998.

[31] H. Ohshima, "Approximate analytic expression for the electrophoretic mobility of a spherical colloidal particle", *Journal of Colloid and Interface Science*, vol. 239, pp. 587-590, 2001.

[32] F. Carrique, F. J. Arroyo, and A. V. Delgado, "Electrokinetics of concentrated suspensions of spherical colloidal particles: Effect of a dynamic Stern layer on electrophoresis and DC conductivity", *Journal of Colloid and Interface Science*, vol. 243, pp. 351-361, 2001.

[33] F. Carrique, F. J. Arroyo, and A. V. Delgado, "Sedimentation velocity and potential in a concentrated colloidal suspension - Effect of a dynamic Stern layer", *Colloids and Surfaces a-Physicochemical and Engineering Aspects*, vol. 195, pp. 157-169, 2001.

[34] T. B. Jones, *Electromechanics of Particles*. New York: Cambridge University Press, 1995.

3 Separation methods and devices

3.1 Introduction

With the onset of miniaturised diagnostic technology and micro total analysis systems (μ-TAS) [1-7], the demand for microfluidic based characterisation, fractionation and pumping techniques has increased rapidly. In this section several existing and developing technologies and theoretical concepts relating to the AC electrokinetic manipulation and fractionation of colloidal particles will be outlined. Firstly, travelling wave dielectrophoresis is described with its two-fold application in inducing movement in both particles and fluid due to discrete or continuous variations in permittivity. Alluded to are the underlying principles of fluid motion as a result of a general non-homogeneous E-field, which may or may not have travelling wave characteristics. These are particularly noteworthy with reference to Chapter 9. Work in field flow fractionation, where particles are separated on the basis of their position in a laminar flow, is also reviewed and illustrated by a design devised in the course of this project for application to sub-micron particles. The concept of Brownian ratchets, systems inducing transport of a dissipative ensemble by the application of a pulsed, asymmetric potential, is subsequently expounded and lastly, electro-osmotically driven global fluid motion is examined on an asymmetric structure. These concepts, while providing a background to the field of small scale transport and separation, are also elucidated for the purpose of clarifying the argument and analysis in Chapters 6-9.

3.2 Travelling Wave Systems

The travelling wave device has its roots in work by Melcher [8] who first demonstrated that waves of electric fields travelling perpendicular to a liquid interface or a continuous conductivity/permittivity gradient induce charges at the interfaces or in the liquid bulk. Subsequent interaction of these charges with the field, under certain circumstances, results in two types of motion [9, 10].

i) The propagation through the fluid of dipolar particles

ii) Net fluid pumping as a consequence of charge inhomogeneities in the fluid

The former is known as travelling wave dielectrophoresis [11], although the latter also depends on the dielectric response of the medium [10].

3.2.1 Principle

A moving electric field – or travelling wave – can be set up by having 4-phase interdigitated electrodes so that there is a phase lag of π/2 between each consecutive electrode (Figure 3-1).

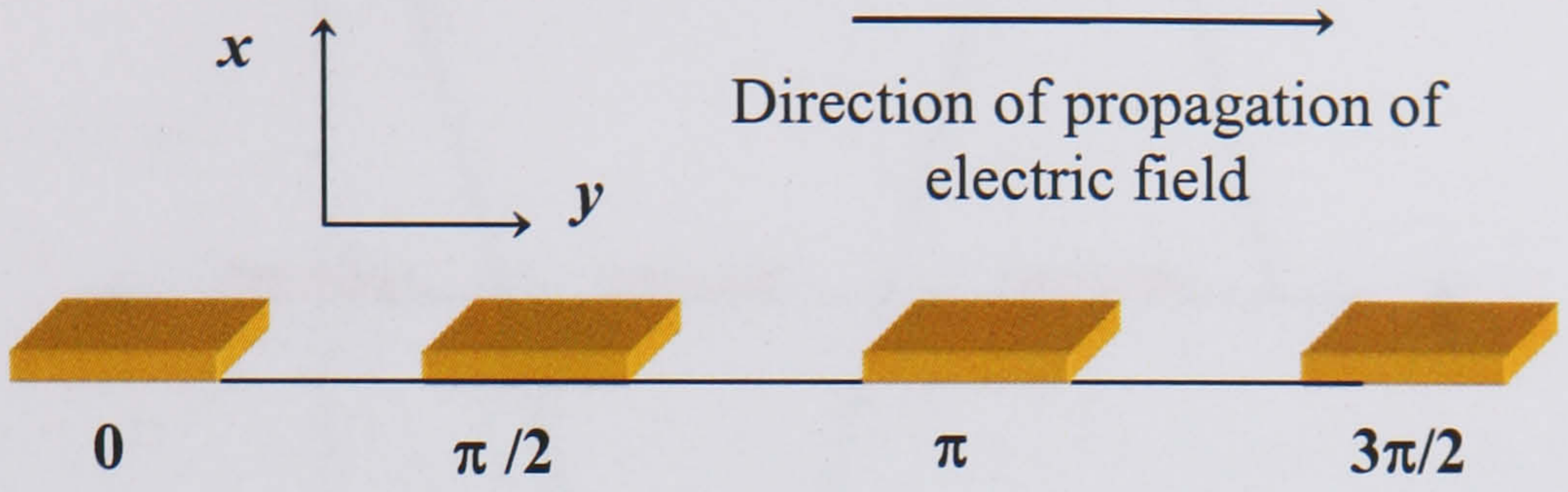

Figure 3-1
Phases of four applied signals on consecutive electrodes in a travelling wave construction. Fluid or particles are transported in the y-direction.

3.2.2 Particle motion

The initial approach to quantifying induced motion in this system was to express the field as a perfect sinusoid [12], where the amplitude component in the *x*-direction, perpendicular to the direction of propagation, was written simply as:

$$E_x(x,y,t) = A(x)\cos\left(\omega t - \frac{2\pi y}{\lambda}\right)\underline{a_x} \tag{3-1}$$

where λ is the distance between same-phase electrodes, and $\underline{a_x}$ is the unit vector of the x-component.

From this field, the induced dipole moment, m_x, was quantified as [13]:

$$m_x(0,y,t) = 4\pi\varepsilon_m r^3\left\{\cos\left(\omega t - \frac{2\pi y}{\lambda}\right)\mathrm{Re}[f(\varepsilon_p^*,\varepsilon_m^*)] - \sin\left(\omega t - \frac{2\pi y}{\lambda}\right)\mathrm{Im}[f(\varepsilon_p^*,\varepsilon_m^*)]\right\}A(0) \tag{3-2}$$

with the corresponding force on a real dielectric particle thus given by [12]:

$$F(\omega) = \frac{-4\pi^2\varepsilon_m r^3\,\mathrm{Im}[K]E^2}{\lambda} \tag{3-3}$$

i.e. proportional only to the imaginary part of the Claussius-Mossotti factor. Movement with or against the direction of the travelling wave being dependent on the phase lag between the field and the induced dipole moment.

Another approach has been taken by Morgan et al [14] in the derivation of the travelling wave and DEP forces from an interdigitated electrode array by expanding an approximation of the *static* field in a Fourier series (Figure 3-2), before extending the concept to include complex fields, thus allowing the inclusion of a phase dependent, travelling wave force.

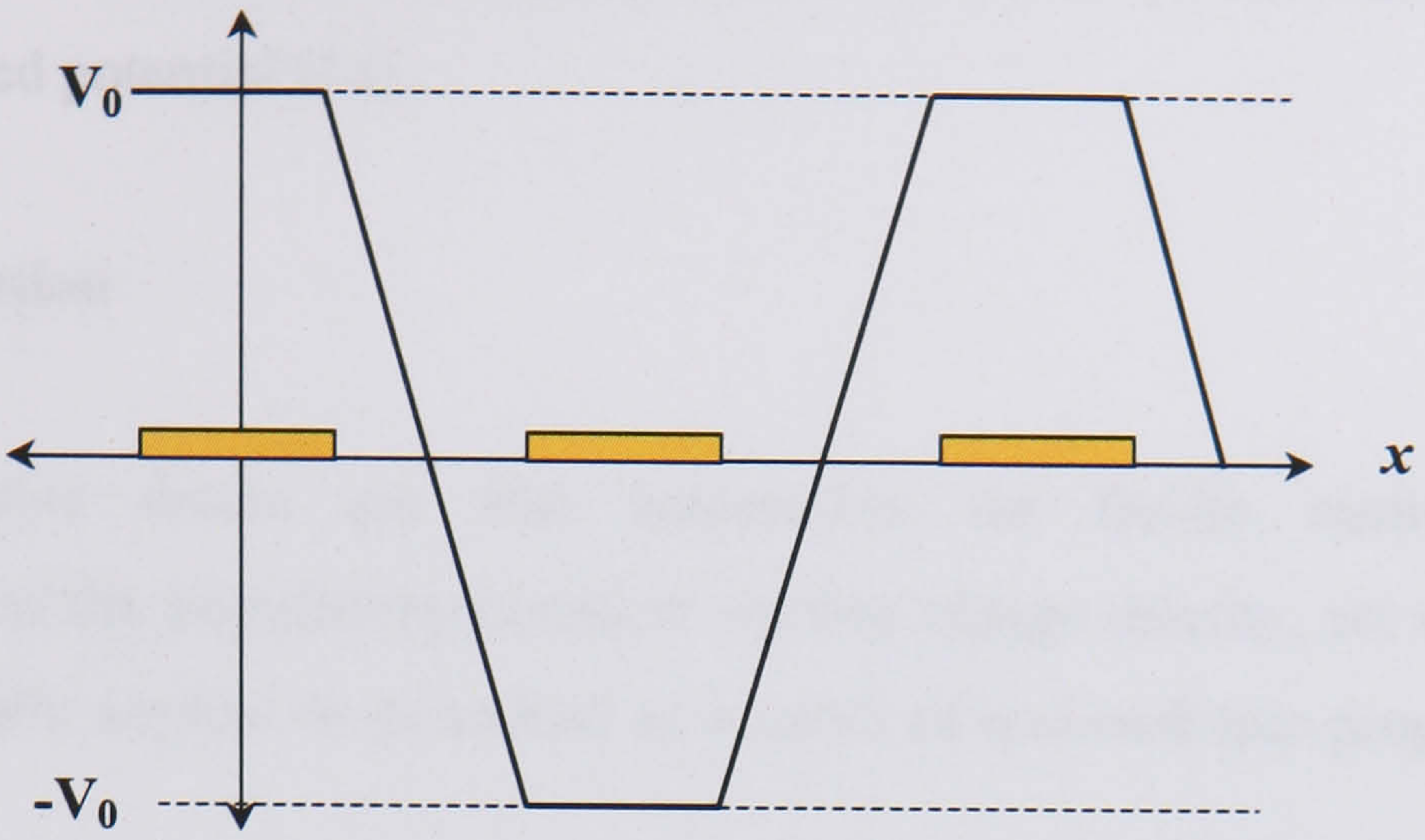

Figure 3-2
Static field approximation used in Fourier series derivation for interdigitated electrode array [14].

For the particular case of equal electrode width and spacing, d, the primary co-efficient is:

$$A_1 = \frac{16V_0}{\pi^2}\left[\cos\left(\frac{\pi}{8}\right) - \cos\left(\frac{3\pi}{8}\right)\right] \tag{3-4}$$

with the x and y components of the DEP force, generalised to include the case of phasor source fields, given by:

$$\langle F_x(t)\rangle = -v\,\mathrm{Im}[\alpha_p]\left(\frac{\pi}{4d}\right)^3 A_1^2 e^{-(\pi/2d)y} \tag{3-5}$$

$$\langle F_y(t)\rangle = -v\,\mathrm{Re}[\alpha_p]\left(\frac{\pi}{4d}\right)^3 A_1^2 e^{-(\pi/2d)y} \tag{3-6}$$

where α_p is the effective polarisability.

The first term alone of the series is valid for heights grater than $1.5d$, otherwise higher order terms must be included. This more closely fits the existing experimental data than previous approaches. However, the field approximation is somewhat crude and in a subsequent publication [15] has been improved by numerical simulation using the finite element differential equation solver FlexPDE, giving a travelling wave force of:

$$\langle F_{TW-DEP}\rangle - \frac{1}{2}v\,\mathrm{Im}[\alpha_p]\frac{V_0^2}{d^3}\left(\nabla' \times \left(\nabla'\phi_R' \times \nabla'\phi_I'\right)\right) \tag{3-7}$$

where v is the particle volume, ϕ' is a non-dimensional potential scaled with the applied voltage and ∇' is a non-dimensional nabla operator based on the definition of displacement $\mathbf{x}' = \mathbf{x}/d$, where d is the distance between the electrodes.

All these analyses have in common that the travelling wave force is dependent on the imaginary part of the polarisability, highlighting the need for a phase lag of less than π between applied signals and therefore the need for more than two inputs. While the most common scenario is the use of four signals, as stated, TWD has been achieved also with a three phase applied potential [16].

3.2.3 Fluid motion

Travelling wave forces are also responsible for fluidic motion if there are inhomogeneities in the permittivity/conductivity/free charge density, set up by temperature gradients, externally applied or generated as a result of non-isotropic properties of the field or medium.

The basic governing equations in fluid motion are the (steady state) Navier-Stokes relationship between the applied force and pressure gradient and the viscous response of the medium:

$$-\nabla p + \eta \nabla^2 \underline{u} + \rho \langle f_e \rangle = 0 \tag{3-8}$$

where the first term is the pressure gradient - possibly imposed as well as self generating from the force term, $\langle f_e \rangle$ - with the non-linear velocity term being due to viscous drag where η is the constant of viscosity. This is generally used in the case of an incompressible fluid – i.e. where the continuity equation is:

$$\nabla . \underline{u} = 0 \tag{3-9}$$

The force term is due primarily to non-homogeneity of temperature within the medium. A temperature gradient can be externally imposed or it can be self generating within the system due to local Joule heating by the electrodes [10]. In the latter case the energy balance equation must be used to calculate the temperature field [17]. This can be expressed in the steady state as:

$$k \nabla^2 T + \langle \sigma E^2 \rangle - \rho_m c_p \underline{u} . \nabla T = 0 \tag{3-10}$$

where c_p is the specific heat at constant pressure and k is the thermal conductivity. This version of the equation does not include viscous dissipation, since this is of the order of 10^{-10} smaller than the Joule heating (second term) [17]. The third term is due to convection which, having a ratio to heat diffusion (first term) of $\sim 3 \times 10^{-3}$, is small enough also to be neglected [18]. Since conductivity and permittivity are, respectively, directly and inversely proportional to temperature, a temperature increase results in a decrease of the free charge relaxation time of the medium, defined as (Appendix 3-1):

$$\tau = \frac{\varepsilon_m}{\sigma} \tag{3-11}$$

Thus, there is a gradation in the effective dipole relaxation time of each incremental layer of fluid. Each layer can be approximated as consisting of discrete particles – or packets of fluid – which respond dielectrophoretically in an analogous way to real dielectric particles.

3.2.4 The electrothermal force

The electric force density on an element of fluid with permittivity ε and charge density ρ_q can be written as (Appendix 3-2):

$$f_e = \rho_q E - \frac{1}{2} E^2 \nabla \varepsilon \tag{3-12}$$

If Gauss's law :

$$\rho_q = \nabla.(\varepsilon E) \tag{3-13}$$

and the charge conservation equation :

$$\frac{\partial \rho_q}{\partial t} + \nabla.(\rho_q u) + \nabla.(\sigma E) \tag{3-14}$$

are expanded for the case of a time varying field with frequency ω, neglecting the convection term in equation (3-14) due to its negligible contribution compared to conduction, we obtain:

$$\rho_q(\sigma + i\omega\varepsilon) = \sigma\nabla\varepsilon.E_0 - \varepsilon\nabla\sigma.E_0 \tag{3-15}$$

Substituting the charge density as expressed here into the force equation, (3-12), and defining quantities :

$$\alpha = \frac{1}{\varepsilon}\left(\frac{\partial \varepsilon}{\partial T}\right) \text{ and } \beta = \frac{1}{\sigma}\left(\frac{\partial \sigma}{\partial T}\right) \tag{3-16}$$

in recognition of the fact that gradients in permittivity and conductivity are due to inhomogeneities in the temperature we can write the time averaged force as [18]:

$$\langle f_e \rangle = \frac{1}{2}\mathrm{Re}\left(\frac{\sigma\varepsilon(\alpha - \beta)}{\sigma + i\omega\varepsilon}(\nabla T.E_0)E_0^* - \frac{1}{2}\varepsilon\alpha|E_0|^2\nabla T\right) \tag{3-17}$$

In the specific case of TWD the real and imaginary parts of the E-field must be explicitly included in the calculation to obtain the correct force.

3.2.5 Electrorotation

An analogous system to that of TWD as applied to particle manipulation is that of electrorotation. This differs from conventional TWD in that the electrodes are arranged in a circular as opposed to linear fashion so that particles can be characterised through their angular velocity without net fluid pumping [19-22].

3.2.6 Applications and recent work

Subsequent to Melcher's foundational and early developmental research on liquid pumps [8, 9], much work has been done on the design and fabrication of various devices capable of acting as travelling wave pumps [10, 23] Masuda et al first demonstrated the application of travelling wave DEP to manipulate small bio particles and red blood cells [16, 24] and since then the technique has been applied to yeast cells [12, 25] pollen, cellulose and liquid droplets [11, 26] and latex beads [27]. A wide assortment of devices have been fabricated from Fuhr's micromanipulator [28], through Goater's combined travelling wave and electrorotation device [29] to multi-layer constructions [27, 30] and lab on a chip orientated prototypes [31, 32].

3.3 Field Flow Fractionation

The technique of field flow fractionation (FFF) was first described by Giddings in 1966 [33]. Since then electric and sedimentation field flow fractionation have been developed for a variety of applications ranging from cell separation [34] and the manipulation of colloidal biological particles such as viruses, proteins and river water colloids [35-37] to the characterisation of emulsions and colloidal adsorption complexes [38-40]. More recently, thermal fields [41] and DEP [14, 15, 27, 42-55] have been used in FFF devices.

The basic FFF method entails the application of a lateral external field to a particulate sample contained in a ribbon-like channel so that the forces which act on the sample balance, causing a steady-state distribution profile to be set up in the relaxed system. Particles to be separated should be affected by the imposed field in a manner relating to their particular characteristics (e.g. mass, electric charge) so that their equilibrium positions are different. Imposing a force to pump the fluid along the channel in a non turbulent manner – i.e. with a definable velocity profile – allows a longitudinal flux to be calculated for each lateral co-ordinate and so the output predicted. The nature of the field (eg gravitational, electrical, etc) and the velocity profile (eg pressure gradient, travelling wave) characterise the system.

The forces to be balanced in the DEP case are usually the negative DEP force with gravity. However, in the case of sub-micron particles, with higher diffusion co-efficients, this type of stratification is difficult to achieve (see 3.3.2) – particularly with the large electrode systems commonly used [53] which introduce perturbations in the direction of flow large in comparison with the sub-micron scale. DEP levitation of particles in this realm could possibly be achieved by lowering the electrode scale in order to both decrease the perturbative effects experienced by the particles in the course of the flow and increase the field strengths possible at low applied voltages. In the absence of adequate negative DEP stratification, then, the basic forces to be balanced for sub-micron particles are diffusion and positive DEP.

3.3.1 Example of DEP- FFF device design for sub-micron particles

In order to describe the principle of dielectrophoretic field flow fractionation for the case of sub-micron particles, a device designed in the course of this project is illustrated. A basic schematic is shown in Figure 3-3 and a fabricated prototype of the device described in Appendix 3-3. The electrodes are 10 μm width/gap and are at the top and bottom of the device chamber in order to increase the active area of the lateral field and possibly focus particles in the centre using negative DEP (although this is not essential). If particle populations experience differing strengths of positive DEP forces then the concentration gradients required to support an equilibrium distribution will be different and so their mean positions will not be the same. The laminar flow driving force is a pressure gradient along the channel, applied by means of an external pump.

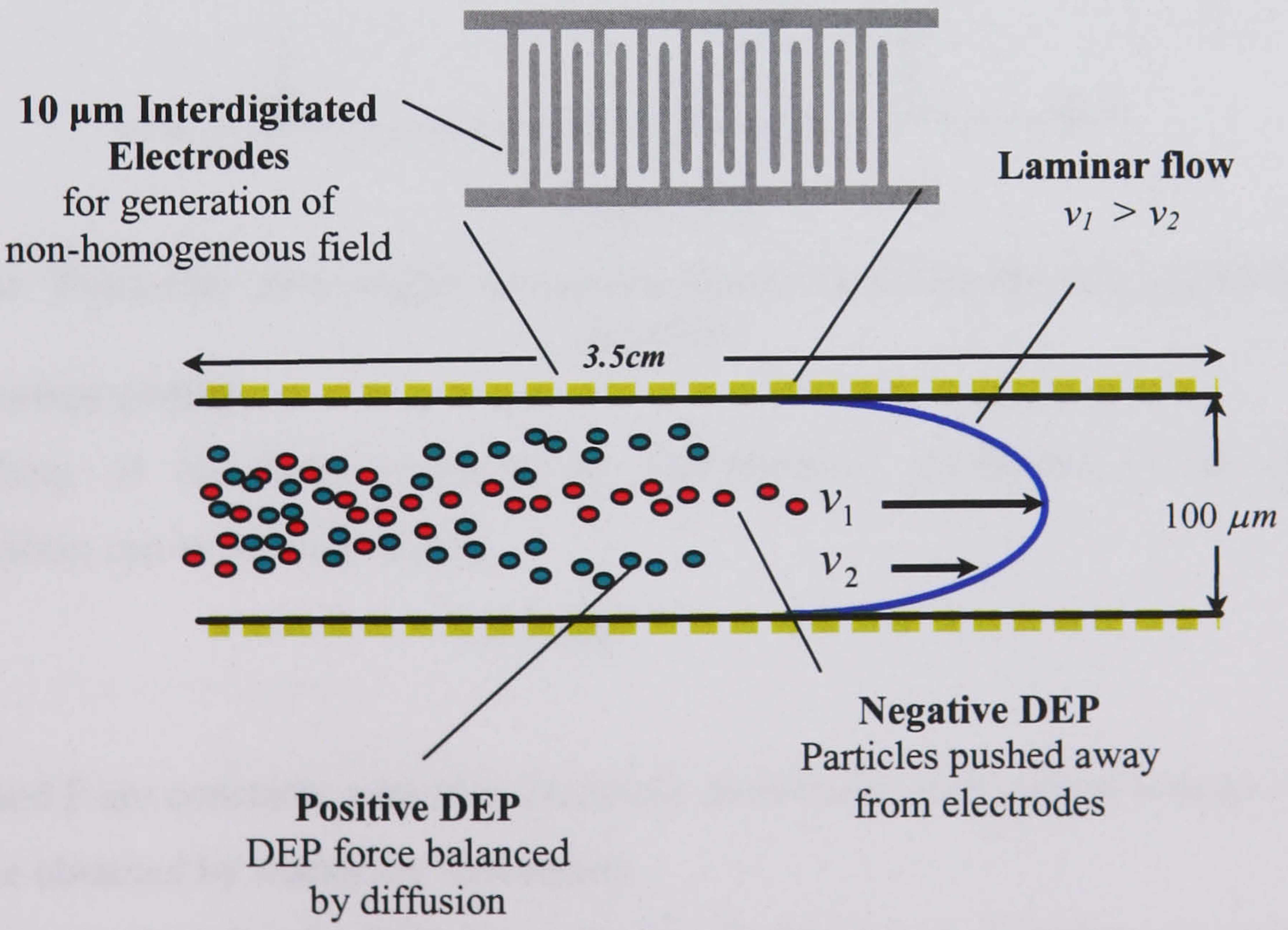

Figure 3-3

Schematic of DEP-FFF device concept for use with sub-micron particles, illustrating FFF separation principle

Velocity Profile

In the case of the applied force being a pressure gradient, the resulting laminar flow through an enclosed channel, known as Poiseuille flow, is well defined. The total force on the fluid, including viscous drag, is given by the Navier-Stokes equation:

$$F = -\nabla p + \eta \nabla^2 v_x \tag{3-18}$$

Again in steady state, friction is balanced by the pressure gradient and so, on substitution of p and x differentials with characteristic scales, i.e, where Δp is the change in pressure over a characteristic length L_0, such that:

$$\nabla p = \frac{dp}{dx} \approx \frac{\Delta p}{L_0} \tag{3-19}$$

Equation (3-18) is easily integrable with zero flow boundary conditions to give a parabolic velocity distribution (Figure 3-4):

$$v_x(y) = \frac{\Delta p(h-y)y}{2L_0\eta} \tag{3-20}$$

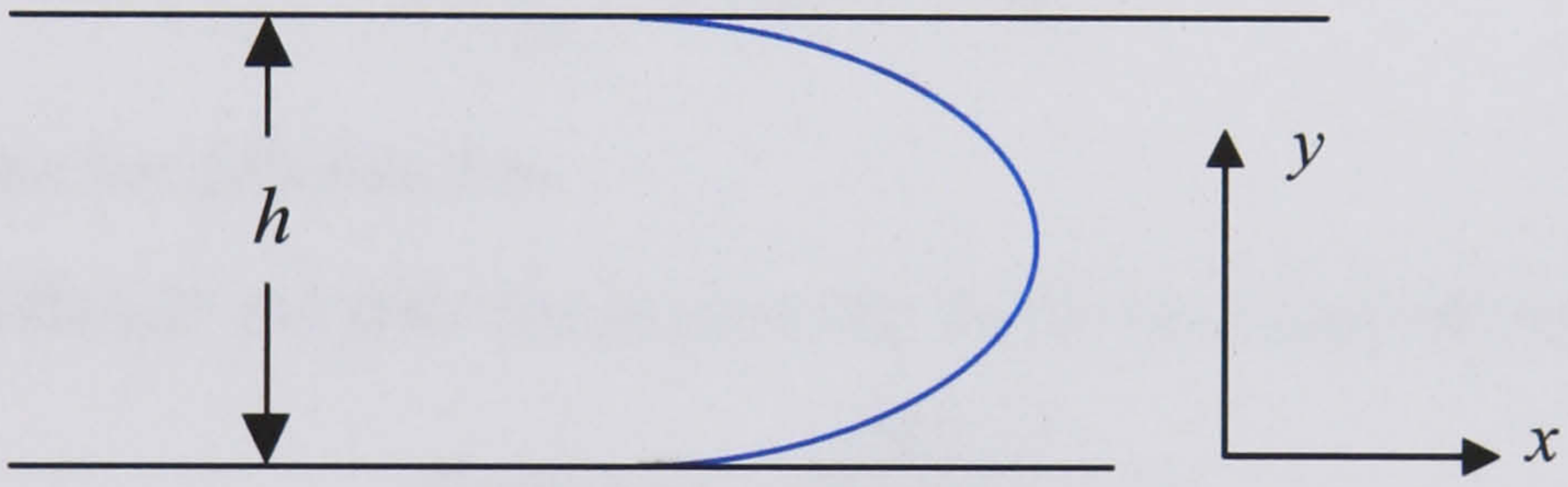

Figure 3-4

Laminar 'Poiseuille' flow profile across the channel as the result of an applied pressure gradient

Concentration profile

The form of the field produced by interdigitated electrodes in the long range approximation can be written as [56]:

$$|E| = \beta e^{-\alpha y} \tag{3-21}$$

where α and β are constants related to electrode dimensions and applied voltage respectively and can be obtained by numerical simulation.

Particles acted on by the DEP force can be assumed to instantaneously reach terminal velocity, v_t, balancing with the Stokes force:

$$F_{Stokes} = -6\pi\eta r v_t(y) \tag{3-22}$$

such that:

$$F_{Stokes} + F_{DEP} = 0 \tag{3-23}$$

This produces a DEP induced flux:

$$J_{DEP} = C(y)v_T(y) \tag{3-24}$$

where C(y) is the concentration profile across the width of the channel.

Fick's second law states that the time rate of change of the concentration is proportional, via the diffusion constant, *D*, to its second spatial derivative, i.e.:

$$\frac{\partial C}{\partial t} = D\frac{\partial^2 C}{\partial y^2} \tag{3-25}$$

Assuming steady state:

$$D\frac{\partial^2 C}{\partial y^2} = 0 \tag{3-26}$$

which can be integrated to give:

$$D\frac{\partial C}{\partial y} = Const. = J_{Diff} \tag{3-27}$$

where J_{Diff} is the net diffusion flux.

Balancing the diffusion and DEP fluxes gives the first order, linear differential equation:

$$v(y)C(y) - D\frac{\partial C(y)}{\partial y} = 0 \tag{3-28}$$

which can be easily solved to obtain a concentration profile across the channel (Appendix 3-4).

$$C = \frac{ye^{\frac{v}{D}y}}{A} + Be^{\frac{v}{D}y} \tag{3-29}$$

where A and B are constants of integration.

From (3-22) and (3-23), it can be seen that $v_T \propto F_{DEP}$ so that from (3-21) $v_T \propto e^{-2\alpha y}$, thus the concentration distribution across the channel has the form of a double exponential. In the case of the system under consideration, the total field is of the same form and by superposition of the two arrays is given by:

$$E = \beta e^{-\alpha y} + \beta e^{-\alpha(h-y)} \tag{3-30}$$

The resulting generic concentration profile (plotted on Mathematica™) is shown in Figure 3-5.

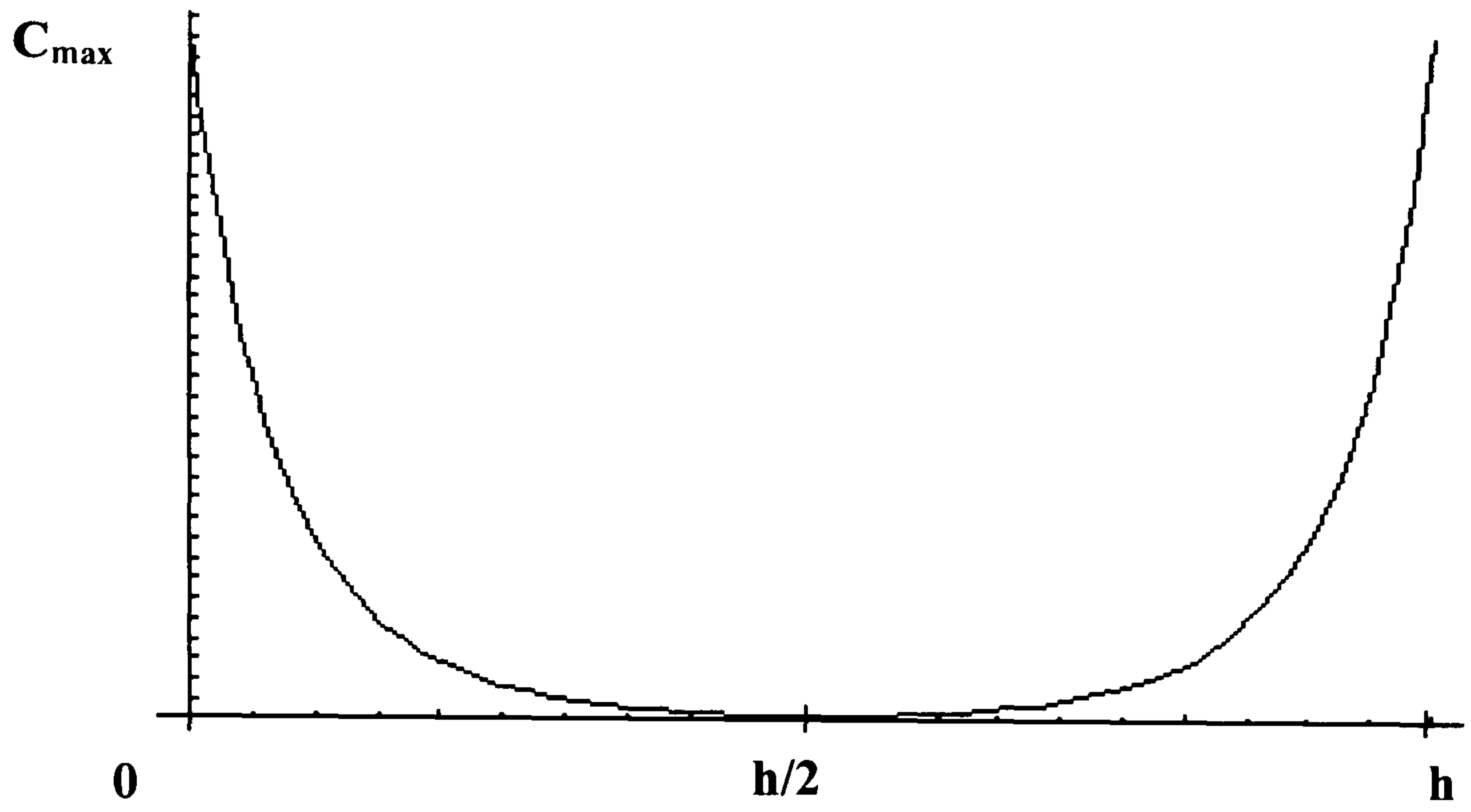

Figure 3-5

Generic concentration profile across the channel obtained by balancing positive DEP forces with diffusion. The profile would be steeper closer to the walls if the particles experienced a stronger DEP force.

According to the laminar flow profile given by (3-20), a velocity can be assigned to each concentration increment in order to predict the output of the device. Particles with mean position closer to the channel walls should be eluted after those entrained in the higher velocity flow closer to the centre.

3.3.2 Research in Dielectrophoretic Field-flow-fractionation

The concept of using DEP as a force field for FFF was first introduced by Davis and Giddings [57] who described theoretically how positive or negative DEP could be used to this effect. Ajdari *et al* [58] later made theoretical predictions on the separation of DNA with a series of dielectric traps controlled by an AC electric field, showing that 1 Mbp (mega base pair) fragments, differing by 10 kbp would lie 2mm apart after one hour. The same level of separation would take 100 hours or more using pulsed gel electrophoresis, therefore this suggests an improvement of several orders of magnitude. This work was followed up experimentally by Washizu [59], who used a flow through device to separate protein and DNA molecules based on the differing strengths of positive DEP experienced by each. This was achieved, however, by trapping or elution of samples experiencing strong or weaker DEP forces respectively and not by the layering effect described above, although this was one of the aims of the experiment. Failure to achieve this was attributed to microfluidic injection problems, as in dealing with such diffusive particles minutely accurate control is necessary. Preliminary levitation studies with a view to hyperlayer DEP-FFF have been conducted by Markx et al using latex particles of 0.5 μm-6 μm [60], based on work by Kaler and Jones [61] and Fuhr *et al* [62]. Various DEP-FFF devices based on levitation and trapping have since been designed and built [46, 52, 53] and have been applied to various biological entities and latex beads. Wang *et al* [53] have effected DEP levitation based separation of 9.5 μm and 10.5 μm beads on a 360mm channel from which they were eluted one minute apart at a flow rate of 200 μl/min. Separation of 15 μm, 10 μm and 6 μm particles was also achieved in this study in around 15 minutes, following an initial relaxation time of 25 minutes. Particles of less than 1μm, however, have not been observed to levitate on a sufficiently thin plane due to the perturbing effects of Brownian motion being much stronger for this particle size range with the relatively large feature sizes of the devices so far built [52]. DEP-FFF is currently being applied most commonly to cell fractionation techniques [43, 50, 55], with a foundational precedent having been set by Becker *et al* managing to extract leukaemia and breast cancer cells from blood [63].

3.4 Brownian Ratchets

Brownian ratchets are in essence constructs wherein net directional motion can be produced without need of a non-zero average force – simply by the application of an asymmetrical and periodic constraint to a system containing random dissipation. The phenomenon of biasing Brownian motion in this way has been known about, at least theoretically, for quite some time. Pierre Curie first proposed that spatially asymmetric, periodic structures may act as ratchets for Brownian particles in the presence of diffusion or other sources of time-reversal symmetry breaking [64] (referenced in [65]). The idea was later discussed by Smoluchowski [66] before Feynman [67] gave final credibility to the concept by silencing claims that Brownian ratchets extract work from thermal energy fluctuations in direct violation of the second law of thermodynamics. The energy to drive the ratchet must be non-zero – unlike the net force – and therefore an external power source is required. At the interface between the macroscopic and microscopic Newtonian and Brownian worlds and hovering on the border between stochastic and deterministic, however, some of the enigma of Brownian ratchets remains.

3.4.1 Brownian Motion

Brownian motion is the movement of small particles in a fluid as a result of bombardment – or thermal agitation – by the rapidly moving molecules in the liquid suspension. Discovery of this effect is attributed to Robert Brown who in 1927 first reported microscopically observed, rapid, irregular movement of pollen grains in aqueous suspension. Many decades of speculation ensued - with suggestions of the origin of this motion ranging from illumination effects to unknown electrical phenomena – and even, quite correctly linking it with the newly affirmed kinetic theory. It was not until Einstein, however, that it was given a full quantitative analysis. He equated it to the basic mechanism of diffusion, despite this having been popularly ruled out due to the apparently marked difference in velocity scales of molecular motion and diffusion. In his PhD thesis he derived that the average distance, x, travelled by a particle in a diffusing ensemble at time t is given in the singular dimensional case by:

$$\langle x \rangle = \sqrt{2Dt} \tag{3-31}$$

Comparing this to the standard deviation, σ, in a normal – or Gaussian – distribution:

$$f_g(x) = \frac{1}{\sqrt{2\pi\sigma^2}} e^{\frac{-(x-a)^2}{2\sigma^2}} \tag{3-32}$$

it can be seen that this profile adequately describes the distribution of a diffusing collection of particles after time t, where:

$$\sigma^2 = 2Dt \tag{3-33}$$

3.4.2 Principle of operation

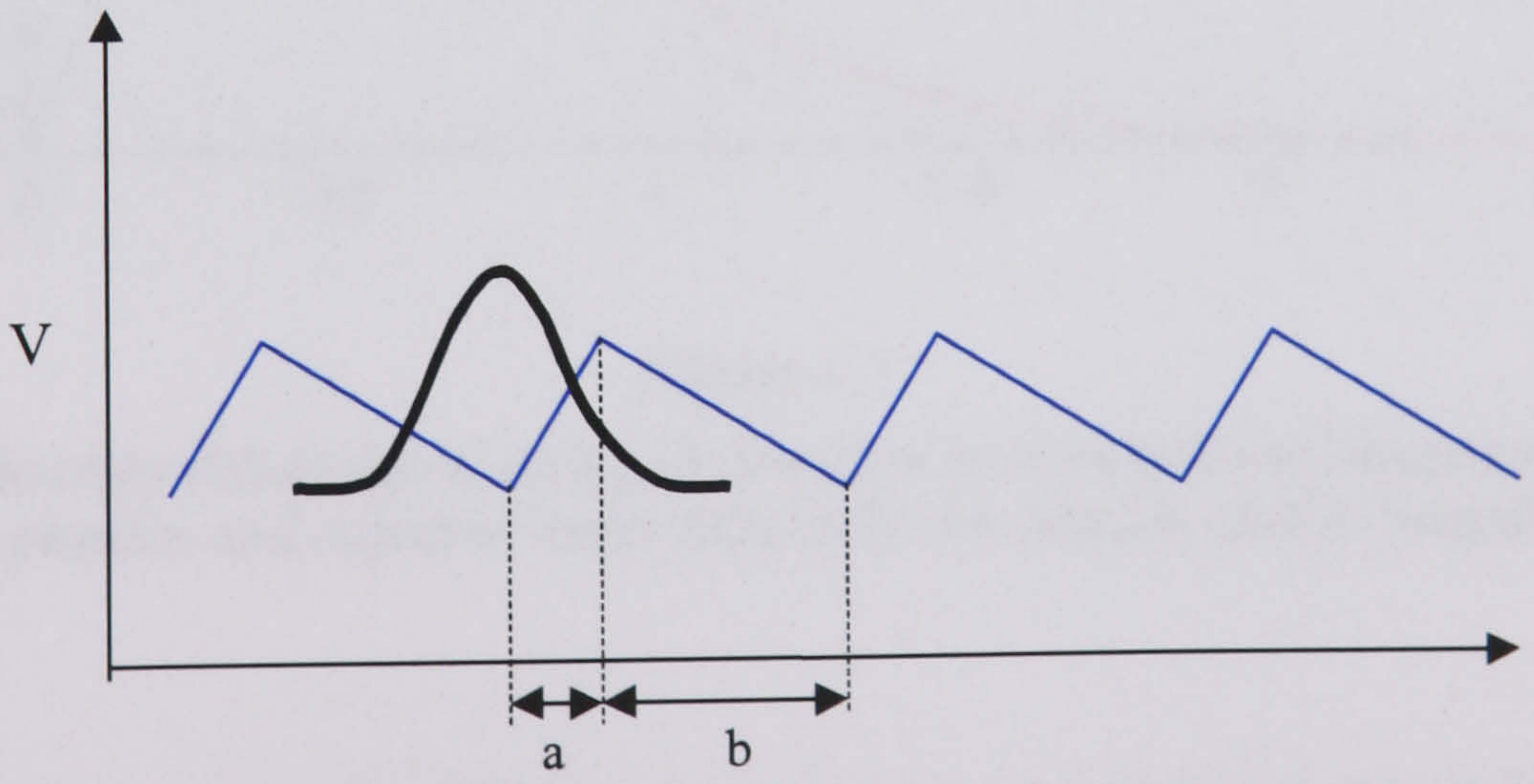

Distance in direction of transport

Figure 3-6

Illustration of asymmetric potential with superimposed diffusion profile of particles previously trapped in a potential minimum

The basic mechanism of the ratchet is the periodic application of the illustrated asymmetric potential shown in Figure 3-6. When the potential is switched on, the particles are trapped in the minima shown. When it is switched off, they diffuse in a time dependant Gaussian distribution, given by:

$$f_g(x) = \frac{1}{\sqrt{4\pi Dt}} e^{\frac{-x^2}{4Dt}} \tag{3-34}$$

The error function (Figure 3-7):

$$erf(x) = \frac{2}{\sqrt{\pi}} \int_{-x}^{x} e^{-u^2} du \tag{3-35}$$

represents the area under a normalised Gaussian curve between the limits x and $-x$.

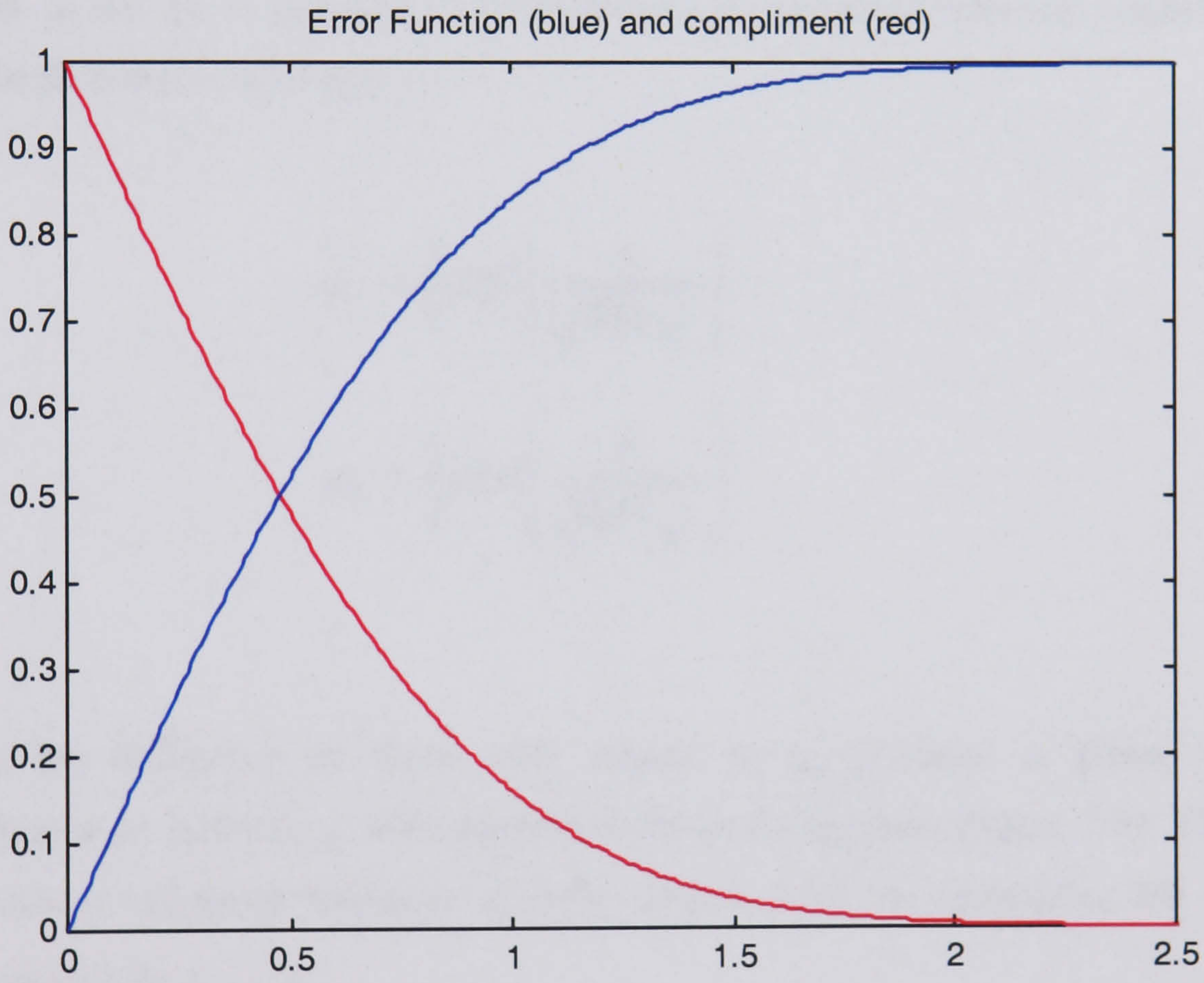

Figure 3-7

The error function (blue) representing the fraction of a normalised Gaussian contained between the positive and negative limits defined by the domain, and its compliment (red).

Therefore, integrating the semi infinite *complimentary error function* (1-*erf*) from the limits a and b respectively gives the total segment of the area bounded by the curve to have passed either of these two points after a specified diffusion time, t_{off}, Figure 3-8.

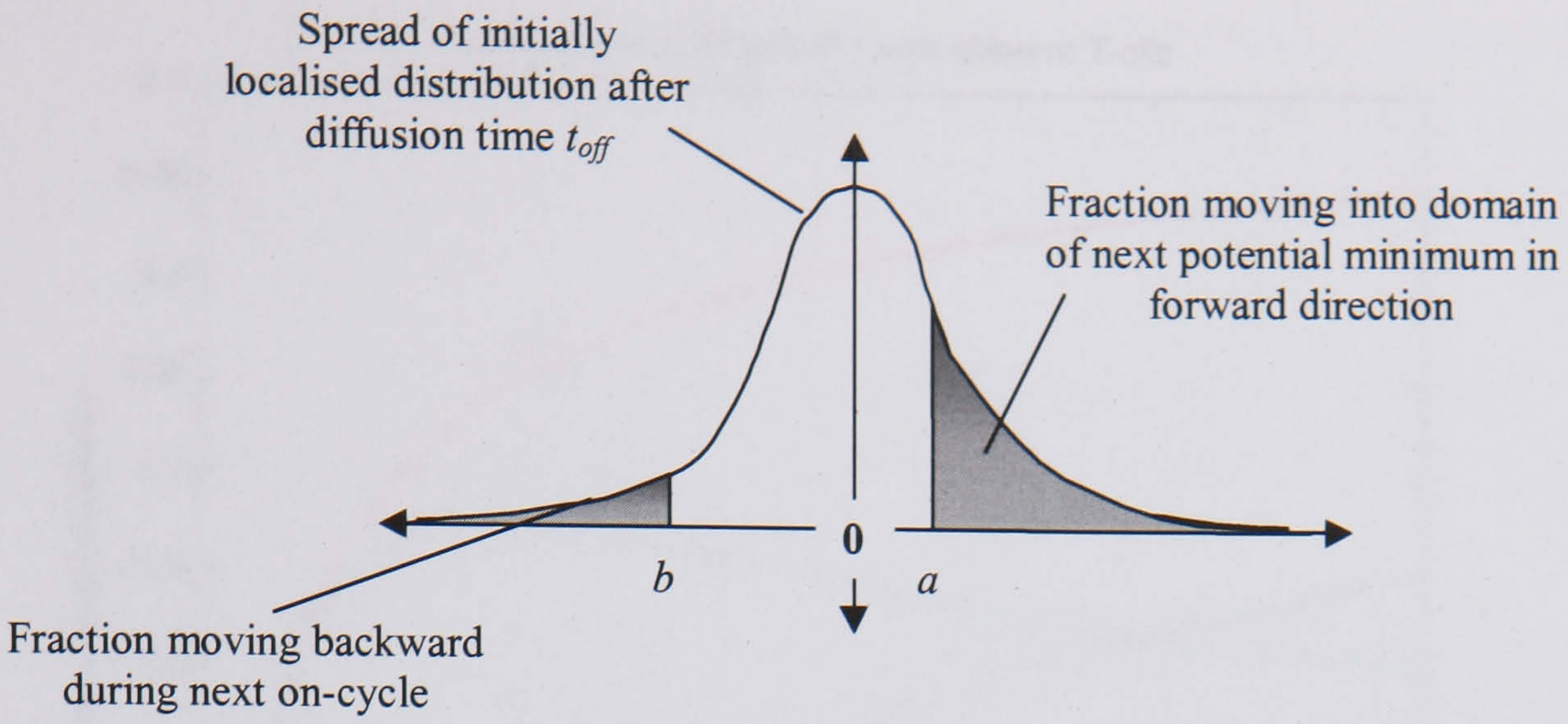

Figure 3-8

Comparison of particle quantities diffusing past boundaries a *and* b *in a fixed time interval, from a potential minimum centred at the origin.*

Because diffusion is by nature stochastic, this is a direct representation of the *probabilities*, p_f and p_b, of propulsion in the forward or backward direction respectively, the next time the potential is activated, i.e:

$$p_f = \frac{1}{2} erfc\left(\frac{a}{\sqrt{4Dt_{off}}}\right) \tag{3-36}$$

$$p_b = \frac{1}{2} erfc\left(\frac{b}{\sqrt{4Dt_{off}}}\right) \tag{3-37}$$

Plotting the difference of these with respect to t_{off} produces a global maximum corresponding to an optimal t_{off} with maximum forward transport (Figure 3-9). This can be translated into a maximum transport *velocity,* Figure 3-10, by optimising the combined difference divided by t_{off} , i.e:

$$\frac{p_f - p_b}{t_{off}} \tag{3-38}$$

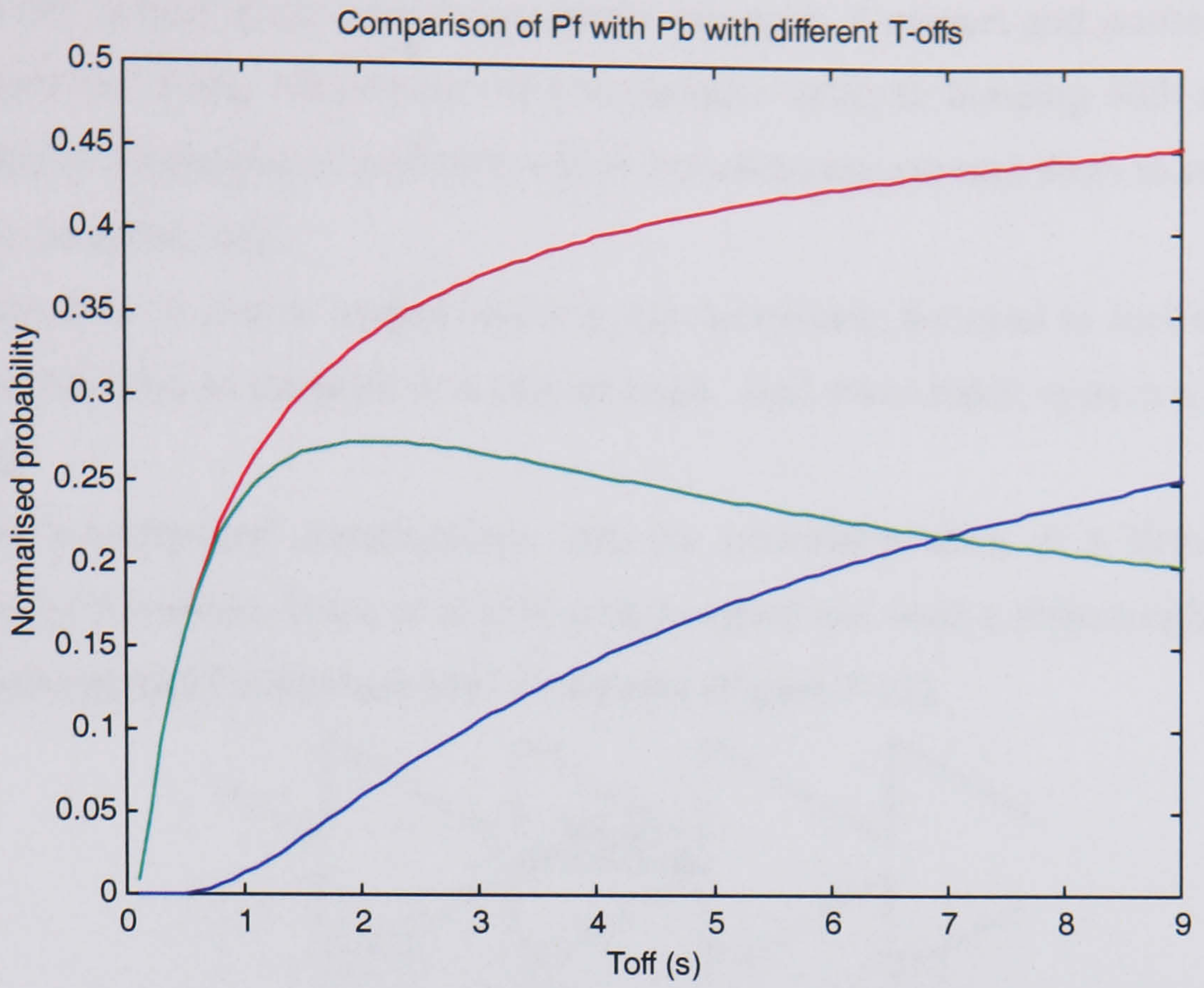

Figure 3-9

Comparison of forward (red) and backward (blue) transport probabilities for 0.5μm particles in a Brownian ratchet of a:b = 1:3 μm, showing a peak in the difference (green)

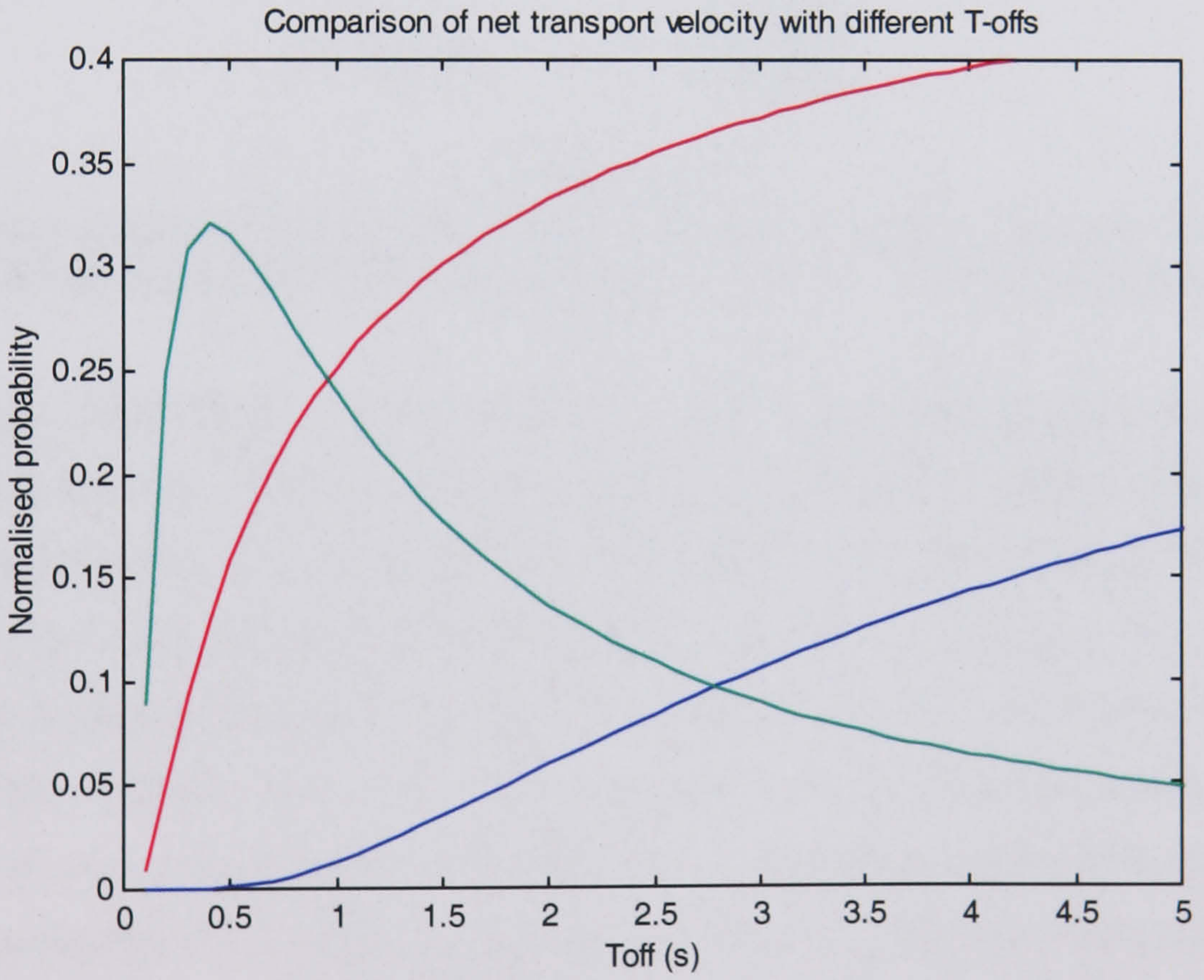

Figure 3-10

Net transport probability (green) scaled by T_{off} to predict transport velocity peak

3.4.3 Brownian ratchets in operation

Initially a curiosity, the concept of Brownian ratchets first attracted serious academic interest as a transport mechanism in motor proteins - individual nano-scale proteins responsible for muscle action and intra-cellular transport. Compact and positively charged, they are propelled along biopolymers due to periodic catalytic bonding with a neutralising ATP (adenosine triphosphate) molecule which intermittently exposes them to an asymmetric electrostatic potential [68].

Given the drive to shrink analysis tools to the microscale, the need to find efficient ways to transport sub-micron particles is a critical issue. And what better system to imitate than nature itself?

The first experimental investigations into the microfabrication of a Brownian ratchet device were by Rousselet, Prost *et al* [69] who designed and built a dielectrophoretic system utilising interdigitated "Christmas tree" electrodes (Figure 3-11).

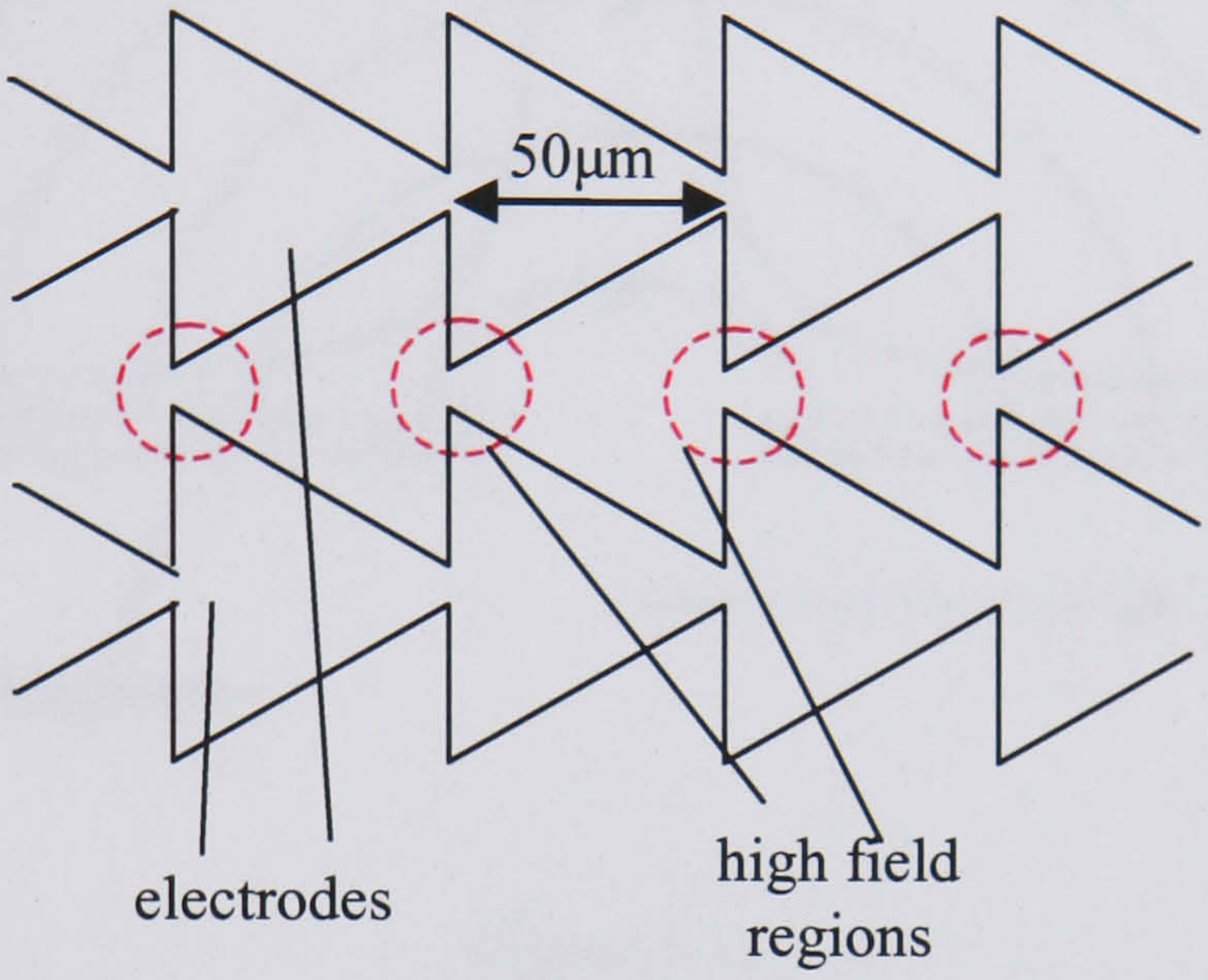

Figure 3-11

DEP-Brownian ratchet electrode design [69], with an asymmetric DEP potential originating in the different electric field gradients on either side of the high field regions

Due to the difference in the rate of change of the electric field gradient on either side of the high field regions[11], this arrangement generates an asymmetric dielectrophoretic force - so with pulsed application could be used to transport colloidal particles. This work was followed up by Gorre-Talini *et al* [70], who used a parallel 3-d arrangement consisting of a blazed optical grating ("factory roof" shape) and plane electrode to transport functionalised latex colloids. Schnelle *et al*, [71] have also very recently devised another 3-d design consisting of two planar arrays of interdigitated electrodes, sandwiched on the top and bottom of a channel, with negative DEP used to drive the flow. An electrophoretic system has been constructed by Bader and Hammond [72, 73] which has been used to transport oligonucleotides with a view to fractionation according to size. Optical tweezers [74] and sieve like structures [75, 76] have also been proposed as a means to exploiting the potential of Brownian ratchets.

---

[11] points of closest approach of electrodes

3.5 Electro-osmosis

A recently published fluid flow mechanism occurs on the surface of polarised electrodes as the result of the interaction of the double layer with a divergent AC inter-electrode field [77]. The observed effect of this electro-osmosis is the fluid (as followed by the tracer particles) being pushed towards the *centre* of the electrodes at frequency regions where usually they should be undergoing positive DEP (Figure 3-12).

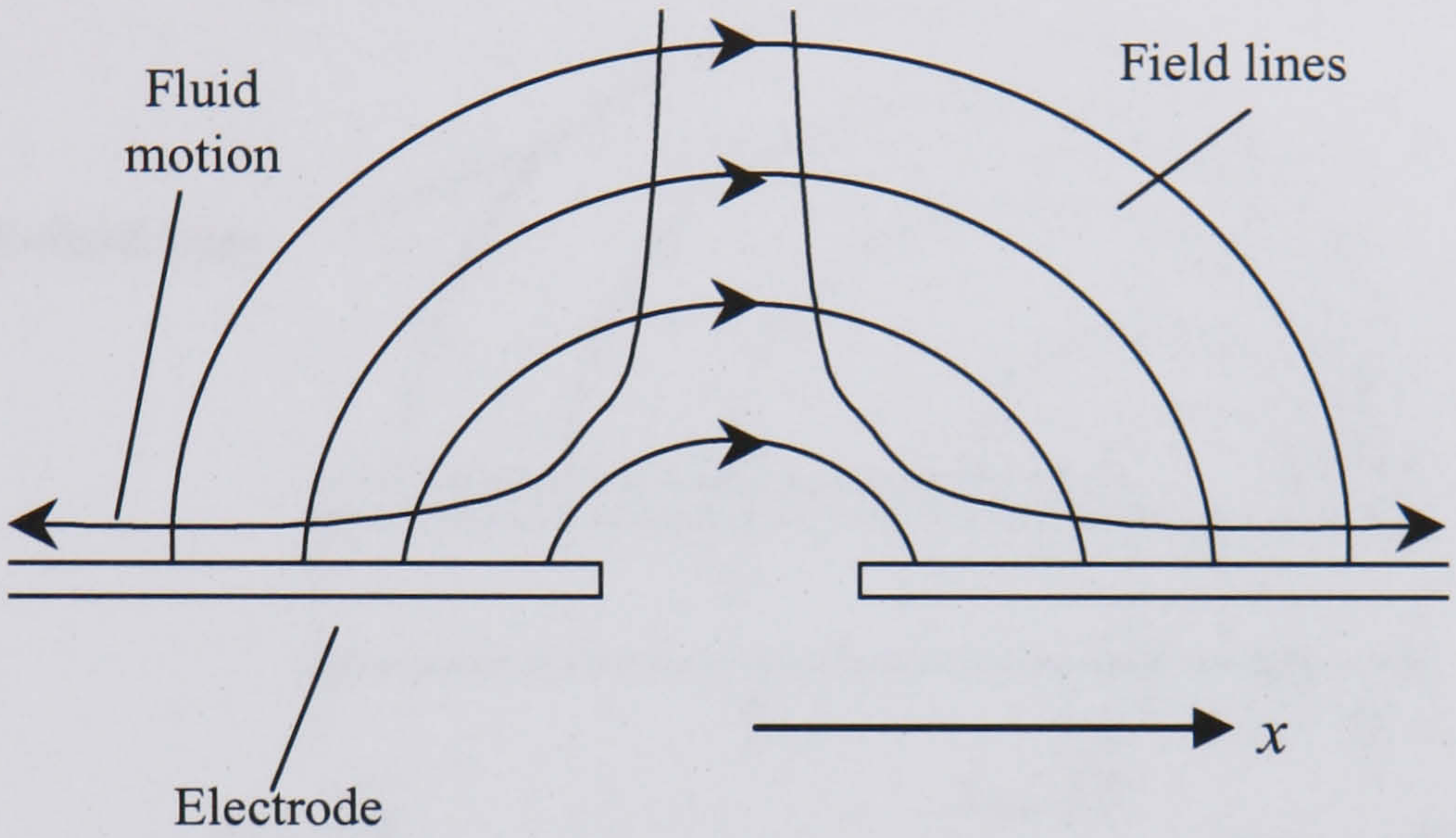

Figure 3-12

Electro-osmotic flow pattern produced on parallel electrodes as the result of the tangential component of the AC electric field acting on double layer charge. The force has constant direction due to the simultaneous change of field direction and the sign of the counter charge.

The basic force is that due to the tangential field component which acts on the induced layer of counter charge built up on the electrode surface. When the field changes direction so does the sign of the counter charge and therefore the force is monodirectional. In the linear double layer approximation Ramos et al [78] have derived the time averaged velocity across the electrodes to be (Appendix 3-5):

$$\langle v \rangle = \frac{1}{8}\frac{\varepsilon V_0^2 \Omega^2}{\pi x \left(1+\Omega^2\right)^2} \tag{3-39}$$

where:

$$\Omega = \frac{\omega}{\sigma}\frac{\pi}{2} x \kappa \tag{3-40}$$

This gives rise to fairly good predictions for the frequency dependence of velocity but with inconsistency in the order of magnitude. Further theoretical work has been carried out by

Gonzales et al using a linear double-layer analysis and taking into account also the capacitance of the Stern layer [79].

3.5.1 Electro-osmotic pumping

Brown *et al* [80] have used this principle to build an electro-osmotic pump by fabricating an interdigitated electrode array which is pair-wise asymmetric (Figure 3-13).

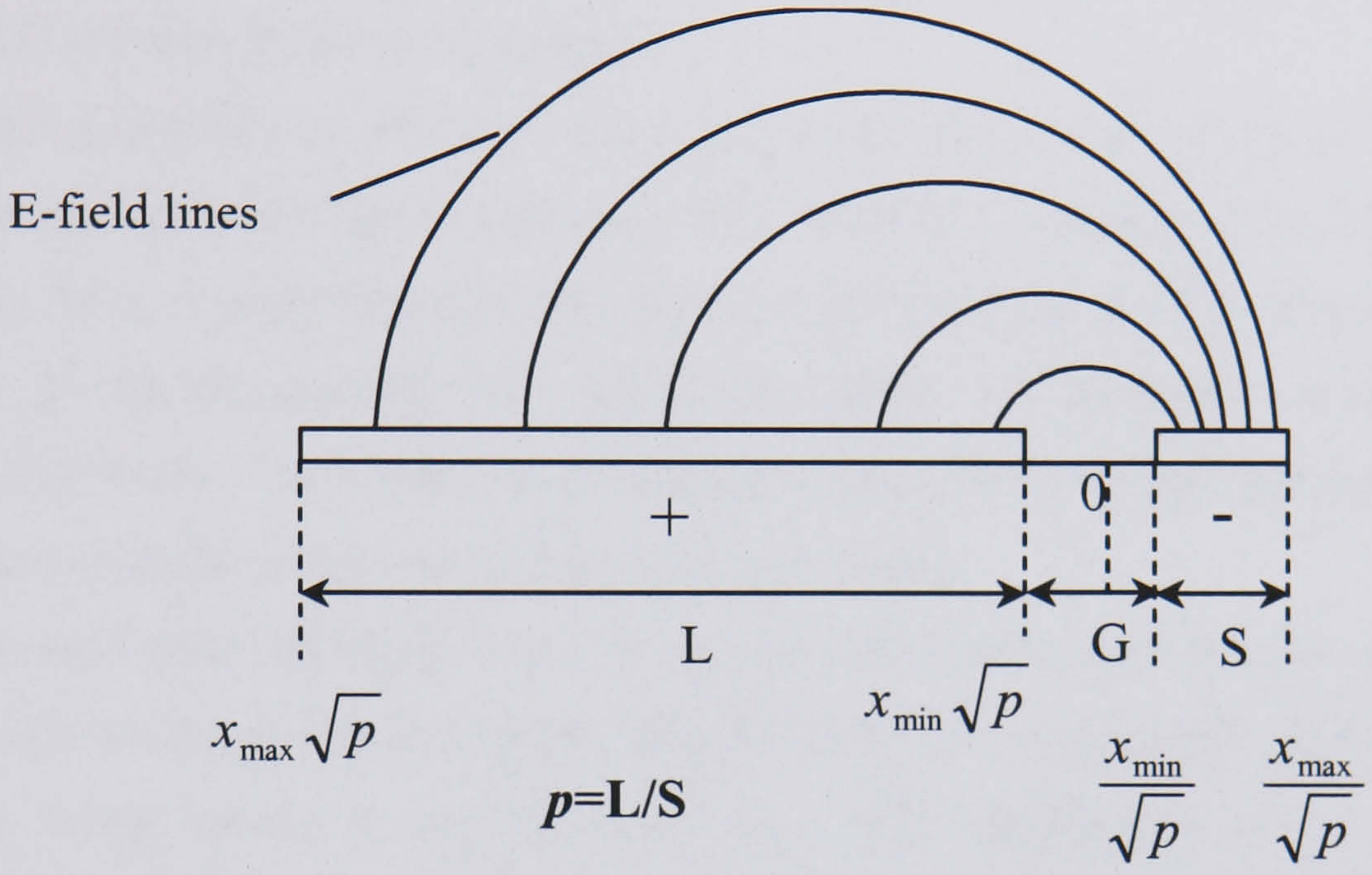

Figure 3-13

Schematic of asymmetric interdigitated electrodes and co-ordinate system devised by Brown et al *for asymmetry induced electro-osmotic pumping.*

In this way the opposing flows are imbalanced and so the fluid has a net velocity. The frequency at which the maximum occurs has been calculated by Brown *et al* to be:

$$\omega_{\max} = \frac{\omega_0}{\sqrt{x_{\min} x_{\max}}} \qquad (3\text{-}41)$$

where $\omega_0 = 2\kappa\sigma / \varepsilon\pi$ and x_{min} and x_{max} are shown in Figure 3-13, with p given by L/S - the ratio of the large to small electrode.

3.6 Summary

An extensive body of literature exists in the field of micro-scale transport and particle fractionation technologies. The three main fractionation groups highlighted, - travelling wave, field-flow-fractionation and Brownian ratchets – all have the capability, potential or otherwise, to differentiate dielectrophoretically between particles with different surface properties, although with varying degrees of applicability to sub-micron particles. This has been largely explored in travelling wave applications, with increasing success due to the rapid growth of micro-fabrication techniques.

In field-flow-fractionation, the restrictions are mainly due to the difficulty in achieving adequate stratification of Brownian particles. This limitation is considerable with the use of DEP since the force is proportional to the third power of the radius and therefore falls off rapidly with decreasing particle size while the effects of Brownian motion become increasingly significant. The separation of colloids using field-flow-fractionation, therefore, has been most successful using non-dielectrophoretic means.

The Brownian ratchet principle, however, is most applicable to sub-micron particles – its primary requirement being that the sample *should* behave in a substantially diffusive manner and therefore firmly belong to the Brownian realm. DEP applications in this field, while intriguing, are as yet somewhat scarce and a great deal of unexplored potential remains.

The liquid pumping principles highlighted - electrothermal, in the context of travelling wave and otherwise, and electro-osmosis, newly harnessed by the use of asymmetric structures – also carry significant scope for investigation with a view to micro-fluidic applications in the context of the manipulation of colloidal particles.

Appendix 3-1 Charge relaxation time

The charge relaxation of a slightly conducting medium is effectively what governs its response to the action of travelling fields and thereby what determines the frequency distribution of any resultant motion.

In an electric field system the field equations are:

$$\nabla \times E = 0 \tag{3-42}$$

$$\nabla.\varepsilon E = \rho_f \tag{3-43}$$

$$\nabla.J_f + \frac{\partial \rho_f}{\partial t} = 0 \tag{3-44}$$

where J_f is the free current density and the other symbols have their usual meaning.

The conduction of free charge can be accounted for using Ohm's law

$$J_f = \sigma E + \rho_f v \tag{3-45}$$

combining (3-44) and (3-45):

$$\nabla.\sigma E + \nabla.\rho_f v + \frac{\partial \rho_f}{\partial t} = 0 \tag{3-46}$$

Assuming the medium to be stationary, this can be expressed, using (3-43), only in terms of the free charge and medium characteristics as:

$$\frac{\partial \rho_f}{\partial t} + \frac{\sigma}{\varepsilon}\rho_f = 0 \tag{3-47}$$

which has general solution:

$$\rho_f(x, y, z, t) = \rho_0(x, y, z)e^{-(\sigma/\varepsilon)t} \tag{3-48}$$

Thus a characteristic relaxation time for the medium can be defined as:

$$\tau = \frac{\varepsilon}{\sigma} \tag{3-49}$$

Appendix 3-2 Forces and the Maxwell Stress tensor

The Lorentz force on a charged particle is given by:

$$f = qE \tag{3-50}$$

A more useful quantity, however, is the force *density*:

$$F = \rho_f E \tag{3-51}$$

This allows the introduction of more general tensorial notation. The stresses on each of the faces of a cubic segment of fluid can be depicted as shown in Figure 3-14.

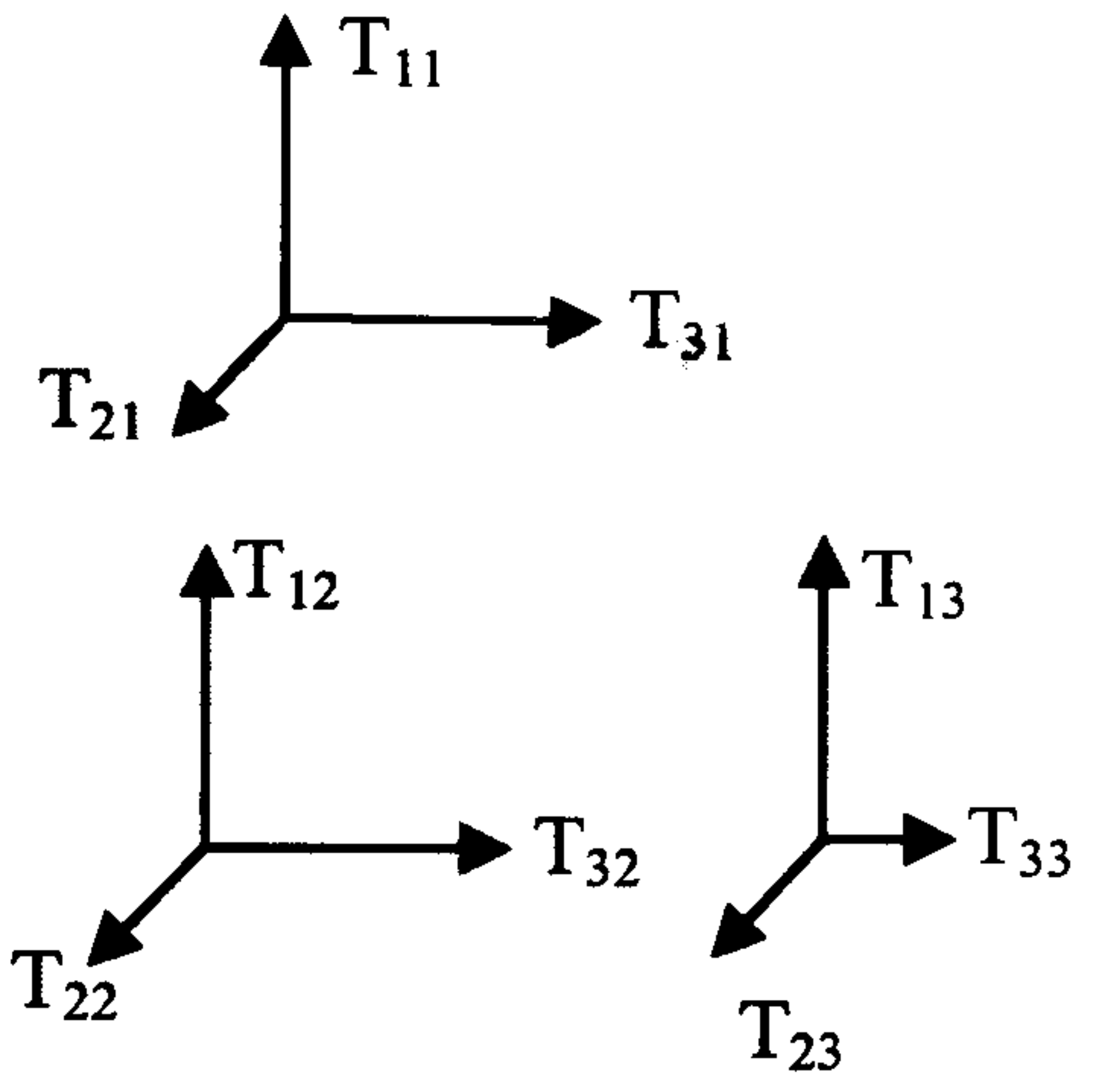

Figure 3-14
Tensorial stress components on fluid segment

A tensor T_{mn} can be used to define each component of stress on every face in all directions such that the m^{th} component of the force density is given by:

$$F_m = \frac{\partial T_{mn}}{\partial x_n} \tag{3-52}$$

where repeated indices denote the Einstein summation convention.

In order to express the electric force density (3-43) in these terms, we consider the fact that for non-magnetic systems $\nabla \times E = 0$ which allows us to write:

$$F = (\nabla.\varepsilon E)E + (\nabla \times E) \times \varepsilon E \tag{3-53}$$

Rearranging using a standard vector identity on the last term gives:

$$F = (\nabla.\varepsilon E)E + \varepsilon(E.\nabla)E - \frac{1}{2}\varepsilon\nabla(E.E) \tag{3-54}$$

whereby the m$^{\text{th}}$ component can be expressed as:

$$F_m = \frac{\partial}{\partial x_n}(\varepsilon E_m E_n) - \frac{\varepsilon}{2}\frac{\partial}{\partial x_m}(E_k E_k) \tag{3-55}$$

This can be put into the desired form:

$$F_m = \frac{\partial T_{mn}}{\partial x_n} \tag{3-56}$$

by use of the Kronecker delta to write:

$$\frac{\partial}{\partial x_m} = \delta_{mn}\frac{\partial}{\partial x_n} \tag{3-57}$$

so that the Maxwell stress tensor for electric field systems is given by:

$$T_{mn} = \varepsilon E_m E_n - \frac{\varepsilon}{2}\delta_{mn} E_k E_k \tag{3-58}$$

If ε is non constant, the derivative of the stress tensor also produces effectively a DEP force term, proportional to $\nabla\varepsilon$ giving the total force density as:

$$F = \rho_q E - \frac{1}{2}E^2\nabla\varepsilon \tag{3-59}$$

n.b. If first order compressibility of the fluid is taken into account there is also an additional term known as electrostriction, given by [81]:

$$f_{electrostriction} = \frac{1}{2}\left(\rho_m\left(\frac{\partial\varepsilon}{\partial\rho_m}\right)\right)_T E^2 \tag{3-60}$$

However, this can be combined with the induced pressure gradient term in the Navier-Stokes equations and omitted from explicit reference in the calculations [18].

Appendix 3-3 Fabricated prototype of a μ-DEP-FFF device

Electrodes

The electrodes consisted of an interdigitated finger array and were designed on a scale smaller than previously utilised in a DEP-FFF system in order to accommodate the particles in the sub-micron domain. The larger field gradients from this array means that particle distributions will achieve equilibrium positions less widely spaced than with larger electrodes and therefore the array should be long enough to effect separation of closely distributed populations.

The channel was made as wide as possible to allow a maximum sample through and minimise edge effects. The final dimensions are those shown in Figure 3-15. This amounts to a very large area on which to avoid short circuits, therefore with such a comparatively small electrode feature size, e-beam direct write on a prefabricated mask plate was used (see Chapter 7). A photograph of the edge of the fabricated array is shown also in Figure 3-15.

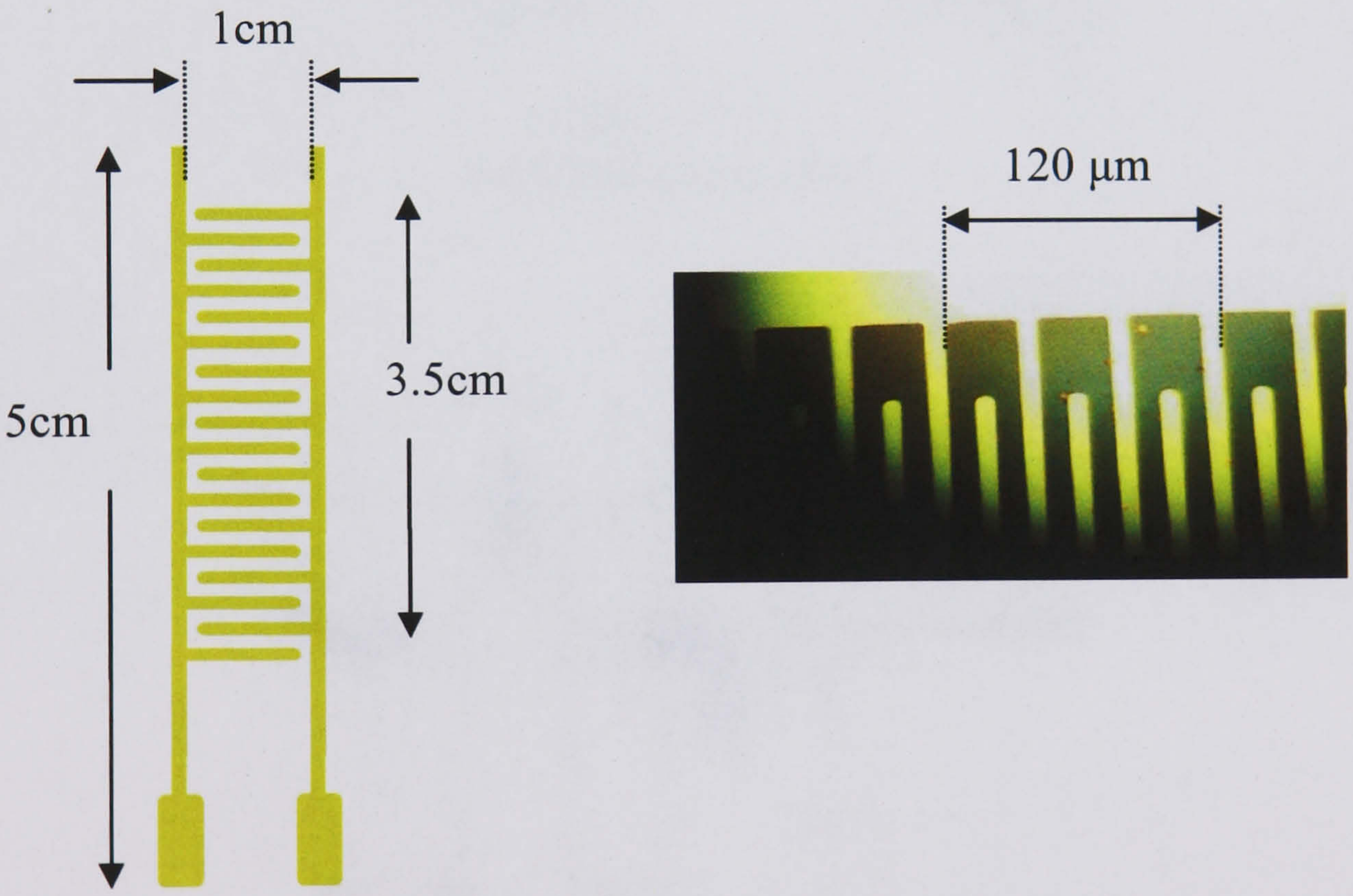

Figure 3-15

Schematic of 10μm electrode array highlighting macroscopic dimensions, with photograph of electrode edges, fabricated using e-beam lithography.

Spacer

The electrodes were sandwiched in a staggered arrangement to allow access to the bonding pads (Figure 3-16).

Various materials were tried for the spacer (Figure 3-17) including SU8 and PDMS (see Chapter 7) and 100µm bonding film. Adhesion problems, resulting in inadequate sealing were encountered with the first two. Even after PDMS oxidation following a recipe developed by Duffy *et al* [82] the large areas were an obstacle. The bonding film proved satisfactory although the channel shape could only be crudely cut and the device could not be reopened for cleaning.

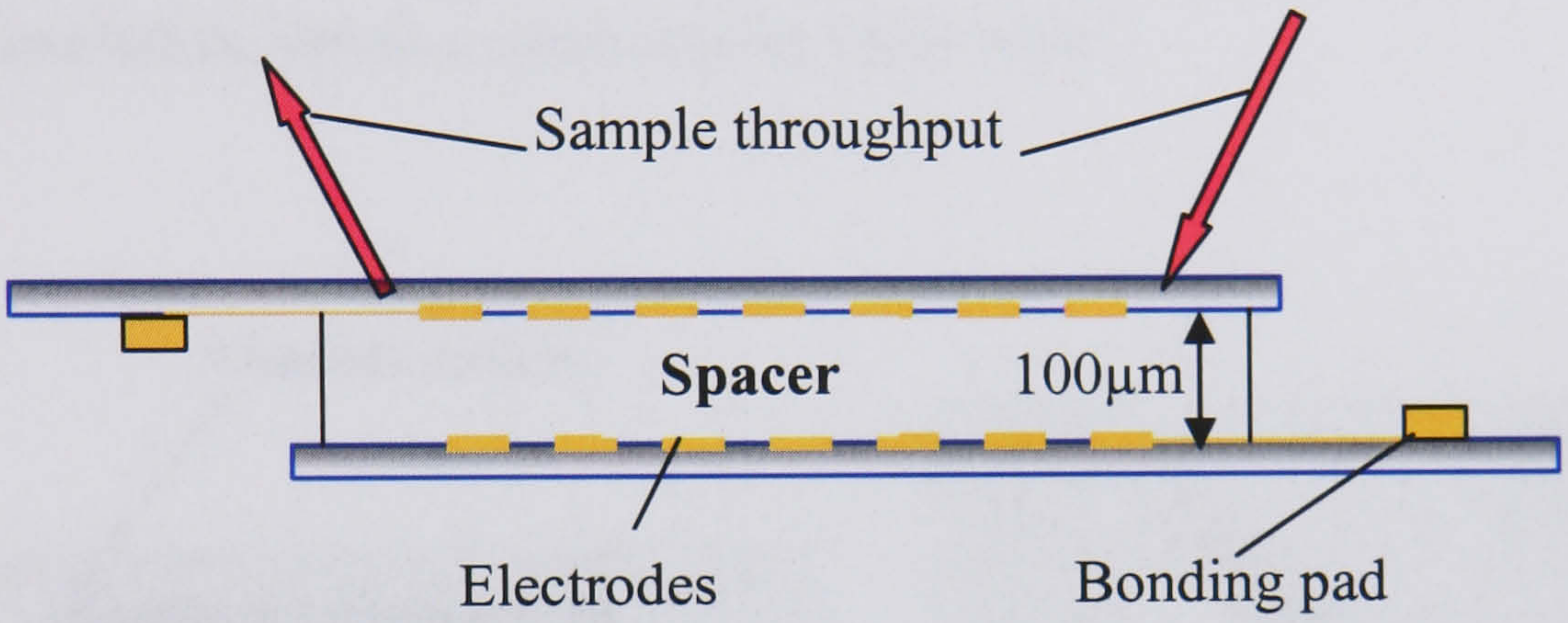

Figure 3-16
Alignment of electrodes

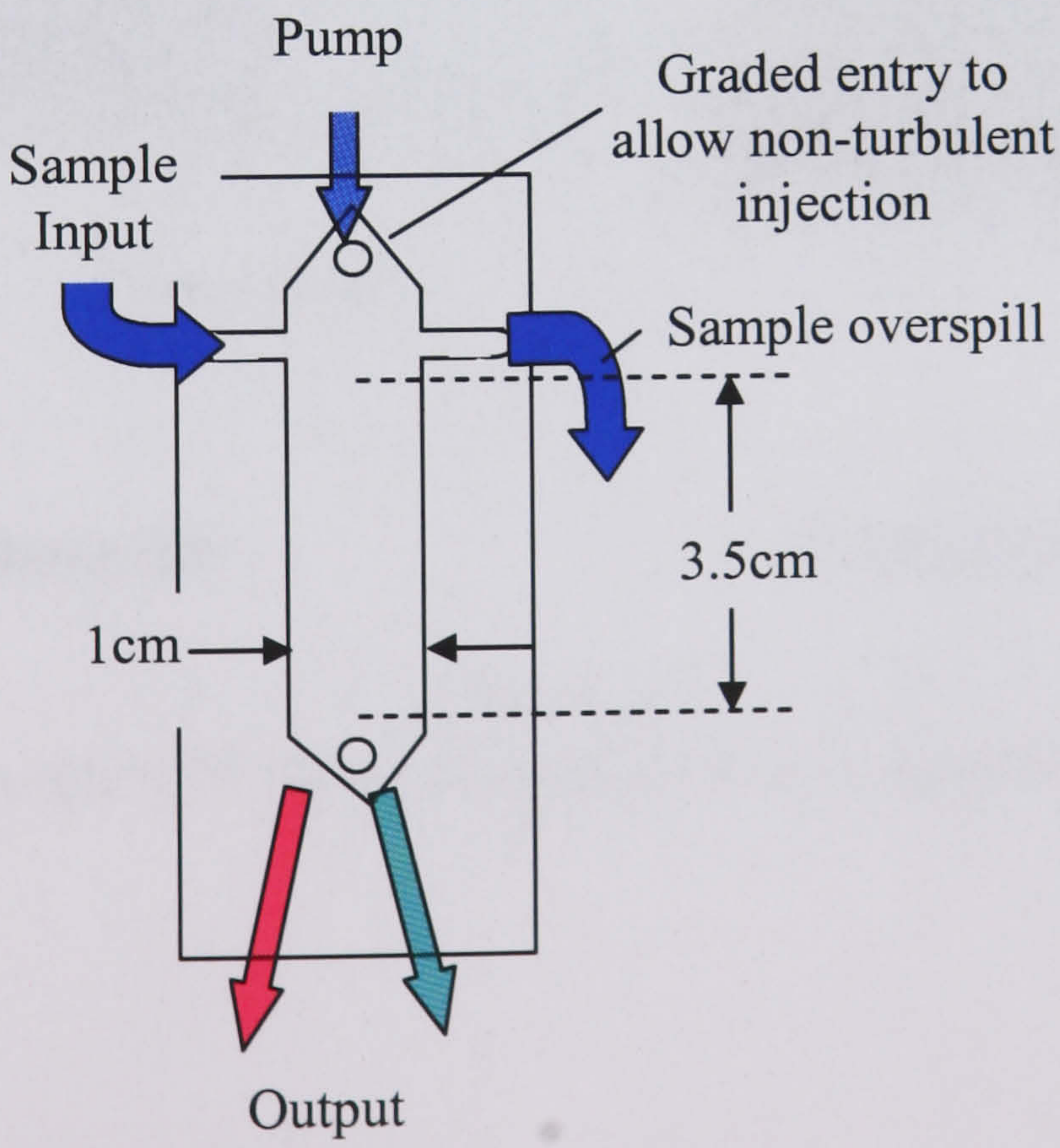

Figure 3-17
Schematic of channel in 100 µm thick spacer

Device construction

Perspex blocks with threaded receptors for syringe fittings were fixed to the device on 1mm holes drilled at the pump input and elution points. Cross-bar sample introduction points were omitted at this stage due to the low level of precision afforded by the channel fabrication procedure in contrast to that attainable using lithographic techniques.

The prototype was tested using three sub-micron bead sizes. Separation under these circumstances, however, was not achieved. A much higher level of microfluidic control would be necessary for initial sample localisation (as also alluded to in [59]), combined, possibly with a better optimisation of channel/electrode dimensions for this scale of particle. This does, nonetheless, remain an open area for future work!

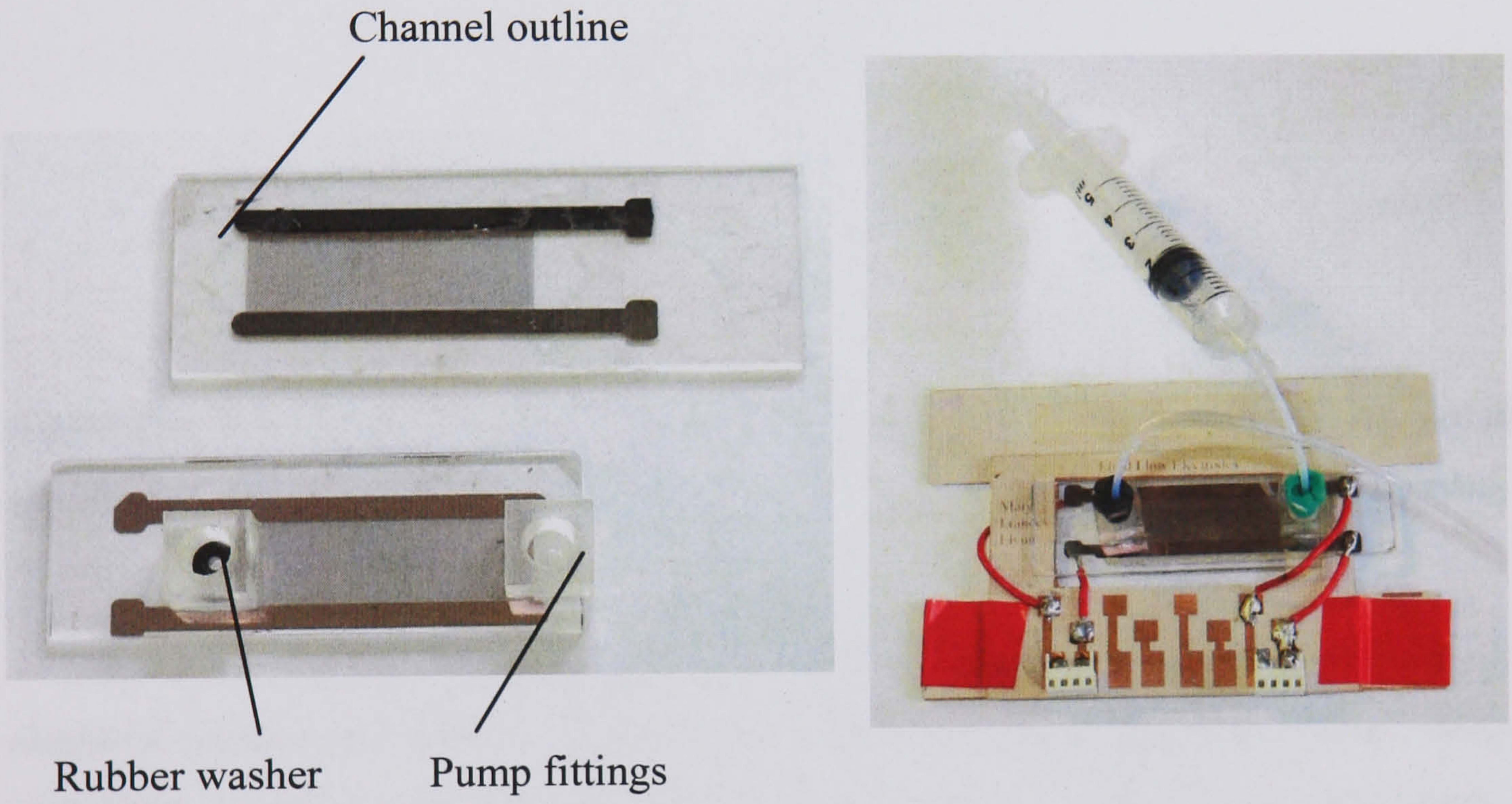

Electrodes **Prototype device**

Figure 3-18
μ-DEP-FFF electrodes and final device construction

Appendix 3-4 Generic concentration profile solution across a channel when DEP forces are balanced by diffusion

Rewriting Equation (3-28) as:

$$\frac{\partial C}{\partial y}-\frac{v}{D}C=0 \qquad (3\text{-}61)$$

it can be observed that an integrating factor is:

$$e^{\int -\frac{v}{D}\partial y} \quad \text{i.e.} \quad Ae^{-\frac{v}{D}y}$$

so that:

$$\frac{\partial}{\partial y}\left(Ae^{-\frac{v}{D}y}C\right)=0$$

i.e.

$$C=\frac{ye^{\frac{v}{D}y}}{A}+Be^{\frac{v}{D}y}$$

Appendix 3-5 1st order derivation of electro-osmotic flow velocity on parallel electrodes

[77, 78, 83] As a first approximation it is illustrative to model the system in terms of electrical components with voltage drop across the electrodes represented by an array of capacitors in series with the medium resistance (Figure 3-19). From this figure, an incremental capacitance can be defined as:

$$\Delta C=\varepsilon\Delta x\kappa \qquad (3\text{-}62)$$

where κ is the inverse Debye length.

Similarly, the resistance, R, of a flux tube through the medium can be written as:

$$R=\frac{\pi x}{\sigma\Delta x} \qquad (3\text{-}63)$$

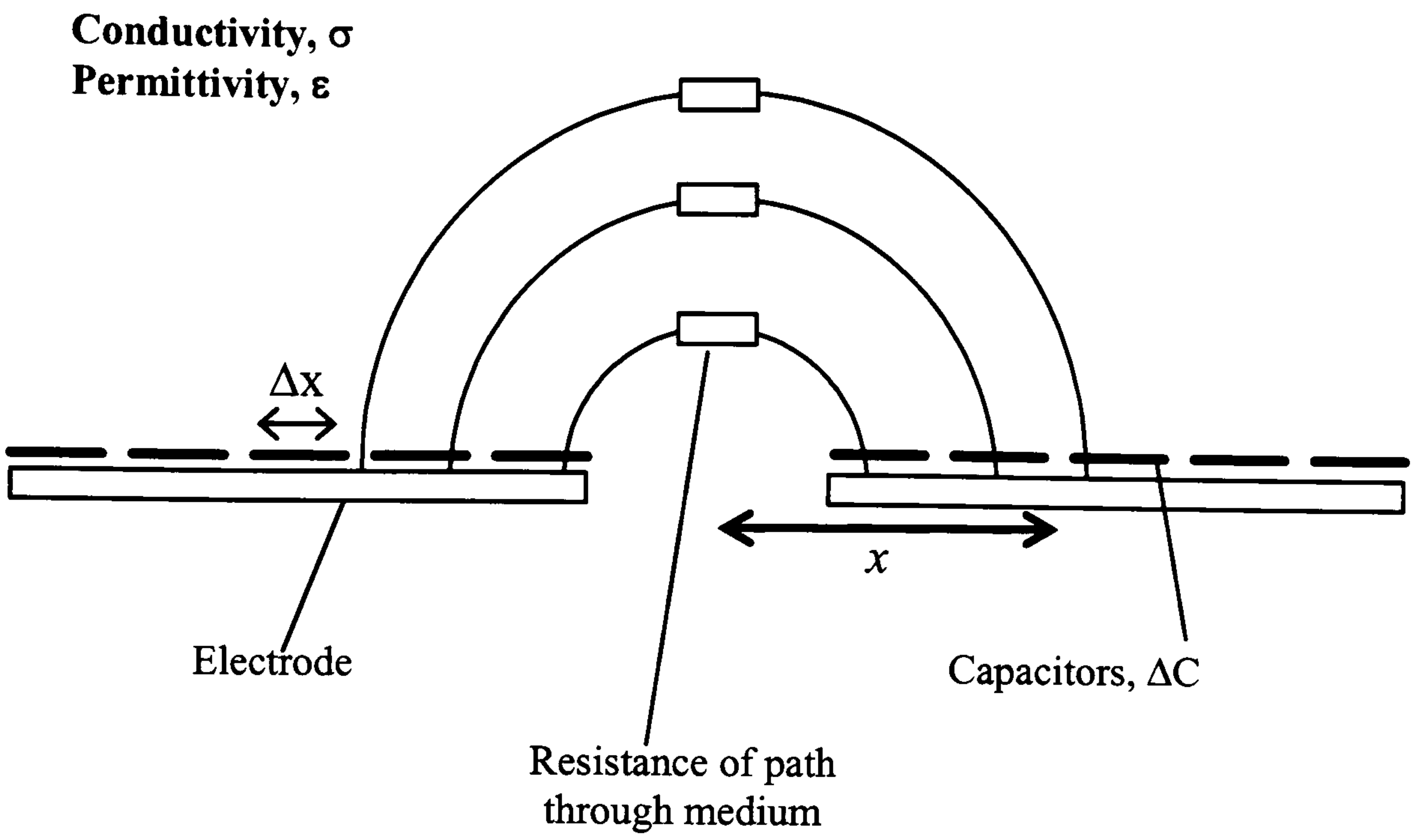

Figure 3-19
Schematic representation of resistive/capacitive components of ac parallel electrodes immersed in a fluid medium

Considering the complex impedance of a capacitor is given by:

$$Z_C = \frac{1}{j\omega C} \tag{3-64}$$

the total impedence of a flux tube is therefore:

$$Z_T = 2Z_C + R \tag{3-65}$$

i.e.

$$Z_T = \frac{2}{j\varpi\varepsilon\Delta x\kappa} + \frac{\pi x}{\sigma\Delta x} = \frac{1}{j\omega\varepsilon\Delta x\kappa}\left(2 + \frac{\pi x j\varpi\varepsilon\kappa}{\sigma}\right) \tag{3-66}$$

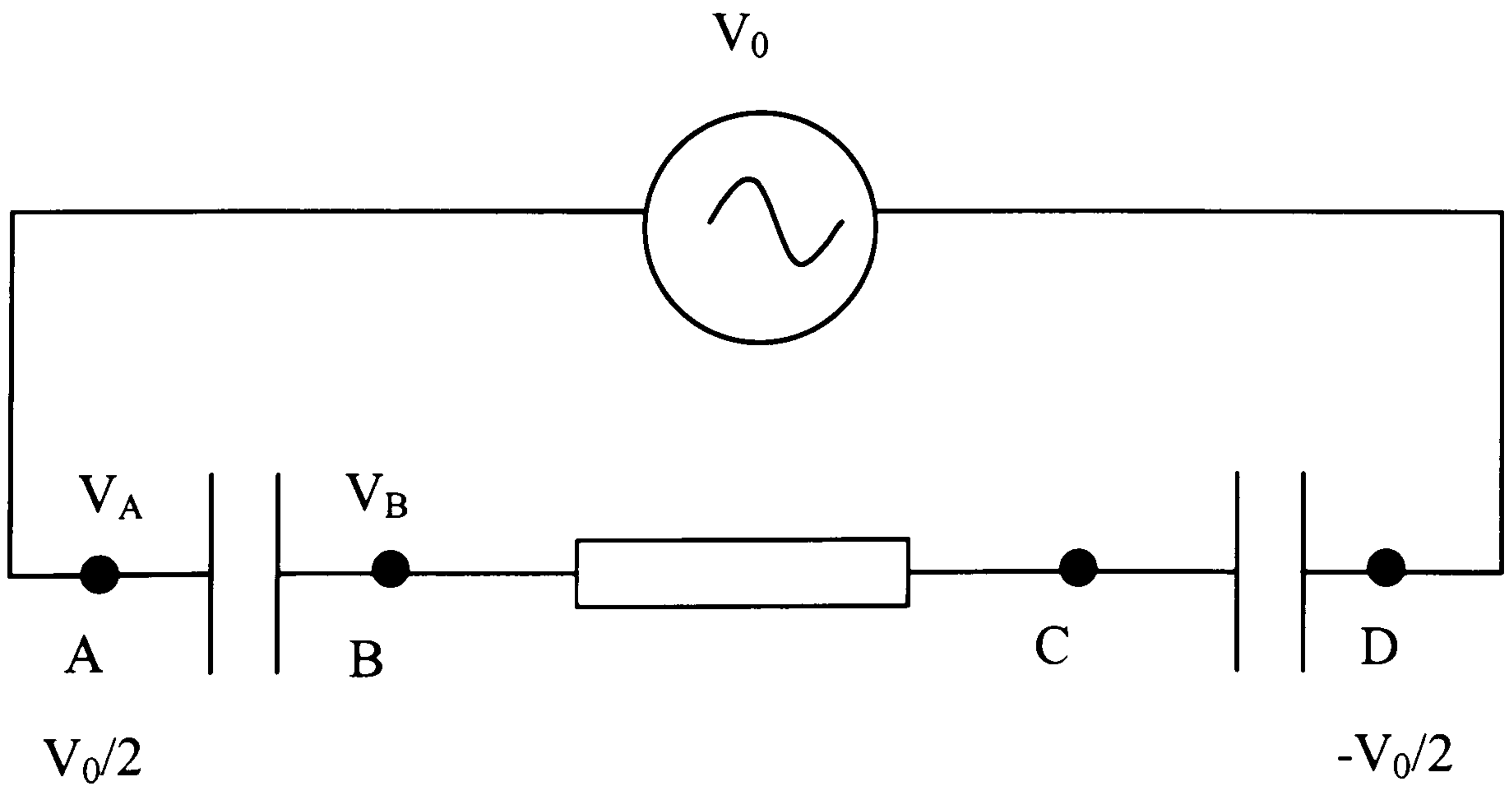

Figure 3-20
Equivalent RC circuit of current flow between parallel electrodes through a liquid medium

From Figure 3-20, the potential dropped across the double layer is:

$$\Delta V = V_A - V_B = Z_C I \tag{3-67}$$

$$I = \frac{V_0}{Z_T} \tag{3-68}$$

$$\Delta V = \frac{Z_C}{Z_T} V_0 = \frac{\dfrac{V_0}{j\omega\varepsilon\Delta x\kappa}}{\dfrac{1}{j\omega\varepsilon\Delta x\kappa}\left(2 + \dfrac{\pi x j\omega\varepsilon\kappa}{\sigma}\right)} \tag{3-69}$$

i.e:

$$V_{dl}(x) = \frac{V_0}{2 + \dfrac{\pi x j\omega\varepsilon\kappa}{\sigma}} \tag{3-70}$$

This gives the voltage across the double layer as a function of x, the distance from the centre of the electrode pair. From this the tangential component of the electric field, $\frac{\partial V_{dl}}{\partial x}$, can be calculated and the charge density at each point on the electrodes is correspondingly $\Delta\sigma(x) = \varepsilon\kappa V_{dl}$.

From the relationship between mobility, μ, and ζ-potential :

$$\mu = \frac{v}{E} = \frac{\varepsilon\zeta}{\eta} \tag{3-71}$$

it can be seen that in the Gouy-Chapman linear double layer approximation [84] the induced electro-osmotic velocity v is given by:

$$v = \frac{E_t \Delta\sigma}{\kappa\eta} \tag{3-72}$$

i.e.

$$\langle v \rangle = \frac{1}{2}\mathrm{Re}\left\{\frac{\Delta\sigma E_t^*}{\eta\kappa}\right\} = \frac{1}{8}\frac{\varepsilon V_0^2 \Omega^2}{\pi x\left(1+\Omega^2\right)^2} \tag{3-73}$$

where:

$$\Omega = \frac{\omega}{\sigma}\frac{\pi}{2} x\kappa \tag{3-74}$$

3.7 References

[1] P. A. Greenwood and G. M. Greenway, "Sample manipulation in micro total analytical systems", *Trac-Trends in Analytical Chemistry*, vol. 21, pp. 726-740, 2002.

[2] S. C. Jakeway, A. J. de Mello, and E. L. Russell, "Miniaturized total analysis systems for biological analysis", *Fresenius Journal of Analytical Chemistry*, vol. 366, pp. 525-539, 2000.

[3] J. Khandurina and A. Guttman, "Bioanalysis in microfluidic devices", *Journal of Chromatography a*, vol. 943, pp. 159-183, 2002.

[4] A. Manz, D. J. Harrison, E. Verpoorte, and H. M. Widmer, "Planar Chips Technology For Miniaturization of Separation Systems - a Developing Perspective in Chemical Monitoring", *Advances in Chromatography*, vol. 33, pp. 1-66, 1993.

[5] S. Shoji, "Fluids for sensor systems", in *Microsystem Technology in Chemistry and Life Science*, vol. 194, *Topics in Current Chemistry*, 1998, pp. 163-188.

[6] S. Shoji, "Micro Total Analysis System (mu TAS)", *Electronics and Communications in Japan Part Ii-Electronics*, vol. 82, pp. 21-29, 1999.

[7] X. Yi, J. C. T. Eijkel, and A. Manz, "Miniaturized total analysis system: mu-TAS", *Chinese Journal of Analytical Chemistry*, vol. 28, pp. 1295-1299, 2000.

[8] J. R. Melcher, "Travelling Wave induced Electroconvection", *The Physics of Fluids*, vol. 9, pp. 1548-55, 1966.

[9] R. M. Ehrlich and J. R. Melcher, "Bipolar Model For Traveling-Wave Induced Non-Equilibrium Double-Layer Streaming in Insulating Liquids", *Physics of Fluids*, vol. 25, pp. 1785-1793, 1982.

[10] G. Fuhr, T. Schnelle, and B. Wagner, "Traveling Wave-Driven Microfabricated Electrohydrodynamic Pumps For Liquids", *Journal of Micromechanics and Microengineering*, vol. 4, pp. 217-226, 1994.

[11] R. Hagedorn, G. Fuhr, T. Muller, and J. Gimsa, "Traveling-Wave Dielectrophoresis of Microparticles", *Electrophoresis*, vol. 13, pp. 49-54, 1992.

[12] Y. Huang, X. B. Wang, J. A. Tame, and R. Pethig, "Electrokinetic Behavior of Colloidal Particles in Traveling Electric-Fields - Studies Using Yeast-Cells", *Journal of Physics D-Applied Physics*, vol. 26, pp. 1528-1535, 1993.

[13] Y. Huang, R. Holzel, R. Pethig, and X.-B. Wang, *J. Phys D; Appl. Phys.*, vol. 25, pp. 881-888, 1992.

[14] H. Morgan, A. G. Izquierdo, D. Bakewell, N. G. Green, and A. Ramos, "The dielectrophoretic and travelling wave forces generated by interdigitated electrode arrays: analytical solution using Fourier series", *Journal of Physics D-Applied Physics*, vol. 34, pp. 1553-1561, 2001.

[15] N. G. Green, A. Ramos, and H. Morgan, "Numerical solution of the dielectrophoretic and travelling wave forces for interdigitated electrode arrays using the finite element method", *Journal of Electrostatics*, vol. 56, pp. 235-254, 2002.

[16] S. Masuda, M. Washizu, and M. Iwadare, "Separation of Small Particles Suspended in Liquid By Nonuniform Traveling Field", *Ieee Transactions On Industry Applications*. vol. 23, pp. 474-480, 1987.

[17] A. Castellanos, *Electrohydrodynamics*. New York: Springer, 1998.

[18] N. G. Green, A. Ramos, A. Gonzalez, A. Castellanos, and H. Morgan, "Electrothermally induced fluid flow on microelectrodes", *Journal of Electrostatics*, vol. 53, pp. 71-87, 2001.

[19] T. B. Jones, *Electromechanics of Particles*. New York: Cambridge University Press, 1995.

[20] H. A. Pohl, *Dielectrophoresis*. Cambridge: Cambridge University Press, 1978.

[21] H. Ying, R. Holzel, R. Pethig, and X. B. Wang, "Differences in the Ac Electrodynamics of Viable and Nonviable Yeast-Cells Determined Through Combined Dielectrophoresis and Electrorotation Studies", *Physics in Medicine and Biology*, vol. 37, pp. 1499-1517, 1992.

[22] A. D. Goater and R. Pethig, "Electrorotation and dielectrophoresis", *Parasitology*, vol. 117, pp. S177-S189, 1998.

[23] T. Muller, W. M. Arnold, T. Schnelle, R. Hagedorn, G. Fuhr, and U. Zimmermann, "A Traveling-Wave Micropump For Aqueous-Solutions - Comparison of 1-G and Mu-G Results", *Electrophoresis*, vol. 14, pp. 764-772, 1993.

[24] S. Masuda, M. Washizu, and I. Kawabata, "Movement of Blood-Cells in Liquid By Nonuniform Traveling Field", *Ieee Transactions On Industry Applications*, vol. 24, pp. 217-222, 1988.

[25] Y. Huang and R. Pethig, "Electrode Design For Negative Dielectrophoresis", *Measurement Science & Technology*, vol. 2, pp. 1142-1146, 1991.

[26] G. Fuhr, R. Hagedorn, T. Muller, W. Benecke, B. Wagner, and J. Gimsa, "Asynchronous Traveling-Wave Induced Linear Motion of Living Cells", *Studia Biophysica*, vol. 140, pp. 79-102, 1991.

[27] L. Cui, D. Holmes, and H. Morgan, "The dielectrophoretic levitation and separation of latex beads in microchips", *Electrophoresis*, vol. 22, pp. 3893-3901, 2001.

[28] G. Fuhr, S. Fiedler, T. Muller, T. Schnelle, H. Glasser, T. Lisec, and B. Wagner, "Particle Micromanipulator Consisting of 2 Orthogonal Channels With Traveling-Wave Electrode Structures", *Sensors and Actuators a-Physical*, vol. 41, pp. 230-239, 1994.

[29] A. D. Goater, J. P. H. Burt, and R. Pethig, "A combined travelling wave dielectrophoresis and electrorotation device: applied to the concentration and viability

determination of Cryptosporidium", *Journal of Physics D-Applied Physics*, vol. 30, pp. L65-L69, 1997.

[30] L. Cui and H. Morgan, "Design and fabrication of travelling wave dielectrophoresis structures", *Journal of Micromechanics and Microengineering*, vol. 10, pp. 72-79, 2000.

[31] R. Pethig, J. P. H. Burt, A. Parton, N. Rizvi, M. S. Talary, and J. A. Tame, "Development of biofactory-on-a-chip technology using excimer laser micromachining", *Journal of Micromechanics and Microengineering*, vol. 8, pp. 57-63, 1998.

[32] L. Cui, T. Zhang, and H. Morgan, "Optical particle detection integrated in a dielectrophoretic lab-on-a-chip", *Journal of Micromechanics and Microengineering*, vol. 12, pp. 7-12, 2002.

[33] J. C. Giddings, *Separation Science*, vol. 1, pp. 123, 1966.

[34] J. C. Bigelow, T. Koch, K. Kataoka, and J. C. Giddings, "Cell-Separation and Characterization By Field-Flow Fractionation and Related Techniques", *Abstracts of Papers of the American Chemical Society*, vol. 193, pp. 144-ANYL, 1987.

[35] C. R. Yonker, K. D. Caldwell, J. C. Giddings, and J. L. Vanetten, "Physical Characterization of Pbcv Virus By Sedimentation Field Flow Fractionation", *Journal of Virological Methods*, vol. 11, pp. 145-160, 1985.

[36] M. E. Hansen, R. Beckett, and J. C. Giddings, "Particle-Size Analysis of River Water Colloids By Sedimentation Field-Flow Fractionation", *Abstracts of Papers of the American Chemical Society*, vol. 192, pp. 84-ENVR, 1986.

[37] P. Li, M. Hansen, and J. C. Giddings, "Separation of lipoproteins from human plasma by flow field-flow fractionation", *Journal of Liquid Chromatography & Related Technologies*, vol. 20, pp. 2777-2802, 1997.

[38] M. Dunkel and K. D. Caldwell, "Adsorption-induced shifts in colloid electrokinetic behavior: A study by electrical field-flow fractionation", *Abstracts of Papers of the American Chemical Society*, vol. 214, pp. 183-ANYL, 1997.

[39] M. Dunkel, N. Tri, R. Beckett, and K. D. Caldwell, "Electrical field-flow fractionation: A tool for characterization of colloidal adsorption complexes", *Journal of Microcolumn Separations*, vol. 9, pp. 177-183, 1997.

[40] J. C. Giddings, K. D. Caldwell, and H. K. Jones, "Measuring Particle-Size Distribution of Simple and Complex Colloids Using Sedimentation Field-Flow Fractionation", *Acs Symposium Series*, vol. 332, pp. 215-230, 1987.

[41] J. Janca, "Micro-thermal field-flow fractionation of colloidal particles: Effect of temperature on retention and relaxation processes", *Collection of Czechoslovak Chemical Communications*, vol. 68, pp. 672-695, 2003.

[42] A. P. Brown, W. B. Betts, A. B. Harrison, and J. G. O'Neill, "Evaluation of a dielectrophoretic bacterial counting technique", *Biosensors & Bioelectronics*, vol. 14, pp. 341-351, 1999.

[43] P. R. C. Gascoyne, Y. Huang, X. J. Wang, J. Yang, G. DeGasperis, and X. B. Wang, "Cell separation by conventional dielectrophoresis combined with field-flow-fractionation", *Biophysical Journal*, vol. 70, pp. TU412-TU412, 1996.

[44] P. Gascoyne, C. Mahidol, M. Ruchirawat, J. Satayavivad, P. Watcharasit, and F. F. Becker, "Microsample preparation by dielectrophoresis: isolation of malaria", *Lab On a Chip*, vol. 2, pp. 70-75, 2002.

[45] P. R. C. Gascoyne and J. Vykoukal, "Particle separation by dielectrophoresis", *Electrophoresis*, vol. 23, pp. 1973-1983, 2002.

[46] Y. Huang, X. B. Wang, F. F. Becker, and P. R. C. Gascoyne, "Introducing dielectrophoresis as a new force field for field- flow fractionation", *Biophysical Journal*, vol. 73, pp. 1118-1129, 1997.

[47] M. P. Hughes, "Strategies for dielectrophoretic separation in laboratory-on-a- chip systems", *Electrophoresis*, vol. 23, pp. 2569-2582, 2002.

[48] T. Kawabata and M. Washizu, "Dielectrophoretic detection of molecular bindings", *Ieee Transactions On Industry Applications*, vol. 37, pp. 1625-1633, 2001.

[49] G. H. Markx and R. Pethig, "Dielectrophoretic Separation of Cells - Continuous Separation", *Biotechnology and Bioengineering*, vol. 45, pp. 337-343, 1995.

[50] G. H. Markx, J. Rousselet, and R. Pethig, "DEP-FFF: Field-flow fractionation using non-uniform electric fields", *Journal of Liquid Chromatography & Related Technologies*, vol. 20, pp. 2857-2872, 1997.

[51] H. Morgan, M. P. Hughes, and N. G. Green, "Separation of submicron bioparticles by dielectrophoresis", *Biophysical Journal*, vol. 77, pp. 516-525, 1999.

[52] J. Rousselet, G. H. Markx, and R. Pethig, "Separation of erythrocytes and latex beads by dielectrophoretic levitation and hyperlayer field-flow fractionation", *Colloids and Surfaces a-Physicochemical and Engineering Aspects*, vol. 140, pp. 209-216, 1998.

[53] X. B. Wang, J. Vykoukal, F. F. Becker, and P. R. C. Gascoyne, "Separation of polystyrene microbeads using dielectrophoretic/gravitational field-flow-fractionation", *Biophysical Journal*, vol. 74, pp. 2689-2701, 1998.

[54] X. J. Wang, F. F. Becker, and P. R. C. Gascoyne, "Membrane dielectric changes indicate induced apoptosis in HL-60 cells more sensitively than surface phosphatidylserine expression or DNA fragmentation", *Biochimica Et Biophysica Acta-Biomembranes*, vol. 1564, pp. 412-420, 2002.

[55] J. Yang, Y. Huang, X. B. Wang, F. F. Becker, and P. R. C. Gascoyne, "Cell separation on microfabricated electrodes using dielectrophoretic/gravitational field flow fractionation", *Analytical Chemistry*, vol. 71, pp. 911-918, 1999.

[56] P. Lorrain, D. R. Corson, and F. Lorrain, *Electromagnetic Fields and Waves*. New York: W.H. Freeman and Company, 1988.

[57] J. M. Davis and J. C. Giddings, "Feasibility Study of Dielectrical Field-Flow Fractionation", *Separation Science and Technology*, vol. 21, pp. 969-989, 1986.

[58] A. Ajdari and J. Prost, "Free-Flow Electrophoresis With Trapping By a Transverse Inhomogeneous Field", *Proceedings of the National Academy of Sciences of the United States of America*, vol. 88, pp. 4468-4471, 1991.

[59] M. Washizu, S. Suzuki, O. Kurosawa, T. Nishizaka, and T. Shinohara, "Molecular Dielectrophoresis of Biopolymers", *Ieee Transactions On Industry Applications*, vol. 30, pp. 835-843, 1994.

[60] G. H. Markx, R. Pethig, and J. Rousselet, "The dielectrophoretic levitation of latex beads, with reference to field-flow fractionation", *Journal of Physics D-Applied Physics*, vol. 30, pp. 2470-2477, 1997.

[61] K. Kaler, T. B. Jones, and R. Paul, "Low-Frequency Micromotions of Dep-Levitated Plant-Protoplasts .1", *Journal of Colloid and Interface Science*, vol. 175, pp. 108-117, 1995.

[62] G. Fuhr, W. M. Arnold, R. Hagedorn, T. Muller, W. Benecke, B. Wagner, and U. Zimmermann, "Levitation, Holding, and Rotation of Cells Within Traps Made By High-Frequency Fields", *Biochimica Et Biophysica Acta*, vol. 1108, pp. 215-223, 1992.

[63] F. F. Becker, X. B. Wang, Y. Huang, R. Pethig, J. Vykoukal, and P. R. C. Gascoyne, "Separation of Human Breast-Cancer Cells From Blood By Differential Dielectric Affinity", *Proceedings of the National Academy of Sciences of the United States of America*, vol. 92, pp. 860-864, 1995.

[64] P. Curie, *J. Phys.(Paris) III*, vol. 3, 1894.

[65] J. Prost, J. F. Chauwin, L. Peliti, and A. Ajdari, "Asymmetric Pumping of Particles", *Physical Review Letters*, vol. 72, pp. 2652-2655, 1994.

[66] M. v. Smoluchowski, *Phys. Z*, vol. 13, pp. 1069, 1912.

[67] R. P. Feynmann, R. B. Leighton, and M. Sands, *The Feynmann Lectures on Physics*, vol. 1. New York: Addison-Wesley, 1966.

[68] M. Bier, "Brownian ratchets in physics and biology", *Contemporary Physics*, vol. 38, pp. 371-379, 1997.

[69] J. Rousselet, L. Salome, A. Ajdari, and J. Prost, "Directional Motion of Brownian Particles Induced By a Periodic Asymmetric Potential", *Nature*, vol. 370, pp. 446-448, 1994.

[70] L. Gorre-Talini, J. P. Spatz, and P. Silberzan, "Dielectrophoretic ratchets", *Chaos*, vol. 8, pp. 650-656, 1998.

[71] T. Schnelle, T. Muller, G. Gradl, S. G. Shirley, and G. Fuhr, "Dielectrophoretic manipulation of suspended submicron particles", *Electrophoresis*, vol. 21, pp. 66-73, 2000.

[72] J. S. Bader, R. W. Hammond, S. A. Henck, M. W. Deem, G. A. McDermott, J. M. Bustillo, J. W. Simpson, G. T. Mulhern, and J. M. Rothberg, "DNA transport by a micromachined Brownian ratchet device", *Proceedings of the National Academy of Sciences of the United States of America*, vol. 96, pp. 13165-13169, 1999.

[73] R. W. Hammond, J. S. Bader, S. A. Henck, M. W. Deem, G. A. McDermott, J. M. Bustillo, and J. M. Rothberg, "Differential transport of DNA by a rectified Brownian motion device", *Electrophoresis*, vol. 21, pp. 74-80, 2000.

[74] L. P. Faucheux, L. S. Bourdieu, P. D. Kaplan, and A. J. Libchaber, "Optical Thermal Ratchet", *Physical Review Letters*, vol. 74, pp. 1504-1507, 1995.

[75] T. Duke, "Separation techniques", *Current Opinion in Chemical Biology*, vol. 2, pp. 592-596, 1998.

[76] D. Ertas, "Lateral separation of macromolecules and polyelectrolytes in microlithographic arrays", *Physical Review Letters*, vol. 80, pp. 1548-1551, 1998.

[77] A. Ramos, H. Morgan, N. G. Green, and A. Castellanos, "AC electric-field-induced fluid flow in microelectrodes", *Journal of Colloid and Interface Science*, vol. 217, pp. 420-422, 1999.

[78] A. Ramos, A. Gonzalez, A. Castellanos, H. Morgan, and N. G. Green, "Fluid flow driven by AC electric fields in microelectrodes", in *Electrostatics 1999*, vol. 163, *Institute of Physics Conference Series*, 1999, pp. 137-140.

[79] A. Gonzalez, A. Ramos, N. G. Green, A. Castellanos, and H. Morgan, "Fluid flow induced by nonuniform ac electric fields in electrolytes on microelectrodes. II. A linear double-layer analysis", *Physical Review E*, vol. 61, pp. 4019-4028, 2000.

[80] A. B. D. Brown, C. G. Smith, and A. R. Rennie, "Pumping of water with ac electric fields applied to asymmetric pairs of microelectrodes", *Physical Review E*, vol. 63, 2000.

[81] J. A. Stratton, *Electromagnetic Theory*. New York: McGraw-Hill, 1941.

[82] D. C. Duffy, J. C. McDonald, O. J. A. Schueller, and G. M. Whitesides, "Rapid Prototyping of Microfluidic Systems in Poly(dimethylsiloxane)", *Anal. Chem.*, vol. 70, pp. 4974-4984, 1998.

[83] A. Ramos, H. Morgan, N. G. Green, and A. Castellanos, "Ac electrokinetics: a review of forces in microelectrode structures", *Journal of Physics D-Applied Physics*, vol. 31, pp. 2338-2353, 1998.

[84] Hunter, *Zeta Potential in Colloid Science*: Academic Press Inc., 1981.

4 DEP Characterisation – Materials and Methods

4.1 Introduction

This chapter outlines the concept of particle characterisation following surface modification via **dielectrophoretic (DEP) crossover** measurements, with the aim of using DEP to discriminate between particles on the basis of their surface properties and predict fundamental parameters of the interface. Following the definition of the crossover, the experimental set-up and surface modification materials and methods are described. Independent ζ-potential measurement techniques are also outlined, since as highlighted in Chapter 2, this parameter influences surface conductance and therefore may be possible to predict from DEP crossover data, using current theories of the double-layer.

4.2 Concept and Context

The DEP force derived in chapter 2[12]:

$$F_{DEP} = \pi a^3 \varepsilon_m \operatorname{Re}(K(\omega))\nabla|E|^2 \tag{2-56}$$

provides a discriminatory mechanism based on the combination of complex particle and medium permittivities through the Claussius-Mossotti factor:

$$K(\omega) = \frac{\varepsilon_p^* - \varepsilon_m^*}{\varepsilon_p^* + 2\varepsilon_m^*} \tag{2-57}$$

The force term also contains a factor relating to the gradient of the square of the electric field, thus various electrode geometries have been designed with well defined high and low field regions [1-4]. If the particle is more polarisable than the medium, $K(\omega)$ will be positive, compelling movement towards the high field regions and if less polarisable, the particle will correspondingly be pushed in the direction of the low field strength [5]. DEP has been used for some time in the characterisation of cells and other microscale biological entities via observation of this movement [6-10] and more recently, with improved electrode miniaturisation techniques, sub-micron particles also have begun to be characterised in this way [11-16].

---

[12] Expressed in terms of voltage amplitude to facilitate use in an experimental context

4.3 Definition of Crossover

The crossover is defined to be the frequency at which $\mathrm{Re}\{K(\omega)\}=0$ i.e. the frequency at which there is no force on the particle (Figure 4-1). Altering the frequency around this point therefore should cause the migration of particles to different field regions corresponding to their becoming more or less polarisable than the medium. The resultant crossover distribution as measured with reference to suspending medium conductivity should resemble Figure 4-2 – assuming the surface conductance of the particles to be finite and constant[13].

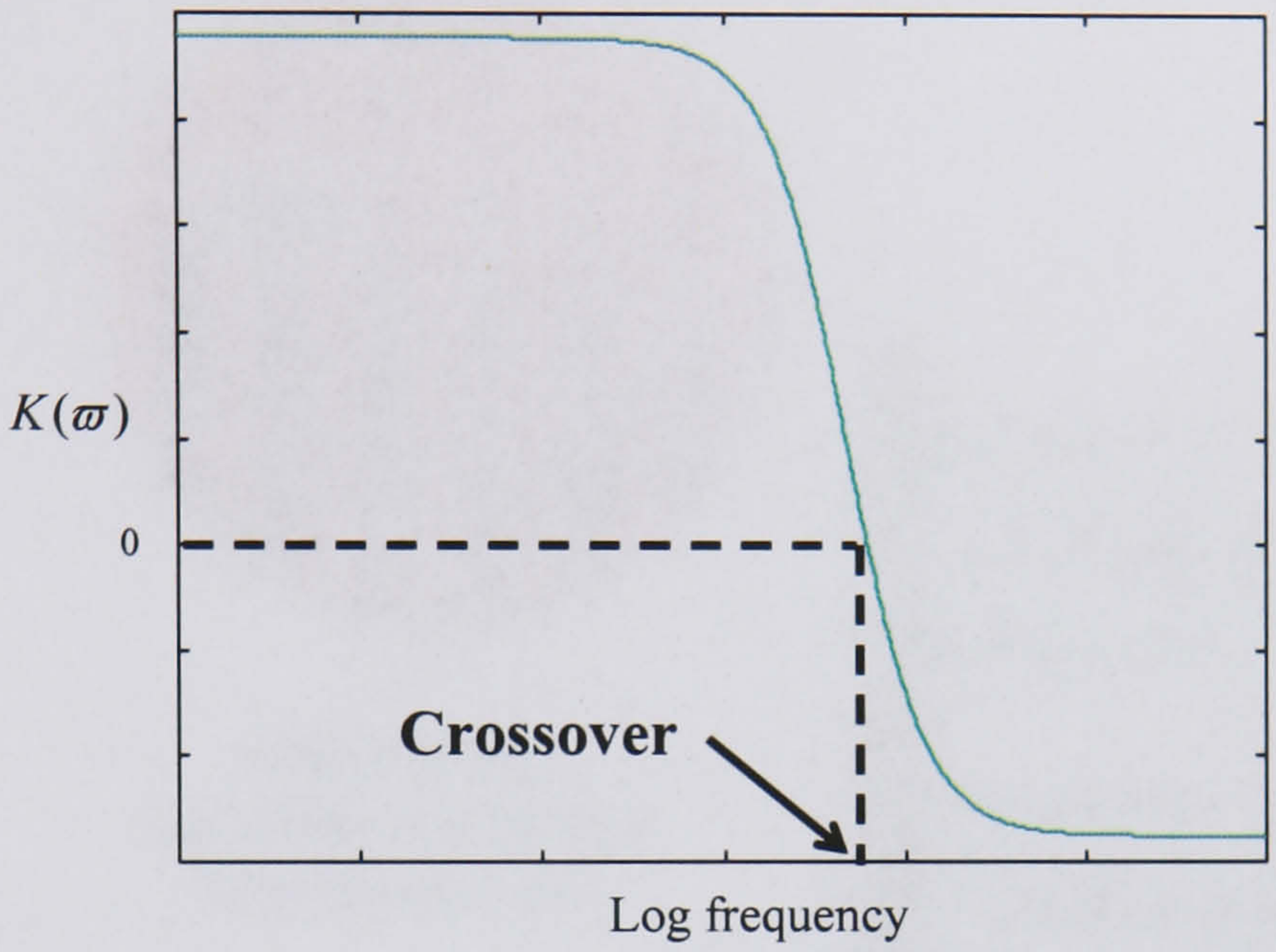

Figure 4-1

Schematic of the Claussius-Mossotti factor/frequency relationship showing definition of crossover

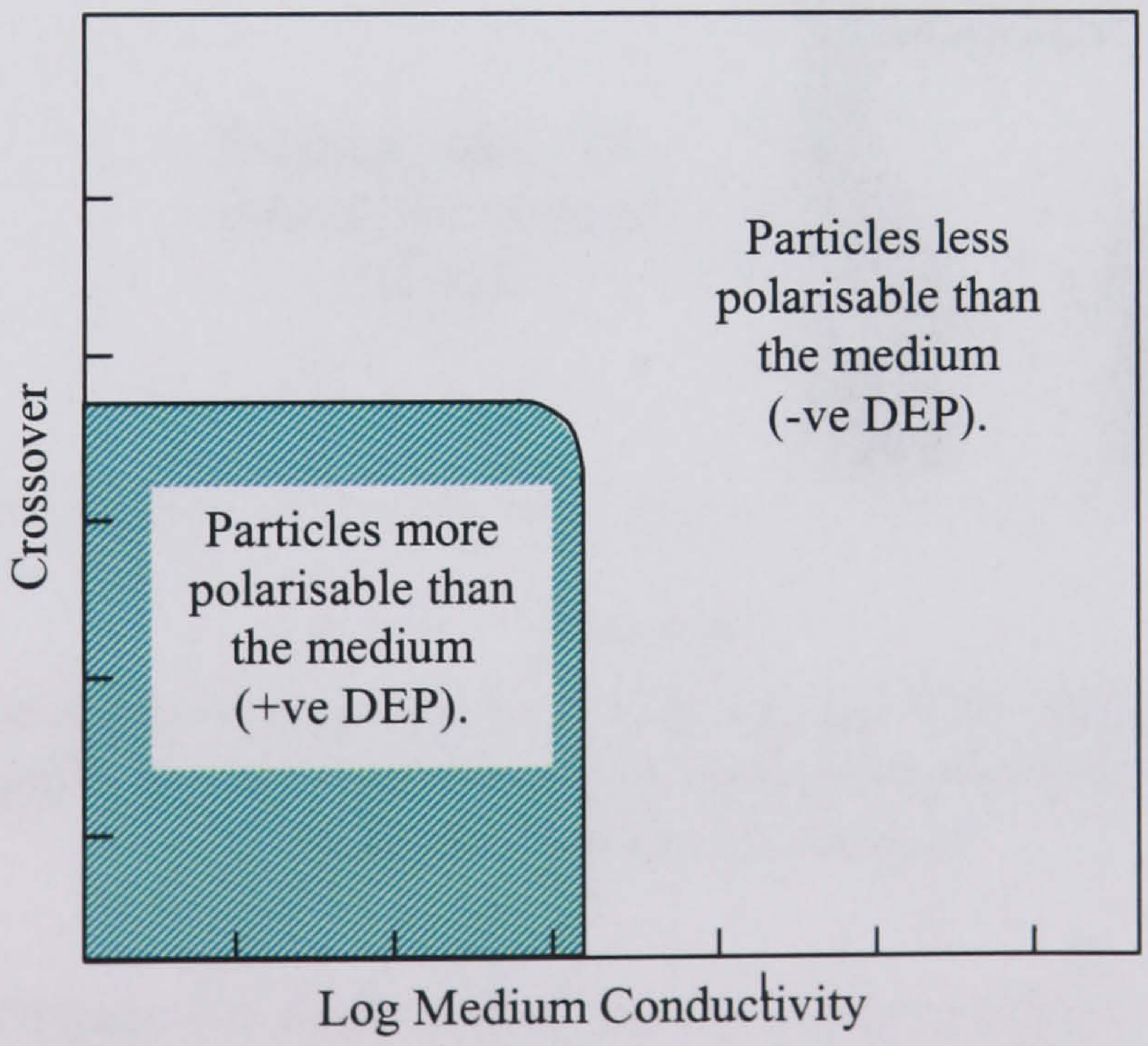

Figure 4-2

Indication of the frequency/conductivity ranges where positive and negative DEP should be observed

---

[13] Since it is the surface conductance that effectively controls the polarisation of real particles which have a lower permittivity than their suspending medium.

4.4 Electrodes

Interdigitated electrodes were fabricated in a castellated design [3] by direct write E-beam lithography (see Chapter 7). Figure 4-3 shows the basic schematic, previously utilised by Green *et al* who devised the final device structure shown in Figure 4-6 [11]. This has been modified so that more than one sample may be examined simultaneously without the intermingling of fluids (Figure 4-7).

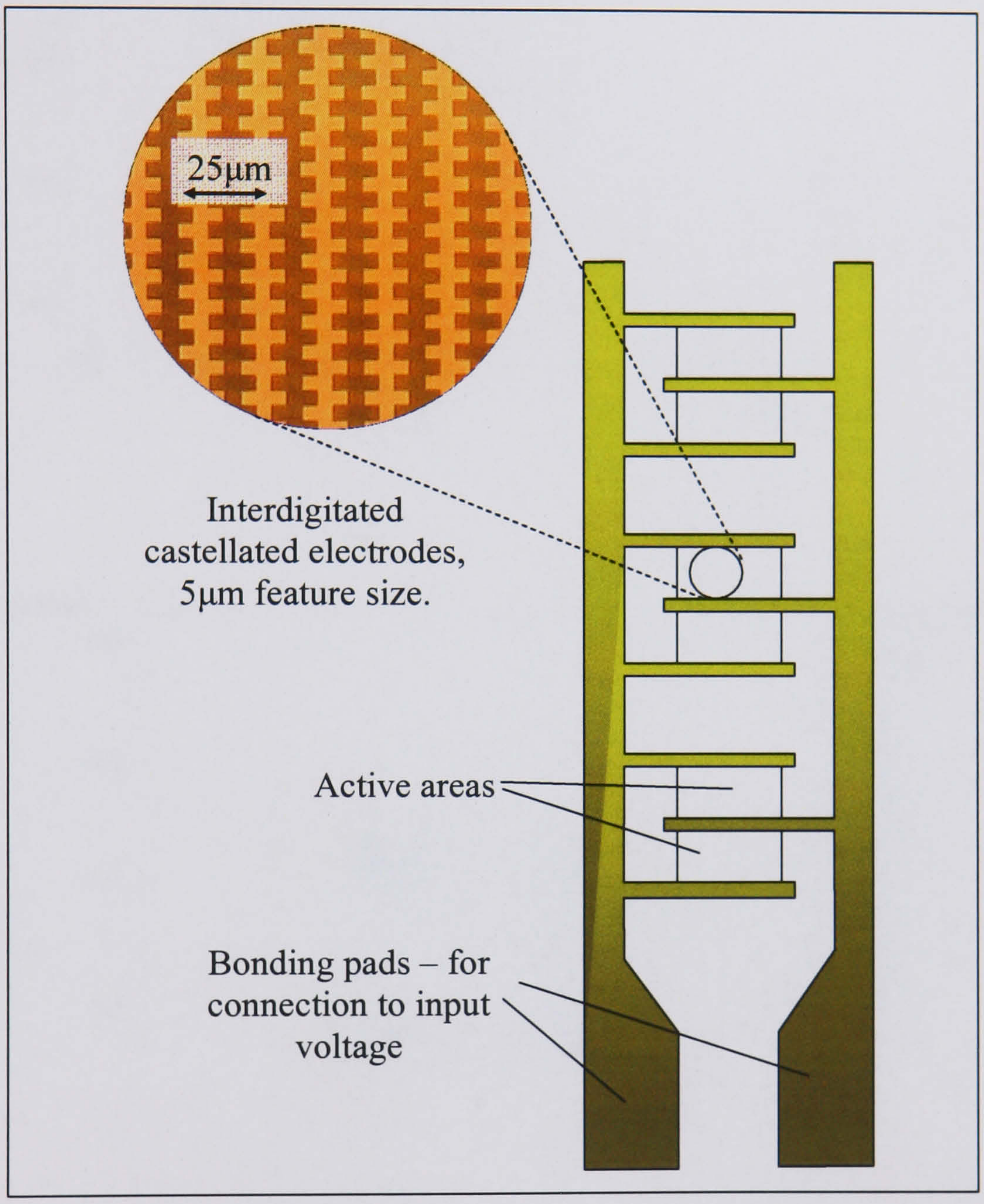

Figure 4-3

One of four electrode sets on the device constructed for DEP crossover characterisation, with shpe designed for the generation of non-homogeneous field. Aqueous samples are deposited on the active areas.

Figure 4-4 and Figure 4-5 show the electric and DEP potentials - the latter defined as $\boldsymbol{E}^2$, since the resultant force is a linear multiple of $\nabla \boldsymbol{E}^2$ - of both electrode arrangements, modelled using the finite element method [17] (see Chapter 6), highlighting the inhomogeneous nature of the field in this design. The high field points can be observed on the corners and edges of the electrodes and the low field points in the gaps in between. These are the areas where particles should collect under positive and negative DEP respectively [9].

1)

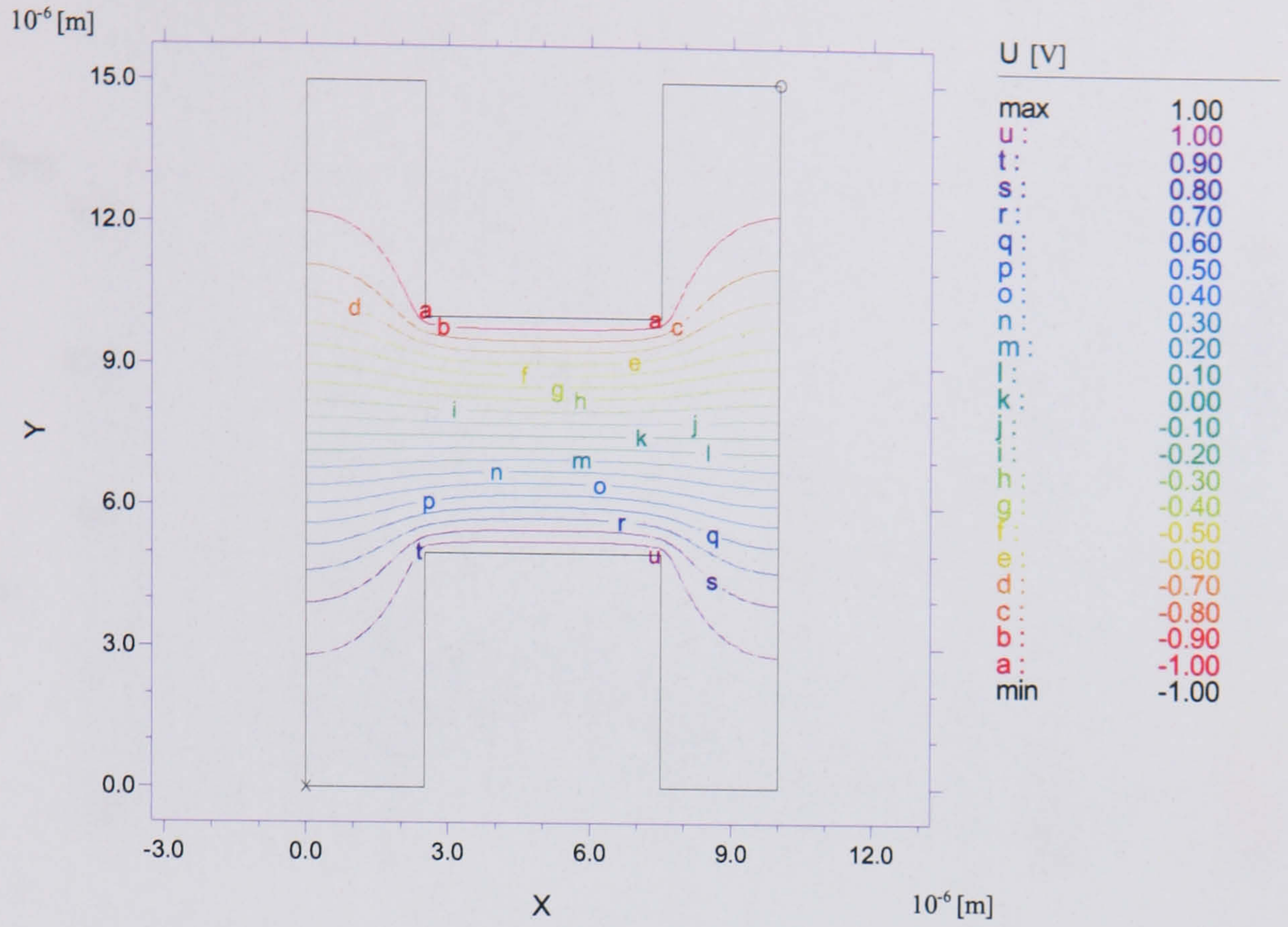

2)

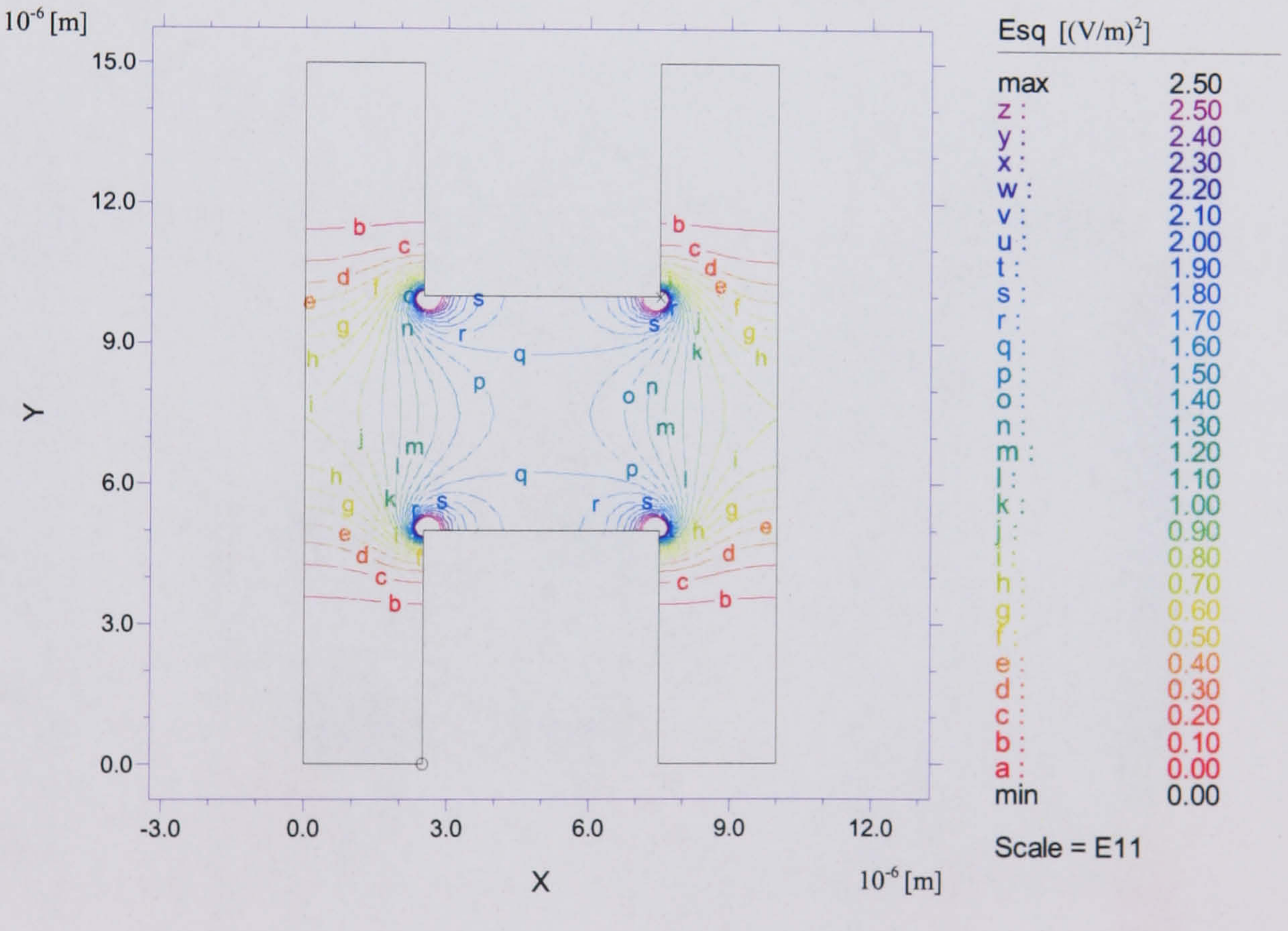

Figure 4-4

Flex PDE solutions of 1) electric and 2) dielectrophoretic potential (V and (V/m)^{2}resp.) of one cell of the symmetric castellated design. High electric field regions can be seen at the points of closest approach of the electrode, with points of strongest positive DEP on the protruding electrode corners. Negative DEP regions are correspondingly in the bays.

Reflective cell boundaries represented by vertical lines on the perimeter extremities, otherwise lines denote electrode boundaries. Length scale in metres.

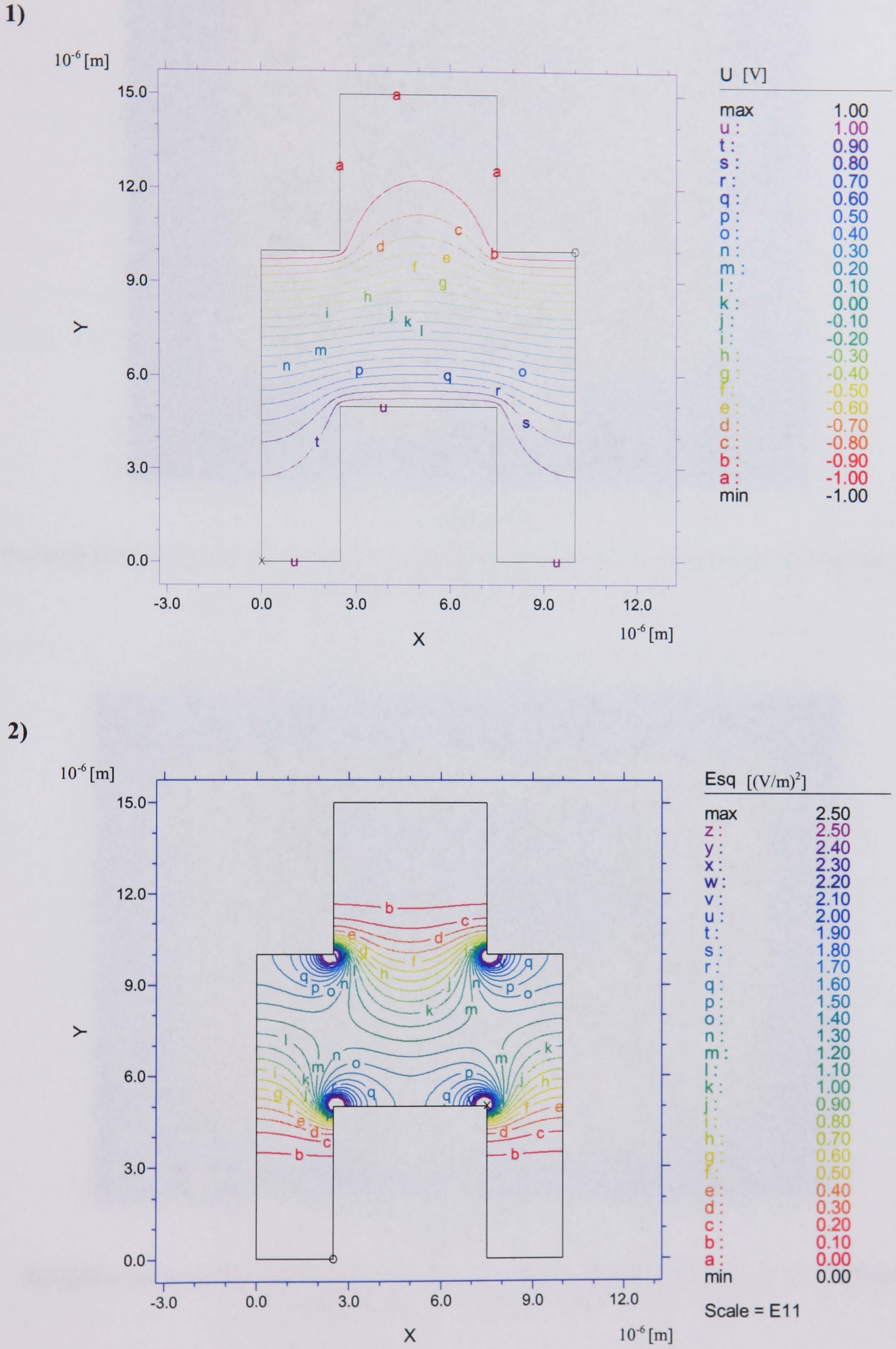

Figure 4-5

Antisymmetric castellated design, showing 1) electrical and 2) DEP potentials

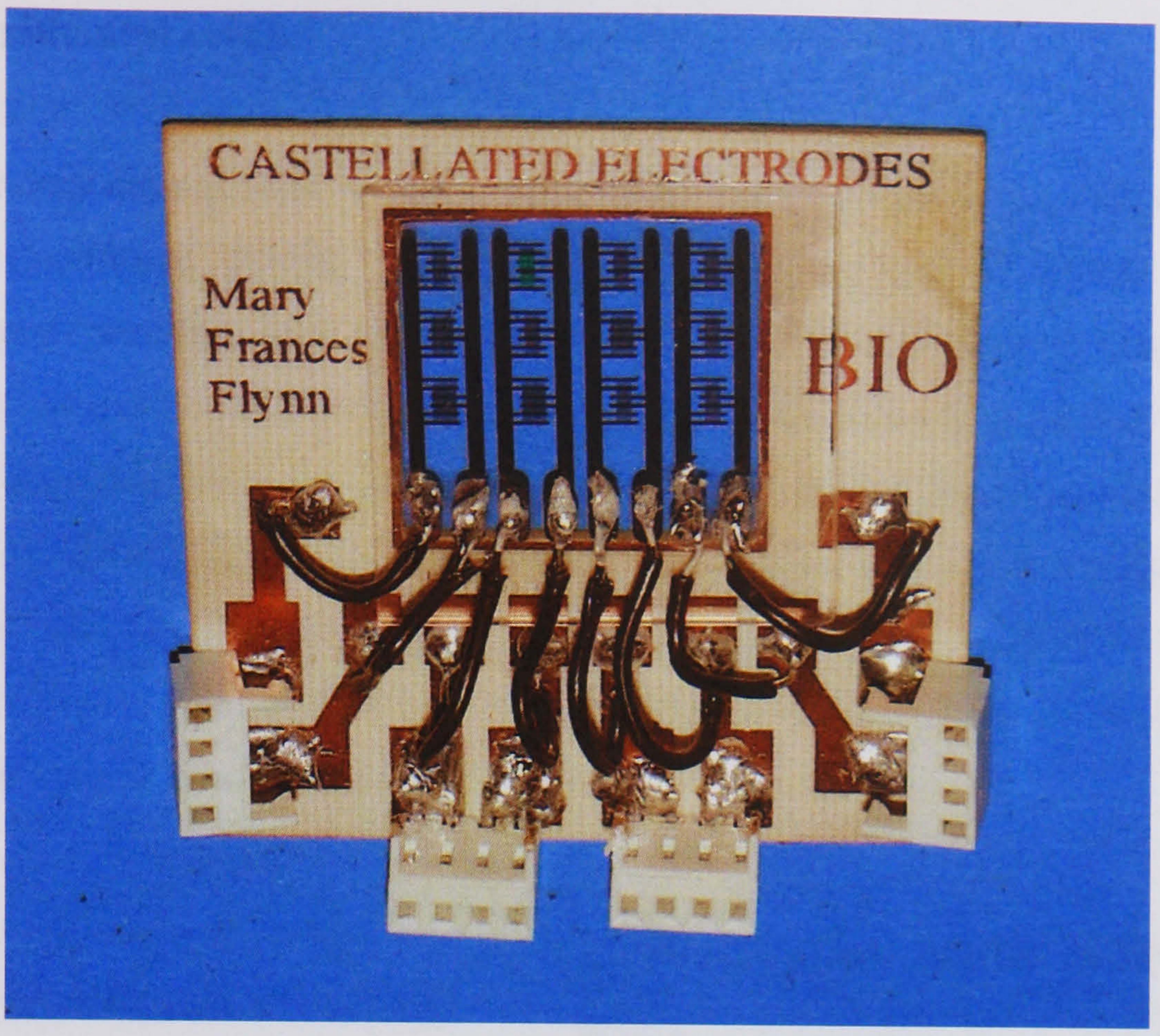

Figure 4-6

Working castellated device. Glass electrode substrate is fixed to a printed circuit board with connections soldered to molex receptors.

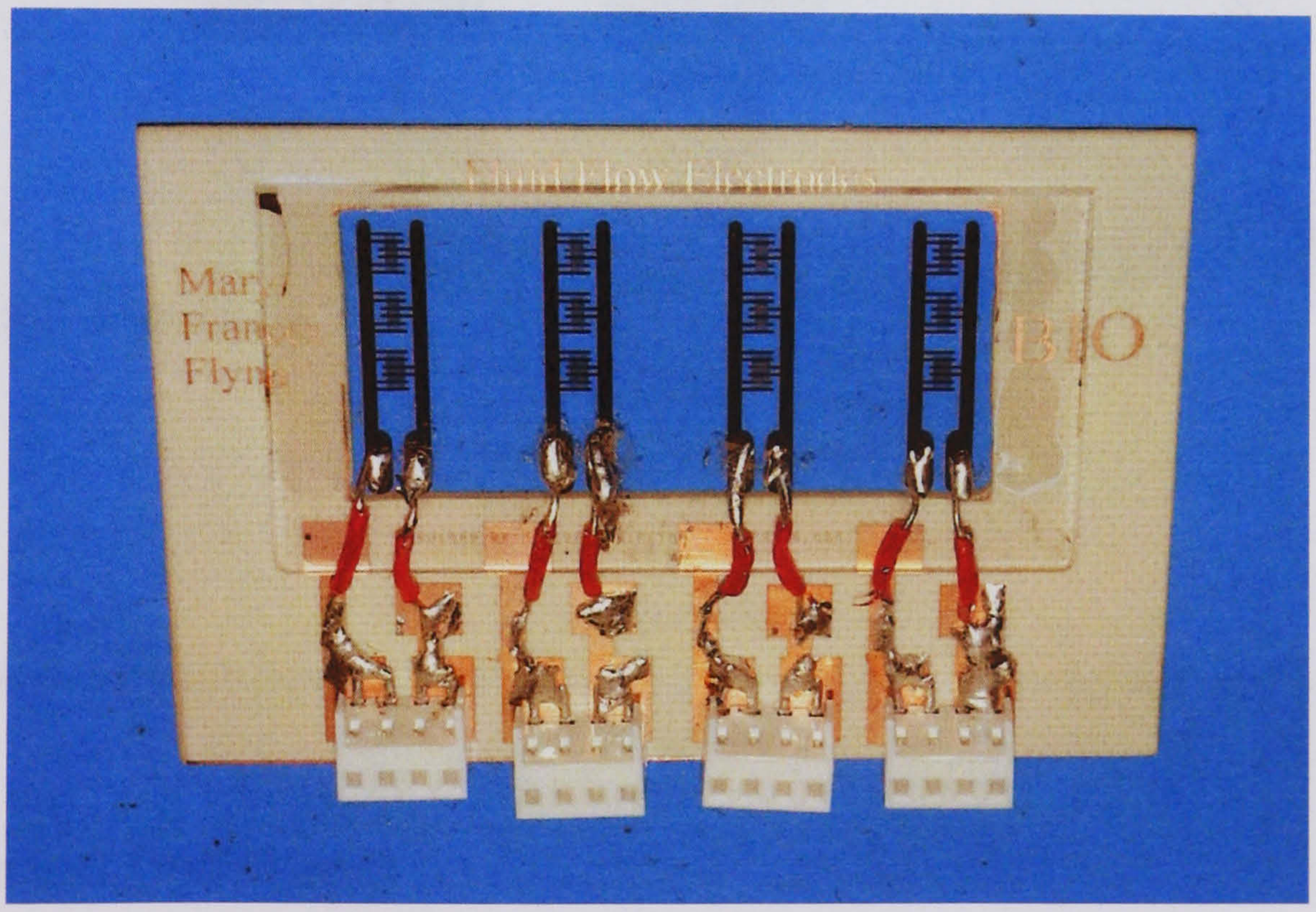

Figure 4-7

Modification to design with increased electrode pair spacing allowing the simultaneous deposition of multiple samples

4.5 Experimental setup

The laboratory arrangement is outlined in Figure 4-8. The electrodes were powered by an oscilloscope monitored 20MHz signal generator. For beads below ~0.3μm diameter, a 100MHz signal generator was used since positive DEP was frequently observed above 20MHz. The electrode resonance at high frequencies is therefore documented in Appendix 4-1. Data was gathered by a Nikon fluorescence microscope and digital camera, and a VCR used to record the images which were converted to AVI format using Miro image processing software. Samples were prepared in 1ml aliquots at a dilution of 1/1000 of the bottle concentration (2% solids), deposited in 30μl volumes on the active area of the device with a Gilson pipette and covered with glass coverslips.

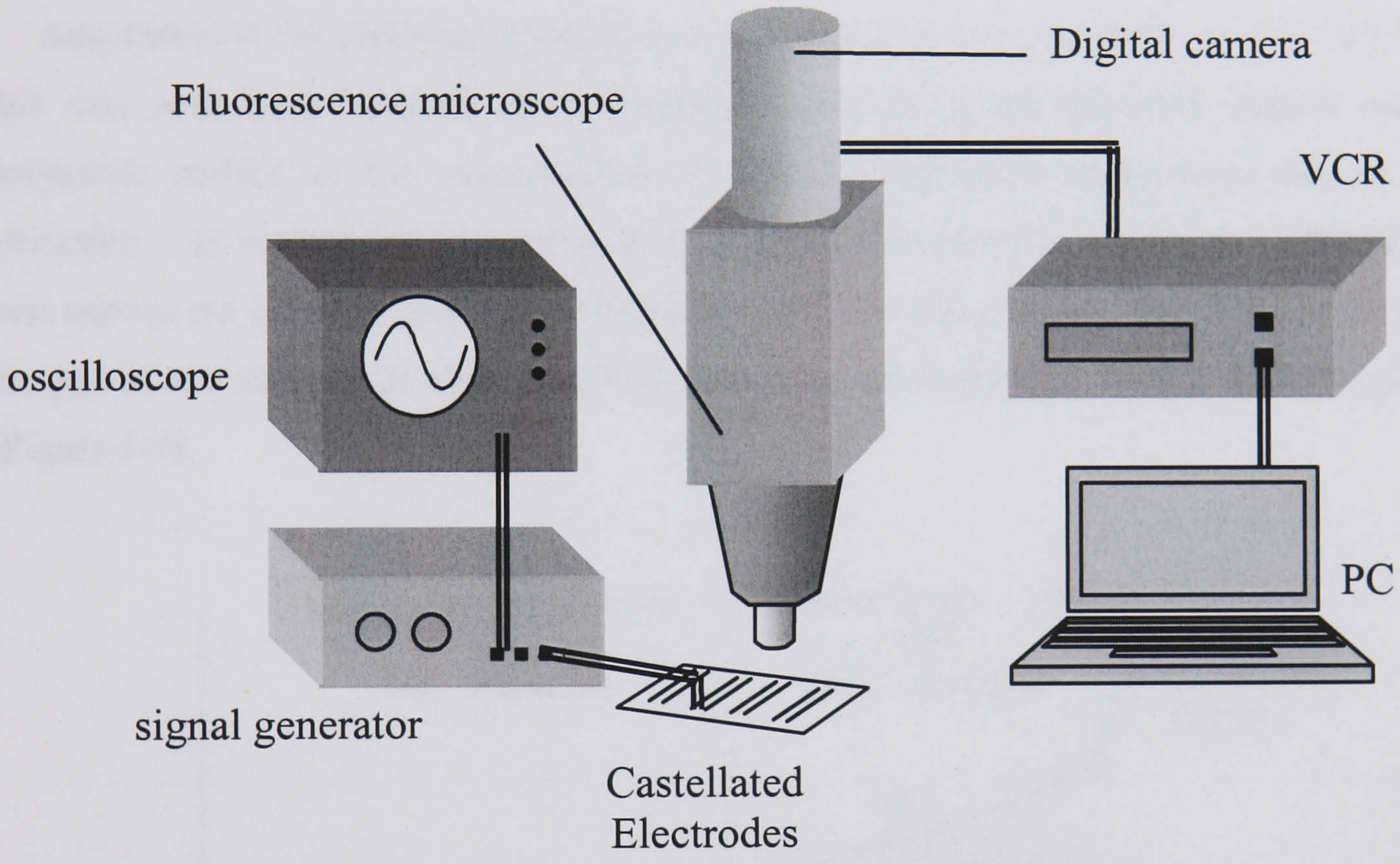

Figure 4-8

Experimental arrangement consisting of signal generation and monitoring, data collection and processing.

4.6 Surface Modification

The polarisation of latex being essentially due to surface conductance suggests that the DEP behaviour of colloidal latex particles would be affected by biological surface modification [18]. Possible applications of this include affinity separation technology and immunologically based tests and assays as well as other areas of medical diagnostics such as localisation techniques, enrichment and recombinant genetics. Surface modification is also of interest from a fundamental perspective with the insight it may give into the possible mechanisms of the relaxation process and the physical parameters of the system.

4.7 Coupling Mechanisms

There are currently many different techniques available for the attachment of biomolecules to solid phase supports [19]. These essentially fall into three generic categories:

- Adsorption
- Covalent attachment to functionalised substrates
- Coupling via generic binding proteins

4.7.1 Adsorption

Adsorption at the solid-liquid interface is due primarily to hydrophobic forces [20] i.e. in this case attractions between the hydrophobic portions of the adsorbed ligands and the polymeric surface of the microspheres. In order to minimise interference due to ionic attraction – an undesirable phenomenon due to its environmental sensitivity – adsorption is best carried out on or around the isoelectric point (pI) of the protein. This is the point where the pH of the solution is such that there is no net electrokinetic charge on the molecule (Figure 4-9).

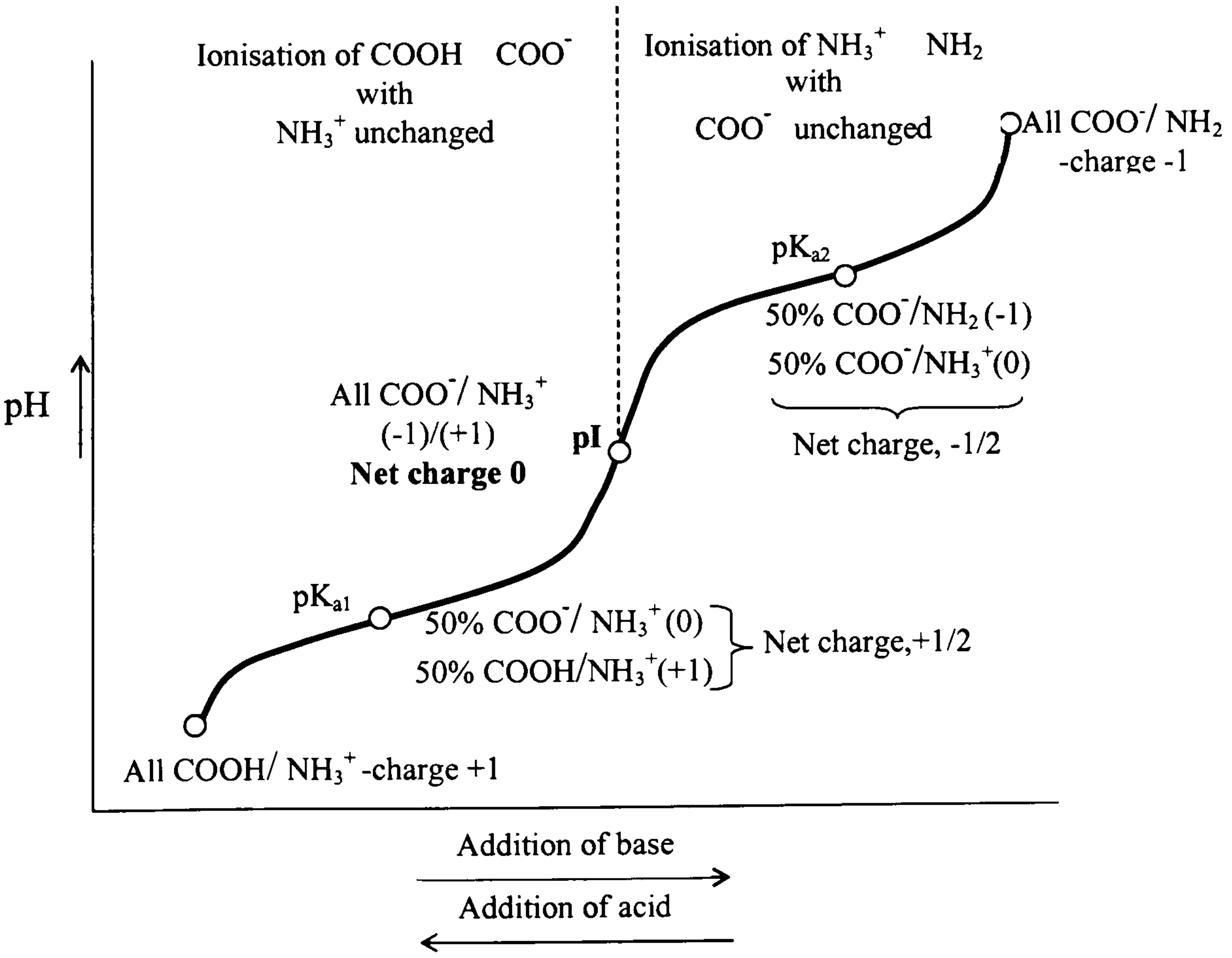

Figure 4-9

Illustration of the pH/pI relationship of an amino acid (protein building block) with respect to the pK$_a$ values

With respect to the bead surface, a distinction should be made between the pI, often referred to as the point of ζ reversal (p.z.r.), and the point of zero charge (p.z.c.). The p.z.r. corresponds to the net balancing of electrokinetic charge on the bead such that no movement is induced under the action of an applied E-field whereas the p.z.c. denotes the point where there is *no* native charge on the bead surface (Figure 4-10). In the latter case, however, the particle may still possess electrokinetic charge due to the presence of specifically adsorbed ions i.e. covalently linked moieties or Van der Waals adsorbates. Only in the absence of specific adsorption do the p.z.r. and the p.z.c. co-incide.

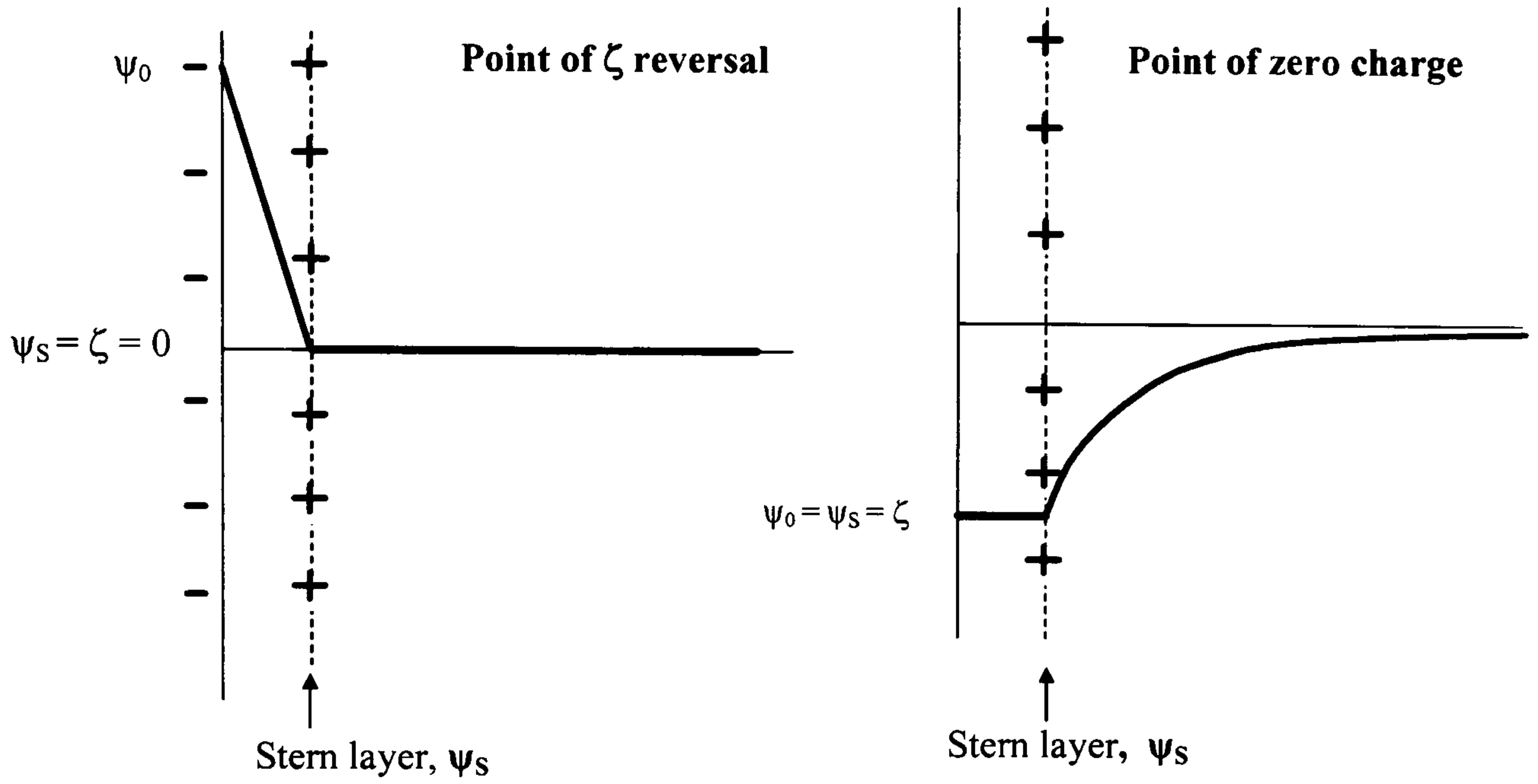

Figure 4-10
p.z.r and p.z.c. on a phase boundary, illustrating the effect on the Stern and diffuse layers [20]

4.7.2 Covalent Attachment

Covalent attachment of biological ligands basically involves the chemical activation of the surface molecular groups on the substrate (or ligand) so that there is an accessibility to bonding with complimentary groups on the ligand (or substrate). This procedure must be carried out in conditions favourable to the reaction in terms of pH, temperature and agitation level and must be blocked on termination so that no further contaminant adsorbates may have access to unoccupied binding sites.

4.7.3 Biotin-Avidin binding

Forming one of the strongest non-covalent bonds in nature – with a dissociation constant of 10^{-15} [21]- the biotin-avidin complex is being used increasingly in many modified-surface methodologies [22]. Apart from the high affinity with the vitamin biotin or biotin containing complexes other main advantages of using avidin or its relatives include ease of binding, using most adsorption or covalent protocols, with retention of biological activity [22].

4.8 Surface modification materials

4.8.1 Substrate

The substrate to be modified was in all cases carboxylated latex particles purchased from Molecular Probes (Oregon) (Figure 4-11). These were fluorescently loaded, emitting in the green (505-515 nm) or red (535-575nm) and ranging in diameter from 216-1000nm. The specified pI of these beads is ~2 [23].

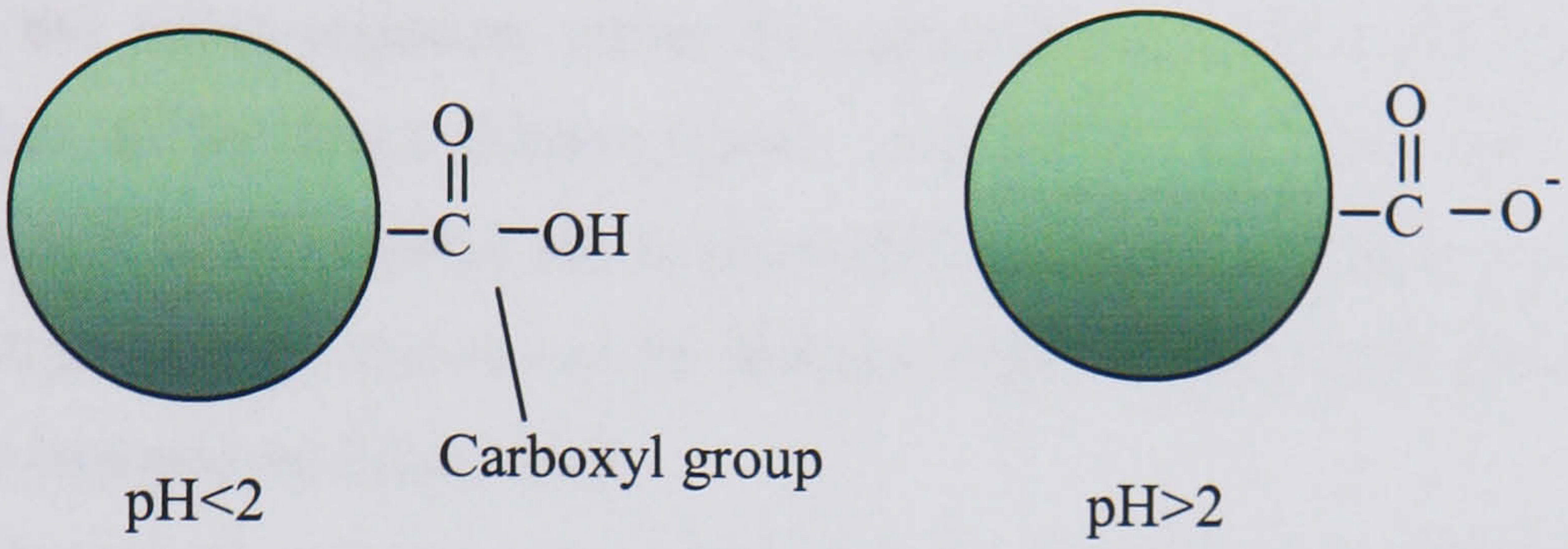

Figure 4-11

Fluorescent microsphere with highlighted carboxyl group. These are predominantly de-protonated at pH>2 giving beads a net negative charge.

4.8.2 Suspending medium

The suspending medium used was potassium chloride (KCl) salt solution prepared at various molarities using water deionised by reverse osmosis (RO). The molarity/conductivity relationship, as measured with a hand held dc probe meter, is linear, as shown in Figure 4-12. Molarity increments were defined on a logarithmic basis so that log-log plots of the crossover data could be made.

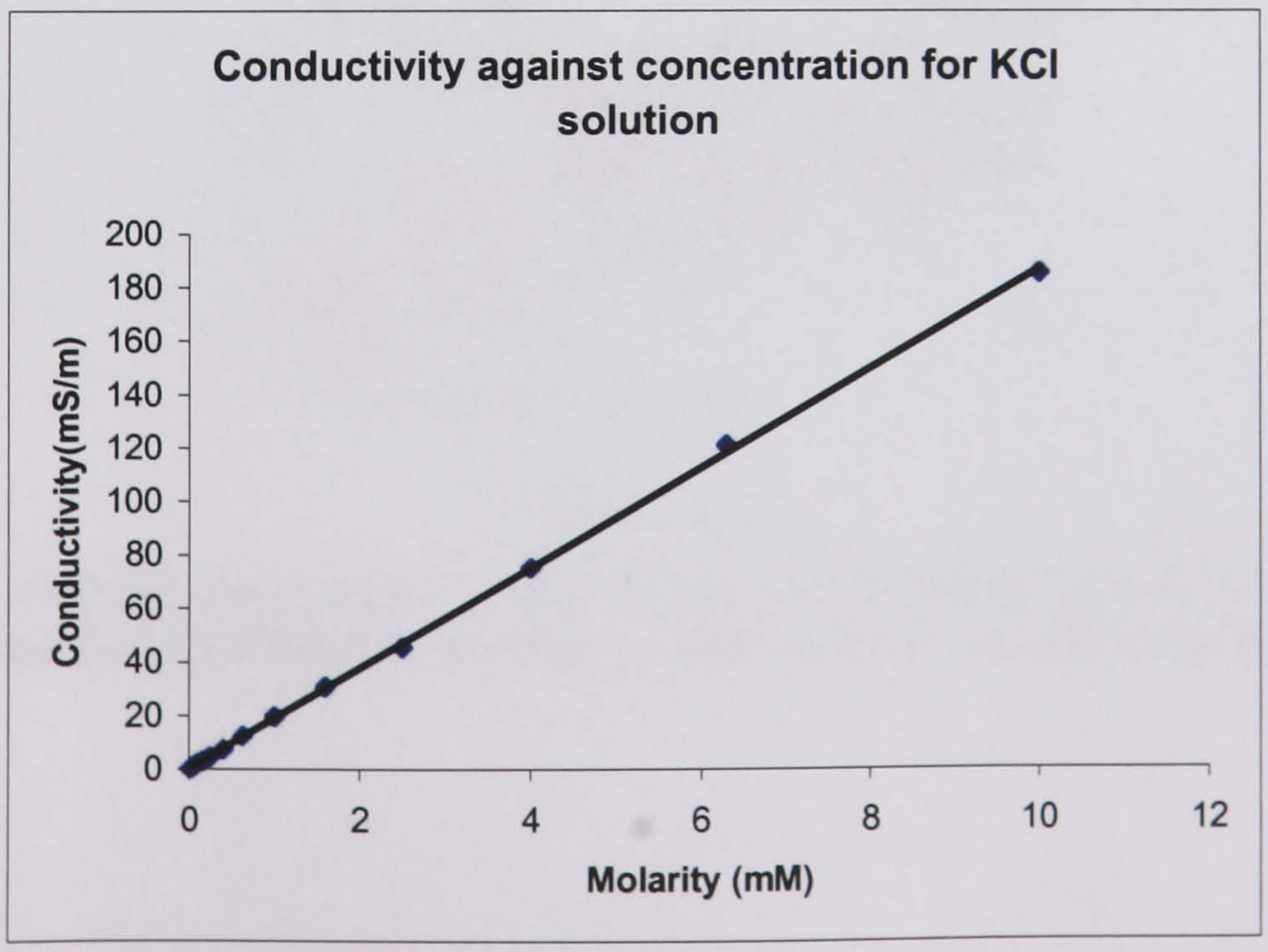

Figure 4-12

Linear relationship between molarity and conductivity of KCl solution.

4.8.3 Immunoglobulin G Antibody

Antibodies [24, 25] are specifically structured proteins that are produced in the body as part of the immune response to the presence of a foreign agent. They are manufactured by the B-lymphocytes on encountering the macromolecular structures on the invader surface known as antigens. The antibodies attach themselves to the antigens which can lead to uptake by lymphocytes or activation of other parts of the immune system leading to the destruction of the micro-organism either by agglutination, where the foreign cells are clumped together, or by direct disintegration – cell lysis. Complementary antibodies are formed as the result of introducing the primary antibodies into a foreign host, so that these are now the antigen carriers and cause the immune response described above. They bind to spieces specific epitopes on the primary.

Antibodies belong to a group of proteins known as the immunoglobulins (Ig). Their structure consists of two identical heavy chain protein molecules and two identical light chains linked and stabilised by disulphide bridges. There are five classes of Ig molecules as determined by the different antigenic and structural properties of the H chains. The most common in plasma or serum is Ig Gamma (IgG), shown schematically in Figure 4-13. The antibody specific section is outlined with the stem, known as the F_c group, defining the axis of symmetry of the molecule.

The proteins used for surface modification of the carboxylated beads were mouse IgG and its complementary antibody, which have a molecular weight of 150 kDa and a near neutral pI [26].

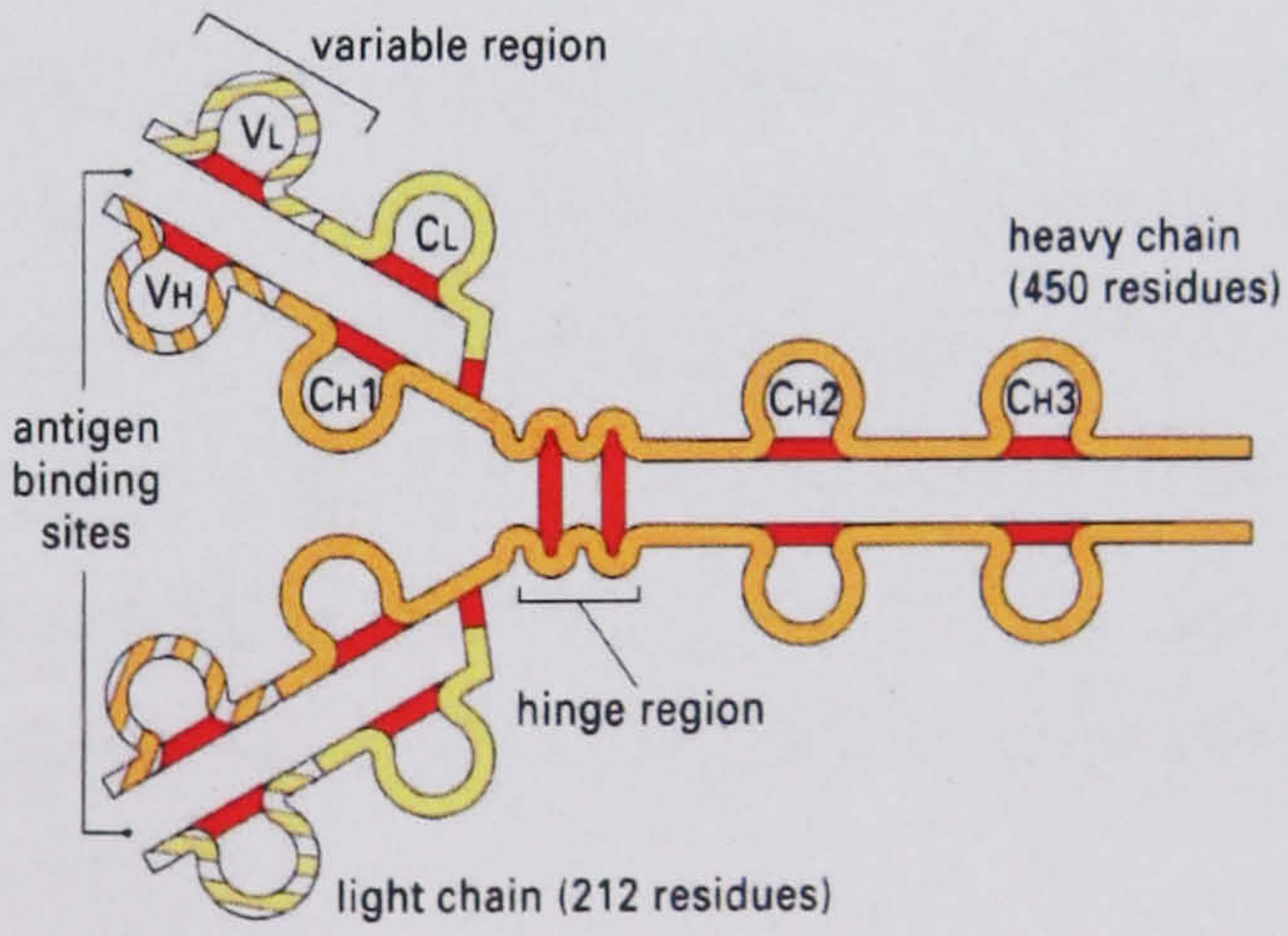

Figure 4-13

IgG Structure, showing heavy chains, light chains, and antibody specific groups [27]. The horizontal heavy chain (F_c section) is inactive in the uptake of antibodies.

4.8.4 Biotin

Biotin (also known as vitamin H) is a small, non-aromatic heterocyclic molecule with a 4-carboxybutyl tail (Figure 4-14). A variety of its derivatives are available in which the biotin moiety is connected (through the 4-carboxybutyl group) to a linker molecule that can be attached directly to various biological ligands, rendering them suitable for subsequent immobilisation via avidin or its derivatives. It has a molecular weight of 224.31Da.

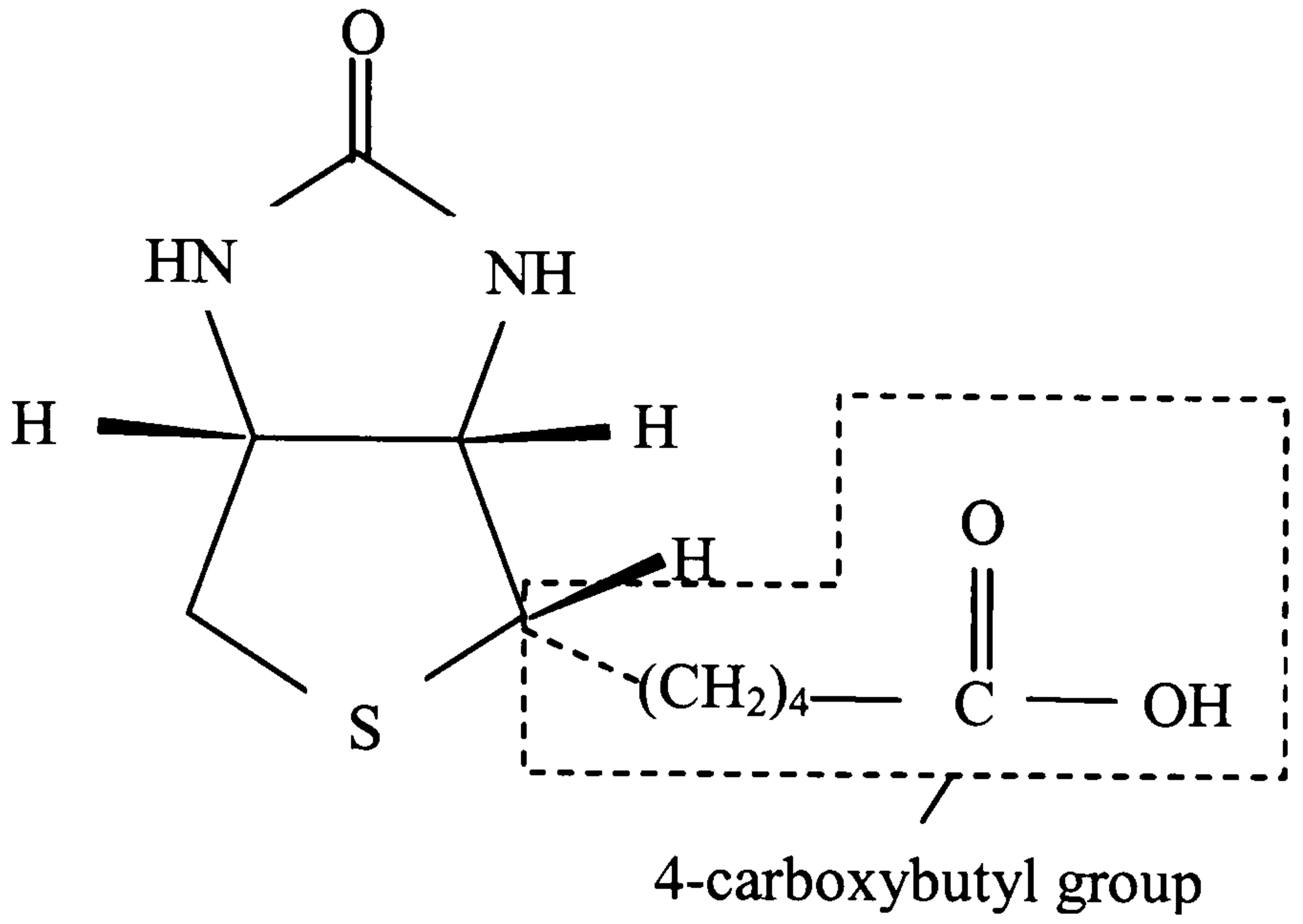

Figure 4-14
Molecular structure of the biotin molecule.

4.8.5 Avidin

Avidin, [21, 28, 29] synthesized in the hen oviduct, is a glycoprotein of molecular weight 68kDa which occupies about 0.05% weight/weight (w/w) of the total protein content of the hen egg white. Native avidin is a tetrameric protein composed of four identical subunits. Each subunit is glycosylated (i.e. contains a sugar tail) and has one binding site for biotin. The isoelectric point of native avidin is 10.5. Avidin, native or modified is highly soluble in water or salt solution at physiological pH (7.5-8.0). Its basic glycoprotein nature, however, can result in some non-specific binding, as observed in various studies. For a representation of the structure of avidin, see [29].

4.8.6 Streptavidin

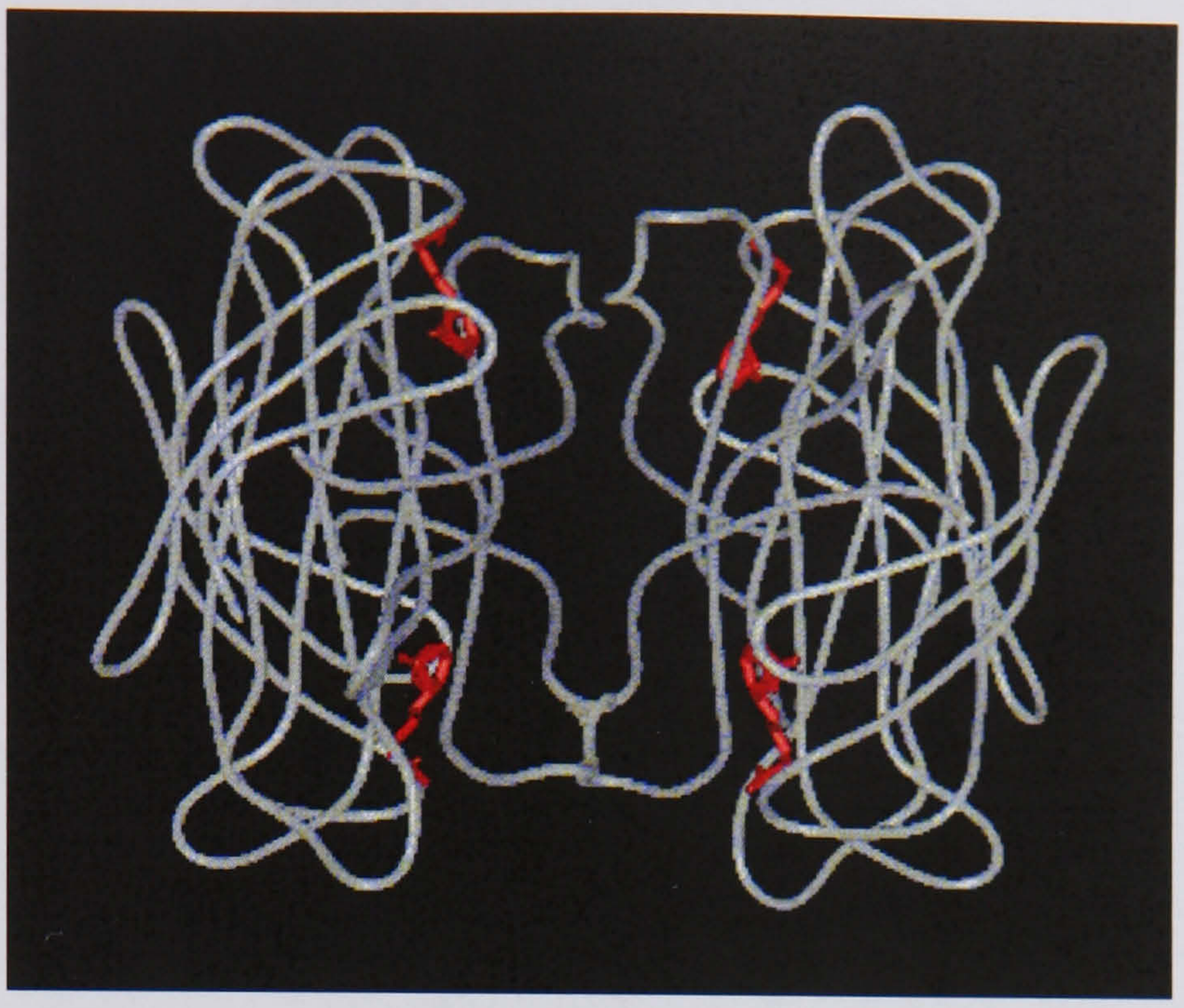

Figure 4-15[14]

Folded structure of streptavidin with biotin binding sites highlighted in red.

Streptavidin, shown diagrammatically in Figure 4-15, is a bacterial analogue of avidin isolated from streptomyces avidinii [30]. It has a near neutral pI and is non-glycosylated therefore does not show the non-specific binding attributed to the native avidin. The absence of the carbohydrate tails brings down its molecular weight to 64kDa. The biotin-binding subunits of streptavidin are the same as those of avidin, however, and therefore it has similar biotin affinity, localising 4 moles per mole of protein with high selectivity.

4.8.7 Biotinylated oligonucleotide

Oligonucleotides are small fragments of deoxyribonucleic acid (DNA) [31]– the famous, spiral molecular blueprint for most of the constituents of life. DNA is made up of sequences of four different units called nucleotides - adenine, guanine, cytosine, thymine or, by convention, A, G, C and T – with a phosphate sugar appendage. These are linked together by means of a backbone comprised of the phosphate-sugar groups with a certain directionality, the syntax for which is "5 prime to 3 prime" (5'-3') – where 5' denotes the position of the phosphate group. Each base has an affinity for one particular partner – A with T and G with C. Complementary strands can thus be formed which interweave in opposing sequences (5' end matched with 3') to form the well-known 'double helix' structure (Figure 4-16).

---

[14] Figure obtained from: http://www.amber.ucsf.edu/amber/tutorial/streptavidin/

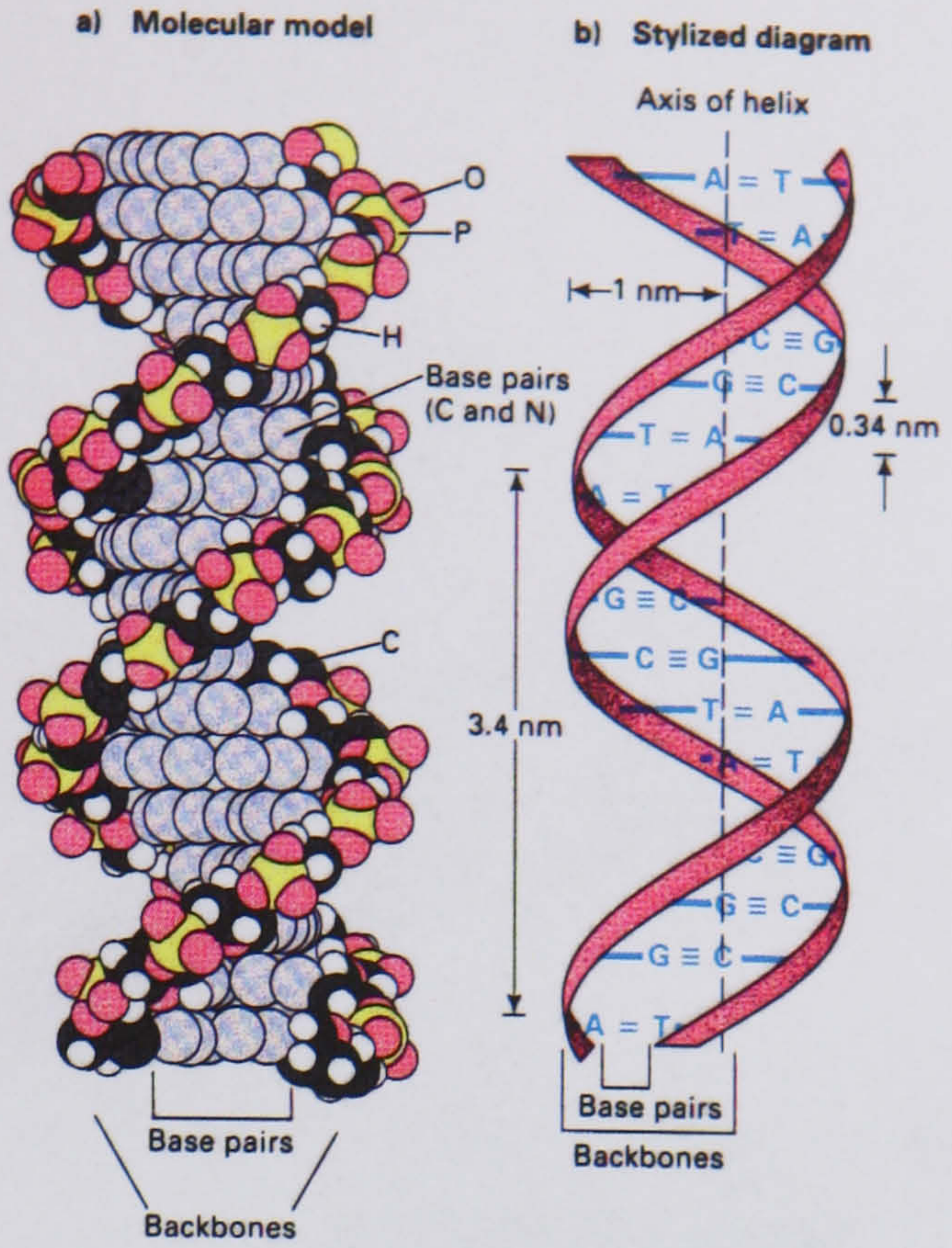

Figure 4-16

Section of DNA, highlighting length scale and base pairing [32]

In this study, 20 base, single stranded oligonucleotides were used, purchased from MWG Biotech, with a base sequence of 5' TAT CGA TAA GCT TGA TAT CGA ATT GCA GCC 3'. These were biotin labelled at the 5'end. Non-biotinylated complementary strands were also purchased.

4.9 BCA assay

The amount of protein on the beads was assessed using the Pierce™ BCA protein assay which operates on the principle of the reduction of Cu^{2+} ions in bicinchoninic acid to Cu^{+} on reaction with protein in an alkaline medium. This produces a purple complex, the amount of colour depending on the number of peptide bonds in the protein, and varying linearly over a wide range of protein concentrations [30].

4.9.1 Method

Samples were mixed at an 8-1 ratio with the working reagent complex and incubated at 37 degrees for 30 minutes. Spectrophotometer measurements were done at 562nm against a standard of uncoated beads or alternatively the supernatant saved after spin-down and a comparison made with the original protein solution. Where possible a calibration curve of bovine serum albumin (BSA) was used and the results quantified using a conversion table supplied by the manufacturers of responses normalised against this particular protein. Otherwise, a separate calibration curve had to be produced using the protein in question (Figure 4-17).

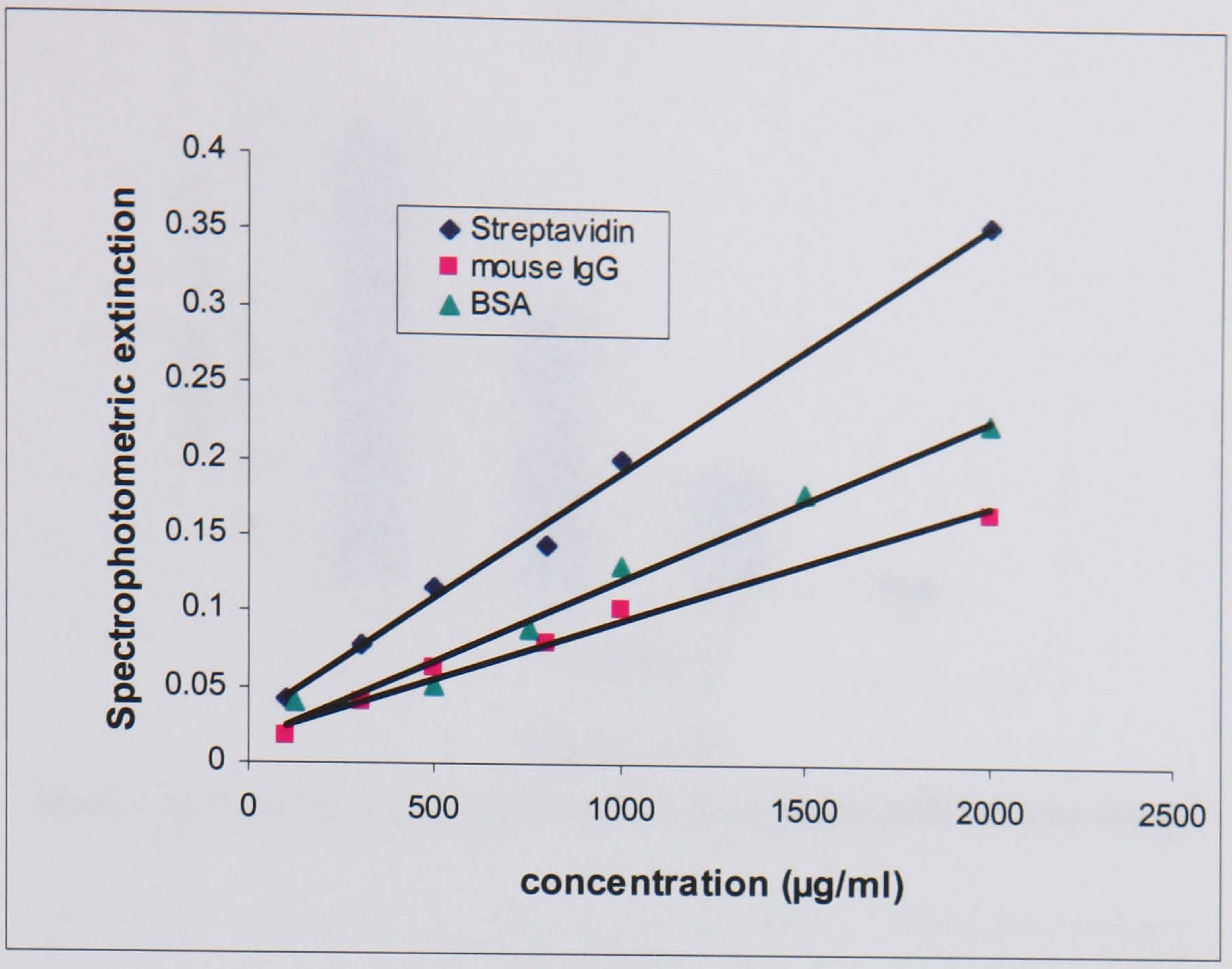

Figure 4-17

BCA assay response of various proteins. The linear scale facilitates calibration.

4.10 Surface modification procedures

4.10.1 Adsorption

Buffers were prepared with a range of pH's from 5.8-8 using citric acid and sodium phosphate. The beads were mixed with the buffers and the protein for 2-4 hours with agitation at room temperature. The microspheres were added to the protein rather than vice versa in order to maximise efficiency, making an even distribution more likely [33]. The pH ranges for IgG and streptavidin were those specified as the region containing the pI [26]. The pI of avidin, however, at 10.5 is far from the neutral pH experimental conditions intended for crossover measurements. Since adsorption is highly susceptible to a back reaction [20] the large change in the pH required for the DEP experiments could greatly affect the amount of protein on the beads. Therefore the adsorption test was carried out around the neutral pH in order to observe directly the amount of protein which was initially stable under these conditions. The amount of protein on the beads was measured using the BCA assay by directly analysing the protein coated bead samples and subtracting the reading from an uncoated control. The results can be seen in Figure 4-18-Figure 4-20.

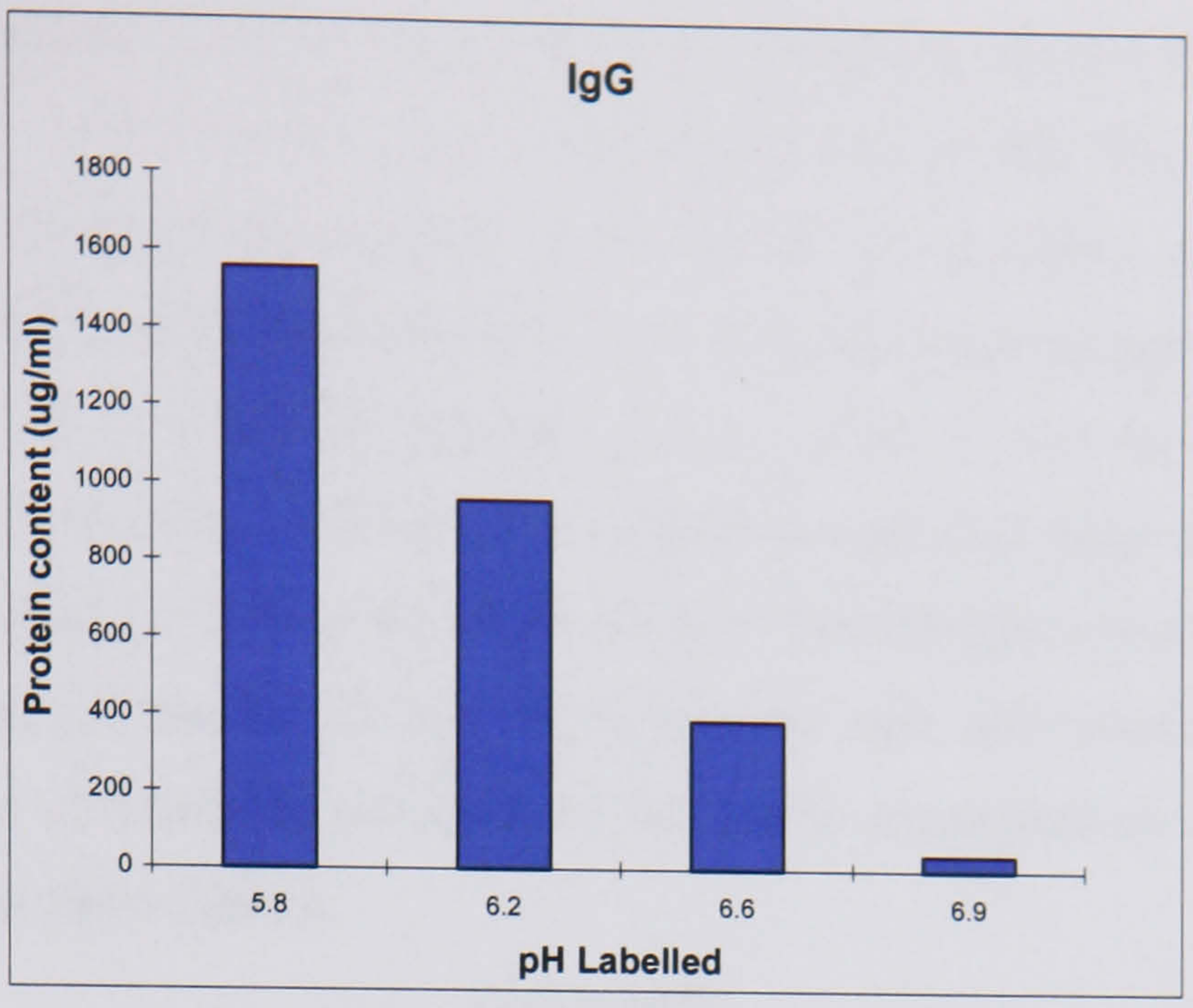

Figure 4-18

Mouse IgG adsorption response at various buffer pHs around the pI.

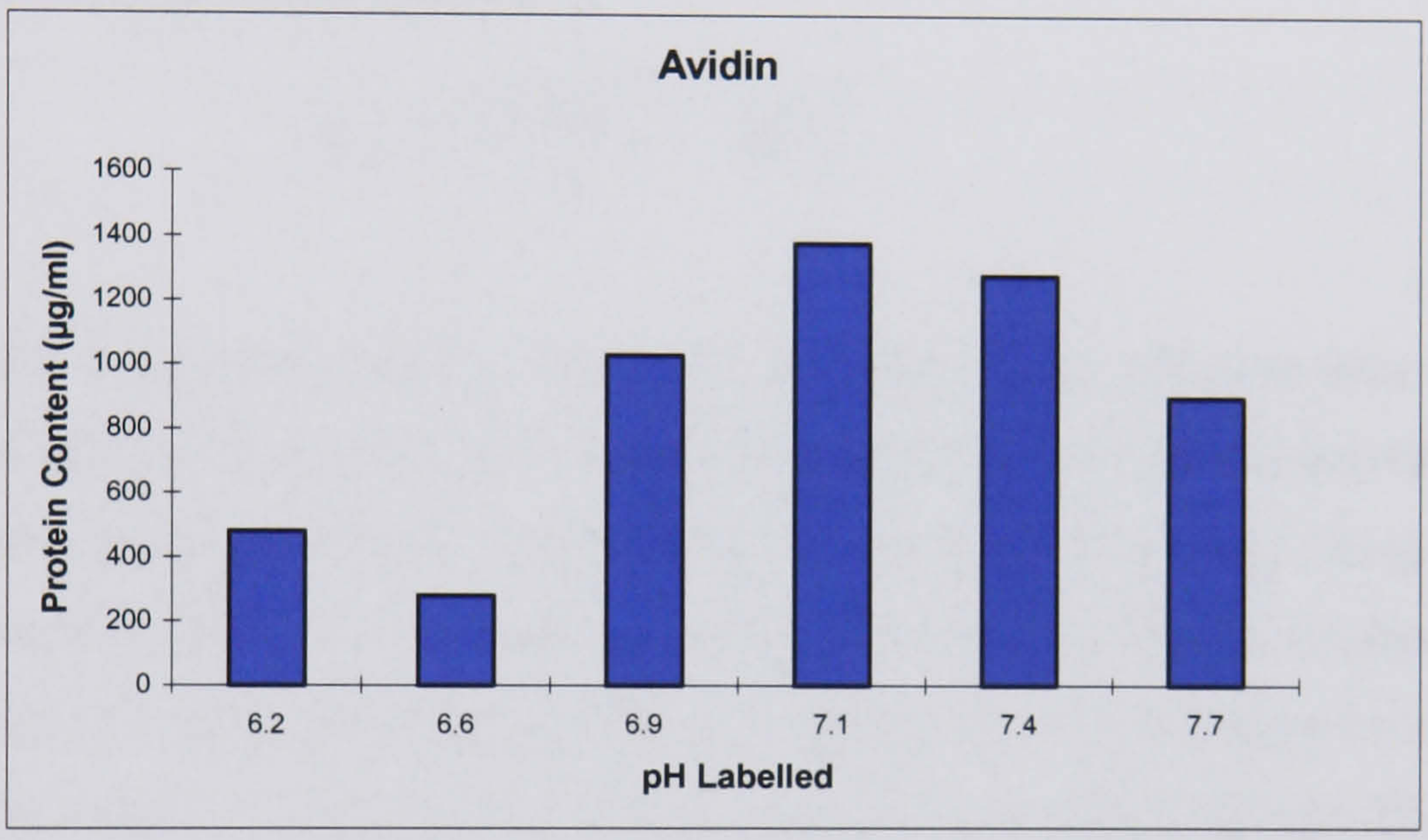

Figure 4-19

Avidin adsorption in the neutral pH range, far from the pI of 10.5

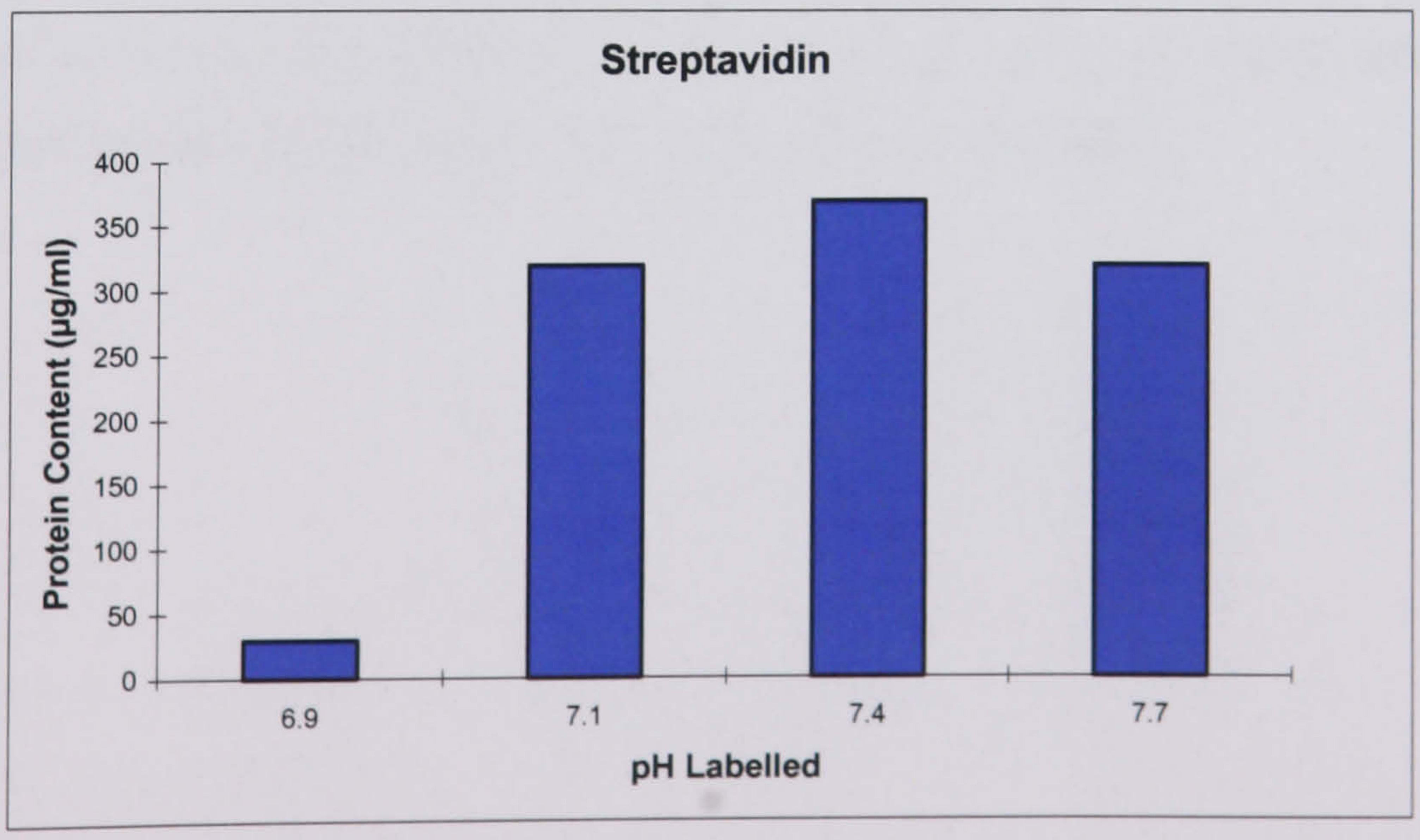

Figure 4-20

Streptavidin adsorption in the pH range around the pI.

Because the adsorption of IgG appeared to be increasing toward the lower end of the specified pH range, with very little adsorption around neutral pH, this was not deemed an adequate surface modification method with which to conduct consistent crossover experiments. Avidin, by contrast, produced a very high adsorption around a neutral pH. This was undoubtedly due to large electrostatic forces, since it was so far away from the isoelectric point. Streptavidin coverage also peaked around this range although with lower absolute quantities of protein. In order to assess how this translates into molecular coverage of the bead surface the amount of protein molecules were calculated by multiplying the molar quantities by Avogadro's number. At the bottle concentration of 2% volume, the number of beads per micro litre is:

$$n = \frac{0.02 \times 10^{-9}}{\frac{4}{3}\pi a^3} \tag{4-1}$$

And therefore the total surface area/μl is:

$$A_{tot} = \frac{6 \times 10^{-11}}{a} \quad \left[m^2\right] \tag{4-2}$$

Streptavidin is generally tightly compacted and takes up an effective area of 5nm×5nm [30] and therefore the maximum number of potential binding sites for streptavidin per micro-litre for 216nm beads is 2.2×10^{13}. The peak spectrophotometer reading, taking into account the sample volume of 0.4μl, corresponds to 1.4×10^{15} molecules with the number of available sites on the 40μl of beads calculated according to the above criteria being 8.9×10^{14}. This then corresponds to around 1.5 monolayers which suggests reasonable coverage. The higher than unity value may be attributed to the fact that some free protein may still be in solution, to the possibility of irregular, overlapped positioning of the adsorbed proteins and also to the approximations used. The number of avidin molecules is 3.5 times higher than this suggesting an extremely disordered and dense coverage. However, since there was still a finite amount of protein on the beads DEP measurements were made.

4.10.2 Covalent attachment

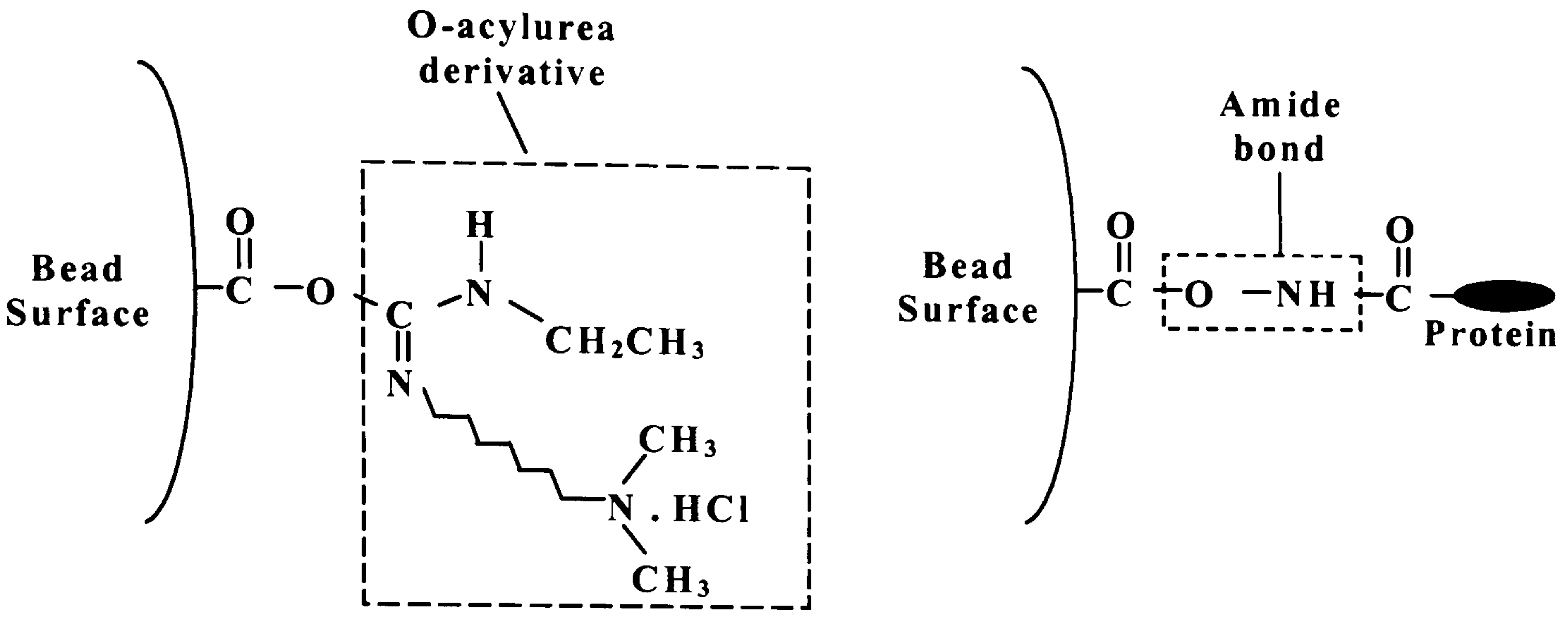

Figure 4-21
Carbodiimide activated carboxyl group on the bead surface showing O-acylurea derivative and subsequent replacement by protein, covalently linked via an amide bond.

The concept of binding globulin to polystyrene latex, first developed by Singer *et al* in 1971, [34] has led to the widespread use of antibody coated microspheres for various diagnostic purposes. The basic method generally used for this type of substrate is covalent linkage of the amino group on the protein to the carboxyl group on the bead surface following intermediate activation by a water soluble carbodiimide. This takes place in two stages, first by the formation of a preliminary complex, involving, in this case, the coupling of EDAC (1-Ethyl-3–(3-dimethylaminopropyl) carbodiimide hydrochloride) to the surface so that it forms the activated O-acylurea derivative [35](Figure 4-21). This water soluble compound is then released on substitution of the protein which forms an amide bond with the carboxyl group.

Method[15]

20-250 µl of the carboxylated microspheres were washed twice by dilution and centrifuge in 100mM sodium carbonate buffer, prepared by titrating 20mM Na_2CO_3 to 100mM $NaHCO_3$ until pH 9.6 was reached. Being far from the highly acidic PI of the beads, this ensured that they were highly negatively charged so that uniform resuspension was easily achieved. The optimal pH for the formation of the O-acylurea complex is 4-5, therefore the washing buffer was substituted after a further centrifugation with 20mM sodium phosphate, pH 4.5, prepared as above, by titration of mono and dibasic solutions, NaH_2PO_4 and $NaHPO_4$. The carbodiimide was dissolved in this buffer at 2% weight/volume (w/v) and added dropwise to an equal volume of the bead solution, resuspended at the 2% solids bottle

---

[15] Adapted from www.polysciences.com, technical data sheet #238C

concentration. This was mixed gently for 2 hours at room temperature. After this time. the mixture was centrifuged twice for 20-30 minutes at 11-13,000rpm (depending on sample volume and particle size) to remove excess carbodiimide with the pellet resuspended each time in phosphate buffer. Centrifugation was again carried out, this time resuspending in 200mM Borate buffer, with the pH adjusted to 8.5 using 1M NaOH. This buffer is favourable for the addition of protein since the amino groups are predominantly unprotonated at this high pH, and flocculation of the microspheres is also minimised, being at the other end of the scale from their Ip. The protein was added at 2-5 times excess to ensure adequate coverage and left overnight on an end to end mixer. A small quantity (~4% v/v) of 250mM ethanolamine was subsequently used to block any remaining sites before centrifugation to remove the excess protein. The supernatant was reserved for protein determination and the pellet resuspended for immediate use in RO water at 1% solids (half the original microsphere stock concentration). Alternatively, for longer term storage a potassium phosphate buffer was made up at pH 7.4 containing 10mg/ml BSA, 5% glycerol and 0.1% NaN_3.

Being a well established procedure, this generally produced around a monolayer of protein coverage, measured in the ways previously described.

4.10.3 Biotin-avidin binding

Streptavidin coated beads were used in this procedure. Since the biotin-avidin complex is effective for a wide range of pH, biotinylated moieties for immobilization were mixed at small excess with streptavidin coated samples in pH 7.4 phosphate buffer. These were then left with agitation for 2 hours before centrifugation and resuspension in RO water at 1% solids for immediate transferral to KCl solutions for crossover measurements.

4.11 ζ-potential measurement techniques

The main techniques employed for the measurement of ζ-potential can be summarised as follows [20, 36].

i) **Streaming** – where a potential difference is set up in a capillary channel with an established double layer as a result of an applied pressure gradient to pump the fluid. This fluidic movement of charges from the hydrodynamically mobile part of the double layer gives rise to an equilibrating back current which can be measured.

ii) **Electro-osmosis** – The movement of a fluid over a charged interface due to the action of an applied electric field on the diffuse layer charges.

iii) **Surface charge titration** – where the volume of added acid or alkali to a particulate sample is measured along with the pH on establishment of equilibrium and compared to the corresponding pH change in the suspending solution only. This must be carried out in the absence of specific ion adsorption and at several different electrolyte concentrations in order to obtain an absolute value of surface charge (see section 4.7.1)

iv) **Electrophoresis** – the movement of charged particles under the action of an applied electric field.

Traditionally, these methods have produced highly incongruent results [37]. The method employed in this thesis is electrophoresis, using the Coulter DELSA™ ζ-potential analyser. DELSA, as expanding the acronym makes evident, works on the principle of Doppler Electrophoretic Light Scattering Analysis. Particles are placed in a small fluid filled chamber where they move under the action of an applied electric field. The fluid also is induced to move electro-osmotically but since the chamber is sealed there is a corresponding back flow at the edges. Measurements are performed, therefore, at the stationary plane between the regions of opposing flow (Figure 4-22) in order to observe the velocity of the particle relative to the liquid.

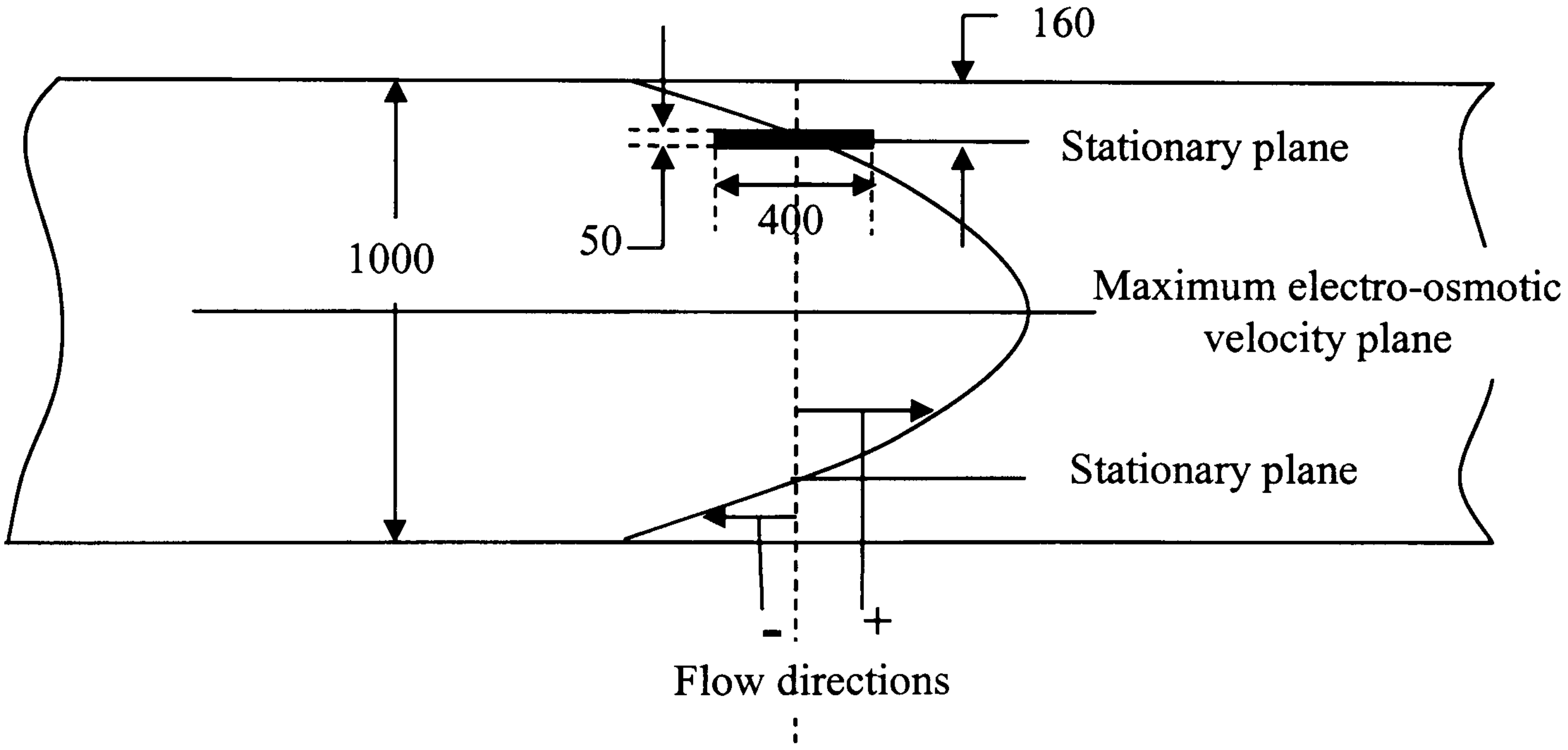

Figure 4-22
Laminar flow profile inside the sealed DELSA chamber, highlighting the stationary layer. Dimensions in microns [38].

Incident laser light from a single transmitter is scattered by the moving colloids and detected by photodiodes at 4 fixed angles, 7.5°, 15 °, 22.5 °, and 30 ° (Figure 4-23).

The Doppler shift is given by:

$$\Delta v = v_0 \frac{V}{c} \tag{4-3}$$

where ν_0 is the frequency of the scattered wave, **V** is the speed of the particle relative to the detector, and c is light speed. This depends on the scattering angle, θ, according to:

$$\Delta\nu = \frac{2n\underline{V}\,sin\left(\dfrac{\theta}{2}\right)}{\lambda_0} \tag{4-4}$$

where n is the index of refraction of the medium and λ_0 is the wavelength of light in a vacuum. The small frequency shift is measured by observing the interference fringes between the scattered light and 4 reference beams aimed at each of the detectors, produced from and therefore coherent with the original beam (Figure 4-23).

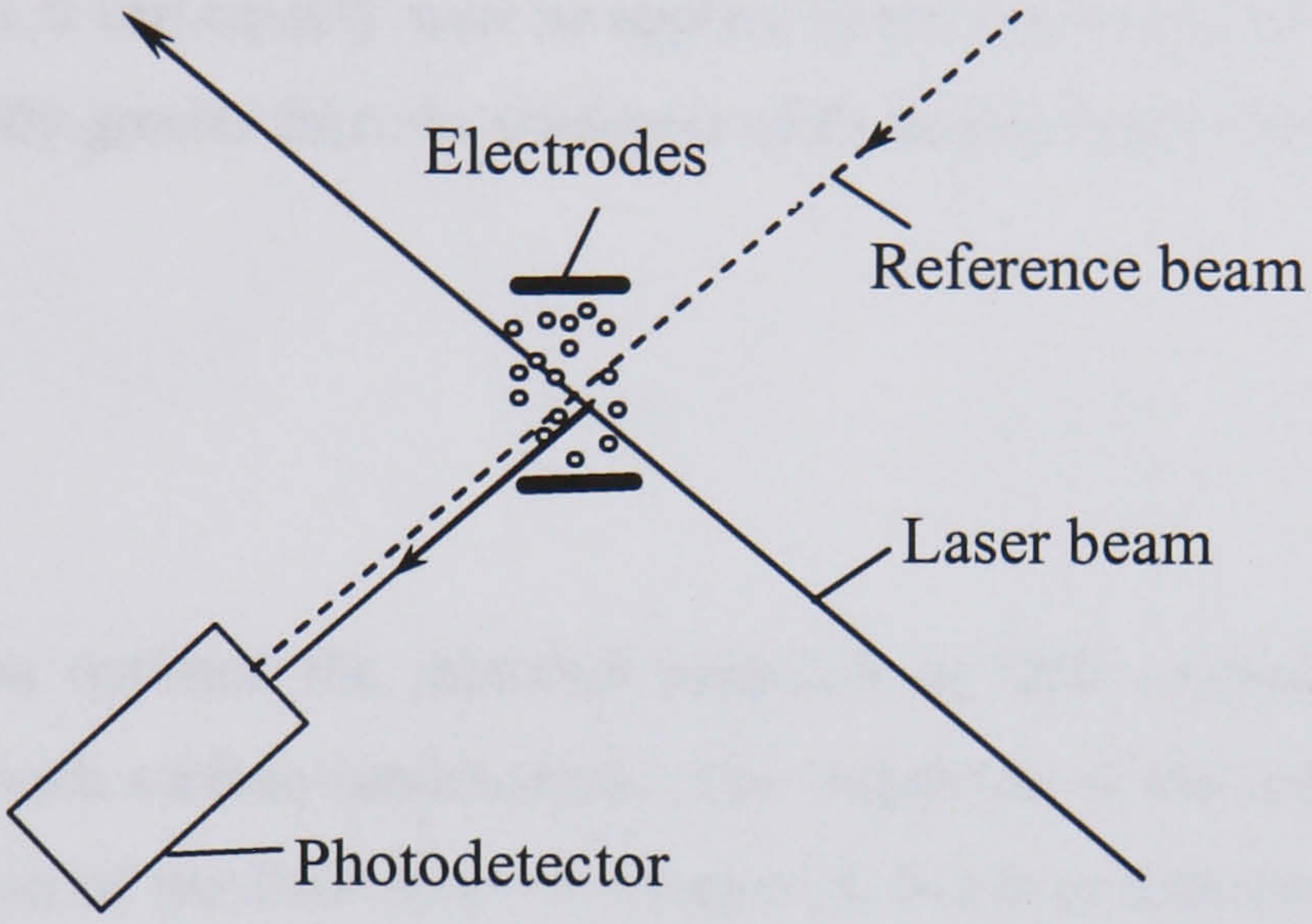

Figure 4-23

DELSA chamber, showing incident laser beam and one of four reference beams with photodetector [38]

As illustrated in Figure 4-24, the beating envelope function is of much lower frequency than the light beams themselves and therefore easily discernable by the photodetectors.

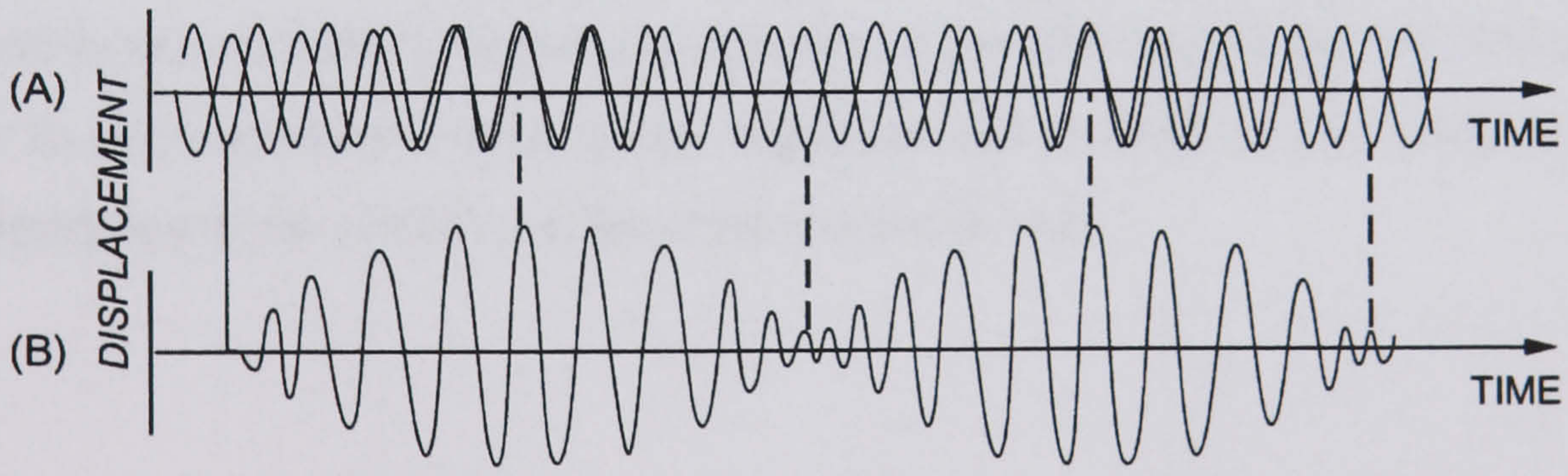

Figure 4-24

Combination of two waves slightly differing in frequency, highlighting the resultant lower frequency beat pattern [38]

The resulting intensity spectra are normalised and superimposed to check for data consistency – spurious peaks suggesting non-homogeneity of the sample.
The electrophoretic mobility is defined as:

$$U = \frac{V}{E} \tag{4-5}$$

which, from (4-4), can be expressed as:

$$U = \frac{\Delta \nu \lambda_0}{2nE \sin\frac{\theta}{2}} \tag{4-6}$$

The ζ-potential is calculated from this mobility using the Smoluchowski approximation [20]:

$$U = \frac{\varepsilon_o \varepsilon_r \zeta}{\eta} \tag{4-7}$$

where η is the viscosity of the medium and the other symbols have their usual meanings. Although this formula was originally derived for electro-osmosis in a capillary [39] (referenced in [20]), it can equally well be applied to the electrophoretic motion of a particle of radius significantly greater than the thickness of its double layer if the suspending liquid is fixed [20].

4.12 Summary

This chapter has outlined the intended approach to DEP crossover measurements on colloidal particles with surface modification. The definition of the crossover, following the theoretical derivation of the DEP force in Chapter 2, has been clarified in the context of an experimental situation, with a finite element modelled illustration of the positive and negative DEP regions on the electrodes used. Surface modification techniques have been outlined in terms of their generic categories to establish a context for the specific methods employed in this thesis. Preliminary studies have been carried out to examine the effect of a neutral pH on protein absorption in order to assess the level of necessity of employing the more complex but well established and reliable method of carbodiimide coupling. The background to experimental ζ-potential measurement has also been described with particular reference to electrophoresis which is the technique that is used in this study in order to independently assess the viability of the crossover predictions.

Appendix 4-1 Resonance measurements on castellated electrodes

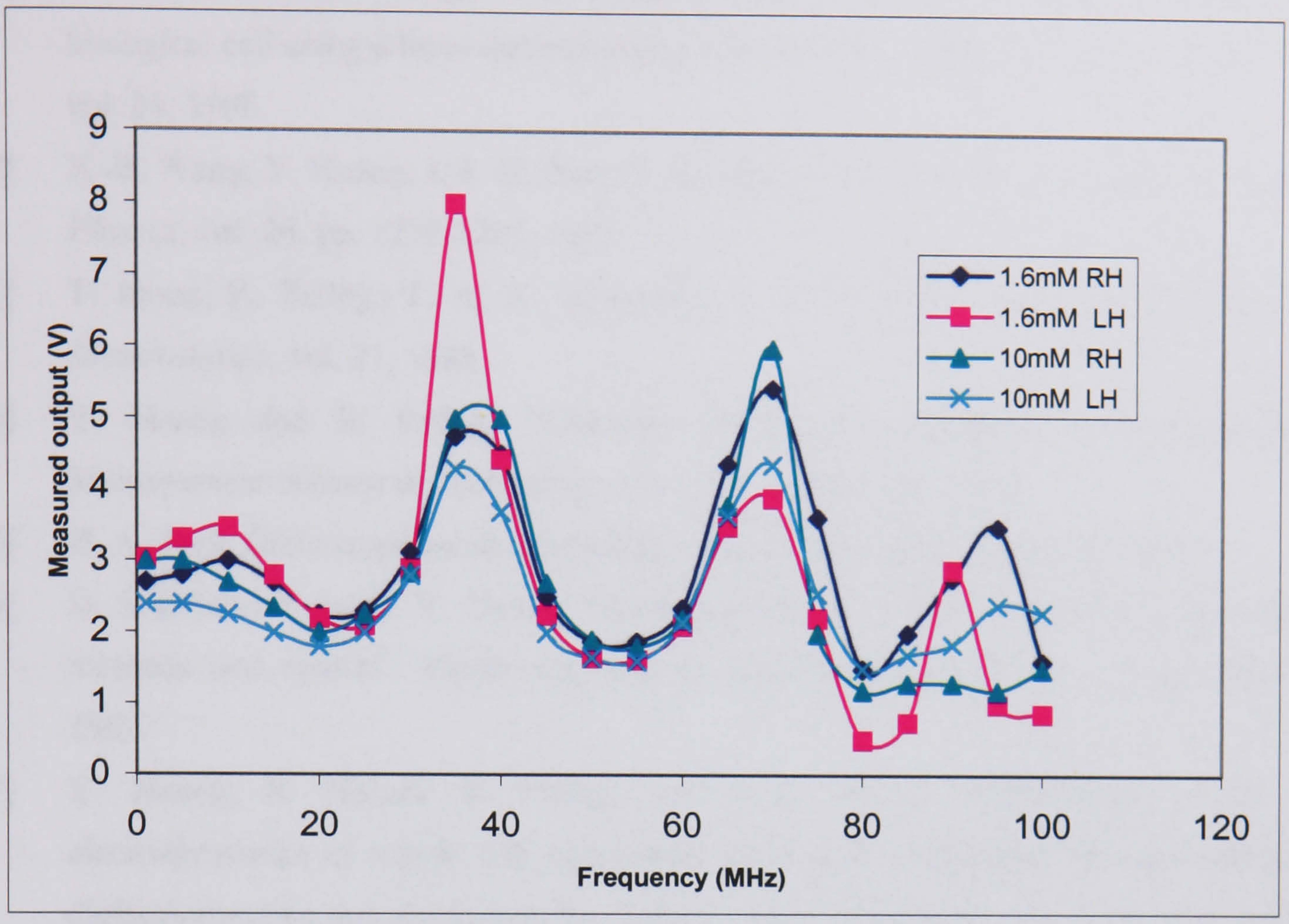

Figure 4-25

Resonance measurements on castellated electrodes for two different sets (RH and LH) and two medium conductivities.

At frequencies higher than ~20MHz resonance effects due to high frequency reflections in the coaxial cable were documented (Figure 4-25) and dealt with by terminating the cable with a 50Ω resistor. The problem, nonetheless, still remained to a significant degree since the sample resistance varied with medium conductivity and the termination was not always adequate. Resonance still occurred at regular frequency intervals when the source voltage wavelength was comparable to the length of the cable. This was partially resolved in the case of a crossover co-inciding with a point of high resonance by temporarily changing the length of the cable or by observing whether or not positive DEP re-occurred at higher frequencies. The high frequency crossovers, therefore, are correspondingly less accurate than those in the lower range.

4.13 References

[1] J. Suehiro and R. Pethig, "The dielectrophoretic movement and positioning of a biological cell using a three-dimensional grid electrode system", *J. Phys.D: Appl. Phys.*, vol. 31, 1998.

[2] X.-B. Wang, Y. Huang, J. P. H. Burt, G. H. Markx, and R. Pethig, , *J. Phys. D: Applied Physics*, vol. 26, pp. 1278-1285, 1993.

[3] T. Inoue, R. Pethig, T. A. K. Al-Ameen, J. P. H. Burt, and J. A. R. Price, , *J. Electrostatics*, vol. 21, 1988.

[4] Y. Huang and R. Pethig, "Electrode Design For Negative Dielectrophoresis", *Measurement Science & Technology*, vol. 2, pp. 1142-1146, 1991.

[5] H. A. Pohl, *Dielectrophoresis*. Cambridge: Cambridge University Press, 1978.

[6] D. S. Dimitrov and D. V. Zhelev, "Dielectrophoresis of individual cells: Experimental methods and results", *Bioelectrochemistry and bioenergetics*, vol. 17, pp. 549-557, 1987.

[7] Y. Huang, R. Holzel, R. Pethig, and X.-B. Wang, "Differences in the AC electrodynamics of viable and non-viable yeast cells determined through combined dielectrophoresis and electrorotation studies", *Phys. Med. Biol.*, vol. 37, pp. 1499-1517, 1992.

[8] J. P. H. Burt, R. Pethig, and P. R. C. Gascoyne, , *Biochim. Biophys. Acta*, vol. 1034, pp. 93-101, 1990.

[9] R. Pethig, Y. Huang, X.-B. Wang, and J. P. H. Burt, "Positive and negative dielectrophoretic collection of colloidal particles using interdigitated castellated microelectrodes", *J. Phys. D: Appl. Phys.*, vol. 24, 1992.

[10] P. R. C. Gascoyne, X.-B. Wang, Y. Huang, and F. F. Becker, "Dielectrophoretic Separation of Cancer Cells from Blood", *IEEE Transactions on Industry Applications*, vol. 33, 1997.

[11] N. G. Green, "Dielectrophoresis of sub-micron particles" in *Electrical and Electronic Engineering*: University of Glasgow, 1998, pp. 270.

[12] N. G. Green and H. Morgan, "Dielectrophoretic investigations of sub-micrometre latex spheres", *J. Phys. D: Appl. Phys.*, vol. 30, pp. 2626-2633, 1997.

[13] N. G. Green and H. Morgan, "Separation of submicrometre particles using a combination of dielectrophoretic and electrohydrodynamic forces", *Journal of Physics D-Applied Physics*, vol. 31, pp. L25-L30, 1998.

[14] M. P. Hughes, H. Morgan, and F. J. Rixon, "Measuring the dielectric properties of herpes simplex virus type 1 virions with dielectrophoresis", *Biochimica Et Biophysica Acta-General Subjects*, vol. 1571, pp. 1-8, 2002.

[15] M. P. Hughes, H. Morgan, and F. J. Rixon, "Dielectrophoretic manipulation and characterization of herpes simplex virus-1 capsids", *European Biophysics Journal With Biophysics Letters*, vol. 30, pp. 268-272, 2001.

[16] T. Schnelle, T. Muller, G. Gradl, S. G. Shirley, and G. Fuhr, "Dielectrophoretic manipulation of suspended submicron particles", *Electrophoresis*, vol. 21, pp. 66-73, 2000.

[17] O. C. Zienkiewicz and R. L. Taylor, *The Finite Element Method*, 4 ed. London: McGraw Hill Book Company, 1989.

[18] M. P. Hughes, M. F. Flynn, and H. Morgan, "The dielectrophoretic behaviour of latex spheres: Influence of surface conductance", *Journal of Colloid and nerface Science*, vol. 220, pp. 454-457, 1999.

[19] T. Cass and F. S. Ligler, *Immobilized Biomolecules inAnalysis*: Oxford University Press, 1998.

[20] Hunter, *Zeta Potential in Colloid Science*: Academic Press Inc., 1981.

[21] M. Wilchek and E. A. Bayer, "The Avidin-Biotin Complex in Bioanalytical Applications", *Analytical Biochemistry*, vol. 171, pp. 1-32, 1988.

[22] M. Wilchek and E. A. Bayer, *Immobilised Biomolecules in Analysis*. New York: Oxford University Press, 1998.

[23] A. Y. Menshikova, I. B. Dmitrieva, V. I. Kuchuk, Y. O. Skurkis, T. G. Evseeva, and B. M. Shabsels, "Electrosurface Properties of Poly(styrene-co-acrolein) Latexes with the Protein Modified Surface", *Kolloidnyi Zhurnal*, vol. 61, pp. 799-808, 1999.

[24] T. Boenisch, A. J. Farmilo, and R. H. Stead, *Immunochemical Staining Methods*. California: DAKO corporation, 1989.

[25] M. B. V. Roberts, *Biology - a functional approach*. Surrey: Nelson, 1986.

[26] *CRC handbook of Chemistry and Physics*: http://www.hbcpnetbase.com/.

[27] L. Herzenberg, D. M. Weir, and L. Herzenberg, *Weir's Handbook of Experimental Immunology*, 5 ed: Blackwell Science Inc., 1996.

[28] N. M. Green, , *J. Biochem*, vol. 89, pp. 599, 1963.

[29] L. Pugliese, A. Coda, M. Malcovati, and M. Bolognesi, "3-Dimensional Structure of the Tetragonal Crystal Form of Egg- White Avidin in Its Functional Complex With Biotin At 2.7- Angstrom Resolution", *Journal of Molecular Biology*, vol. 231, pp. 698-710, 1993.

[30] S.-C. Huang, H. Swerdlow, and K. Caldwell, "Binding of Biotinylated DNA to Streptavidin-Coated Polystyrene Latex", *Analytical Biochemistry*, vol. 222, pp. 441-449, 1994.

[31] C. R. Calladine and H. R. Drew, *Understanding DNA*. London: Academic Press, 1997.

[32] P. J. Russel, *Fundamentals of Genetics*. USA: Harper Collins, 1994.

[33] "Technical note #204", *http://www.bangslabs.com/*.

[34] J. M. Singer and R. M. Plotz, , *Am. J. Med*, vol. 31, pp. 766, 1971.

[35] D. Sehgal and I. K. Vijay, "A Method for the High Efficiency of Water-Soluble Carbodiimide-Mediated Amidation", *Analytical Biochemistry*, vol. 218, pp. 87-91, 1993.

[36] J. Lyklema, *Fundamentals of Interface and Colloid Science*, vol. 2. New York: Academic Press, 1995.

[37] J. Lyklema, H. P. van Leeuwen, and M. Minor, "DLVO-theory, a dynamic re-interpretation", *Advances in Colloid and Interface Science*, vol. 83, pp. 33-69, 1999.

[38] Coulter-DELSA, *440 Training course Workbook*: Coulter Electronics Limited, 1997.

[39] M. v. Smoluchowski, *Handbuch der Electrizitat und des Magnetismus*, vol. 2. Leipzig: Graetz, 1921.

5 DEP Characterisation - Results

5.1 Introduction

The aim of this chapter is to present crossover data obtained for polystyrene beads of various sizes before and after surface modification with biological entities. This data is compared to current theories of charge relaxation and a fitting mechanism proposed. Parameters such as ζ-potential and Stern layer conductance are inferred and, within the scope of the investigation, compared to independent experimental analysis using non-dielectrophoretic techniques.

5.2 Experimental Results

Applying the methods outlined in chapter 4, the experimental results were as follows.

5.2.1 Latex Beads

Crossover measurements were taken on beads of various sizes. Figure 5-1 illustrates how the crossover was observed, showing the effect of a small alteration of frequency around this point.

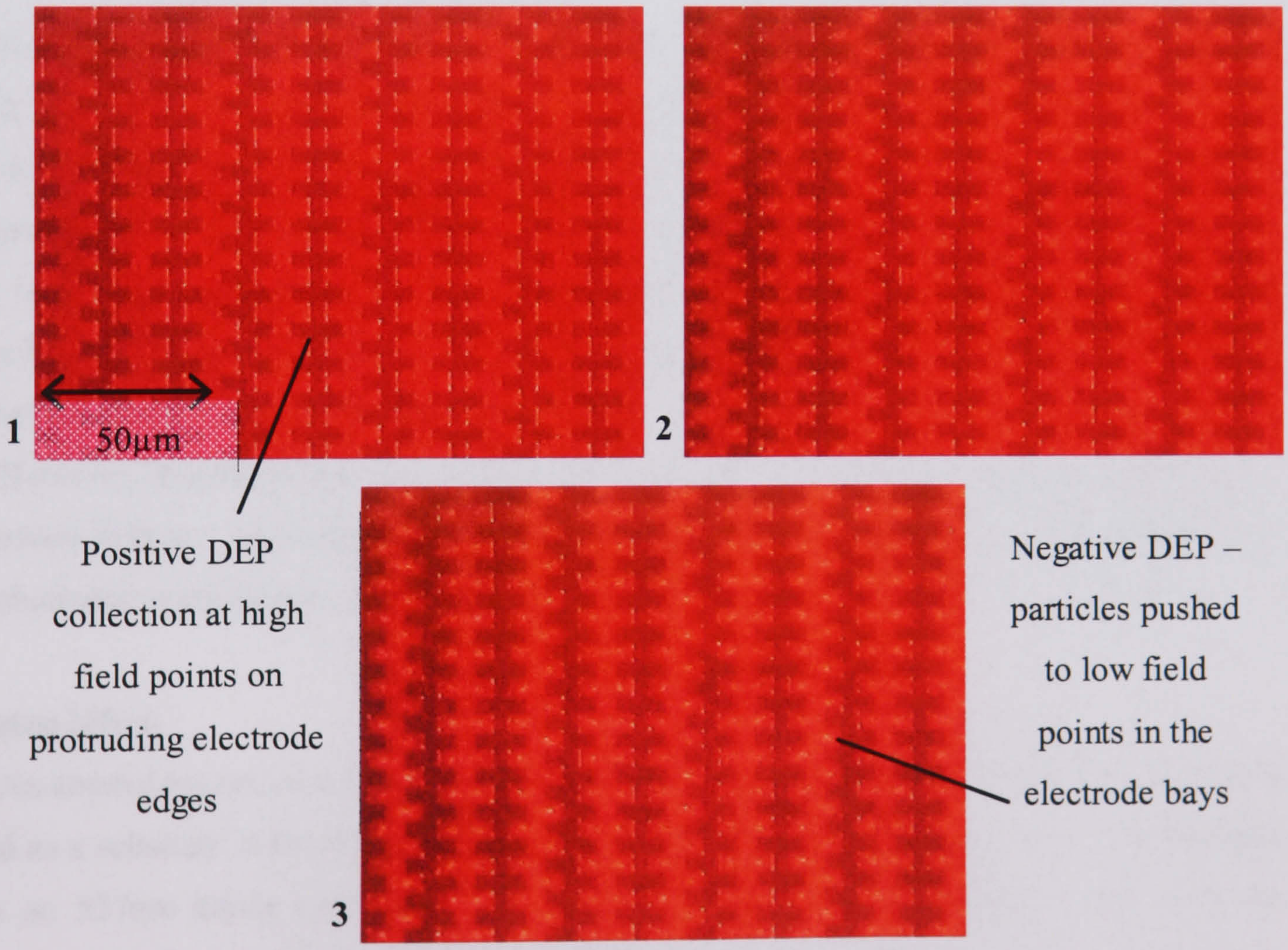

Figure 5-1

*Crossover of 216nm latex beads showing transition from positive to negative DEP with 3V signal **1)** Positive DEP collection on protruding electrode edges ,7MHz, **2)** particles begin to move away from electrodes as frequency is increased, 8MHz, **3)** most particles in the negative DEP regions, 9MHz*

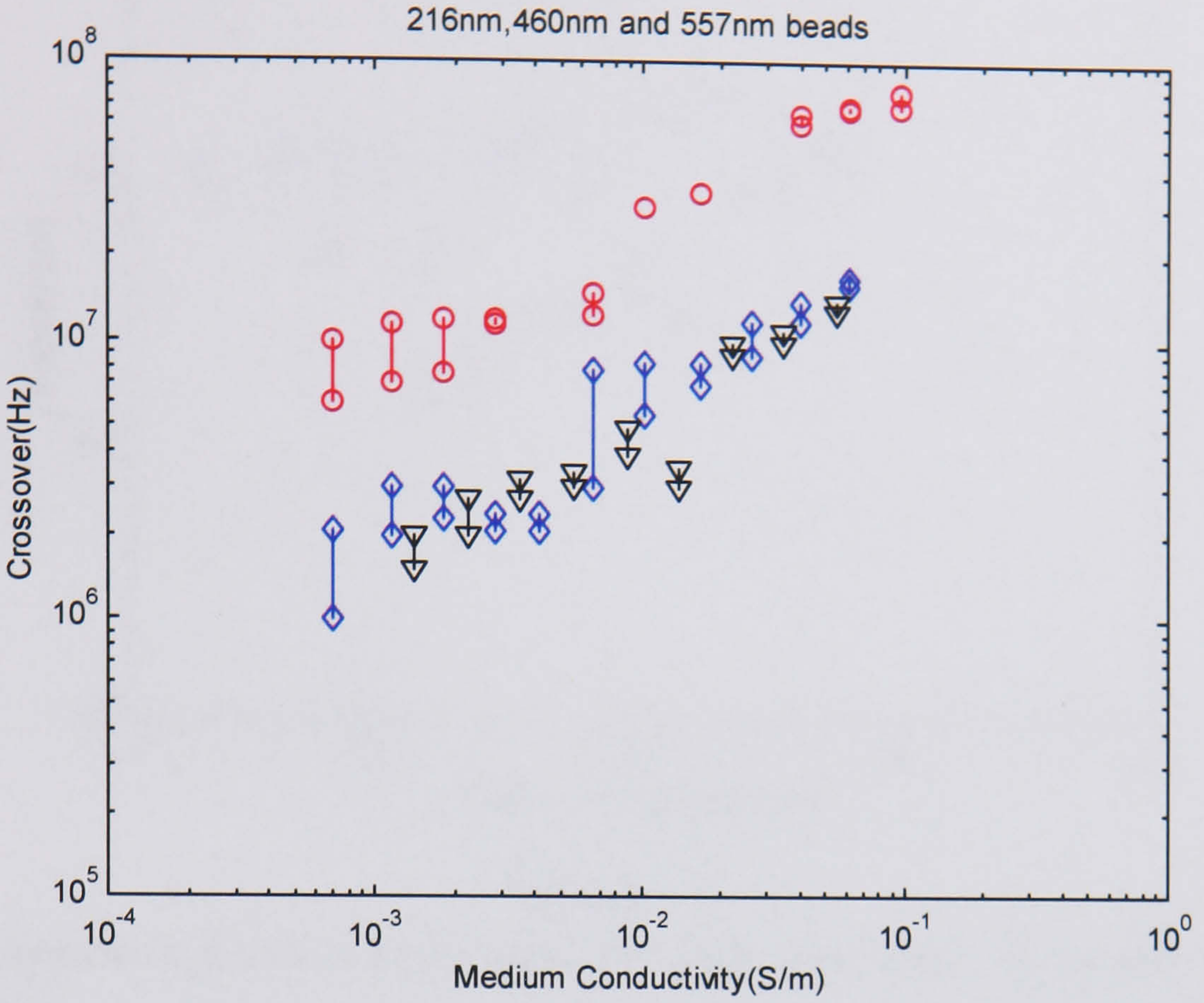

Figure 5-2
DEP Crossovers of uncoated 216nm (o), 460nm (◇)and 557nm (▽) latex beads.

It can be seen from Figure 5-2 that the crossovers are effectively bead size dependent, with the ~0.5 μm beads manifesting significantly lower crossovers than the 216nm microspheres, as would be expected from the basic predictions of dielectric theory derived in chapter 2 for a lossy dielectric sphere. The fact that there is no marked distinction between the two larger bead sizes can feasibly be attributed to differing surface properties and experimental uncertainty limits since the ratio of their diameters is much smaller than that of either compared to the 216nm beads.

However, in general they rise with medium conductivity in a manner not predicted by the Maxwell-Wagner interfacial polarisation mechanism with simple, constant surface conductance as previously described (Figure 5-12).

Ageing effect

An anomalous occurrence which should be mentioned here since all sizes of beads will be used as a substrate is the effect of ageing on the bead crossovers (Figure 5-3). The first data sets on 557nm beads were gathered 18 months before the second and in that time the crossovers had changed considerably. The beads, however, still remained responsive to surface modification and so continued to be used as a substrate in the interests of experimental consistency i.e. when repeating modifications previously carried out on them.

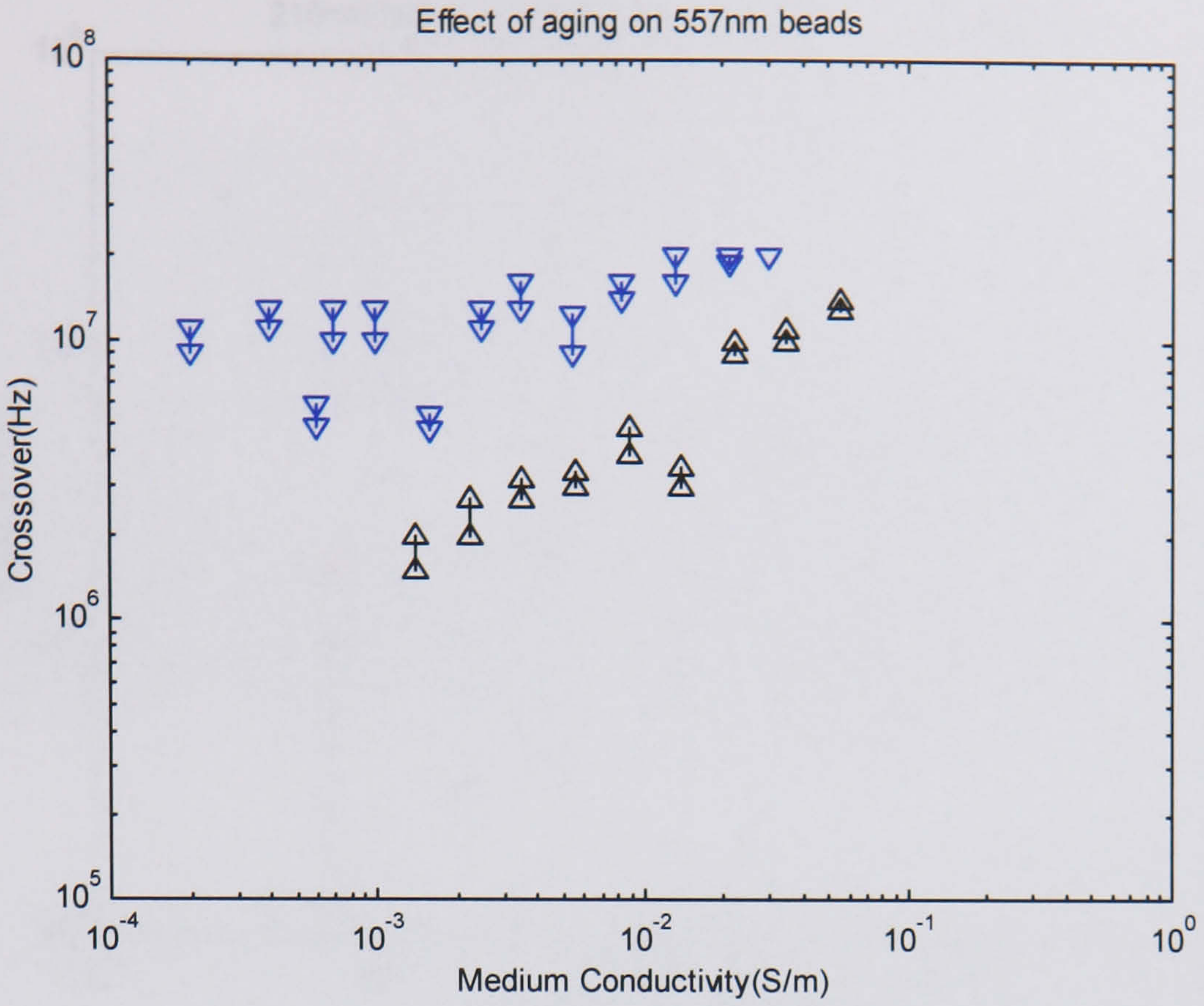

Figure 5-3

Crossovers of 557nm beads taken 18 months apart (first : △, second: ▽)

5.2.2 Beads with IgG

Sequential images of frequency increase around the crossover for IgG modified beads are shown in Figure 5-4. Samples were generally less mono-disperse after protein attachment and negative DEP was difficult to observe. The crossover results can be seen in Figure 5-5, also following subsequent attachment of the complementary antibody.

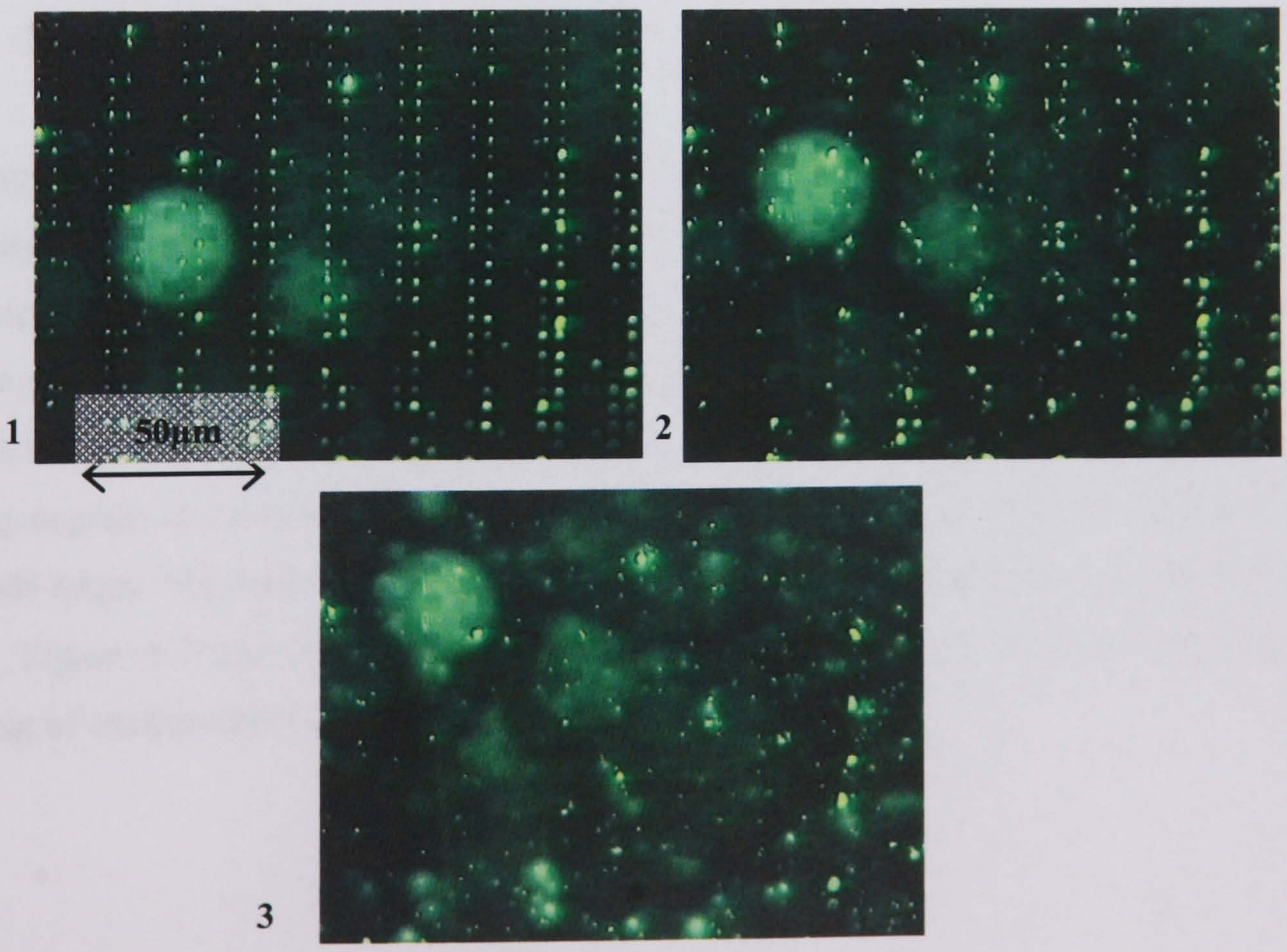

Figure 5-4

Crossover of IgG labelled beads, showing the break up of positive DEP
1)1.2MHz 2)1.5MHz 3)1.9MHz

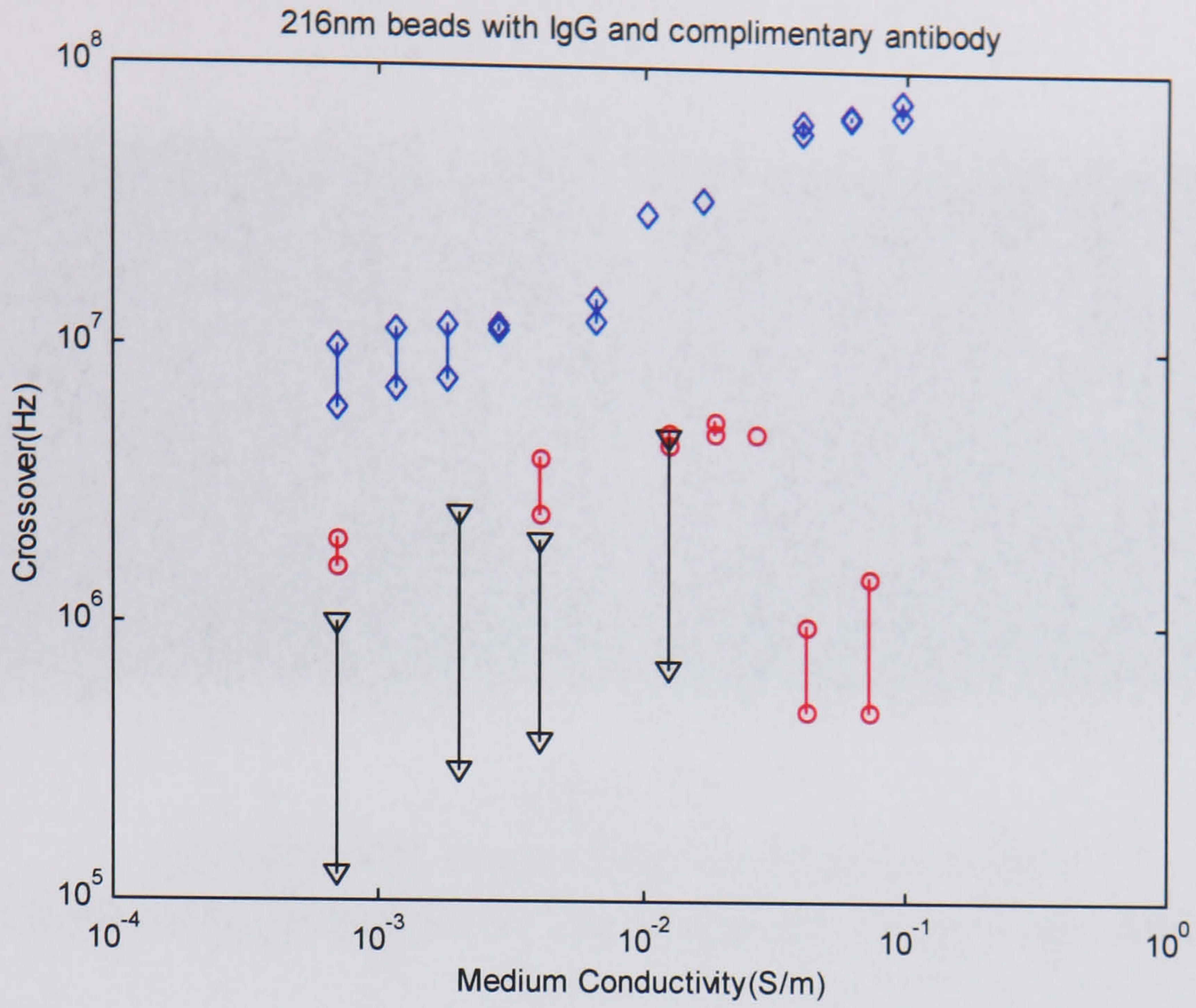

Figure 5-5
Uncoated 216nm beads (◊), with IgG (o) and complimentary antibodies (∇).

It can be seen from Figure 5-5 that on attaching the IgG, the crossovers are generally lower. There are, in addition, some low frequency crossover points in the high conductivity regime for the labelled beads. Secondary labelling results in a lowering of the crossover still further, with a much larger spread in the measurements.

5.2.3 Beads with Streptavidin

Streptavidin was attached to the surface of 216nm beads by covalent coupling and by adsorption as outlined in Chapter 4. Figure 5-6 shows two images before and after a small frequency change around what was generally accepted as the crossover point. At this frequency there was a visible adjustment of the bead positions with a general flux away from the electrodes – although a sizable number of beads remained. This could be due again to varying degrees of coverage of the bead surface or it could be attributed to adhesion to the electrode edges. The latter is undoubtedly a factor as some beads remain on switching off the signal. Figure 5-7 and Figure 5-8 show the crossover data for covalent and adsorptive coupling of streptavidin to 216nm beads.

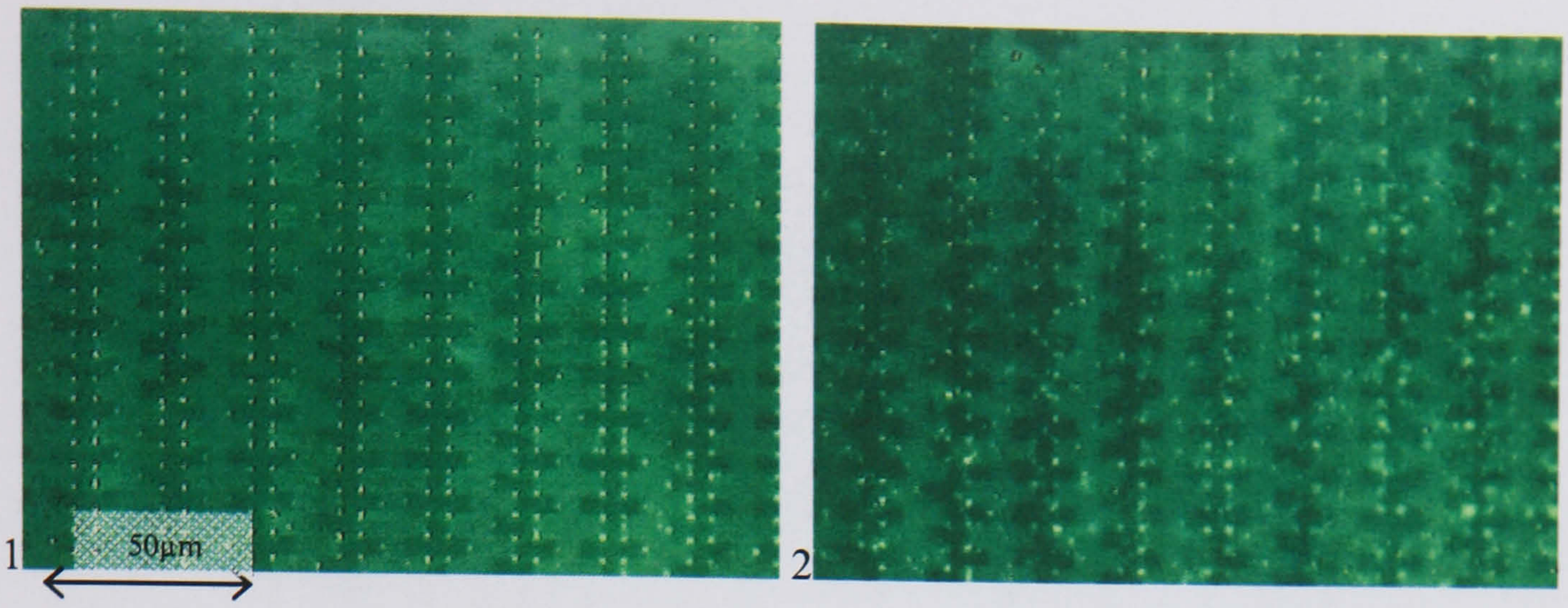

Figure 5-6

1. Positive DEP of streptavidin coated beads, 3.9MHz

2. Some sticking of beads to the electrodes beyond the crossover, 4.9MHz

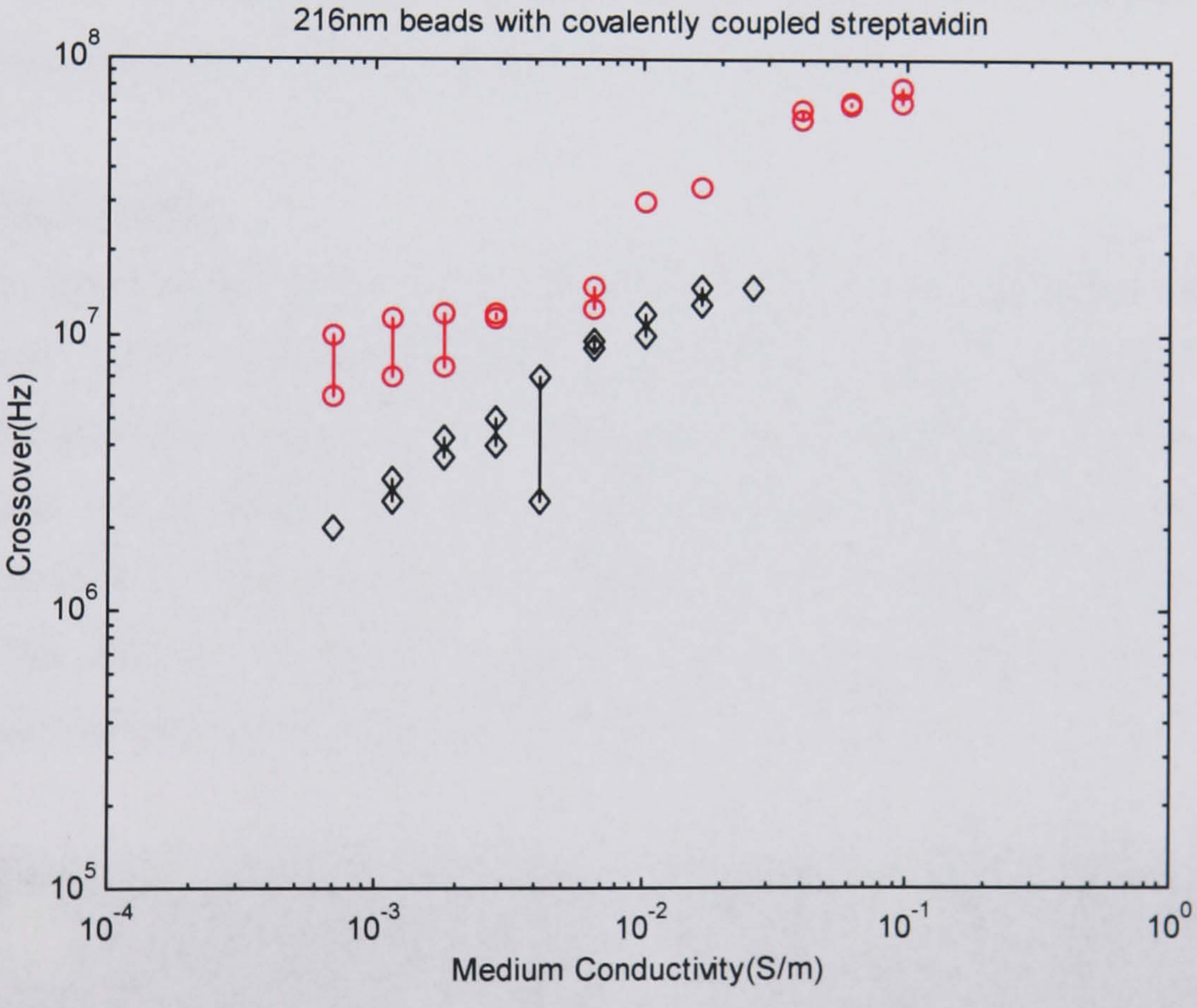

Figure 5-7

Covalently coupled streptavidin (◊) on 216nm beads (o)

As shown in Figure 5-7, a difference is again observed between the labelled and unlabelled samples.

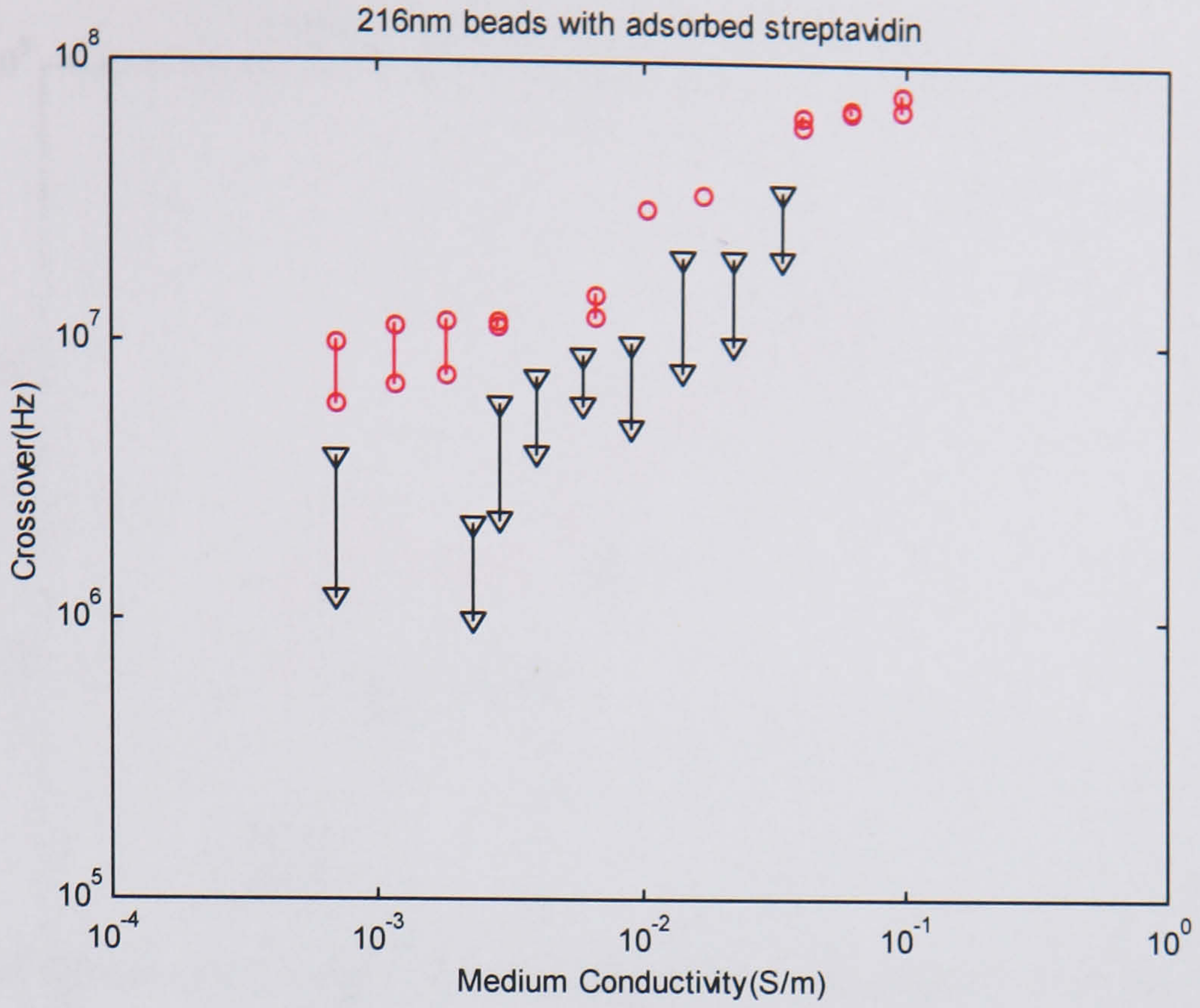

Figure 5-8
Adsorbed streptavidin (∇) on 216nm beads (○)

As can be seen from Figure 5-8 the error bars are large for the adsorbed streptavidin sample with the crossovers approaching those of uncoated beads.

5.2.4 Avidin Coupling

Due to the discrepancy between the high Ip of avidin and the approximately neutral pH of the suspending media used in the DEP measurements sample clumping was greatly augmented. Larger beads, 460nm in diameter, were used in an attempt to reduce this effect and the protein was covalently coupled in order to increase the regularity of the ligand distribution. Crossover measurements were nonetheless very difficult to perform on these beads due to the still high level of coagulation and were were generally defined by repeated observation of individual beads (Figure 5-9). The results can be seen in Figure 5-10.

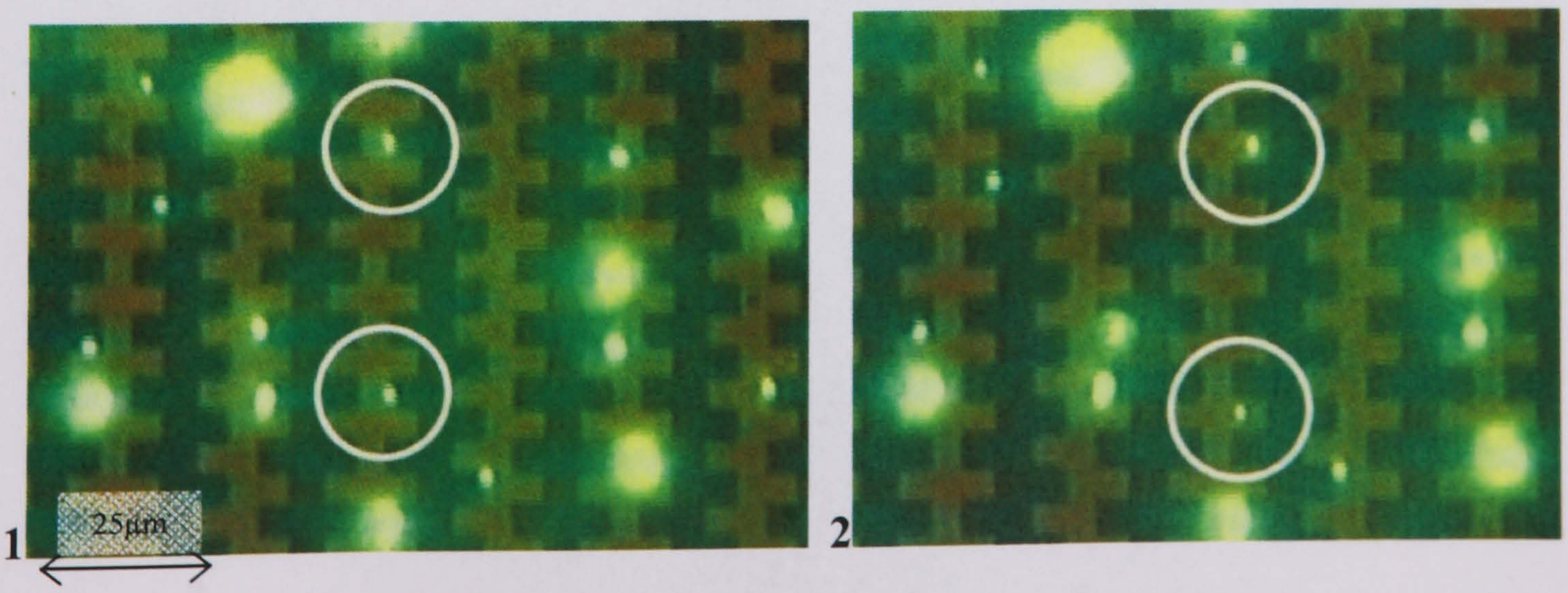

Figure 5-9
Two single bead transitions from positive to negative DEP in a highly coagulated sample of avidin coated beads.1)800kHz 2)1MHz

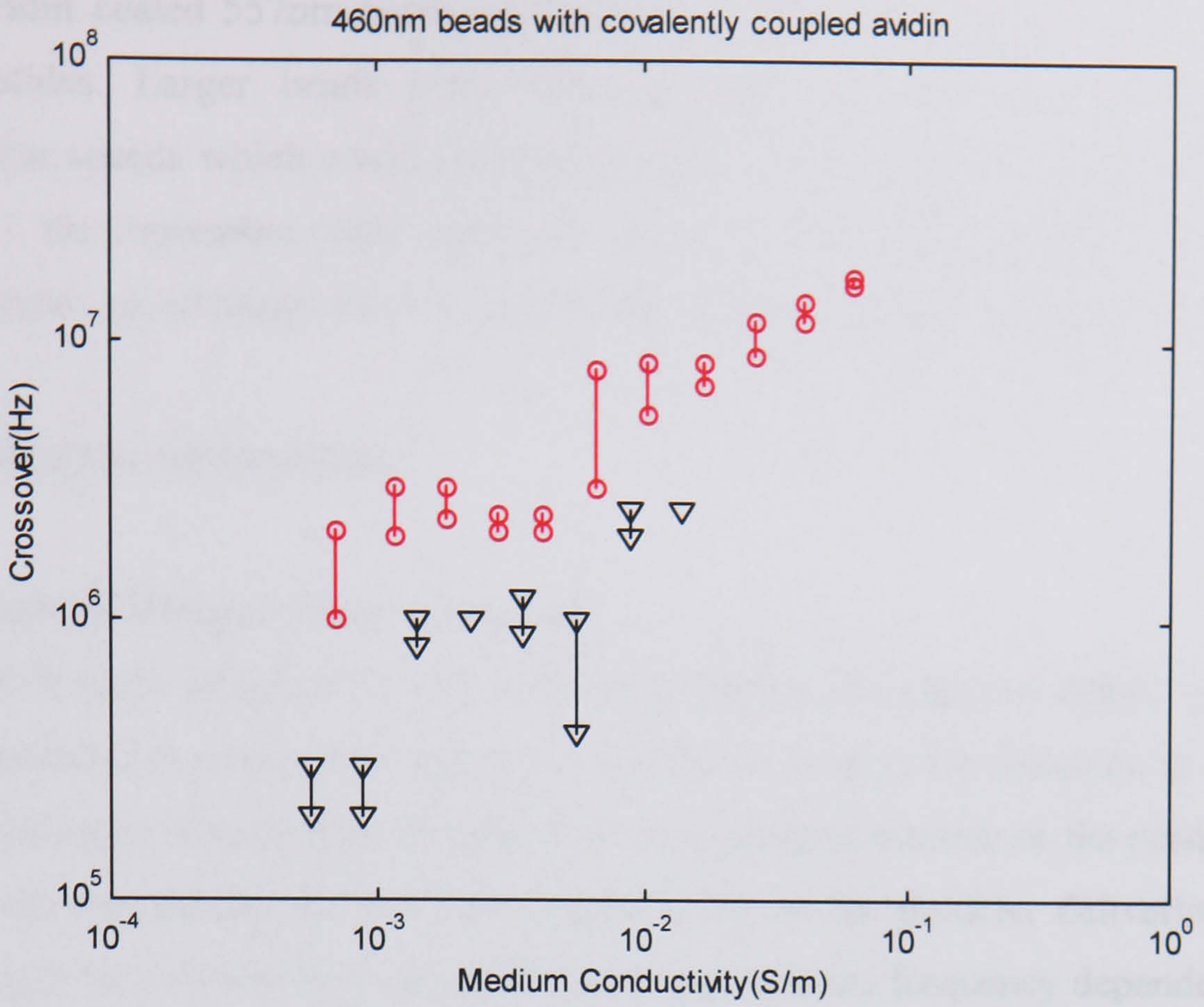

Figure 5-10

460nm beads (○) with covalently coupled avidin (▽)

5.2.5 Beads with oligonucleotides

Due to the clearer crossover results and better monodispersivity, covalently coupled streptavidin was used as the linking protein for the biotinylated oligonucleotides. These were attached at neutral pH according to the method indicated in Chapter 4.

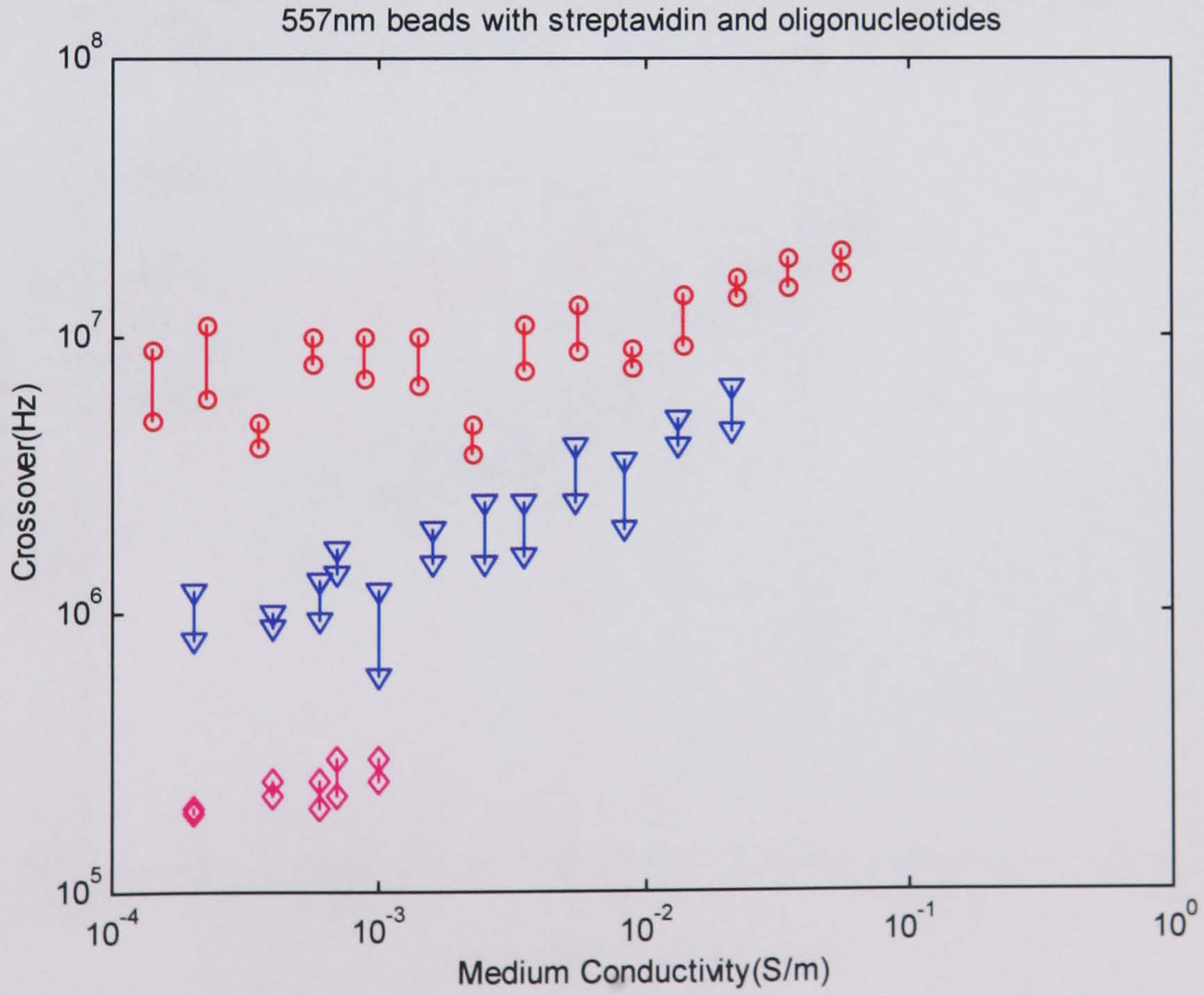

Figure 5-11

557nm beads (○) modified with streptavidin (▽) and oligonucleotides (◇)

Streptavidin coated 557nm beads were chosen as the substrate on which to attach the oligonucleotides. Larger beads were used in order to avoid the necessity of high centrifugation speeds which could cause aggregation of the sample. As can be seen from Figure 5-11 the crossovers were again reduced, with no positive DEP observed on the oligonucleotide coated beads above a suspending medium conductivity of 10^{-3} S/m.

5.3 Relaxation mechanisms

5.3.1 Maxwell-Wagner-Gouy-Chapman

Maxwell-Wagner polarisation can cause the formation of a positive dipole in a dielectric particle suspended in a region of higher permittivity as long as the dielectric is not ideal. A surface conductance is necessary in order that a polarisation current on the particle-medium interface will compensate for the lower permittivity of the particle, delivering sufficient counter charge for external field cancellation. In this way the frequency dependent response of the Clausius-Mossotti factor is obtained as illustrated in Chapter 4. However, the nature of the surface conductance component necessitates a definition. If a simple, non-variable surface conductance is assumed, as for example in the Gouy-Chapman theory, the predicted profile is essentially constant. It does not account for the characteristic rise apparent in so much of the data (Figure 5-12).

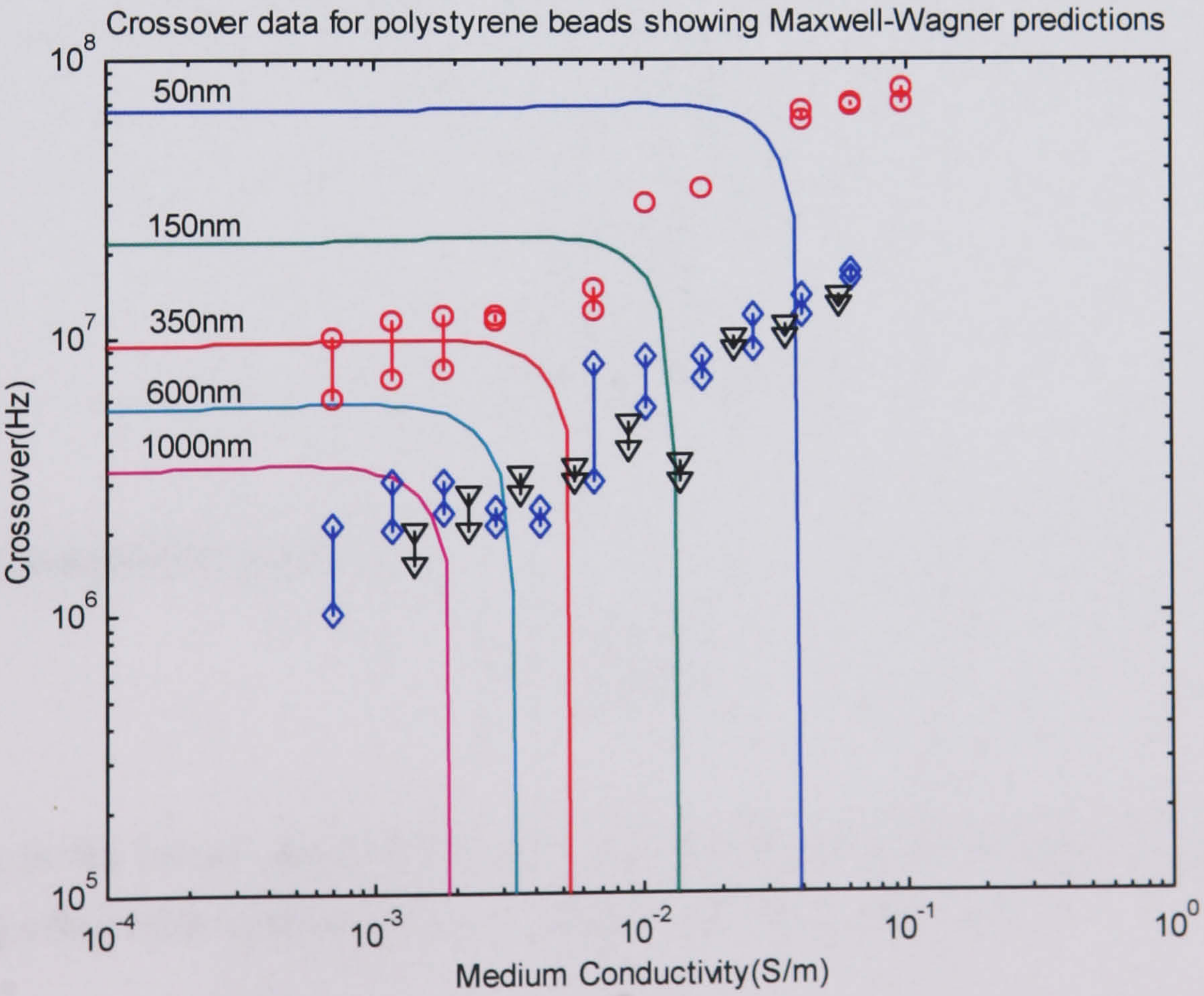

Figure 5-12

Illustration of the incompatibility of the data with the Maxwel-Wagner model applied with constant surface conductance. Curves represent bead radii from 50nm-1000nm

5.3.2 Summary of other investigated models

Attempts have been made [1] to fit Maxwell-Wagner curves to crossover data for latex spheres by introducing into the O'Konski surface conductance (2-31) a term involving the inverse Debye length, κ, in addition to arbitrary scaling factors C_1 and C_2, in order to take into account that an alteration in medium conductivity may affect the surface conductance of the particle. The complete expression for the conductance of the particle is given by:

$$\sigma_p = \sigma_b + C_0 \frac{2\lambda_s}{a}\left(C_1 + C_2 \kappa a\right) \tag{5-1}$$

where the symbols have their usual meanings and the right hand term constitutes the surface conductance. This equation produced reasonable fits for the data at low medium conductivity but in the absence of a satisfactory physical interpretation of the constants C_1 and C_2 did not provide insight into the parameters of the system.

Low frequency relaxation effects thought to be due to ion fluxes around the particle (known collectively in the literature as the α-relaxation) were also included in an attempt to model the complete data set including the reported observance of low frequency data points in the high conductivity regime. The models used were those of Schwarz [2], O'Brien [3] and Lyklema [4] who proposed, respectively, relaxation frequencies given by:

$$f_1 = \frac{D}{\pi a^2} \tag{5-2}$$

$$f_2 = \frac{D\kappa^2}{\pi} \tag{5-3}$$

$$f_2 = \frac{MD}{\pi a^2} \tag{5-4}$$

With the parameter M, given by:

$$M = 1 + \frac{F\rho_b}{RTC_d} \tag{5-5}$$

where ρ_b is the bound charge density behind the slip plane. (5-4) takes into account the screening effect of the diffuse layer as quantified in a capacitance term:

$$C_d = \varepsilon_m \kappa \cosh\left(\frac{F\zeta}{2RT}\right) \tag{5-6}$$

These models, however, do not present convincing fits to the data. Their associated relaxation times, τ, have, in addition, been inserted in a modified surface conductance postulated by Zhou [5] including a Debye like formulation such that:

$$\sigma_p = \sigma_b + \frac{2\lambda_s}{a} + \left(\frac{A}{1 + (j\omega\tau)^B} \right) \tag{5-7}$$

where A and B again are arbitrary constants. This approach also failed to clarify the interpretation of the data or make convincing predictions of the system parameters. It may be, however, that the low frequency crossover data being modelled in this instance was not due to a dielectric dispersion at all but to a misinterpretation of fluid effects, prevalent in the crossover regime at high medium conductivities. Since no such relaxation has been unequivocally observed in this thesis, the α-relaxation was not modeled further.

5.3.3 Gouy-Chapman-Graham-Stern surface conductance

Using the data gathered in this investigation, another approach was taken. Instead of a single, constant surface conductance, the component parts of the double layer as outlined in Chapter 2 were considered separately. The inner (Stern) layer was assumed to conduct only by lateral movement in response to the field with no hydrodynamic component.

Charge transport in the diffuse layer was assumed to take place in the manner expounded by Bikerman and later authors [6-9] with an added hydrodynamic component enhancing the delivery of charge. For a symmetrical electrolyte this is given by:

$$K_s^d = \frac{\left(4F^2cz^2D^d\,(1+3m/z^2)\right)}{RT\kappa}\left(\cosh\left[\frac{zF\zeta}{2RT}\right]-1\right) \tag{2-44}$$

Plots of this with respect to suspending medium conductivity and ζ-potential are shown in Figure 5-13.

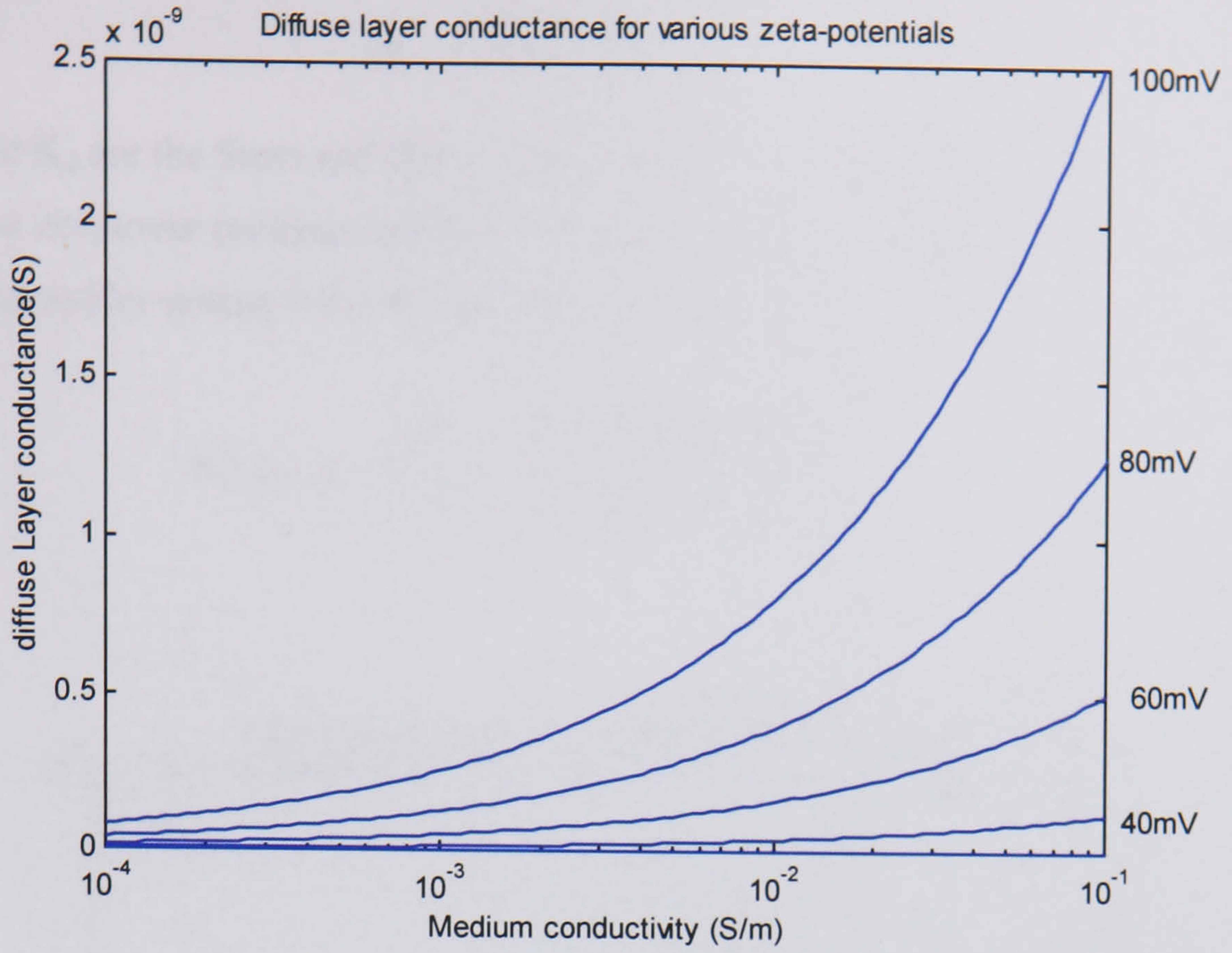

Figure 5-13

Diffuse layer conductance as a function of frequency for various ζ-potentials

It can be seen that the suspending medium conductivity may play an important role in the polarising process, particularly in the high conductivity regime, where the diffuse layer conductance is increasing rapidly[16]. The Stern layer conductivity can be written as the product of charge density and mobility as outlined in Chapter 2, but since little as yet is known conclusively of the ion mobility in this region the total magnitude is the most significant quantity.

5.4 Crossover predictions

O'Konski's term converting surface conductivity of a spherical particle into a specific conductance was derived by considering the radial charge motion in interfacial polarisation as well as current flow around the particle [10]. The mechanism for the latter charge transport in O'Konski's theory is purely conduction. However, the addition of the Bikerman electro-osmotic component could be equated to a simple increase in charge transport so considering this as an extra surface conductivity term in O'Konski's analysis would not be incompatible with his theoretical derivation. Since the Stern layer has no electro-osmotic component this must be dealt with separately. It is assumed that the two conductivities are non-interacting – a reasonable proposal given the rigid confinement of charge in the Stern layer - and so they are combined by summation in the O'Konski expression to give a total surface conductance:

---

[16] between an exponential and cosh function depending on the co-ion/counter-ion ratio

$$\sigma_p = \frac{2K_s + K_d}{R} \qquad (5\text{-}8)$$

where K_s and K_d are the Stern and diffuse layer conductances respectively.

The resultant crossover predictions using this expression are illustrated in Figure 5-14. The plots are obtained by setting $K(\omega)=0$ and solving for ω to give:

$$\omega_{crossover} = \left[\frac{(\sigma_m - \sigma_p)(\sigma_p + 2\sigma_m)}{(\varepsilon_p - \varepsilon_m)(\varepsilon_p + 2\varepsilon_m)}\right]^{\frac{1}{2}} \qquad (5\text{-}9)$$

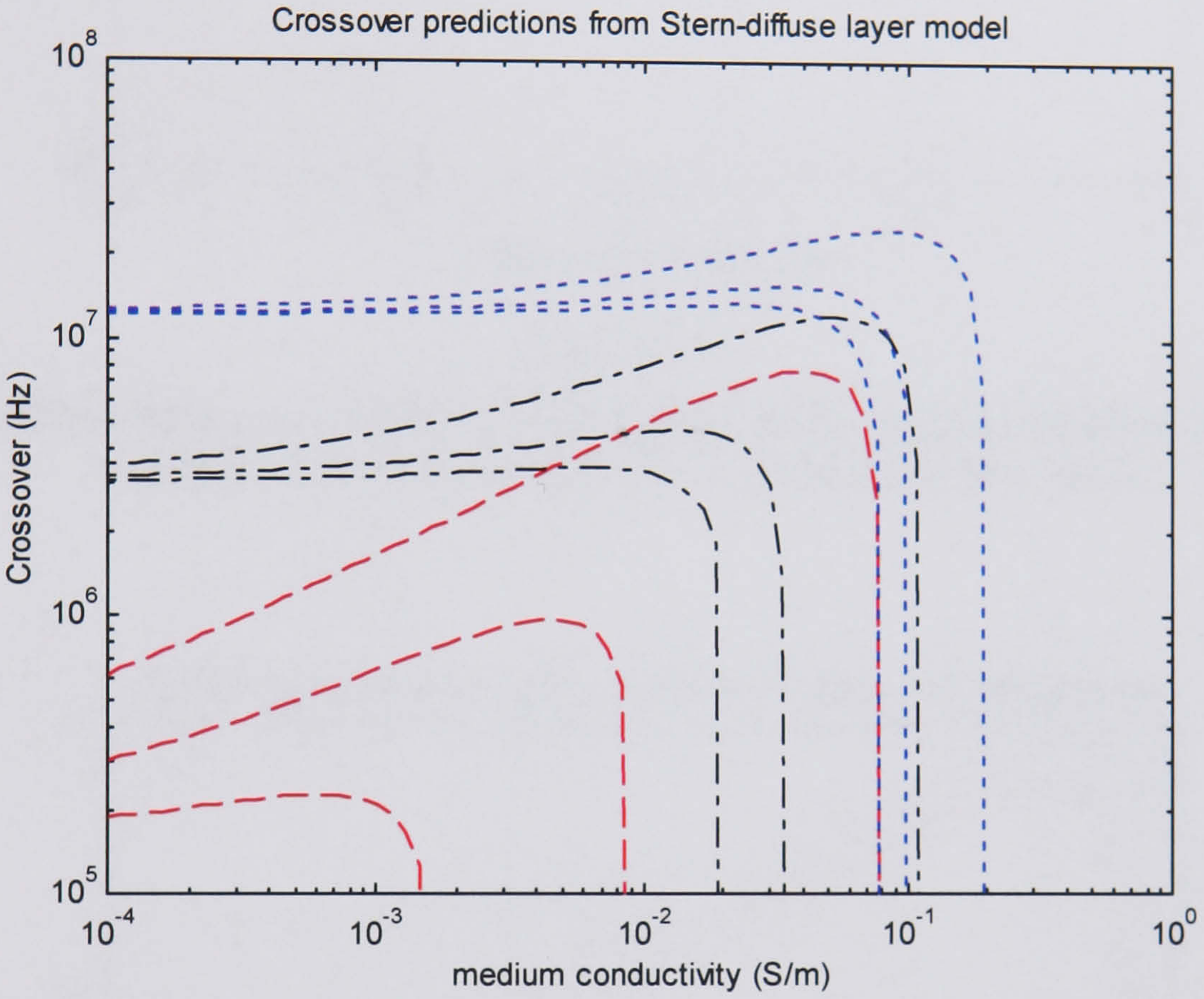

Figure 5-14

Stern-diffuse model shown for 3 Stern layer conductances, dashed line-K_s=0.1, dot-dash-K_s=2, dotted K_s=8, each with ζ-potential 50mV, 100mV and 200mV.

As can be seen, the slope before the fall-off is governed by the ζ-potential, the increase of which results in a steeper gradient of the crossover predictions in a log-log plot. The Stern layer conductance parameter by contrast can be used to adjust the general height of the graph with higher conductances resulting in an increase in the average crossovers.

It can be seen, in addition, that at low ζ-potentials the Stern layer conductance dominates in determining the point where positive DEP is no longer observed (Figure 5-15), whereas at high ζ-potentials the Stern layer conductance has little prediction power of this parameter (Figure 5-16). Here instead the inner layer conductance may be more readily estimated by fitting to the low medium conductivity data.

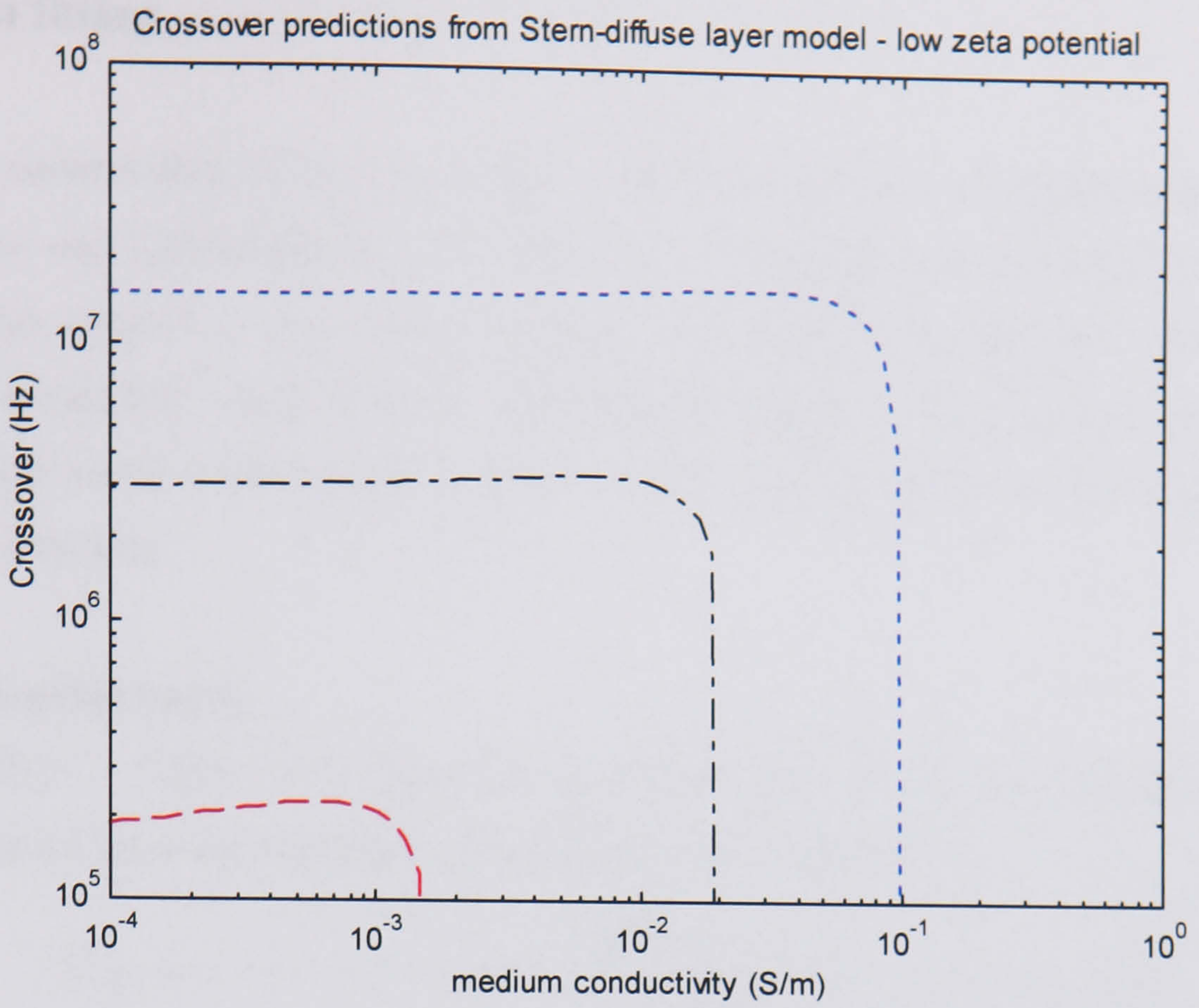

Figure 5-15

Low ζ-potential behaviour (50mV) of Stern-diffuse model showing variation in Stern layer conductance over 2 decades (0.1, 2, 10nS) for 216nm beads.

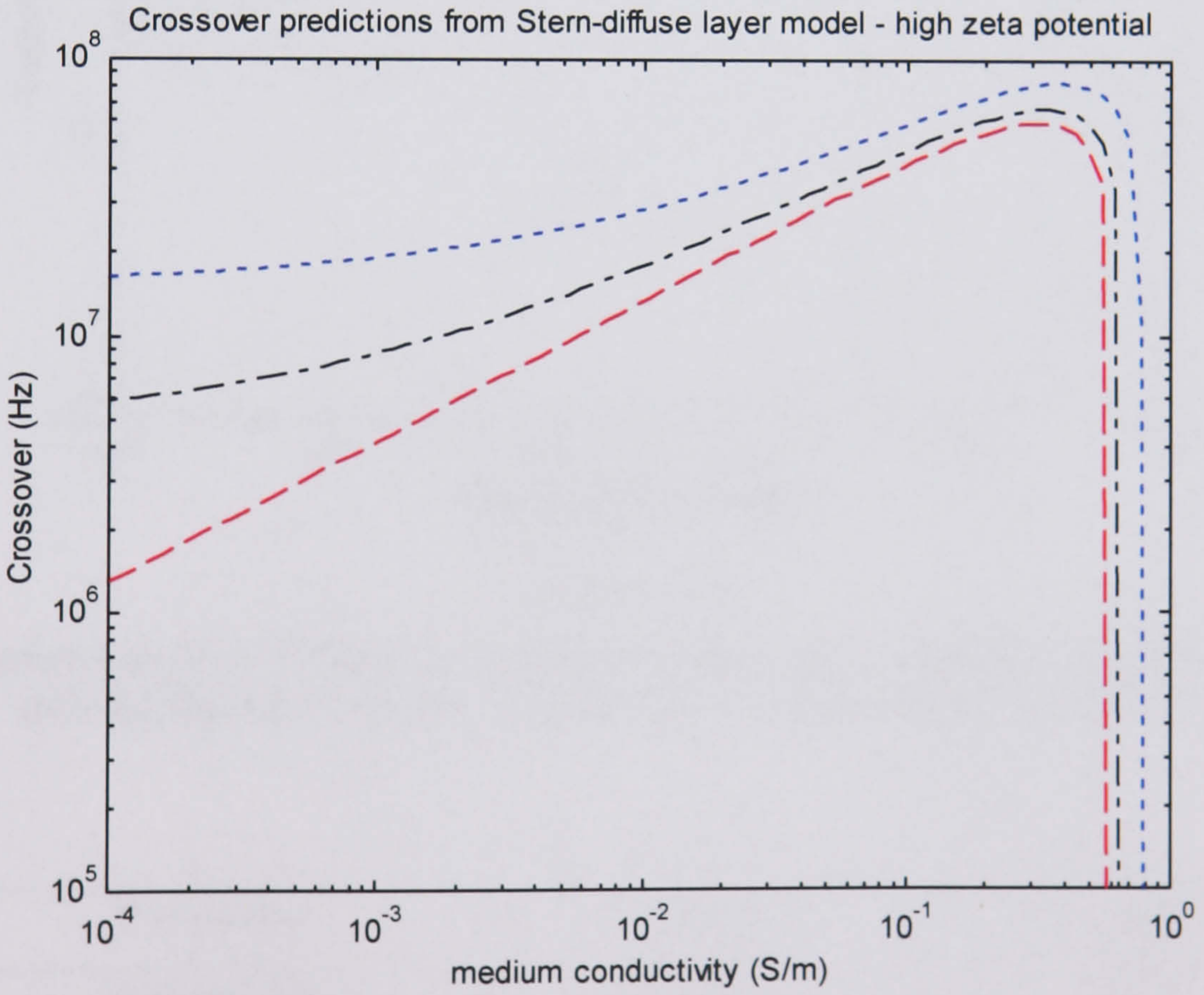

Figure 5-16

High ζ-potential behaviour (200mV) of Stern-diffuse model showing variation in Stern layer conductance over 3 decades (0.01, 3, 10nS) for 216nm beads.

5.5 Data fitting

A least squares data-fitting routine was written to simultaneously optimise the Stern layer conductance and ζ-potential for each data set. The minimising procedure used was the Nelder-Mead simplex (direct search) method. It is based on evaluating a function at the vertices of a simplex[17], then iteratively shrinking the simplex as better points are found until some desired bound is obtained [11]. Below can be seen the results of the fitting procedure on various data sets.

5.5.1 Uncoated beads

Figure 5-17 - Figure 5-19 show the optimized data fits on the uncoated beads with comparisons of the initial and final values in Table 5-1-Table 5-3.

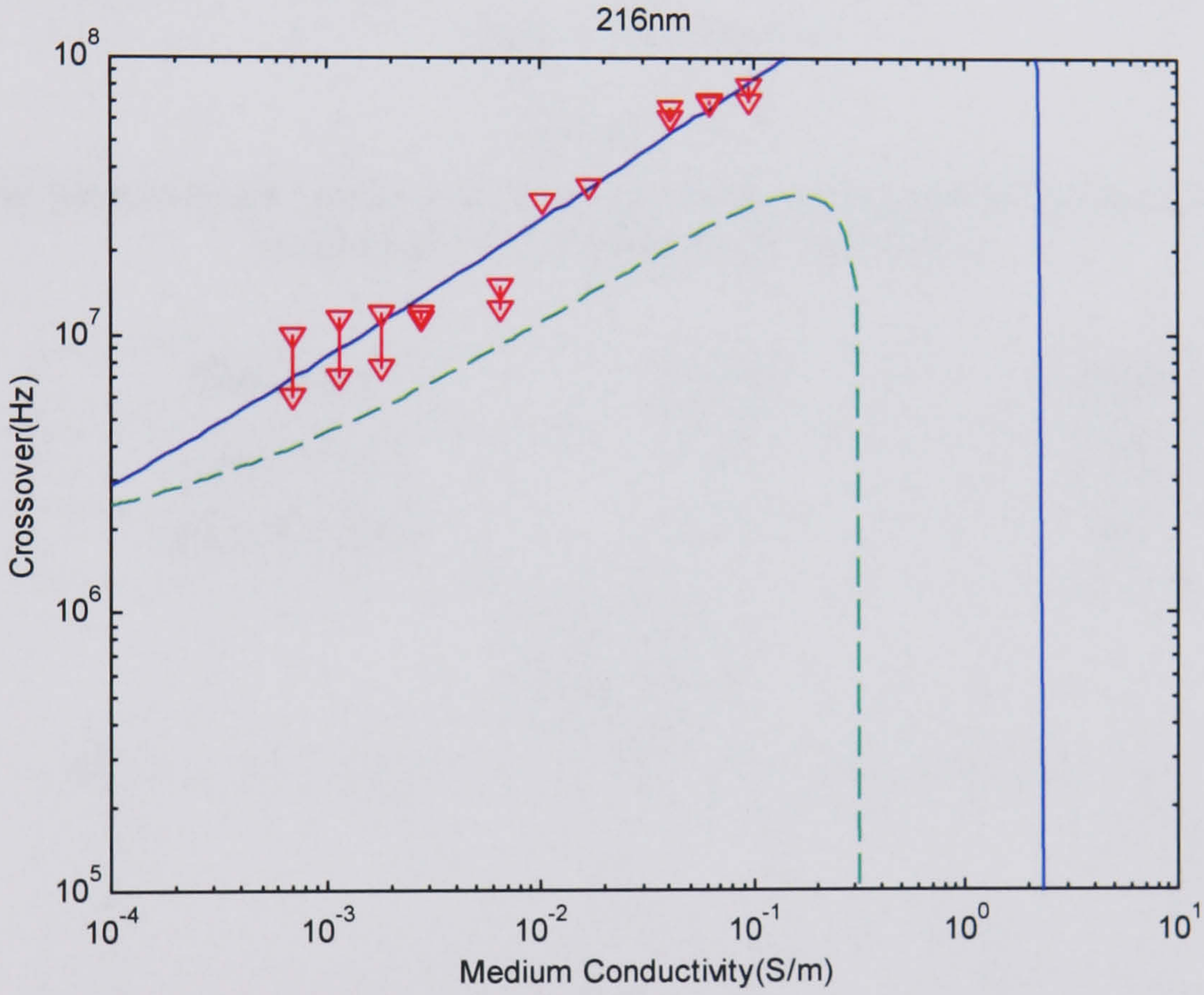

Figure 5-17

Least squares data fit of 216nm beads with combined diffuse and Stern layer conductances showing the initial attempt (dashed line) and optimised fit (solid line).

Parameter	K_s(nS)	ζ (mV)
starting value	0.500	150
optimised value	0.125	199

Table 5-1

216nm beads

---

[17] The generalization of a tetrahedral region of space to *n* dimensions

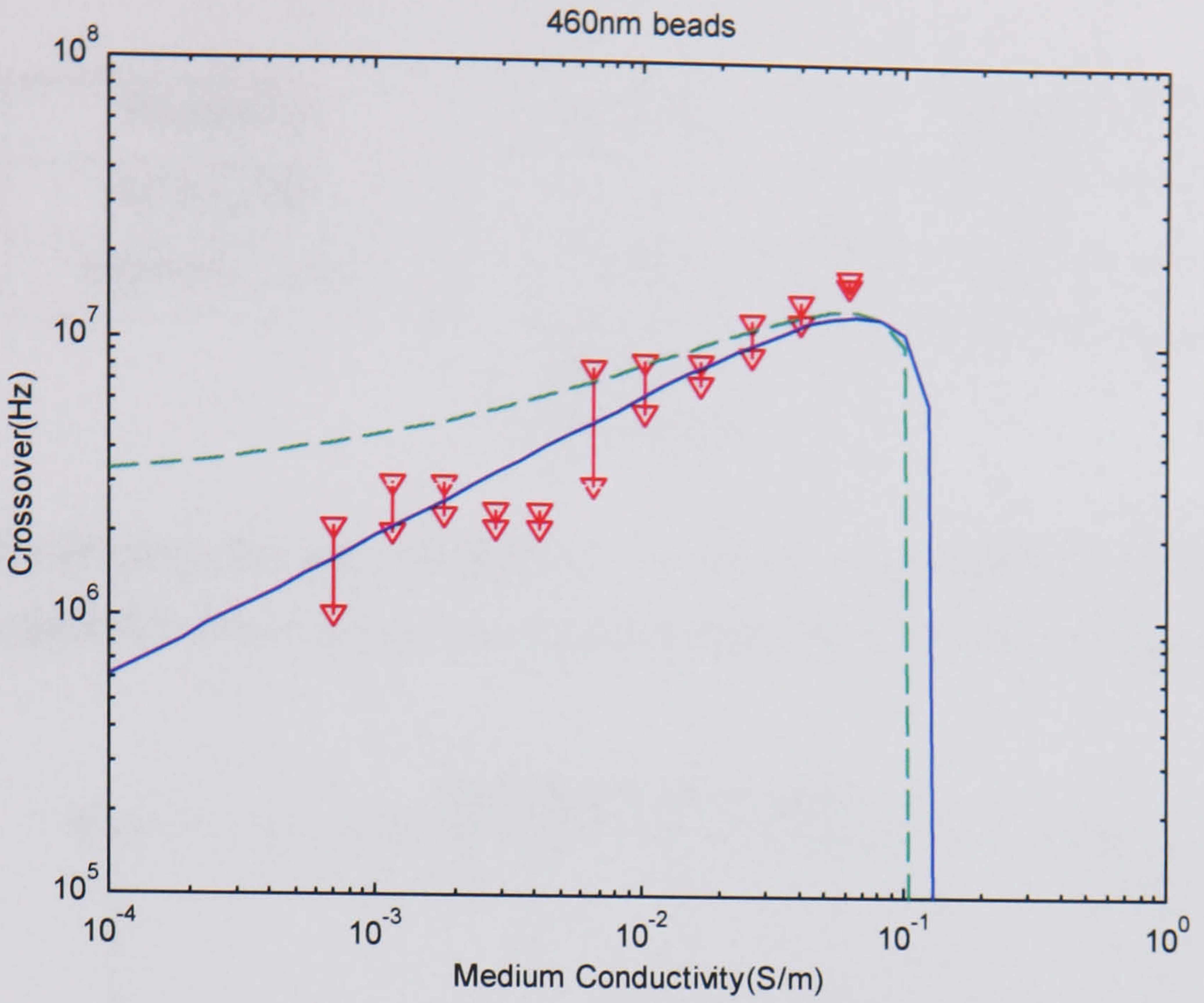

Figure 5-18

Data fit of 460nm beads using combined conductance model showing the initial attempt (dashed line) and optimised fit (solid line).

Parameter	**K_s(nS)**	**ζ (mV)**
starting value	2.0	150
optimised value	0.0	159

Table 5-2

460nm beads

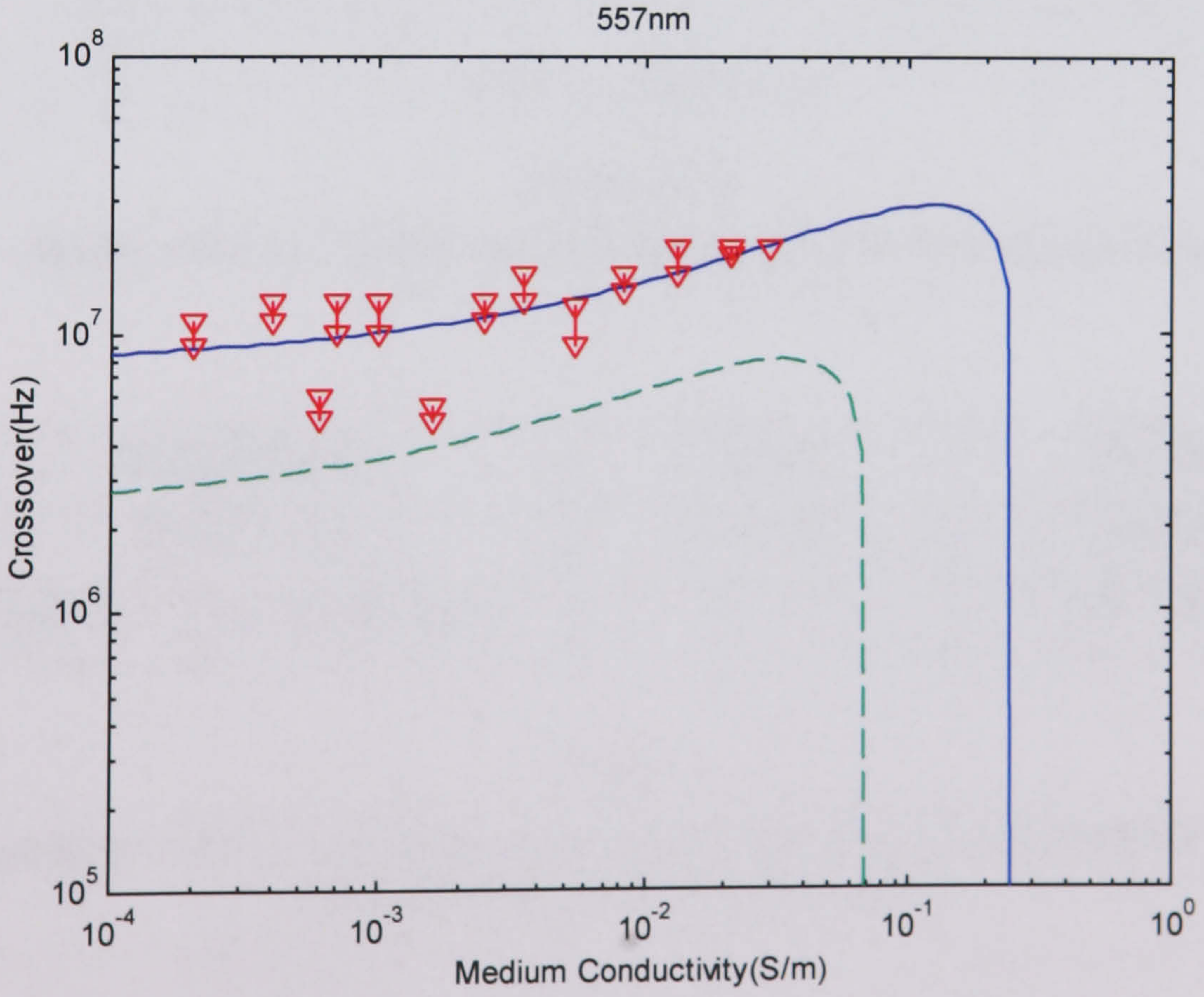

Figure 5-19

Data fit of 557nm beads using combined conductance model - initial attempt (dashed line) and optimised fit (solid line).

Parameter	**K_s(nS)**	**ζ (mV)**
starting value	2.0	150
optimised value	6.59	181

Table 5-3

557nm beads

When the optimum fits were obtained, the sensitivity to modification of the parameters around the predicted values was also investigated within the error range of the data.

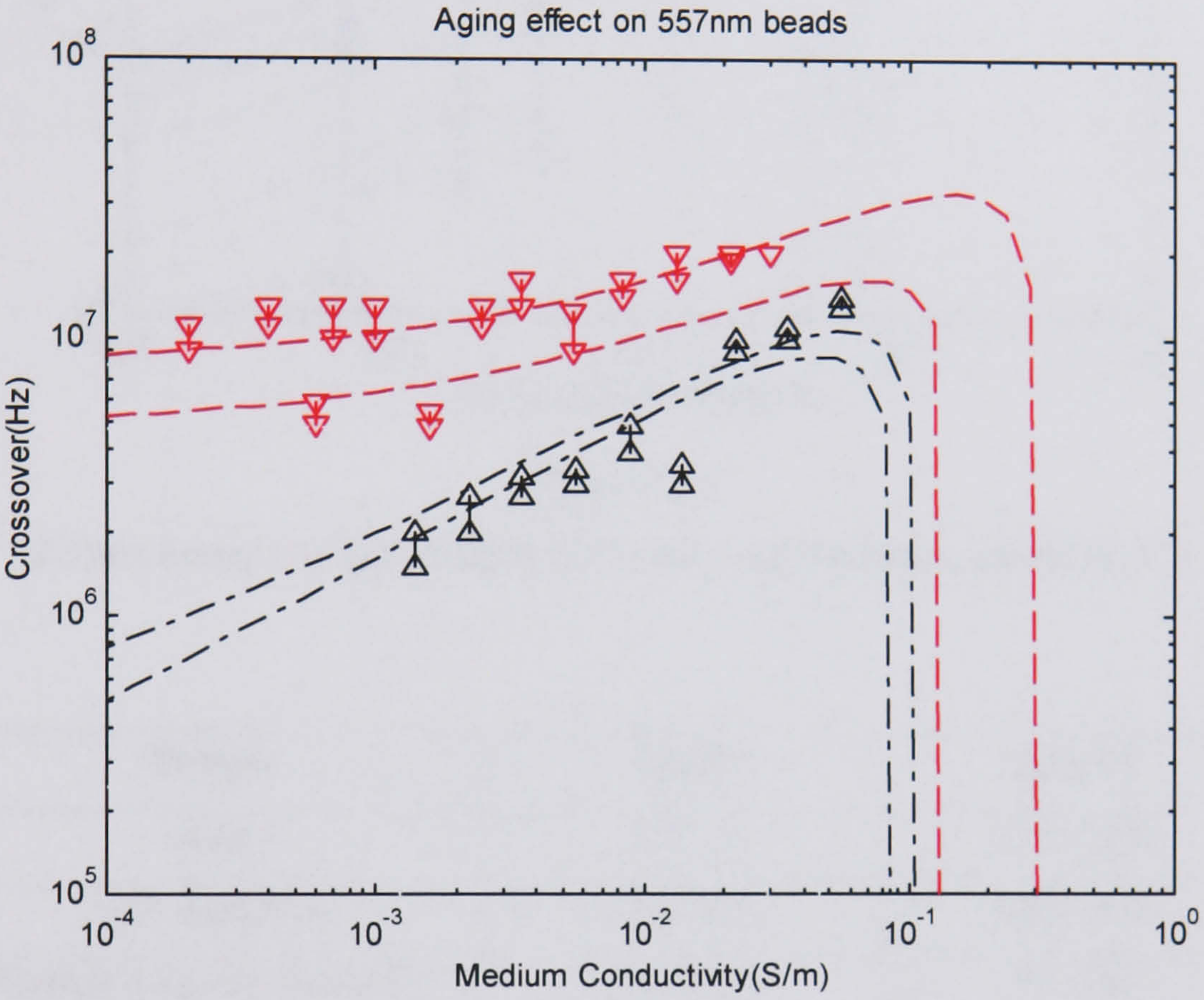

Figure 5-20

Ageing effect on 557nm beads showing upper and lower fitting limits.

Measurements	**K_s(nS)**	**ζ (mV)**
Batch 1 (△)	0.0 -0.4	159-163
Batch 2 (▽) (18 months later)	4 – 6.7	160 - 182

Table 5-4

Effect of ageing on Stern layer conductance and ζ-potential of 557nm beads for 2 batches of measurements made 18 months apart.

5.5.2 IgG and complimentary antibody labeled

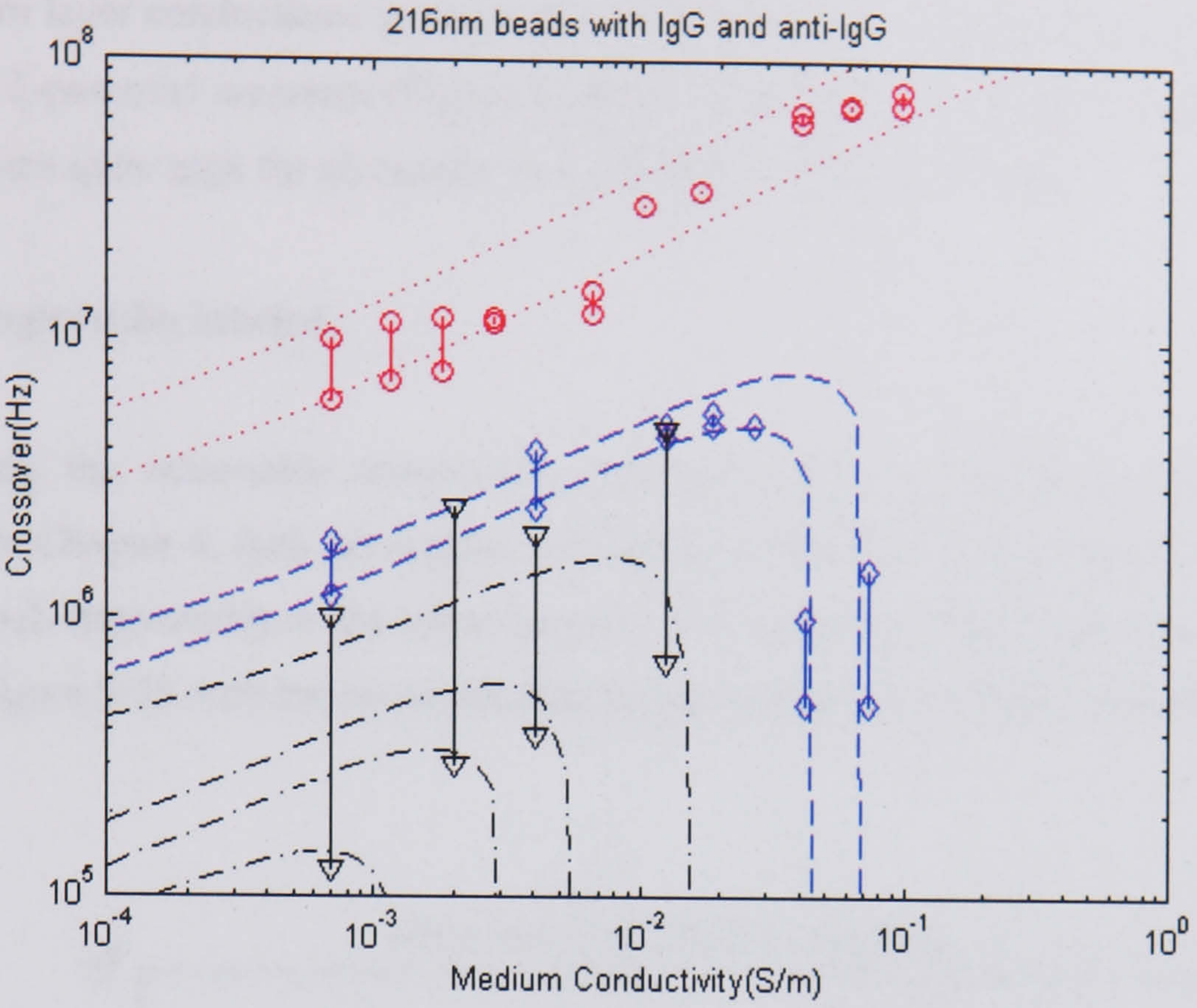

Figure 5-21

216nm beads (○) IgG modified (◊) with complimentary antibody (▽).

Sample	**K_s(nS)**	**ζ (mV)**
beads	0.0 - 2	177 - 210
IgG modified	0.0 -0.4	103 - 120
Complimentary antibody	0.0– 0.07	45 - 80

Table 5-5
216nm IgG/anti-IgG modified beads

The IgG modified fits produced a fairly narrow band of ζ-potential values due to the low error ranges in the crossover data. This suggests fairly uniform coverage has been achieved. Adding the complimentary antibody, however, produces a much larger spread in the data, implying that the degree of attachment has been much more variable.

In this case, it is proposed that various positive DEP cut-off points occur corresponding to a variation in ζ-potential, with particles of low ζ-potential and Stern layer conductance not undergoing positive dielectrophoresis above a certain conductivity threshold and therefore not contributing to the crossover observations beyond this point. This is equivalent to saying that the observed crossovers at higher conductivity are due to a sample with a proportionally higher fraction of particles of larger ζ-potential. Several curves are needed, therefore, to adequately fit all the data.

The Stern layer conductance is much less well defined and becomes correspondingly less accurate as ζ-potential increases (Figure 5-16). In fact, only upper bounds can be established which become quite high for all but the complimentary antibody sample.

5.5.3 Streptavidin labeled

Following the reasonable streptavidin adsorption results obtained at neutral pH, as described in Chapter 4, both adsorption and carbodiimide mediated covalent coupling were used to attach streptavidin to the microspheres. The crossover results can be seen in Figure 5-22 and Figure 5-23 with the corresponding fitting parameters in Table 5-6 and Table 5-7.

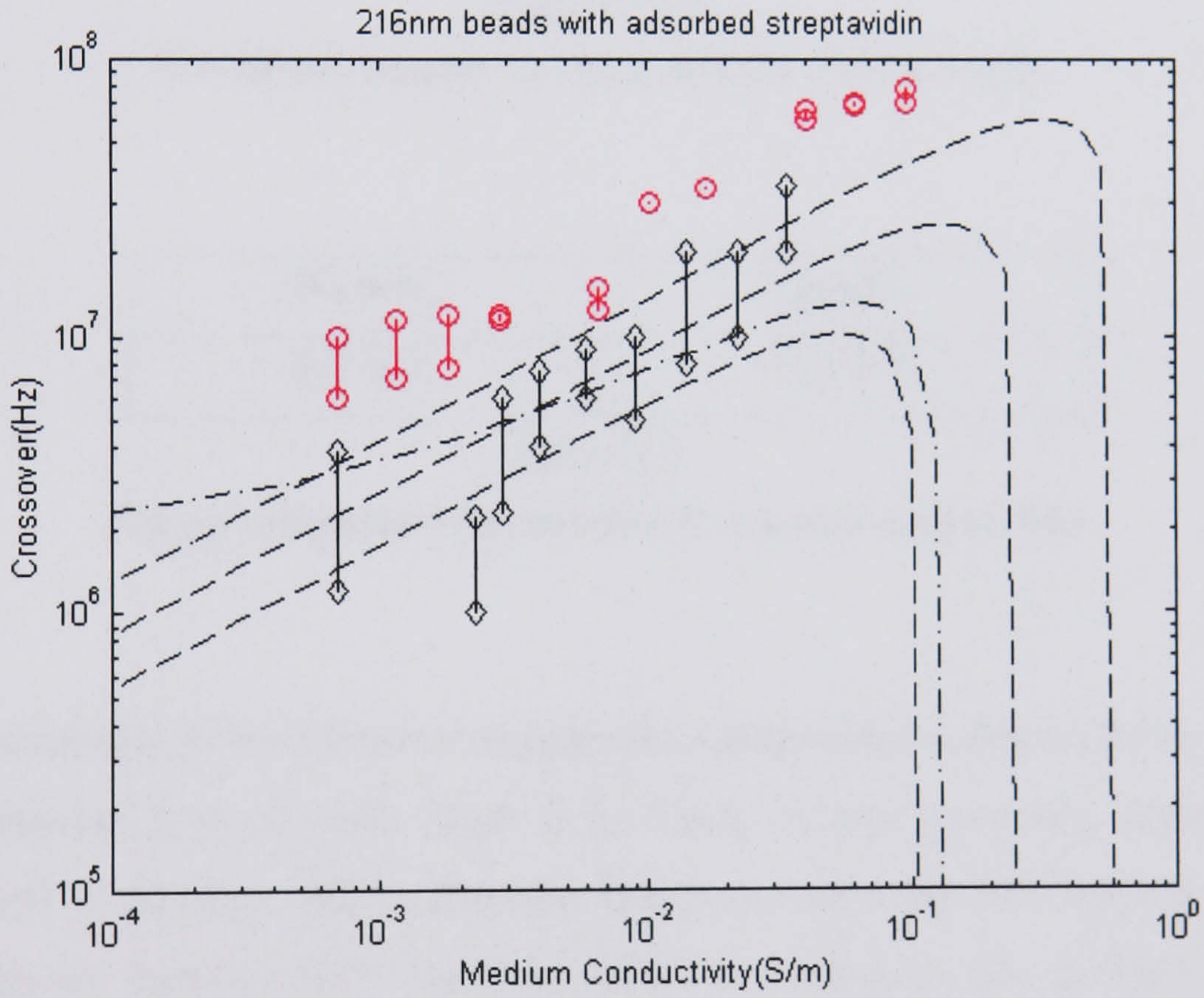

Figure 5-22

216nm beads with adsorbed streptavidin showing a range of possible data fits. Dashed line - K_s=0nS, ζ-potential =120-160mV, dot-dash - K_s=0.6nS, ζ-potential =120mV

K_s(nS)	ζ (mV)
0.0-0.6	120 - 160

Table 5-6

Adsorbed streptavidin fitting parameter ranges

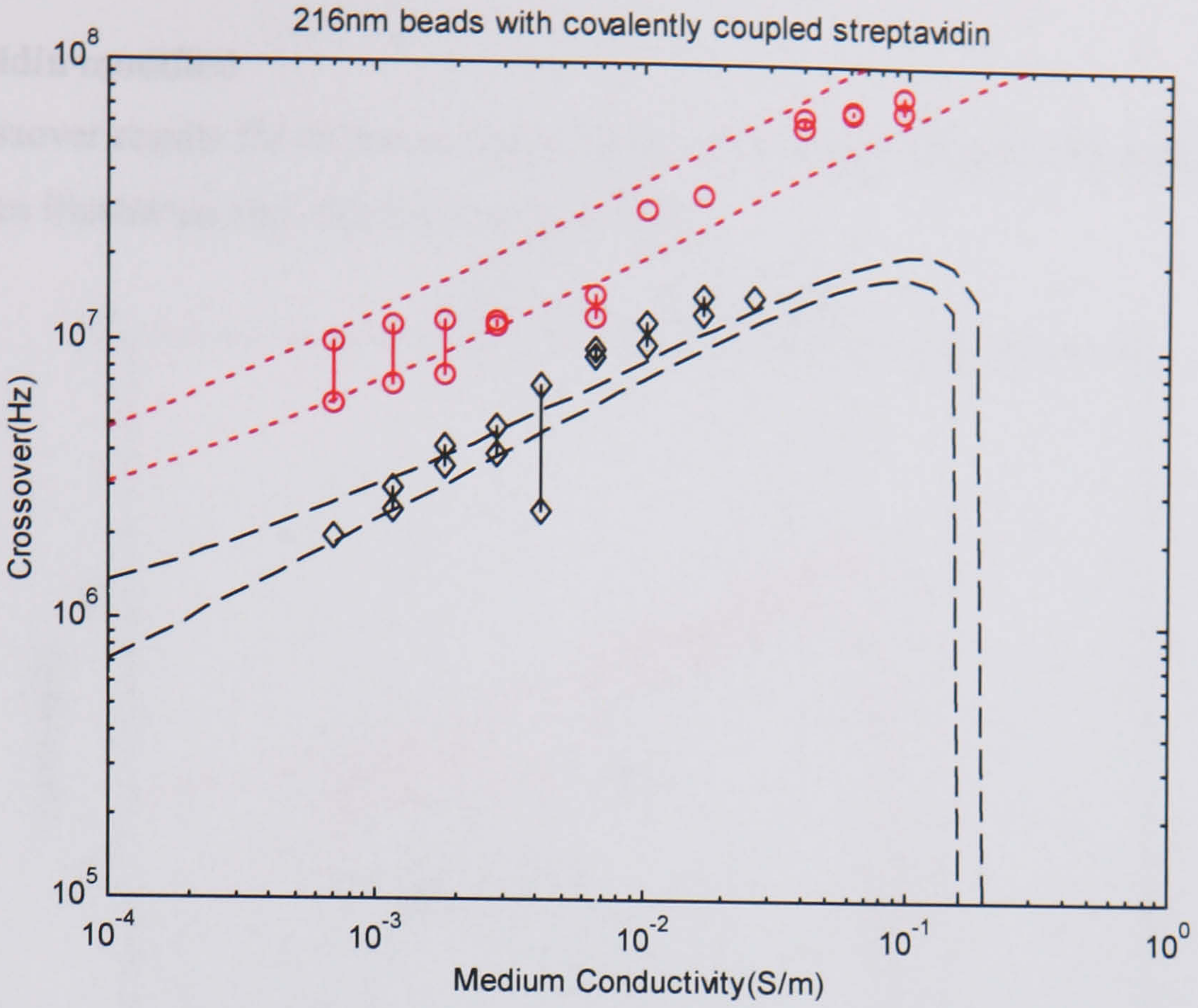

Figure 5-23

Covalently coupled streptavidin on 216nm beads

K_s(nS)	ζ (mV)
0.0-0.2	132-135

Table 5-7

Fitting parameters for covalently coupled streptavidin

The non-uniformity of the adsorbed streptavidin sample means that it can be covered by a range of ζ-potentials (Figure 5-22, Table 5-6). These do not accurately correspond to the observed cut-off in positive DEP collection, however, implying that there may have been higher conductivity positive DEP that was difficult to observe due to fluid perturbations (refer to Chapter 9) or, possibly, heating effects – most likely the former as higher frequency naked bead crossovers are observable in this region. The ζ-potentials are again too high to accurately define *Ks*. The upper bound for this parameter is shown by the dot-dash line in Figure 5-22, corresponding to the lower bound of ζ-potential. This better defines the cut-off point and is within the error range of the low conductivity data so is not an unrealistic estimate. The ζ-potential range for the covalently coupled sample is much narrower. But being within the range established for the adsorbed sample they are still too high for *Ks* to be ascertained with a reasonable degree of precision.

5.5.4 Avidin modified

The crossover results for avidin modified beads are shown in Figure 5-24 with additional fitting curves illustrating the effect of low ζ-potential.

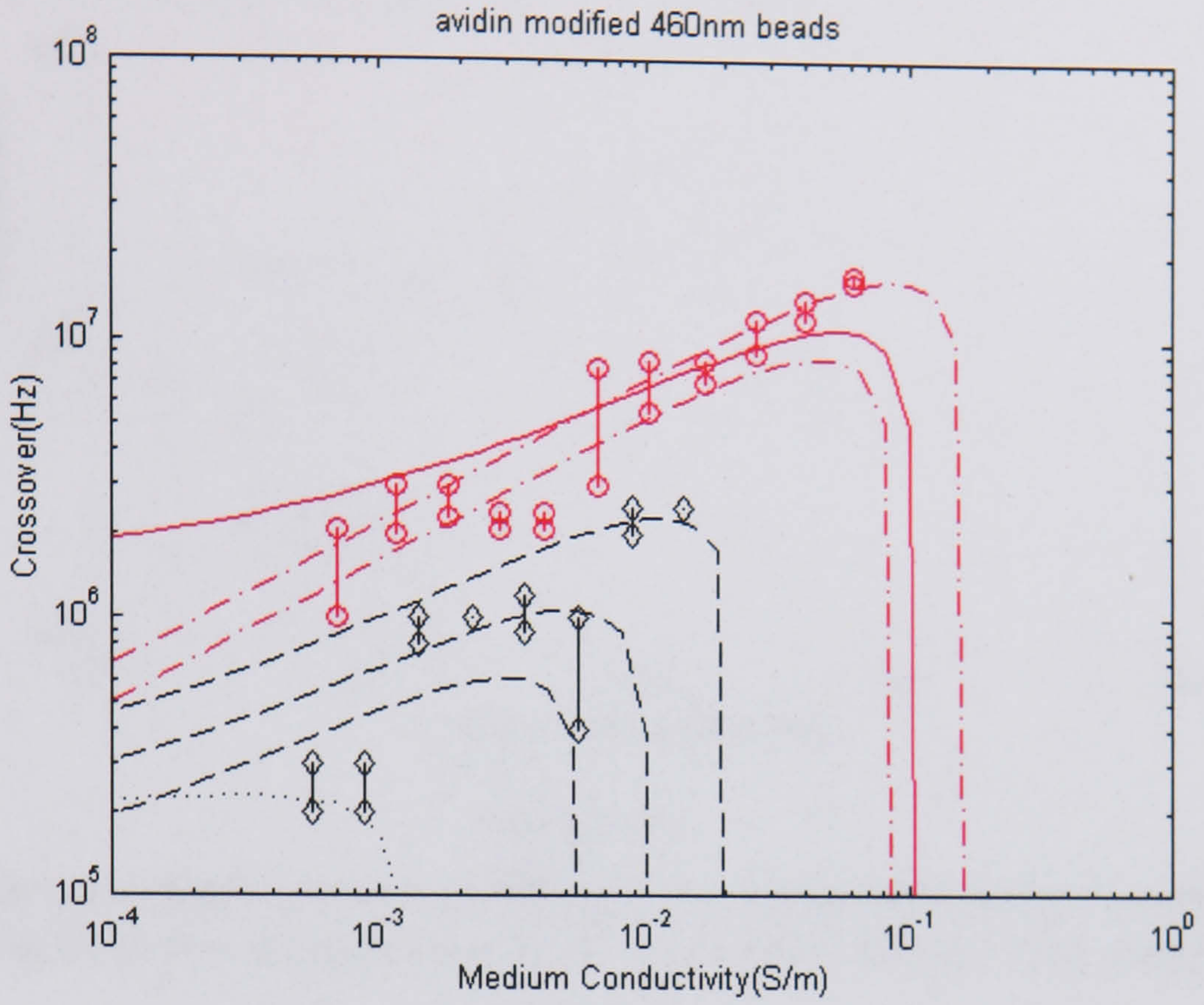

Figure 5-24

*460nm beads (**o**) with covalently coupled avidin (◊) Lines: Dot-dash– low K_s, upper and lower ζ limits; solid – upper K_s, lower ζ. Dash lines, highest to lowest, d=0.15nS; zeta=117mV; d=0.1nS; zeta=100mV; d=0.05nS; zeta=90mV. The dotted line shows the high K_s limit, 0.15nS, with ζ=0mV as a point of reference*

Sample	K_s(nS)	ζ (mV)
beads	0.0 – 1.0	150 -165
with avidin	0.0 – 0.15	90 - 117

Table 5-8

Fitted data range for avidin modified beads

5.5.5 Oligonucleotides

The crossover fitting results for streptavidin and secondary layer biotinylated oligonucleotide samples are shown in Figure 5-25 with a summary of fitting parameters given in Table 5-9. The marked reduction in crossovers on oligonucleotide attachment means that much narrower bounds for the Stern layer conductance can be gauged, with correspondingly low ζ-potential.

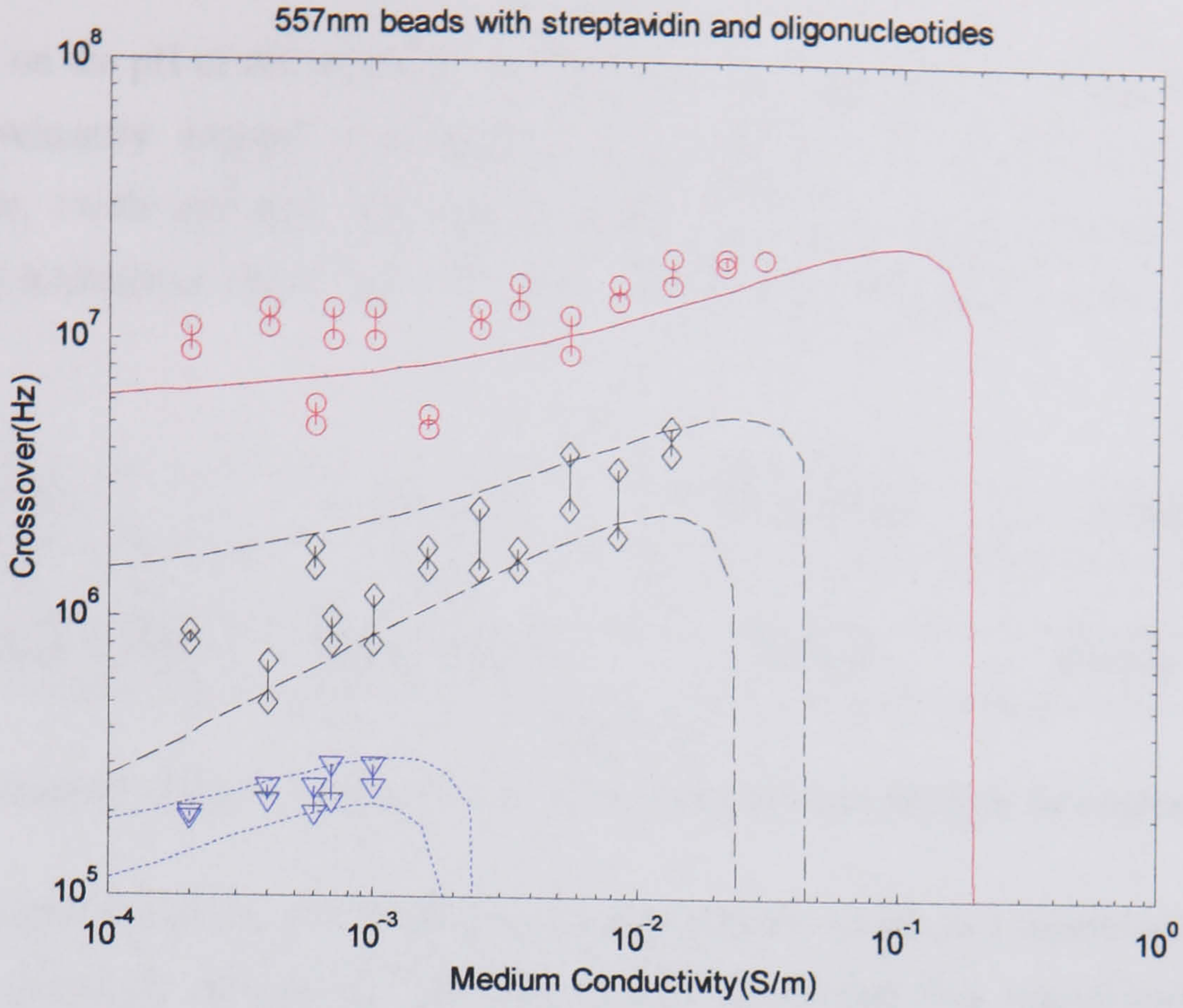

Figure 6-25

557nm beads (○) modified with streptavidin (▽) and oligonucleotides (◊). Dashed and dotted lines showing upper and lower limits of K_s and ζ for each sample

Sample	**K_s(nS)**	**ζ (mV)**
beads	4 – 6.5	150 - 180
streptavidin	0.0 - 1	130-139
oligonucleotides	0.04 – 0.1	70 - 80

Table 6-9

Fitting parameters for beads with streptavidin and oligonucleotides

6.6 ζ-potential and surface modification

The general trend following surface modification of the latex beads appears to be that the ζ-potential is lowered. This shows some compatibility with expectations in that much of the native negative charge on the bead originating from the ionized carboxyl groups would be neutralized by the formation of covalent bonds with the linked proteins. Whether the protein itself effectively adds counter or co-ionic charge is the second point of consideration since the proportional nature of the fixed charge is the ζ-potential defining element. If the additional charge introduced into the Stern layer is comprised of counter-ions the ζ-potential will be lowered by surface modification. Likewise if the net added charge consists of co-ions it would be increased. The overall charge on a coupled protein may be positive or negative depending on the pH of the solution i.e. pertaining to whether the amino or carboxyl groups are predominantly ionised. Considering the position of the three primary proteins, streptavidin, avidin and IgG with respect to their isoelectric points in a neutral medium reasonable estimations (from fig 4-9) of the sign of their net charge can be made (Table 5-10).

Protein	Avidin	Streptavidin	Mouse IgG
Ip	~10.5	~7	~6
Sign of charge at pH 7	Highly positive	Neutral	Weakly negative

Table 5-10

Estimation of sign of charge of the three primary layer proteins in neutral pH

Streptavidin and avidin are at or below their isoelectric points in a neutral medium – i.e. neutral or positively charged and therefore it is plausible that they would contribute to a lowering of the ζ-potential, although some of their amino groups will also be neutralised during the immobilisation. The situation with IgG, however, is less clear. Carrying, possibly, the greatest amount of negative charge this could compensate for the neutralization of the carboxyl groups on covalent bond formation so that the ζ-potential need not necessarily be reduced. Therefore, in order to assess the viability of the ζ-potential predictions of this model it is necessary to make independent measurements of this parameter using another established technique.

5.7 Electrophoretic Mobility Data

The electrophoretic mobility is effectively governed by the ζ-potential since this potential originates from the fixed charge on the bead surface i.e. that which moves with the bead under the action of a static electric field. Electrophoretic mobility observations were therefore carried out on the Coulter DELSA^{TM}, which was used to assess the effect of protein layers using the mouse/anti-mouse specimen. Sample profiles are shown in Figure 5-26. The four curves shown in each of the graphs represent the output from each of the photodetectors. As can be observed from the consistency of the data from all the measured angles, uncoated beads and those with one protein layer were largely homogenous allowing a realistic assessment of the mobility. The measurements at various medium conductivities can be seen in Figure 5-27 and Figure 5-28. These agree well with similar mobility analyses [12-14]. The clumping of some particles with two layers of protein, however, meant that these samples were too poly-disperse to measure and generally had substantial peaks at zero mobility.

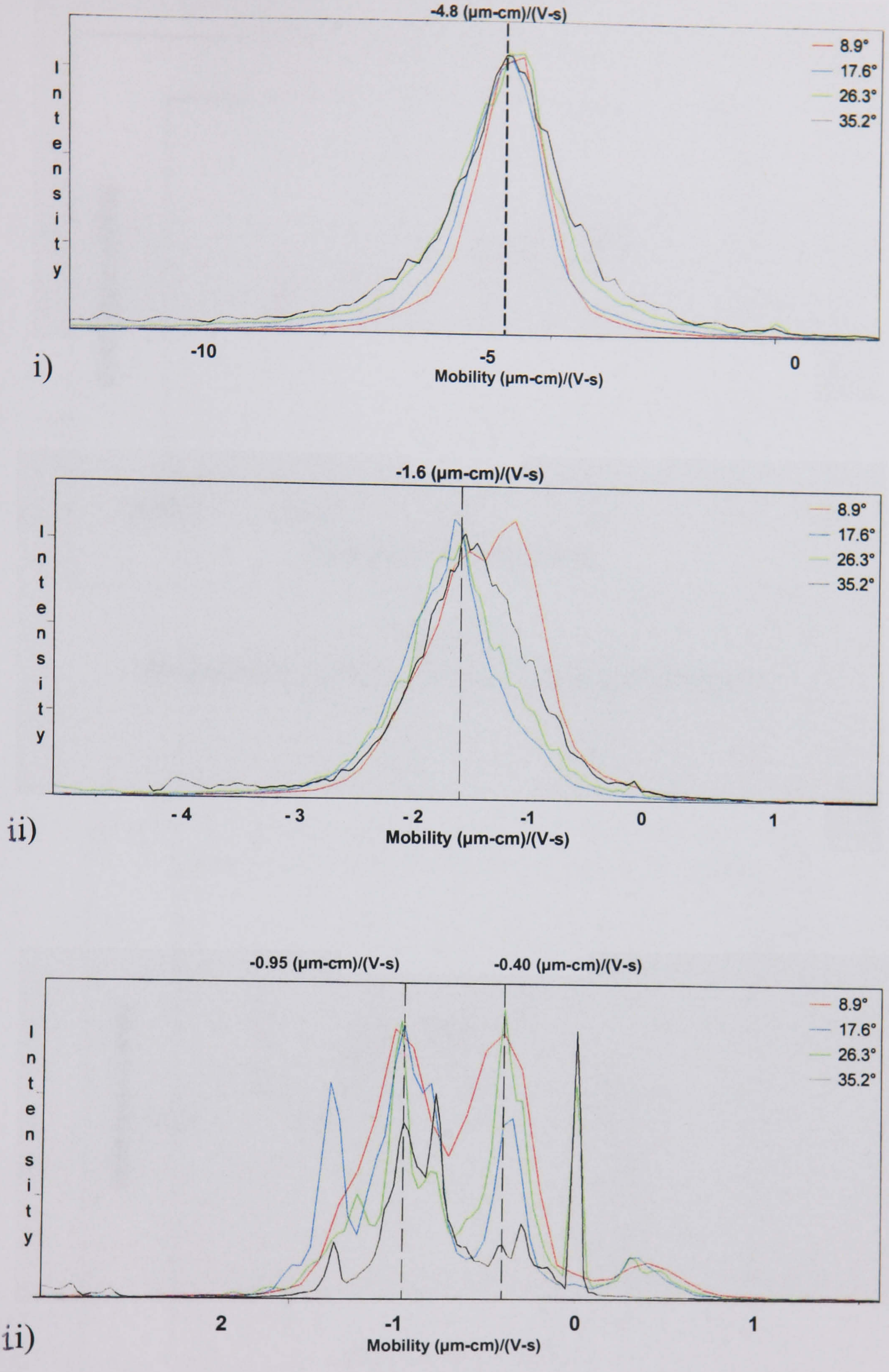

Figure 5-26

Sample DELSA graphs for 216nm beads in KCl i) unmodified ii) with a single layer of Mouse IgG protein and iii) with Mouse IgG and complimentary antibodies. i) and ii) show high consistency between all four detectors implying good levels of sample homogeneity, whereas iii) is very poly-disperse due to bead cross-linking with the result that the detector readings are incongruent and no conclusive mobility measurement can be made.

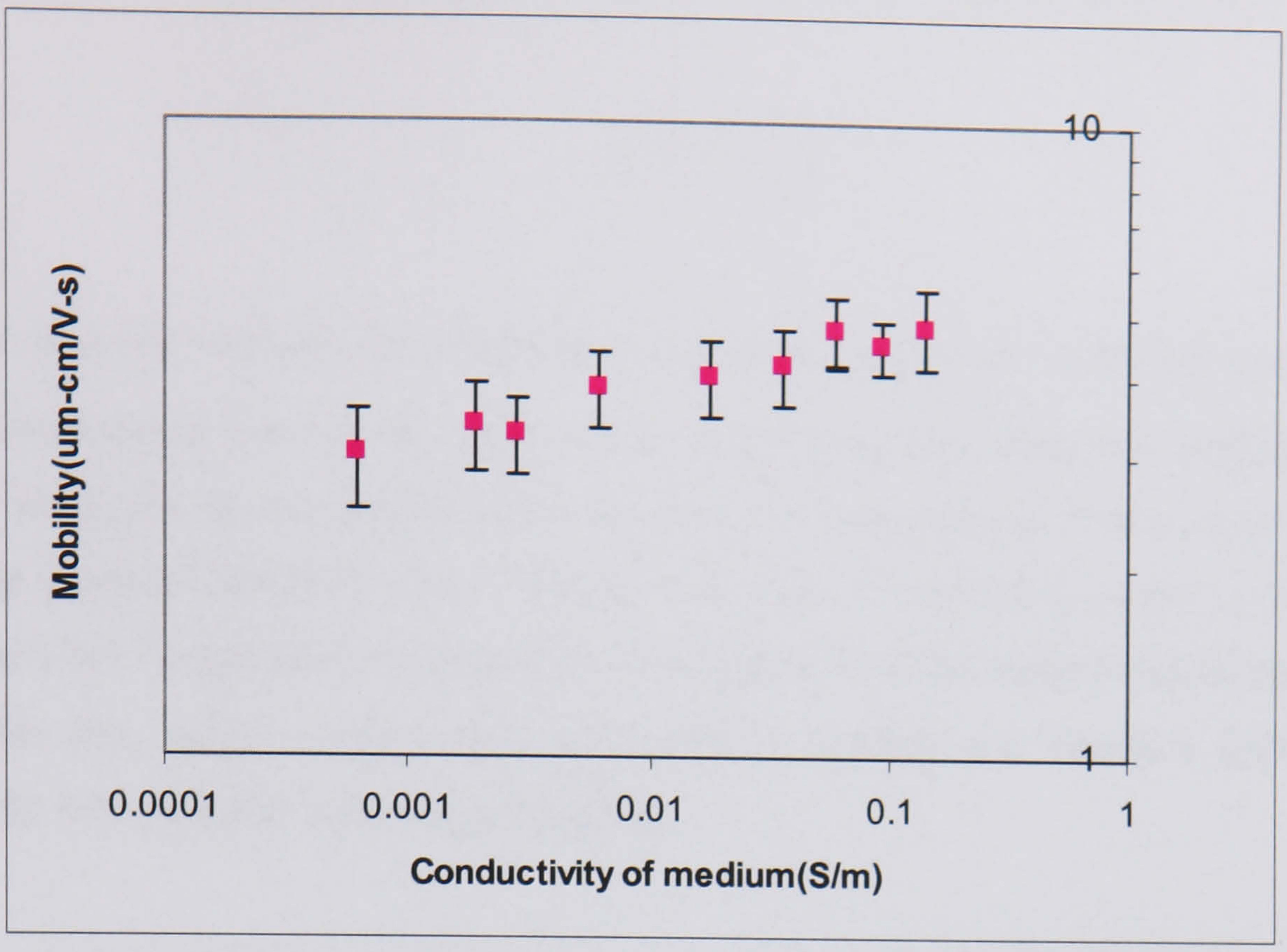

Figure 5-27
Electrophoretic mobility of 216nm carboxylated latex beads

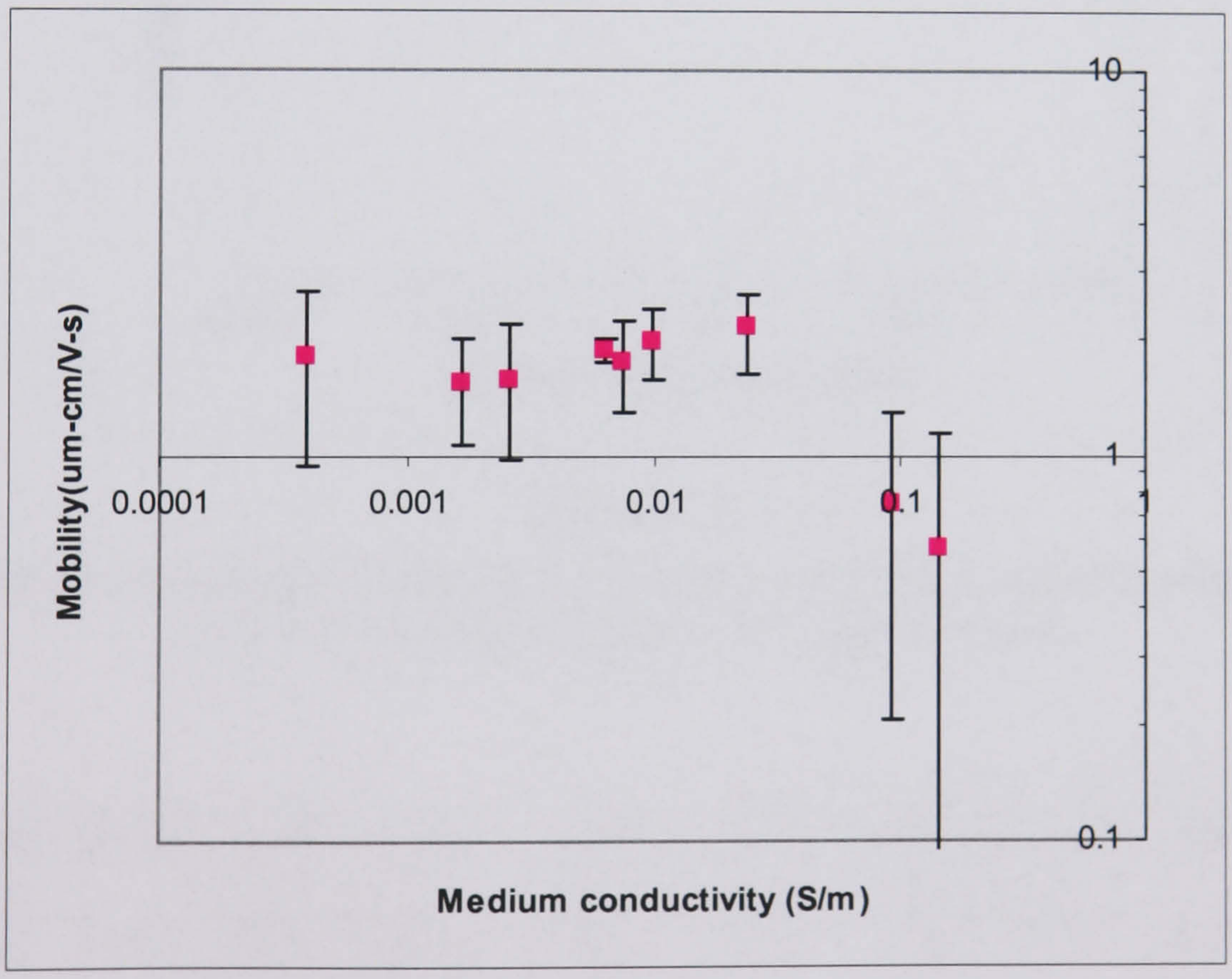

Figure 5-28
Electrophoretic mobility of 216nm beads with a monolayer of protein

The Smoluchowski relation converting ζ-potential to mobility, U, is given by:

$$U = \frac{\varepsilon_o \varepsilon_r \zeta}{\eta} \tag{4-7}$$

where η is the viscosity of the medium, applicable to particles with thin double layers and no conductance behind the shear plane. Converting the measured mobilities to ζ-potential using this approximation, however, produced systematically lower absolute values than those predicted (Figure 5-29 and Figure 5-30 with corresponding values in Table 5-11 and Table 5-12). Nonetheless it is apparent from Figure 5-31 that surface modification of the latex beads does indeed cause a substantial drop in mobility and therefore ζ-potential in accordance with the DEP crossover predictions.

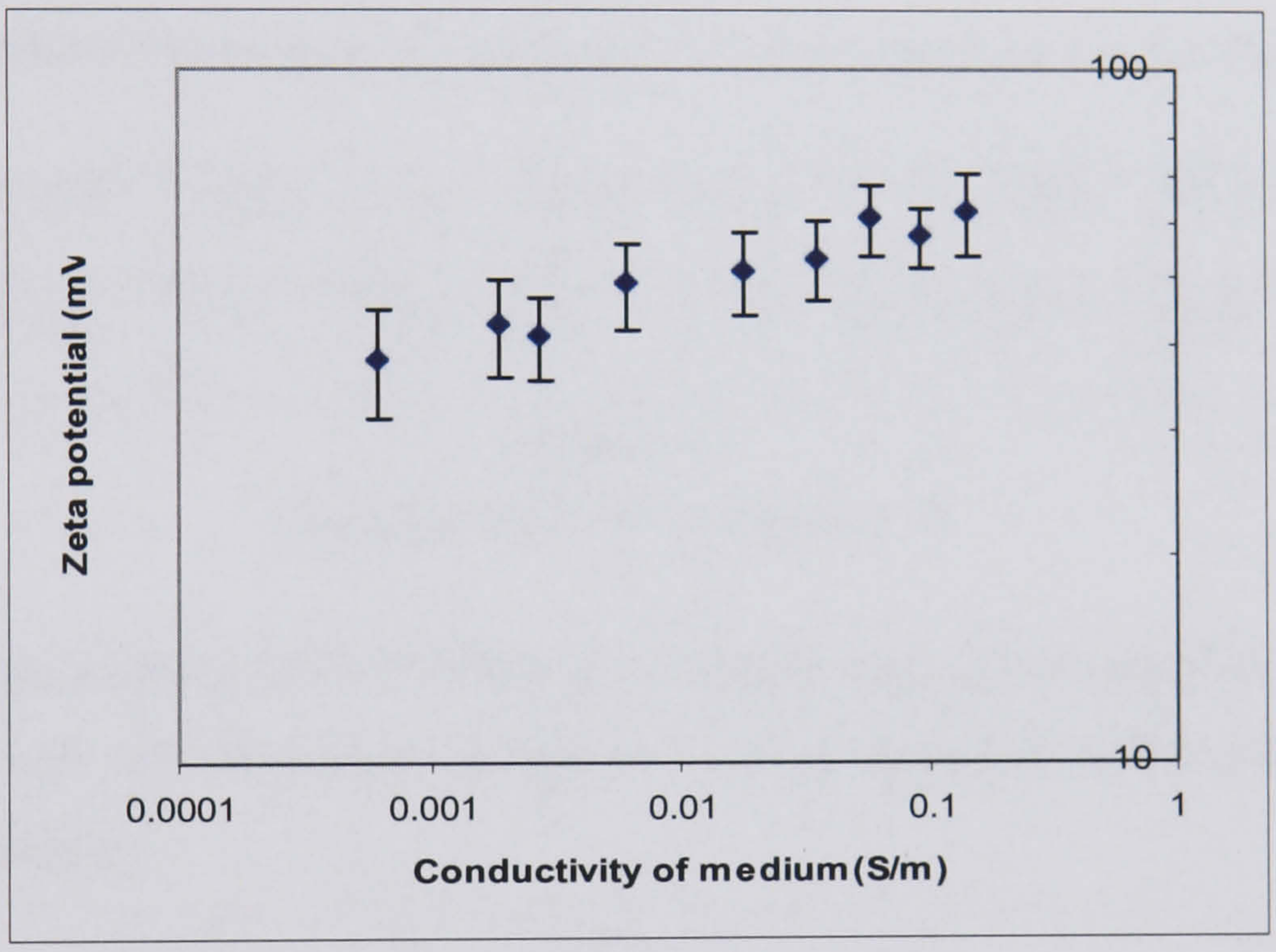

Figure 5-29

ζ-potential of carboxylated 216nm beads calculated from DELSA mobility measurements using the Helmholtz-Smoluchowski approximation

Conductivity (mS/m)	0.623	1.89	2.76	6.17	17.8	36	92.1	58.6	142.7
ζ-potential (mV)	38.3	43	41.3	49.1	51.2	53.4	57.5	61.1	62.5

Table 5-11

ζ-potentials shown in Figure 5-29.

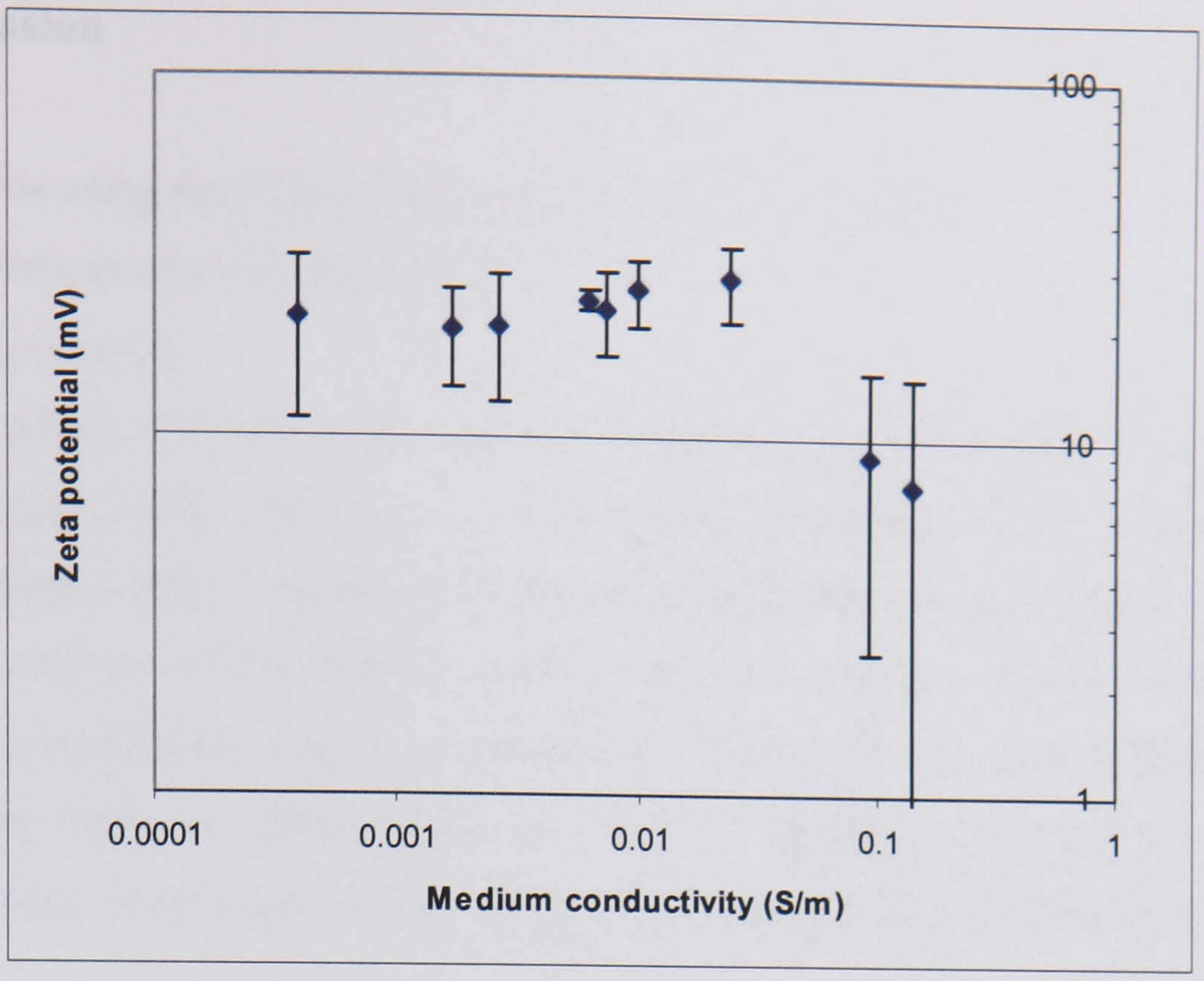

Figure 5-30

Helmholtz-Smoluchowski ζ-potential for 216nm beads with mouse IgG

Conductivity (mS/m)	0.385	1.661	2.6	6.23	7.32	9.79	23.9	93.2	142
ζ-potential (mV)	21.3	19.7	20.3	24	22.5	25.5	27.4	8.91	7.35

Table 5-12

ζ-potentials shown in Figure 5-30.

The last 2 data points in Table 5-12 are due to sample aggregation caused by double layer contraction at high salt concentrations and are not representative of the ζ-potential in a monodisperse sample.

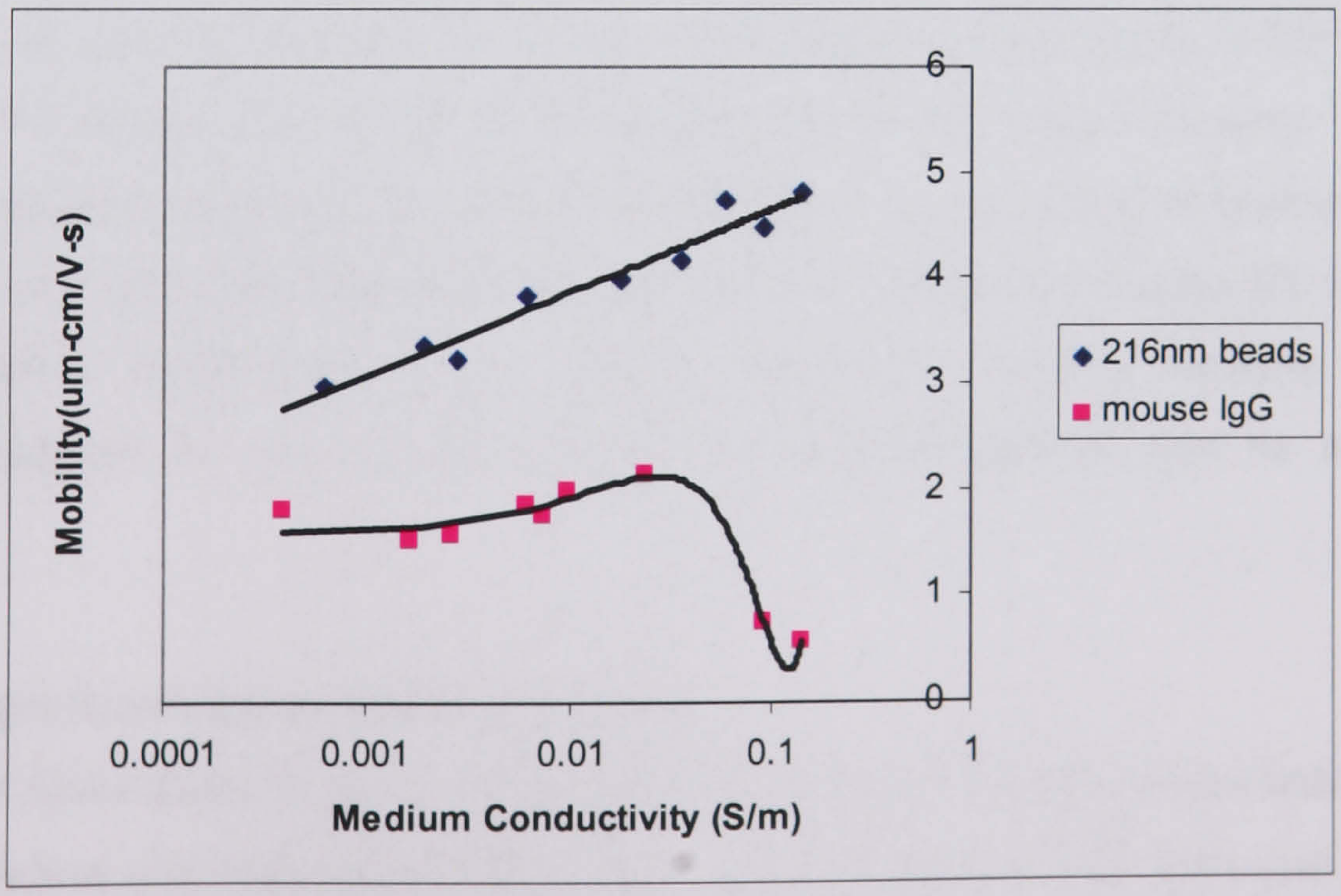

Figure 5-31

Comparison of the mobilities of 216nm beads before and after surface modification

5.8 Discussion

The data fits using the model described allow the prediction of:

i) the Stern layer conductance and

ii) the ζ-potential

The latter allows the inference of diffuse layer charge transportation although, given the additional hydrodynamic quantity, *m*, which must be specified it is not unique in doing so. The general pattern tends to be that both are decreased by varying amounts on the attachment of biological entities. The mechanism of how surface conductance may be altered and the validity of the predictions remain to be discussed. This involves a closer inspection of charge transport in the Stern and diffuse layers and therefore primarily gives rise to the question as to how and where, with respect to the bead surface, the ζ-potential may be defined.

5.8.1 Interpretation of ζ-potential

The idea that the ζ-potential defining plane and the shear plane may not coincide is common throughout the literature [15-17]. Uncertainty remains, nonetheless, as to how this may be interpreted. Since the ζ-potential determines the induced motion of a particle under the action of an externally applied E-field, the potential determining ions responsible for the motion can be defined as those which move with the particle (neglecting for the moment the retardation effects caused by diffuse layer hindrance). The extent of this charge would coincide with the shear plane if the distribution was uniform [18]. However, in the case of a surface with attached moieties the situation is less clear. Irregularity of the Stern surface is introduced as proteins are attached covalently or adsorbed with finite spacing, which means that the shear plane is not automatically defined. In general with attached ligands it could be interpreted as moving outwards [18] since more charge moves rigidly with the particle. However, the roughening of the Stern surface may affect charge transport mechanisms within the stagnant layer and therefore the shear plane cannot simply be approximated as a flat surface at a mean distance within the immobilized charge distribution [9]. Other effects such as particle coagulation can be taken into account in order to estimate the level of surface roughness so that possible charge transport mechanisms may be more clearly identified.

5.8.2 Experimentally measured ζ-potential

The first observation on the electrophoretic mobility data for IgG coated beads is that the measured values rise with suspending medium conductivity. This is due most probably to falling levels of diffuse layer hindrance as a result of the contraction of the double layer - brought about by the fact that electrolytes of higher concentrations can support greater double layer charge density gradients. This has been examined by Huckel [19] who derived a correction factor of 2/3 to account for the retardation effects of thick double layers. Comparing this to the DELSA ζ-potentials which are calculated assuming negligible diffuse-layer retardation it can be seen that for the uncoated beads the ratio of the low and high ζ-potentials limits is quite close to this value. This implies that the low and high conductivity regimes measured are effectively equivalent to the thick and thin double layer limiting cases respectively. The best estimate of the ζ-potential, then, could be inferred to be closer to the highest values measured. The magnitudes are, nonetheless, still considerably lower than the dielectrophoretically deduced values. Insertion of the DELSA values into the Stern-diffuse layer model, however, does not account for the measured increase in the crossover data with suspending medium conductivity (Figure 5-32).

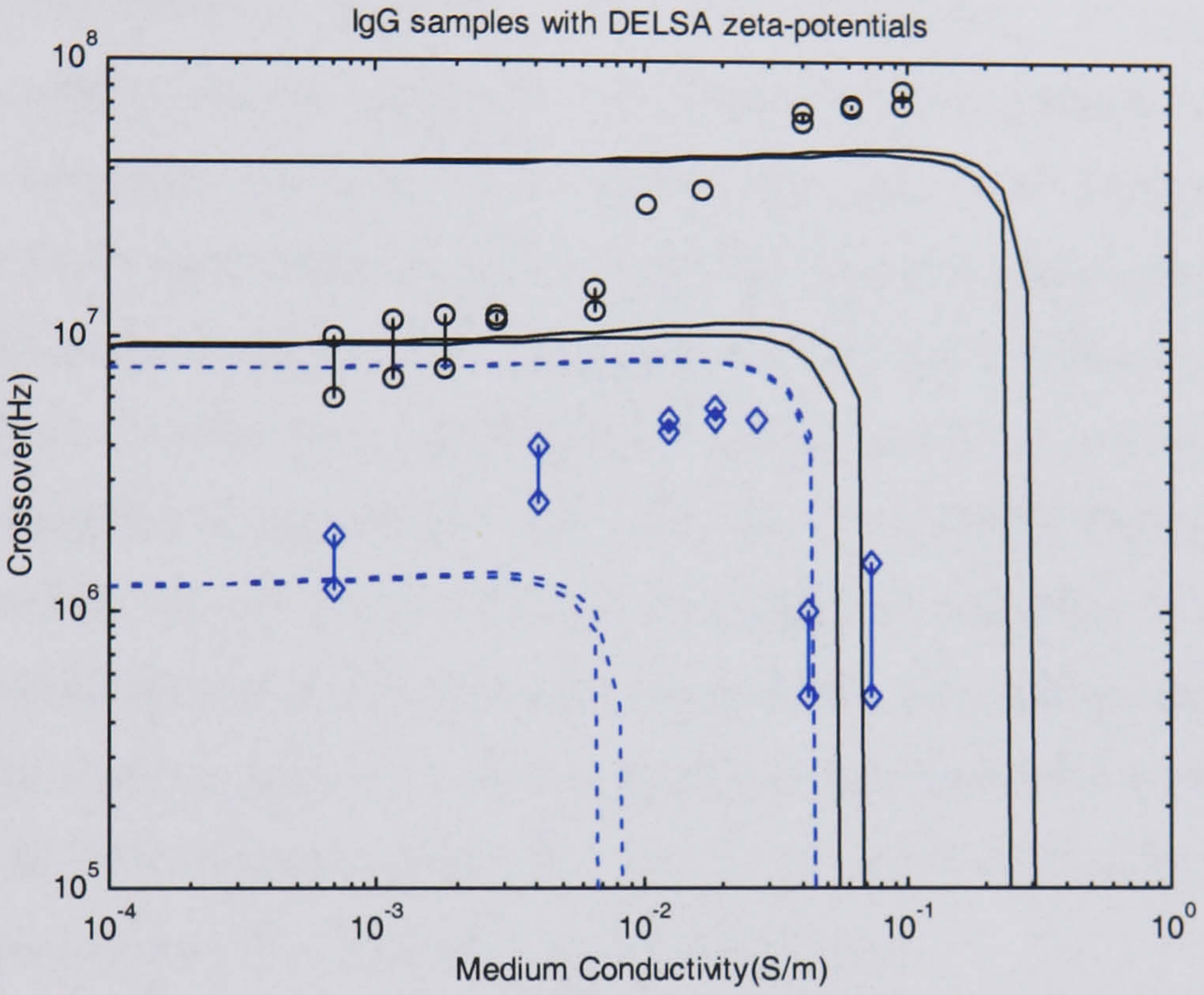

Figure 5-32

Crossover predictions with DELSA measured ζ-potentials. Uncoated 216nm beads (solid lines) protein coated samples (dotted lines).

Sample	**K_s(nS)**	**ζ (mV)**
216nm beads	3-14	38.3-62.5
with IgG	0.4-2.5	19.7-27.4

Table 5-13

K_s *ranges corresponding to DELSA measured ζ-potentials for uncoated and IgG modified beads.*

At these ζ-potentials, Stern layer conductance is the dominating curve determining parameter. If upper and lower limits are placed on this parameter corresponding to the highest and lowest data points in each set this implies large variation in Stern layer conductance with conductivity of the medium, contradicting the basic assumption in the model that this conductance is due to the densely packed ions behind the slip plane, which have no hydrodynamic mobility and are unlikely to be affected by the salt concentration in the ambient medium. Moreover, substitution of these low ζ-potentials forces the Stern layer conductance to be unrealistically amplified (Table 5-13).

The electrophoretic response of a particle, however, may be quite sensitive to the nature of the particle surface. Surface roughness, for example, has been shown to dramatically affect the electrokinetic potential of latex particles. One study [14] comparing them to bitumen-in-water emulsions, which have a smoother surface although similar surface charge densities, has shown the electrophoretically derived ζ-potentials of the latter to be ~100% higher than for latex. The effects of heating the latexes above their glass transition temperature in order to smooth the surface has also been shown in this article to significantly increase the electrophoretic mobility. The underestimation of ζ-potential from electrophoretic mobility data as compared with other ζ-potential measurement techniques has also been frequently discussed [7-9, 20-26]. This has been attributed mainly to unaccounted for Stern layer conductance which has been found to cause considerable errors in ζ-potential calculations. In particular, underestimation of 200%-300% have been noted, where mobility data for polystyrene latexes and alumina suspensions have been compared with results from surface charge titration [27]. Therefore, it is conceivable that the DELSA measured ζ-potentials are also out by a factor of this order of magnitude in which case the original Stern-diffuse layer model data fits are not unrealistic. The underestimation of ζ from the electrophoretic mobility data, then, would imply that the K_s values are always close to the higher limit of the DEP predicted range, but significantly lower than those listed in Table 5-13, corresponding to the low DELSA ζ-potential predictions.

It is also quite probable that use of DEP, which is an AC electrokinetic phenomenon, results in the considerable *overestimation* of ζ-potential, since the polarising current relates to the *total* charge – not only the net charge – on the bead surface.

5.8.3 Mechanisms of surface conduction

Diffuse layer conductance

In order to assess the alteration of diffuse layer conductance it is necessary to consider possible changes in both the charge carrier quantity and mobility. The quantity of ions is related exponentially to the ζ-potential through the Poisson-Boltzmann equation thus the ζ-potential dependence of the conductivity in the diffuse region as outlined. The electrophoretic mobility of the ions however is barely impeded with increasing concentration as even with density conditions as extreme as in the Stern layer this has been found comparable to the bulk [7].

The hydrodynamic impedence, however, may be affected by surface modification due to the protrusion of proteins into the diffuse layer. Considering the scale of the entities involved, this is not improbable with the extent of the diffuse layer of a monovalent electrolyte approximately in the range of 1-10nm for a solute concentration of 0.1M-1mM. Tightly compacted, streptavidin has a physical extent of around 5nm, avidin is a similar size although includes the extra carbohydrate moieties and IgG is around 6nm, therefore interference with fluid movement in the diffuse region could well take place. This has been alluded to recently by Dukhin *et al* [9] who pointed out that liquid entrapped in cavities formed by the local curvature of a rough solid surface would interfere with data evaluation based on the conventional model. Although realistically quantifying this effect is beyond the scope of this study an upper bound of the influence it might have can be estimated by maximising the viscosity term, η, in the parameter m, characterising the electro-osmotic contribution, which was given by:

$$m_{\pm} = \left(\frac{RT}{F}\right)^2 \frac{2\varepsilon_0\varepsilon}{3\eta D_{\pm}}$$

The effect of $m \to 0$, then, on the expected crossover data is illustrated in Figure 5-33 for three Stern layer conductance and ζ-potential magnitudes.

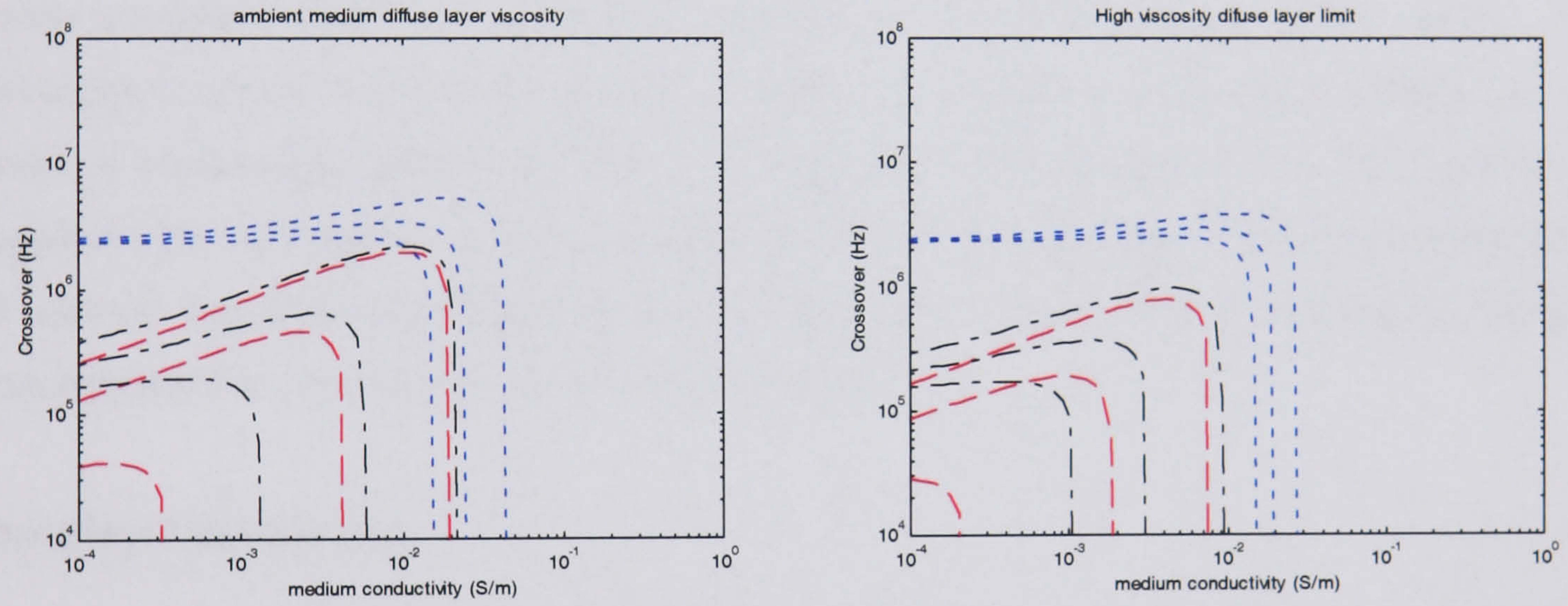

Figure 5-33

Effect of reducing to zero the electro-osmotic parameter, m, on the model predicted curves. The first graph shows results for the permittivity and viscosity of water and ion diffusivity of the bulk, the second when the combination of these factors is minimized. ζ-potentials illustrated are 45 mV, 90 mV and 120mV with K_S values 0.01nS, 0.09 nS, and 1.5 nS – dash, dot-dash and dotted lines respectively.

The primary result appears to be an alteration of the cut-off point of the curves – i.e. a decrease in the suspending medium conductivity where positive DEP no longer occurs. It can be seen that this effect increases with lowering Stern layer conductance as would be expected given the corresponding proportional dominance of the diffuse layer in the total surface conductance (section 5.8.5.) This could explain the apparently early cut-off in some of the crossover data with respect to an otherwise well fitting curve – e.g. covalently coupled and adsorbed streptavidin. The validity of this modification should depend on the physical size and distribution of the attached moiety. One indication of the level of surface roughness in a particle suspension is that it is linked, possibly, with flocculation effects [28, 29]. This has been analysed quasi-statically by Shulepov through summation of all the interaction energies of the interaction configurations of the system [30], referenced in [8]. A more dynamic approach in support of this is taken by Lyklema [8] where he argues on the basis of particle interaction rates that surface irregularities of the order of κ^{-1} may have a dramatic effect on the electrostatic repulsion between colloids. This result is obtained by considering that since the rotation of particles of radius a through an angle $O(\arcsin(\kappa a)^{-1})$ has time constant:

$$\tau_{rot} = \frac{(\kappa a)^{-2}}{D_{p,rot}}$$

which, for typical rotational diffusion constants $D_{p,rot}$ $O(10^3)s^{-1}$, can be as small as $10^{-7}s$, on the timescale of a Brownian collision rough particles have time to readjust in order to minimise the repulsive energy between them, thus suppressing electrostatic repulsion. The level of coagulation of DEP samples, then, may provide some indication of how far the protein layer protrudes into the diffuse layer and therefore m approximately estimated. The avidin modified beads are a possible example of this manifesting a high degree of flocculation which could be attributed to additional irregular non-covalent coupling as a result of electrostatic adsorption. This is of course a crude estimation of the bead surface properties but nonetheless suggests that protein modified samples may have varying degrees of surface irregularities which should be taken into account when considering charge transport mechanisms on both sides of the slip plane.

Stern layer conductance

The Stern layer, although generally only a few molecular diameters thick [8] can contain 90% of the surface charge [18]. As alluded to in the previous section, recent studies have also shown that although the fluid is immobilized in this region the ions can retain a high level of electrophoretic mobility – frequently only slightly different from their bulk values [7, 8, 31]. A mobility ratio of 0.96, for example, has been calculated for K^+ ions on silica [32]. This, however, is a smooth, solid surface. There is no indication, as yet, that rough surfaces can be treated in the same way.

How attached substances influence conduction in the Stern layer is an ongoing point of debate [9, 18, 32-35]. In general the measured DEP crossovers decrease with surface modification corresponding to a decrease in Stern layer conductance (Figure 5-14).

This could imply that:

i) some kind of frictional effects take precedence over electrical forces - i.e. the inclusion of ligands into the Stern layer causes added impedance to charge carriers that is not fully compensated for by any additional carriers introduced [18]

or

ii) the irregularity of the Stern layer and the nature of the introduced moieties cause additional electrical impedance.

A possible mechanism for i) is not clear since protein layers are frequently to be regarded as porous and easily permeable to small electrolyte ions [33]. In support of ii) it could be argued that attached ligands may polarise, causing local field cancellation at intervals along the bead surface. Clearly, however, further investigation is required.

Since hydrodynamic transport is by definition absent from the Stern layer, additional frictional impedance effects on the fluid in this region should also be negligible. But as highlighted in section 5.8.1, the ζ-potential and shear plane evade conventional interpretation in the case of a surface with attached moieties. In an irregular surface possessing locally uniform surface properties, the nature of the Stern layer could also be approximated to be locally invariant. This would imply that the Stern layer would follow the outer boundary of the surface with an essentially constant thickness [9]. Although the nature of the stagnant layer on proteins has not been definitively established it is justifiable to assume that they do indeed have one, since as stated by Lyklema [32] present day insight suggests that stagnant layers exist not only because of electrostatic attraction but are general properties of fluids on any phase boundary. The fact alluded to that small ions are not rigidly confined to planar movement on the surface due to porosity, however, implies that a conventionally defined inner Helmholtz plane may not exist. Instead, Stern layer characteristics could more closely resemble that of the outer Helmholtz plane as defined on a flat surface consisting of immobilised water molecules and hydrated ions.

How charges move in the various parts of the stagnant layer has been most progressively tackled by Lyklema et al [32] through numerical molecular dynamics simulations. The results support layering effects in the Stern region analogous to the inner and outer Helmoltz planes although they are not so rigidly defined. These studies also point to a considerable anisotropy between the normal and radial components of the viscosity. While retardation in the tangential plane is low – up to a factor of 2 compared with the bulk – the viscosity factor in the radial direction can be increased as much as 5 times. Thus if the Stern layer were highly irregular, global ionic drift parallel to the bead surface could be impeded. Charge carriers may still move relatively freely tangentially to the irregular stagnant layer defined by the attached substances. This path, however, could take on an almost fractal nature and so the effective distance across the surface may be increased by orders of magnitude - quite feasibly lowering the observed Stern layer conductance!

Despite the radial impedance, another interesting prediction of this study is that ions may often hop between layers. Ion exchange across the shear plane has also been discussed by Goff and Luner [36]. This appears to be more of a stochastic effect, where, due to the random nature of ionic collisions occasionally some have enough energy to overcome the substantial Stern layer radial viscosity. As modelled by Lyklema, however, this radial impedance is not uniform within the Stern layer, being stronger closer to the interface. This would imply that ions in the OHP would be statistically more likely to overcome the energy barrier and leap to the diffuse layer. Therefore the protrusion of proteins into the diffuse layer with their previously postulated OHP-like stagnant layer would quite possibly enhance this effect, shifting the equilibrium of ion exchange between the two layers. This suggests a resulting decrease of net electrokinetic charge since there is proportionally less rigid charge confinement than would be expected in a Stern layer on a flat surface which would have less discrepancy between the quantity of charge in the inner and outer Helmholtz planes. The overall surface conductance, however, need not be altered since the double layer as a whole is still effectively a closed system. A summary of these postulates is illustrated in Figure 5-34.

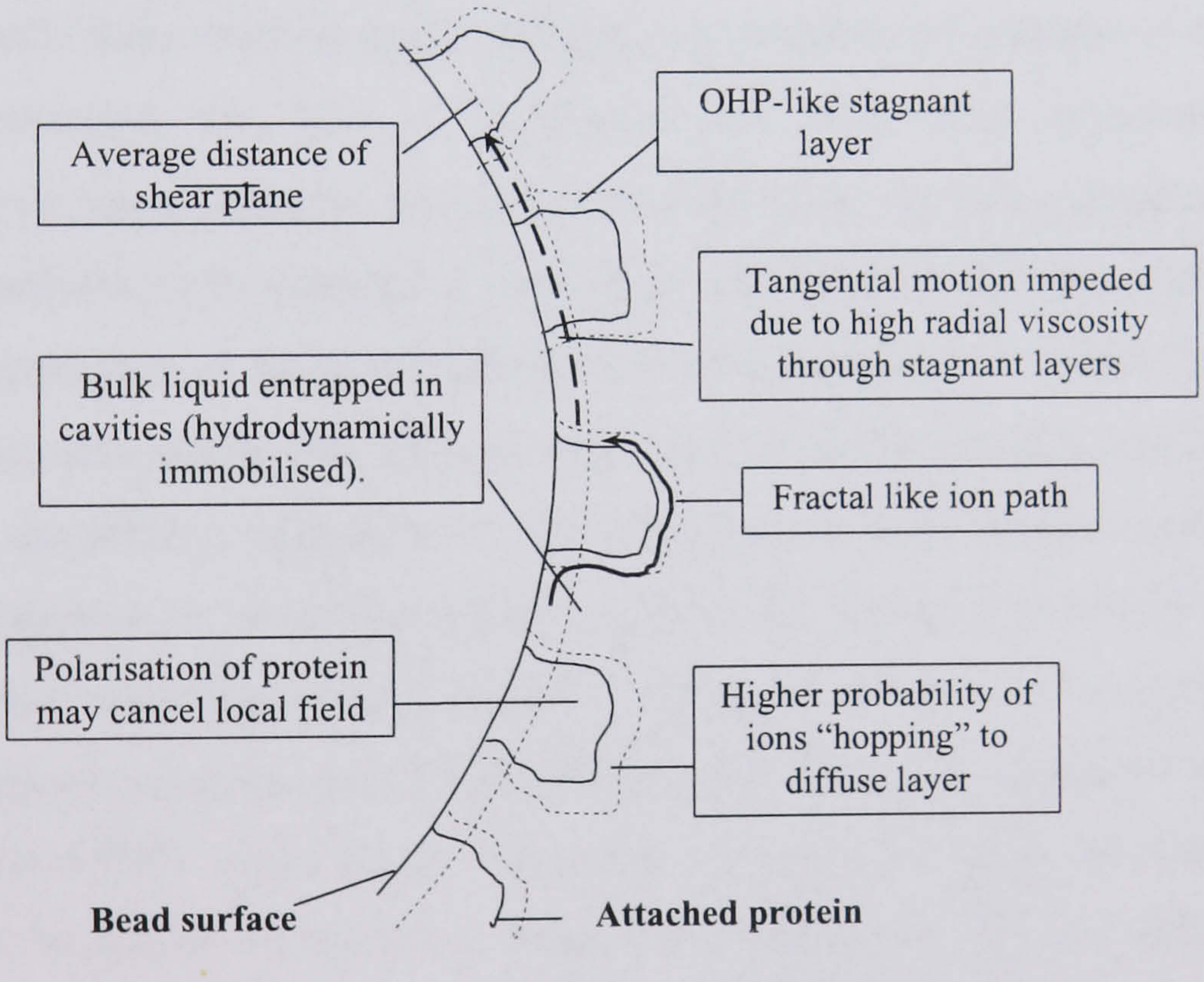

Figure 5-34

Schematic of possible effects on surface conductance mechanisms that may occur on protein immobilization

5.8.4 Secondary layers

The secondary layers - anti-IgG and oligonucleotides - appeared to cause a further reduction in crossovers. In both cases, particularly that of the oligonucleotides, this could be due to increased diffuse layer hindrance. Any extra mobile charge introduced by the secondary labeling does not appear to have a great effect. This is somewhat unexpected in the case of the oligonucleotides as, being DNA fragments, these are highly charged polyelectrolytes possibly possessing a substantial degree of conductivity- or at least semiconductivity [37, 38]. The reported behaviour of DNA, however, continues to be extensively variable, from both theoretical and experimental angles [39] with some indication also of insulating tendencies [40]. Clearly it is out with the scope of this study to speculate on such results, although it would be interesting to observe the effect of several lengths of oligonucleotide on the crossover measurements in order to begin to discern more precisely how surface conductance may be altered.

The quite marked lowering of the crossovers after surface modification with both IgG and oligonucleotides, implies also a considerable effect on the Stern layer. This suggests that some non specific adsorption is occurring on uncoated sections of the bead surface or that an irregular Stern layer does protrude far into the diffuse layer with the implications for ion transport discussed above. The polarization of the oligonucleotides also may have a considerable influence as alluded to in the case of proteins. Since these are potentially highly polarisable entities, the local electric field distribution could be significantly altered some way out into the diffuse layer.

5.8.5 General Commentary on Data fits

In many cases there remains some ambiguity in possible interpretations of the data. As mentioned previously, the ratio of ζ-potential and Stern layer conductance plays an important role in determining the cut-off point of the curve. At high ζ-potential, the general shape is less influenced by changes in Stern layer conductance and vice versa. Figure 5-35 shows the superposition of Stern and diffuse layer conductances for various ζ-potentials. The points of intersection indicate the medium conductivities above which ζ-potential effectively becomes the dominating parameter in the definition of total surface conductance. The conductivity magnitudes where this occurs are plotted in Figure 5-36 for the working range of the parameters. This shows that ζ-potential dominates at a large proportion of the ranges of the parameters in question and is particularly influential in the conductivity region at the cut-off of positive DEP. Since this is usually at the higher end of the medium conductivity range, most of the surface conductance at this point is due to the diffuse layer (Figure 5-13). This means that ζ-potential is generally easier to define than Stern layer conductance from the crossover, being essentially what determines the point where positive DEP is no longer observed (Figure 5-15). In most samples, only a very broad range of Stern layer conductance values can be determined from the crossover data especially where the ζ-potential is high, with the limits for unmodified 216nm beads as wide as 0 – 2nS. This positive DEP cut-off, however, is not always easy to observe in the high conductivity regime as fluid effects come into play (refer to Chapter 9) and so it may be underestimated (Figure 5-23). In this case the slope must be the dominating decisive factor to ascertain ζ-potential – from which it also can be defined within reasonable accuracy. In general this model makes some very concrete predictions – at least establishing bounds for the ζ-potential and Stern layer conductance which could possibly be narrowed by a more statistically viable data set. The accuracy limit of the latter component, however, will never be high in these conditions except in the case of extremely low ζ-potentials.

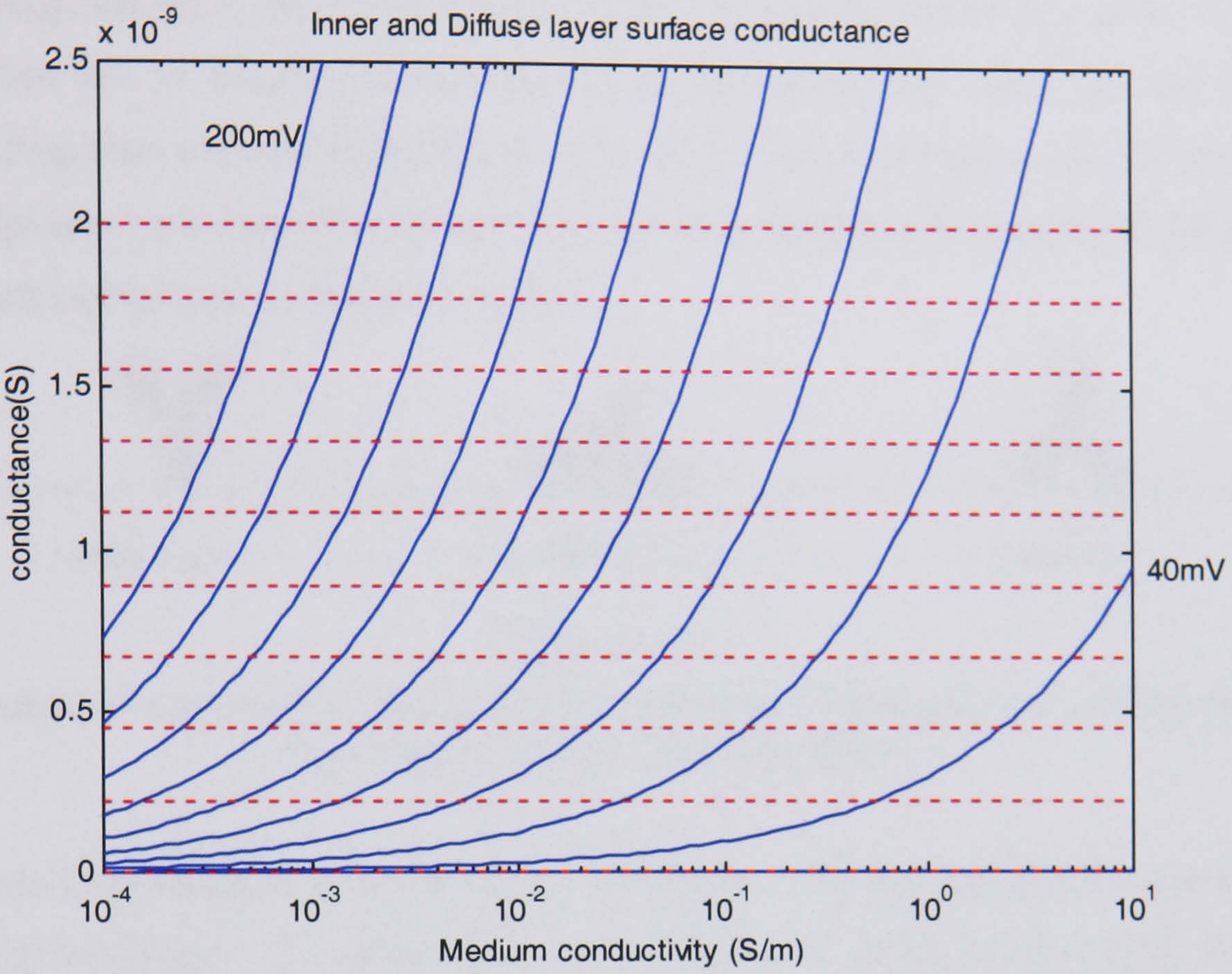

Figure 5-35

Stern layer conductance (dotted line) and diffuse layer conductance for various ζ-potentials with points of intersection corresponding to the medium conductance when diffuse layer conductance becomes dominant.

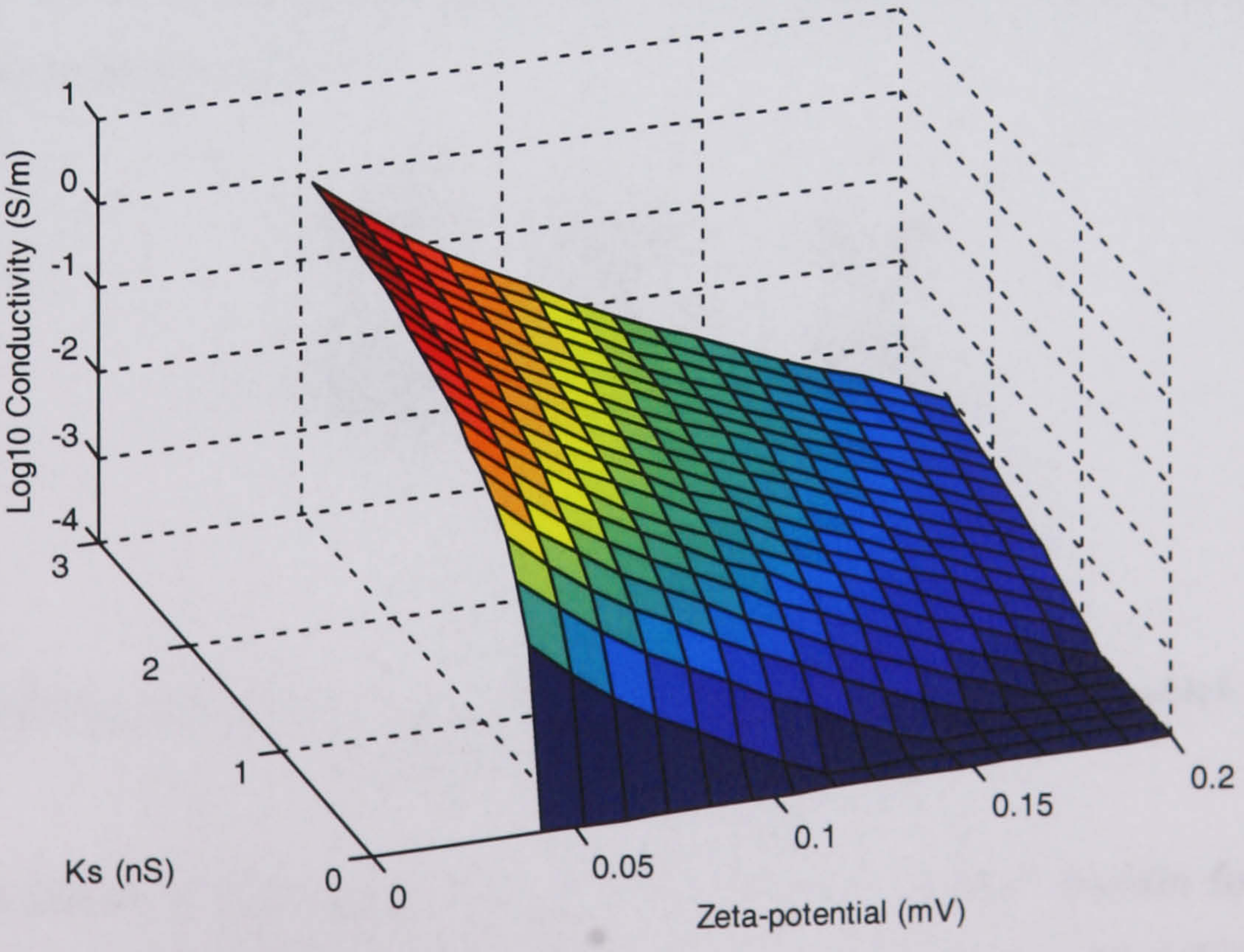

Figure 5-36

Medium conductivity where ζ-potential becomes dominant in determining surface conductance for various Stern layer conductance values and ζ-potentials.

5.8.6 Suggestions for data refinement

Surface modification

Greater control over surface modification, particularly in the binding of secondary layers could provide increased insight into how attached ligands influence conduction in the double layer. The large spread in the crossovers of the IgG sample on attachment of the anti-IgG is most probably due to irregular positioning of the first monolayer such that not all of the antigen binding sites are available (Figure 5-37 [41]). This may happen due to the fact that amino groups are present on all sections of the molecule and therefore randomly attach to the activated carboxyl groups on the bead surface.

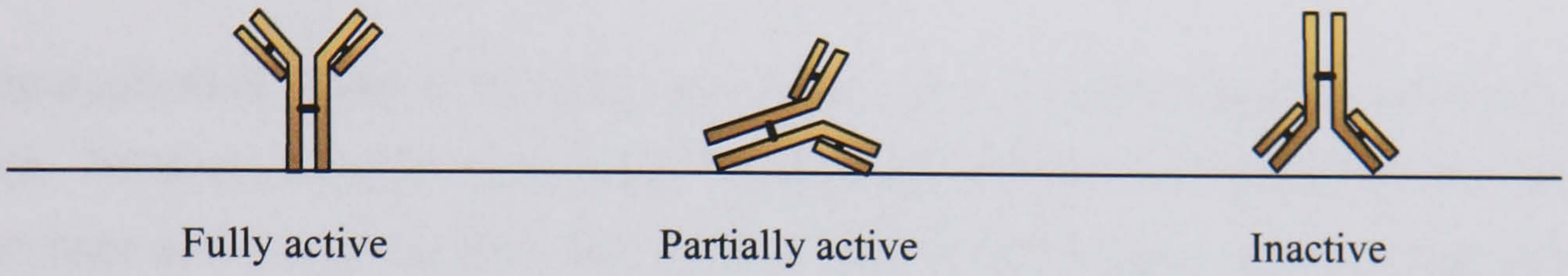

Figure 5-37

Schematic arrangement of IgG antibodies randomly orientated on a solid surface, highlighting antigen binding affinity

Approaches to overcoming the frequently noted loss of biological activity due to random orientation of antibodies on solid surfaces have been reviewed by Lu et al [41]. Two of the methods outlined for achieving orientated antibody coupling are (refer to Figure 4-13):

i) Primary immobilization of a protein possessing F_C receptors, such as protein A, - i.e. those which will bind specifically to the section of the IgG molecule which has no antigen affinity.

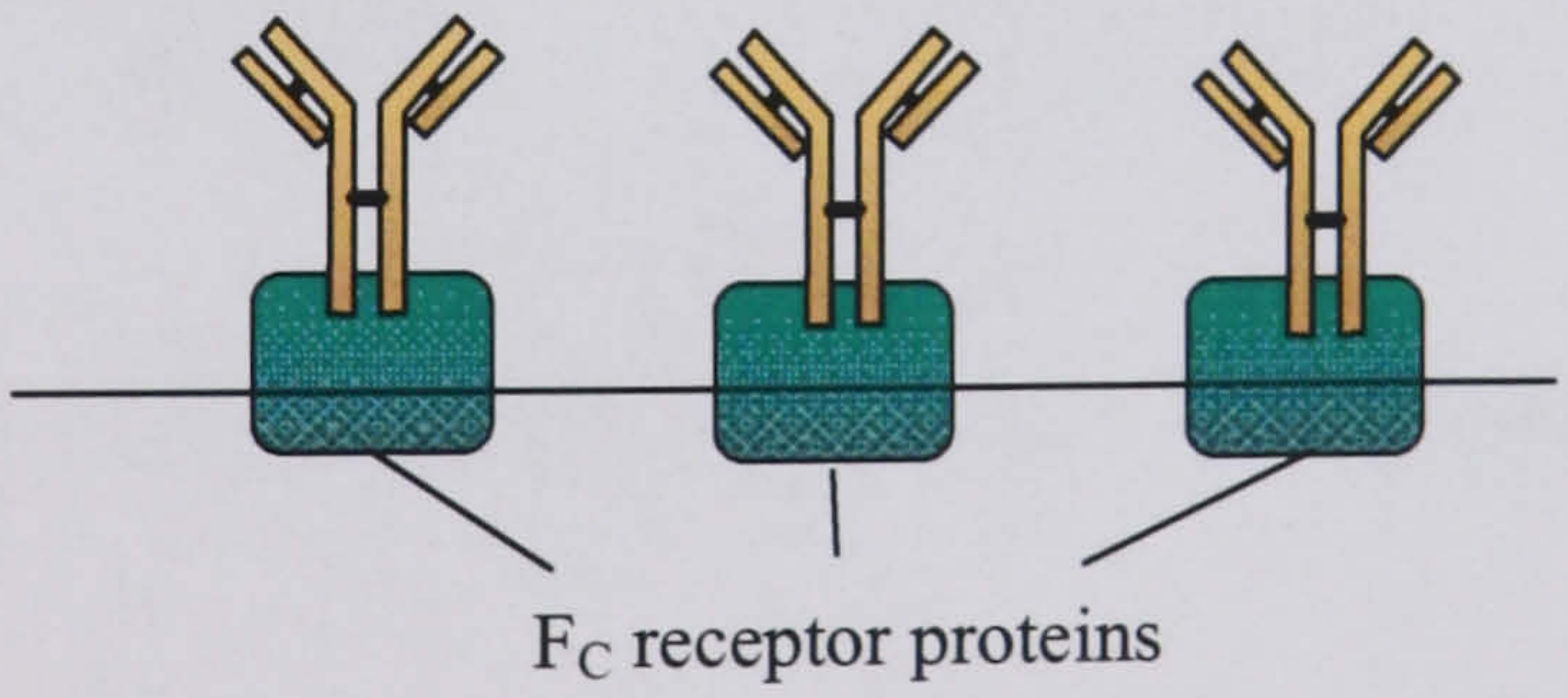

Figure 5-38

Antibodies uniformly orientated on a solid surface through linking proteins which target the F_c portion of the IgG ligand.

ii) Oxidation of the carbohydrate moiety located at the C_H2 domain for covalent bonding to hydrazide modified beads (Figure 5-39). This can be achieved under mild conditions so as not to de-functionalise the active binding groups, and avoids the necessity of an additional linking protein.

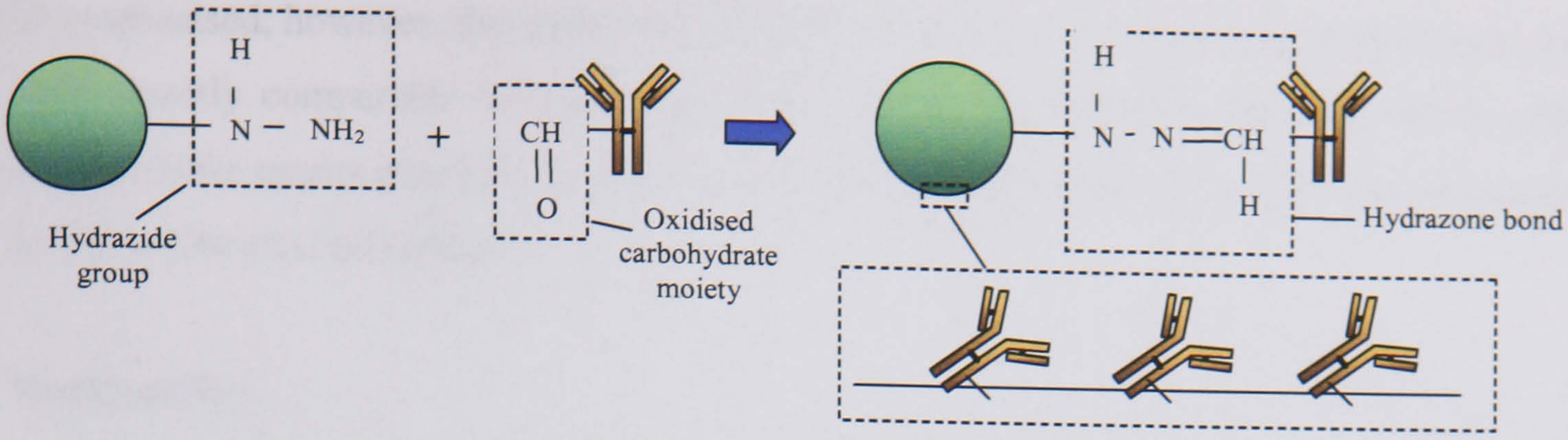

Figure 5-39

An alternative substrate, hydrazide modified beads, can be used to achieve coupling of the IgG through oxidation of the carbohydrate moiety allowing the retention of biological activity.

Oligonucleotide binding through the biotin-avidin complex appears generally more efficient. However, in order to possibly discriminate between hydrodynamic and electrical surface impedance resulting from the attached ligands (as outlined in 5.8.3) oligonucleotide hybridization would be desirable (Figure 5-40). Since the double helices bind tightly this would not alter the physical extent of protrusion into the double layer but could have a significant effect on the polarizability of the complex and electrokinetic charge on the bead surface. Preliminary trials have so far been inconclusive due to inefficient hybridization techniques but this could be a useful area of investigation.

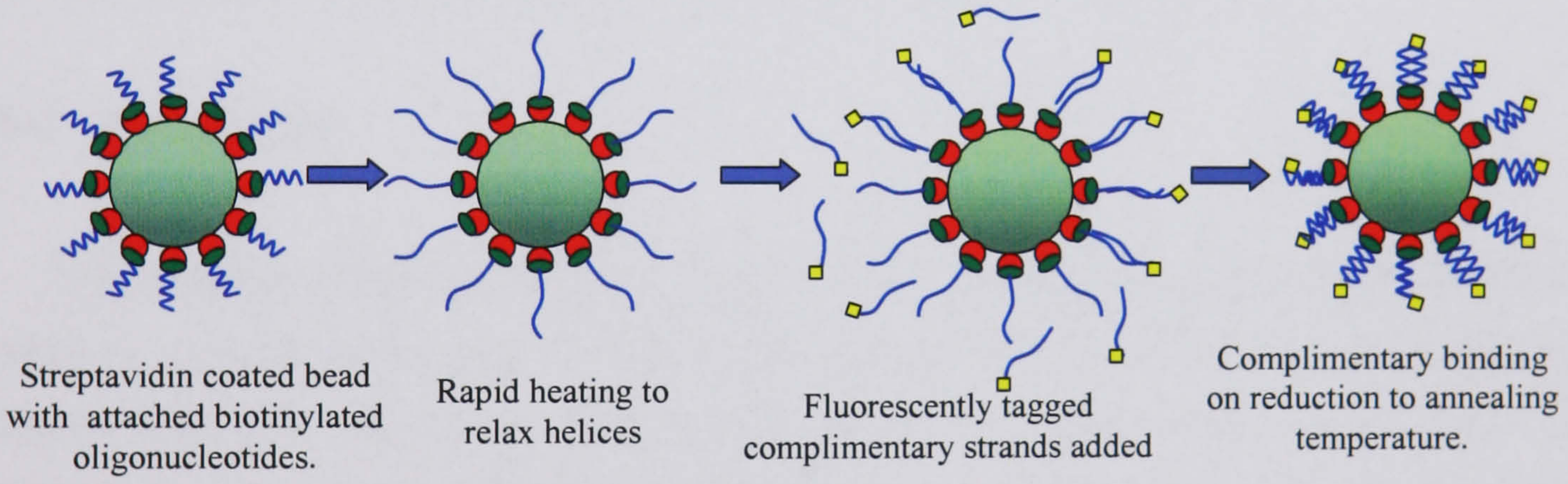

Figure 5-40

Schematic of complementary oligonucleotide binding

ζ-potential data

A more extensive independent assessment of ζ-potential is another requirement if the model predictions are to be adequately validated. Without some indication of the magnitude of conduction behind the shear plane, however, electrophoretic mobility data alone is insufficient. The effect on ζ-potential of attaching biological substances could possibly be assessed using a combination of several other conventional means such as surface charge titration or modifying the walls of a capillary and measuring the streaming current. By comparing the resulting (undoubtedly different) ζ-potentials perhaps some calibration could be established which would allow a reasonable estimate of Stern layer conductance. It must be emphasised, however, that these methods do not involve AC fields and therefore may not yield directly comparable results to those obtained by dielectrophoresis. Nonetheless, AC electrokinetic means may help in some way to resolve the ζ-potential incongruities produced by electrophoretic techniques.

Model utility

Theoretically, the most consistent way of improving the predictions of this model would be to effectively eliminate some variables by conducting experiments at critical pH points such as the p.z.r. of the modified beads or the p.z.c of the bead as it was before surface modification (refer to Chapter 4). In the first case, any charge transport on the bead surface would take place entirely behind the shear plane since there would be effectively no diffuse layer and in the second, the surface conductance would be due only to the charge introduced by surface modification. Some work has been done on the former by Matsumura et al [42] and, as pointed out by Dukhin [9], the experimental evidence of the Stern layer conductance at the isoelectric point is the most reliable proof of the high mobility of adsorbed ions and the dynamic Stern layer concept. Finding these points, however, are complex procedures [18] and indeed maintaining a constant pH in each sample of the modified colloids would severely restrict the conductivity range over which the crossover data could be measured. Moreover, the consistency of the data would not necessarily be reliable as the different pH environments could not be guaranteed to leave the biological layers intact.

5.9 Conclusion

The crossover versus conductivity data for various biological colloids can be fairly well fitted to a model taking into account the stagnant-diffuse layer structure of the electrical double layer and the associated properties of charge transport within each zone. The biological surface modification of latex colloids in the cases measured does indeed tend to produce a change in the DEP response. However, the model used to fit the data is not sensitive enough to provide adequate predictability of the investigated parameters, i.e. ζ-potential and Stern layer conductance. This has been theoretically demonstrated by examining the effect of substantial variations of one parameter while the other is held at a high value. It has been shown, for example, that large variations in diffuse layer conductance when ζ is high produce almost no effect on the shape of the curve, and vice versa. Nonetheless, although the predictive power of the model is limited, the curves do manifest some compatibility with the data - taking into account also the possibility of substantial underestimation of ζ-potential when the Stern layer conductance is not considered - and therefore the underlying assumptions of the model are not contradicted. Moreover, since the inner layer conductance is so vaguely defined it may indeed be the case that it is generally on the higher end of the scale. It could therefore have quite significant consequences on the electroviscous effect thus throwing into question the validity of the electrophoretic mobility data.

In general, however, although the predicted ζ-potential absolute magnitudes are not in immediate agreement with the electrophoretic data, the *relative* predicted change in ζ-potential on surface modification is not in contradiction. There are observable differences in the dielectrophoretic response of samples before and after ligand attachment which implies that DEP techniques could be used to separate, classify and differentiate between colloidal entities on the basis of their surface properties. This would require rigorous calibration with known standards rather than simply model based predictive analysis if absolute parameters are to be adequately assessed. There still remains the problem of degeneracy, however, where different combinations of Stern layer conductance and ζ-potential can feasibly produce similar crossover data. These areas would have to be identified for each particular application, or, where possible, DEP crossover investigations made in environments of highly controlled pH before the technique could be reliably utilised.

5.10 References

[1] N. G. Green, "Dielectrophoresis of sub-micron particles" in *Electrical and Electronic Engineering*: University of Glasgow, 1998, pp. 270.

[2] G. Schwarz, *Journal of Physical Chemistry*, vol. 66, pp. 2636-2642, 1962.

[3] R. W. O'Brien, "The High-Frequency Dielectric-Dispersion of a Colloid", *Journal of Colloid and Interface Science*, vol. 113, pp. 81-93, 1986.

[4] J. Lyklema, *Fundamentals of Interface and Colloid Science*, vol. 2. New York: Academic Press, 1995.

[5] X. F. Zhou, G. H. Markx, R. Pethig, and I. M. Eastwood, *Biochimica et Biophysica Acta*, vol. 1245, pp. 81-93, 1995.

[6] J. J. Bikerman, *Kolloid Z.*, pp. 100, 1935.

[7] J. Lyklema and M. Minor, "On surface conduction and its role in electrokinetics", *Colloids and Surfaces a-Physicochemical and Engineering Aspects*, vol. 140, pp. 33-41, 1998.

[8] J. Lyklema, H. P. van Leeuwen, and M. Minor, "DLVO-theory, a dynamic re-interpretation", *Advances in Colloid and Interface Science*, vol. 83, pp. 33-69, 1999.

[9] S. S. Dukhin, R. Zimmermann, and C. Werner, "A concept for the generalization of the standard electrokinetic model", *Colloids and Surfaces a-Physicochemical and Engineering Aspects*, vol. 195, pp. 103-112, 2001.

[10] C. T. O'Konski, "Electric properties of macromolecules v. theory of ionic polarisation in polyelectrolytes", *Journal of Physical Chemistry*, vol. 64, pp. 605-619, 1960.

[11] J. A. Nelder and R. Mead, "A Simplex Method for Function Minimization.", *Comput. J.*, vol. 7, pp. 308-313, 1965.

[12] J. L. Ortego-Vinuesa, D. Bastos-Gonzalez, and R. Hidalgo-Alvarez, "Comparitive Studies on Physically Adsorbed and Chemically Bound IgG to Carboxylated Latexes, II", *Journal of Colloid and Interface Science*, vol. 176, pp. 240-247, 1995.

[13] A. Y. Menshikova, I. B. Dmitrieva, V. I. Kuchuk, Y. O. Skurkis, T. G. Evseeva, and B. M. Shabsels, "Electrosurface Properties of Poly(styrene-co-acrolein) Latexes with the Protein Modified Surface", *Kolloidnyi Zhurnal*, vol. 61, pp. 799-808, 1999.

[14] R. S. Chow and K. Takamura, "Effects of Surface Roughness (Hairiness) of Latex Particles on their Electrokinetic Potentials", *Journal of Colloid and Interdace Science*, vol. 125, 1987.

[15] A. G. Van der Put and B. H. Bijsterbosch, *Journal of Colloid and Interface Science*, vol. 92, pp. 499, 1982.

[16] M. Rasmusson and S. Wall, "Surface Electric properties of Polystyrene Latex", *Journal of Colloid and Interface Science*, vol. 209, pp. 312-326, 1999.

[17] N. M. Seminikhin and S. S. Dukhin, *Kolloidn. Zh.*, vol. 37, pp. 1123, 1975.

[18] Hunter, *Zeta Potential in Colloid Science*: Academic Press Inc., 1981.

[19] E. Huckel, *Physik. Z.*, vol. 25, pp. 204, 1924.

[20] M. Minor, H. P. van Leeuwen, and J. Lyklema, "Low-frequency dielectric response of polystyrene latex dispersions", *Journal of Colloid and Interface Science*, vol. 206, pp. 397-406, 1998.

[21] M. Minor, A. J. van der Linde, and J. Lyklema, "Streaming potentials and conductivities of latex plugs in indifferent electrolytes", *Journal of Colloid and Interface Science*, vol. 203, pp. 177-188, 1998.

[22] C. S. Mangelsdorf and L. R. White, "The dynamic double layer - Part 1 - Theory of a mobile Stern layer", *Journal of the Chemical Society-Faraday Transactions*, vol. 94, pp. 2441-2452, 1998.

[23] C. S. Mangelsdorf and L. R. White, "The dynamic double layer - Part 2 - Effects of Stern-layer conduction on the high-frequency electrokinetic transport properties", *Journal of the Chemical Society-Faraday Transactions*, vol. 94, pp. 2583-2593, 1998.

[24] C. S. Mangelsdorf and L. R. White, "Effects of Surface Conduction On the Electrokinetic Transport- Properties", *Abstracts of Papers of the American Chemical Society*, vol. 208, pp. 212-COLL, 1994.

[25] F. Carrique, F. J. Arroyo, and A. V. Delgado, "Electrokinetics of concentrated suspensions of spherical colloidal particles: Effect of a dynamic Stern layer on electrophoresis and DC conductivity", *Journal of Colloid and Interface Science*, vol. 243, pp. 351-361, 2001.

[26] A. Moncho, R. Martinez-Lopez, and R. Hidalgo-Alvarez, "Comparitive study of theories of conversion of electrophoretic mobility into zeta-potential", *Colloids and Surfaces (A)*, vol. 192, pp. 215-226, 2001.

[27] F. J. Rubio-Hernandez, R. Ruiz, E., and A. I. Gomez-Merino, "The additional surface conductance: its role in the primary electroviscous effect", *Colloids and Surfaces (A)*, vol. 192, pp. 349-356, 2001.

[28] J. Y. Walz, *Adv. Colloid Interface Sci.*, vol. 74, pp. 119, 1998.

[29] S. Bhattacharjee, C. H. Ko, and M. Elimelech, *Langmuir*, vol. 14, pp. 3365, 1998.

[30] S. Y. Shulepov, : University of Delft, 1997.

[31] M. Lobbus, H. P. van Leeuwen, and J. Lyklema, "Streaming potentials and conductivities of latex plugs. Influence of the valency of the counterion", *Colloids and Surfaces a-Physicochemical and Engineering Aspects*, vol. 161, pp. 103-113, 2000.

[32] J. Lyklema, S. Rovillard, and J. De Coninck, "Electrokinetics: The properties of the stagnant layer unraveled", *Langmuir*, vol. 14, pp. 5659-5663, 1998.

[33] C. Werner, H. Korber, R. Zimmermann, D. Dukhin, and H. Jacobasch, "Extended electrokinetic Characterization of Flat Solid Surfaces", *Journal of Colloid andInterface Science*, vol. 208, pp. 329-346, 1998.

[34] D. A. Saville, *Journal of Colloid and Interface Science*, vol. 222, pp. 137-145, 2000.

[35] J. Lyklema, "A discussion on surface excess entropies", *Colloids and Surfaces a-Physicochemical and Engineering Aspects*, vol. 186, pp. 11-16, 2001.

[36] J. R. Goff and P. Luner, *Journal of Colloid and Interface Science*, vol. 99, pp. 468, 1984.

[37] X. Q. Li and Y. Yan, "Electrical transport through individual DNA molecules", *Applied Physics Letters*, vol. 79, pp. 2190-2192, 2001.

[38] H. Y. Lee, H. Tanaka, Y. Otsuka, K. H. Yoo, J. O. Lee, and T. Kawai, "Control of electrical conduction in DNA using oxygen hole doping", *Applied Physics Letters*, vol. 80, pp. 1670-1672, 2002.

[39] J. S. Hwang, G. S. Lee, K. J. Kong, D. J. Ahn, S. W. Hwang, and D. Ahn, "Electrical transport through poly(G)-poly(C) DNA molecules", *Microelectronic Engineering*, vol. 63, pp. 161-165, 2002.

[40] A. J. Storm, J. van Noort, S. de Vries, and C. Dekker, "Insulating behavior for DNA molecules between nanoelectrodes at the 100 nm length scale", *Applied Physics Letters*, vol. 79, pp. 3881-3883, 2001.

[41] B. Lu, M. R. Smyth, and R. O'Kennedy, "Oriented Immobilization of Antibodies and Its Applications in Immunoassays and Immunosensors", *Analyst*, vol. 121, pp. 29R-32R, 1996.

[42] H. Matsamura, S. V. Verbich, and S. S. Dukhin, *Colloids and Surfaces A*, vol. 271, 1999.

6 Fractionation device design

6.1 Introduction

The aim of this chapter is to report on the design of a microfluidic transport/separation device for colloidal particles based on the utilisation of DEP and the Brownian ratchet induced motion principle. Two types of electrode structure were modelled to compare their potential effectiveness as Brownian ratchets – that is, to simulate the conditions under which they would produce unidirectional net transport with a periodically applied DEP potential.

6.2 Field Modelling

The FlexPDE partial differential equation solver (Version 2.20d ©1996-2001 *PDE Solutions Inc.*) was used to model the field from the postulated electrode structures. This uses the finite element method, dividing the problem space into a grid of triangular elements over which polynomial approximations of the solution are applied, with adaptive mesh refinement until a specified error threshold is reached. Both designs were analysed in the 2-dimensional case, assuming that the length of the electrodes to be much greater than their width.

6.3 Design 1 – Asymmetric electrode pairs

6.3.1 Case 1

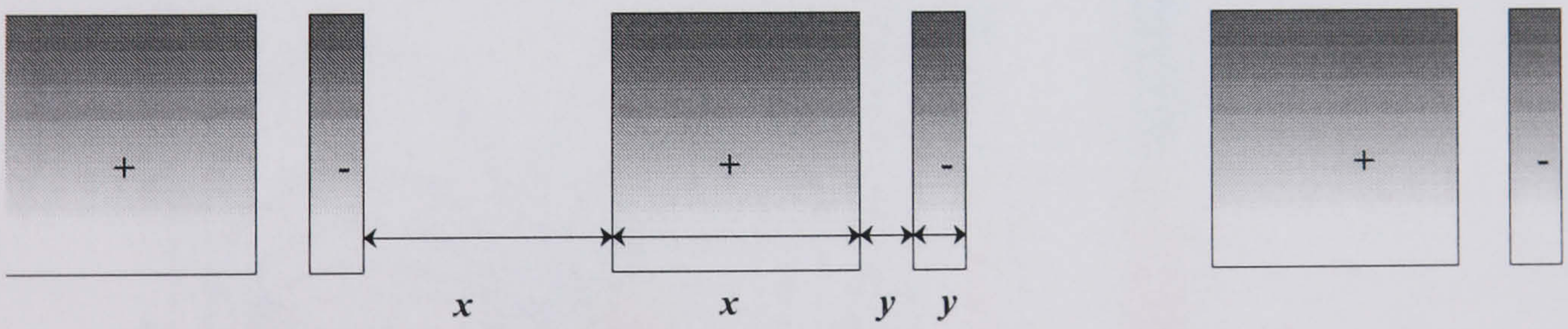

Figure 6-1

Schematic of Design 1 showing asymmetric electrode pairs (lengths not to scale)

This design consisted of an interdigitated array of asymmetric pairs of electrodes, each connected to a single phase alternating voltage source (Figure 6-1). The problem space was divided into a single cell over one electrode period with periodic, non-reflective boundary conditions (Figure 6-2). The substrate for the electrodes was glass and therefore treated as a non-conductor with the ambient medium being RO water. Unit voltages were applied which could subsequently be scaled. The *x*:*y* dimensions were 10μm:2μm, chosen to represent a reasonable scale for diffusion combined with feasibility of fabrication.

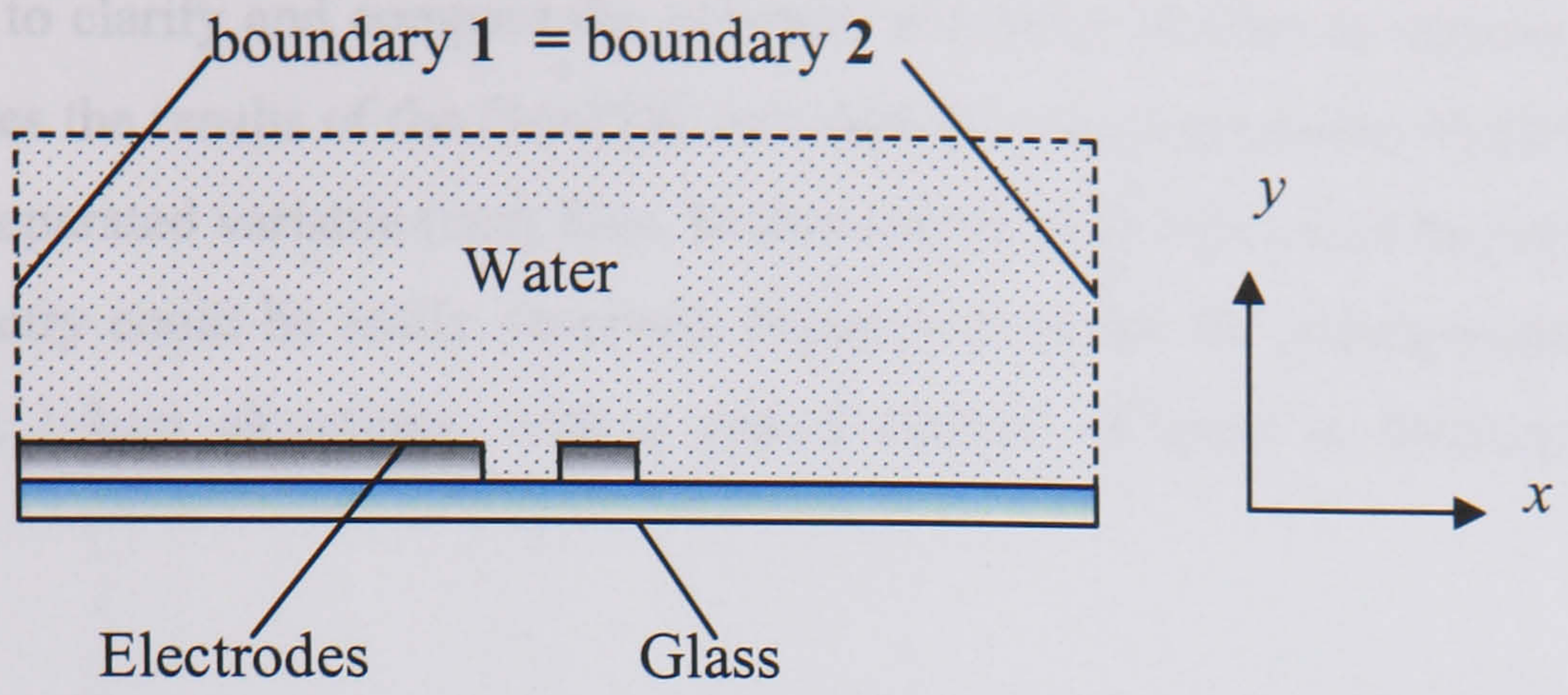

Figure 6-2

Problem space with translationally symmetric boundaries

The electric field was calculated in the electrostatic case, the applied frequency (<10^8Hz) being such that the field always had time to reach a quasi-static state.

The electrical potential, U, and dielectrophoretic potential, defined as $|\boldsymbol{E}|^2$ could then be obtained. From this were transcribed the components of the DEP force so that any asymmetry could be more accurately observed and the height dependence could be envisaged. Figure 6-3 shows the FlexPDE output for the electrostatic potential resulting from this array.

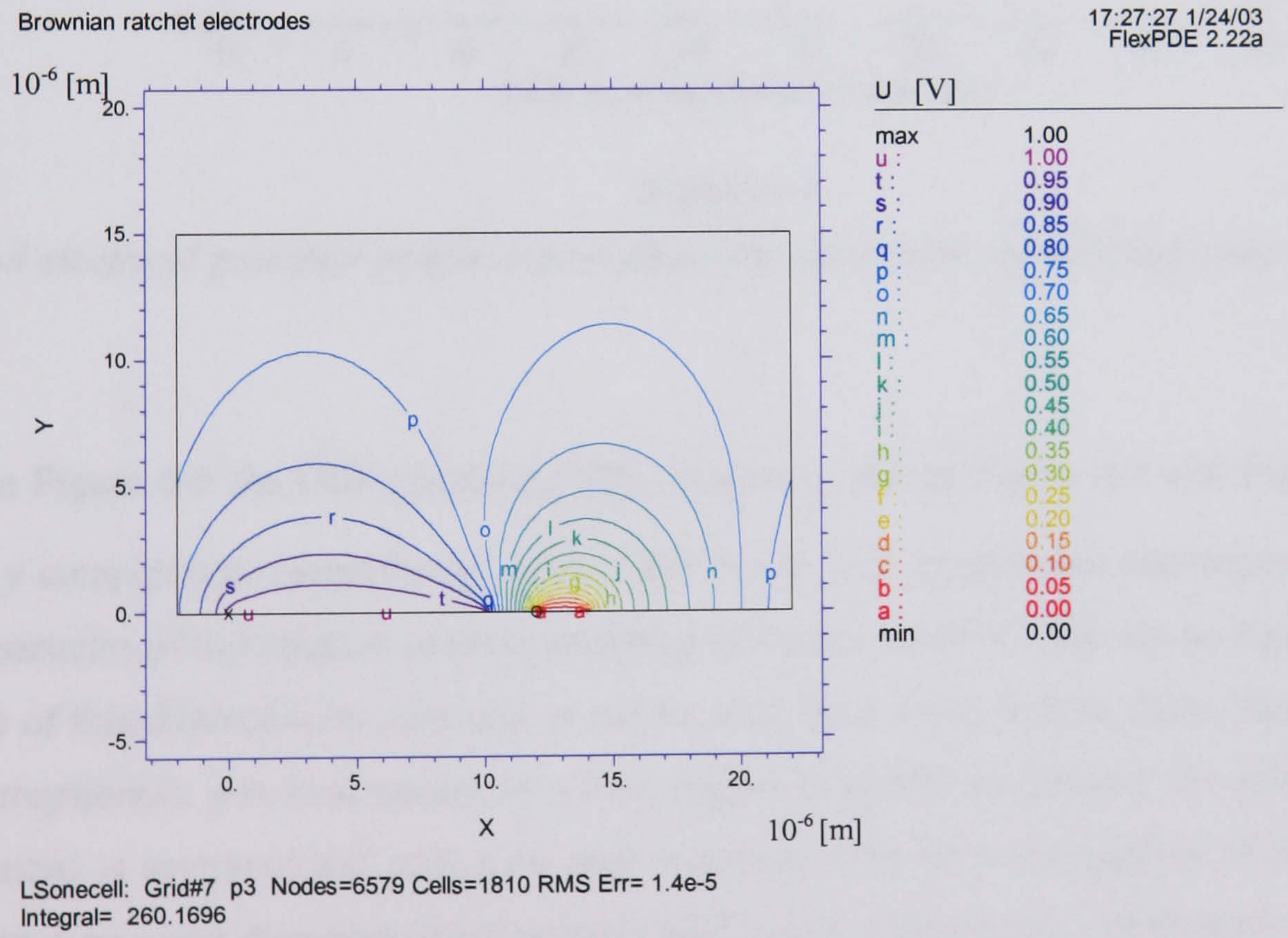

Figure 6-3

Electrostatic potential profile of design 1, case 1

In order to clarify and compare the potential and force profiles at various heights above the electrodes the results of the FlexPDE calculations were imported to Matlab in table form as comma separated variable (csv) files. In this way several cells could be juxtaposed so that any asymmetry could be easily observed. Figure 6-4 shows the corresponding electrostatic potential at 1-3μm elevations, with *a* and *b* marked in order to illustrate the level of asymmetry.

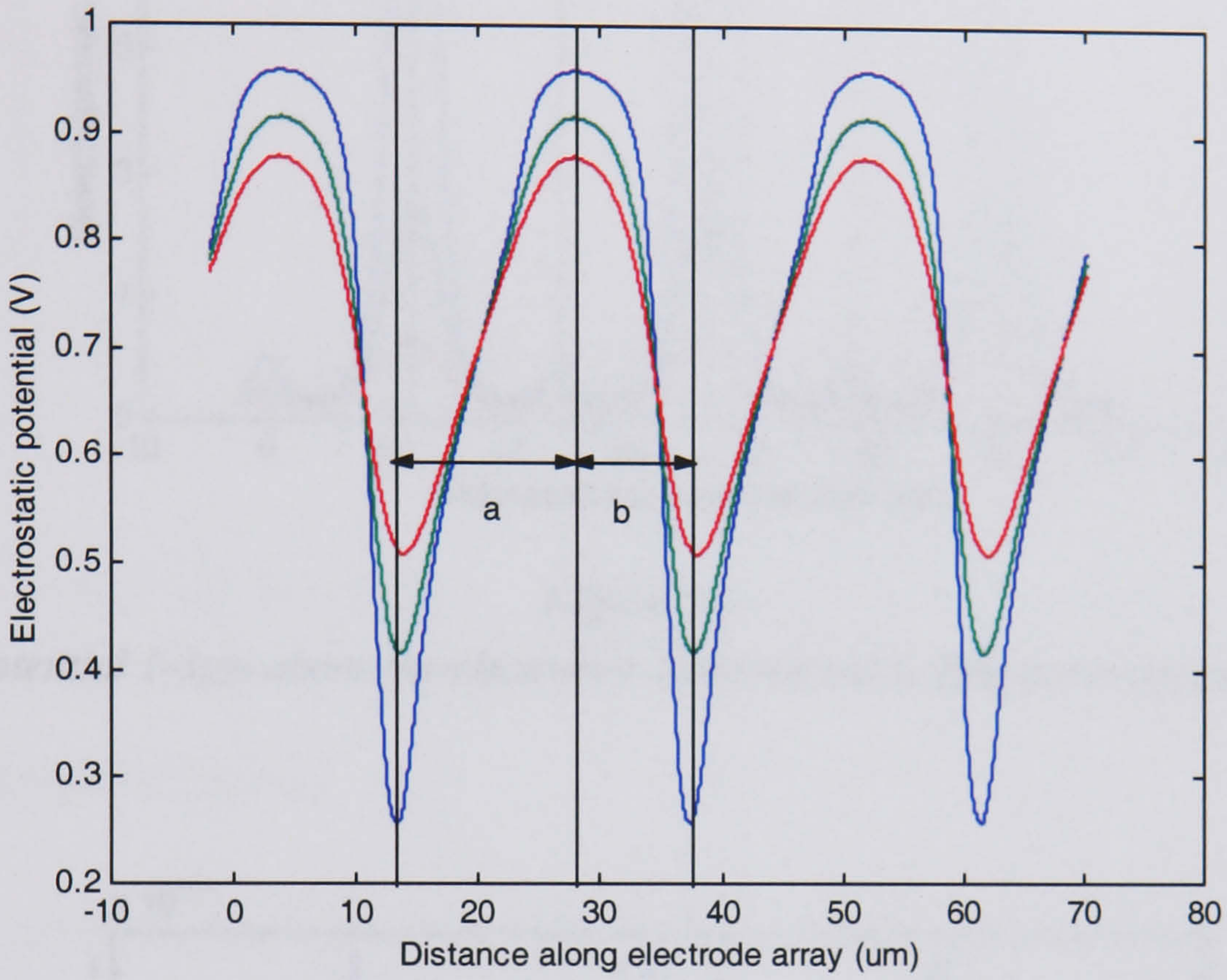

Figure 6-4

1-d electrical potential profile 1-3μm above the electrodes, manifesting some asymmetry

In Figure 6-5 the DEP potential, $|\boldsymbol{E}|^2$, is shown, and in Figure 6-6 and Figure 6-7 the *x* and *y* components, respectively, of the DEP force. The magnitudes correspond to Newtons for particles of unit radii in microns and may be scaled for other radii by multiplication of the cube of this dimension in microns. It can be seen from these figures, then, that although the *electrophoretic* potential possesses a low degree of global asymmetry the dielectrophoretic potential is asymmetrical only over half a period, with the *x*-component of the DEP force acting over equal distances in the positive and negative directions and therefore averaging to zero across one period of the array.

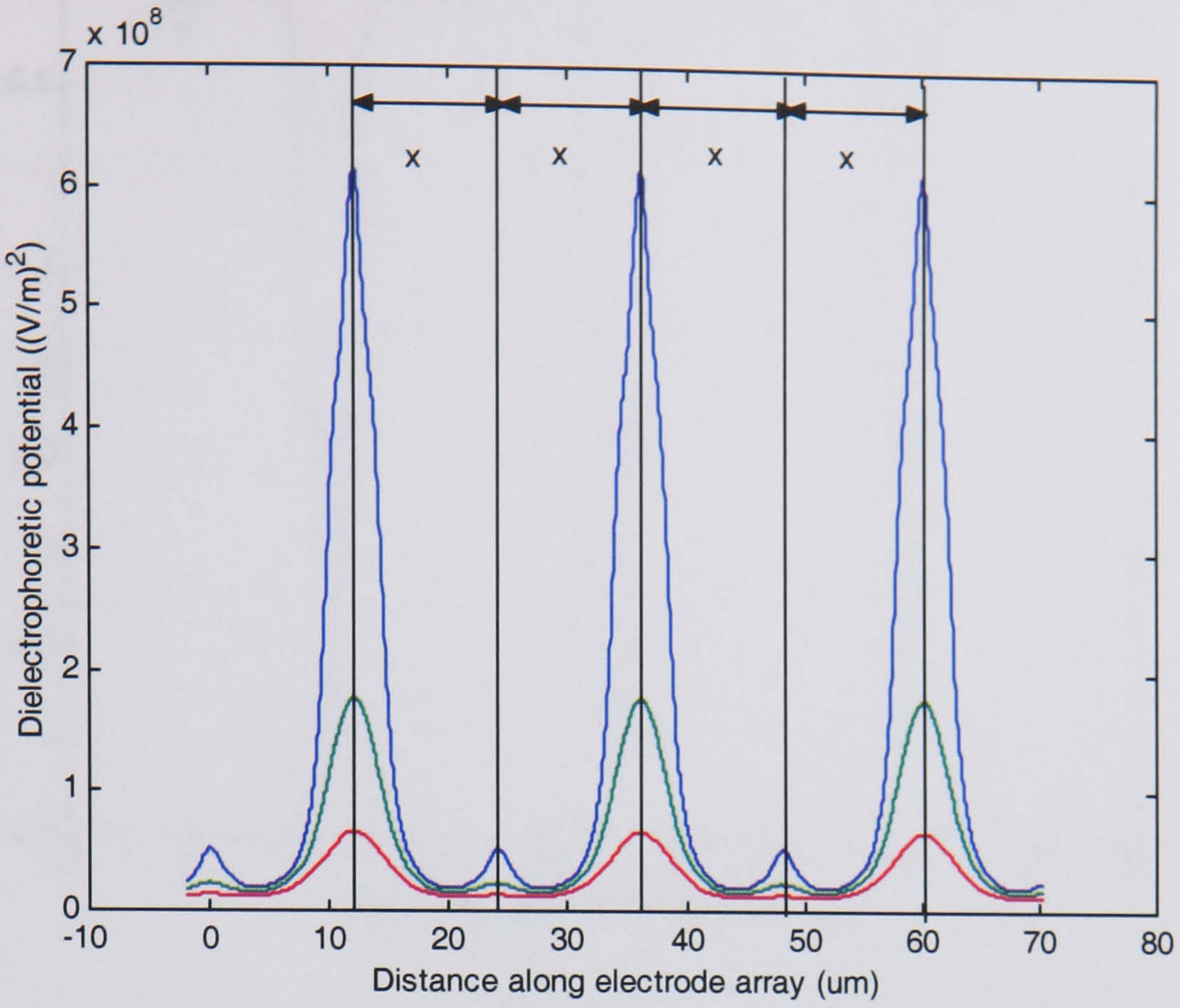

Figure 6-5

DEP potential 1-3μm above the electrodes. Symmetrical to first order approximation.

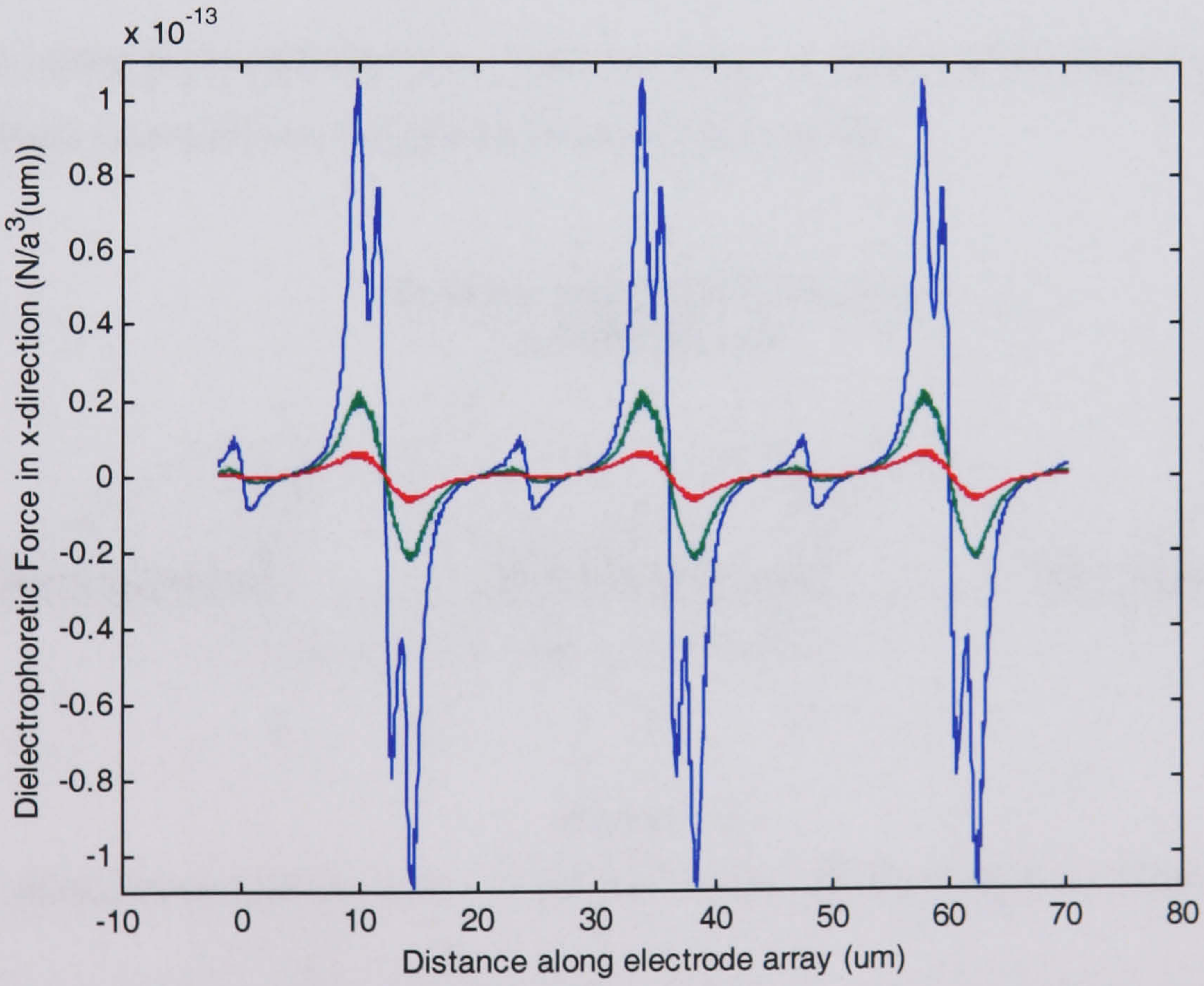

Figure 6-6

x-component of DEP force to first order equally distributed around zero

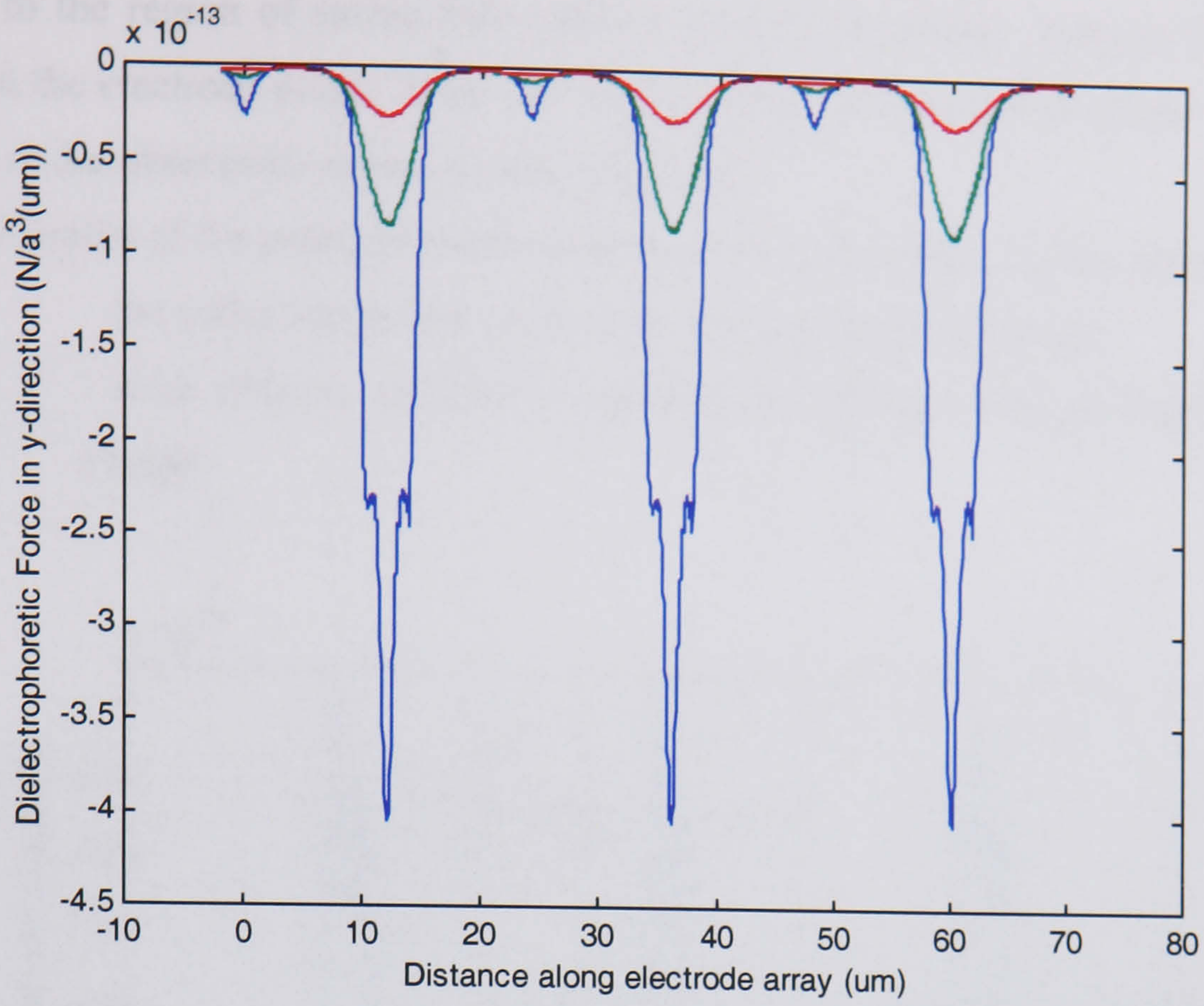

Figure 6-7

y-component of DEP force reflecting the difference in magnitude of high and low field regions

6.3.2 Potential schematic

Over an entire period the deviation from symmetry is small and the trapping potential can be represented essentially by the profile shown in Figure 6-8.

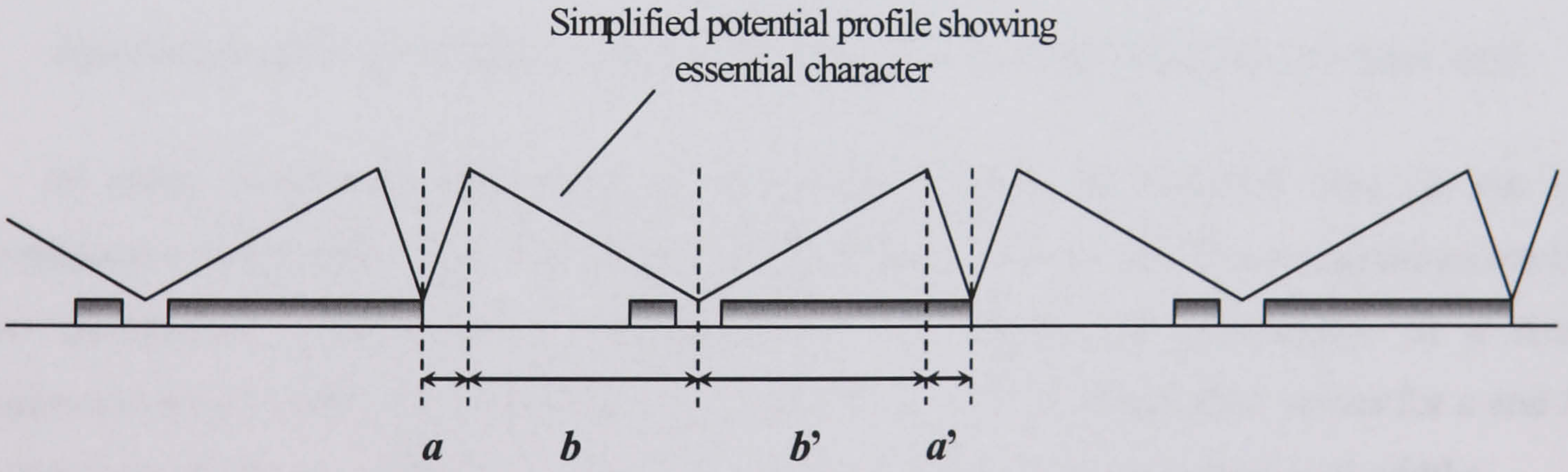

Figure 6-8

Elementary representation of the DEP potential resulting from design 1

The linear potential gradients are of course not representative of the actual potential. This simplified approximation, however, circumvents the complicated dynamical collection problem in the assumption that the on-cycle is sufficiently long so that any particle diffusing beyond the boundary of a potential well will be trapped during the next on-phase. This assumption is validated if the potential considered is that close to the electrodes. Although other particles at higher elevations may remain suspended, the majority should be quickly drawn in to the region of strong force and so will be observable through the microscope focused on the electrode plane. Thus, the on-time could be adjusted to ensure that complete collection in the observable region always occurred.

The equal depths of the potential minima are physically justifiable by the premises that

i) the collection points are assumed to be non-saturable and

ii) once trapped, particles in general do not have enough thermal energy to escape.

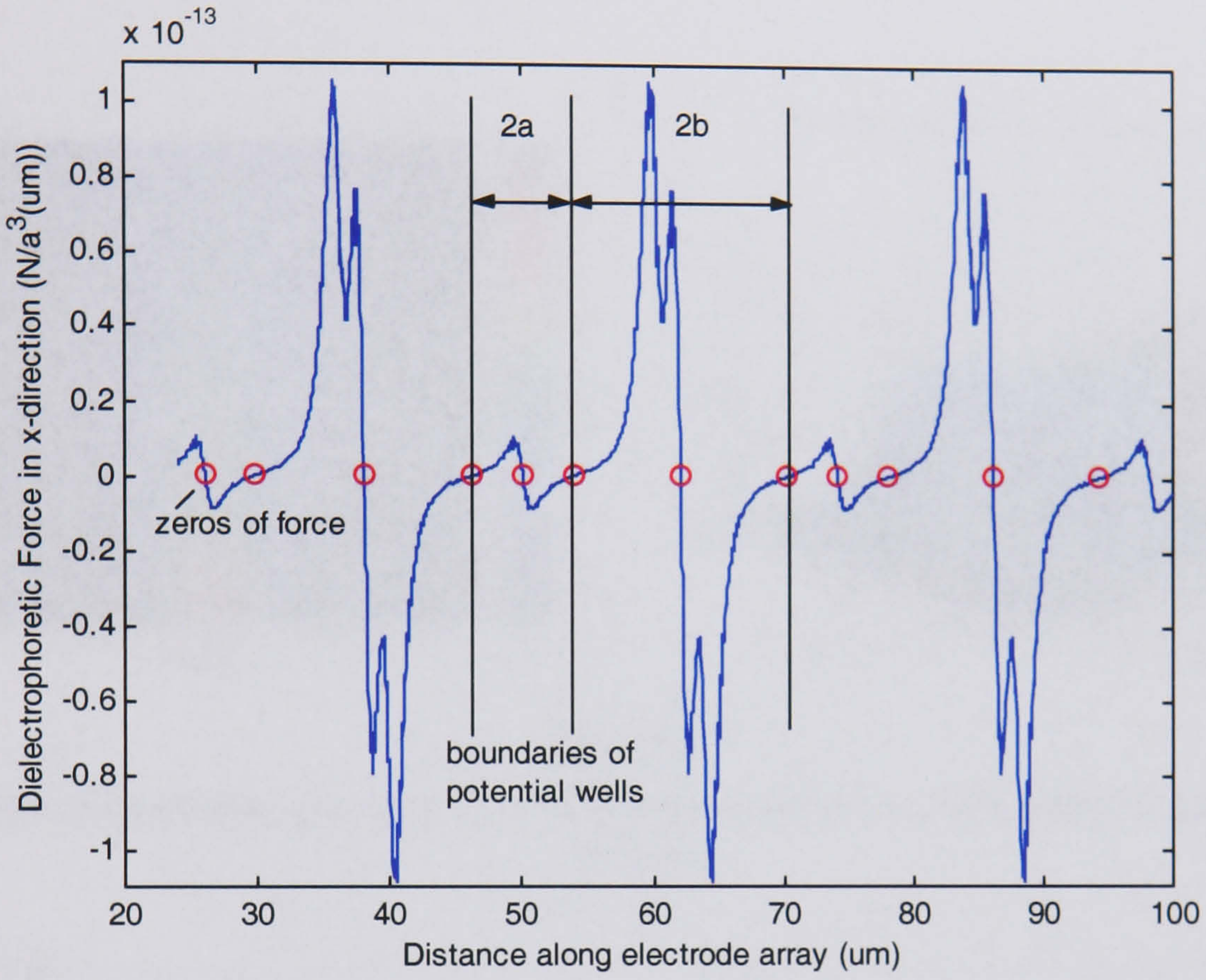

Figure 6-9

Assessment of the scale of a *and* b *from the zero force boundaries of the potential wells*

In order to estimate the widths of the potential wells the FlexPDE data for the x-component of the DEP force was imported to Matlab so that the zero force boundaries could be determined (Figure 6-9). Considering the low degree of asymmetry, as a first approximation a and b were set equal to a' and b' respectively. From this, values for a and b were 4μm and 8μm, defined as half the respective small and large potential well widths.

6.3.3 Simulation of motion

A Matlab program was written to predict the net motion when this potential was periodically applied to a dissipative particle ensemble. This was done on the assumption that the on time, t_{on}, was sufficiently long for collection of all particles diffusing beyond the limits of each trap. As outlined in chapter 3, particles trapped during the on-cycle diffuse in a Gaussian distribution. From Equation (3-29) the probability of diffusing past a potential well boundary is:

$$p = \frac{1}{2} erfc\left(\frac{a}{\sqrt{4Dt_{off}}}\right) \tag{6-1}$$

where a is the distance from the centre of the well. This condition was applied symmetrically to each minimum, according to the definition of the potential wells. Figure 6-10 and Figure 6-11 show 216nm beads diffusing for 20s between on-cycles.

Results

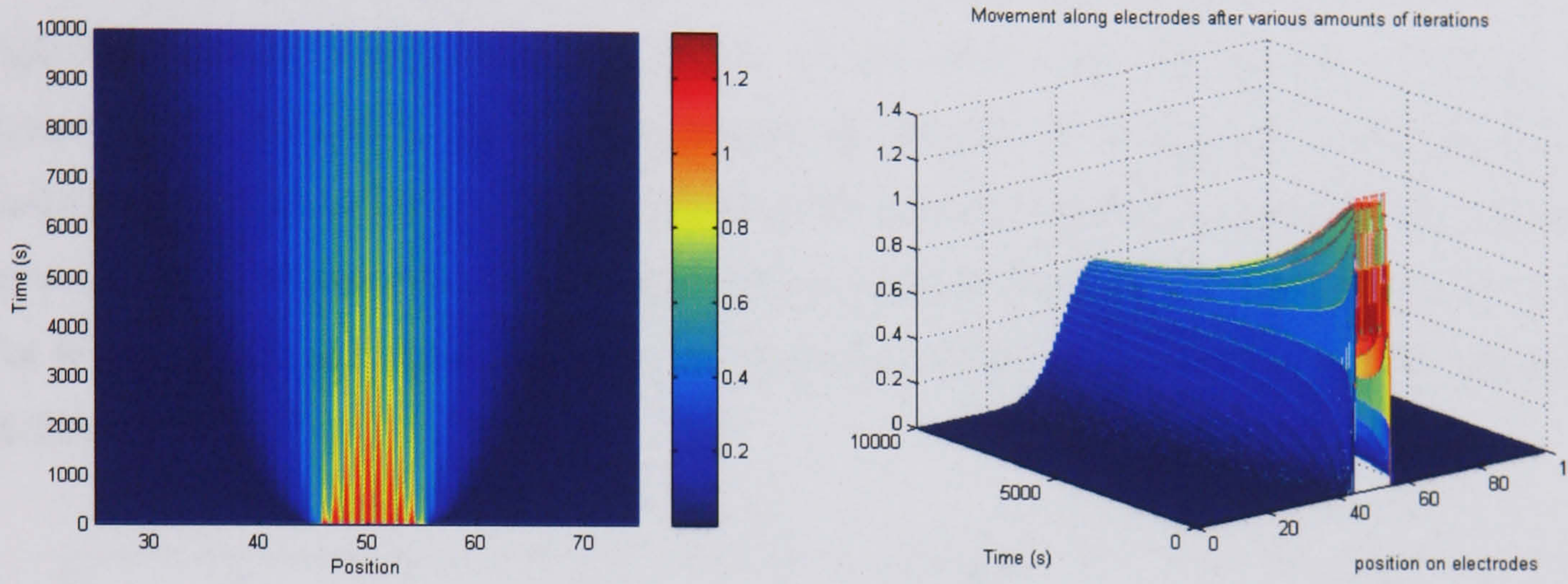

Figure 6-10

Behaviour of a normalised dissipative particle ensemble in electrode design 1 with a=*4μm,* b=*8μm*

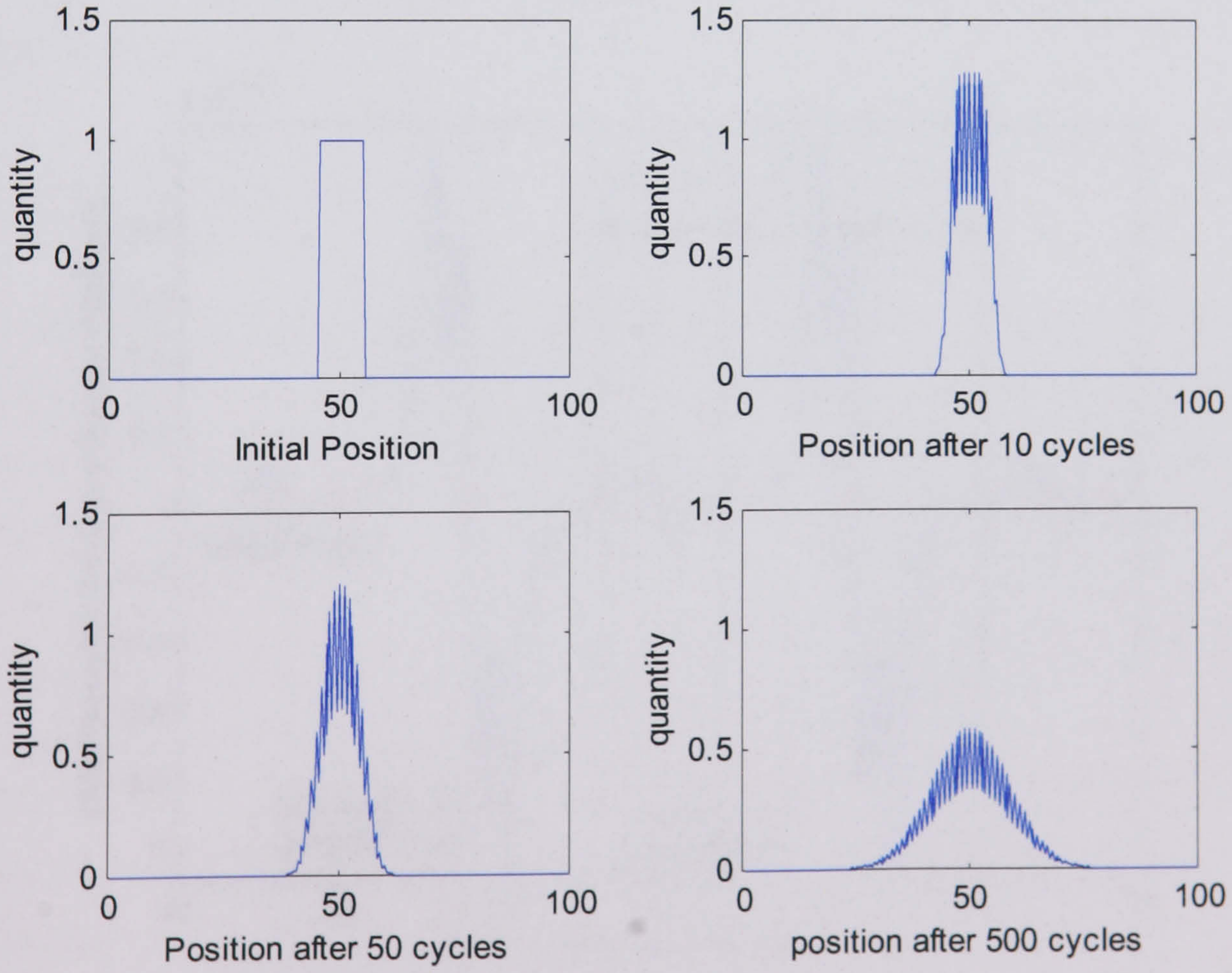

Figure 6-11

Distribution profiles of 216nm beads after various amounts of cycles with 20s off-time

It can be seen from these figures that the theoretical ensemble quickly discretises. This is an indication of the relative distribution of particles with proportionally more particles in the wider wells. There is no global motion, only a small amount of symmetric dissipation around the centre of the initial distribution, with even this curtailed by the lower probability of escape from the outermost wide potential wells. Increasing t_{off} results merely in a greater dissipation of the sample.

6.3.4 Higher order approximation of potential

The real potential profile, of course, is not absolutely symmetrical as the centre of the high field region is not located precisely on the inner edge of the large electrode but somewhere in the small gap. A more accurate description of the system can be obtained by measuring also the positions of the centres of the potential wells, characterised by the x-axis crossing of the x-component of the DEP force between the well boundaries (Figure 6-12). For this $x : y$ ratio of 10μm :2μm the corresponding values of the well boundaries are shown in Table 6-1.

a	a'	b	b'
3.87	3.62	8.38	8.13

Table 6-1
Actual dimensions in microns of potential wells

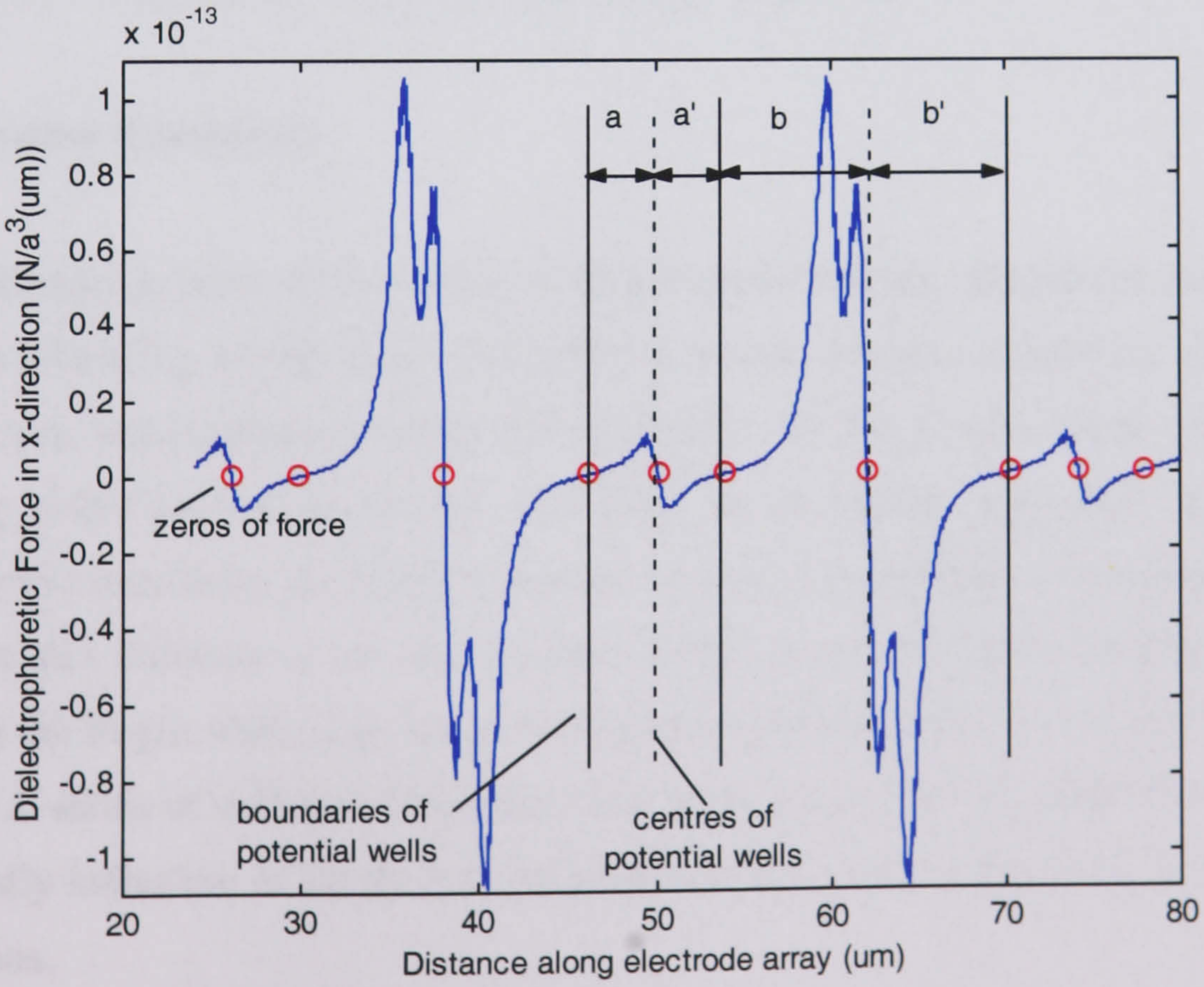

Figure 6-12
Second order assessment of potential profile measuring the degree of well asymmetry from the zeros of the DEP force

Here it must be observed that the asymmetric problem, with $a \neq a'$, $b \neq b'$ is part of a different general class that demands some extra consideration when modelling the resulting motion. In order to clarify the transport properties of this system a modification was introduced into the design – case 2.

6.3.5 Case 2

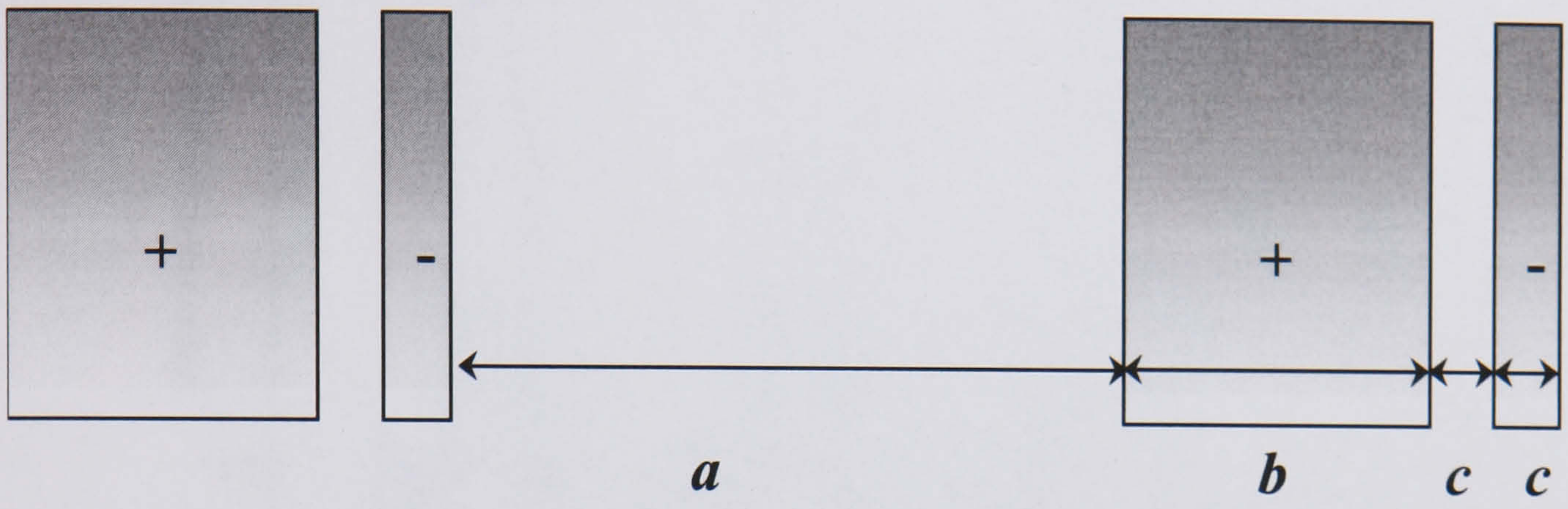

Figure 6-13

Modification to initial design with interdigitated pair spacing not equal to the large electrode width

In an attempt to clearly break the symmetry of the potential the next case modelled was that of independent electrode pair spacing and wide electrode width i.e. with $a \neq b$ (Figure 6-13). This could potentially generate a non-negligible asymmetry due to the smaller potential well being situated off-centre between the larger ones[18].

6.3.6 System dimensions

The influencing factor in the choice of the electrode and gap dimensions was an order of magnitude balancing of the large and small potential minima. Otherwise, the high field generated trap would almost entirely dominate over the lower one and so any asymmetry generating properties would be lost with only an essentially symmetric series of deep potential wells remaining, in a similar manner to case 1. In addition, account had to be taken of the fact that diffusion is an integral part of the system and that from this perspective shortening the length scale of potential well boundaries would result in more efficient global transport. A series of different dimension sets were tried based on adaptive refinement. A trial typically indicative of the general properties of the system is illustrated in the following four sections.

---

[18] Making the small gap and electrode independent variables would not change significantly the class of the problem as it would not allow a much greater alteration of the symmetry of the system, only adding unnecessarily to the number of cases to be simulated for adequate refinement of the solution.

6.3.7 Field modelling

The dimensions of the electrode array illustrated are $a = 15\mu m$, $b = 7\mu m$ and $c = 3\mu m$.

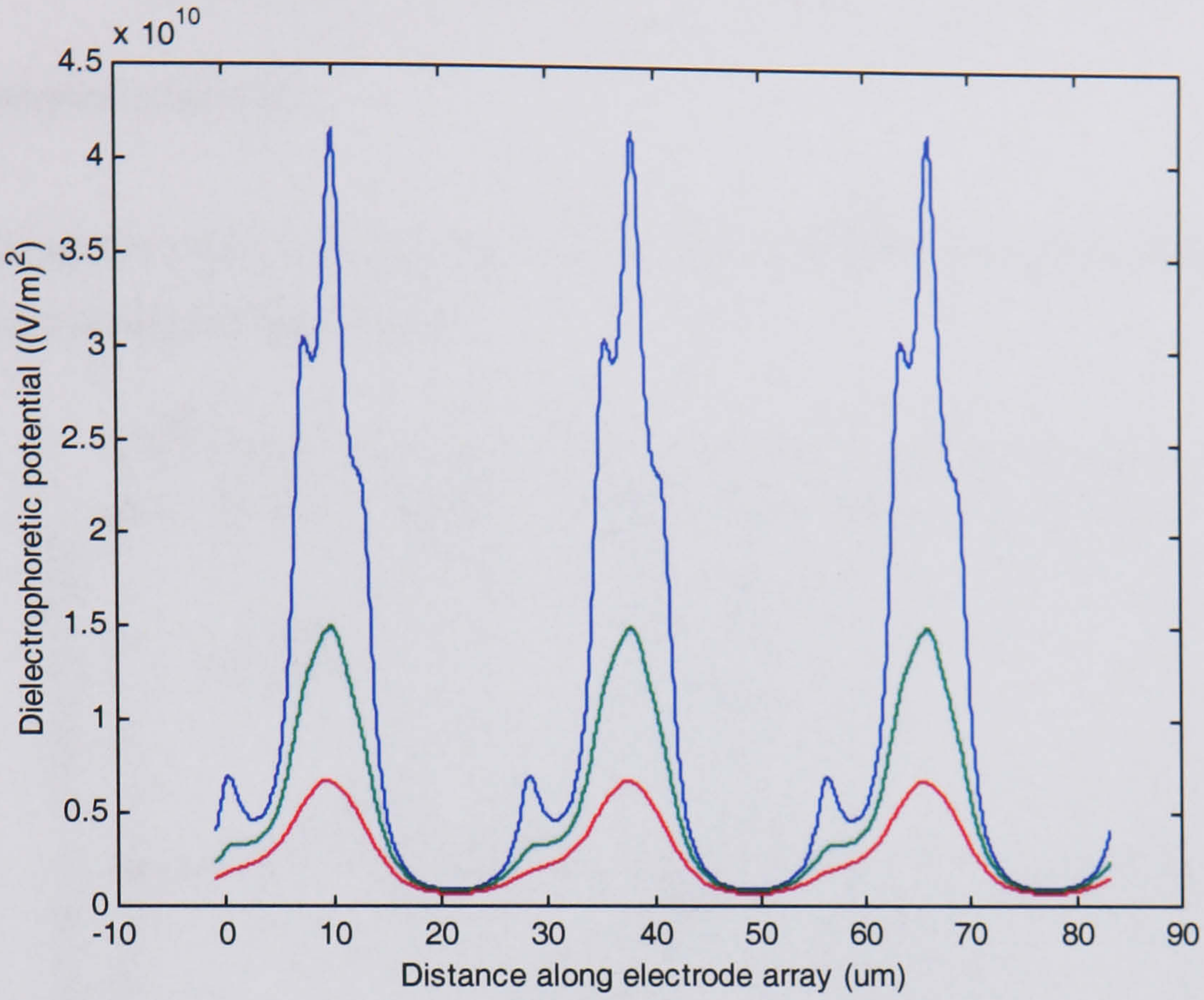

Figure 6-14

DEP Potential of design 1, case 2 at 1-3μm elevation showing increased asymmetry

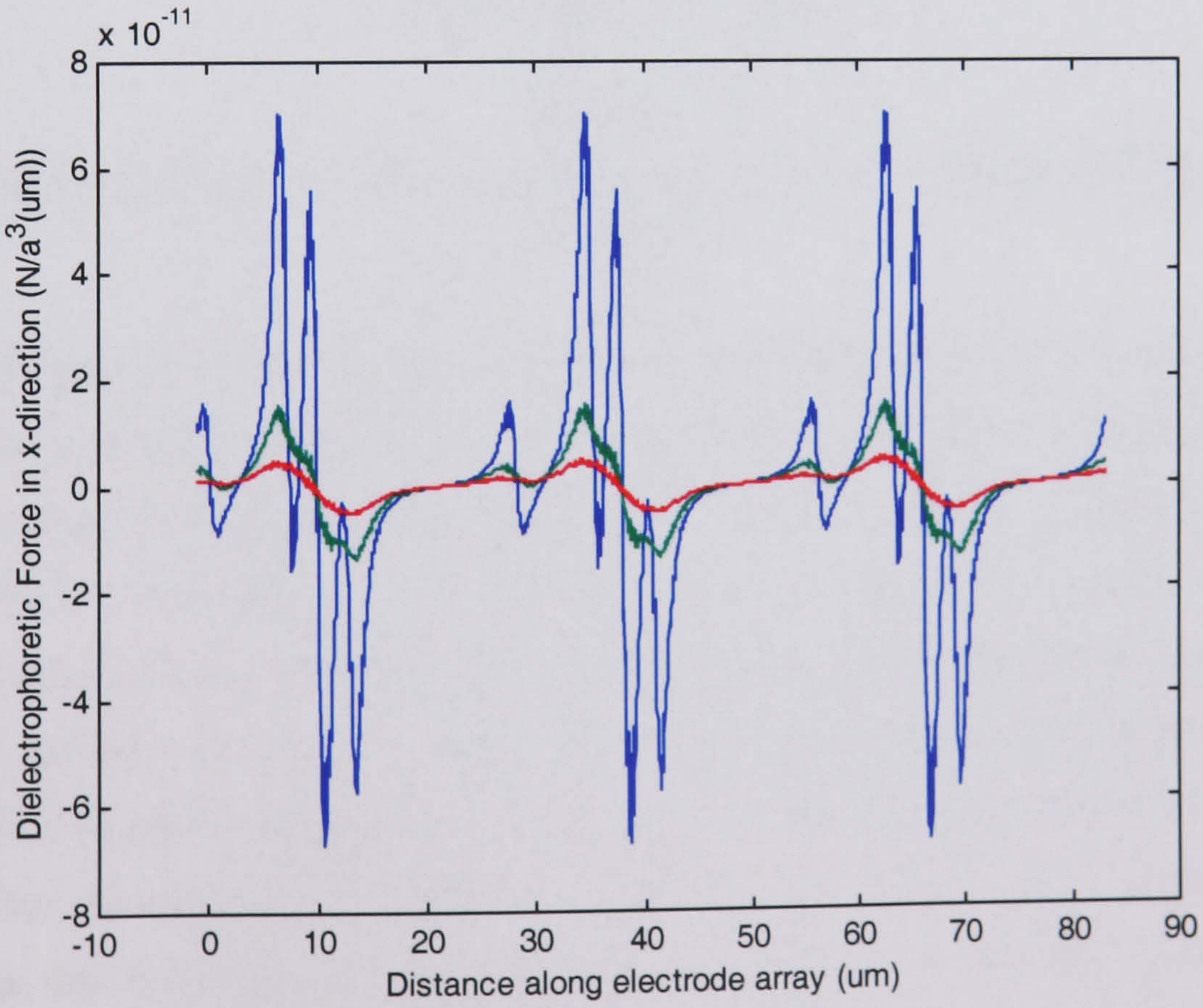

Figure 6-15

Force profile in x *–direction at 1-3μm*

Figure 6-14 shows a definitely asymmetric potential profile with the small potential wells actually defined close to the electrodes. In Figure 6-15 the trapping potential of both wells is further elucidated by illustration of the local direction of the x-component of the DEP force.

6.3.8 Potential schematic

The boundaries of the potential wells were again defined by observing the points of zero force at 1 μm elevation (Figure 6-16).

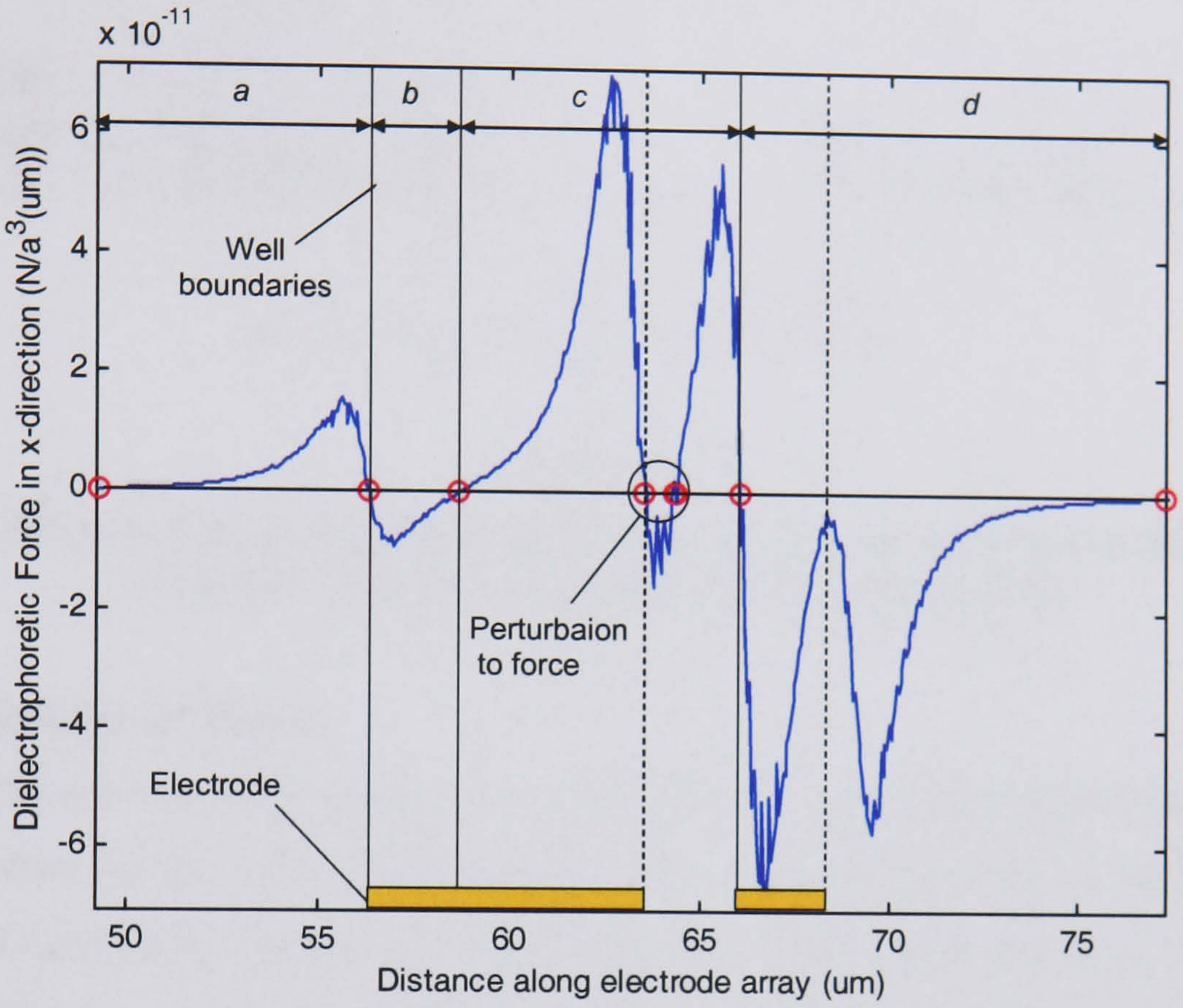

Figure 6-16

Force shown with respect to electrode positions indicating definition of potential well boundaries

The force profile in this instance is slightly more complicated due to the perturbations from the inner and outer edges of the large and small electrode respectively. These are somewhat more prominent than before due to the slightly increased width (and correspondingly lower field) of the small gap, which is necessary in order to achieve the required proportioning of the small and large potential minima. The larger spacing of these perturbing minima from the main trap on the inner edge of the small electrode means that they are not completely subjugated as they were in the previous example. It can be seen, however, that theoretically no collection should occur on the outer edge of the small electrode as the force does not actually reach zero here – although a small amount of collection would still occur on the inner edge of the large electrode. The magnitude of this collection can be estimated by observing the distance in region c over which the force acts in the negative x-direction – i.e. away from the centre of the deep potential well. It can be seen that generally the force in this region is positive apart from a short fragment where there is a weakly negative component. This short section clearly does not substantially contribute to the essential nature of the profile and so may be neglected. This results in a potential profile that can be represented schematically as in Figure 6-17. The noteworthy point is that in this instance the trapping distance on either side of the wells is not equal.

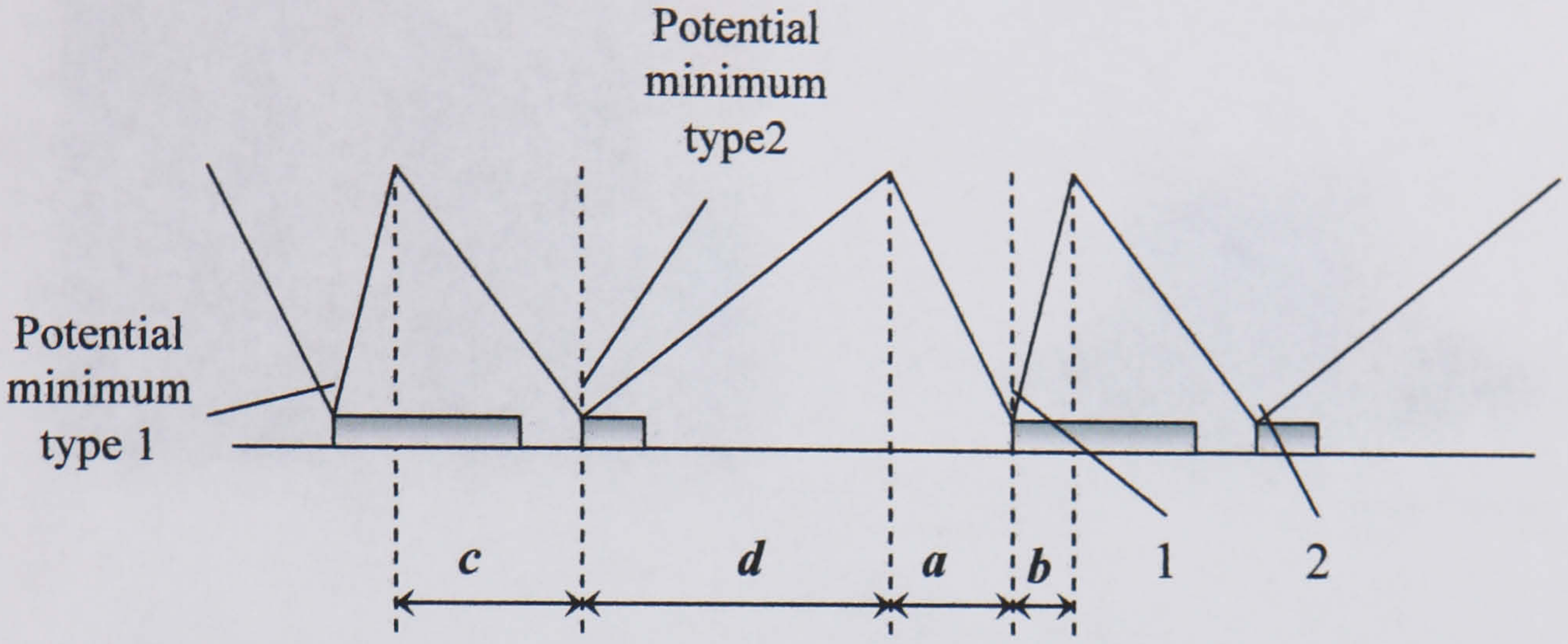

Figure 6-17

Simplified DEP potential profile of asymmetric pairs with arbitrary spacing showing 2 types of minima, classified by distinct width and asymmetry

6.3.9 Simulation of Motion

In this case there are four distances to consider *a, b, c,* and *d.* The motion simulation was written as before but this time taking into account that the probabilities of diffusing beyond two potential boundaries are not equal depending on whether the particle is in a potential minimum of type 1 or 2. For this reason particles diffusing beyond two potential well boundaries were also considered. The dimensions *a, b, c,* and *d* were obtained from Figure 6-14 and Figure 6-15.

a	b	c	d
7.0	2.3	7.3	11.4

Table 6-2

Potential well dimensions in μms for design 1, case 2

The optimum t_{off} was calculated by considering the sum of the fluxes arising from the two types of potential minima. These characteristically transport particles in opposite directions but at different rates so there should be a net imbalance and global asymmetric transport should occur.

Results

The results for t_{off} defined according to the above criteria produced almost no net motion at all (Figure 6-18).

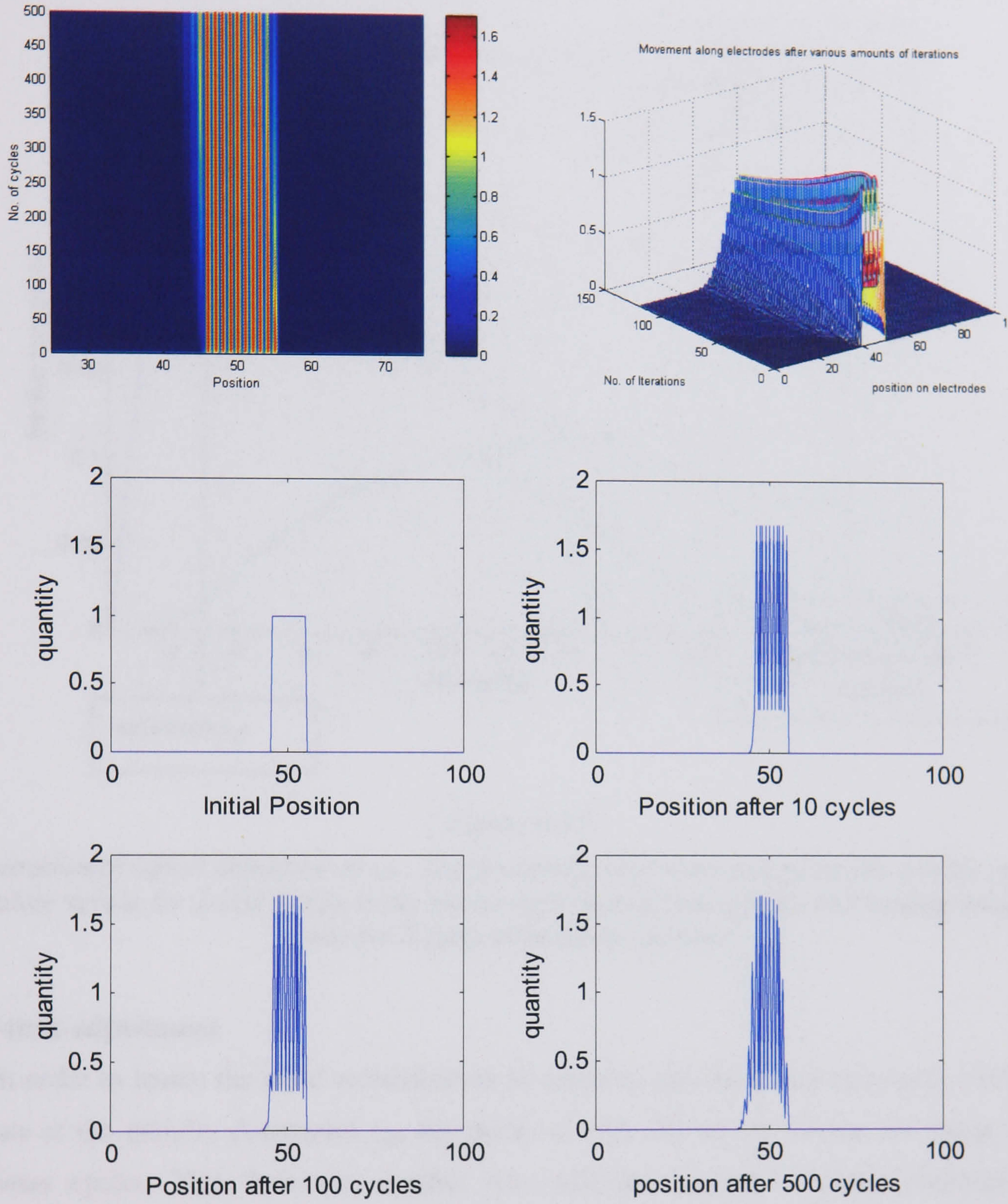

Figure 6-18

t_{off} = 3.2s, defined according to the criteria that, assuming a smooth distribuition, the net flux from the combination of type 1 and 2 minima is maximised

The reason for this is apparent when the magnitude of the forward and backward fluxes from the type 1 and 2 minima respectively is considered (Figure 6-19). Because they are so imbalanced, discretisation of the sample again occurs very quickly, with particles being transported into type 2 minima much faster than they can leave. For this reason the average asymmetry experienced by the particles rapidly becomes much lower than the combination from the two well types. More particles experience the considerably reduced asymmetry of the wider potential well. An interesting effect is that although this transports particles in the opposite direction at a much reduced rate, the increasing proportion of particles in these minima mean that the forward and backward fluxes reach a fluctuating balance. Therefore the widening of the overall profile is constrained but little can be observed of classical Brownian ratchet behaviour.

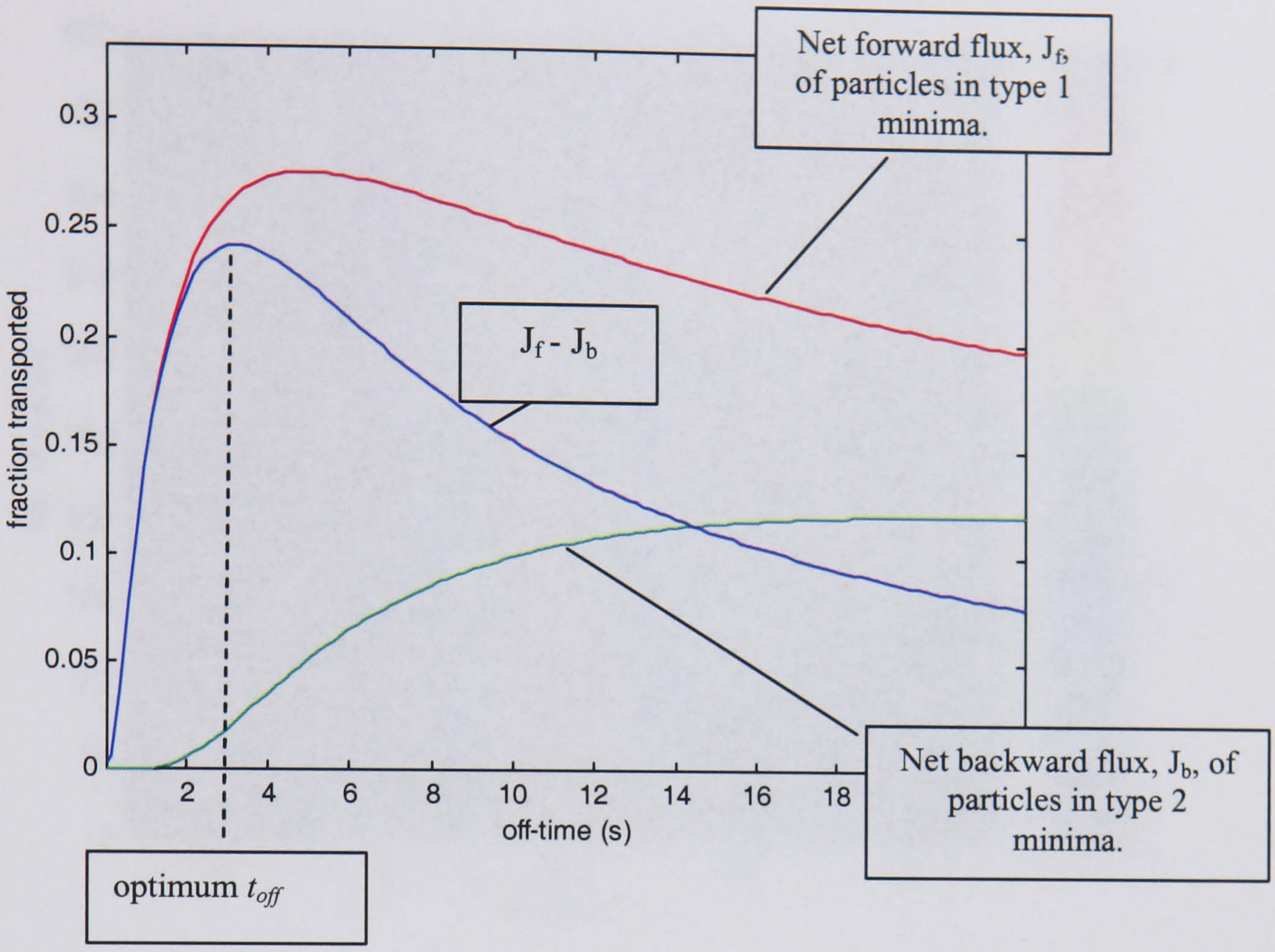

Figure 6-19

Illustration of initial definition of t_{off}. *The problem is that these are generally not the correct absolute values for* J_f *and* J_b *due to the initial even distribution quickly discretising unequally into the 2 types of potential minima.*

Off-time adjustment

In order to lessen the rapid redistribution of particles into the lower symmetry wells that occurs at the initially designated t_{off}, the particles were allowed to diffuse for longer times between cycles. This, however, implies that diffusion beyond a second potential well boundary may become non-negligible and therefore the approximation used would break down. This has been shown to be the case using higher off-times where the distance transported actually peaks and reverse motion eventually takes place due to an unrealistically high number of particles being forced into more asymmetric narrow wells by artificial truncation of the Gaussian tail. In order to avoid this problem, the program was modified to include diffusion past *n* boundaries, where *n* is an off-time dependent cut-off point. In this way the motion could be more accurately simulated and the real optimum t_{off} established by observing the velocity peak. Figure 6-20, shows the distance transported through 500 cycles using $t_{off} = 10s$ with the discretised profiles outlined at various points. Evidently this increase in free diffusion time causes a greater general dissipation of particles although a definite collective drift can be observed.

Figure 6-21 shows the transport expected when the off-time is increased to 30s. The net distance is increased, and from Figure 6-22 it can be seen that the normalized quantity of beads falls off as they begin to be lost from the end of the electrode array.

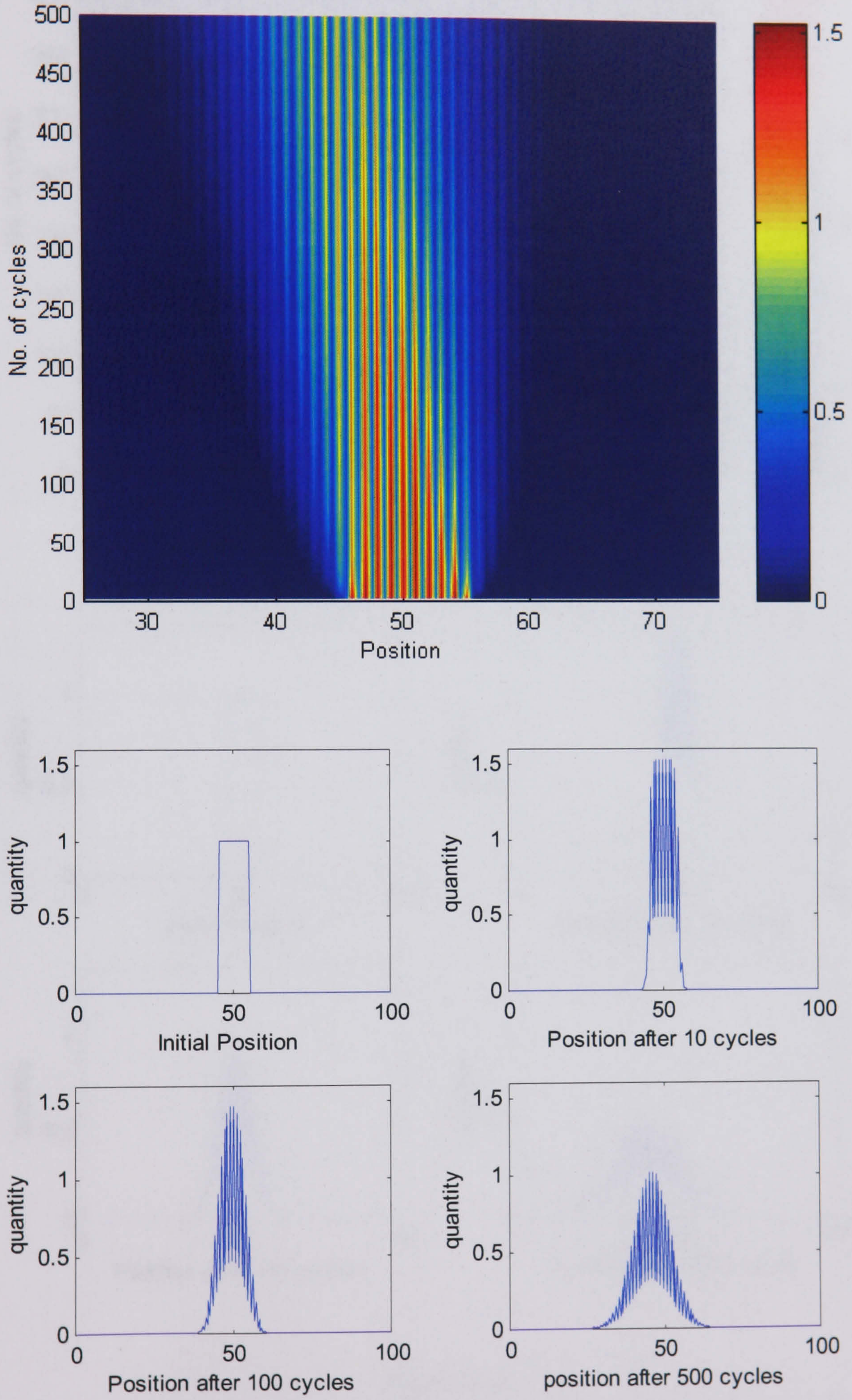

Figure 6-20

216nm beads in device design 2, case 2, with t_{off} 10 second - longer than theoretically optimised in order to reduce competing back flow

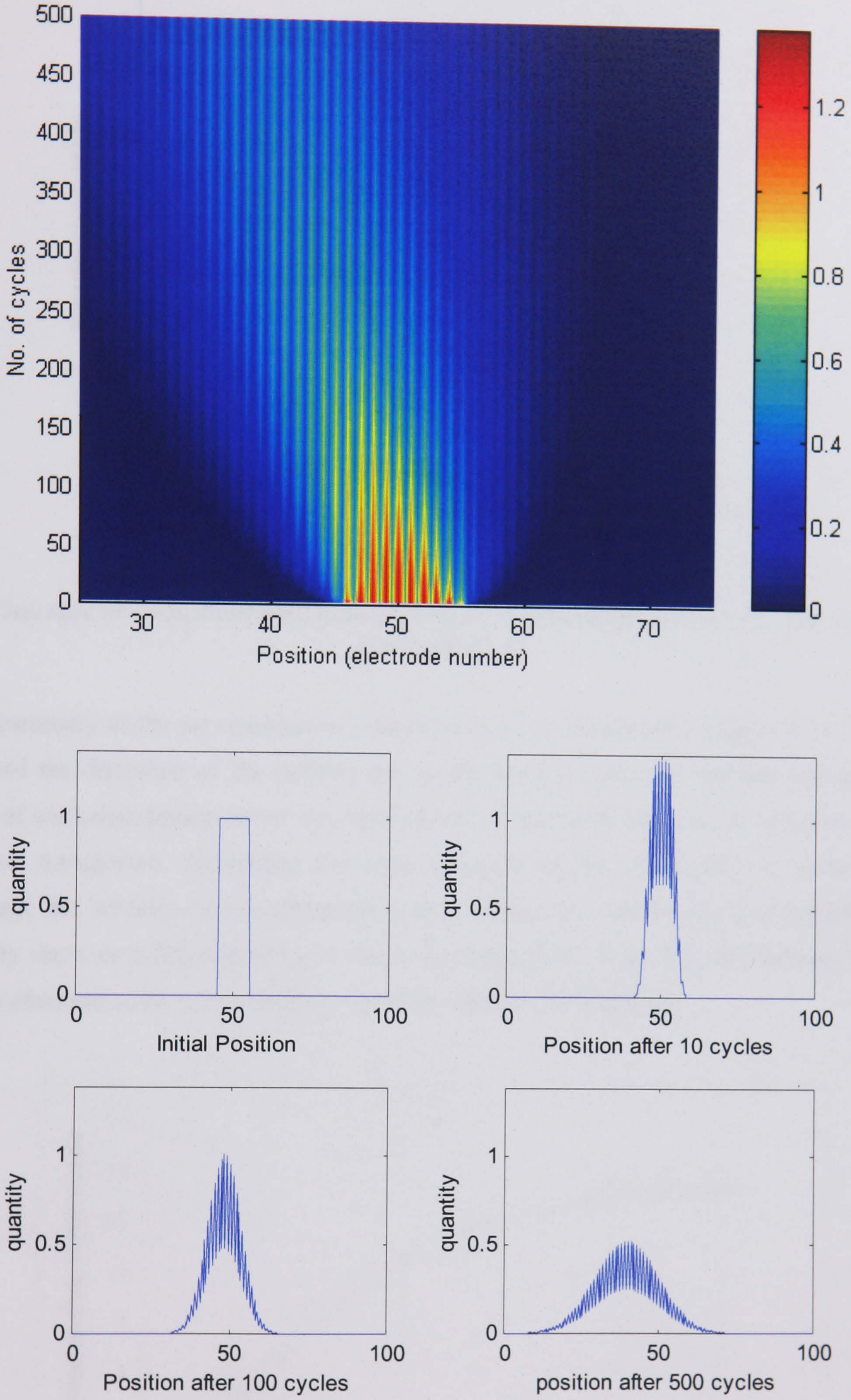

Figure 6-21

216nm beads in device design 2, case 2, with t_{off} increased to 30 seconds - well above the theoretically optimised value in order to reduce competing back flow further and thereby increase forward transport. The sample is correspondingly spread out more across the electrode array.

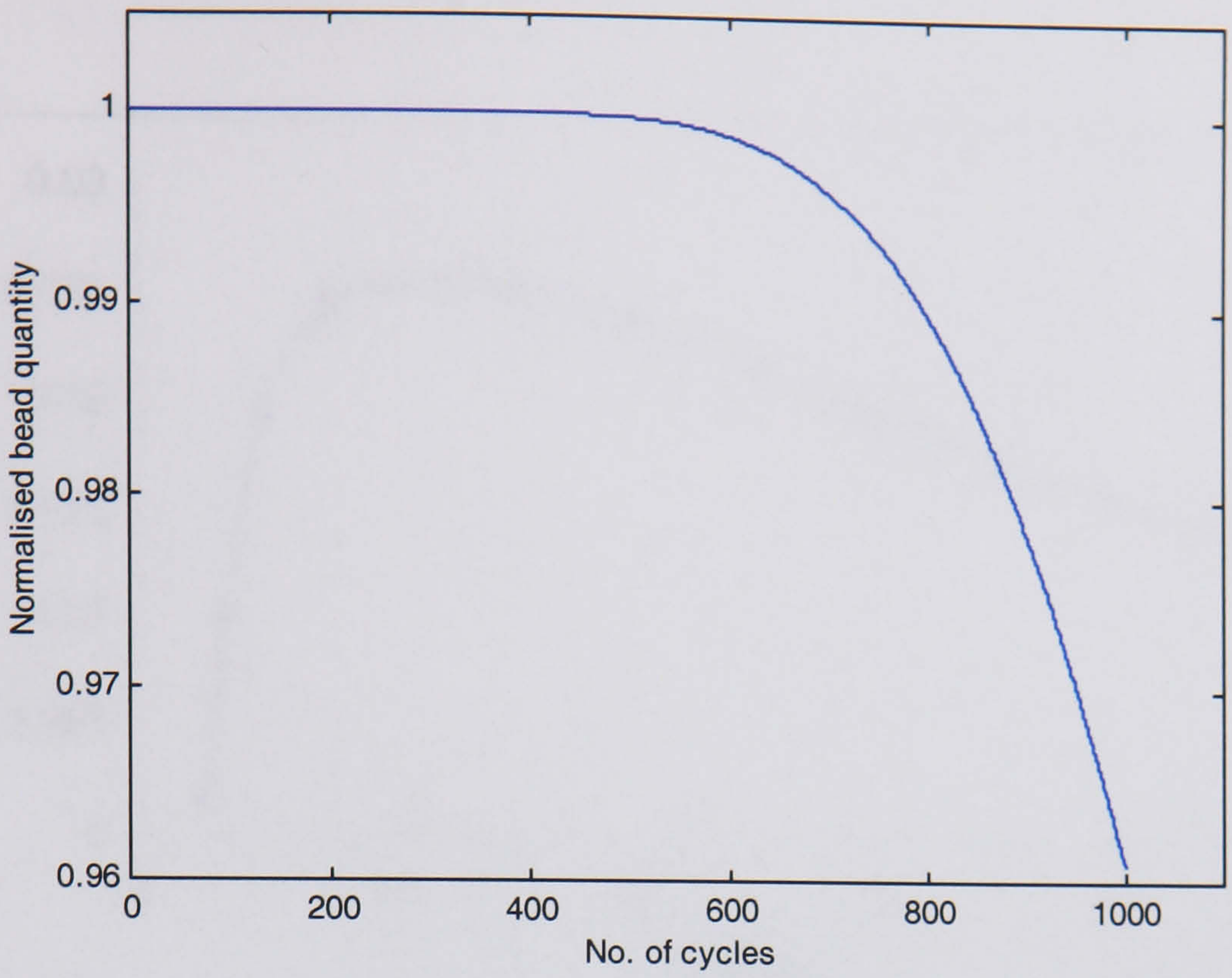

Figure 6-22

Decrease in normalized bead quantity for $t_{off} = 30s$ as particles reach the end of the electrode array

A summary of the net transport as a function of t_{off} is illustrated in Figure 6-23. In order to avoid the distortion of the profiles due to the discrete nature of allowed positions, the mean of each distribution curve was used instead of the peak (median) to calculate the net distance transported. Examining the mean position of the distribution at various time intervals, the velocity can be observed to be constant for a given t_{off}. The corresponding velocity curve as a function of t_{off} is shown in Figure 6-24. From this, the optimal off-time can be observed to be ~10s, resulting in a peak velocity of 0.025μm/s.

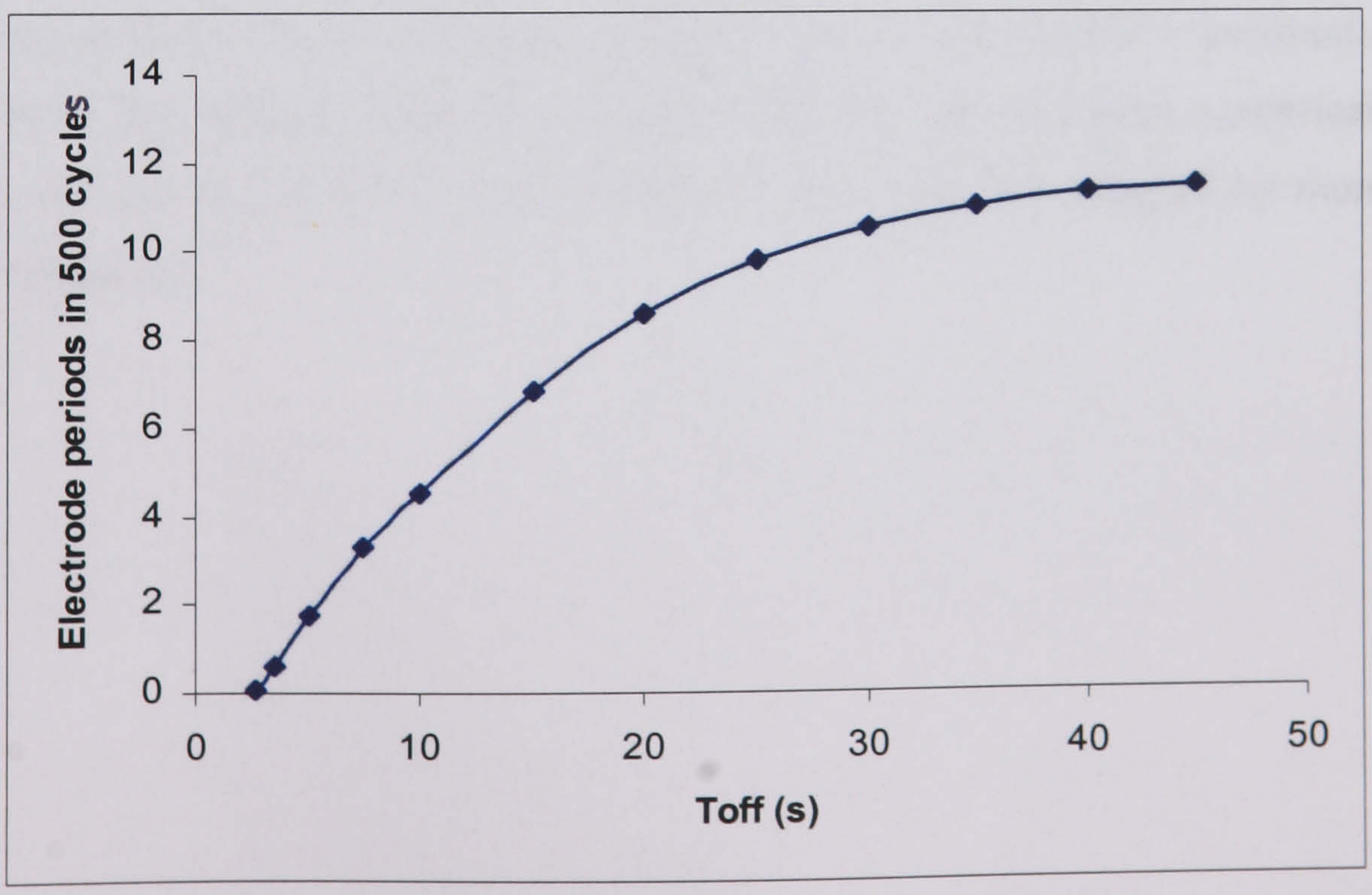

Figure 6-23

The relationship between t_{off} and average distance moved in 500 cycles

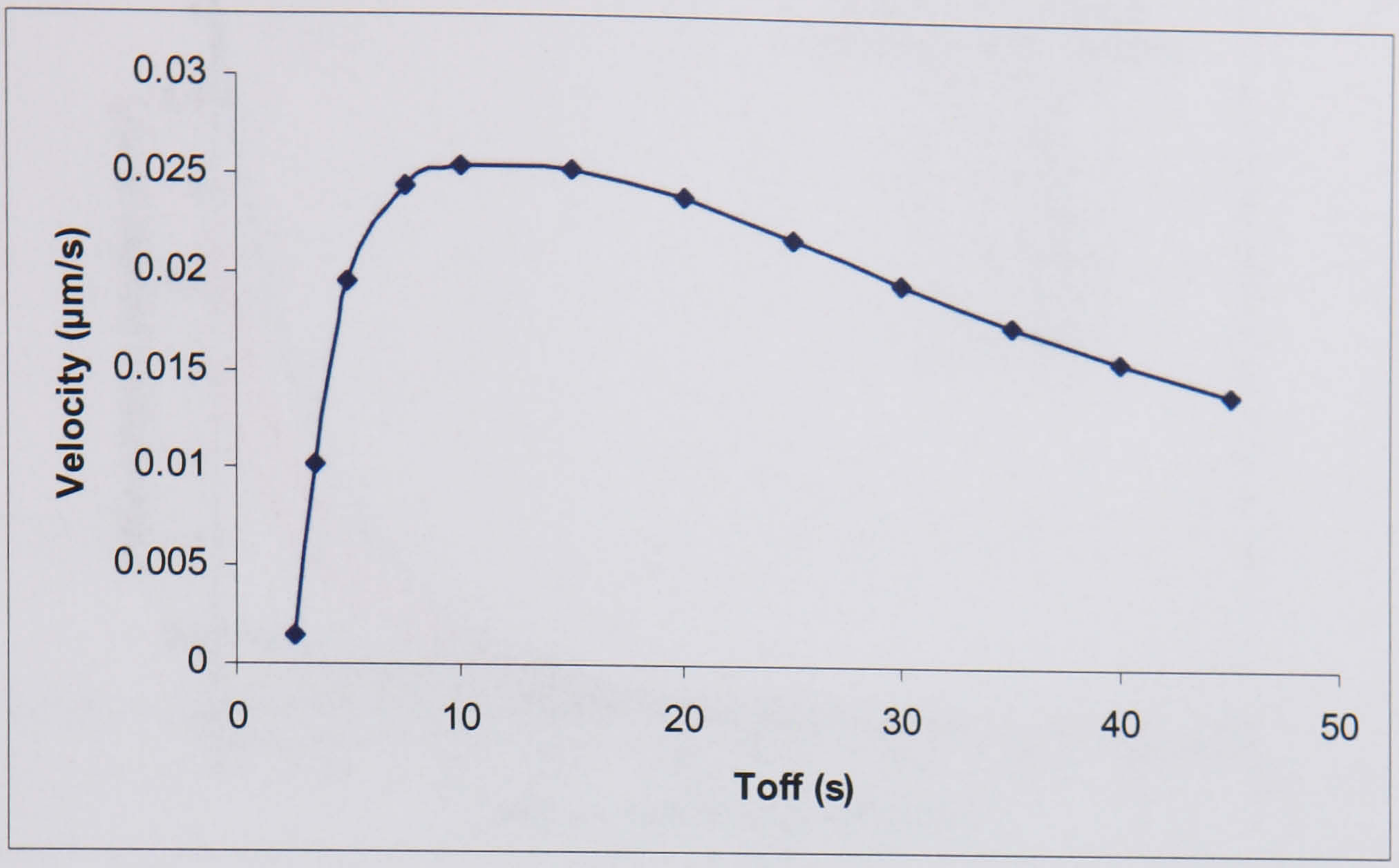

Figure 6-24
Velocity of mean particle distribution as a function of off-time

6.3.10 Field decay

DEP potential magnitude

As illustrated in the selected x-component elevations of the potential and force graphs, the fall-off with height is quite rapid. In Figure 6-25 the height dependence of the potential is illustrated as a continuous *y*-distribution taken at 2μm intervals across one electrode period. The initial field variation is displayed in the different starting values of each curve depending on which point on the device it originated. The curves are shown from a minimum height of 1μm to avoid the artificial distortion generated by the finite element numerical analysis technique. As can be observed, at 5μm elevation, the value has dropped by more than an order of magnitude.

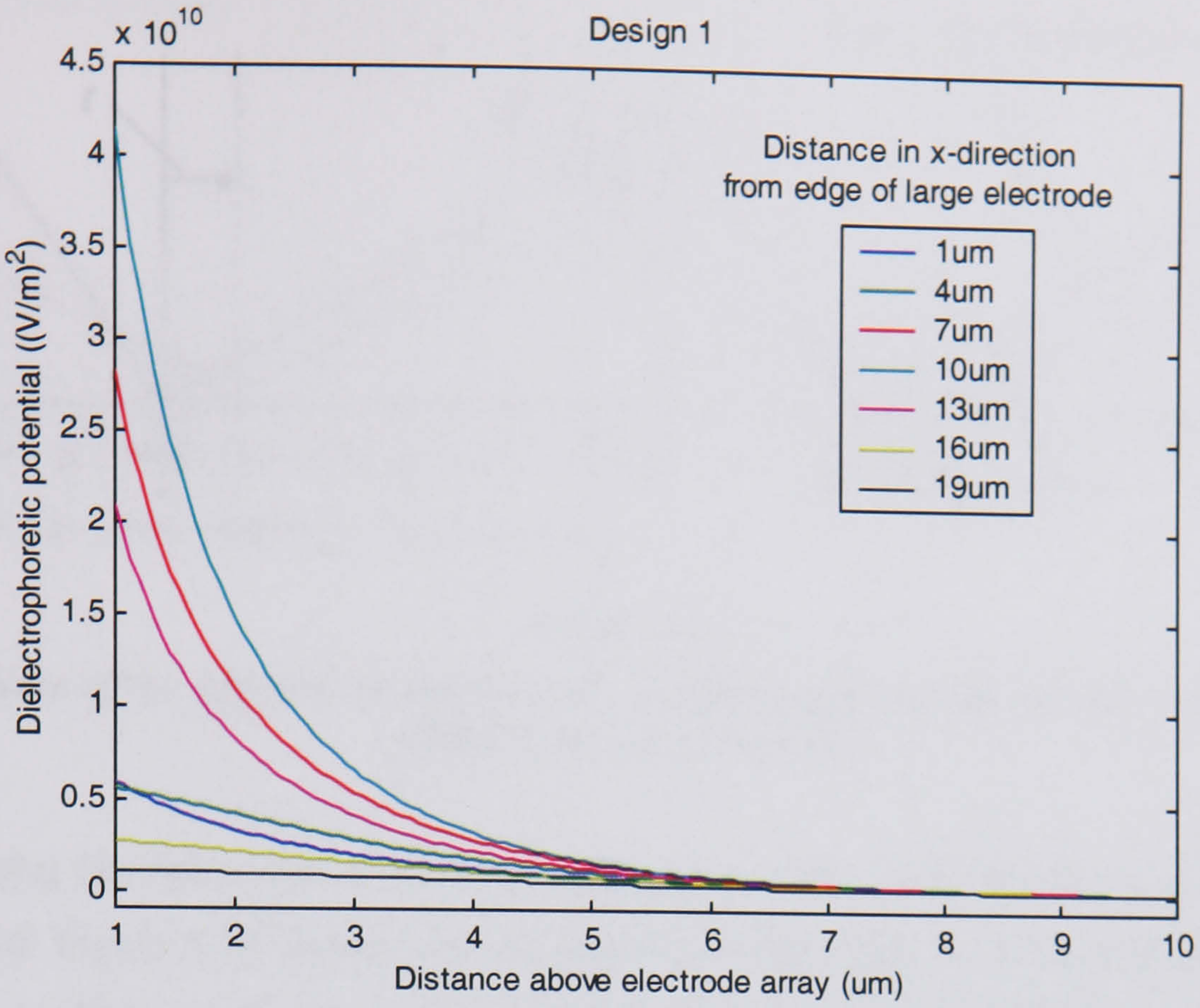

Figure 6-25

DEP potential fall-off with height above the electrodes for discrete points on the array (refer to Figure 6-26). The top curve corresponds to the highest field point on the inner edge of the small electrode.

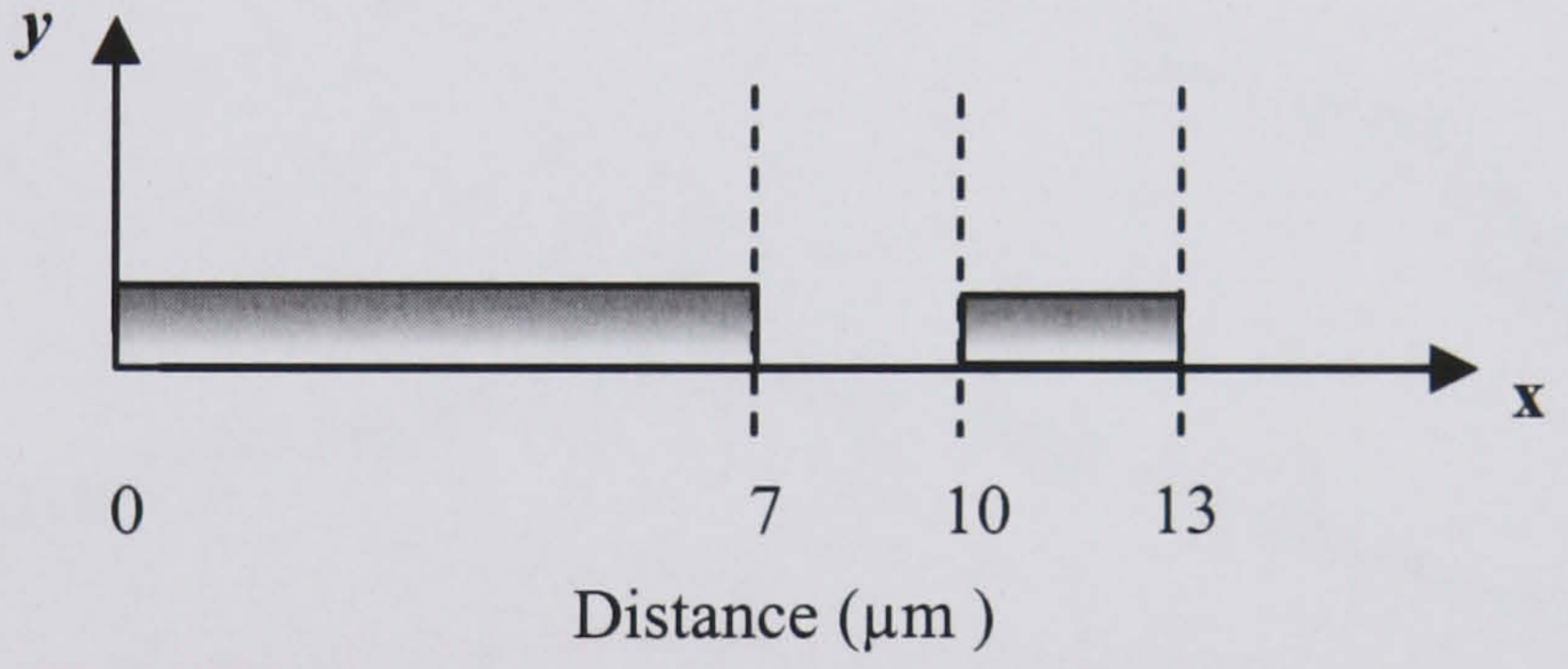

Figure 6-26

Definition of x-co-ordinate *for field calculations in Figure 6-25*

Symmetry

The change in shape of the potential profile is also significant. The degree of symmetry variation may be assessed by observing to what extent there is a change in the relative position of the global maxima and minima with height above the electrodes (Figure 6-27).

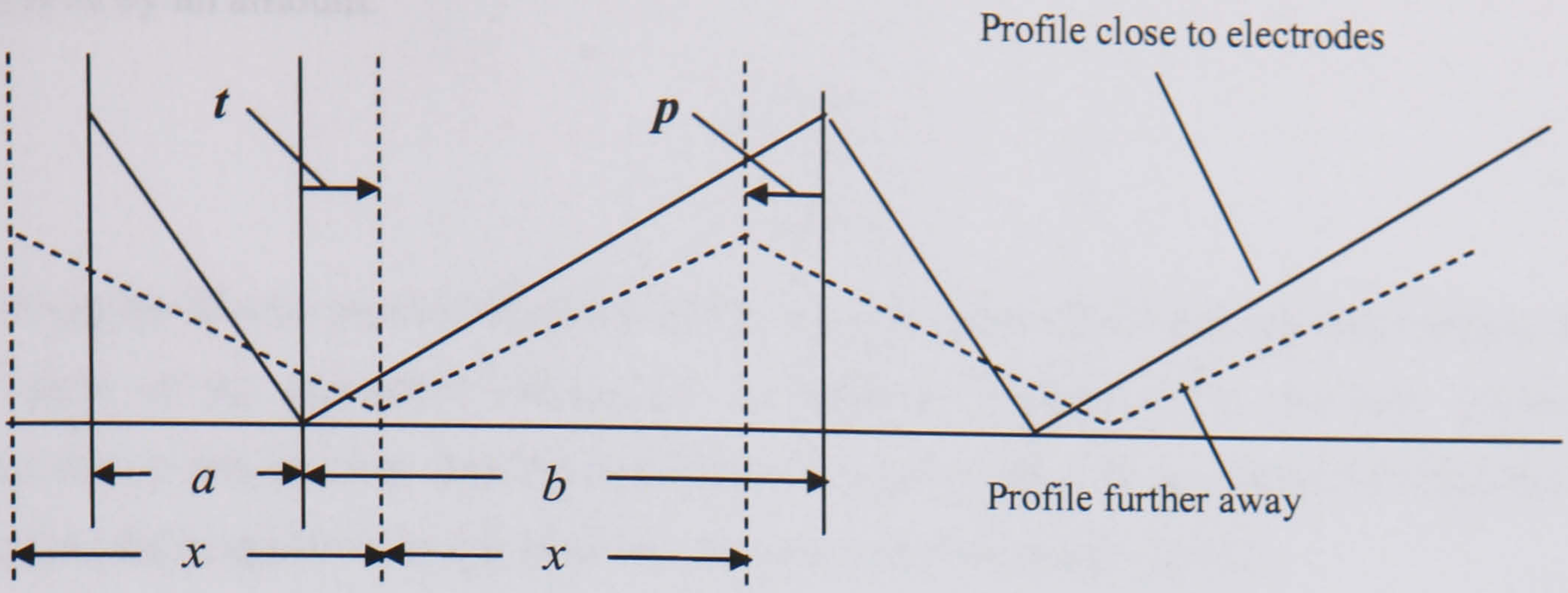

Figure 6-27

Illustration of the effective symmetry change resulting from shifts in the position of the global maxima and minima

Examining the behaviour of these turning points in the potential graphs such a shift can be observed. Figure 6-28 shows how the position of the peak, as defined by Matlab, varies from 1-10μm. The corresponding shift in the minimum is in the opposite direction.

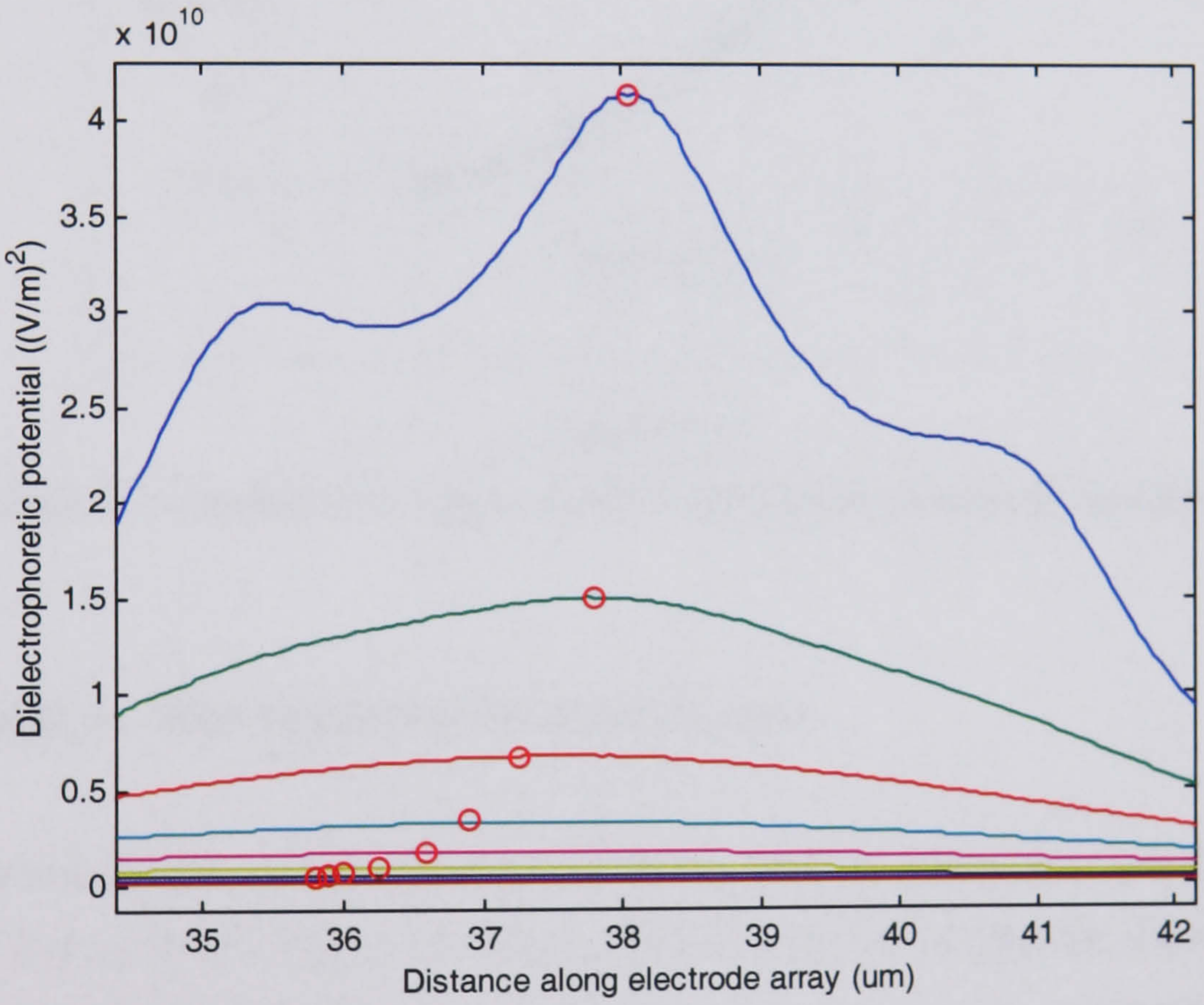

Figure 6-28

Position of the global maxima at 1-10μm elevations

If the positions of the peaks and troughs, as shown in Figure 6-27, undergo a transition of $-p$ and t respectively, on simple algebraic rearrangement it can be shown that the original asymmetry:

$$A = \frac{a}{b}$$

is altered by an amount:

$$\frac{1+A}{1-\dfrac{b}{p+t}}$$

Using the Matlab numerical output of the x co-ordinates of the maxima and minima, then, the scale of the symmetry change can be observed (Figure 6-29). At 5µm above the electrodes it can be seen that the asymmetry has practically disappeared and therefore the resultant field rapidly loses the defining character of a Brownian ratchet.

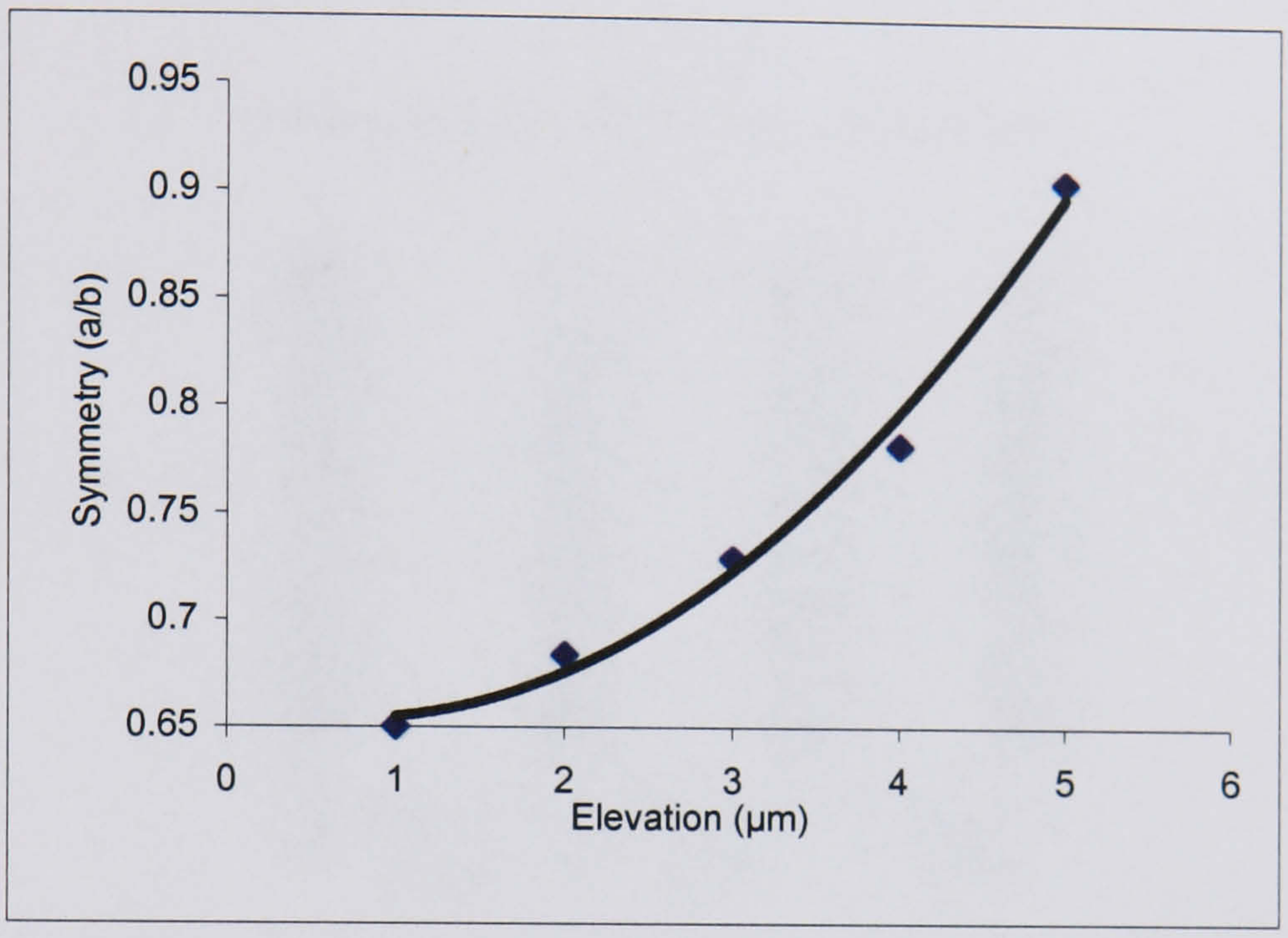

Figure 6-29

Total change in symmetry with height due to combined movement of maxima and minima

6.4 Design 2 – Interdigitated electrode clusters

The second design consisted of arrays of four separately addressable interdigitated finger electrodes (Figure 6-30). This used quite a different principle in that the electrode geometry itself was not periodically asymmetric. It is proposed here that the asymmetry of the DEP potential is generated by the juxtaposition of positive and negative DEP across the consecutive electrode pairs in each group of four. Thus the shape of the effective DEP potential is the result of the frequencies and voltages applied and so is a flexible property of the system. A modification of this design was to have clusters of three electrodes with a common earth in the centre so that the positive and negative DEP zones would be theoretically overlapped (Figure 6-31).

Figure 6-30
4 electrode interdigitated cluster design

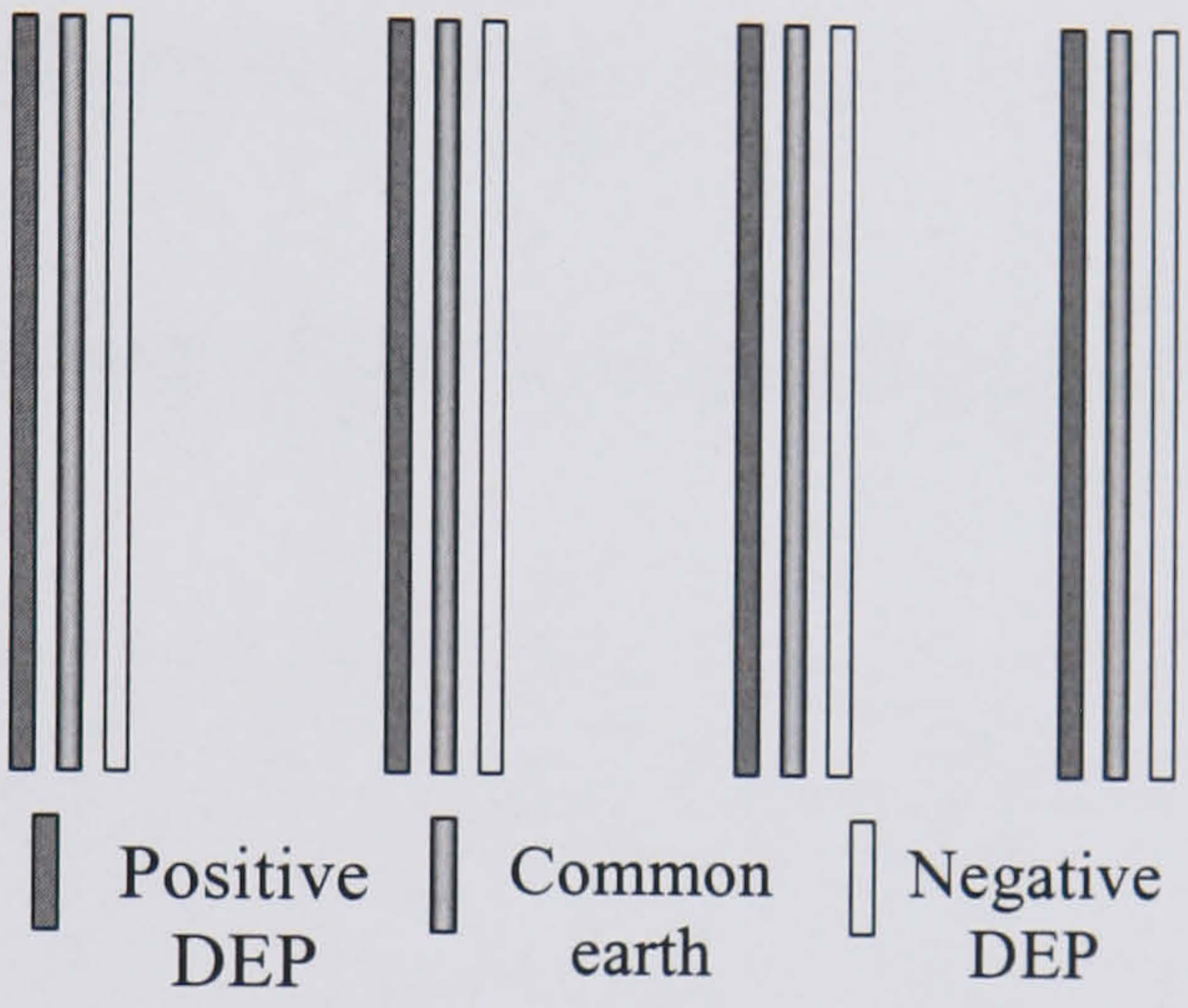

Figure 6-31
3 electrode interdigitated cluster design

6.4.1 Field Modelling

Because the sign of the DEP force depends on frequency it was necessary to model the high and low frequency regimes, corresponding to positive and negative DEP, separately. This could be done assuming the principle of linear superposition of electric fields. For the 4-electrode design, one approach was to model each pair separately using reflective boundary conditions (Figure 6-32).

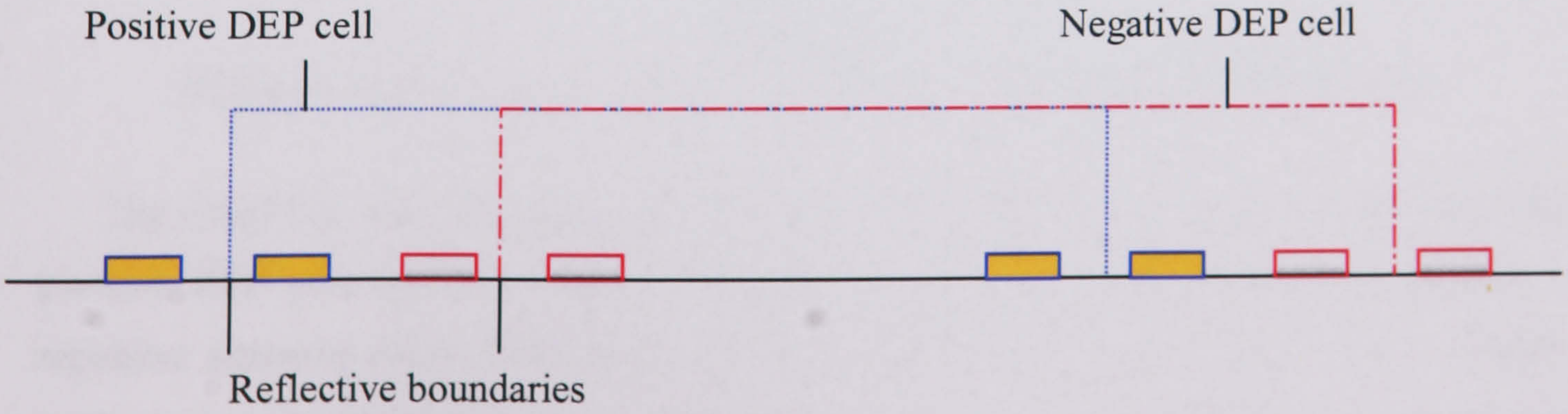

Figure 6-32
Cell boundaries for separate field modelling of positive and negative DEP pairs

A more accurate analysis, however, would be to include all the electrodes in the calculation as earths for the applied frequency (Figure 6-33), superimposing cells with an applied signal on the first and fourth electrode consecutively.

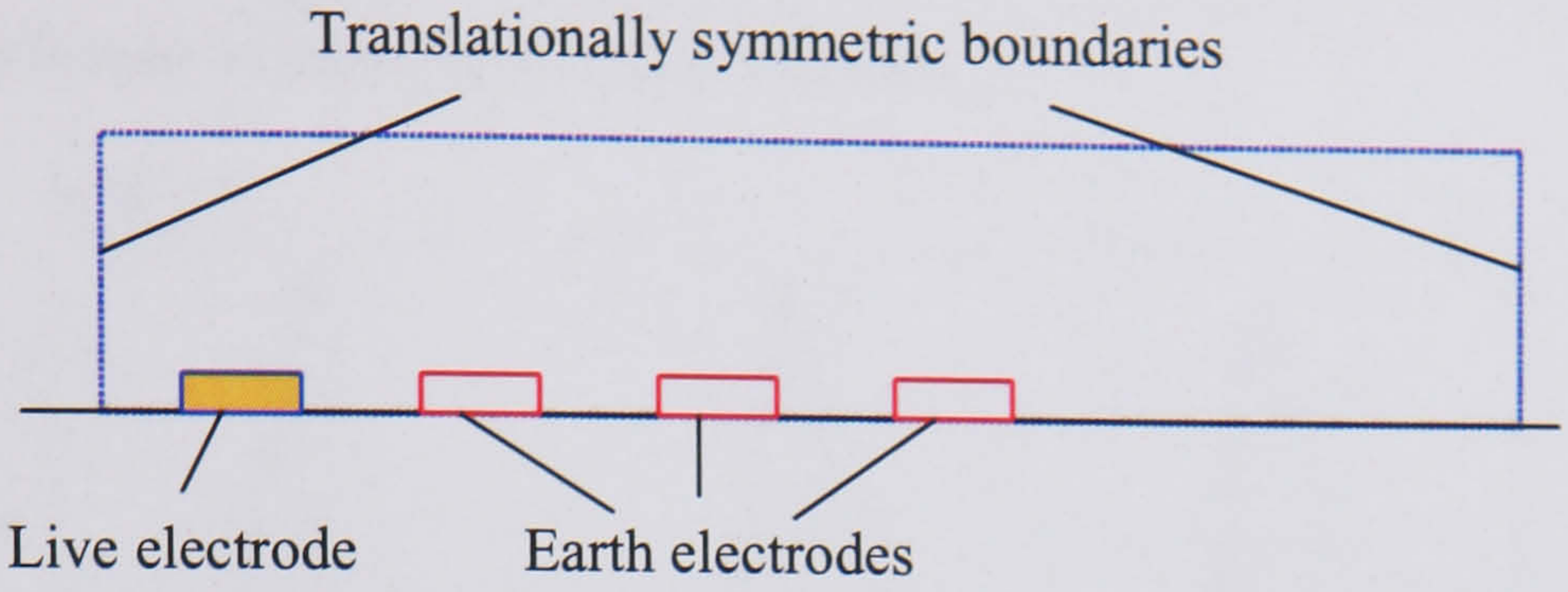

Figure 6-33
One of two superimposed cells used to calculate the DEP potential of the four electrode array

Figure 6-34 shows the Flex PDE output for the DEP potential at 1μm elevation using this cell definition.

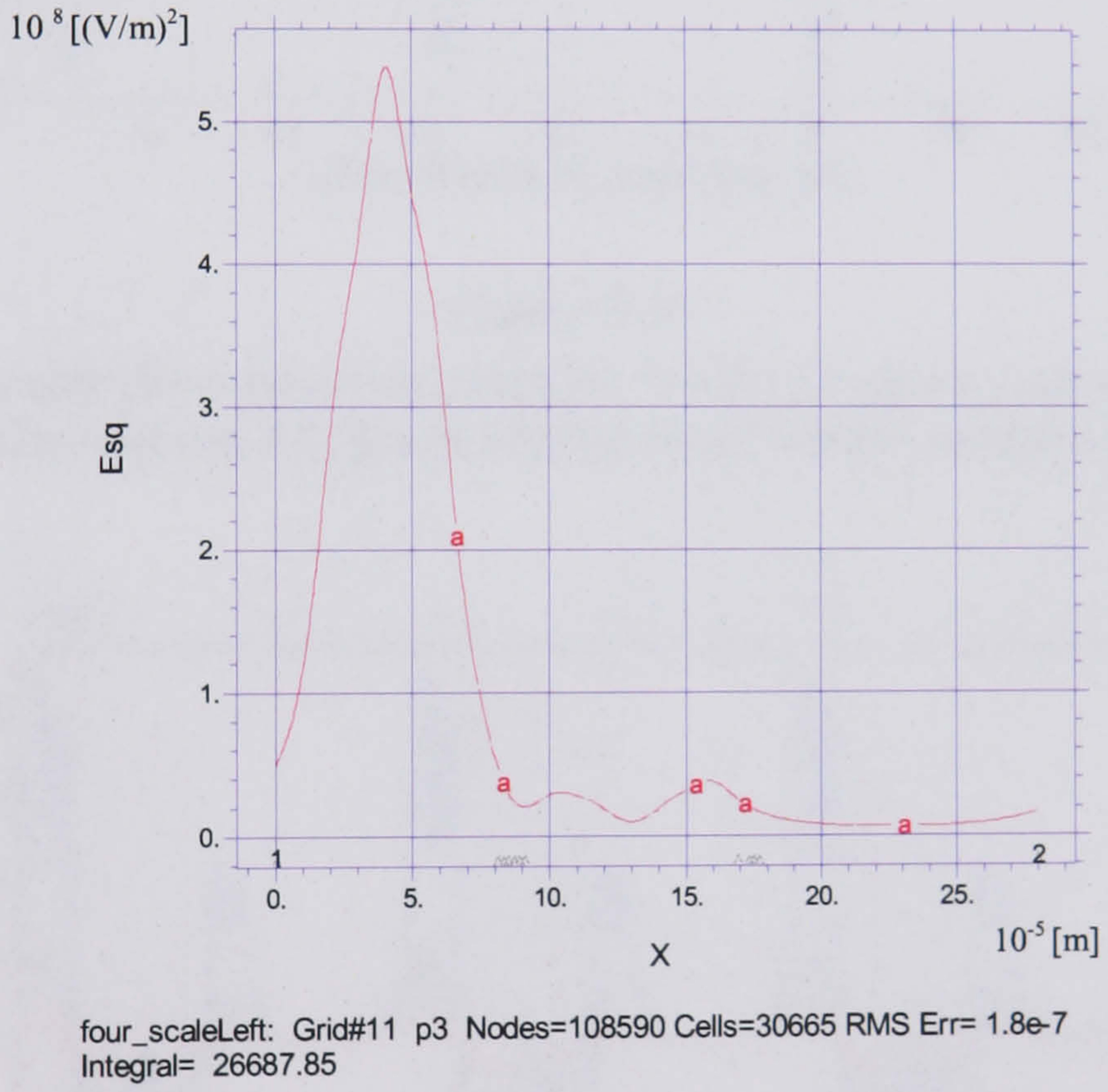

Figure 6-34
DEP potential at 1 μm elevation in the Flex PDE cell defined by Figure 6-33

The FlexPDE data was again transferred to Matlab in csv-file form. In this way the positive DEP potential (E^2) profile could be inverted and scaled in order to represent a repulsive potential force. This produced the profiles exemplified in Figure 6-35 - Figure 6-40, close to the electrodes and up to 10μm above. Figure 6-41 is a summary of the results for the 3-electrode design, which were modelled in the same way. These curves clearly exhibit an asymmetry very much closer to the classical Brownian ratchet potential. Although the short range nature of the DEP force is again sharply visible in the low potential gradient of the large gaps, closer inspection of the force reveals that a substantial unidirectional x-component is still present, which may be scaled on adjustment of the potential inputs. Experimental evidence is nonetheless required to ensure that this force is not subject to perturbations which may hinder asymmetric collection.

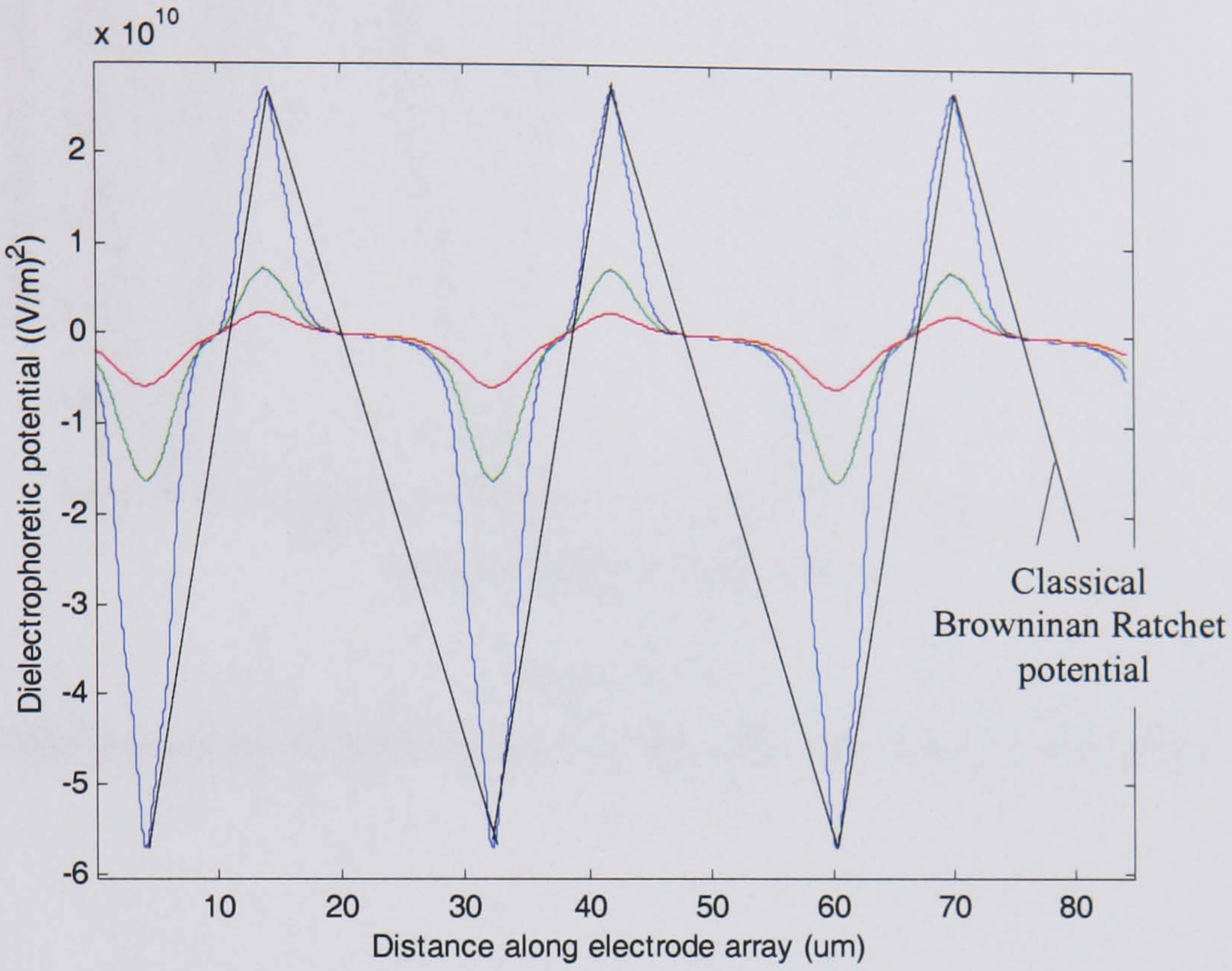

Figure 6-35

DEP potential profile for 4-electrode structure, 1-3μm elevation, with comparison to the classical asymmetric saw-tooth Brownian ratchet potential shape

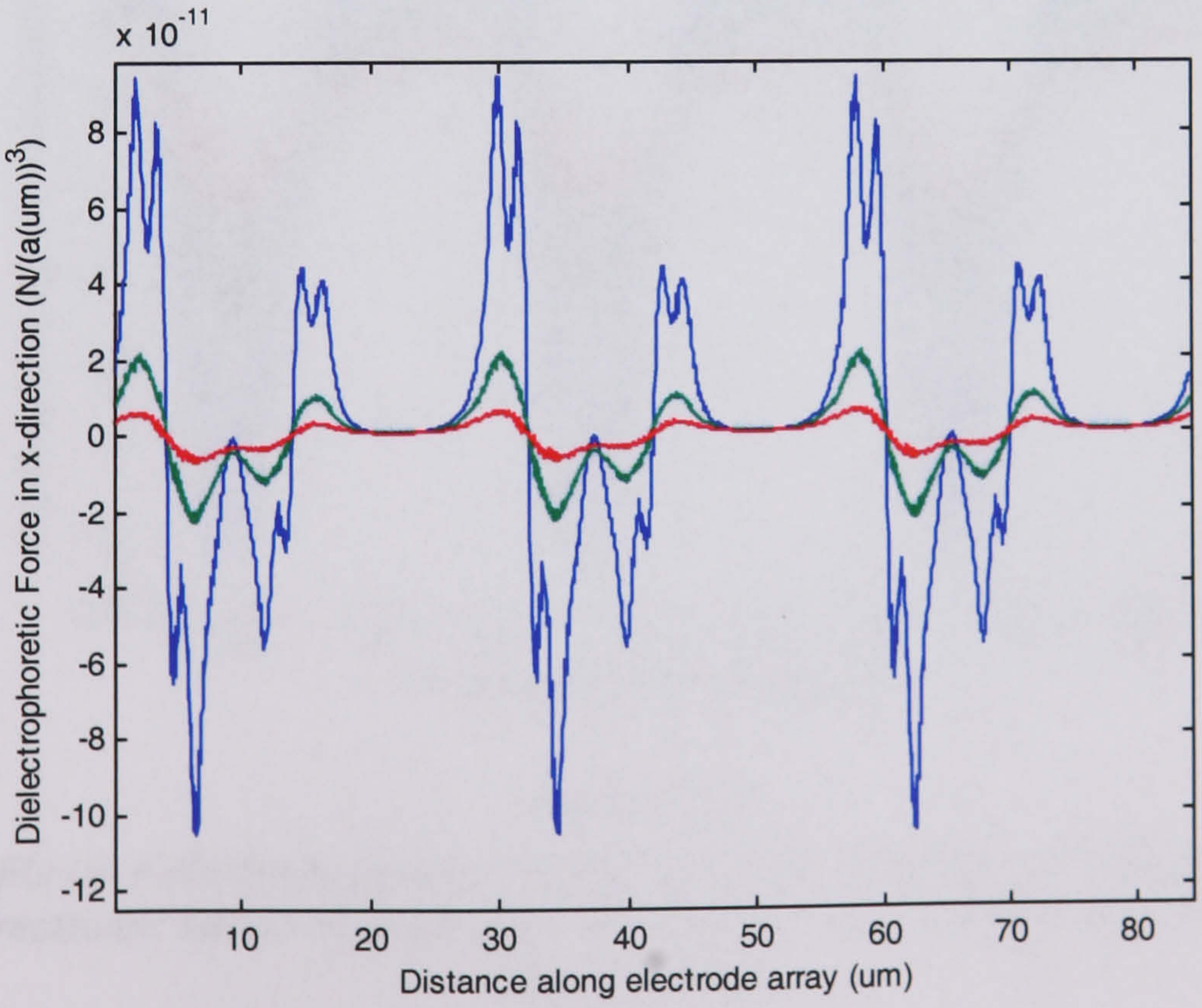

Figure 6-36

DEP force at 1-3μm on four electrode structure. Positive in the large gaps although small in the essentially constant mid sections.

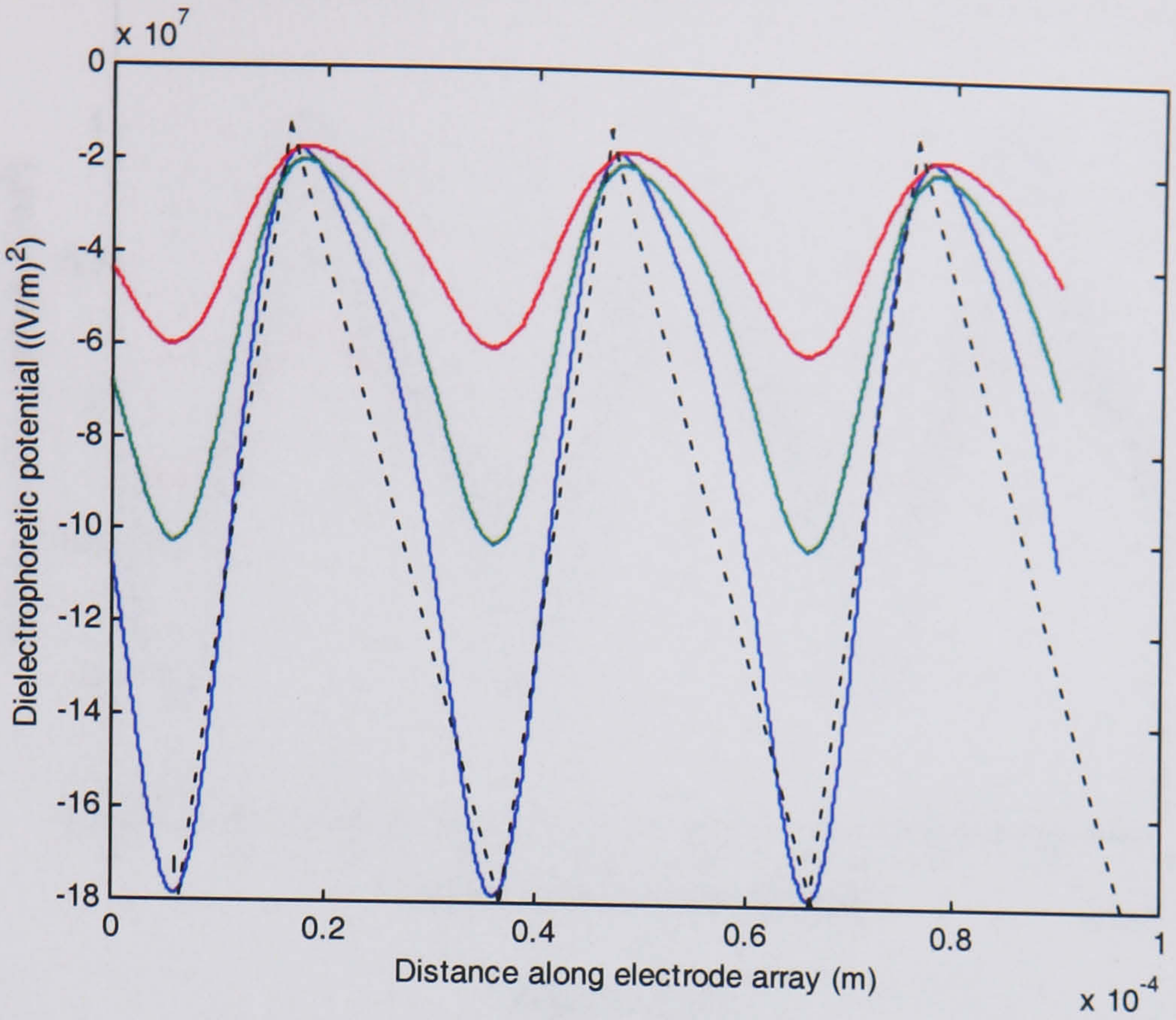

Figure 6-37
DEP potential, 8-10μm elevation, showing retention of asymmetry

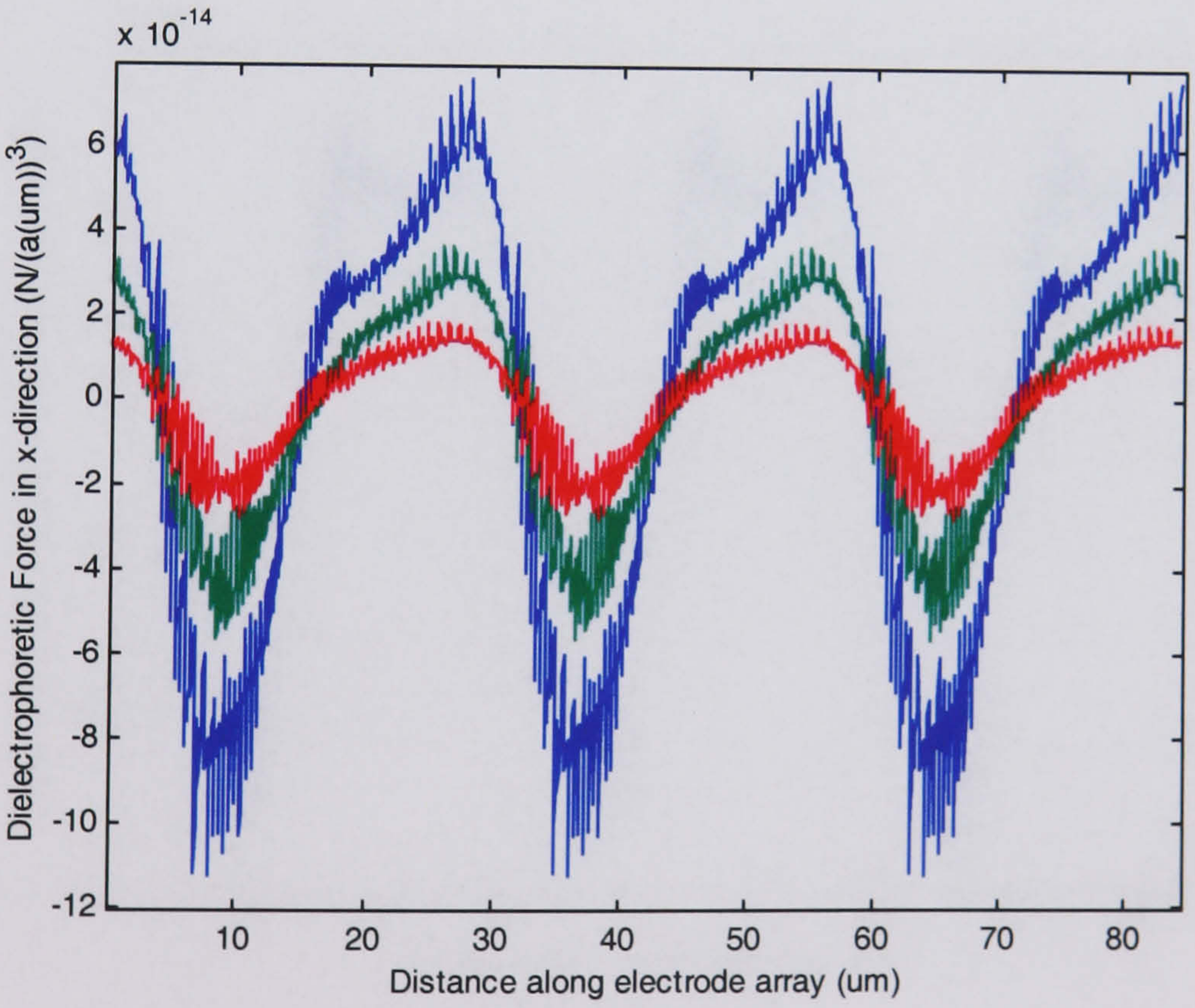

Figure 6-38
Force profile on 4 electrode device 8-10μm above the electrodes. Clearer illustration of unidirectional nature in large gaps. Distortion is due to the finite element grid approximation.

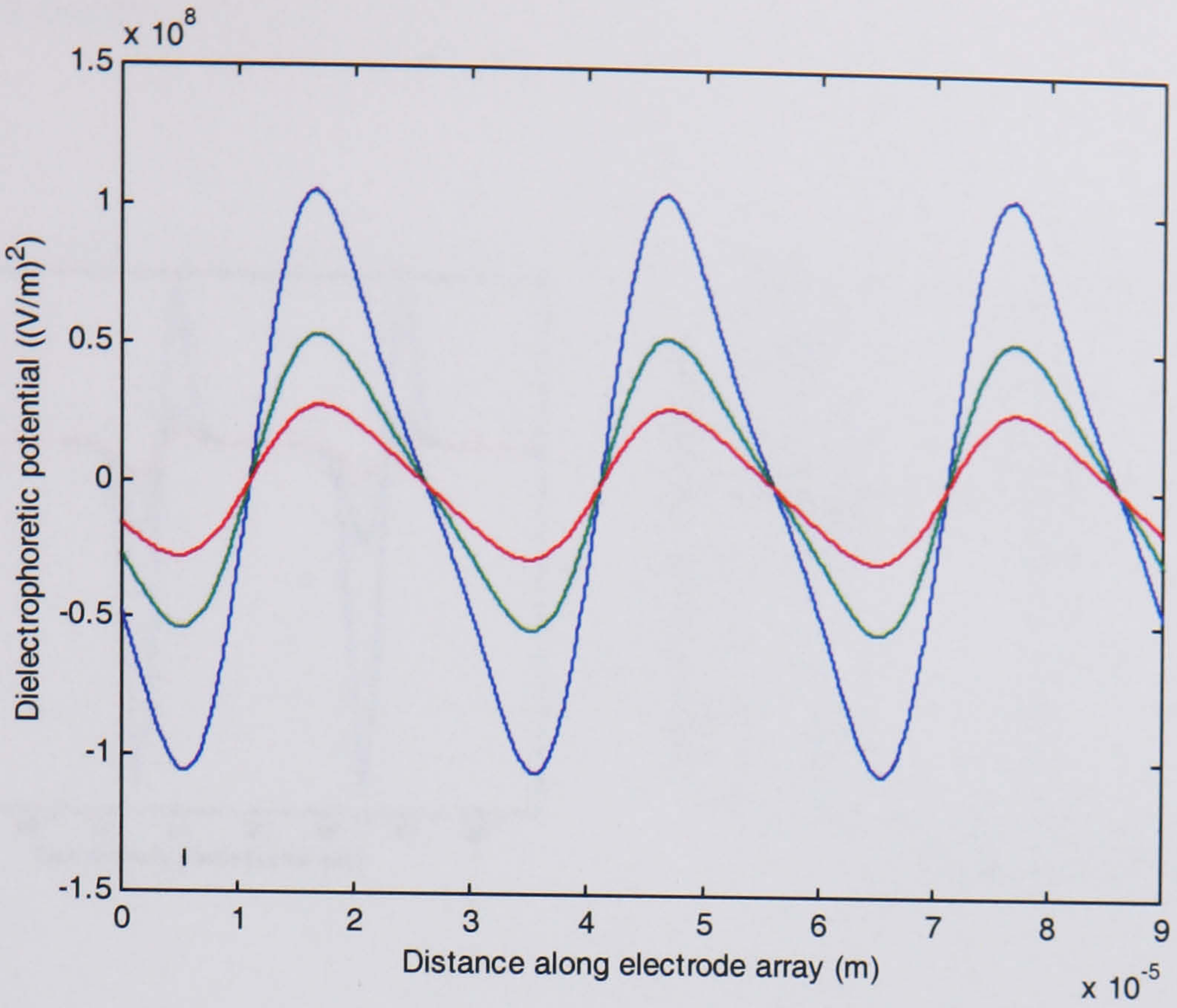

Figure 6-39

DEP potential, 8-10μm, doubling negative DEP potential (increasing V by a factor of $\sqrt{2}$ *). Shape is very similar to the classical Brownian ratchet potential.*

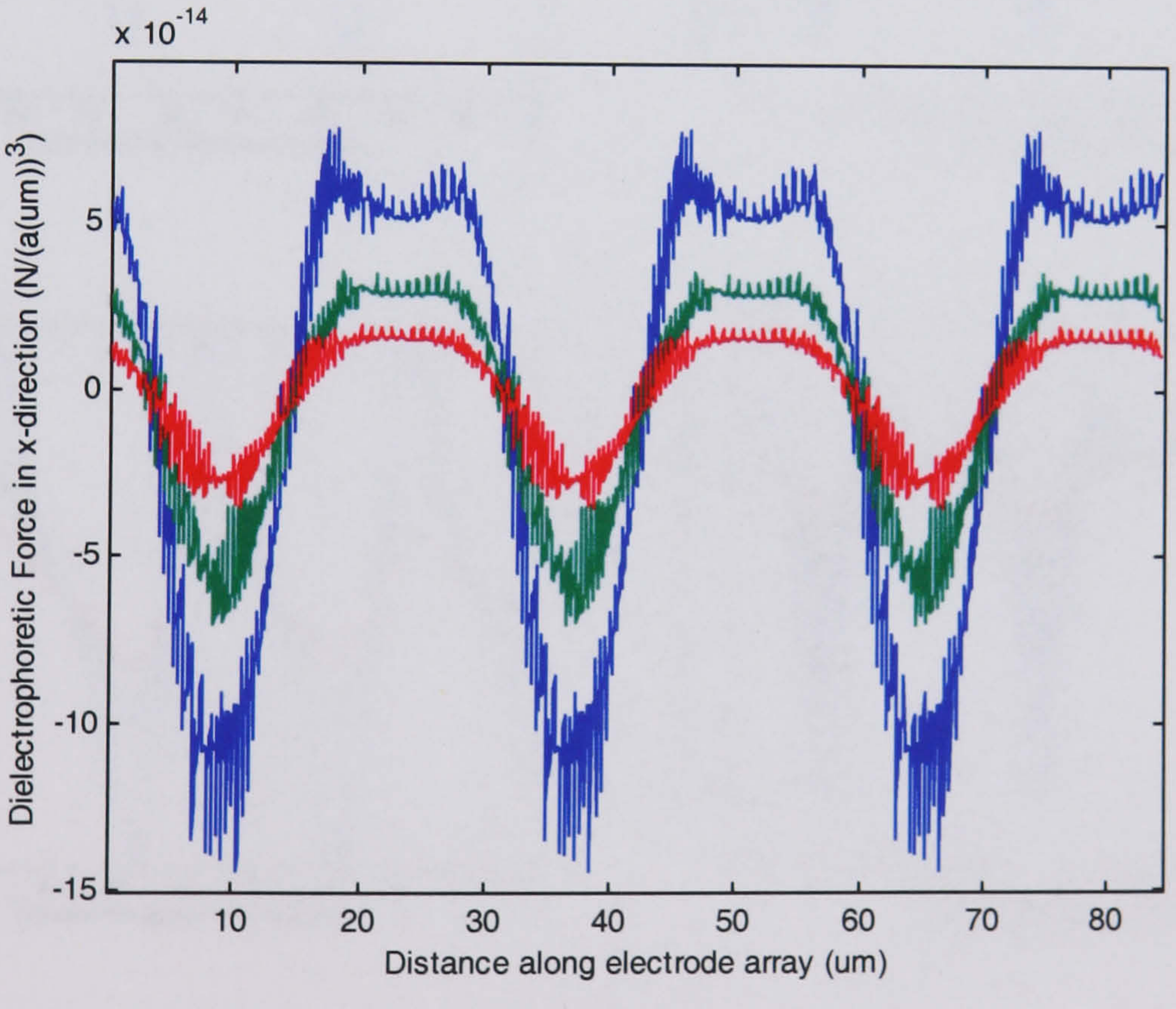

Figure 6-40

DEP force, 8-10μm with doubled negative DEP potential, displaying greater uniformity in the large gaps

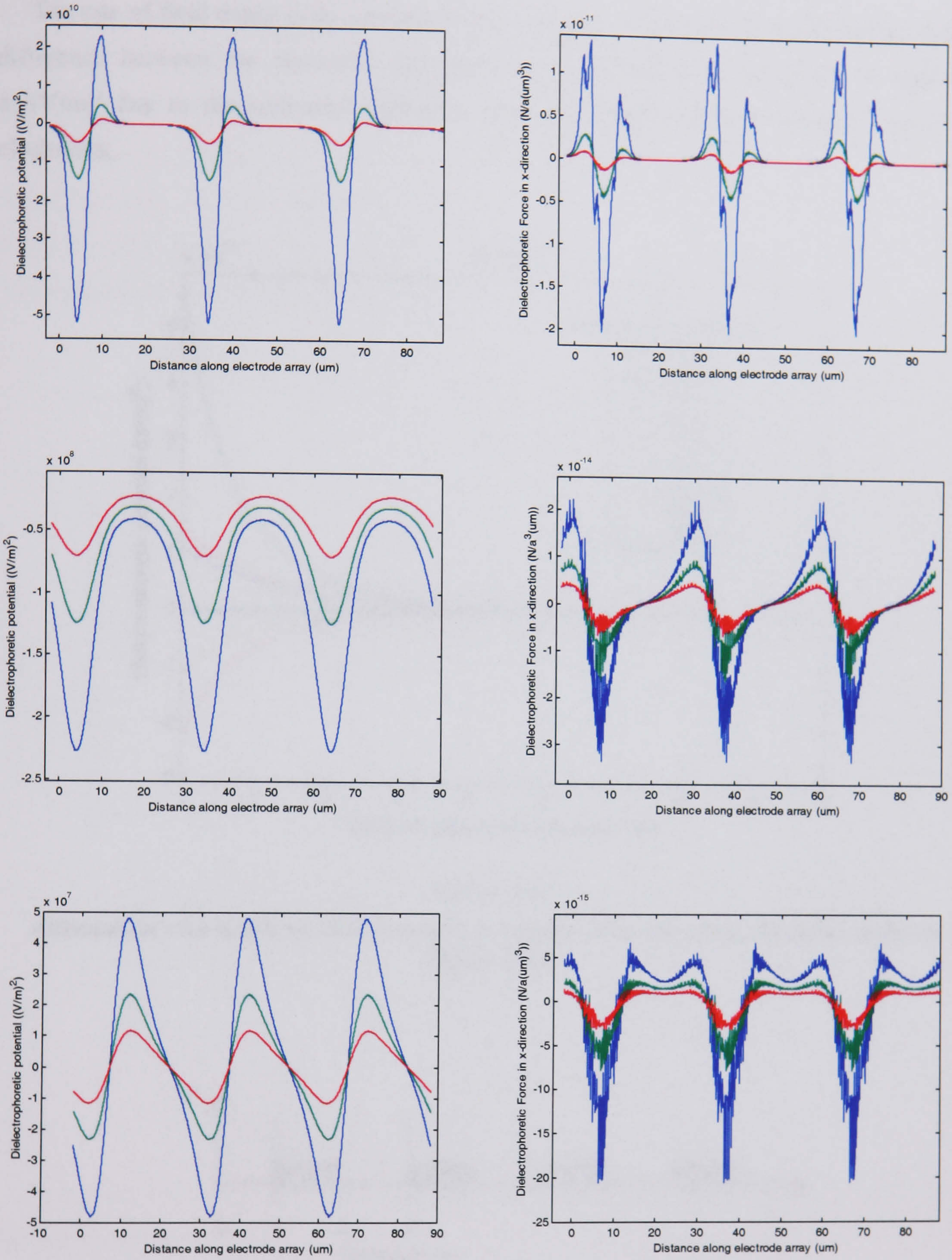

Figure 6-41

3-electrode design DEP potential and x-component force profiles with the same parameters as illustrated for 4 electrodes. These manifest slightly more asymmetry although the force in the gaps is correspondingly reduced.

6.4.2 Field decay

Magnitude

The rate of field decay is on a similar scale to design 1 although the initial DEP potential difference between the maximum and minimum field values is factor of ~2 larger at $8.2(V/m)^2$ due to the additional repulsive force and slightly smaller feature size of the electrodes.

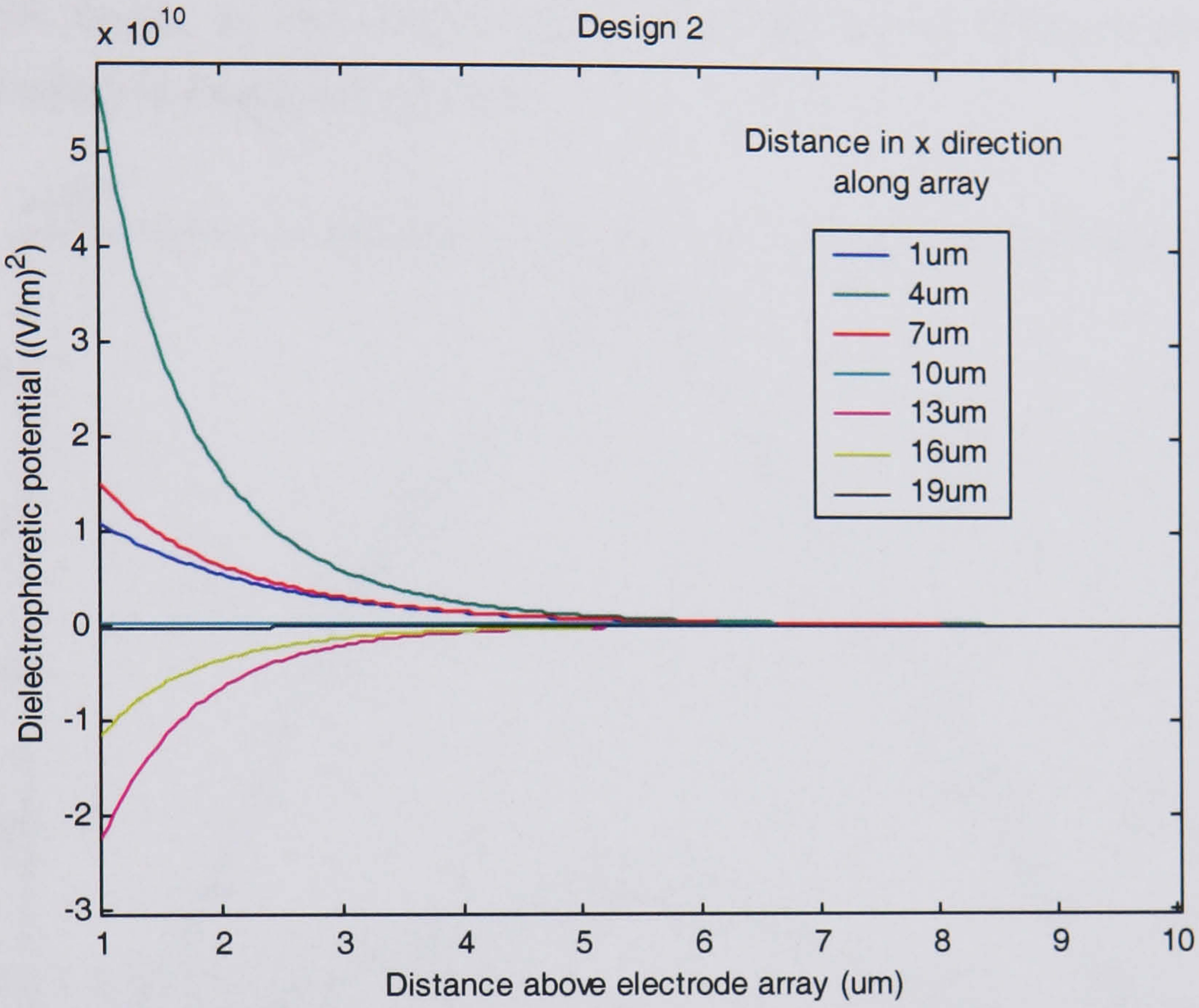

Figure 6-42
Attenuation with height of DEP potential at regular intervals along the array (refer to Figure 6-43)

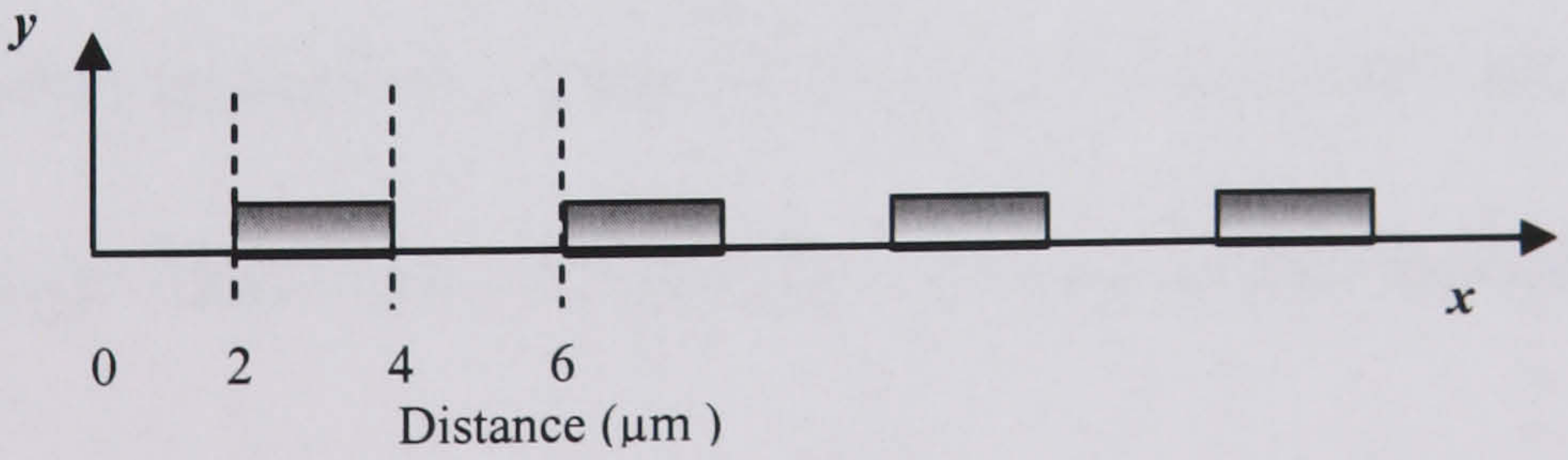

Figure 6-43
Definition of x-co-ordinate for field calculations in Figure 6-42

Symmetry

Although the field is dissipated, the symmetry does not appear to undergo any significant dispersion. Figure 6-44 shows the peak over an equivalent electrode segment length, with the maxima distributed vertically with respect to elevation. This is due to the fact that the asymmetry is not due to an offset produced by a smaller potential well which becomes negligible with height but to a superimposed repulsive force. Both the positive and negative DEP fields are periodically *symmetrical*[19], with the asymmetry of the total DEP potential being due only to the manner of their juxtaposition, therefore they cannot change this property with height as this would result in an *asymmetry* being produced in them individually which is clearly non-physical.

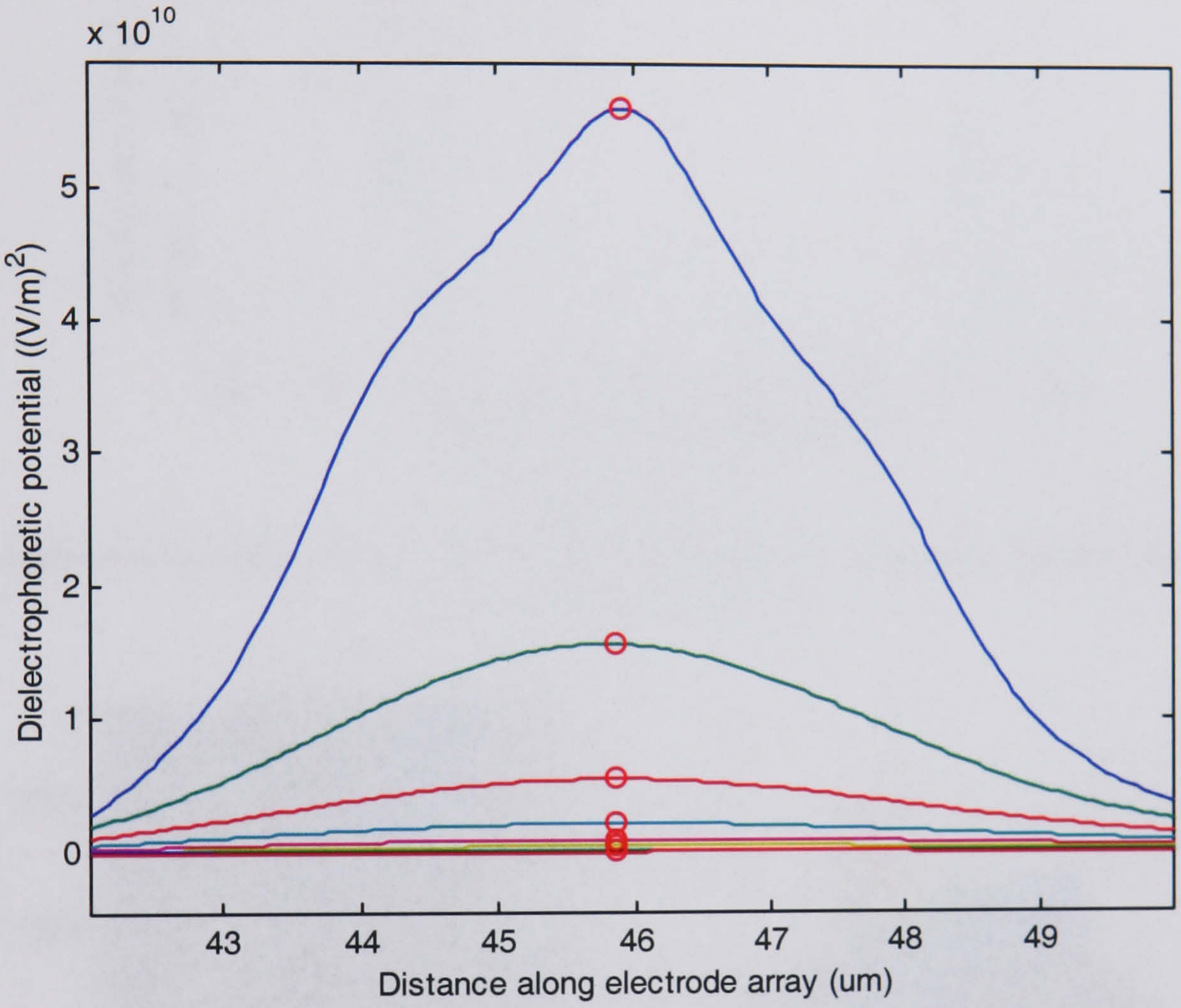

Figure 6-44

Global maxima from 1-10μm showing no shift in the x-direction

Thus, this design retains more consistently the characteristic potential profile of a Brownian ratchet.

6.4.3 Transport Simulation

Particle transport was simulated using Matlab assuming collection would occur from all points in the large gap. Although this is not obvious from the modelled data it is a reasonable assumption to make given that the applied voltages may be adjusted and therefore the

---

[19] apart from the minor perturbations introduced by the earthing effects of the other electrodes

potential shape modified until collection occurs. The *a*:*b* ratios were again obtained from the FlexPDE simulations and this time only diffusion across one boundary considered – a valid assumption given that for forward transport t_{off} should be within a range such that the Gaussian tail migrating as far as the second potential peak is negligible.

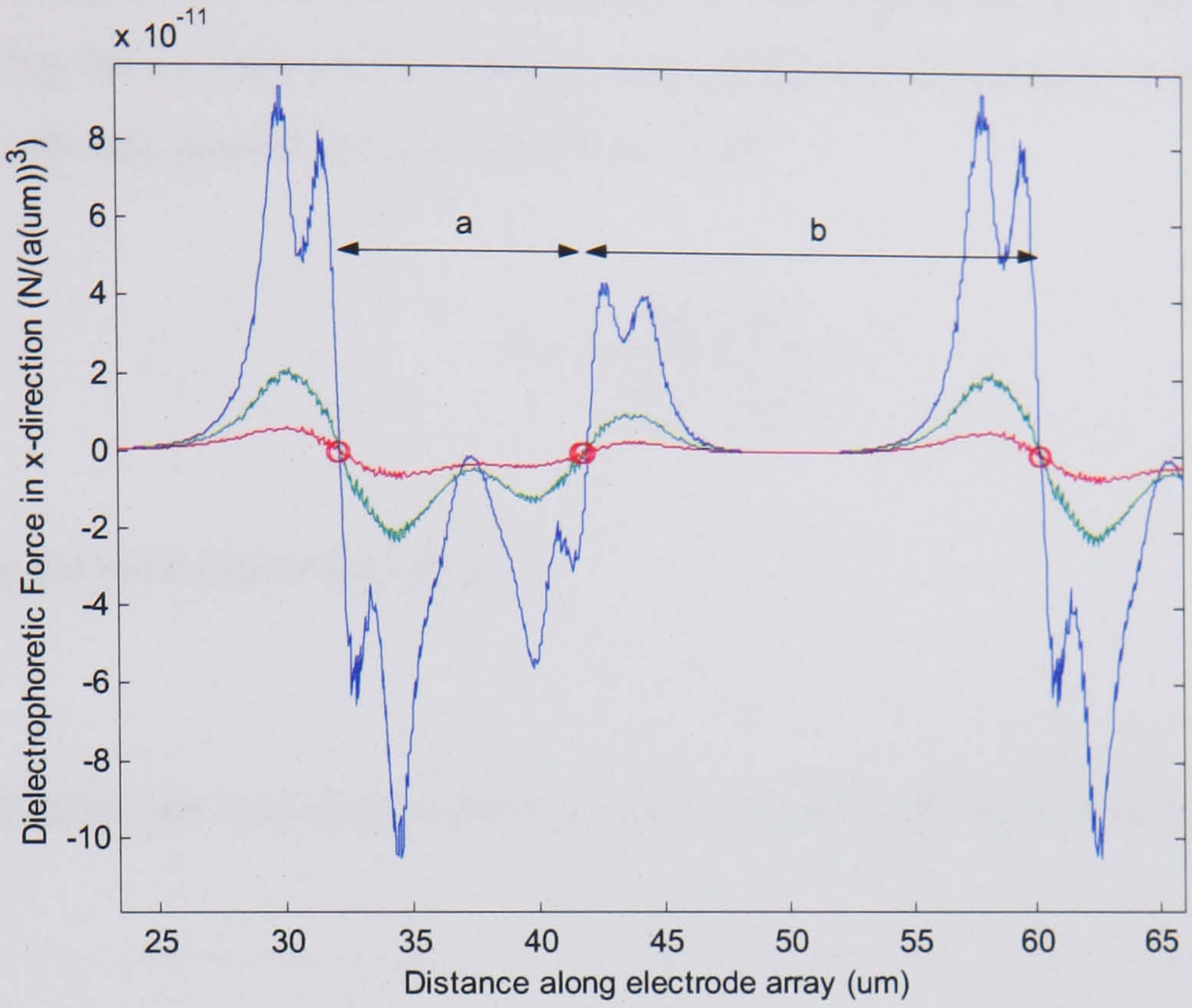

Figure 6-45

Assessment of asymmetry for 4 electrode interdigitated cluster design, resulting in an a:b ratio of 9.8µm :18.2µm

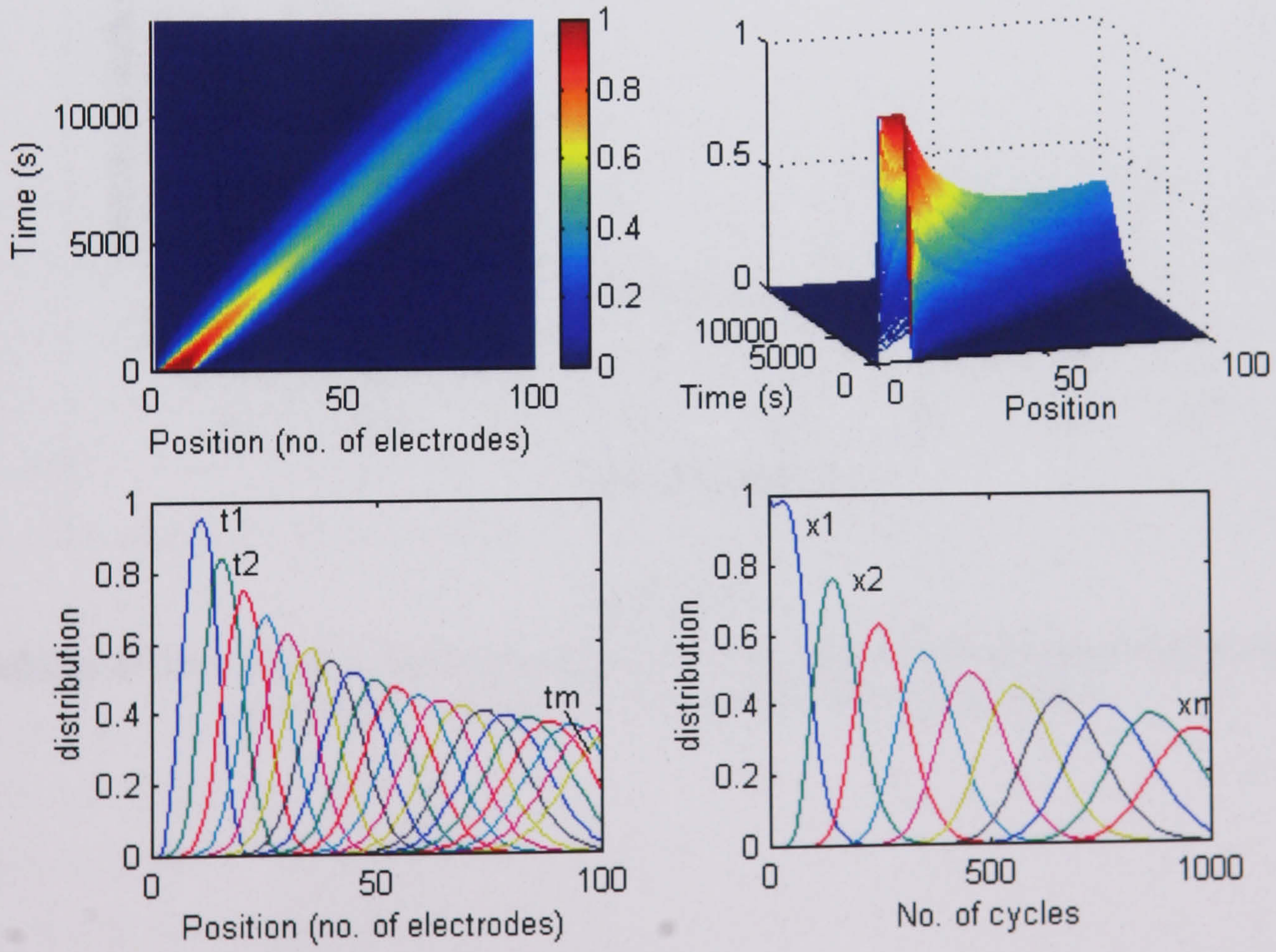

Figure 6-46

216nm beads undergoing transport in the 4-electrode cluster design with optimal t_{off}*=13.81s*

The nature of the resulting particle transport is illustrated in Figure 6-46. The smoothness of the distribution represents the fact that only one type of potential minimum is present. Following the peak of the distribution it can be seen that the motion also possesses a high degree of linearity. Thus a unique velocity may be assigned as before, measured according to net distance transported over total time, which varies with bead size according to Figure 6-47. Excluding the t_{on} factor which will be ascertained experimentally, this agrees with the macroscopic velocity quoted in Gorre-Talini et al [1]:

$$V_m = \frac{(a+b)}{(t_{on} + t_{off})} J$$

where J is the forward probability flux.

The optimum off-times required to produce these velocities are shown in Figure 6-48.

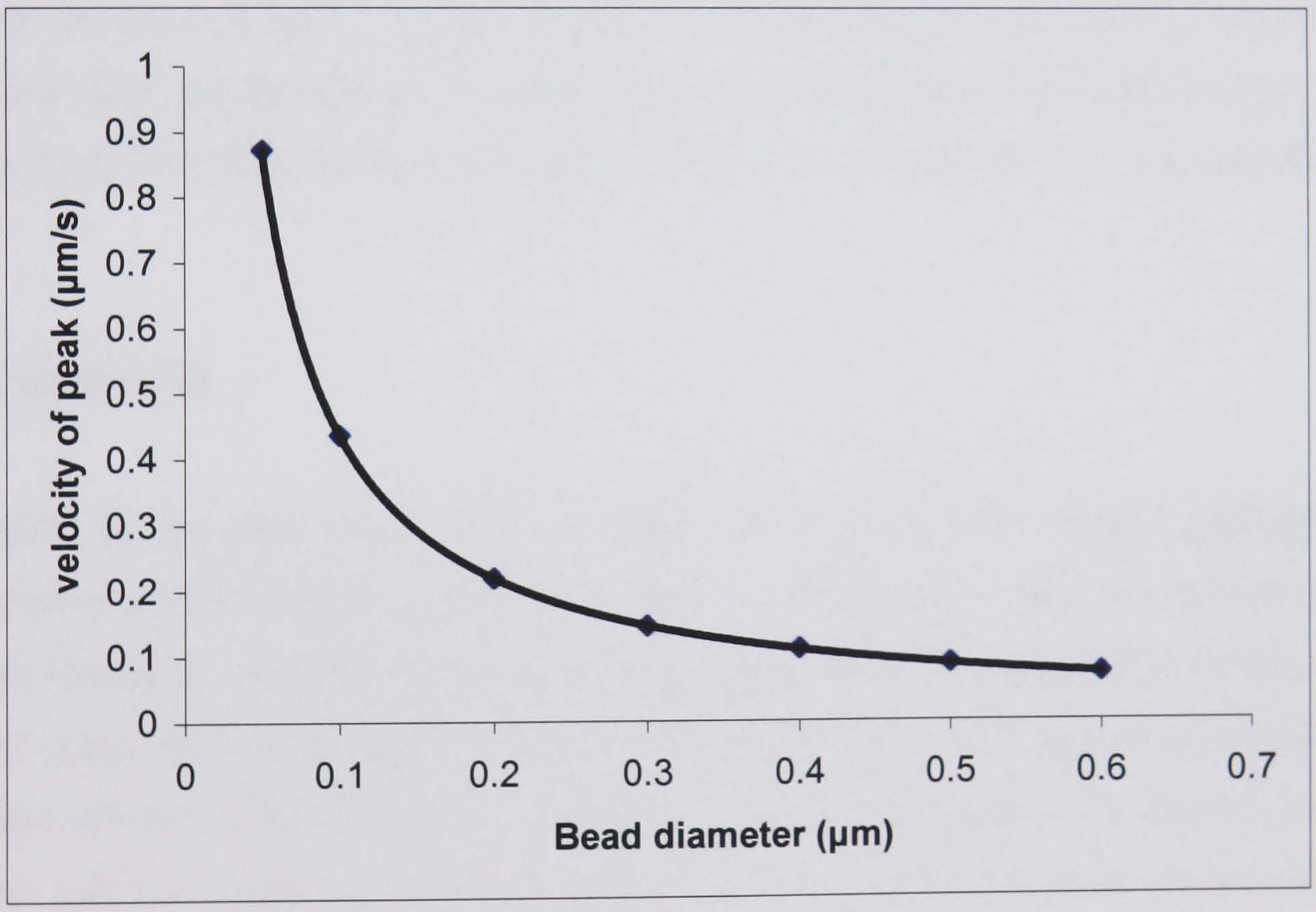

Figure 6-47

Velocity of distribution as a function of bead size, measured from simulation data. Fitting equation is $v=0.04x^{-0.9975}$*, confirming inverse proportion*

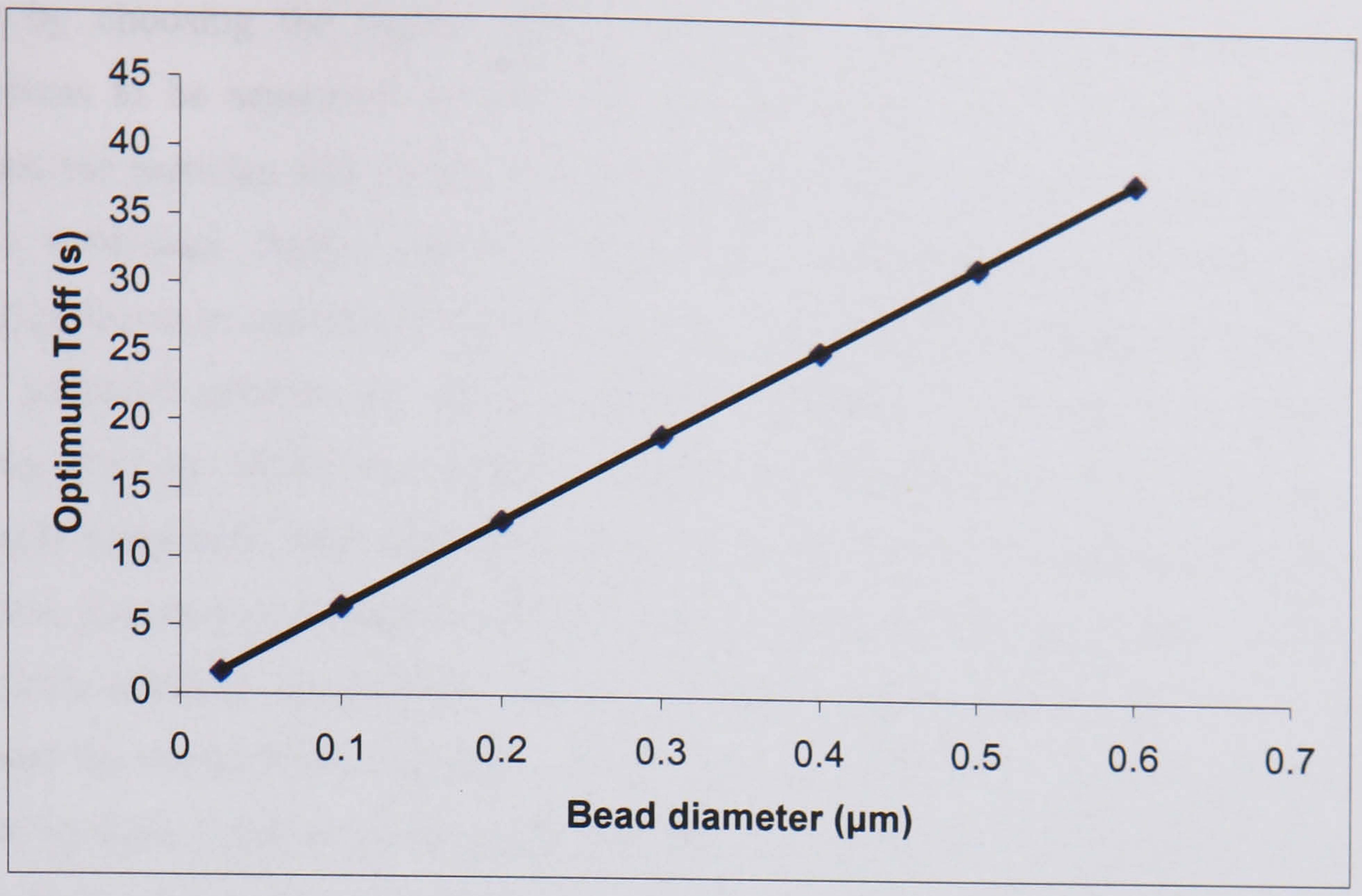

Figure 6-48

t_{off} *required for optimum transport varies linearly with bead size*

Comparing the velocity of 216nm beads, 0.2μm/s, with that resulting from the first electrode design, 0.025μm/s, it can be seen that it is increased by an order of magnitude. In general particles are transported in a much more efficient manner due to the fact that there is no competing back flow since the potential profile is in essence that of a classical Brownian ratchet.

6.5 Conclusion

In terms of the form of the DEP potential and the predicted transport properties, the interdigitated cluster design is largely superior to the asymmetric pairs. This is evident in the essential similarity of the cluster design DEP potential to the standard Brownian ratchet potential shape, known to produce unidirectional transport when applied periodically to a dissipative ensemble. The symmetry dissipation being also negligible, this shape is preserved to higher elevation than in the first design, implying a degree of biased motion some way above the electrodes even though complete collection may not occur.

With the separate addressability of the electrodes the second design also possesses a higher degree of tunability. The shape of the potential may be adjusted to facilitate biased collection by independent alteration of the applied voltages and the pumping direction by interchange of frequencies. This is distinct from existing DEP Brownian ratchets such as the factory roof design [2] and blazed optical grating [1] which have a fixed potential shape. In these designs the pumping direction is altered by changing the sign of the DEP force. Separation can theoretically occur by choosing an intermediate frequency between the crossovers of two particle populations. Likewise, fractionation can occur in the cluster design by choosing the higher applied frequency midway between those of the two populations to be separated. In this way, the device may act as a Brownian ratchet as indicated for particles with lower crossover and a periodic trap without any biased motion for the remaining, higher crossover population. This avoids the potential problem of competing fluxes in opposite directions and also allows a more accurate prediction of motion as the potential minima are always very well defined, in contrast with negative DEP pumping ratchets where the levitation height and therefore the DEP force are not so accurately assessable. The high field exposure resulting from the necessary positive DEP collection, however, may pose problems for certain types of biological entity – although this is probably minimal since DNA, viruses and other colloidal entities have been shown to withstand the strong fields required. Living cells and other fragile organisms which may be affected by these fields are in any case generally not suitable for fractionation in a Brownian ratchet device due to their large size and correspondingly low diffusion constants.

The interdigitated cluster design, then, was chosen for fabrication as despite the higher level of complication necessary for its construction, e.g. multilayer fabrication techniques, it has theoretically interesting and unique features as well as a high probability level that it will function most effectively as a Brownian ratchet. In addition, the full potential of the device cannot be adequately explored theoretically since asymmetric collection rates and unbiased diffusion must be experimentally verified.

6.6 References

[1] L. Gorre-Talini, J. P. Spatz, and P. Silberzan, "Dielectrophoretic ratchets", *Chaos*, vol. 8, pp. 650-656, 1998.

[2] J. Rousselet, L. Salome, A. Ajdari, and J. Prost, "Directional Motion of Brownian Particles Induced By a Periodic Asymmetric Potential", *Nature*, vol. 370, pp. 446-448, 1994.

7 Brownian ratchet Fabrication

The basic fabrication procedure is an adaptation of a method previously utilised on a larger scale in the construction of a travelling wave device [1]. In order to obtain arrays of four separately addressable electrodes, multilayer fabrication techniques were employed. This involved dividing the structure into several parts which are overlaid using semiconductor manufacture methods such as photo and e-beam lithography, chemical deposition and etching. The microfluidics was tackled using moulding techniques derivable from the same technology to produce a silicon elastomer removable channel.

7.1 WAM design

The layout of the device was drawn up using the computer aided design facility of a microwaveguide simulation package produced by Barnard Microsystems called WaveMaker. This allowed the multiple layers to be saved in GDSII point based format before transferral to the beamwriter compatible CATS pattern files. This type of language describes the file in terms of 2-dimensional areas or blocks, the size of which, determined by the specified resolution of the overall shape, governs the spot size of the electron beam. For areas where low resolution is required such as bus bars or bonding pads this can be large and thereby writing time reduced whereas areas with fine detail necessitate correspondingly smaller spot sizes and must be written as a separate layer. The other parameter which should be specified in the beam writer control file is the dose. This controls the electron beam current and is usually determined by a series of multiple dose exposure tests.

This system was employed in the writing of masks used for photolithography and in direct write e-beam lithography. The electrode design was written initially on mask plates for photolithography fabrication. The basic schematic is outlined in Figure 7-1.

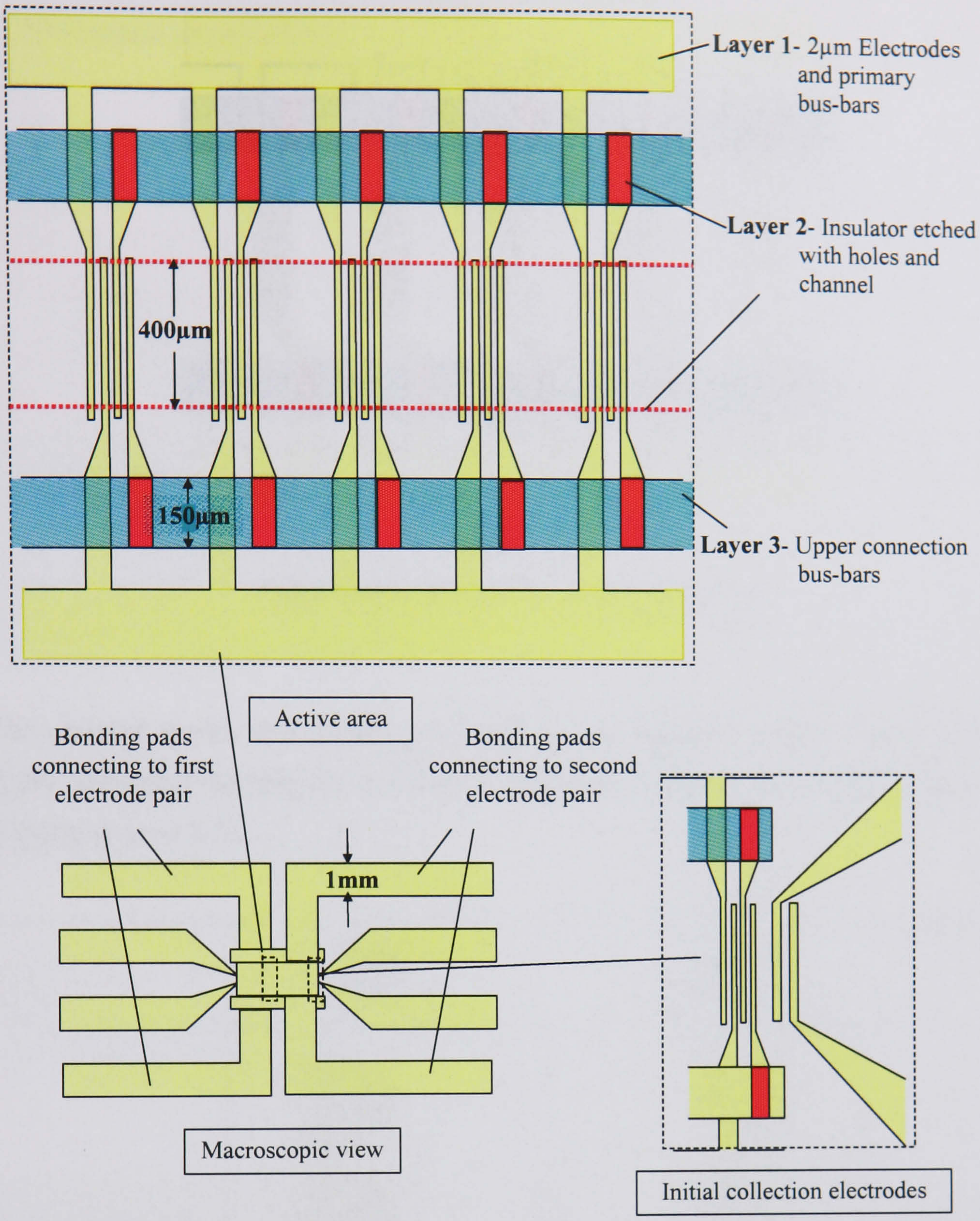

Figure 7-1
Schematic of electrode design

The design consisted of interdigitated electrodes in groups of four (Figure 7-1). In order to obtain the required addressability, each electrode was joined to one of four bus-bars arranged in parallel pairs. Separation between the two sets of bus-bars was achieved by means of an insulating layer, with holes allowing connections to relevant electrodes. The three electrode design was drawn up to be compatible with the same bus-bar and holes masks so that only one extra layer would have to be re-written (Figure 7-2).

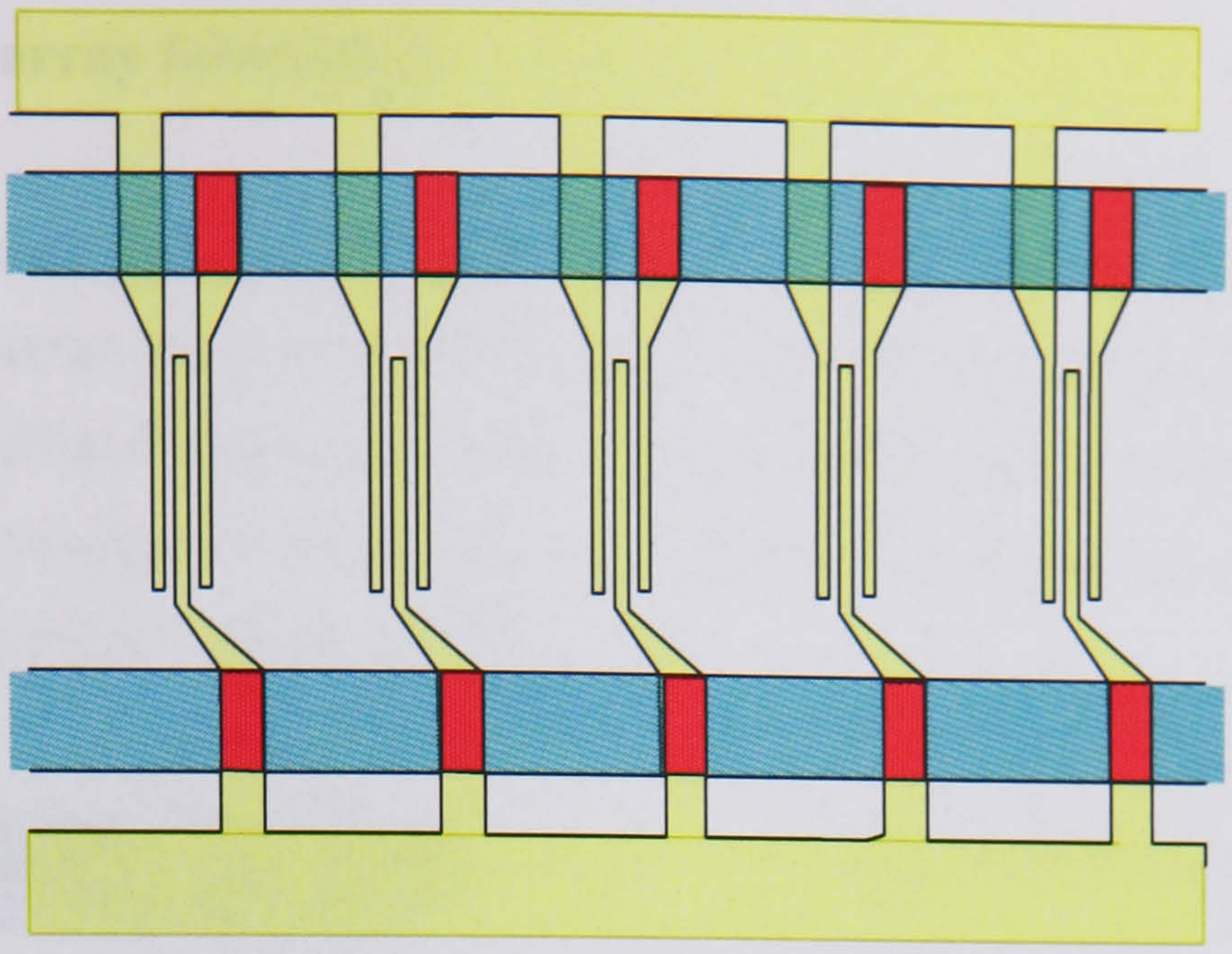

Figure 7-2
3 electrode modification with central earth

The channel design was written as a positive and negative mask in order to explore different fabrication techniques. All layers, including channels, were written on a single mask plate (Figure 7-3).

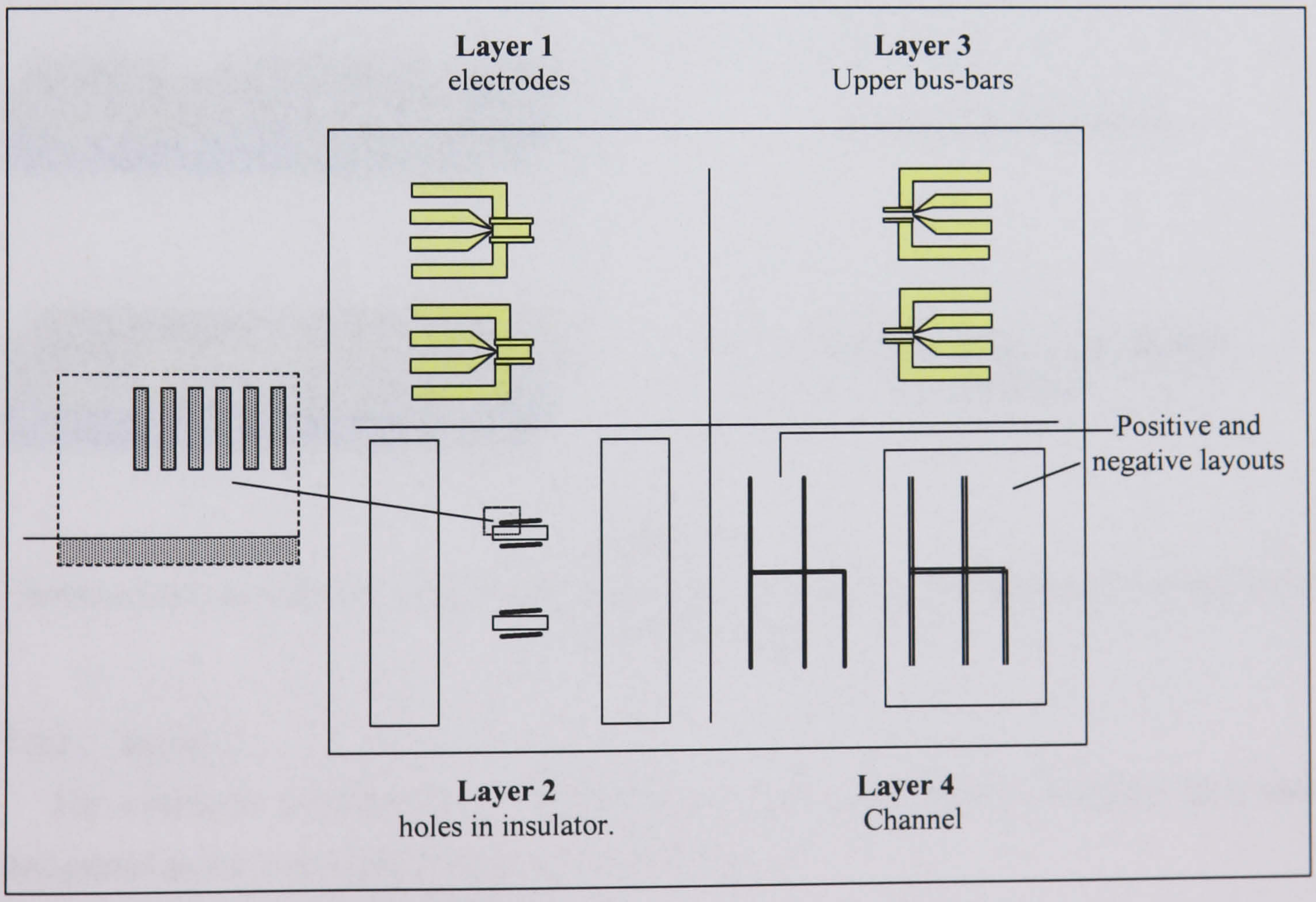

Figure 7-3
Overview of mask plate

7.2 Electrode array fabrication

The first electrode pair in each group was laid down with connections to the primary, outer bus bars whereas the second pair were left with floating connection pads. When the insulating layer had been deposited, holes were etched above these connection pads in order that they could be bonded to the top bus-bars which were overlaid as layer-3. An outline of the fabrication procedure is shown in Figure 7-4.

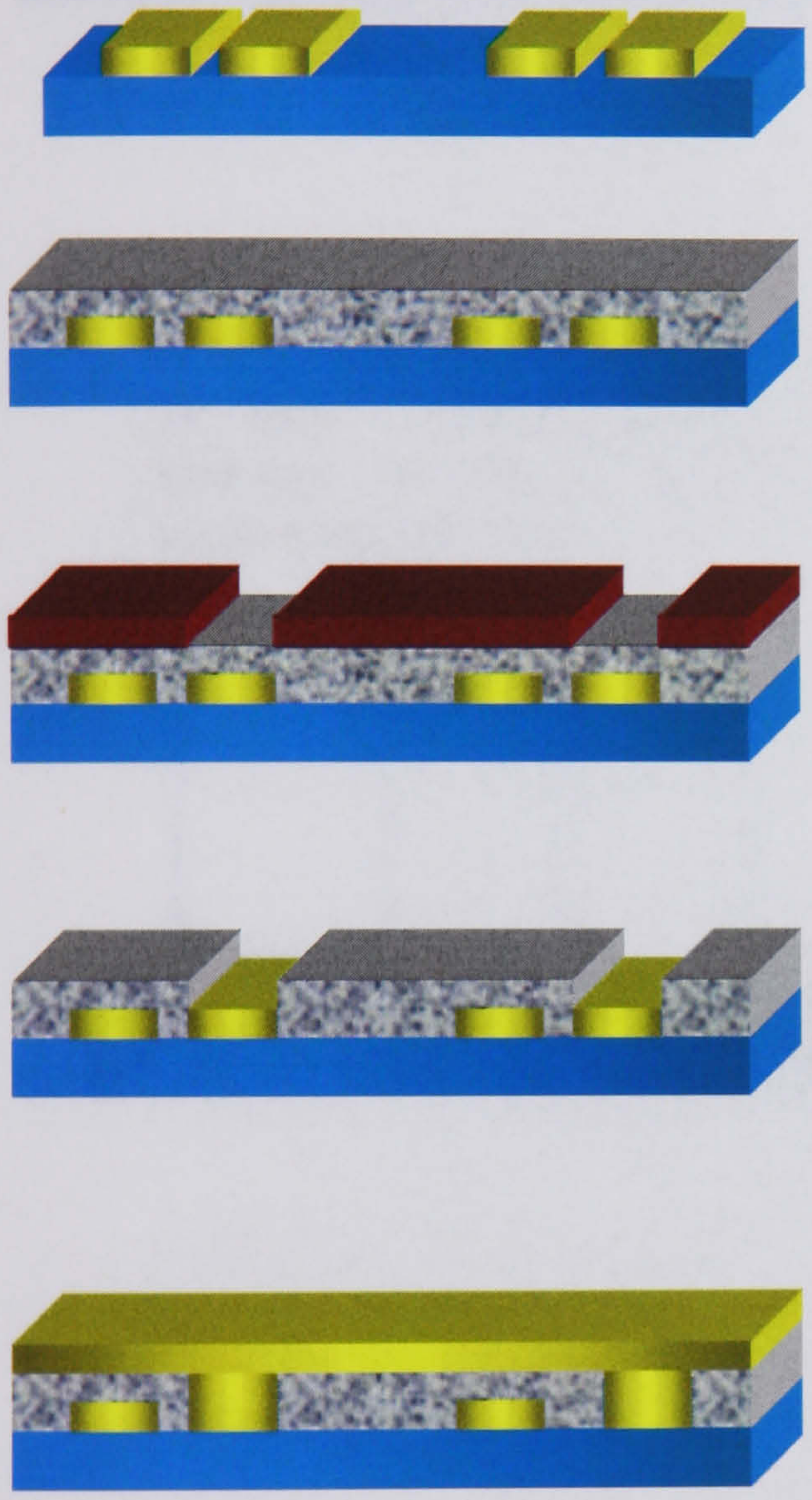

Base electrodes deposited on glass.

Insulating layer deposited on top of electrodes.

Photoresist mask etched delineating connection holes, channel and bonding pads.

Holes etched in insulator.

Top bus-bars and bonding pads deposited.

Figure 7-4

Summary of electrode fabrication procedure showing alternate electrode connections in two juxtaposed groups

7.2.1 Layer 1

The electrodes corresponded to the finest feature size of the device therefore they were designated as the first layer. The metals chosen were:

i) 10nm of Ti, for glass adhesion.

ii) 100nm of Au, for low resistivity.

iii) 20nm of Ti for protection of the top layer from corrosion at low frequencies.

These were deposited in a Plassys™ thin film deposition system. Three techniques, outlined below, were initially employed in order to discern the best and/or most efficient for the large area 2µm features.

Photolithography-lift off

i) Glass microscope slide, cleaned ultrasonically in acetone and methanol

ii) S1818 photoresist spun at 4000rpm, to a thickness of 1.8µm, and baked for 30 mins - soaking in chlorobenzene midway to harden resist, thereby improving lift off.

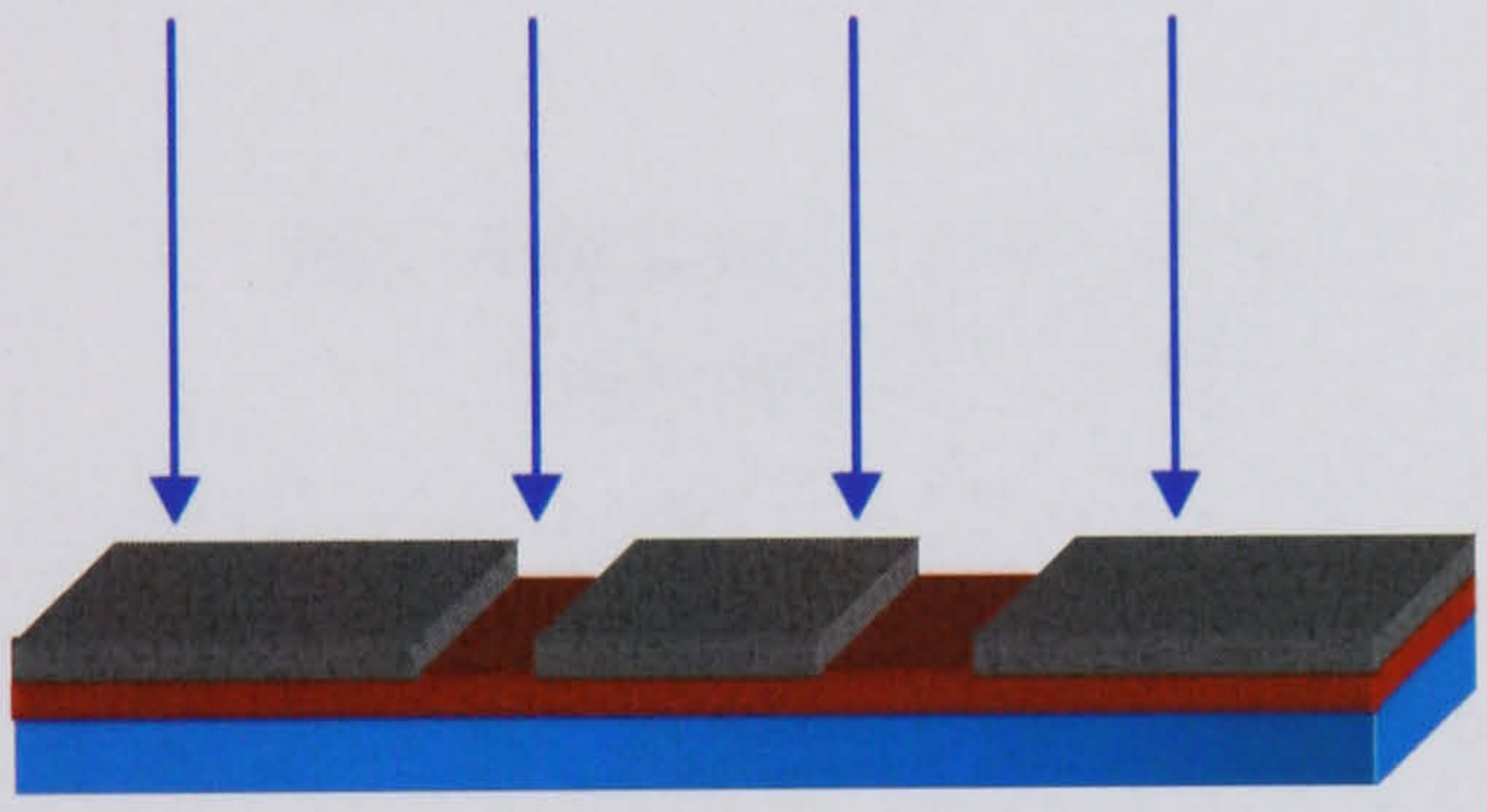

iii) 10-12s exposure on a 200W UV mask aligner .

iv) 75s development in microposit developer (Shipley).

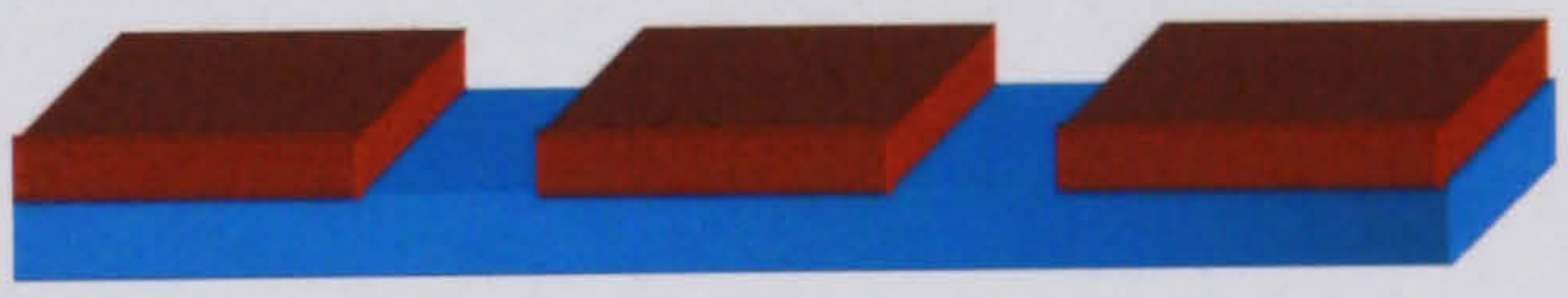

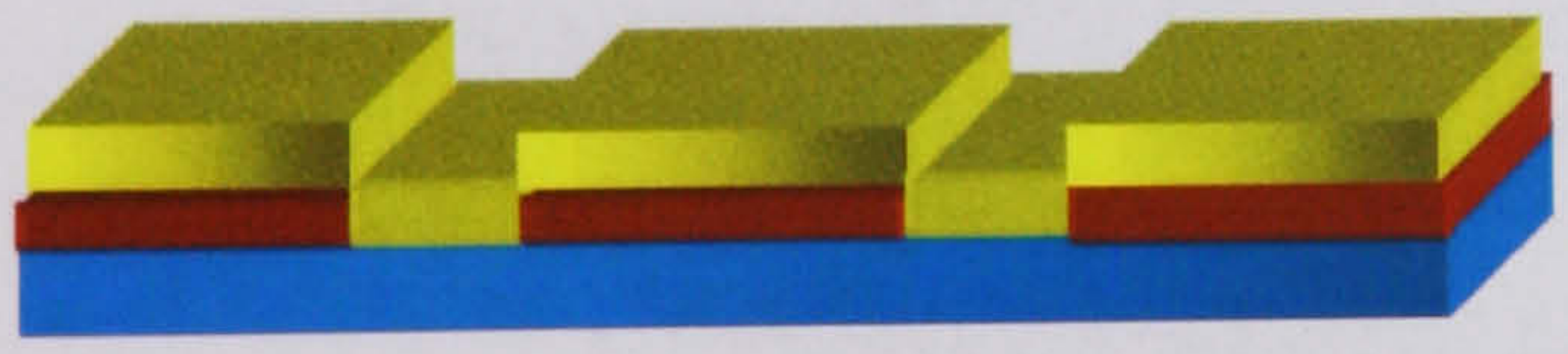

v) Plassys metal evaporation

vi) Lift off – acetone attacks resist, removing unwanted metal

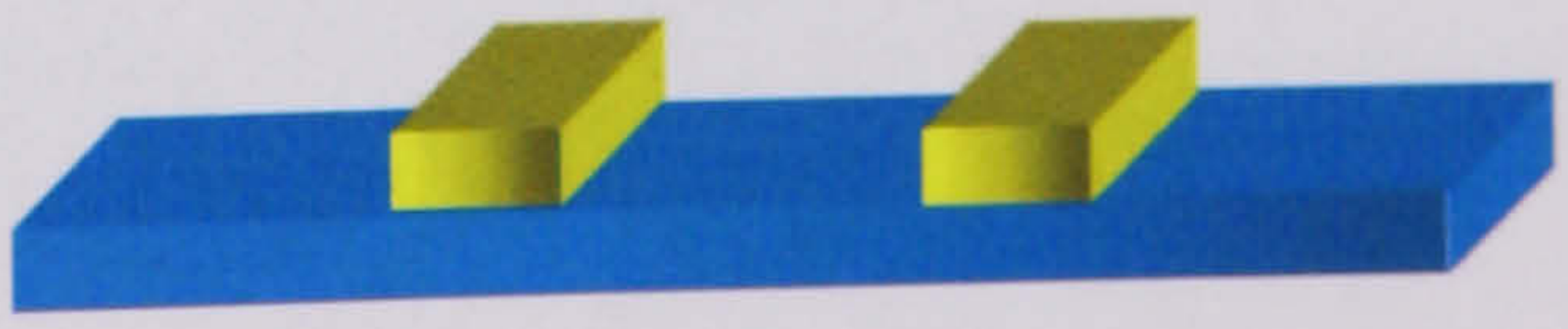

Photolithography - wet etch

This technique was tried in order to decrease the incidence of short circuits caused by metal re-deposition or incomplete metal removal.

i) The glass substrate was cleaned by soaking in a 7:1 mixture of sulphuric acid and hydrogen peroxide for a duration of 5 minutes after the temperature had peaked at 90°C.

ii) TiAuTi layer evaporated

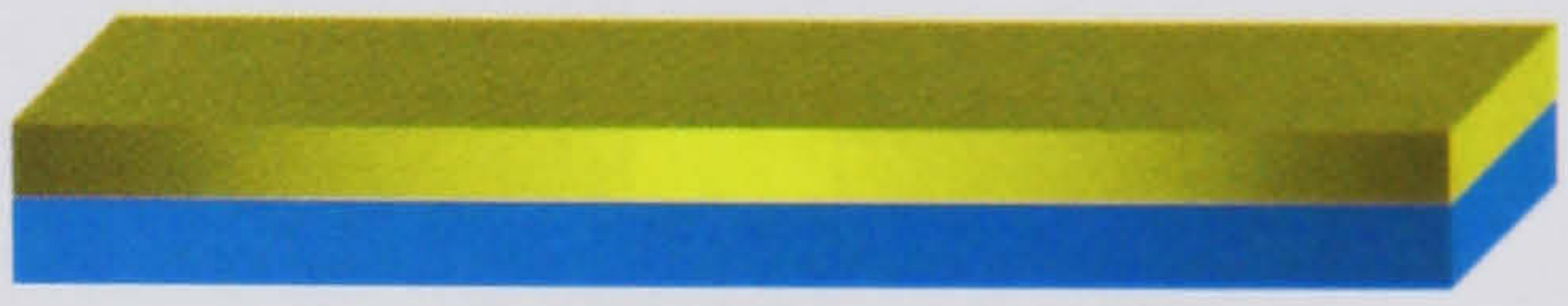

iii) S1818 resist spun on top

iii) Patterned using metal mask and U.V. light

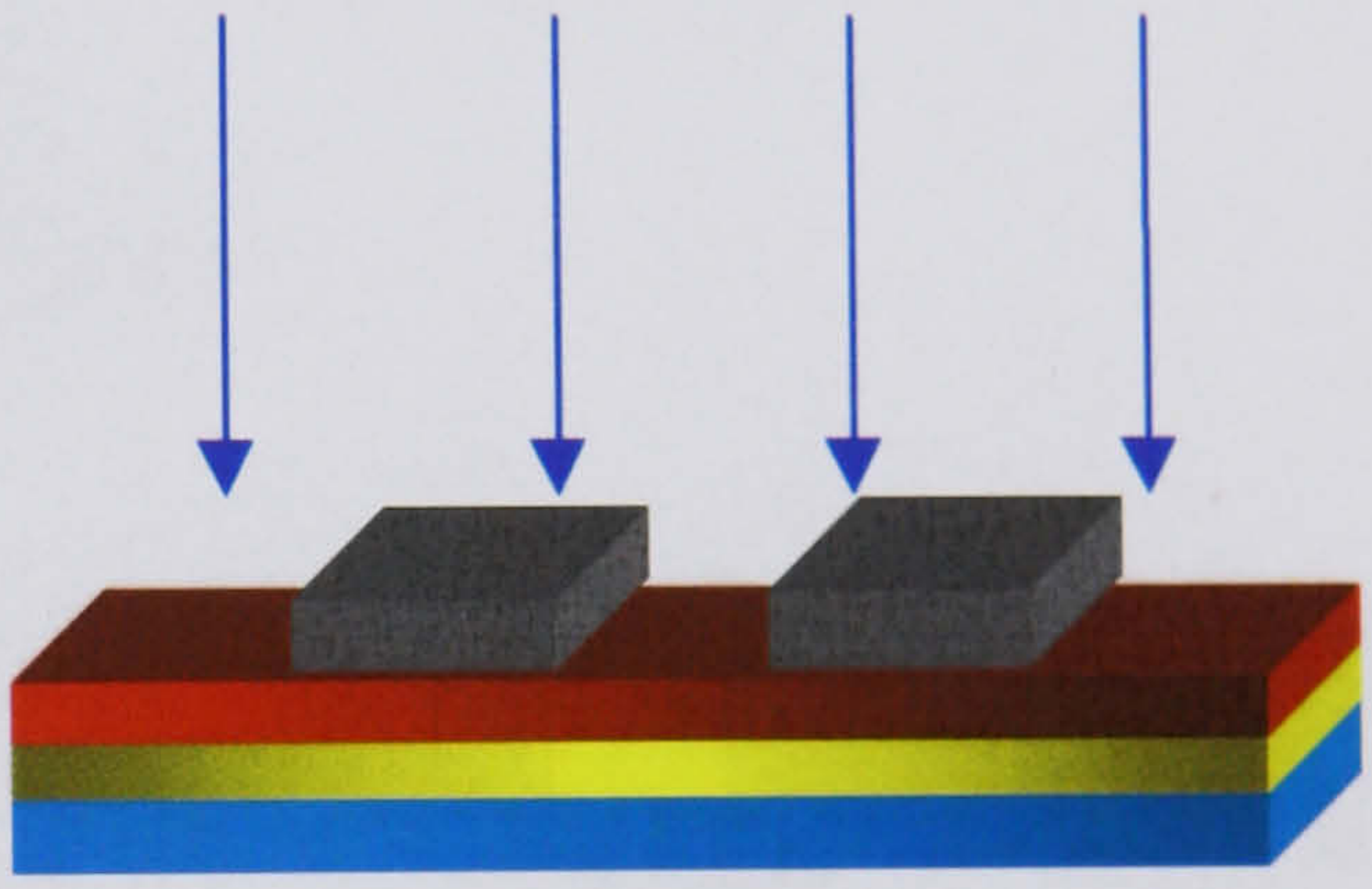

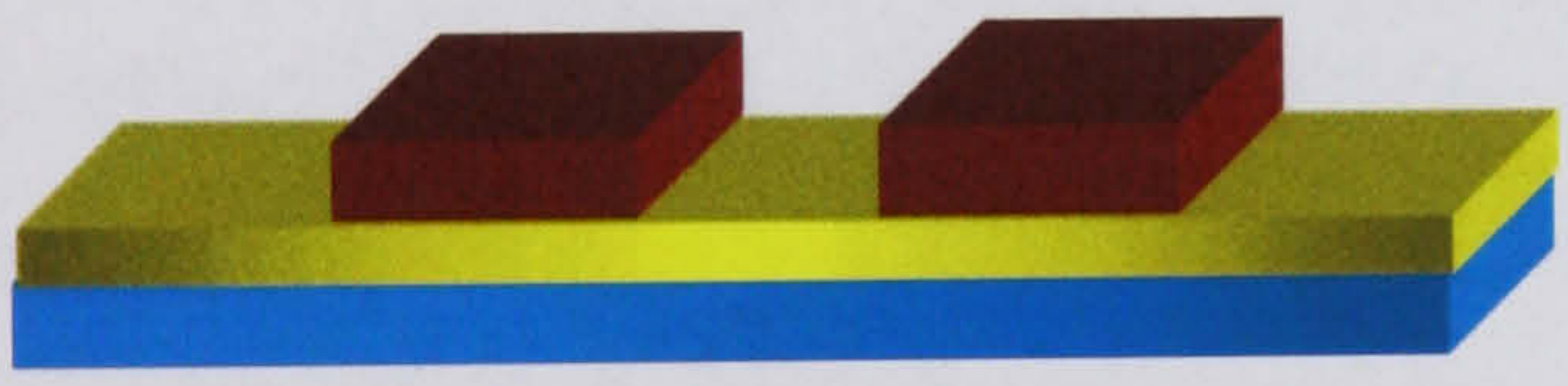

iv) Positive development.

v) Hydrofluoric acid (HF) and gold etch used alternately to remove metals unprotected by resist. Usually results in over-etch, due to the tendency for undercut.

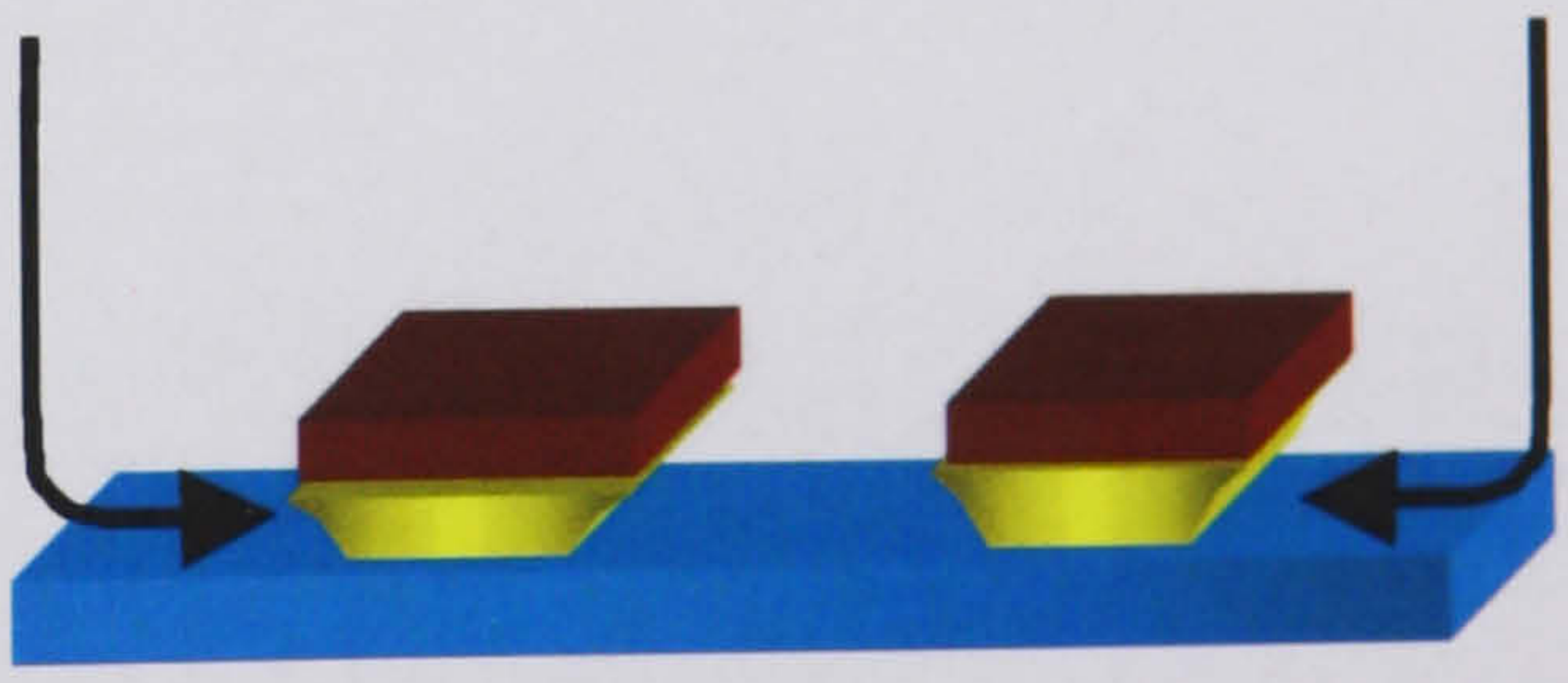

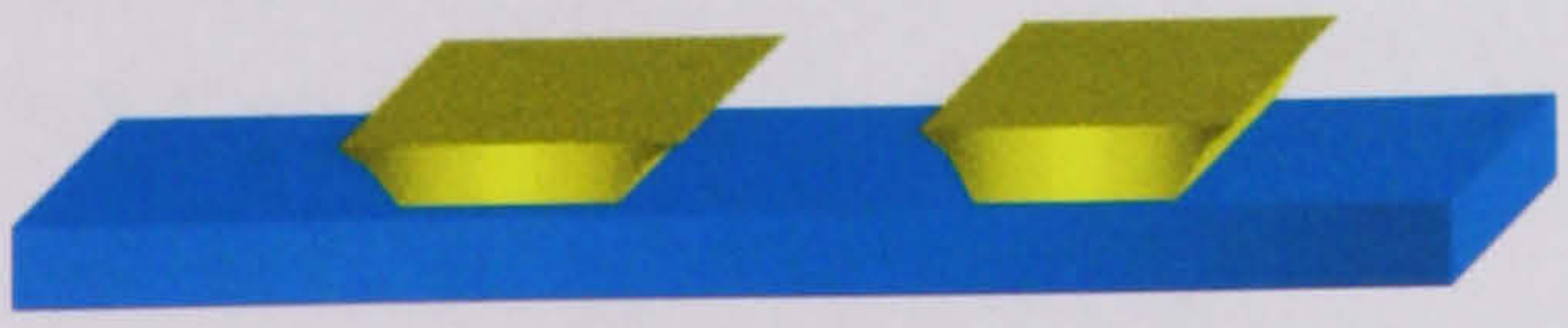

vi) Resist removed in acetone.

E-beam lithography (i)

A higher resolution alternative to photolithography is direct write e-beam lithography (Figure 7-5), where the pattern is written directly onto the sample by means of an e-beam sensitive resist. The resist chosen was UV3 (Shipley). The dose was determined by a series of exposure tests.

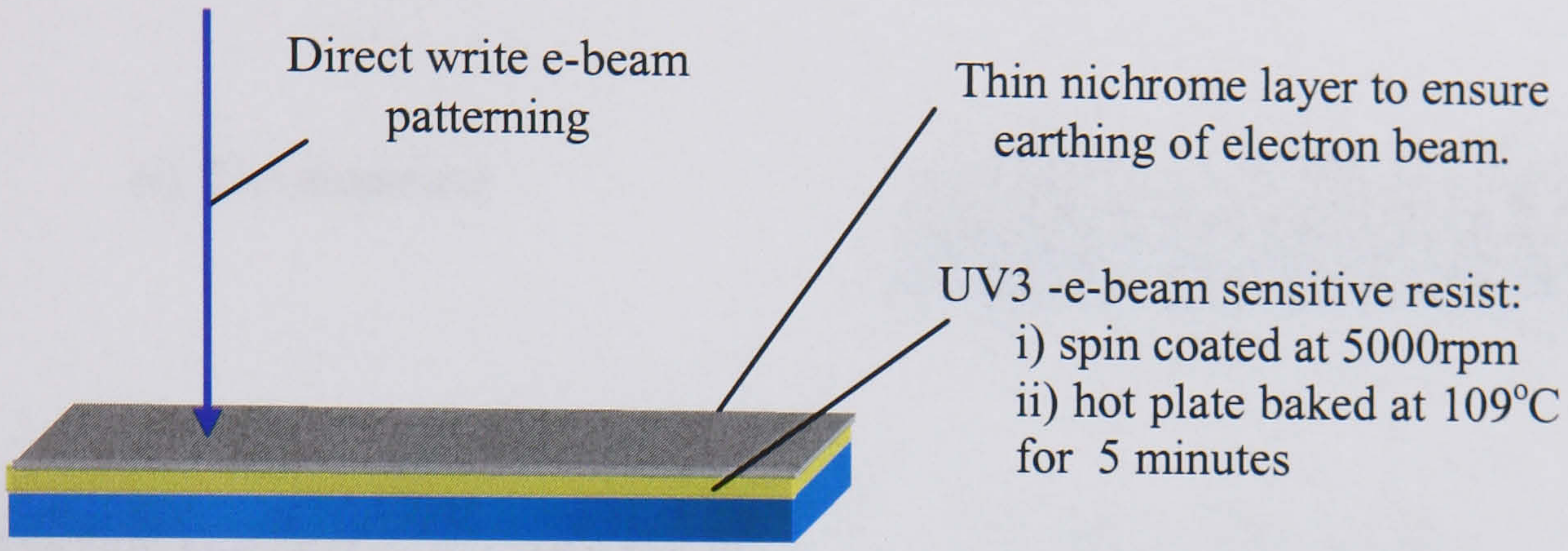

Figure 7-5
UV3 procedure

On removal of the nichrome, the sample is developed and metalised in the same way as for photolithography lift-off. However, although UV3 is used routinely for writing small patterns with feature size ~O(0.5μm) it was not consistently reliable for this relatively large area (~10^6μm^2) since one small imperfection or contaminant could short circuit the device. The lift-off procedure also carried similar potential risk factors with metal re-deposition as in photolithography and therefore there was no significant overall advantage to this technique.

E-beam lithography (ii) [2]

In order to overcome the above weaknesses, a Honda™ mask plate was used as an alternative substrate (Figure 7-6). This minimised the risk of pre-exposure contaminants as well as that of re-deposition as the final etch dissolved away the chrome instead of producing potentially damaging flakes as with lift off.

Figure 7-7-Figure 7-9 show various perspectives of the result.

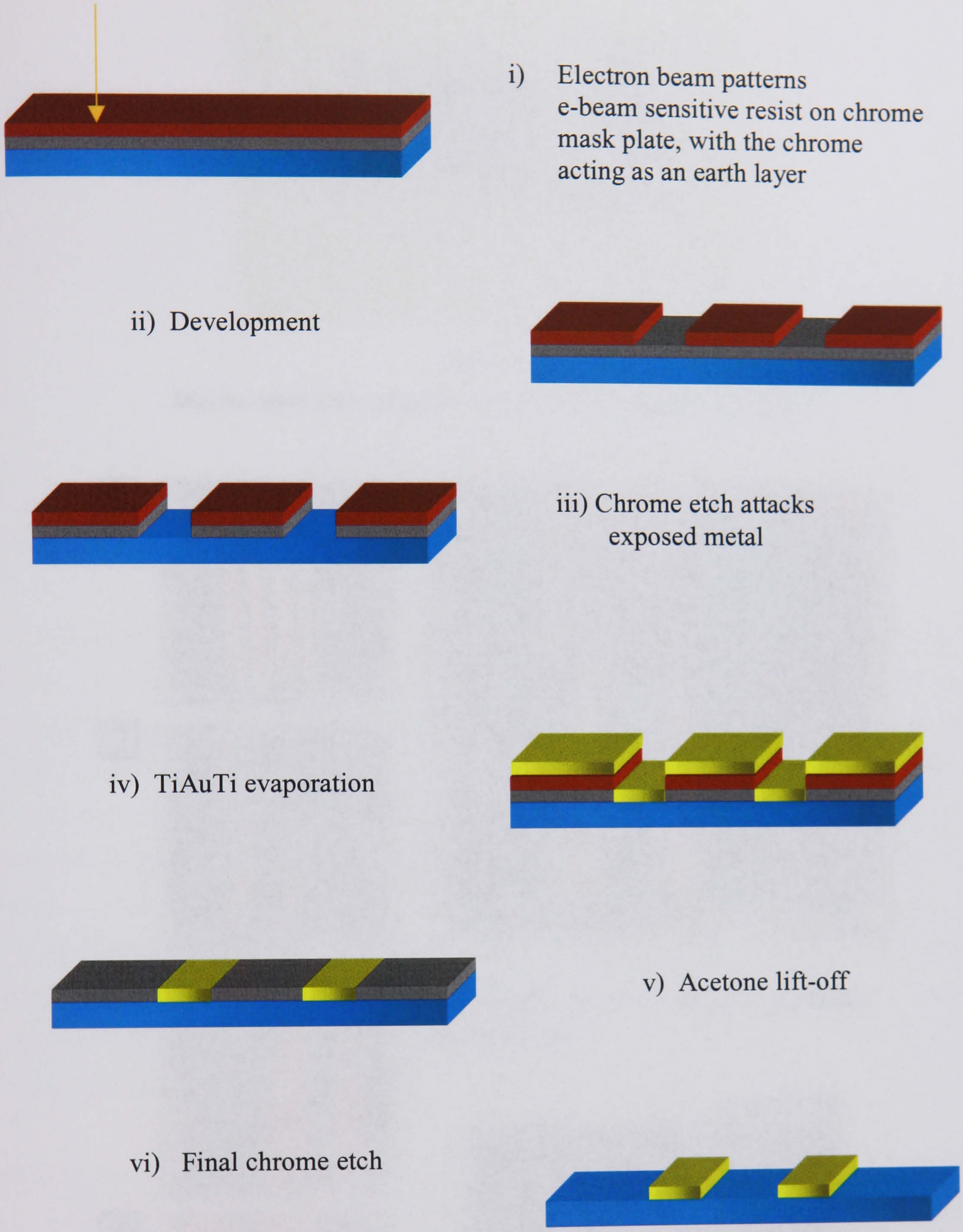

Figure 7-6

Direct write procedure using a pre-metalised mask plate as a substrate.

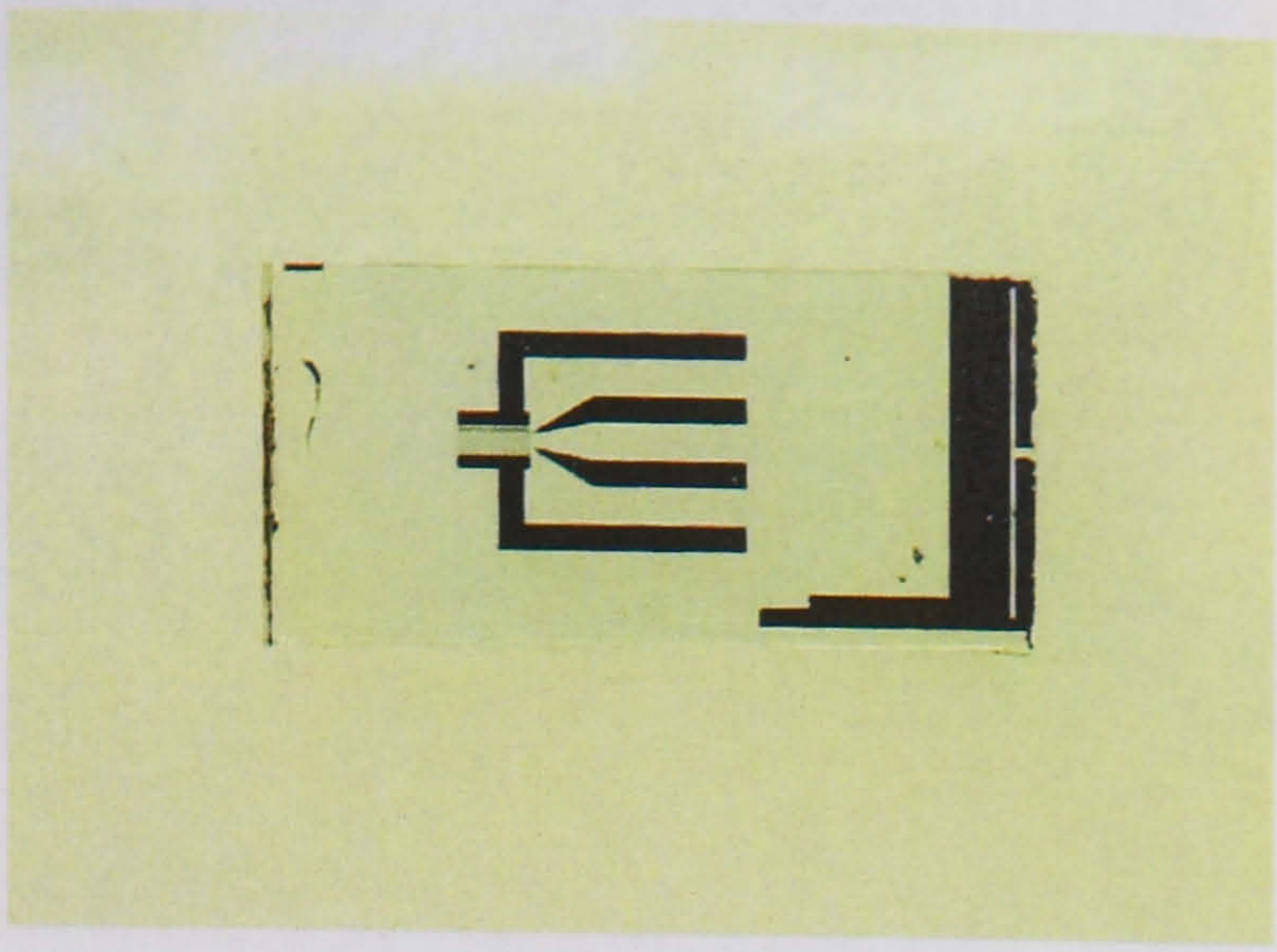

Figure 7-7

Macroscopic view of layer 1 written on a mask plate segment

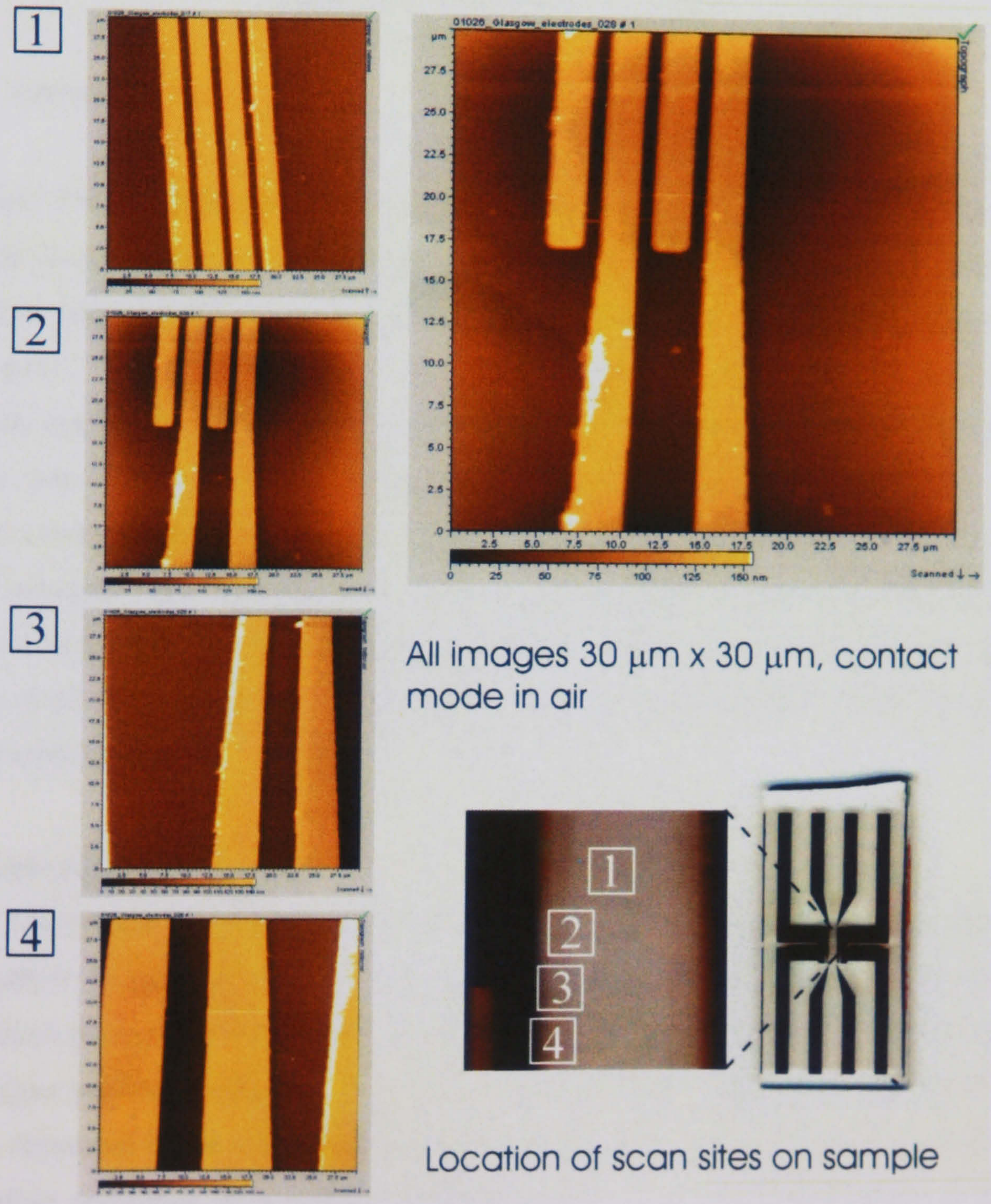

Figure 7-8

Atomic force microscope pictures showing quality of electrode edges. 30μm× 30μm contact mode in air (L.O.T. Oriel Group, http://www.lotoriel.co.uk).

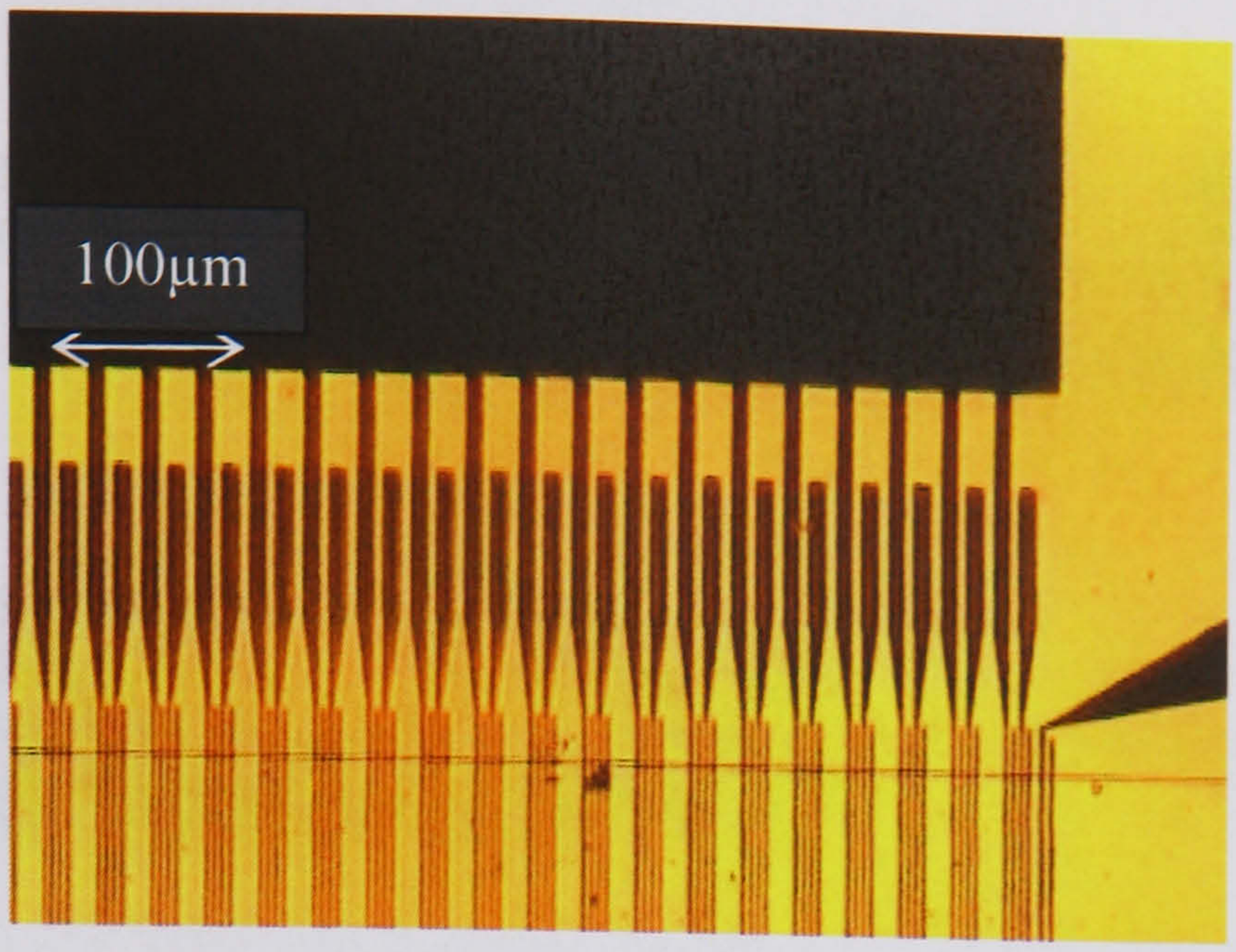

Figure 7-9
Nikon microscope overview of layer 1

7.2.2 Layer 2

Silicon Nitride (SiN) was chosen as the insulation layer because of its non-porosity, which renders it suitable as an insulator even in aqueous conditions. It was deposited in a vapourised form at 300^{0}C using a combination of silane (SiH_4), nitrogen (N_2) and ammonia (NH_3) gases. Several thicknesses were tried ranging from 300-500nm, aiming for good insulation combined with a uniform ohmic connection to the top bus-bars. For the thicker samples, low stress deposition techniques were used to minimise fractures. Given the large areas of overlapping metal and incidences of imperfections in the SiN, it was found that thicker insulation was desirable. The only prospective problem this posed was the potential hindrance to a good connection of the exposed electrodes to the upper bus-bars. However this was dealt with separately with the initial priority being to minimise short-circuits caused by insulation flaws.

Hole patterning

The holes were patterned using photolithography to produce a positive resist mask. Combinations of HF and Carbon-fluoride (C_2F_6) gas and C_2F_6 alone were then used to etch the exposed areas. This was carried out in order to compare the effects of the wall geometry on the upper connection (Figure 7-10), since the insulator thickness was considerably thicker than the deposited metal. The completion of the etch was determined by the measurement of a negligible resistance on a cleared bonding pad and by direct observation of the holes through a polarising filter where any anomalies in the colour of the smaller cleared areas would reveal the presence of a SiN residue.

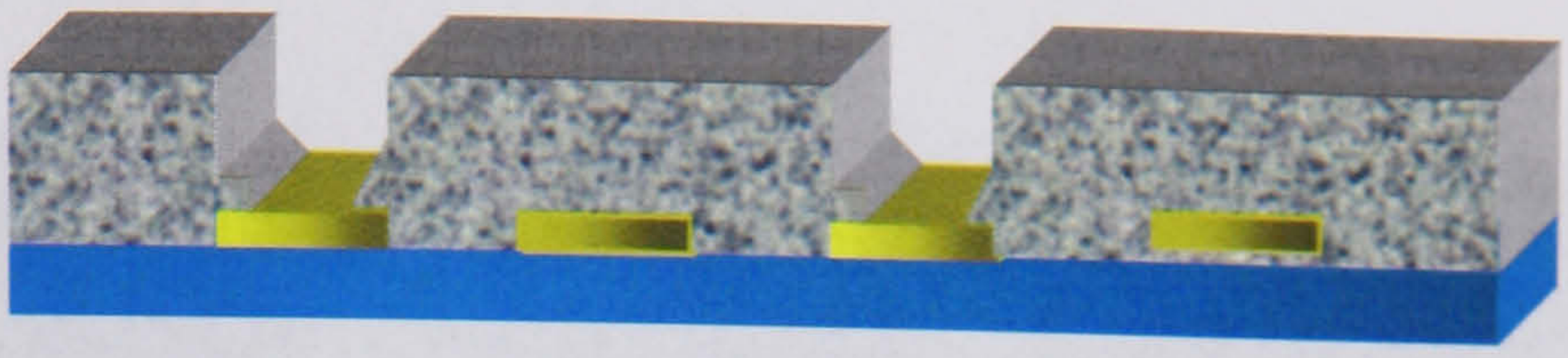

C_2F_6 followed by HF.
Ti acting as a sacrificial
layer

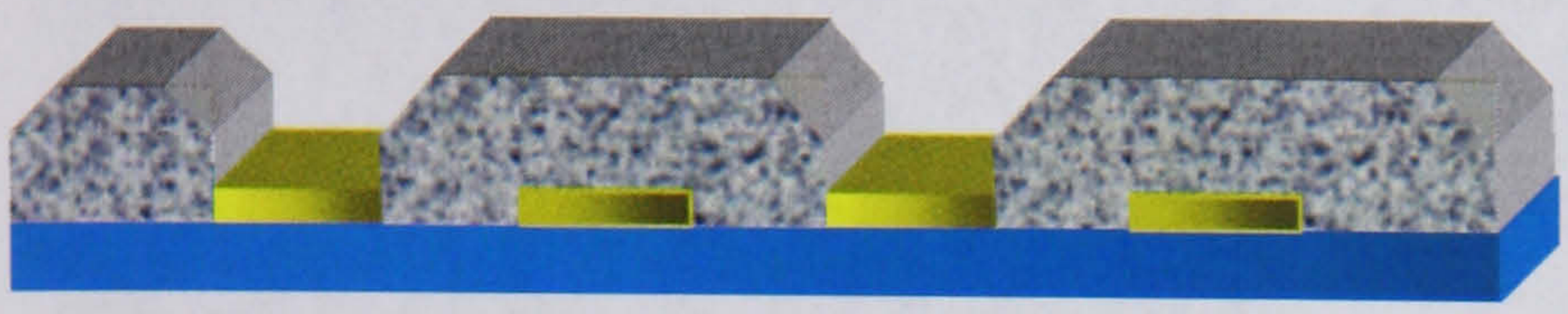

HF followed by C_2F_6

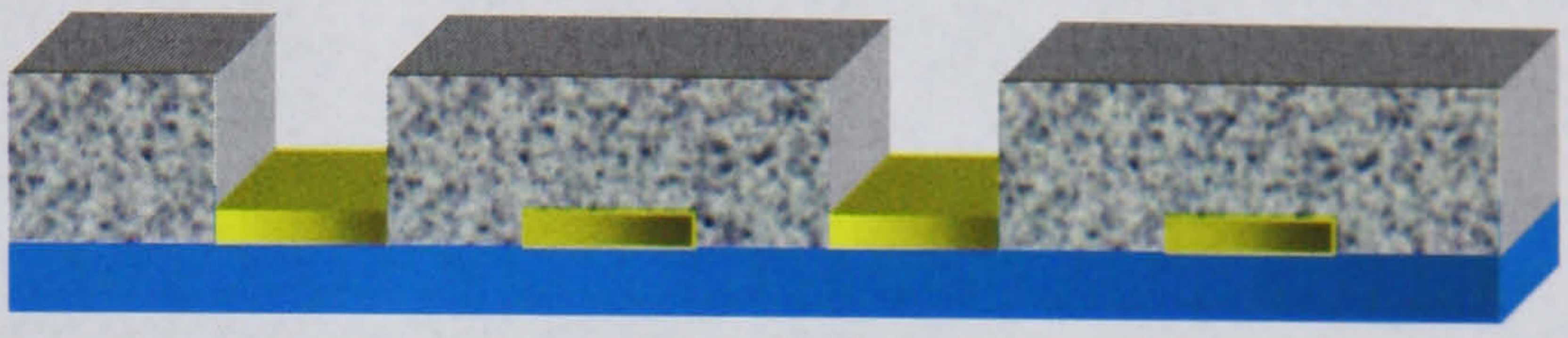

C_2F_6 overetch

Figure 7-10

Approximate profiles of three SiN etches attempted to ensure good ohmic connections of base electrodes to top bus-bars.

It was found upon metal evaporation that over etching with C_2F_6 was optimal since presumably the vertical wall profile maximises the contact area for the upper bus-bar while minimising the chance of consecutive electrode connection. These are essential requirements given the margin of error in alignment. Figure 7-11 shows a series of SEM photographs taken of the etched holes and channel. Part (d) shows some misalignment which although not sufficient in itself to de-functionalise the device is not desirable for connection purposes

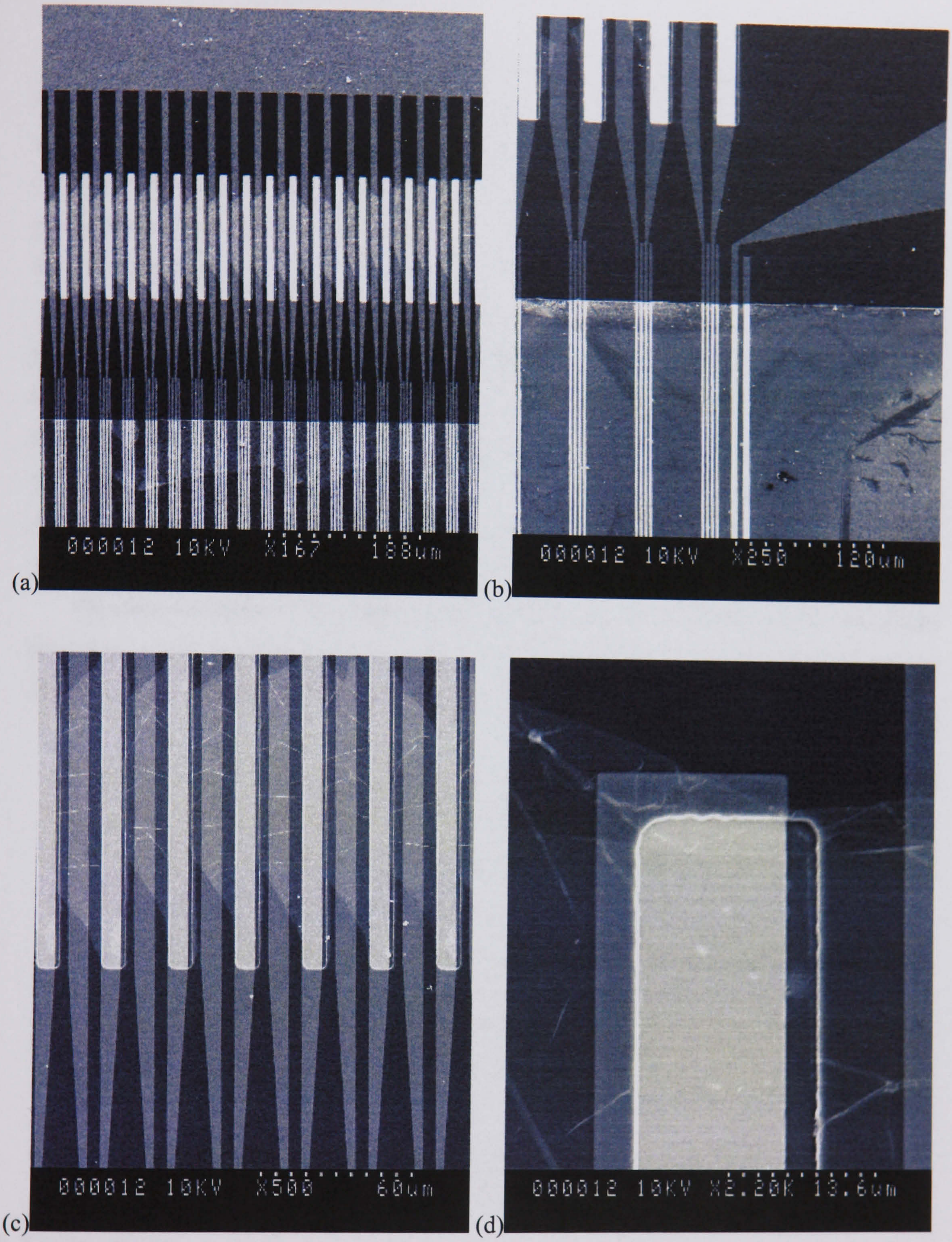

Figure 7-11

Holes etched in the insulating SiN layer to establish the connection of every 4th electrode.

7.2.3 Layer 3

The same metals were chosen with the 10nm layer of Ti retained to promote adhesion to the SiN. Although there was no sloping component to the walls, the divergence of the vapourised metal in the Plassys™ ensured that they were covered. The thickness of the gold of the upper bus-bars was also increased by 50% in order to improve the uniformity of the conduction of this corrugated layer and compensate for the reduced width in comparison to the lower bus-bar.

Here, good adhesion was more difficult to attain and so it was critical that samples had minimal contamination. After etching they were cleaned in water bath heated acetone at 60°C for up to 2 hours to remove any resist residue, hardened or cross-linked by the etching procedure. They were then soaked in hot Opticlear™ to remove any grease picked up in the procedure before being transferred back to the hot acetone to remove the Opticlear residue. After the routine rinsing in methanol samples were air dried and placed for further drying in a 90°C convection oven immediately prior to evaporation.

On some occasions, if the upper bus-bar had any breaks or serious flaws, the lithography procedure could be repeated. This was done successfully on several occasions without further damage to the devices. Figure 7-12 shows the final result on the cut mask plate.

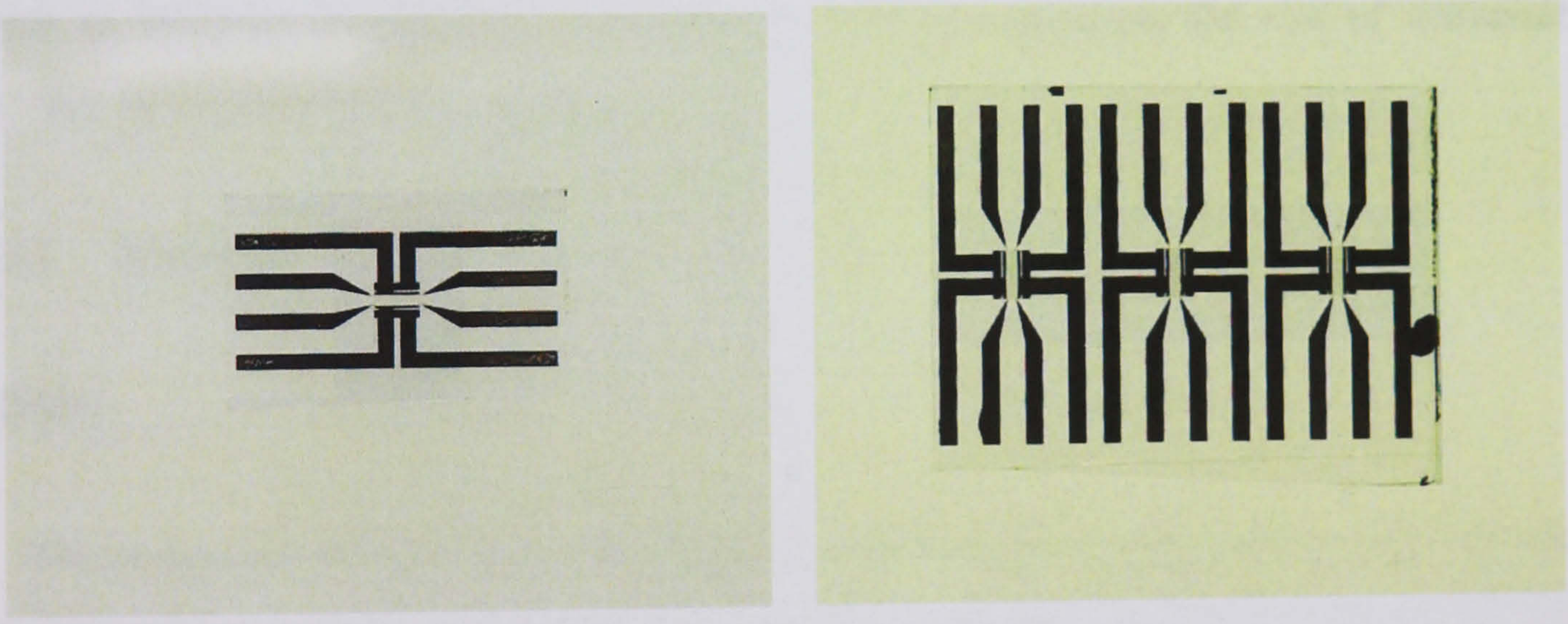

Figure 7-12

Cleaved mask fragments of the finished batch of electrodes

Top insulation

Another SiN layer of 200nm was deposited on the devices and etched using the channel mask above the active area. This served as a protective shield from the potentially damaging repeated repositioning of the channel between experiments and also to minimise interference from bus-bars or electrode edges outwith the active area.

7.3 Channel

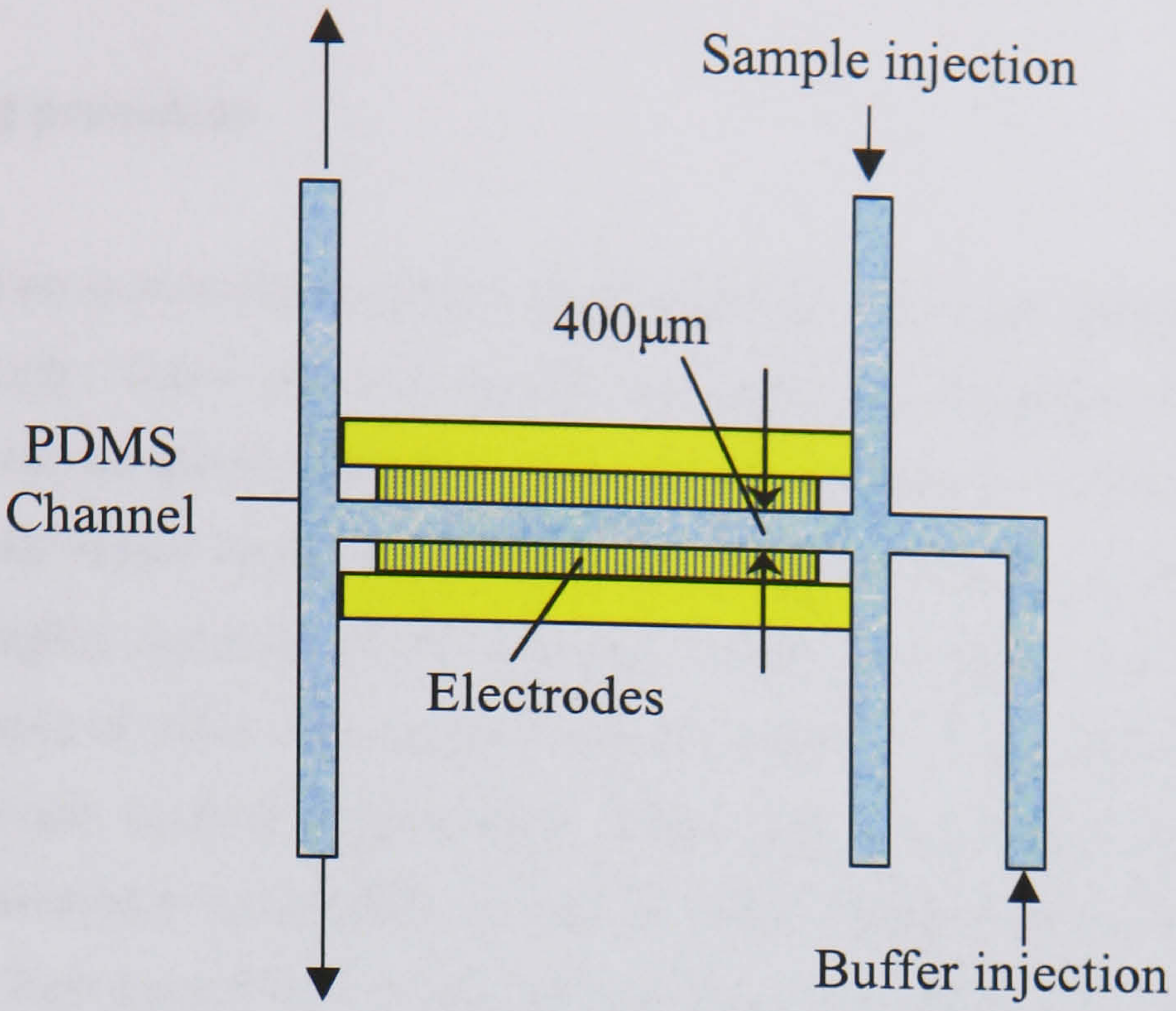

Figure 7-13
Channel design

The channel was added as a top layer in order to constrain the sample when undergoing diffusion in the off-cycle. It was fabricated in SU8 moulded PDMS as a removable entity in order to facilitate cleaning of the device as well as minimising the risk of irreversable damage in the fabrication procedure.

7.3.1 Materials

PDMS

The compound PDMS (Poly (dimethylsiloxane)) is a silicon elastomer widely used with moulding procedures for making capillary channels, with particular application in microscale total analysis systems (μTAS) [3, 4].

SU8

SU-8 is a negative, epoxy-type, near-UV photoresist based on EPON SU-8 epoxy resin (from Shell Chemical) that has been originally developed and patented [5]. It is manufactured for thick and ultra-thick resist applications (SU8-5,10,25,50 100 ranging from 10-2000μm) and generally produces a high aspect ratio. The high resolution obtainable also results in smooth, vertical walls making it suitable for the moulding of microfluidic channels.

7.3.2 Methods

PDMS curing procedure

PDMS comes as two separate parts, fixer and bulk, which are added together at a ratio of 10:1 respectively. These are then mixed thoroughly and de-gassed under vacuum for 15 minutes until no air bubbles remain. The PDMS can then be poured onto the mould and allowed to settle before being oven cured. The thickness, however, is difficult to control. The viscosity is highly sensitive to the accuracy of the fixer:bulk ratio and small variations around the required value can produce variable settling in an unbounded (surface-tension controlled) sample such as a glass slide. While it is not essential in this application that thickness be accurately predictable, it is useful to have it adjustable to the very short working ranges of the high magnification microscope lenses. In addition, if channel height is to be reduced, it is important to have more accurate predictability especially since the use of other constructions – such as PDMS walls with a glass lid – would circumnavigate the problem of having a too high aspect ratio or other filling problems related to the high PDMS surface area/fluid-volume ratio.

PDMS Spinning

Investigations were therefore carried out spinning PDMS onto glass microscope slides using various spin speeds in order to obtain a calibration curve of thickness (measured using a Dektak) against speed (Figure 7-14).

Procedure

1. Clean 7.5:2cm glass microscope slides ultrasonically using acetone and methanol.
2. Mix PDMS according to standard procedure of 1:10 fixer:bulk and de-gas under vacuum for 15 minutes.
3. Apply PDMS to slide spreading with spatula to the edges.
4. Increase spin speed gradually over 10 seconds to desired value.
5. Spin for 40 seconds
6. Oven cure at 75 C for 30 minutes.

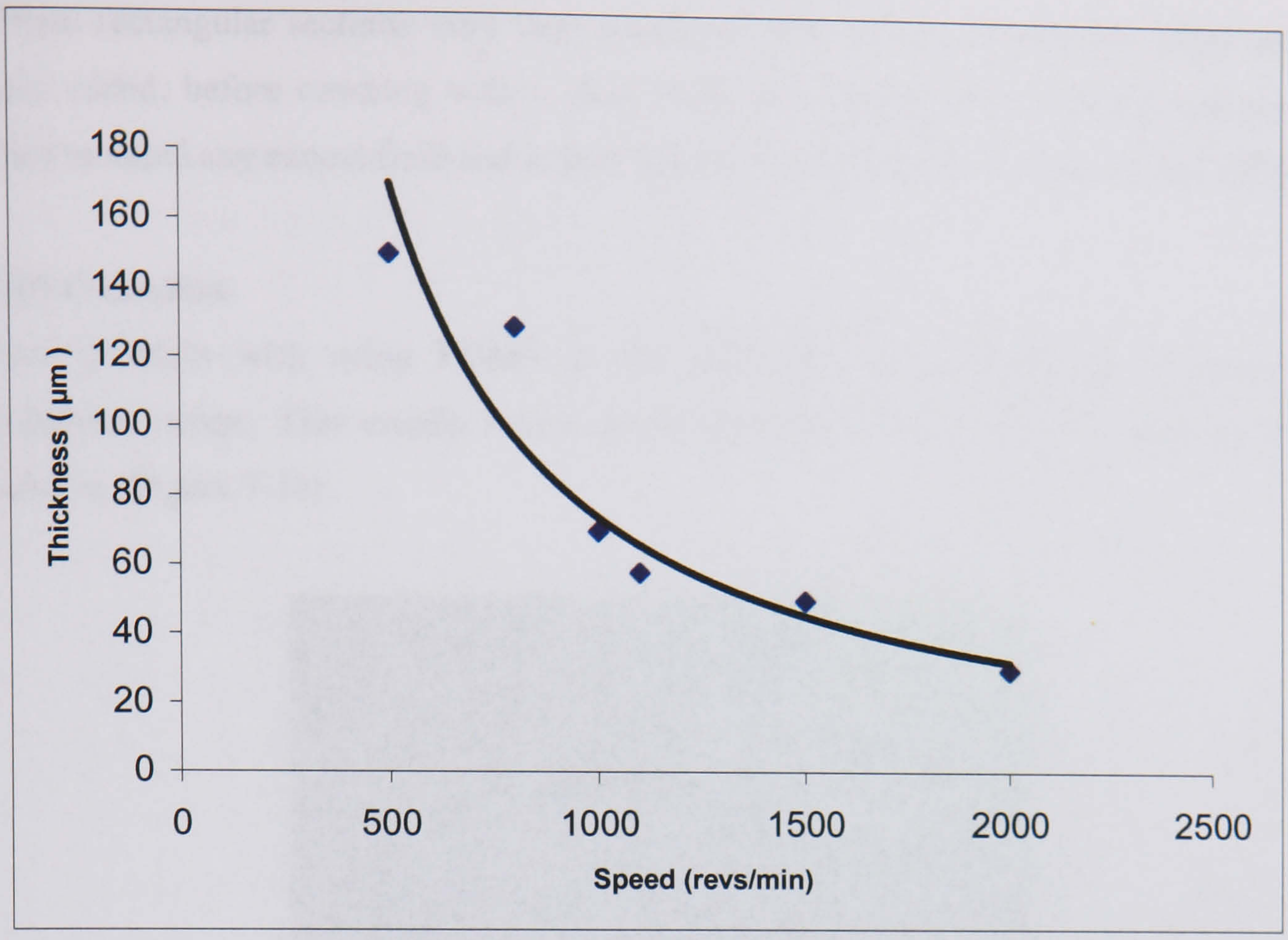

Figure 7-14

Experimental calibration of deposition thickness against spin speed for PDMS on glass

7.3.3 Preliminary constructions

Some preliminary channels were made using several of the spun samples by cutting small, rectangular sections of the PDMS using a scalpel. Because of their small size they could be pealed off with tweezers, in contrast to larger sections of this thickness which could rarely be removed undamaged due to the PDMS-glass adhesion being greater than the strength of the PDMS film.

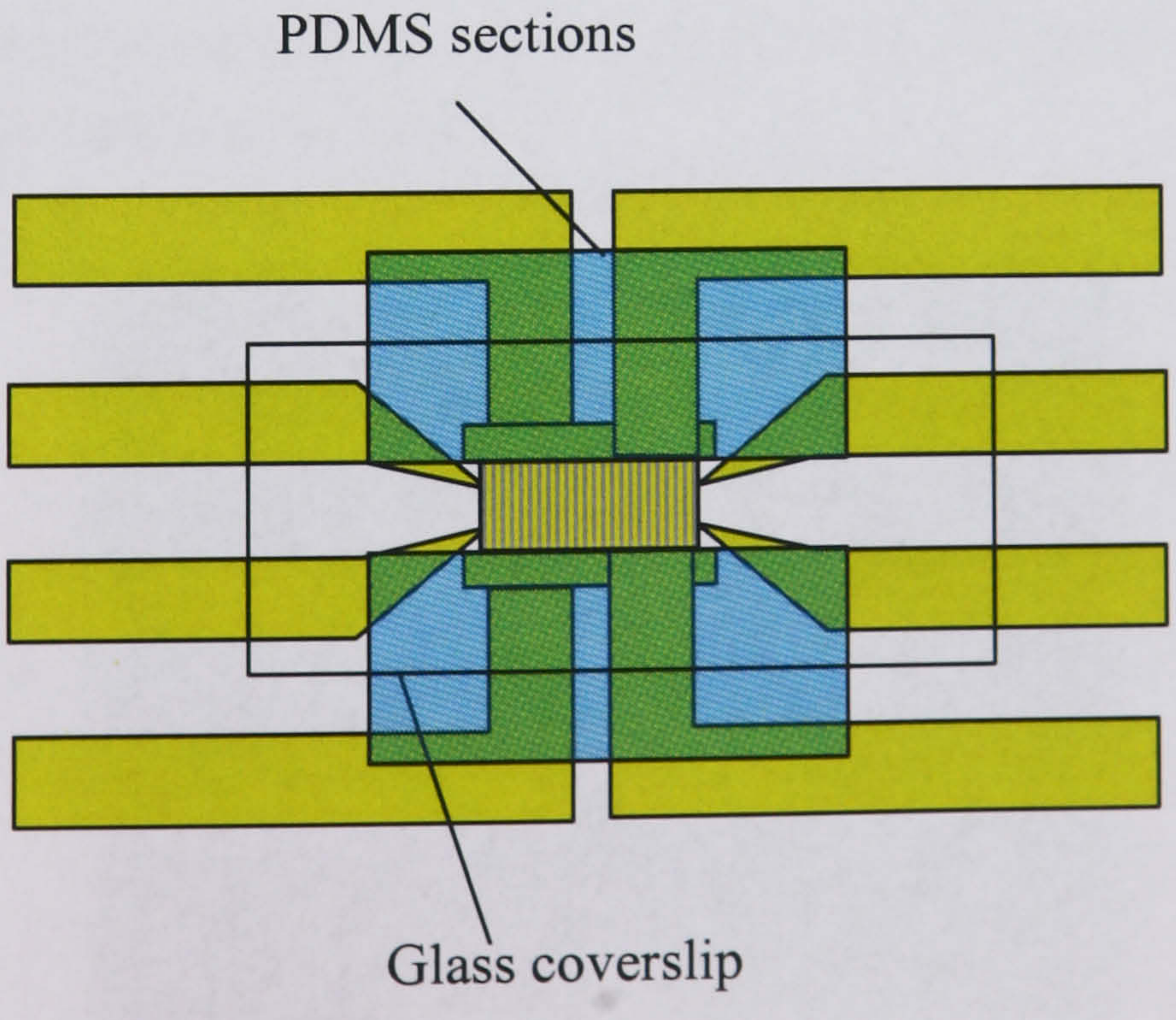

Figure 7-15

Preliminary channel construction using thin, rectangular sections of PDMS with a glass coverslip

These rectangular sections were then positioned carefully at the channel edges and the sample added, before covering with a glass cover slip (Figure 7-15). Gentle pressure was applied to expel any excess fluid and ensure that the channel height was that of the PDMS.

PDMS Oxidation

One problem with using PDMS in the fabrication of a capilliary channel is its hydrophobic nature. This usually results in the formation of a cusp when aqueous fluid is injected in (Figure 7-16).

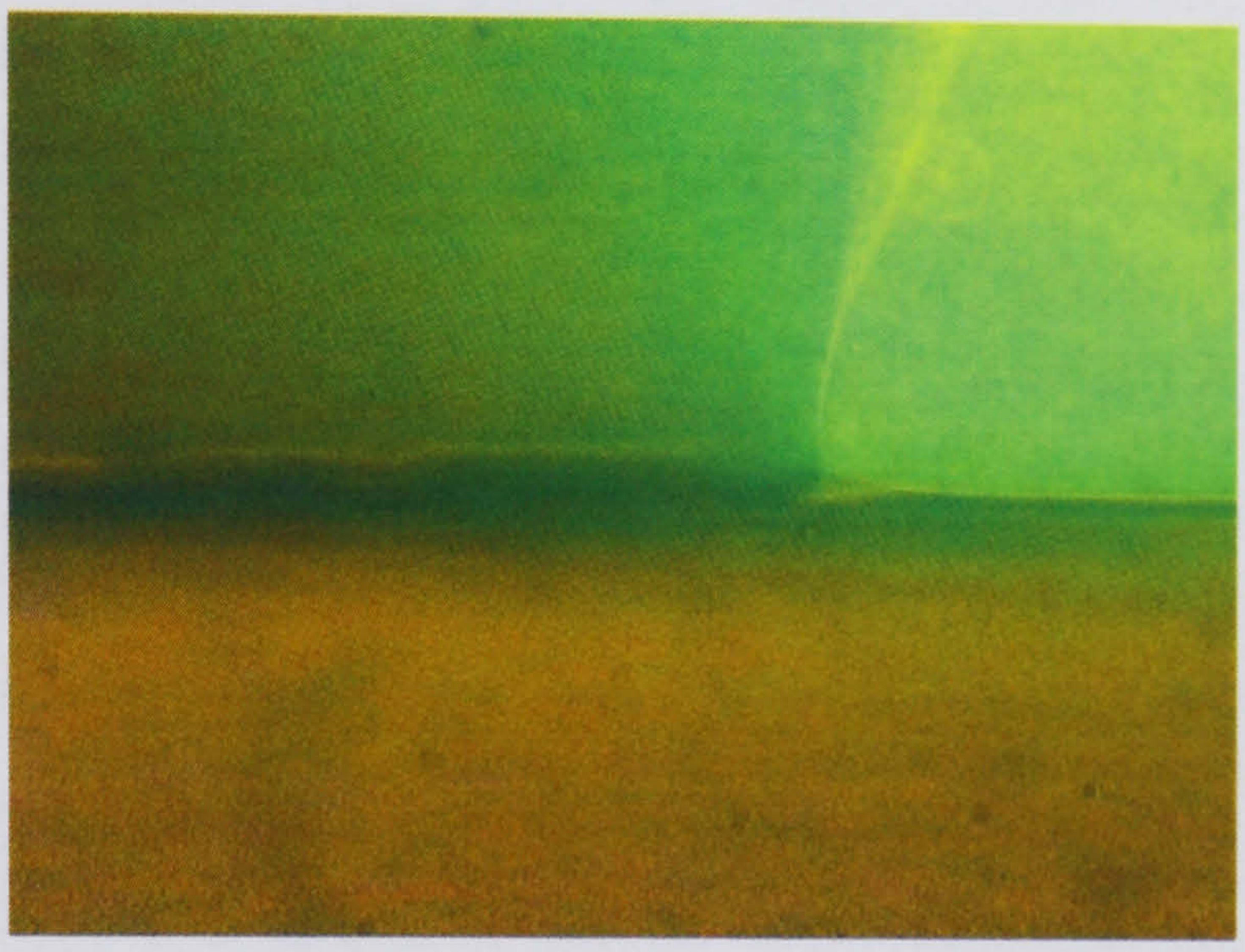

Figure 7-16

Unoxidised PDMS with cusp formation showing resistance of fluid to evenly fill the channel

Modifying a recipe developed by Duffy *et al* [3] the baked PDMS surface was cleaned in ethanol and oxygen plasma etched for a range of different times from 1-10 minutes. This creates silanol groups on the surface $–O_nSi(OH)_{4-n}$ which in neutral or basic solutions, de-protonate producing hydrophylic ionic groups [6], rendering the PDMS channel capable of supporting capillary flow (Figure 7-17).

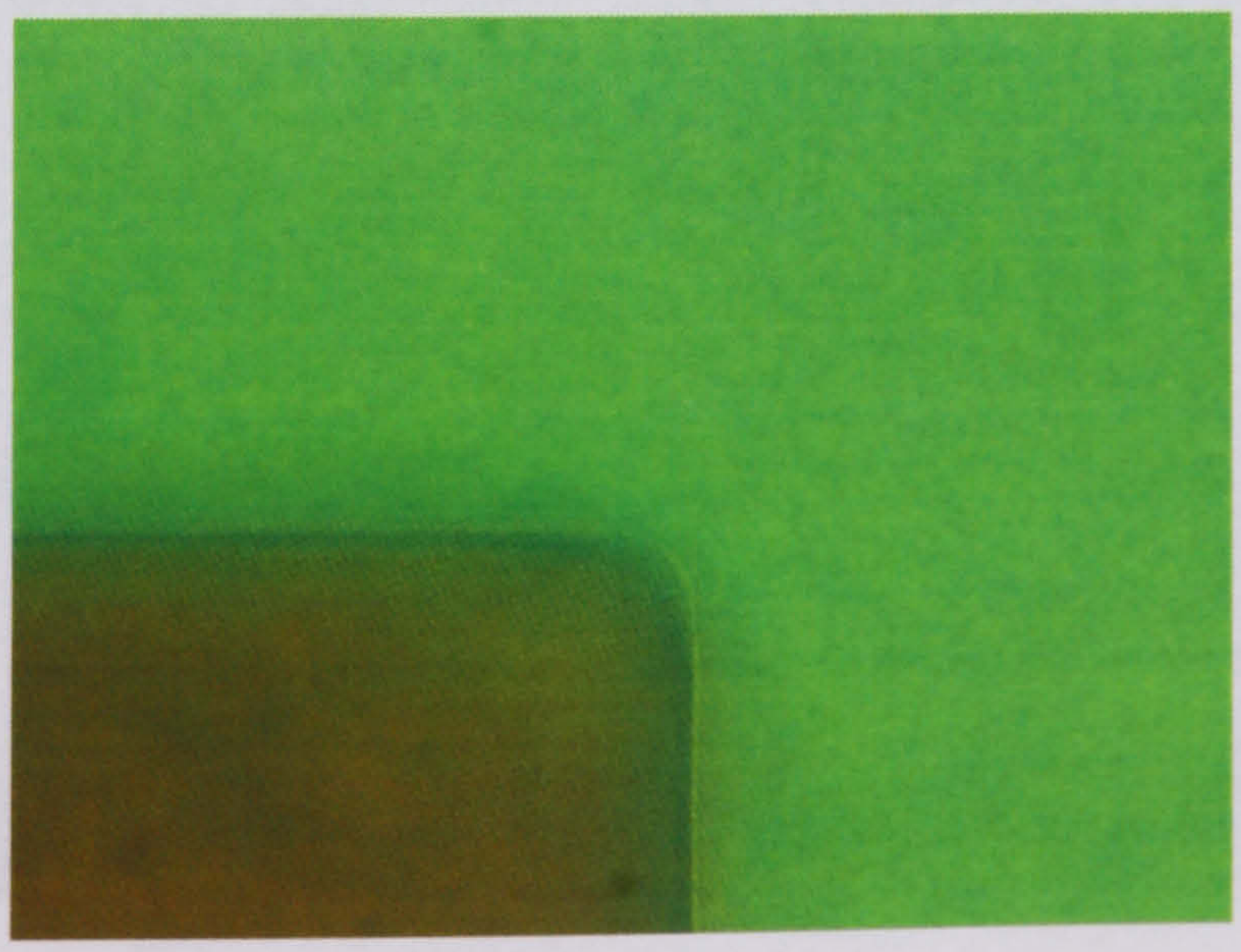

Figure 7-17

Ethanol cleaned and oxidised PDMS capilliary uniformly filled with an aqueous suspension of polystyrene beads

SU8 Lithography Procedure

The moulded channel height was designated to be in an aspect ratio of ~1:3 with the channel width thus supporting a fairly flat PDMS lid. The designated thickness being within the optimal range of SU8-50, this was chosen and etched according to the following lithographic procedure, which has been adapted from data sheets supplied by the company [7].

1. After cleaning, dehydrate glass microscope slides at 120 degrees for 10 minutes.
2. Spin on primer at 2000 rpm for 30 seconds.
3. Dispense SU8-50 using dropper and spreading to edges with spatula.
4. Spin V_1 500 rpm/5s , V_2 1000rpm/30s, V_1 V_2 5s acceleration.
5. Soft bake 5 mins 60 C 2h 95 C 5 mins 60 C(to avoid cracking).
6. Expose at 4mJ/cm^2 for 120s in stages of 15s, allowing 1m between each exposure.
7. Post exposure bake 5 mins 60 C 60 mins 150 C 5 mins 60 C
8. Development - repeated soaking in EC solvent and rinsing in isopropanol for as long as required – usually between 15-20 minutes or until all the white residue produced by the action of the solvent on the SU8 has been rinsed clear by the isopropanol.
9. Blow dry gently.

This procedure proved effective in producing the required structures on glass (Figure 7-18). However, the adhesion was variable and therefore the robustness as an effective mould not guaranteed.

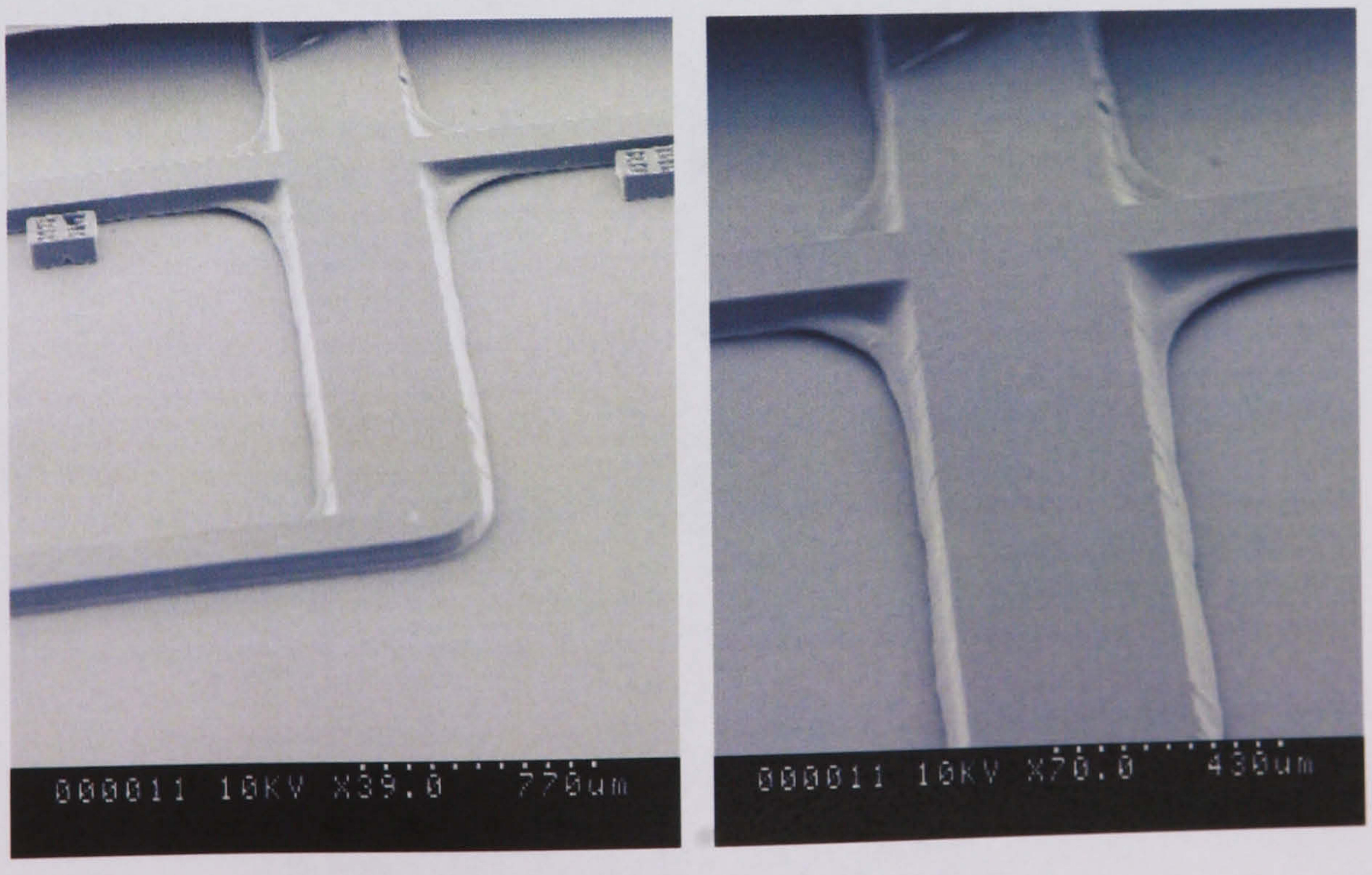

Figure 7-18

SU8 channel mould on glass. Thickness ~100μm.

SU8 Free Structures

In order to promote durability as a mould – i.e. prevent cracking and loosening on channel removal – free structure moulds, not adhering to the glass, were fabricated. The above procedure was modified to allow this by leaving the SU8 structure for longer soaking times in the solvent between rinses with isopropanol. This was sufficient to loosen the cross-linked resist without actually detaching it from the glass. Detachment could then be easily achieved by applying gentle pressure with a spatula to the air dried sample.

SU8 Mould

The final mould was prepared by spinning a 10μm coating of SU8-5 onto a glass slide and heating at 60 C on a hot plate. After a few minutes the previously fabricated channel structure was positioned on the slide using tweezers and left for a further 20 mins or until no spatula imprints could be made in the thin layer 3 mins after removal from the hot plate. This created a very strong adhesion as well as a uniform surface from which even thin PDMS could be easily pealed.

7.3.4 Final channel construction

When the mould was ready, the PDMS was spun on at 600rpm and cured as described. A rectangular section was cut round the channel mould, which was tweezed gently from the SU8 (Figure 7-19). Because of the low adhesion of the SU8 surface, samples were generally removed without damage to the mould nor the PDMS. Figure 7-20 shows the result, focussing on the mid section of the channel. In Figure 7-21 can be seen the channel overlaid on the electrodes.

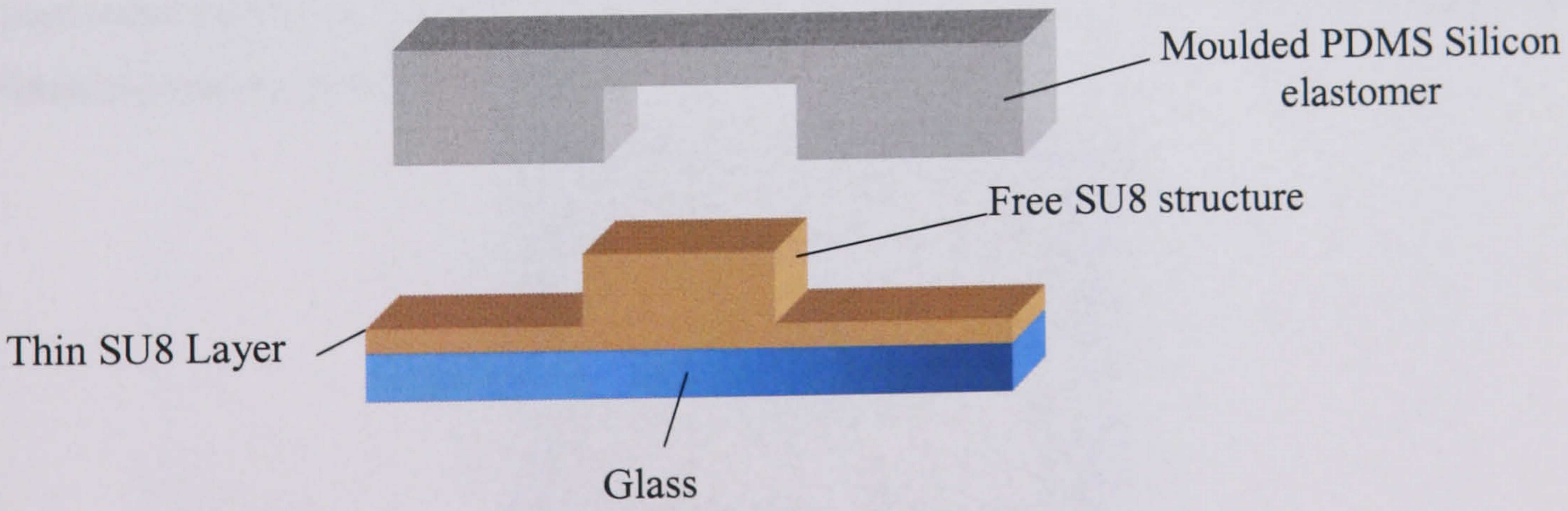

Figure 7-19
Moulded PDMS channel is removed from the SU8

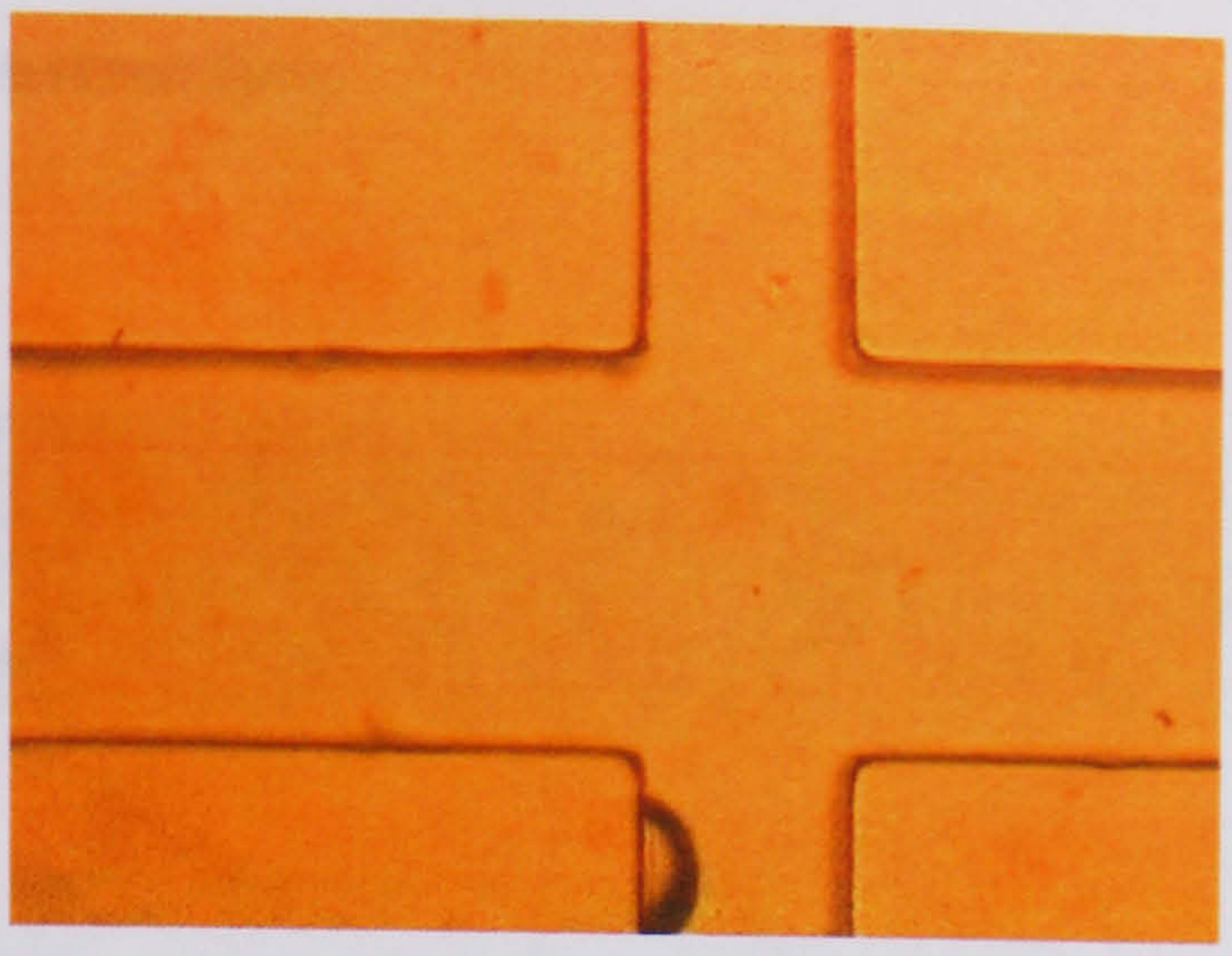

Figure 7-20

Main channel section showing sample injection sub-channels

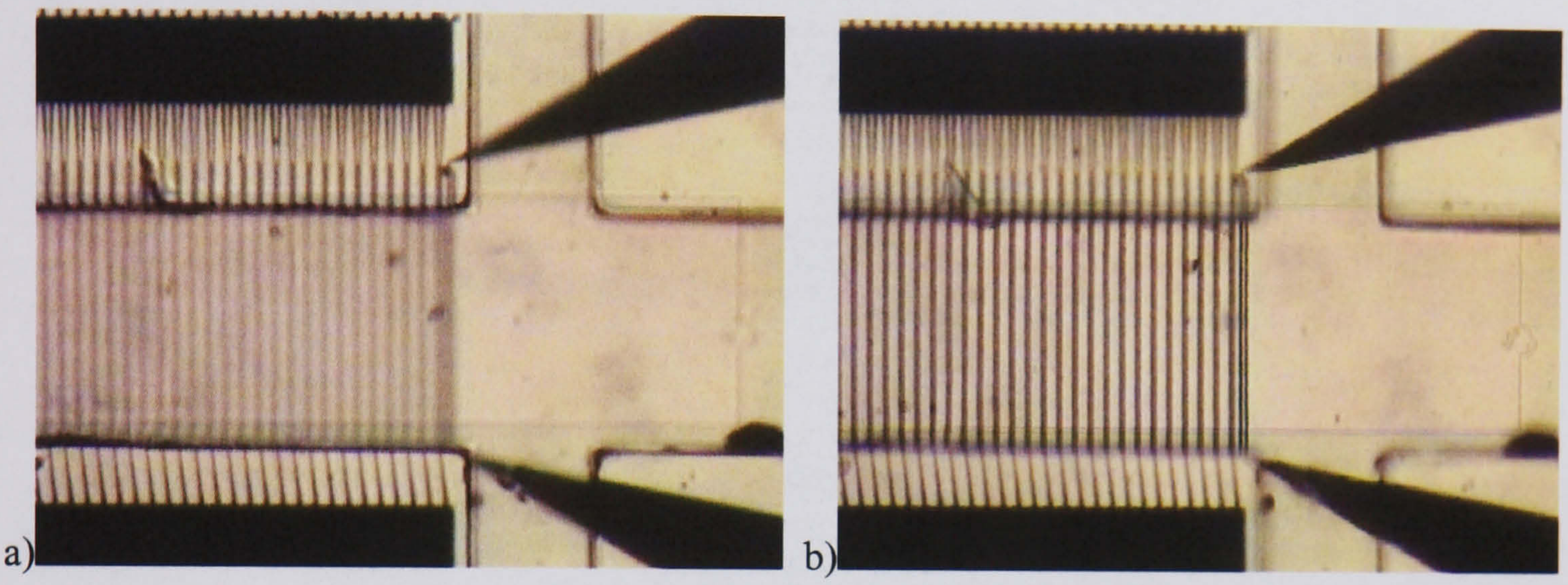

Figure 7-21

Channel positioned on electrodes, focusing on a) channel, b) electrodes.

7.4 Printed Circuit boards

These were fabricated using an acetate mask designed on Corel Draw™ to pattern a photosensitive layer on prefabricated copper coated boards. Exposed copper was removed by ferric chloride and HCl before cleaning in acetone (Figure 7-22).

Figure 7-22

Printed circuit boards for single and triple device layouts

7.5 Final device construction

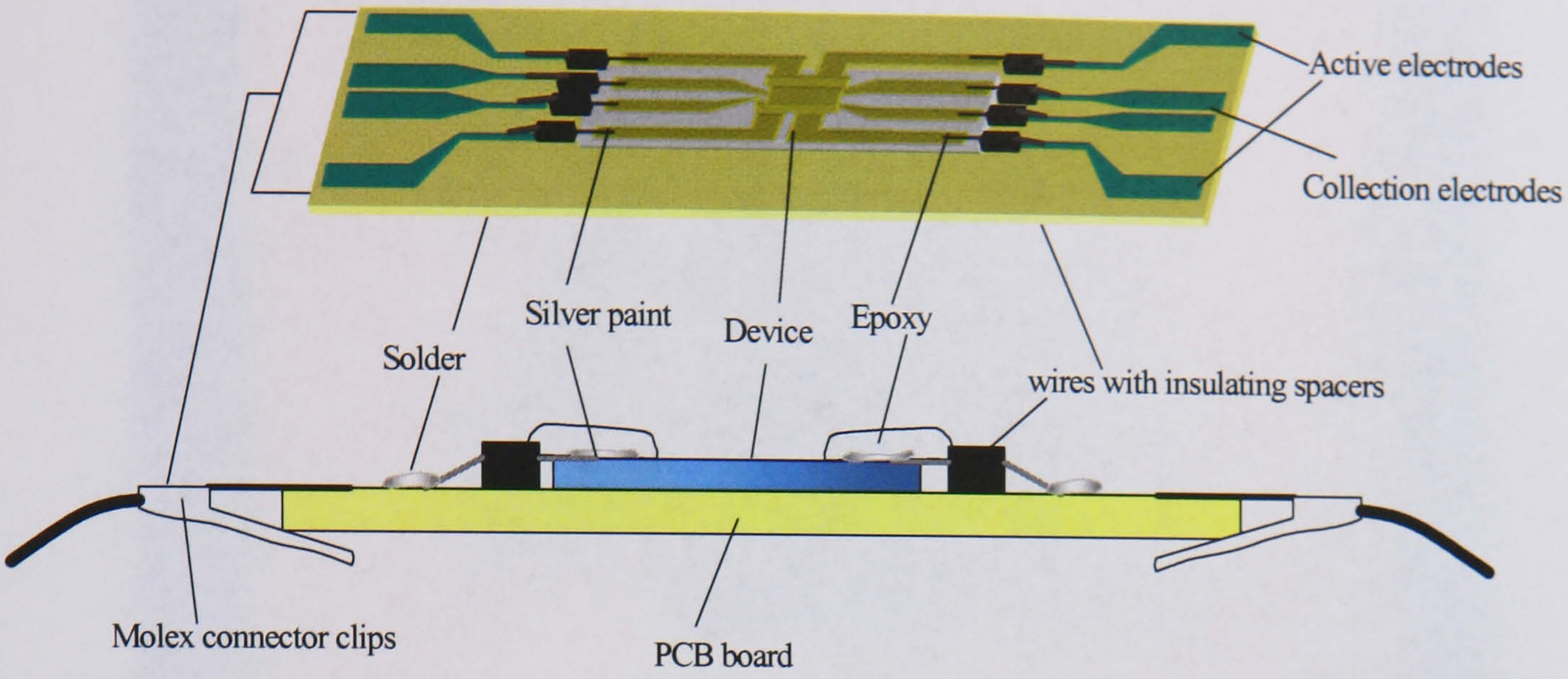

Figure 7-23
Schematic of final device construction

The devices were mounted via insulating wires connected by solder on the PCB. In order to avoid heat damage to the electrodes or insulator, silver paint was used to establish connections on the device and covered with a layer of epoxy for strengthening and to facilitate repeated acetone cleaning. The signals were applied via BNC cables attached to Molex connector clips which could be slotted onto the PCB. A summary of the layout is illustrated in Figure 7-23. In Figure 7-24 and Figure 7-25 the final constructions can be seen in single and triple arrangements.

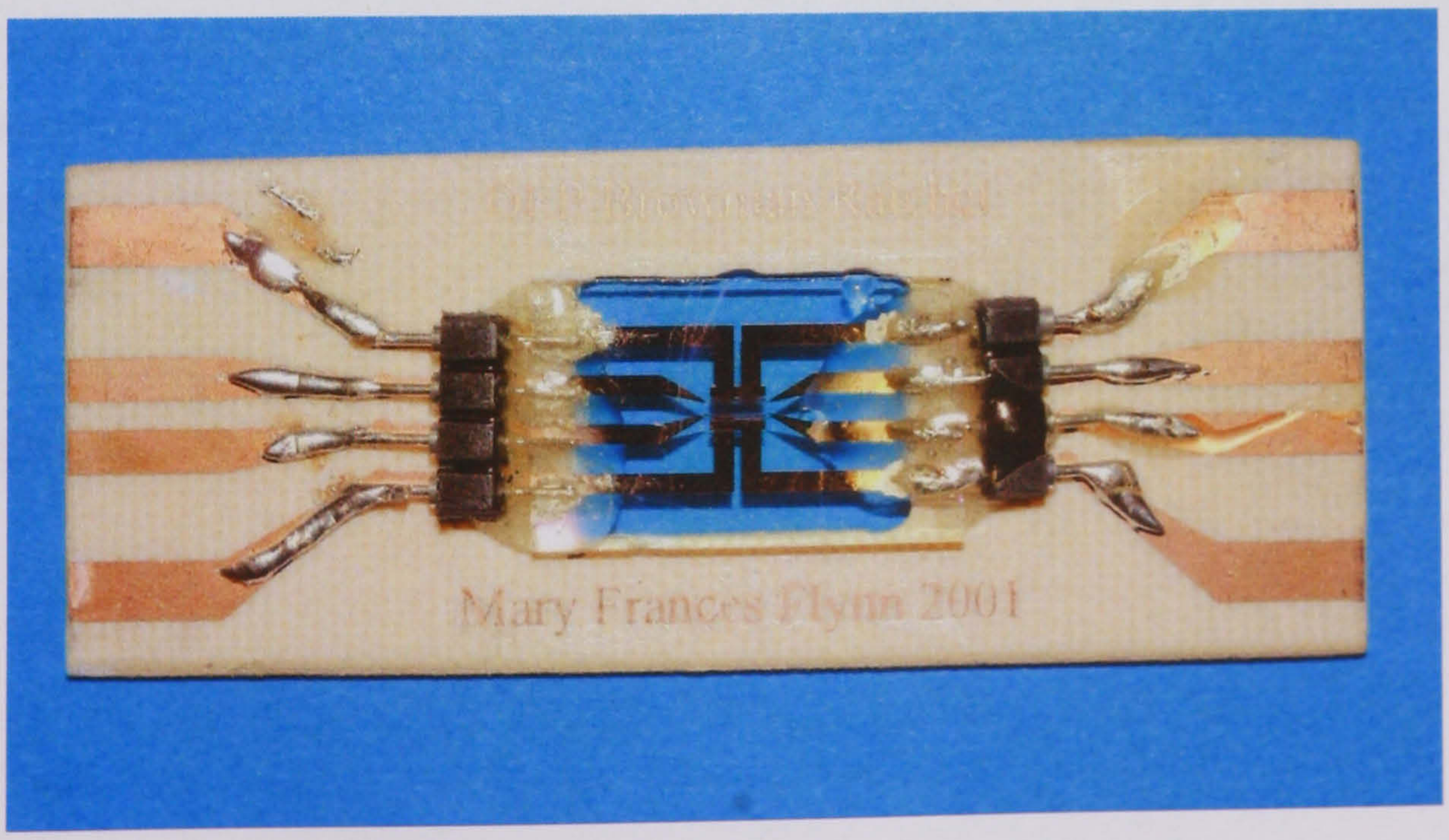

Figure 7-24
Single device

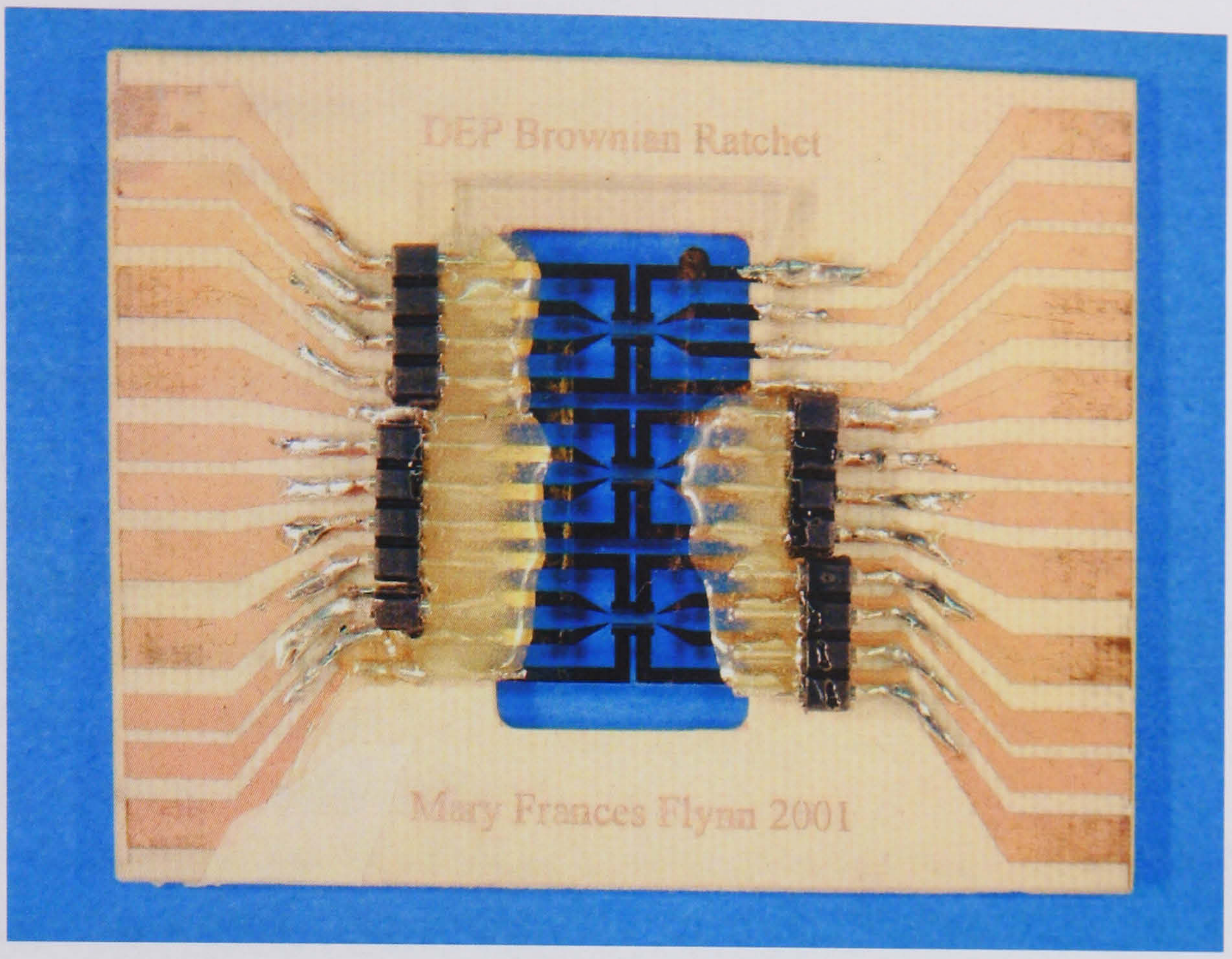

Figure 7-25
Triple device

7.6 Conclusion

The theoretical Brownian ratchet described in Chapter 6 has been designed and built using an adaptation of a method previously utilized on a larger scale. Various modifications have been made in order to accommodate the smaller feature size such as using direct write e-beam lithography for the base electrodes and thicker insulation to overcome the increased likelihood of short circuits. A combination of etch methods has been tried to ensure good connections given the high ratio of insulator width to bonding area with gaseous C_2H_6 found to be optimal. Channel mould functionality has been increased by SU8 bonding of a free SU8 structure thus overcoming the problem of variable SU8-glass adhesion at low surface contact areas. This has resulted in an adequate realization of the requirements of the design concept – in particular the separate addressability of the electrodes and its structuring for use as a microfluidic device.

7.7 References

[1] L. Cui and H. Morgan, "Design and fabrication of travelling wave dielectrophoresis structures", *Journal of Micromechanics and Microengineering*, vol. 10, pp. 72-79, 2000.

[2] N. G. Green, "Dielectrophoresis of sub-micron particles" in *Electrical and Electronic Engineering*: University of Glasgow, 1998, pp. 270.

[3] D. C. Duffy, J. C. McDonald, O. J. A. Schueller, and G. M. Whitesides, "Rapid Prototyping of Microfluidic Systems in Poly(dimethylsiloxane)", *Anal. Chem.*, vol. 70, pp. 4974-4984, 1998.

[4] G. M. Whitesides and A. D. Stroock, "Flexible Methods for Microfluidics", *Physics Today*, pp. 42-48, 2001.

[5] US Patent No. 4882245 , 1989.

[6] P. D. Grossman and J. C. Colburn, *Capillary Electrophoresis: Theory and Practice*. San Diego: Academic Press, 1992.

[7] www.elvisions.com.

8 Particle transport and Separation

8.1 Introduction

The aim of this chapter is to verify experimentally that the postulated new electrode array design does indeed function as a dielectrophoretic Brownian ratchet pump. Ideally, this would involve the visible transportation of a localised group of particles through the device. The functionality of the initial collection electrodes is therefore investigated and the necessity of a channel demonstrated. It has been established that in order to qualify as a Brownian ratchet a system must display two essential properties – an asymmetric potential in the on-cycle and free diffusion around the previous potential minima in the off-cycle. In order to uniquely infer the presence of unidirectional global transport, then, it is enough to demonstrate that asymmetric collection occurs followed by symmetric diffusion. This is investigated via image processing of the microscopic images of the functioning device

8.2 Experimental set up

The experimental arrangement (Figure 8-1) consisted of a pair of signal generators connected via a two way relay to a square wave function generator (Figure 8-2). In this way the signal could be periodically switched by applying a square wave potential from the function generator, where the on-off cycle was governed by the period and symmetry of the signal. The device was mounted on a steel clamp, allowing access to the connector pads which could be attached via removable Molex clips to the power source. A Nikon fluorescent microscope and digital camera were used to observe the images and recordings made onto video tape. A photograph of the complete set-up is shown in Figure 8-3.

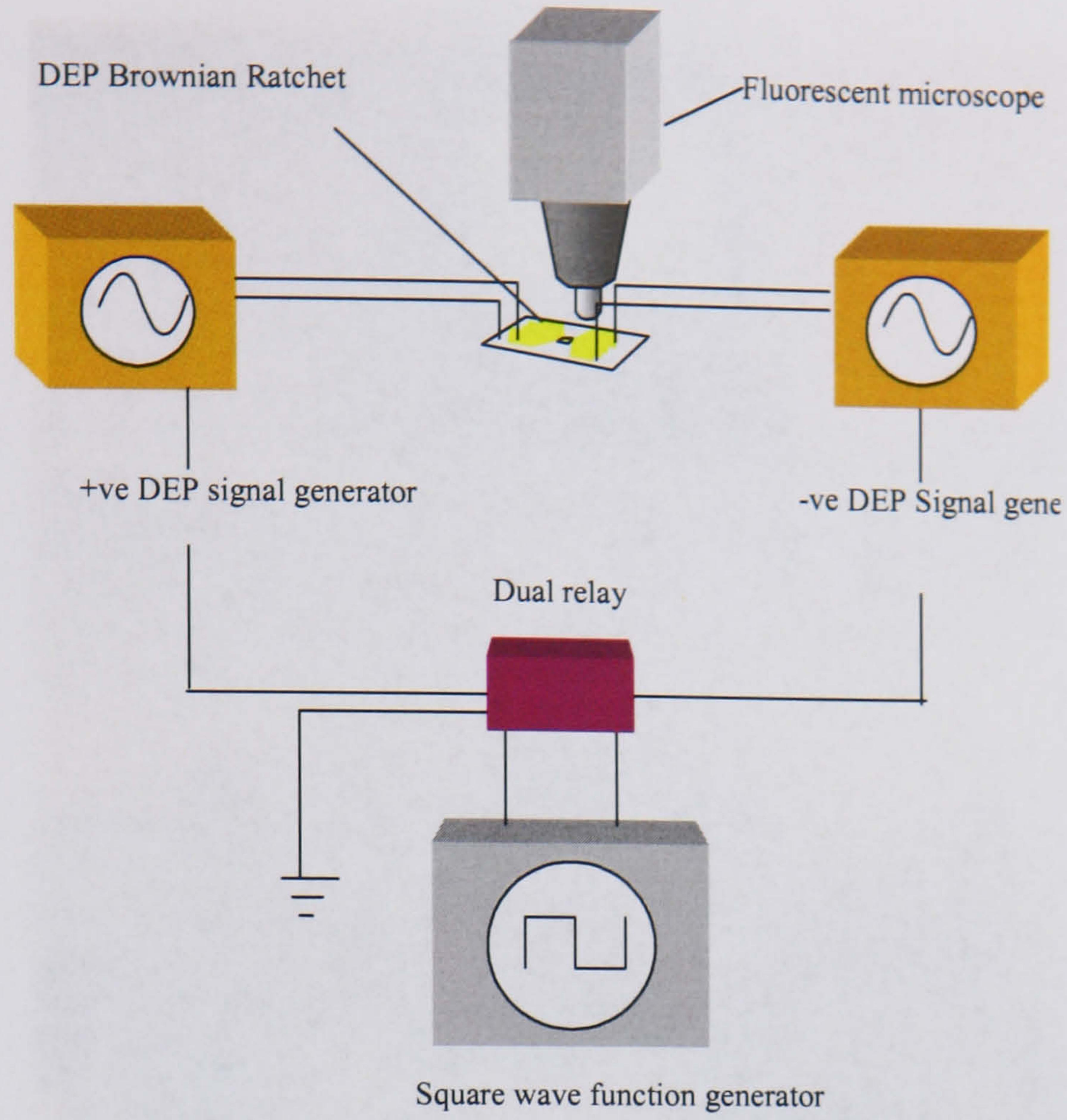

Figure 8-1
Experimental set up

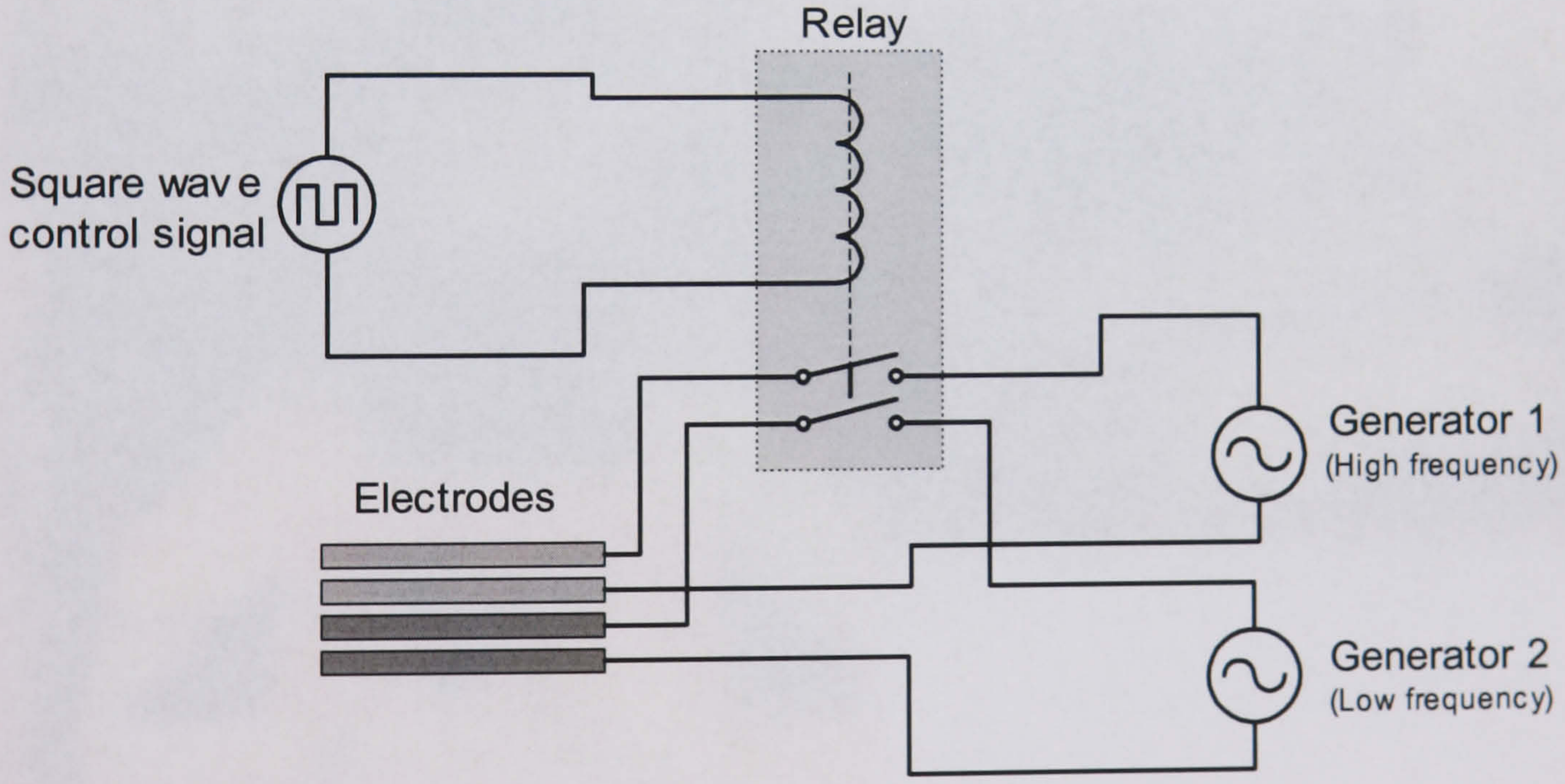

Figure 8-2
Schematic of dual relay system used to synchronise applied signals

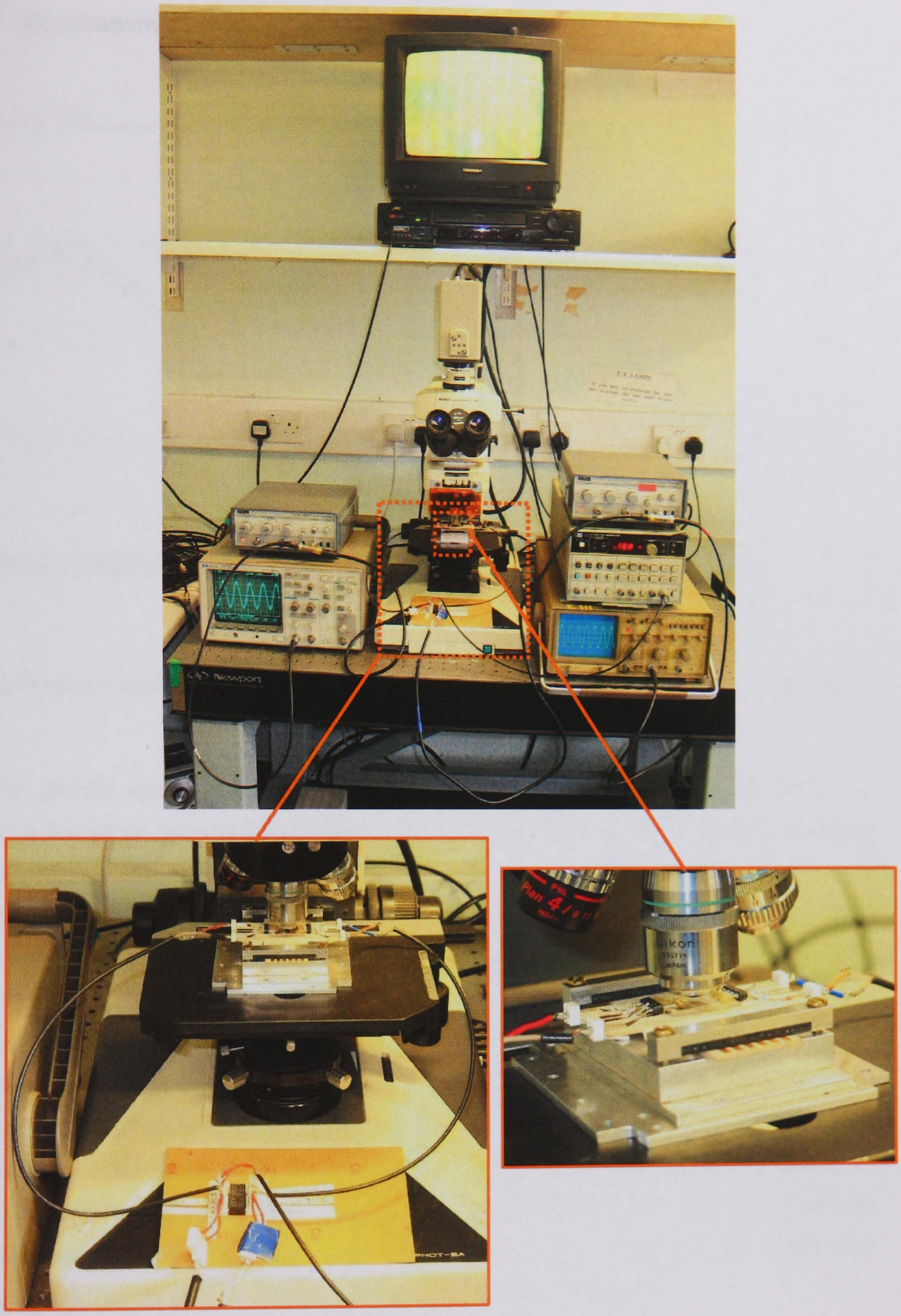

Figure 8-3

Photograph of Brownian ratchet laboratory set-up highlighting relay connections and device fitting on microscope table.

8.3 Simultaneous positive and negative DEP

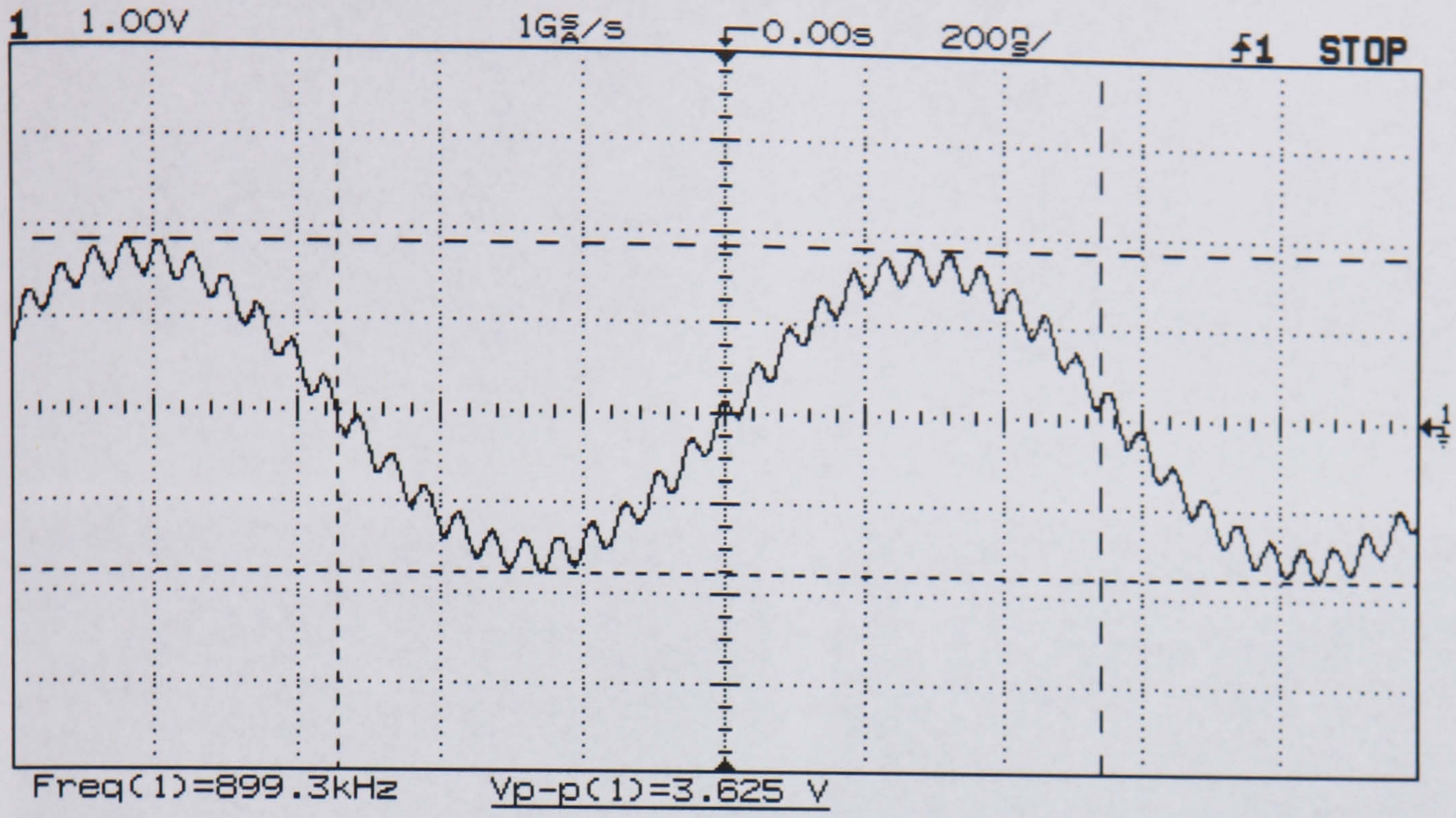

Figure 8-4

Oscilloscope reading on low frequency electrodes showing the effect of the adjacent high frequency

The applied signals on the 4 electrode device were monitored using an oscilloscope in order to assess the level of interference. Due to the proximity of the electrodes combined with induction effects within the relay some mutual influence between the signals was observed. The high frequency superposition on the low frequency signal of the positive DEP electrodes is shown in Figure 8-4. The simultaneous action of high and low frequencies on the juxtaposed pairs was initially investigated. Figure 8-5 shows the result of interchanging the applied frequencies from high/low to low/high. Initially particles are repelled from the left hand (LH) electrode pair. If no signal was applied to them the low frequency field on the RH pair would also cause collection here (as shown in the field simulation, Chapter 6). On increasing the RH frequency to produce negative DEP and lowering that of the LH pair the particles can be seen to move across the gap and collect on the now positively dielectrophoretic LH electrodes. The preservation of the shape of the distribution demonstrates the motion is essentially perpendicular to the electrodes.

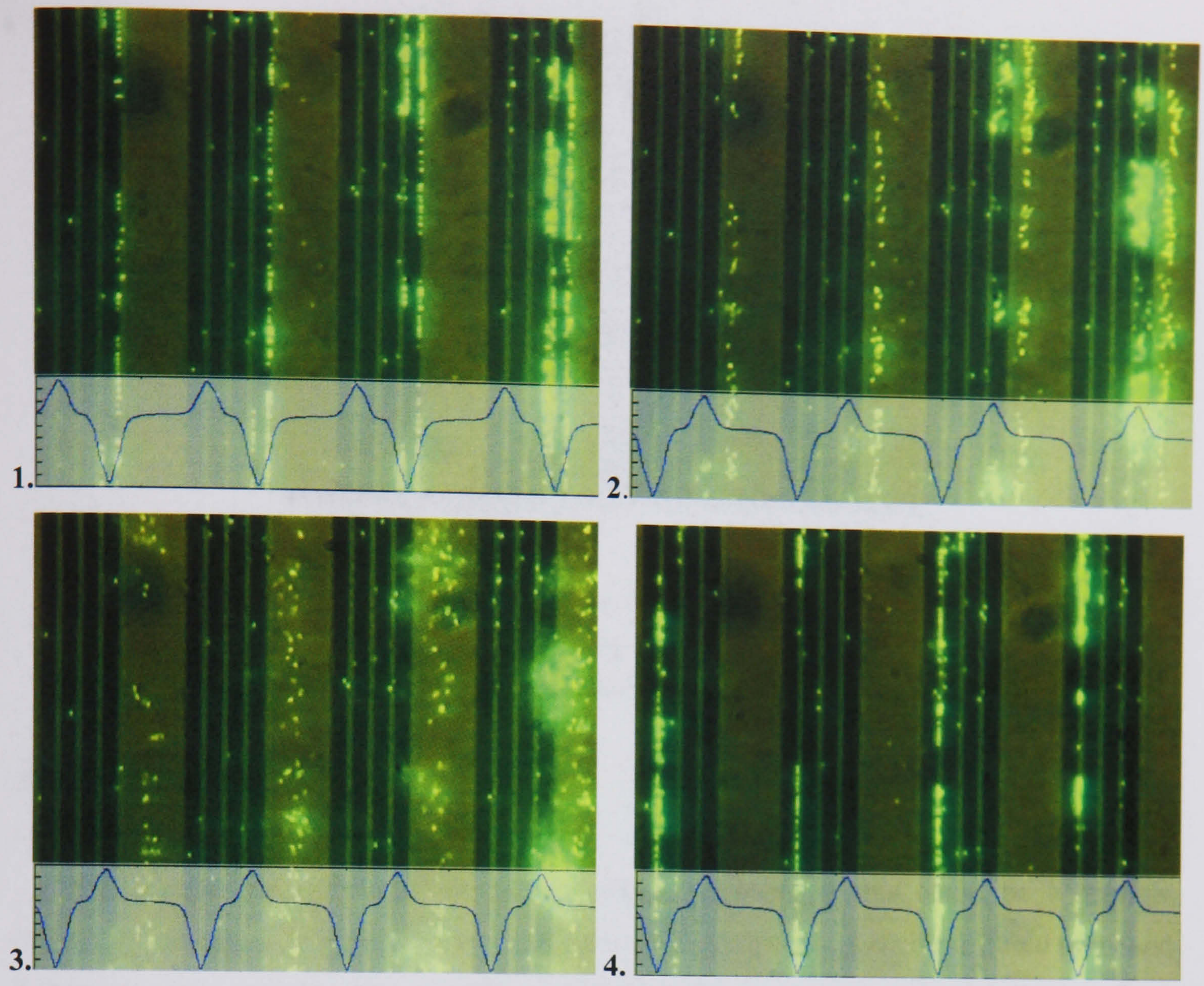

Figure 8-5

Swapping of simultaneously applied high and low frequencies. Trace overlay is the potential simulated in Chapter 6, with the direction switched after plot 1. Time between frames ~ 0.5.

8.4 3-electrode design

The 3-electrode design similarly supported the juxtaposition of positive and negative DEP, although the voltages of the applied signals had to be more in balance to avoid domination of one force over the entire electrode group. Figure 8-6 shows the movement of the positive DEP potential minimum to the outermost electrode edge when a higher voltage is applied to the negative DEP electrodes. This is also possible on the 4-electrode device although the difference in voltages must be significantly greater, alluding to a higher level of flexibility of the potential shape of the latter. The fundamental characteristics of the devices remain the same, however, and therefore they do not require separate analyses in terms of their collection properties – although the 3-electrode device is nonetheless useful for illustration purposes with the localization on a single electrode edge providing greater photographic clarity without need of excessively high negative DEP voltages. The devices are therefore used interchangeably with only minor differences to the observed performances.

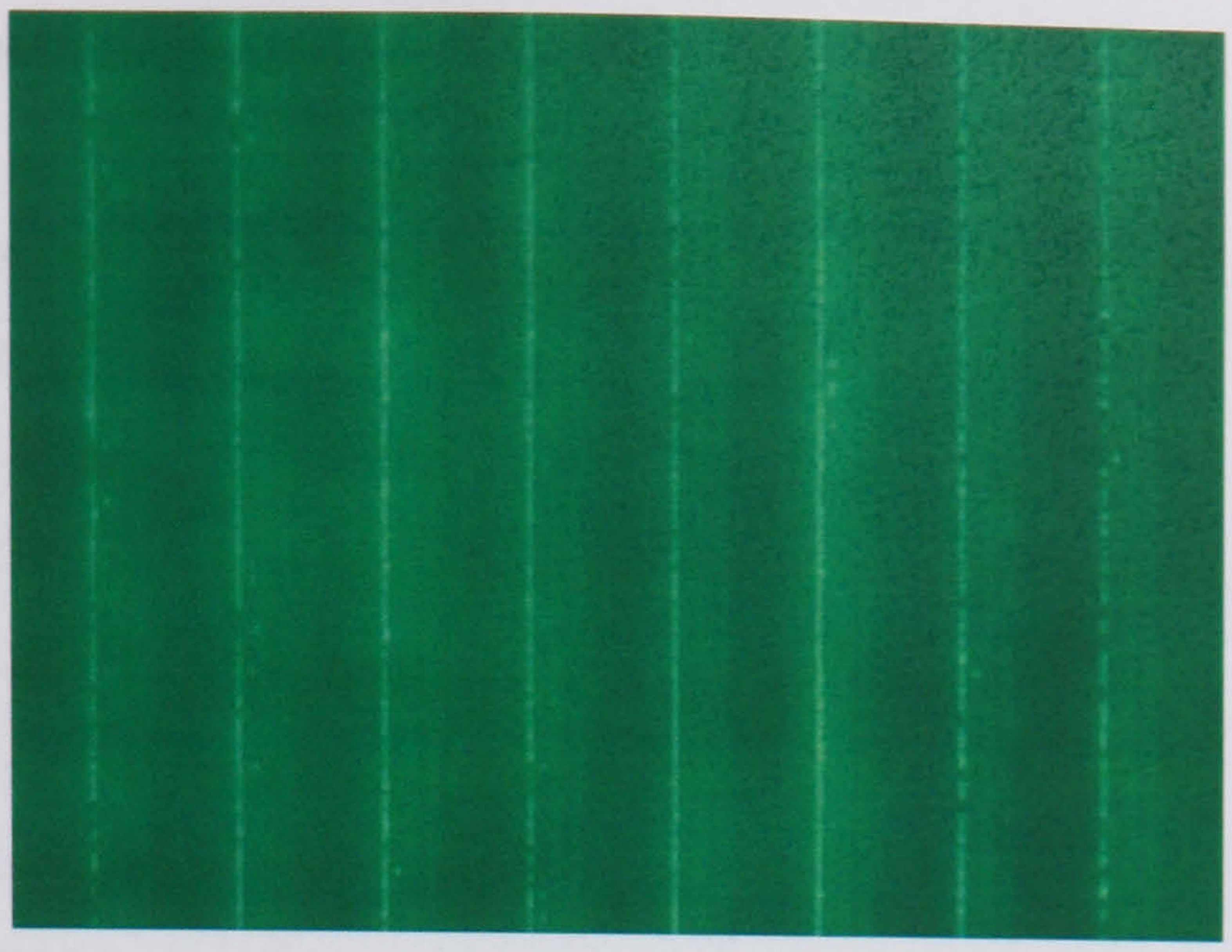

Figure 8-6

3-electrode device showing localisation on a single electrode edge when negative DEP potential is increased

8.5 Channel requirement

The devices were first tested without channels to see if this could be a feasible experimental approximation. However during the off-cycle many particles diffused away and in the on-cycle particles did not collect asymmetrically even at a substantial distance from the electrode ends due to the diffusion flux (Figure 8-7). Therefore one of the two channel constructions described in Chapter 7 was used for subsequent experiments.

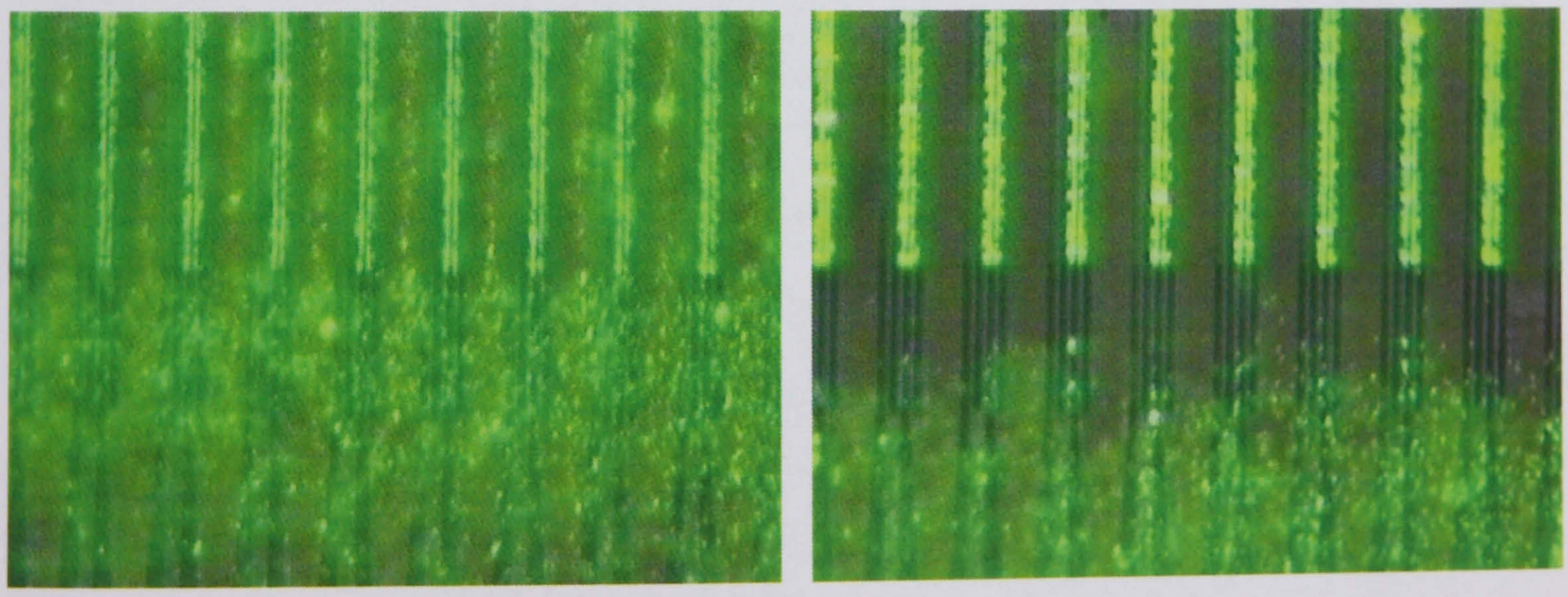

Figure 8-7

Diffusing particles in the on-cycle causing a flow with a parallel component to the electrodes which impedes asymmetric collection.

8.6 Initial Collection

The effectiveness of localising an initial distribution of particles for the purpose of demonstrating a group asymmetric drift was investigated. The device was filled with aqueous buffer and a slug of particles injected into the cross bar of the channel to the activated collection electrodes. However at high particle concentration ($5x10^{-3}$ bottle concentration i.e. $\sim 10^{-4}$ v/v) the particles quickly diffused a substantial distance into the channel (Figure 8-8). Lowering the concentration by a factor of 10 resulted in a somewhat more confined distribution (Figure 8-9) but only at extremely low bead concentrations ($\sim 1/10^6$) was it possible to localise particles only on the collection electrodes (Figure 8-10). However, due to the short range of the DEP force compared to the channel height, many beads still remained suspended above the electrodes and were free to diffuse along the channel. This was evident on activating the Brownian ratchet electrodes which caused extra particles to collect at arbitrary points along the channel, not necessarily only those transported from the previous consecutive electrode group. In order to rigorously demonstrate any ratchet-induced net group drift, then, the channel height would have to be considerably lower (O(~10μm)) so that all injected particles could be within the initial collection range.

8.7 Image Processing

Video sequences were transferred to computer as AVI files using Miro frame-grabbing software and subsequently converted to TIF files using the Morgan codec package. These could be averaged over specified time intervals with Jasc image processing software and analysed using Matlab.

8.7.1 Matlab intensity analysis

In order to measure the quantity of beads present, the basic program strategy was to sum the total intensity of the averaged images along columns parallel to the electrodes. The relationship between intensity and bead quantity was taken to be one of approximate linear proportionality at low bead concentrations. However, as can be seen from section 8.9.2, at higher concentrations overlap results in some saturation of the signal so that the response becomes non-linear and the summed intensity is more representative of the character of the distribution rather than exact numerical quantity.

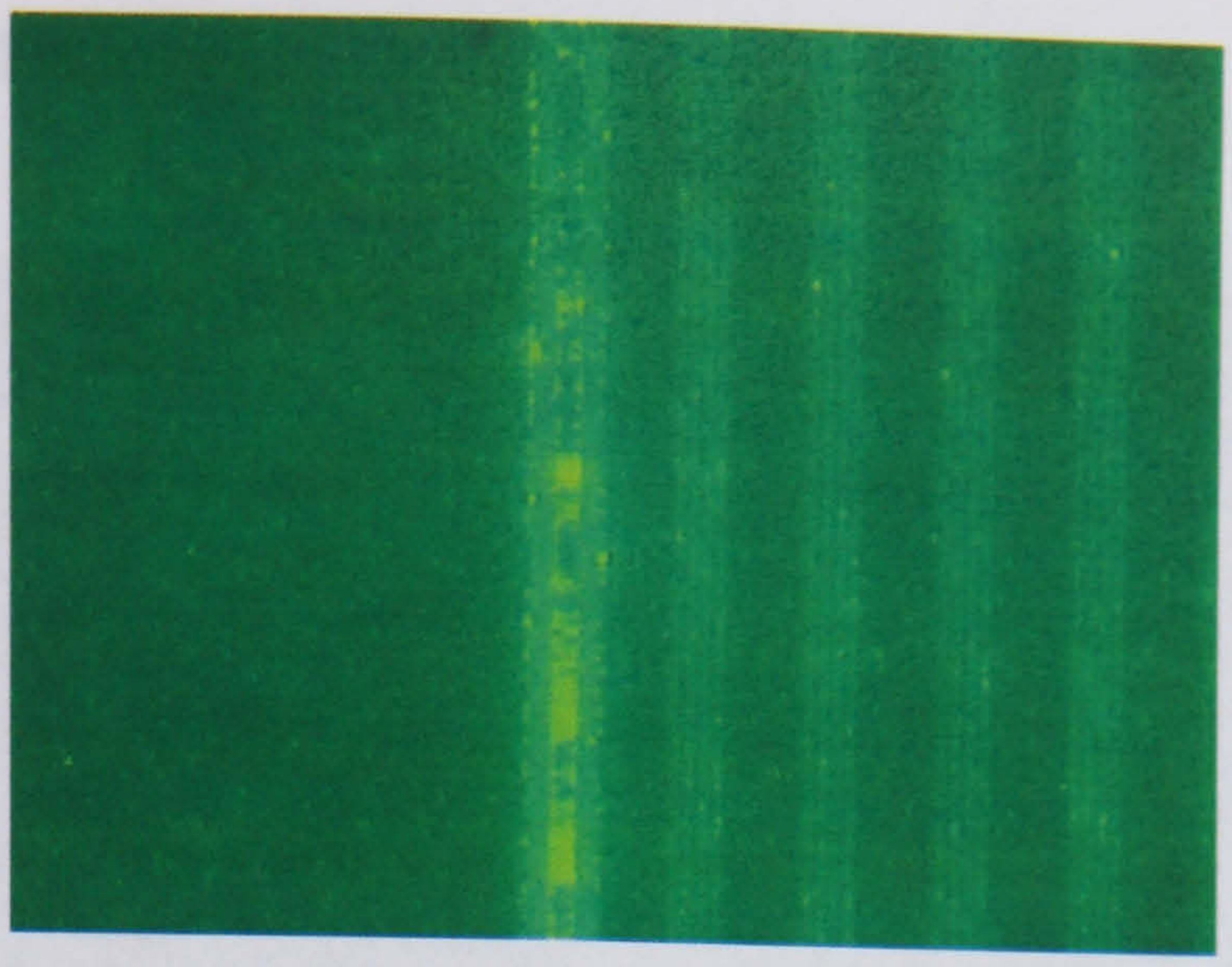

Figure 8-8

Initial collection with high bead concentration (10^{-4}v/v). Beads rapidly diffuse into the channel on saturation of collection electrodes.

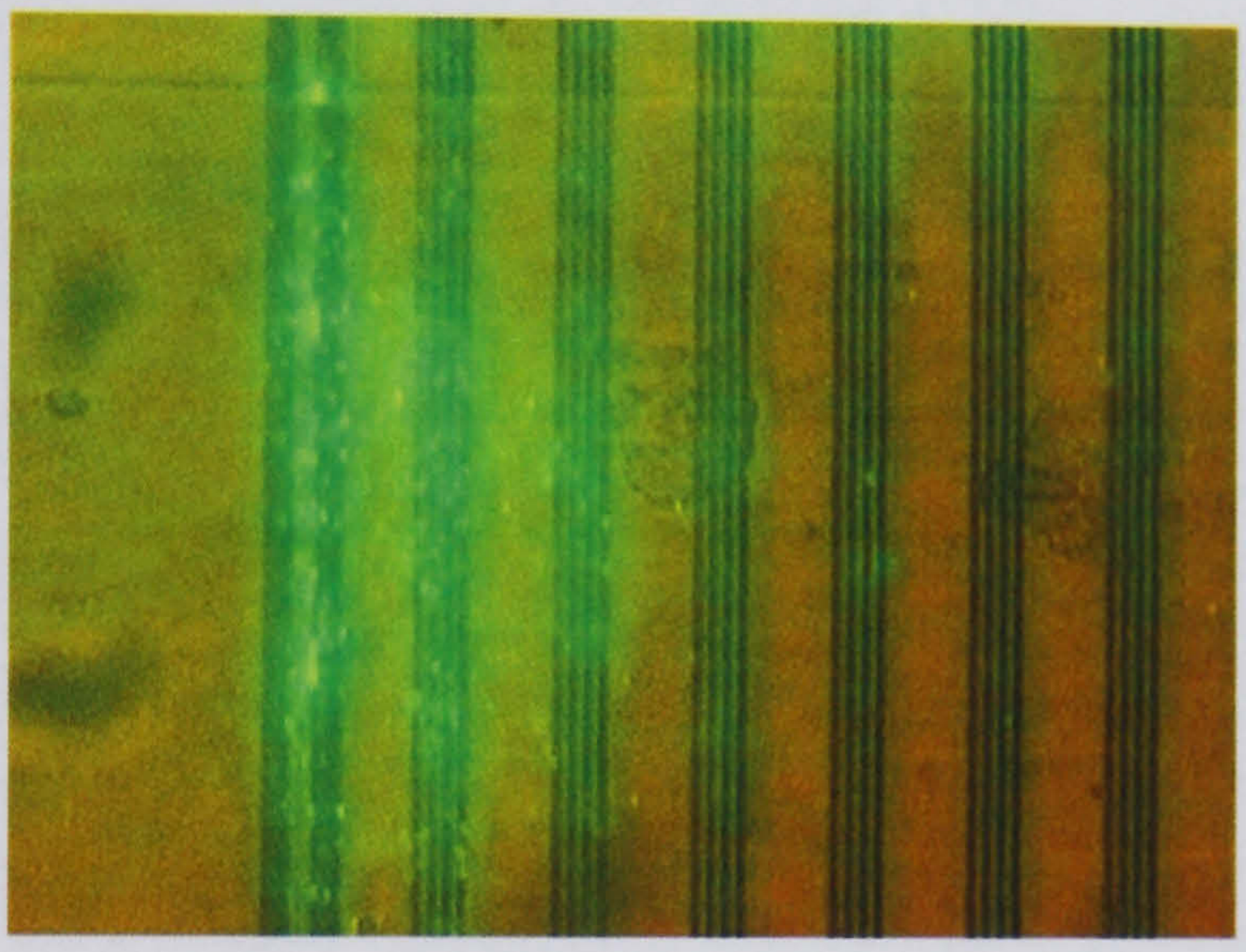

Figure 8-9

Lower bead concentration (10^{-5}v/v)

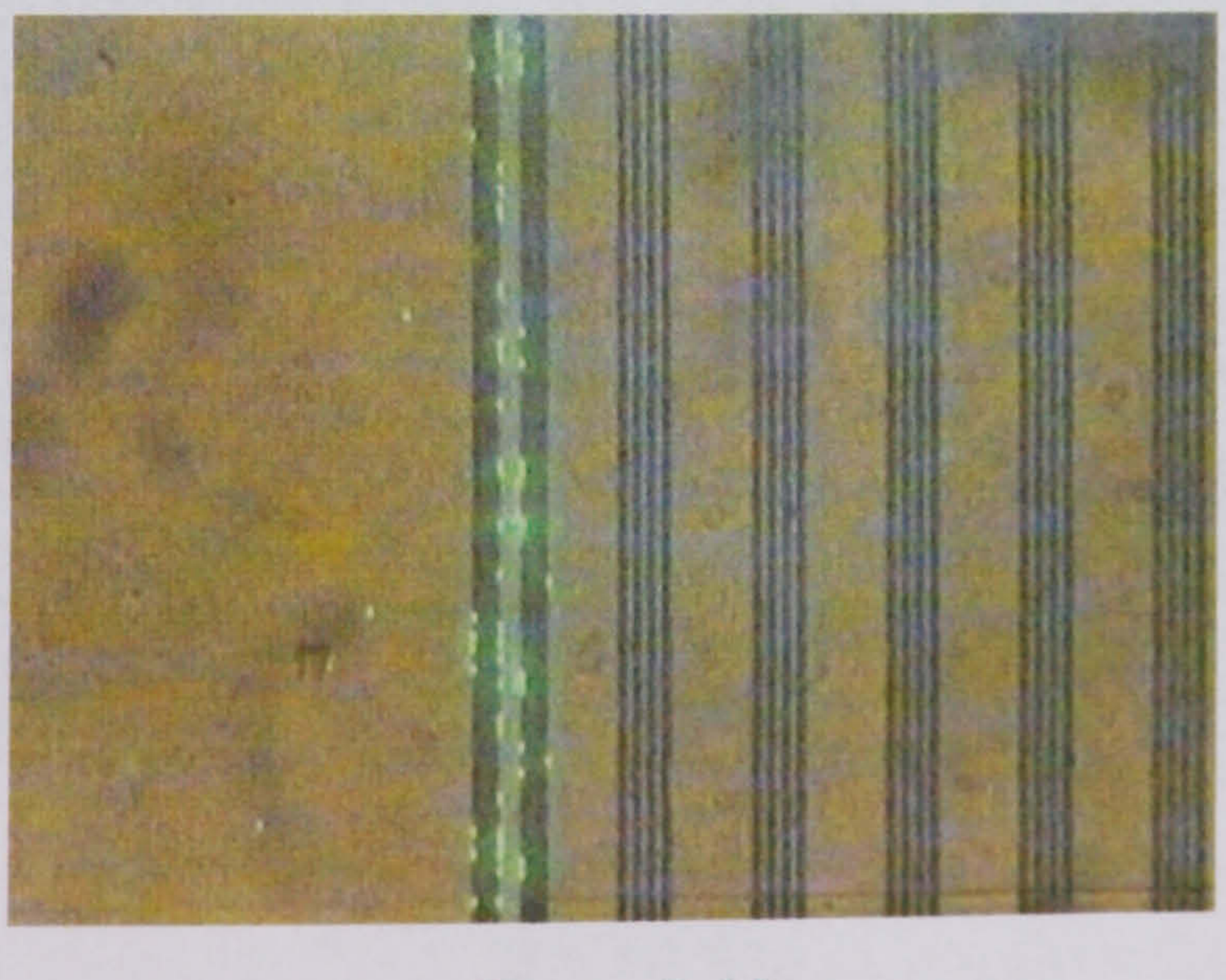

Figure 8-10

Lowest bead concentration (10^{-6}v/v). Localisation is only apparent, however, with a number of beads still suspended above the electrodes.

8.8 Asymmetric Transport

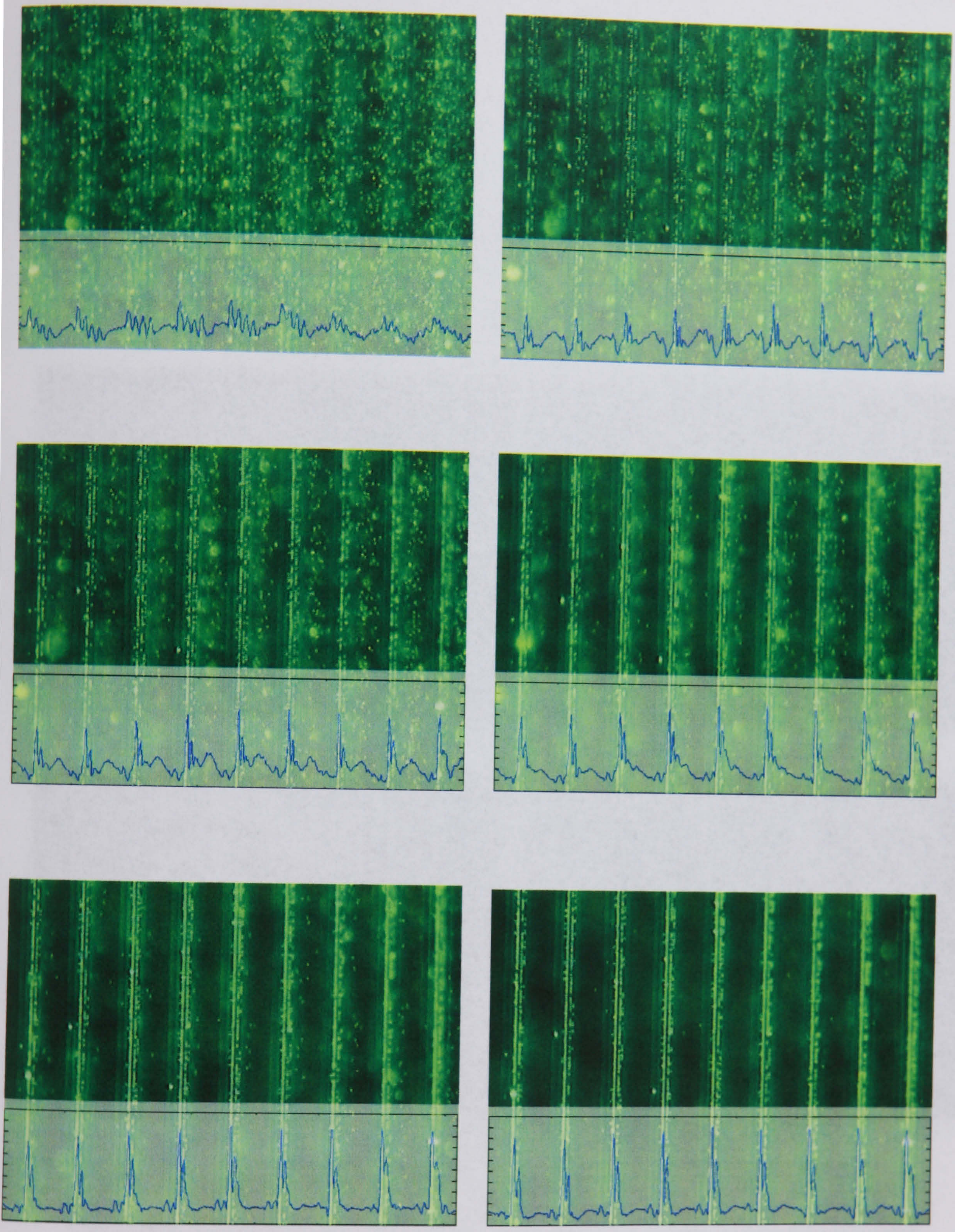

Figure 8-11

Video sequence processed on Matlab to show asymmetric collection over a period of 1.4s

It can be seen from the processed images that the parallel electrode design does indeed induce asymmetric transport in the on cycle (Figure 8-11). The Matlab produced intensity curves show a marked repulsion from the negative DEP electrodes with the beads collecting from any position in the large gap towards the positive electrodes on the left. Thus the potential gradient from maximum (negative DEP electrodes) to minimum (positive) is always negative as predicted.

8.8.1 A closer inspection

Conversion of the images to binary data by threshholding the image to exclude residual light scattering from beads out with the focal plane (Figure 8-12) allowed the movement of the individual beads to be examined more closely.

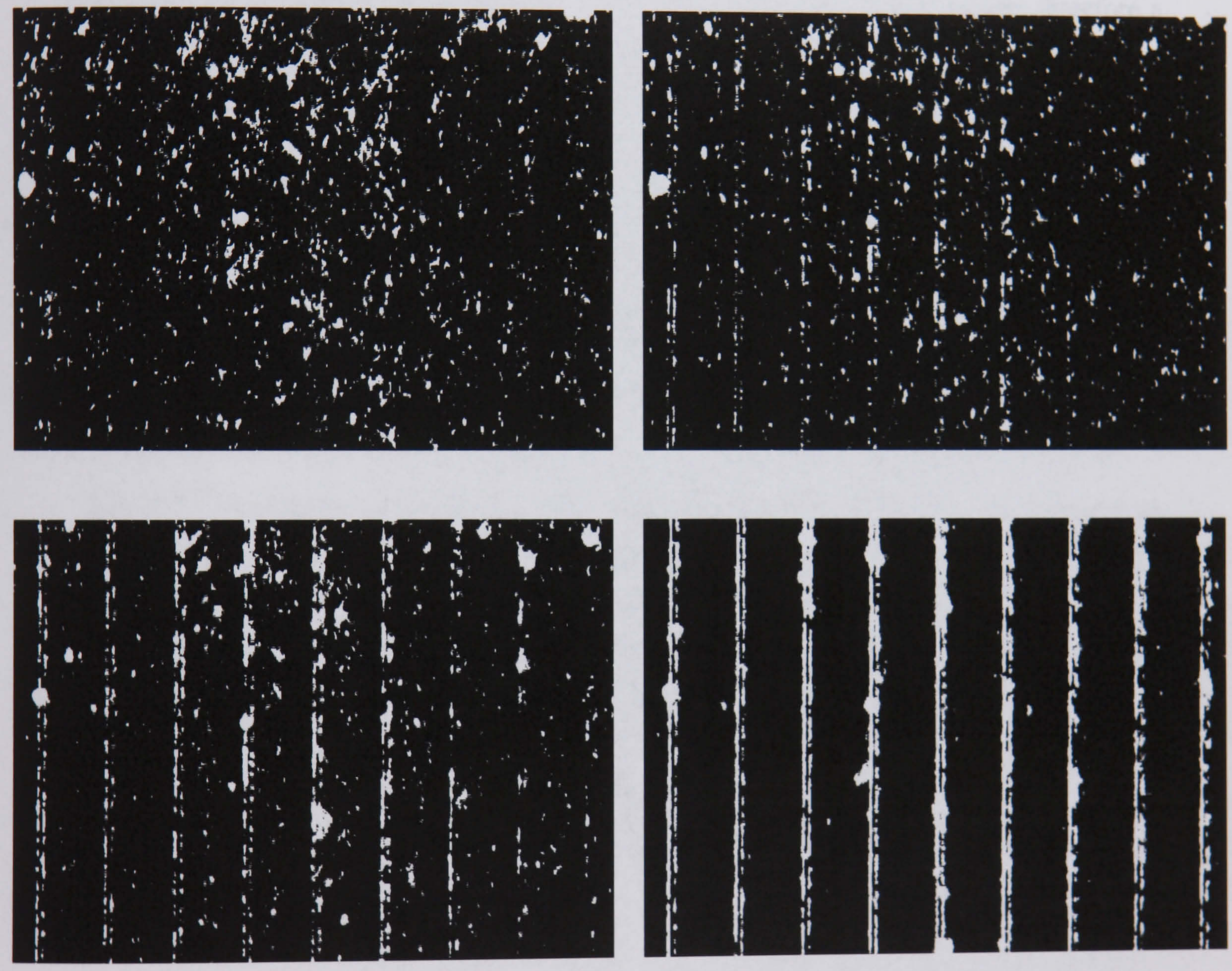

Figure 8-12

Conversion to binary data allows beads to be discerned without interference from residual light scattering

Figure 8-13 shows the Matlab output for one electrode period, where, after this processing, a cluster of beads can be followed moving across the inter-electrode gap.

Observing the shape of the distribution allows an approximate delineation of the potential in this region.

On activation of the electrodes the particles can be seen to be immediately repelled from and attracted to the potential maximum and minimum respectively. The shape of the distribution is rapidly distorted around these areas since the force, as shown in the simulations, is highly non-linear. The repelled beads quickly accumulate on the edge of this region in a distribution which travels along essentially undistorted until reaching the next non-linear region, where attractive tidal forces again cause break up. The motion of the peak of this distribution is shown in Figure 8-14, and is *essentially constant*. This implies the presence of a constant linear force which is balanced by Stokes drag. The potential as predicted by the field analysis, however, is basically flat in the central region, therefore a numerical comparison of the required and actual forces is necessary.

The DEP force required to produce this velocity is

$$F = 2\pi a^3 \varepsilon_m \operatorname{Re}(K(\omega))\nabla E_{rms}^2 = 6\pi\eta r v$$

Substituting in values for a, η and v – 108×10^{-9} m, 10^{-3}Ns/m and, from Figure 8-14, 7.26×10^{-6} m/s respectively, gives a required force to balance Stoke's drag of 1.4×10^{-14} N.

For this size of beads, the DEP force from the simulations at unit amplitude voltages is 6.3×10^{-16} N (Figure 8-15). Scaling for the applied voltages of 4V peak to peak on the positive DEP electrodes and 8V on negative and converting to r.m.s. produces an additional factor of 12 from the DEP force equation, assuming the Claussius-Mossotti factors to be at the positive and negative limits of 1 and -0.5 respectively, i.e:

$$F_{DEP}\ Scale\ factor = 2\times\left(\underbrace{\left(\frac{2}{\sqrt{2}}\right)^2}_{+ve\,DEP} + 0.5\underbrace{\left(\frac{4}{\sqrt{2}}\right)^2}_{-ve\,DEP}\right)$$

Thus the ratio of Stokes drag to the DEP force is 1.75. This is somewhat high although in the right order of magnitude. The measurement of the drift velocity constitutes a considerable approximation which could account for the discrepancy or there may be additional forces in the system. This will be explored further in Chapter 9. Nonetheless, asymmetric transport is clearly observed and therefore one of the two essential criteria of Brownian ratchet pumping fulfilled.

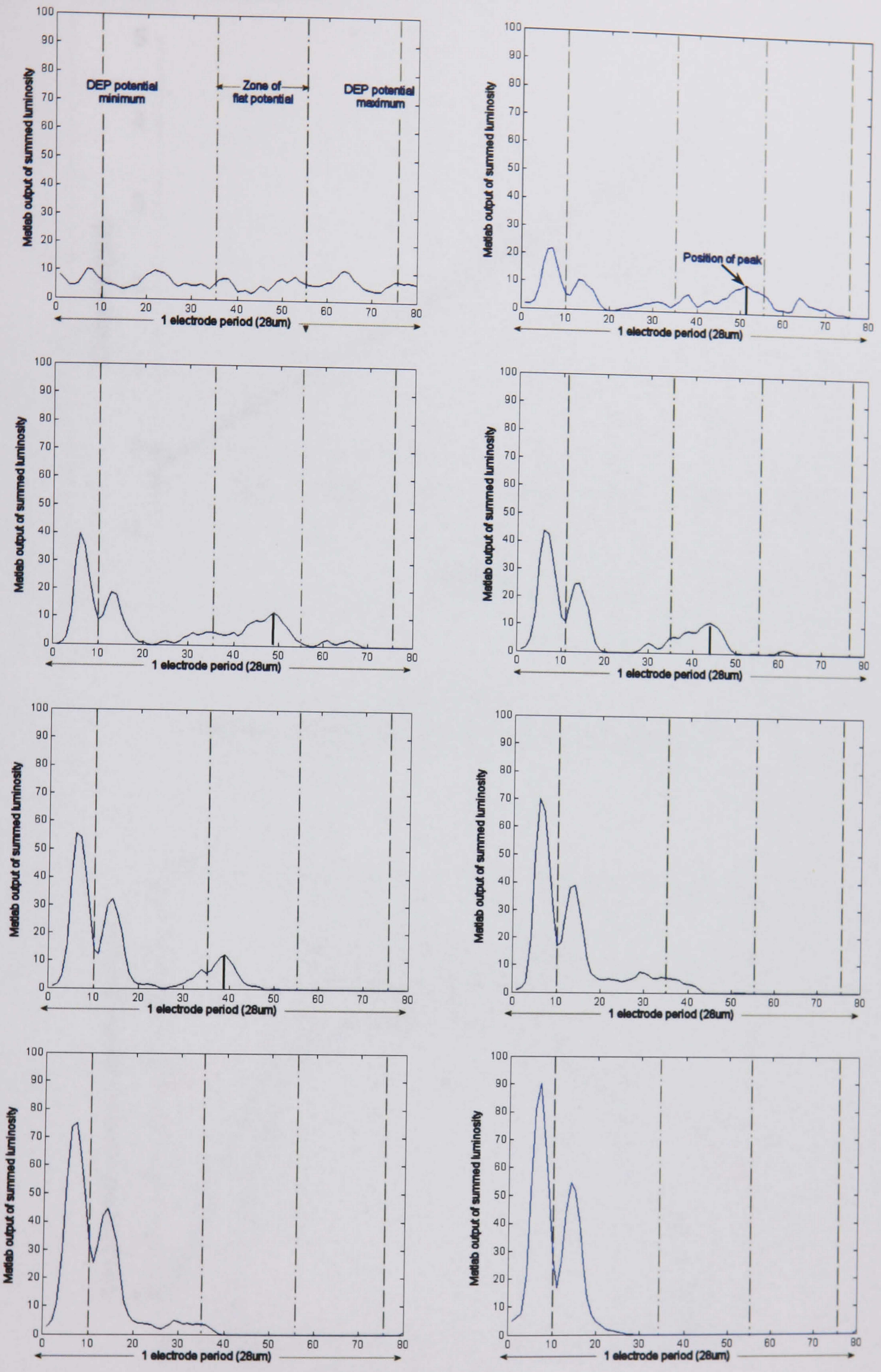

Figure 8-13

Collection of 216nm beads in the device shown at 200ms interval, spatially averaged over 8 electrode period, following image conversion to binary data

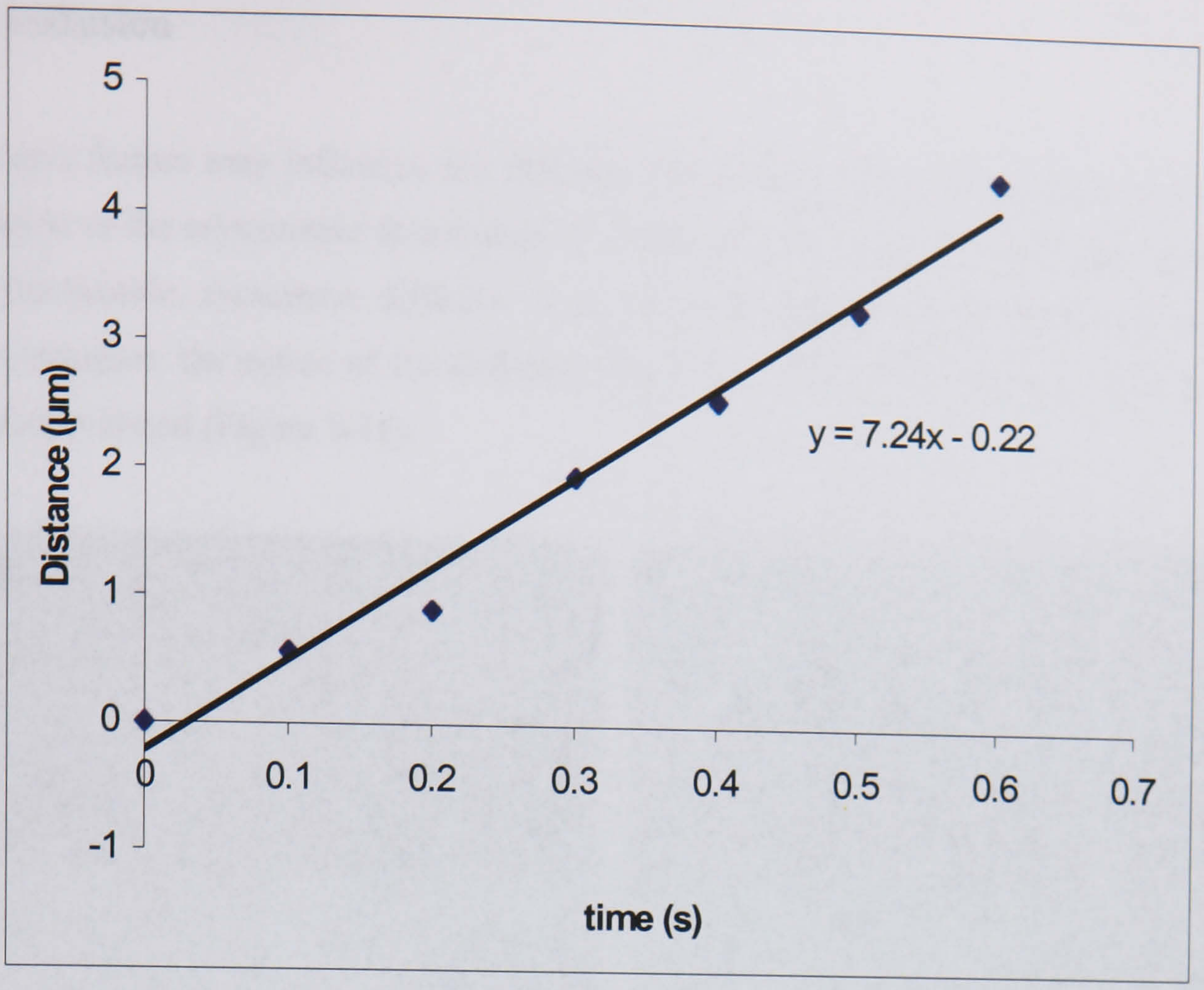

Figure 8-14

Uniform velocity of particles in flat potential section

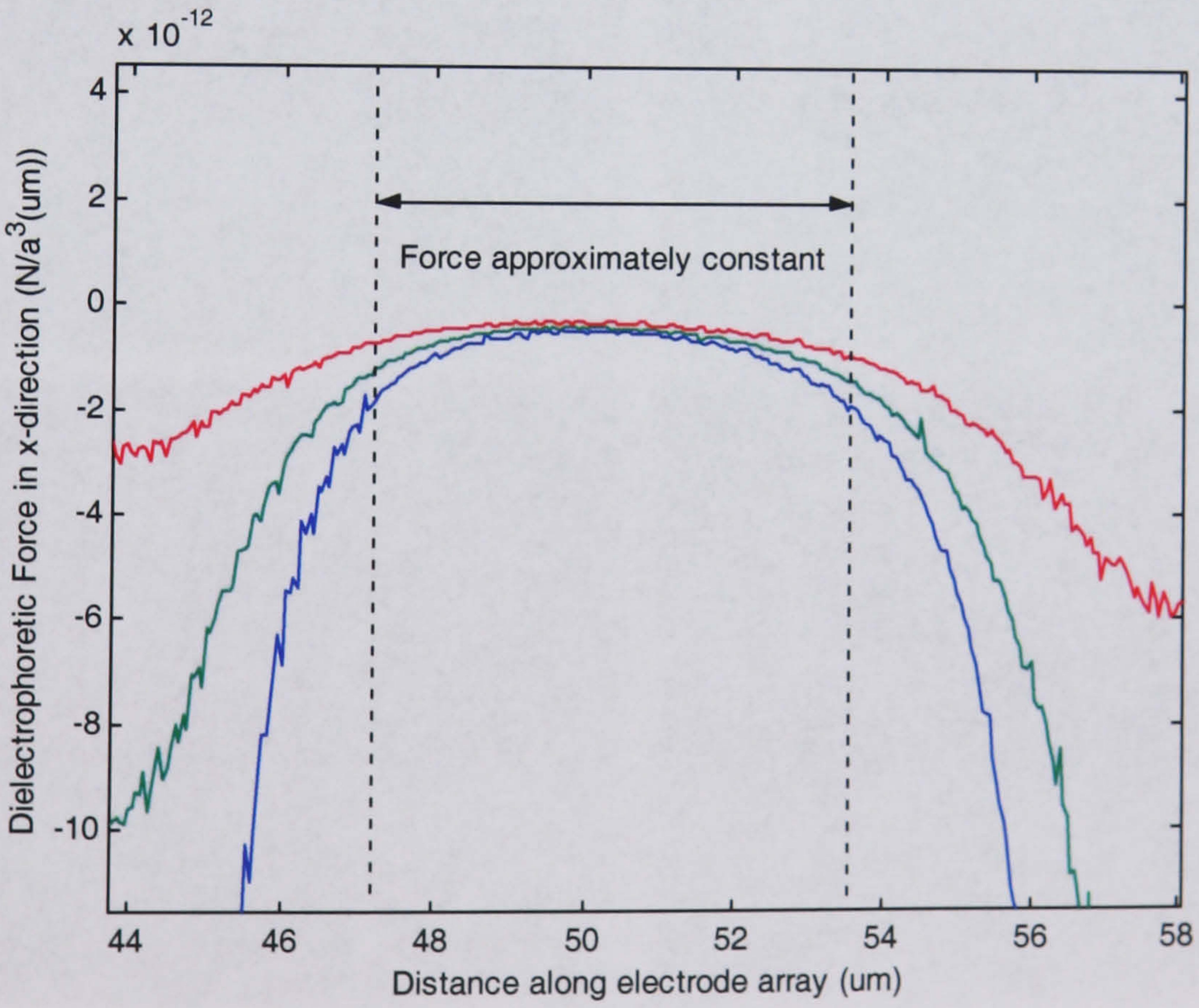

Figure 8-15

Force profile between electrode clusters delineating region highlighted in Figure 8-13

8.9 Diffusion

Several factors may influence the diffusion properties of the system such as a charged suspension or the asymmetric distribution of electrodes with respect to the potential minima. Since predictable, symmetric diffusion is an essential requirement of controlled Brownian ratchet transport, the nature of the diffusion was closely observed using the frame grabbing procedure outlined (Figure 8-16).

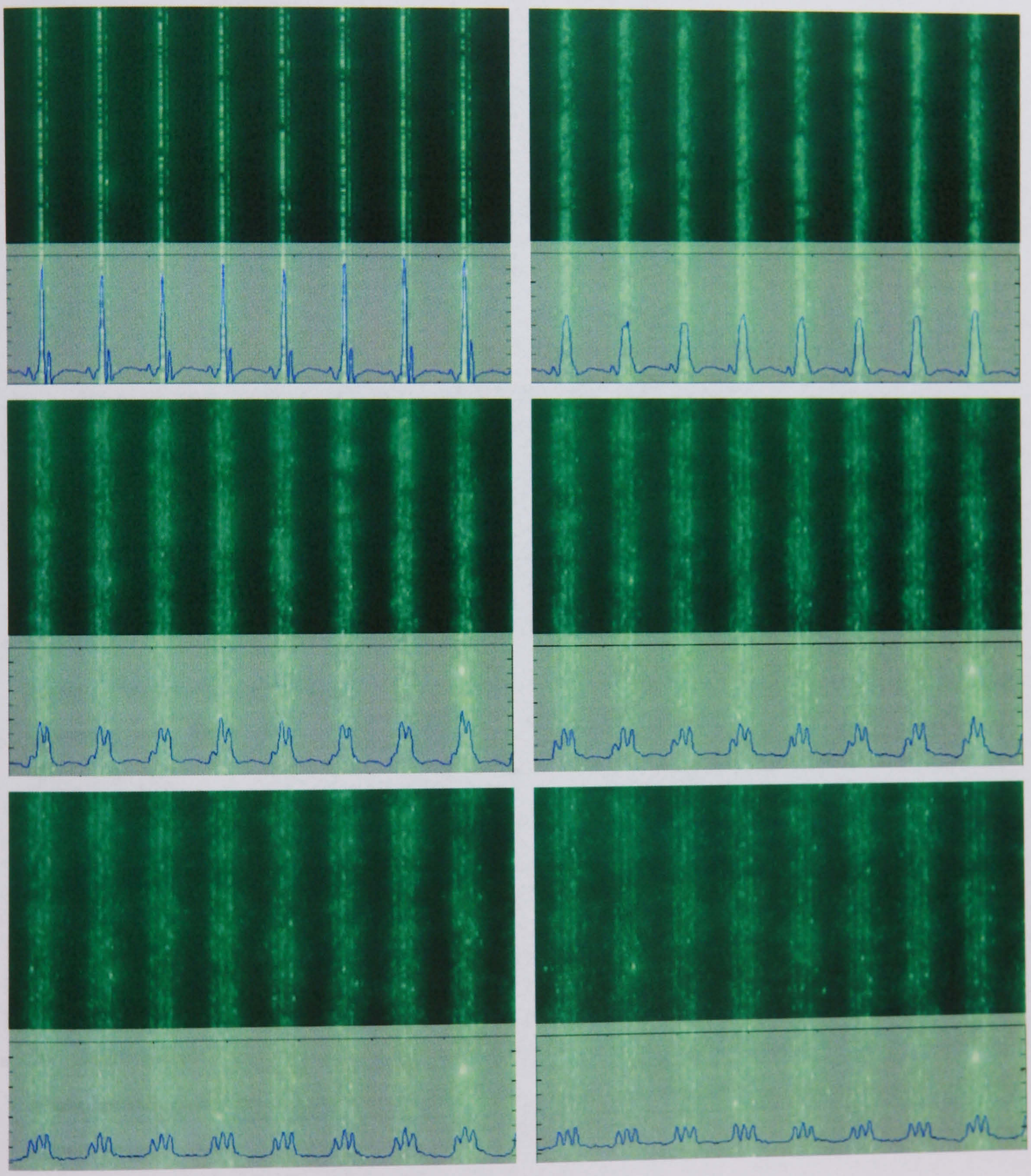

Figure 8-16

Matlab intensity analysis of 216nm beads diffusing in the off-cycle

8.9.1 Spatial averaging

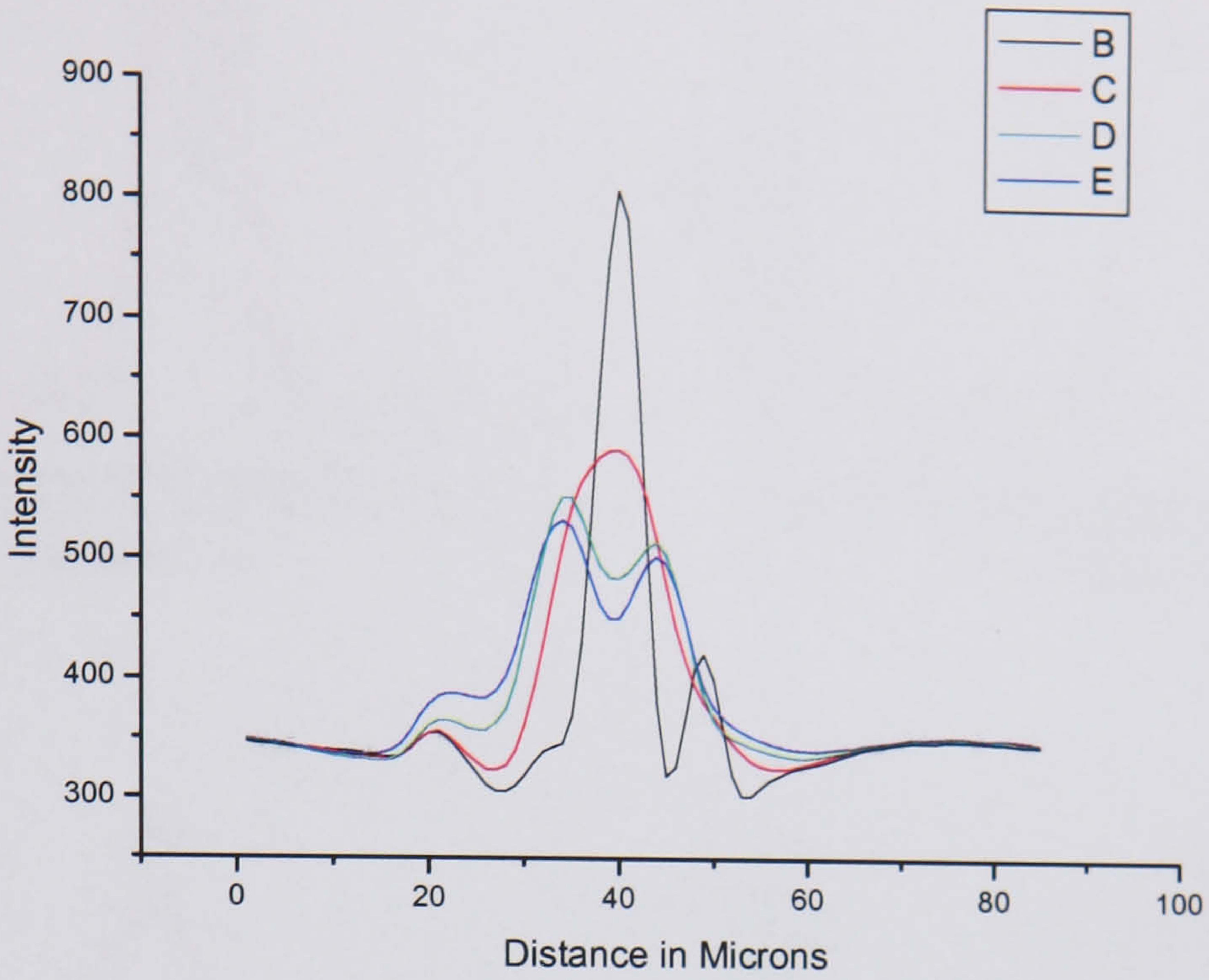

Figure 8-17

Superimposed temporal intensity profiles at 0.5s intervals, spatially averaged over 8 electrode sets

A program was written to average the intensity over all the visible sets of electrodes by measuring the period in pixels and superimposing all the correspondingly partitioned segments. This produced a smoother profile that was more statistically indicative of the general behaviour of the system (Figure 8-17). The results were plotted at various time intervals and fitted with Gaussian profiles using Origin™ statistical analysis software (Figure 8-18).

8.9.2 Intensity-concentration relationship

The resulting curves were not normalised, with variable areas due to differing degrees of non-linearity in the intensity response. The peak width, however, was still a valid quantity as the distribution was finite, with the concentration at positions slightly removed from the dense peaks closer to that producing a more linear intensity-quantity relationship. For this reason peak width was measured as the most representative indication of diffusion rate rather than integrating area segments to obtain bead numbers.

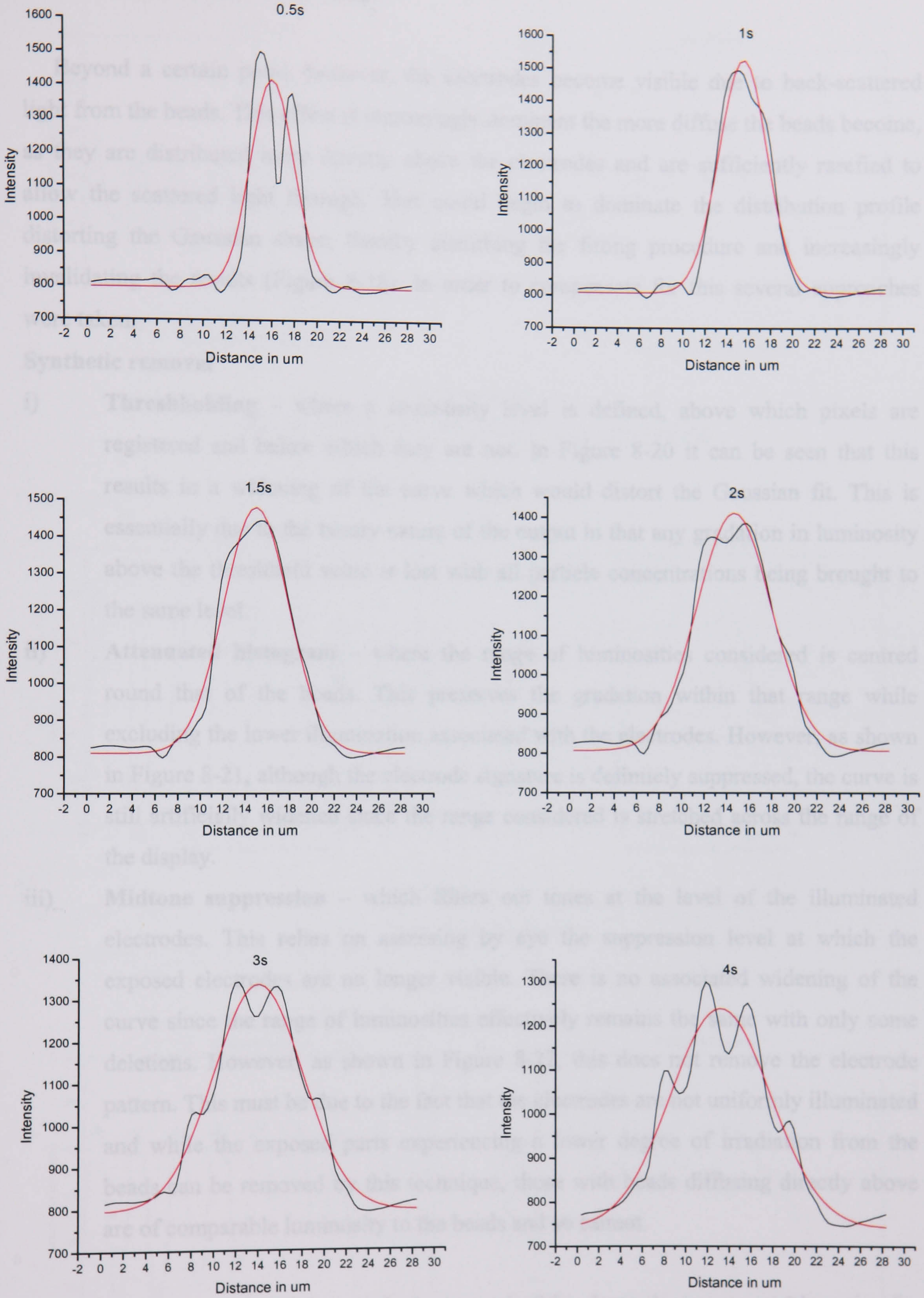

Figure 8-18

Average distributions around potential minima in the off-cycle for 216nm beads with superimposed Gaussian fits

8.9.3 Electrode back-scattering

Beyond a certain point, however, the electrodes become visible due to back-scattered light from the beads. This effect is increasingly dominant the more diffuse the beads become, as they are distributed more directly above the electrodes and are sufficiently rarefied to allow the scattered light through. This could begin to dominate the distribution profile distorting the Gaussian shape, thereby disturbing the fitting procedure and increasingly invalidating the results (Figure 8-18). In order to compensate for this several approaches were taken.

Synthetic removal

i) **Threshholding** – where a luminosity level is defined, above which pixels are registered and below which they are not. In Figure 8-20 it can be seen that this results in a widening of the curve which would distort the Gaussian fit. This is essentially due to the binary nature of the output in that any gradation in luminosity above the threshhold value is lost with all particle concentrations being brought to the same level.

ii) **Attenuated histogram** – where the range of luminosities considered is centred round that of the beads. This preserves the gradation within that range while excluding the lower illumination associated with the electrodes. However, as shown in Figure 8-21, although the electrode signature is definitely suppressed, the curve is still artificially widened since the range considered is stretched across the range of the display.

iii) **Midtone suppression** – which filters out tones at the level of the illuminated electrodes. This relies on assessing by eye the suppression level at which the exposed electrodes are no longer visible. There is no associated widening of the curve since the range of luminosities effectively remains the same with only some deletions. However, as shown in Figure 8-22, this does not remove the electrode pattern. This must be due to the fact that the electrodes are not uniformly illuminated and while the exposed parts experiencing a lower degree of irradiation from the beads can be removed by this technique, those with beads diffusing directly above are of comparable luminosity to the beads and so cannot.

Thus it can be concluded that synthetic removal of the electrodes is not a viable option for the treatment of back scattered light.

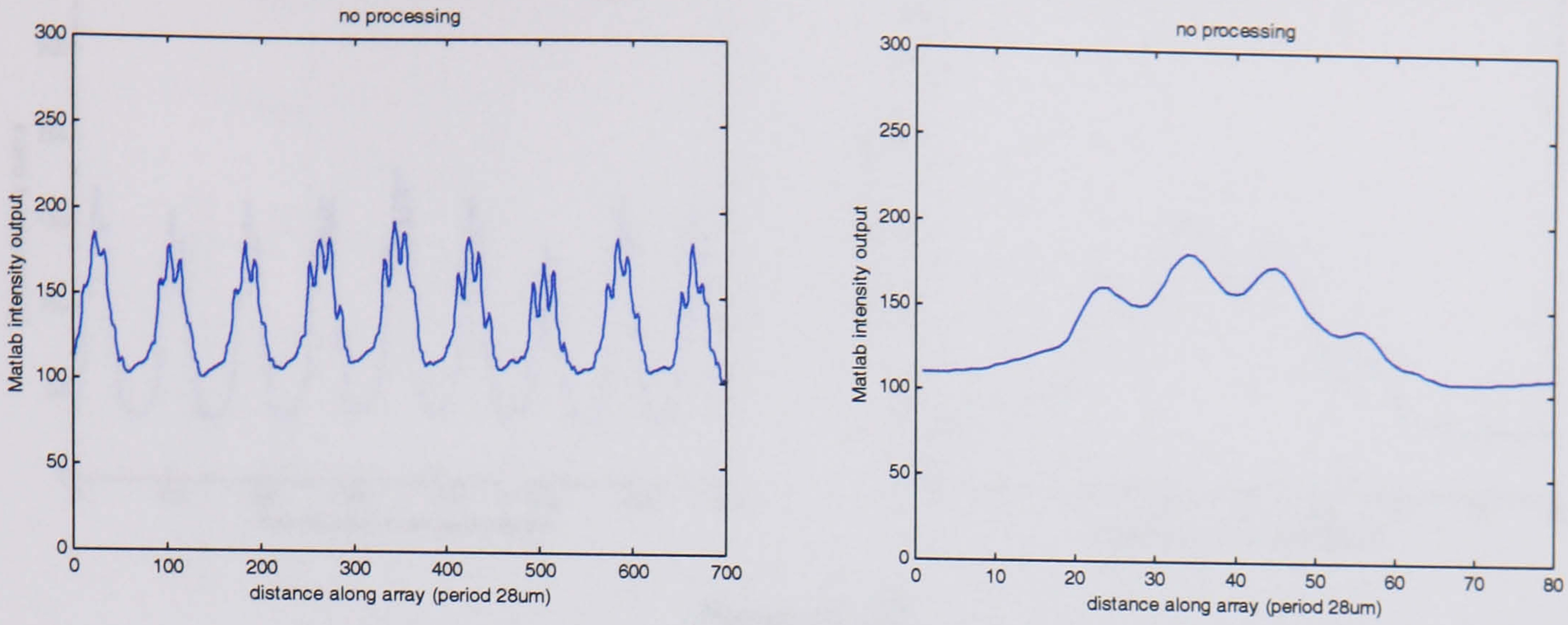

Figure 8-19

Matlab intensity profile without image processing

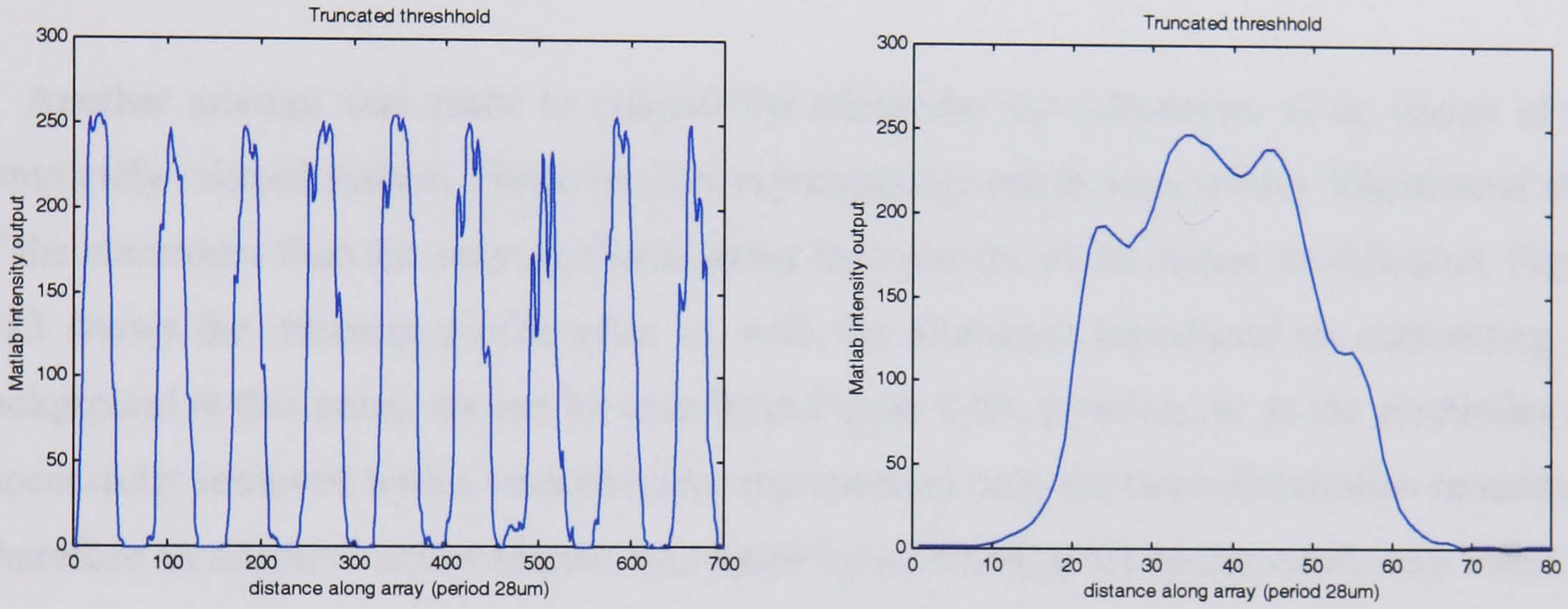

Figure 8-20

Truncated threshold

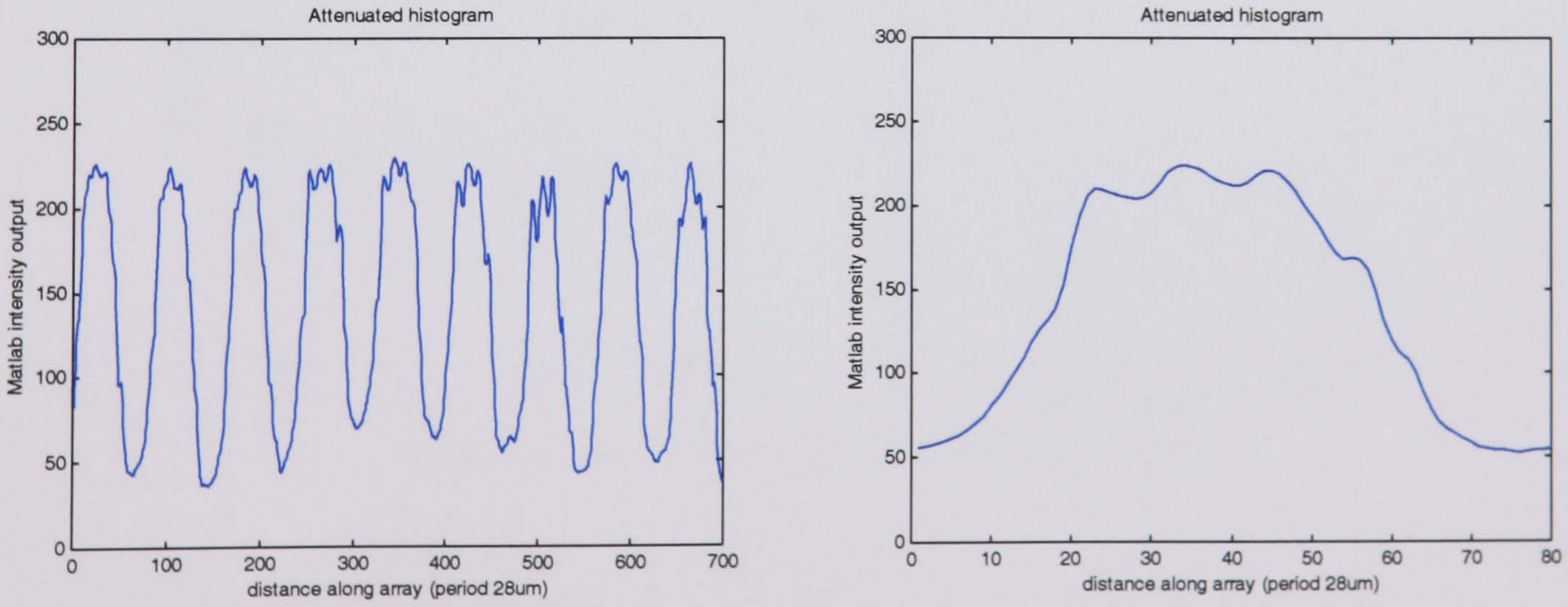

Figure 8-21

Attenuated histogram

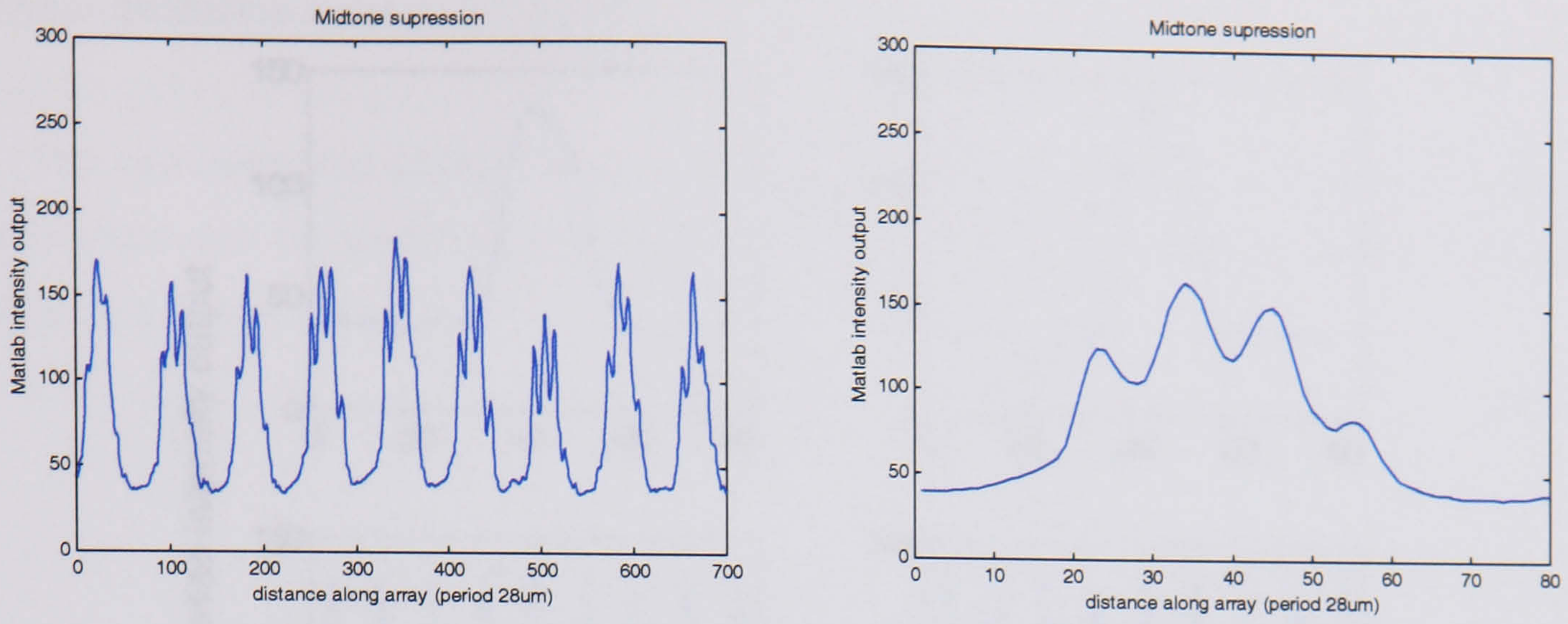

Figure 8-22
Midtone suppression

Background subtraction

Another attempt was made to remove the electrodes by subtraction of an image of the completely relaxed system. However, this represented a much more evenly illuminated state of the electrodes than the varying illumination they receive in the course of diffusion. Figure 8-23 shows the intensity profile after 1s, with the distortion introduced on subtracting the background at this point. As can be seen from Figure 8-24, however, at 4s the electrodes are successfully removed with a smooth curve representing only the bead distribution remaining. Therefore an adaptive ammendment was made by subtracting the background only when the electrodes actually became discernable in the Gaussian profile. Although essentially subjective, the fairly large time interval of 0.5s between curves meant that this point was not too difficult to define without considerable ambiguity.

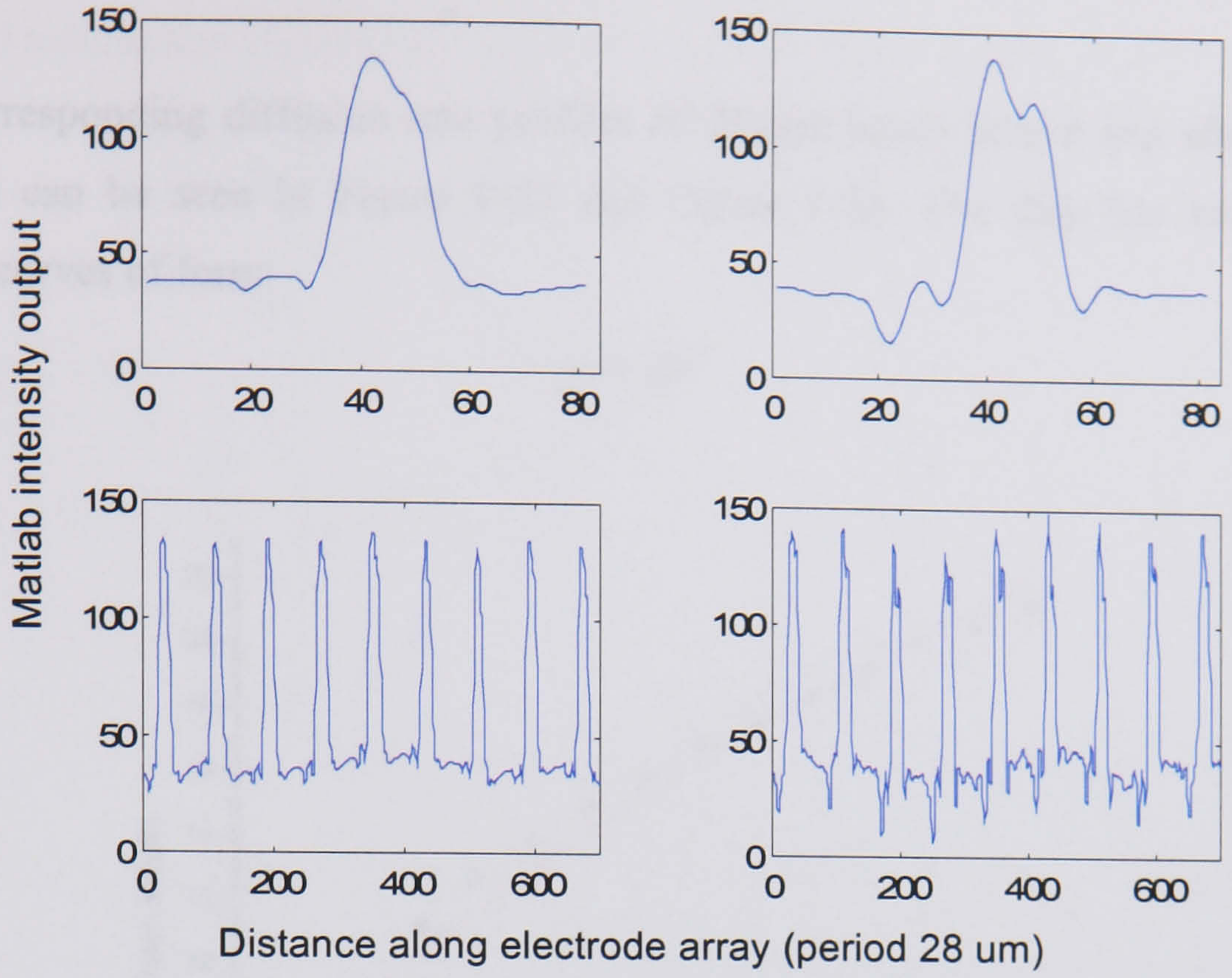

Figure 8-23

Left hand figures show intensity output at 1 second with those on the right manifesting some distortion introduced on background subtraction

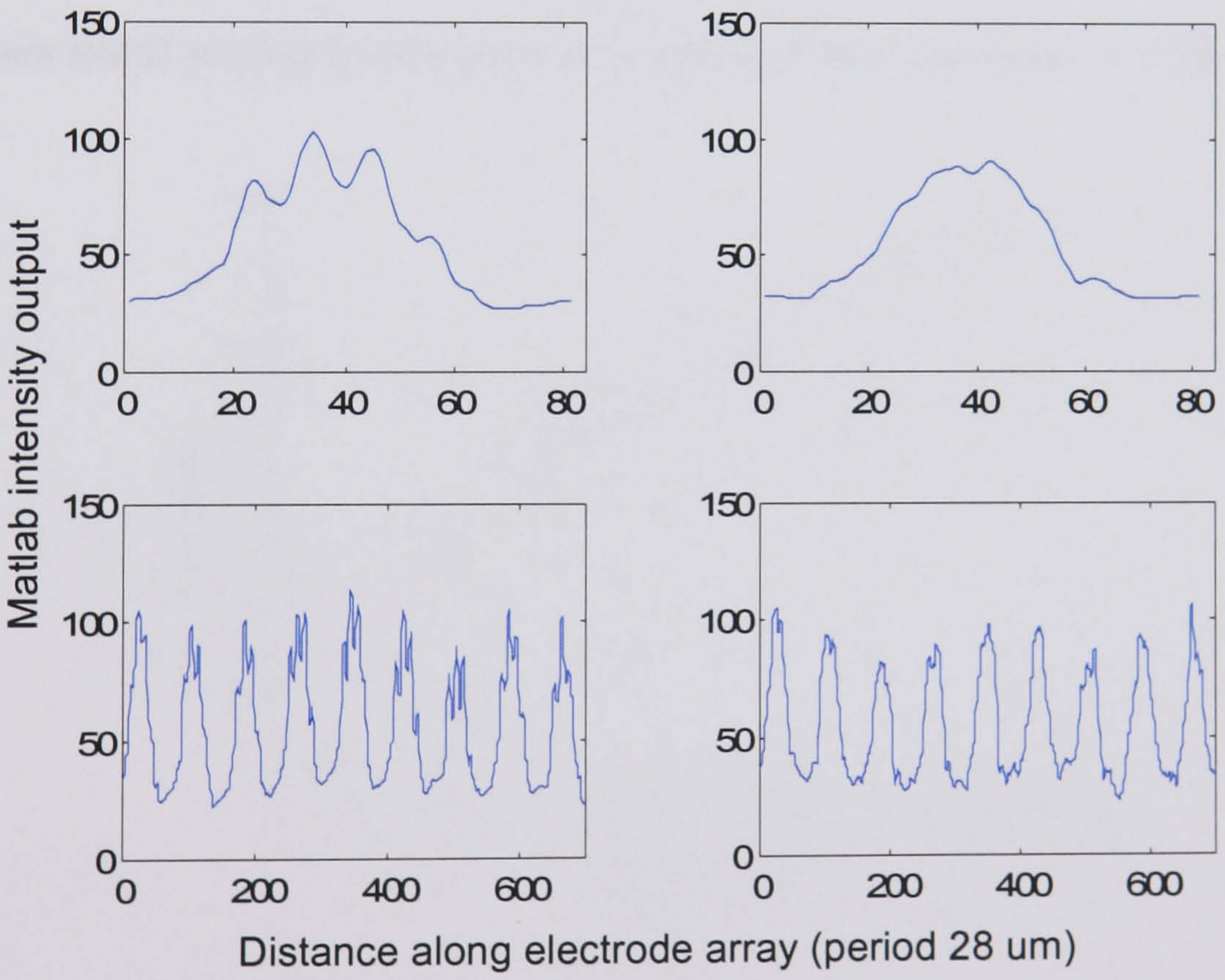

Figure 8-24

Intensity output at 4 seconds with right hand graphs showing smoothing effect on background subtraction

8.9.4 Diffusion rates

The corresponding diffusion rate profiles of 216nm beads before and after background subtraction can be seen in Figure 8-25 and Figure 8-26. The data has been fitted with allometric curves of form:

$$y = At^b \tag{8-1}$$

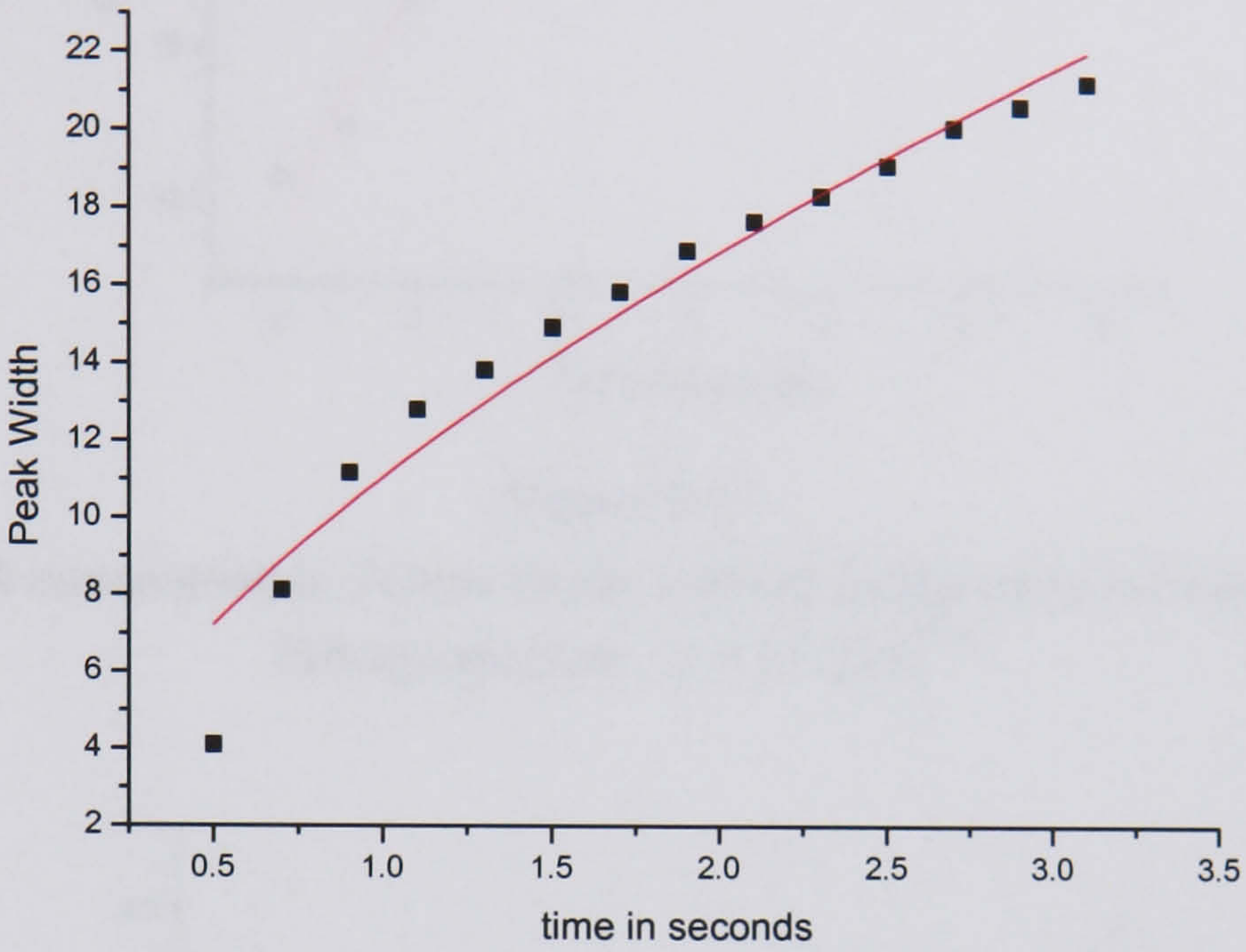

Figure 8-25

216nm beads without background subtraction. Fitting equation, $y = 11.06x^{0.61}$

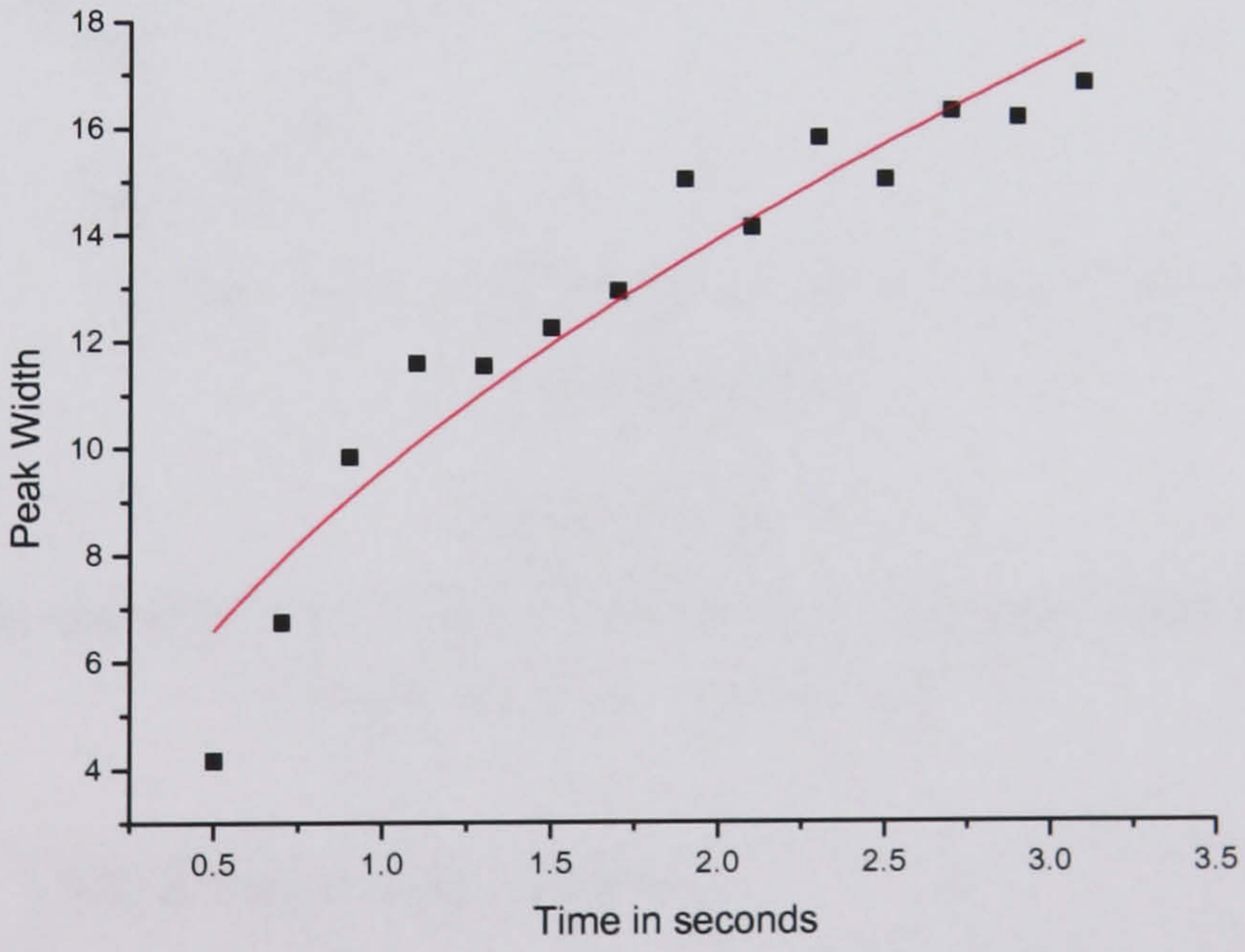

Figure 8-26

216nm beads with background subtraction. Fitting equation, $y = 9.60x^{0.54}$

The data appears more noisy with the background subtraction, although, from equation 3-25, this resulted in a more favourable temporal growth ($\sim\propto t^{1/2}$). The experiment was therefore repeated, doubling the bead concentration in an attempt to reduce the perturbing effects of the background. Figure 8-27 and Figure 8-28 show the results with and without background subtraction. A summary of the fitted parameters can be found in Table 8-1.

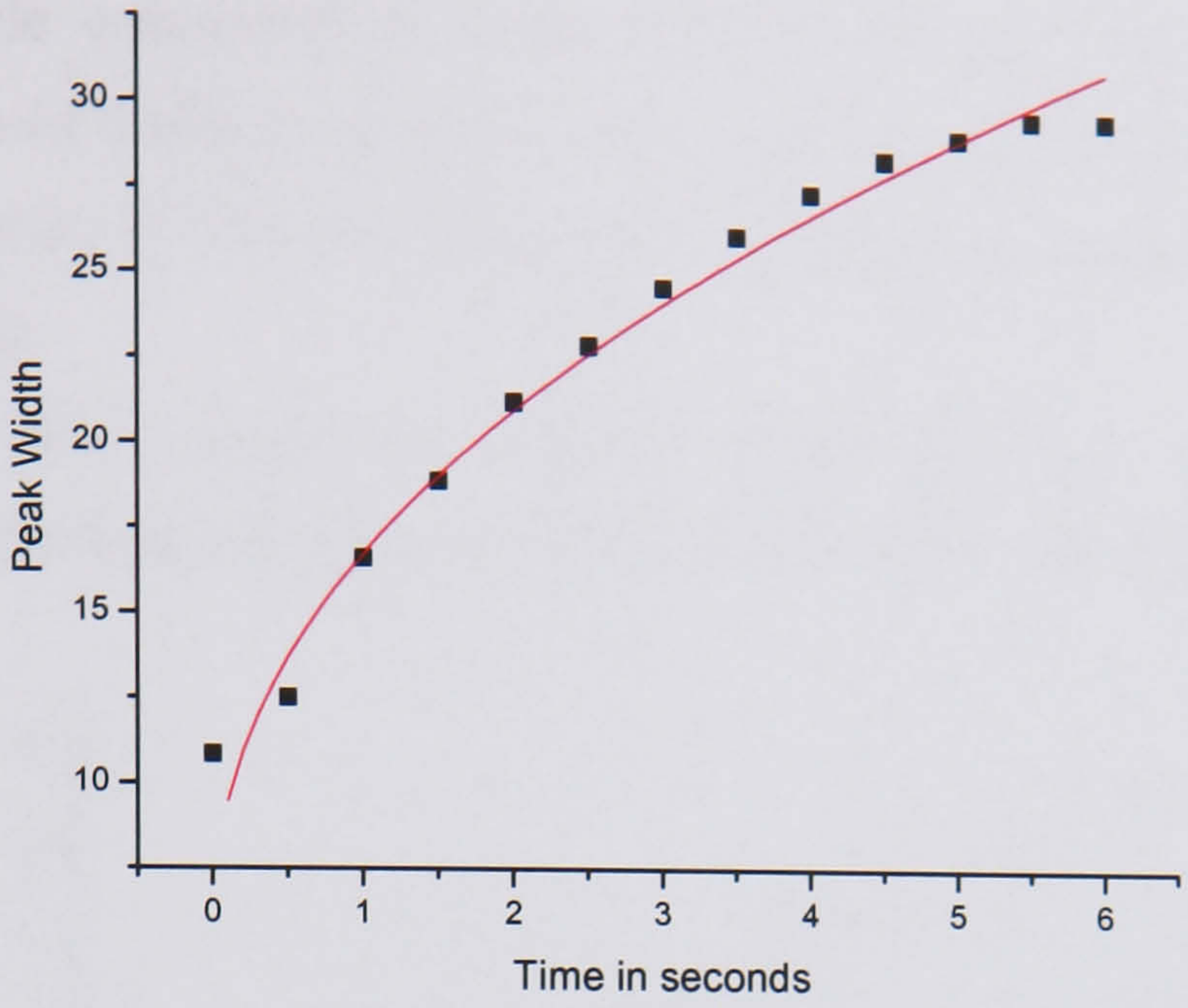

Figure 8-27

High concentration 216nm beads without background subtraction

Fitting equation, $y = 11.16x^{0.46}$

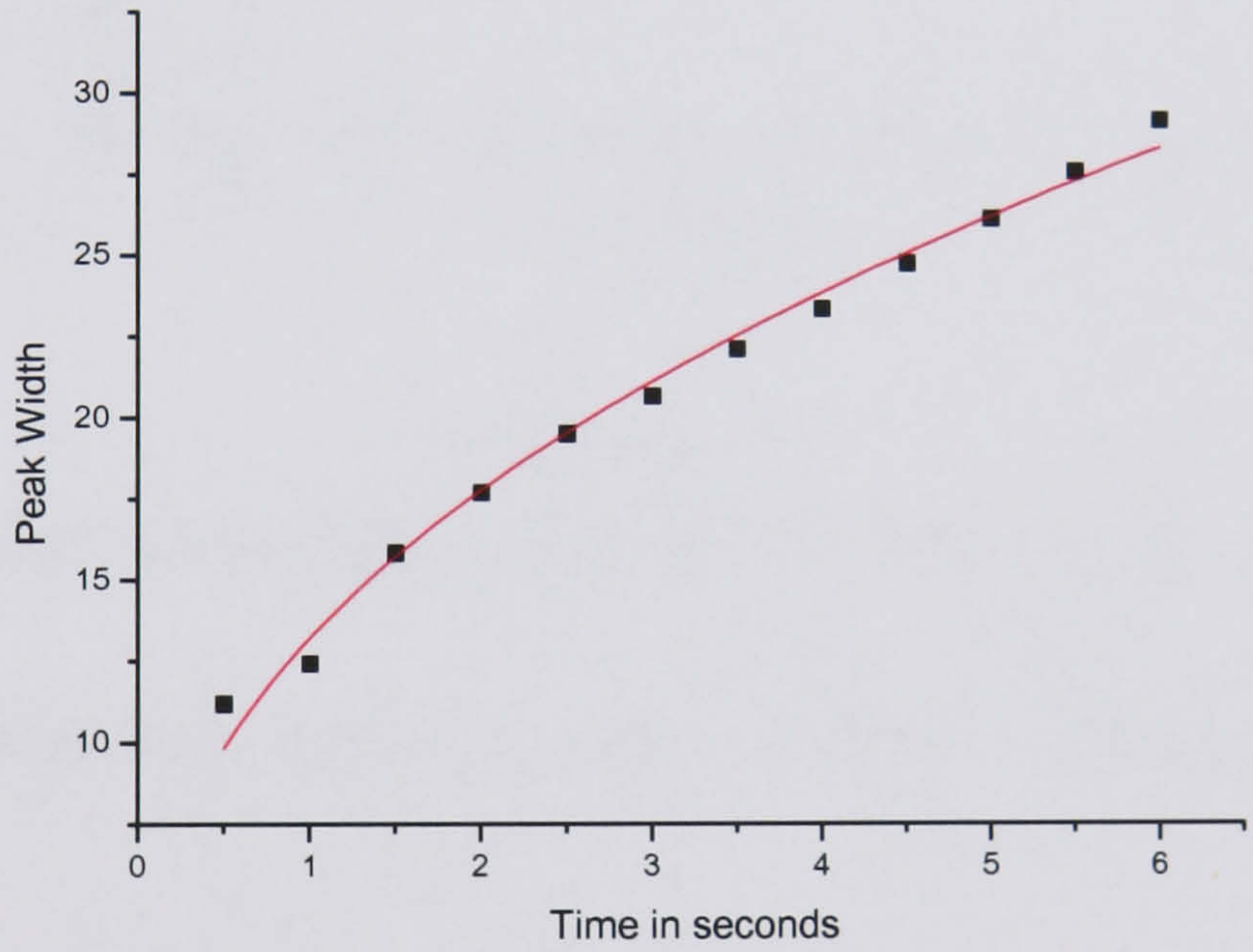

Figure 8-28

High concentration 216nm beads with background subtraction

Fitting equation, $y = 13.21x^{0.43}$

Concentration	Background subtraction	*A*	*b*
Low	Without	11.06	0.61
Low	With	9.6	0.54
High	Without	11.16	0.46
High	With	13.2	0.43

Table 8-1

Comparison of the fitted diffusion parameters for two bead concentrations with and without background subtraction

Examining the results in Table 8-1, then, background subtraction does not appear to be necessary, apparently only introducing a greater variability in the parameter A. Instead, increasing the particle concentration would seem to be the most appropriate way of decreasing the effects of background scattering as this way the electrodes are naturally not visible for a longer period of time allowing a more realistic assessment of temporal growth.

460nm bead diffusion

The diffusion of 460nm beads was analysed in the same way, with the same higher concentration and no background subtraction. The results can be seen in Figure 8-29.

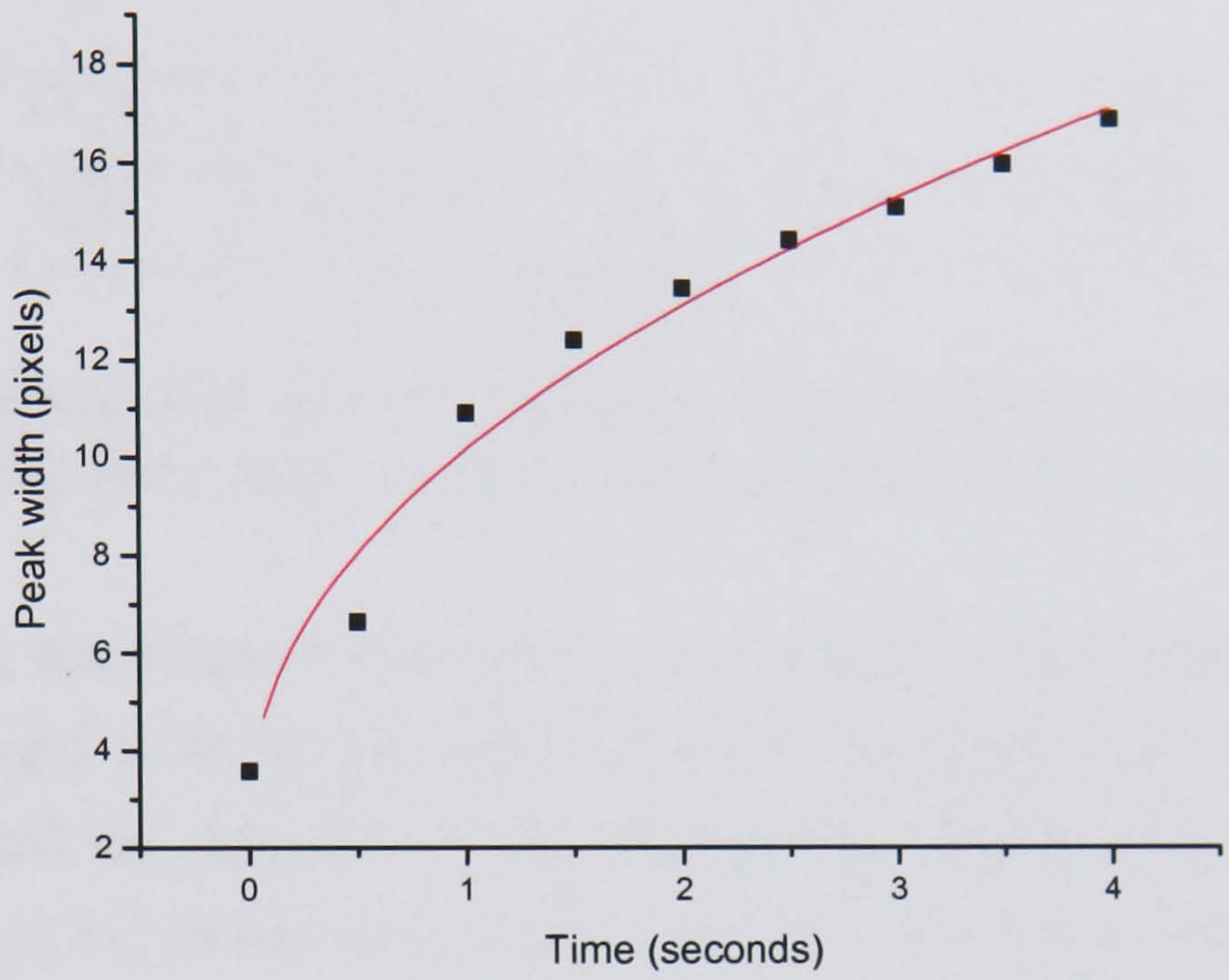

Figure 8-29

Peakwidth against time for diffusing 460nm beads. Fitting equation $y = 7.63x^{0.47}$

The resulting numerical parameters were subsequently compared with theoretical predictions.

8.9.5 Theoretical comparison

The diffusion constant is given by:

$$D = \frac{kT}{6\pi\eta a} \tag{8-2}$$

Substituting in numerical values $k = 1.38 \times 10^{-23} J/K$, $T = 300K$, $\eta = 10^{-3} Ns/m$ gives the theoretical predictions which can be compared to the experimentally measured diffusion constants.

These can be calculated from the fitting parameter A by noting the relation derived in Chapter 3:

$$\sigma^2 = 2Dt \tag{3-27}$$

The peak widths, P.W., measured by Origin are 2σ, thus:

$$P.W. = 2\sqrt{2Dt} \tag{8-3}$$

so that from eq.(8-1), $A = 2\sqrt{2D}$ and $b = \frac{1}{2}$.

Including the conversion factor from pixels to metres, $0.35\text{x}10^{-6}$, the experimentally measured diffusion constants D_{expt} and time exponent b_{theory} compare to those theoretically derived as described in Table 8-2.

Bead Size	A	D_{expt}	D_{theory}	b	b_{theory}
216nm	11.16	1.9×10^{-12}	2×10^{-12}	0.46	0.5
460nm	7.63	8.9×10^{-13}	9.4×10^{-13}	0.47	

Table 8-2

Comparison of theoretically and experimentally obtained diffusion parameters following fitting of the diffusion data with the allometric curve $y = At^b$

As can be seen, the diffusion constants in both cases are slightly below their theoretical value. This can most probably be attributed to the impedance due to the high particle concentration around the electrodes [1] as could also the slightly lower time exponent. In both cases, however, the results seem in good agreement with symmetrical diffusion around the potential minima.

8.10 Separation

With the fulfilment of the two stated criteria of periodic asymmetric collection followed by free, symmetric diffusion unidirectional transport has been established. Separation can thus take place on the basis of two criteria – size and surface properties. Following the convention stated by Gorre-Talini *et a.* [1] the separation of two particle populations moving at respective velocities v_1 and v_2 is defined to be when the distance between the peaks of the distributions is at least that of the wider peak. If D_1 and D_2 are the diffusion constants of the smaller and larger particles respectively then this can be written as:

$$v_1 t - v_2 t = \sqrt{2Dt}$$

which on rearrangement gives the separation time as:

$$t = \frac{2D_1}{(v_1 - v_2)^2} \tag{8-4}$$

Thus, based on the experimentally measured diffusion constants v_1 and v_2 were calculated using the method described in Chapter 6. The t_{off} used was the optimal for the faster 216nm beads, since this was shorter and created a larger discrepancy between v_1 and v_2. This resulted in velocities of 0.188μm/s and 0.064μm/s for the 216nm and 460nm beads respectively. Substituting these values into (8-4) gives a separation time of 4 minutes and 24 seconds. In order to include the total collection time, the measured value from the video analysis of 1.4s[20] (Figure 8-13) was multiplied by the number of cycles. This added an additional 26s, bringing the total separation time to 4 minutes and 50 seconds.

Separation on the basis of surface properties relies on quite a different approach. The object is to utilise the difference between the crossovers of the two populations to be fractionated in order that the device act as a Brownian ratchet for those with higher crossovers and a trap for those with lower. The attachment of biological moieties, as shown in Ch 5, tends to lower the crossover of the particle. Thus, if the higher frequency applied to the electrodesis intermediate between the crossovers of the two bead samples used, then the separation criterion will be satisfied. An example of this is shown in Figure 8-30, which depicts the on-cycle where biotin labelled red beads have been mixed with unlabelled carboxylated green beads which have a much higher crossover frequency. It can be seen that the red beads only collect on the left hand electrode set while the green collect on both. For photographic clarity, larger red beads have been used but the principle of separation on the basis of crossover frequency alone is still the same. Given this result, the device would behave as a Brownian ratchet transporter for the modified beads while being simply a periodic trap for the uncoated beads.

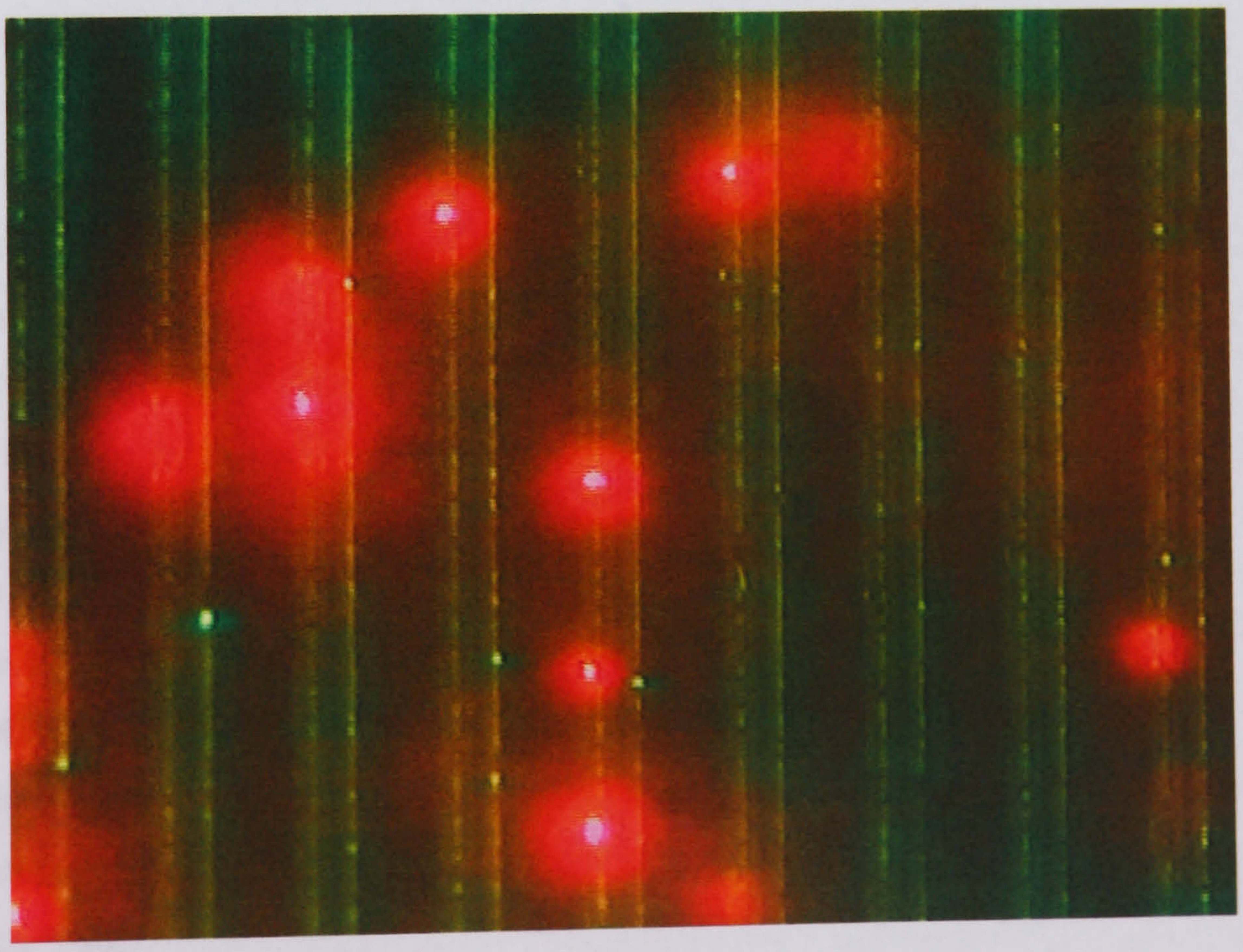

Figure 8-30

Biotinylated red beads with ~500kHz crossover collecting only on the left hand, lower frequency (300kHz) electrodes while the green beads, having a higher crossover (~6MHz), are trapped also by the high frequency set (2MHz).

---

[20] This is not a critical value being easily modified on voltage adjustment.

8.11 Experimental/design refinement

8.11.1 Particle tracking

If software were available which would allow high numbers of particles to be individually tracked constituting a statistically viable data set the current arrangement could be used to observe the net drift. Because of the unequivocally measured asymmetric collection and free diffusion this would be expected to approach that of the predicted results over a large enough particle sample.

8.11.2 Fabrication

In order to produce a working device from which real fractionation with possible collection of differentiated samples could occur, the channel height would have to be considerably lower – of the order of ~5-10μm, since within this range the force has dropped by at least an order of magnitude. This would be necessary for all particles to be included in the Brownian ratchet transportation without excessive collection times. Thus different materials would have to be chosen as the aspect ratio would be too great for PDMS. An SU8 channel would incur the problem of adequate sealing and it is unlikely that this could be achieved while maintaining the height requirements. There is also a high risk of damage in using this resist directly on a working device due to the prolonged baking and long development process with no guarantee of a resulting unblocked channel at the end. A glass etched channel could be fabricated to the optimal dimensions using HF and could be an option, with its hydrophilic properties, if an adequate bonding process could be established. This would lack the versatility of a removable channel, however, and thus not be so practical in terms of cleaning etc. The simplest choice could perhaps be a commercially available 10μm bonding film which could be used in the manner of the preliminary PDMS trials (refer to section 7.3.3) with a glass cover-slip. Sample introduction would have to be dealt with accordingly, since injecting under the channel would not be possible at this height, with possibly the installation of a top fitting pipe entry system.

The transport velocity of the particles could also be improved by increasing the asymmetry of the electrode pattern. This would necessarily involve the down-scaling of the electrodes since simply increasing the gap would necessitate longer collection times. 1μm electrode devices have been fabricated but in preliminary trials have appeared significantly less robust in withstanding the application of high fields. This gives rise to increased collection times which effectively cancel the effect of the slightly shorter optimal diffusion period.

8.12 Conclusion

Although it has not been possible to localise a distribution in order to display the net drift as predicted by the simulations, the two essential requirements which, in the absence of perturbations, are uniquely sufficient to produce Brownian ratchet transportation have been investigated. These are, namely, asymmetric collection and free diffusion in the on and off-cycles respectively and using various image processing techniques both have been unequivocally observed. That is to say if a facility were available to undertake multiple particle tracking on a statistical level then the fulfilment of these two conditions means that drift similar to that characterised in the simulations would be measurable.

On the verification of this action particle separation should take place on the basis of bead size, where diffusion rate is the discriminating factor, and surface characteristics, as defined by DEP crossover frequency. In the former case, experimentally measured diffusion constants have resulted in a predicted separation time of several minutes for two sizes of colloidal particles and in the latter, the trapping of uncoated beads has been demonstrated while for higher crossover biotin coated beads the device simultaneously continues to behave as a Brownian ratchet.

8.13 References

[1] L. Gorre-Talini, J. P. Spatz, and P. Silberzan, "Dielectrophoretic ratchets", *Chaos*, vol. 8, pp. 650-656, 1998.

9 Fluid Flow

9.1 Non-stochastic pumping

In addition to the stochastic pumping documented on the interdigitated Brownian ratchet device, another type of motion was observed. This occurred during the on-cycle causing steady particle transport across a broad range of frequencies, a few microns above the electrode plane. Flows of this type have previously been reported as side effects in experiments involving Brownian ratchet structures [1, 2] but never fully documented in this context. The aim of this chapter is to report on experimental measurements of this motion and discuss the possible mechanisms for it, focussing on electro-osmosis and electrothermal pumping, noting, in addition, the implications for the overall functionality of the Brownian ratchet device. The nature of electro-osmotic flow as theoretically described in Ch3 is examined experimentally and with reference to currently published data, and the possibility of an electrothermal component arising from heat produced by the interaction of the electric field and the fluid is assessed by simulation and theoretical considerations.

9.2 Flow measurements

In order to investigate the apparently non-stochastic linear transport of particles in the device, a series of experiments were performed. It was observed that pumping occurred frequently during the normal functioning of the Brownian ratchet device with the simultaneously applied high and low frequency signals. However, in order to simplify the situation and differentiate between possible explanations of the motion, the effect of the application of a single frequency was also measured.

9.2.1 Experimental method

Initially, an AC signal was applied to each of the four electrodes of the Brownian ratchet in turn while the remaining three were earthed Figure 9-1. This was done by connecting the device in the same manner as with simultaneously applied signals with earth and live on one side of the device, corresponding, say, to the first or second [third or fourth] electrode but this time with a short circuit connection between the remaining two electrodes, to which a muted signal generator was connected in order to establish an earth. The equality of the earths on both sides was confirmed using a volt meter. For the application of two signals the inter-electrode connection was removed. An open PDMS channel was used with a glass coverslip.

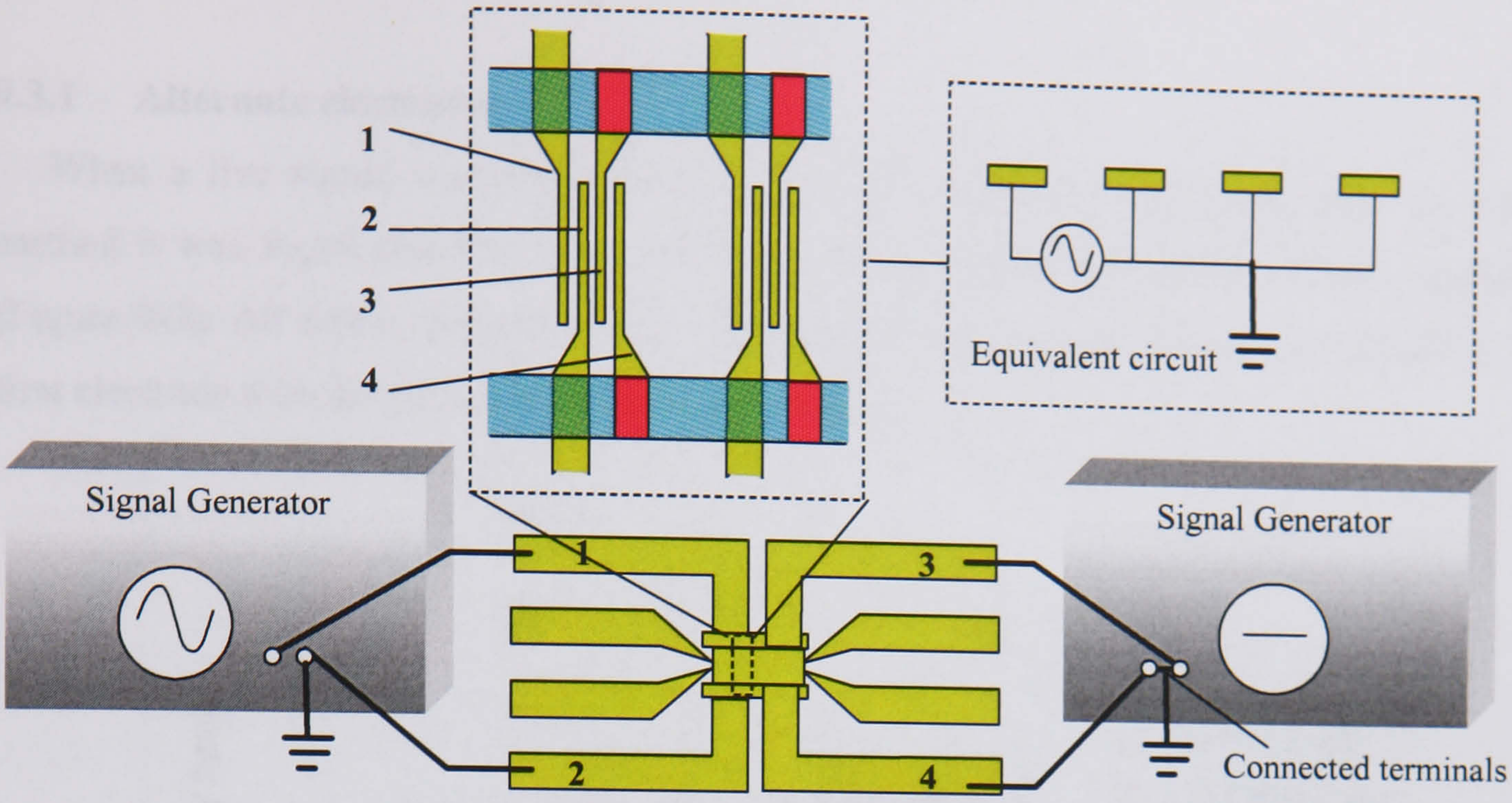

Figure 9-1

Experimental set-up showing electrode connections for the application of one signal to the first electrode.

Close to the electrodes the motion had a significant vertical component resulting in a 'leap-frogging' type of particle trajectory and positive DEP trapping was also frequently observed, therefore the microscope was focussed 15μm above the electrode plane in a zone of more uniform particle motion. Experiments were carried out on both the three and four electrode devices of 2μm electrode width.

Particle tracking

In order to measure the average flow rate, a series of video sequences were made of 460nm tracer particles at various applied frequencies and voltages. The velocity of 4-6 particles at each frequency/voltage was calculated by measuring with a ruler the distance travelled across the TV screen divided by the elapsed time as indicated by the video counter (accurate to the frame rate, 0.04s). This was converted to μm/s by a scaling factor obtained from measurement in centimetres of a fixed number of electrode periods corresponding to a known distance in microns. The average of each set of velocities was plotted. Error bars, corresponding to the range of measured velocities, are not shown as these were generally proportionally very small within a particular sample.

9.3 Results

9.3.1 Alternate electrodes

When a live signal was applied in turn to each consecutive electrode with the others earthed it was found that the outermost electrodes produced the highest velocity pumping (Figure 9-2). All future measurements were therefore carried out using a live signal on the first electrode with the other three connected together.

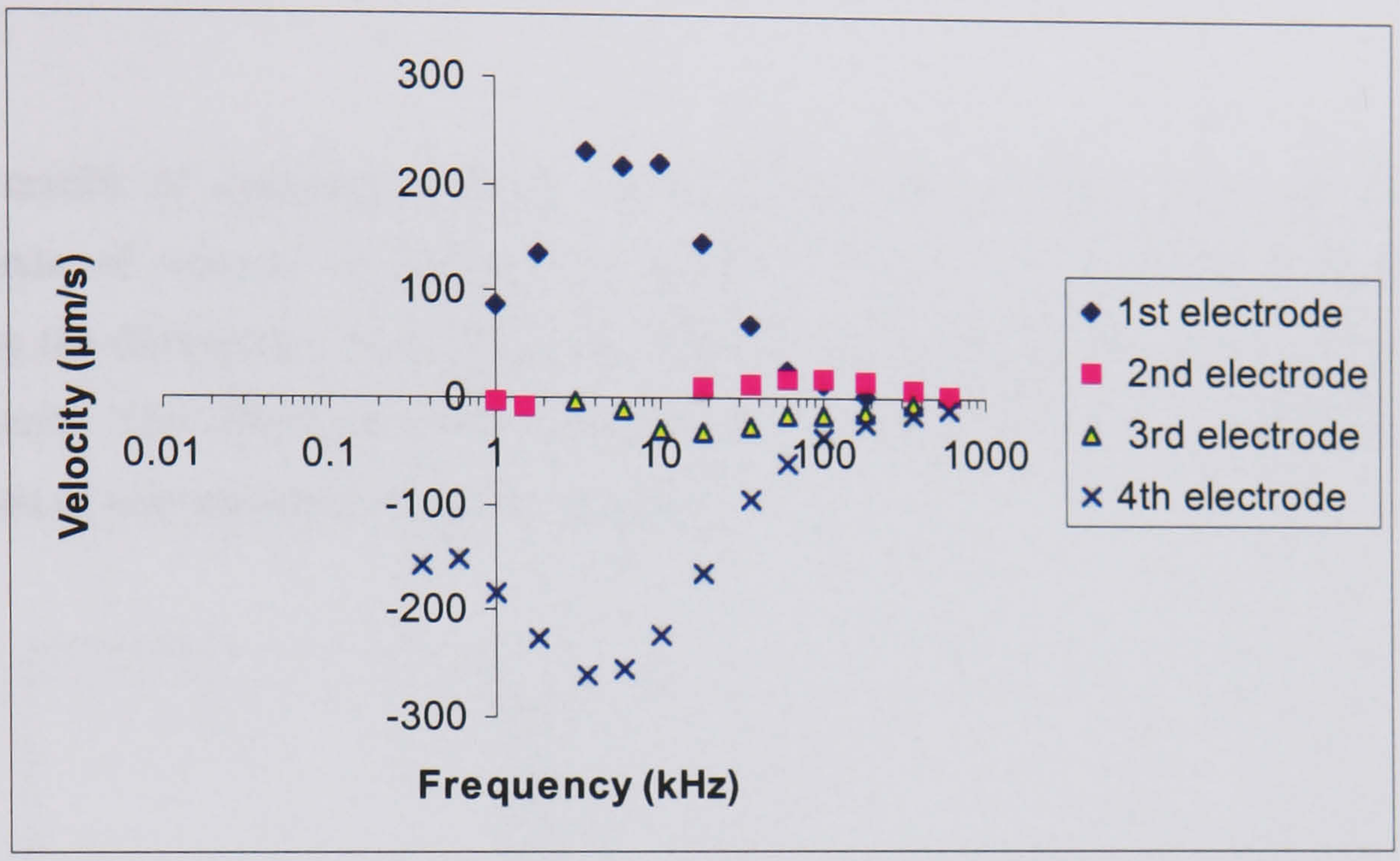

Figure 9-2

Live signal applied alternately to each of the electrodes in turn while the remaining 3 are earthed. RO Water 3.5V.

9.3.2 Variation with medium conductivity

The variation with conductivity was also checked comparing RO water with 0.1mM and 1mM KCl solutions. 10mM KCl was also tried but produced no clearly discernable flow.

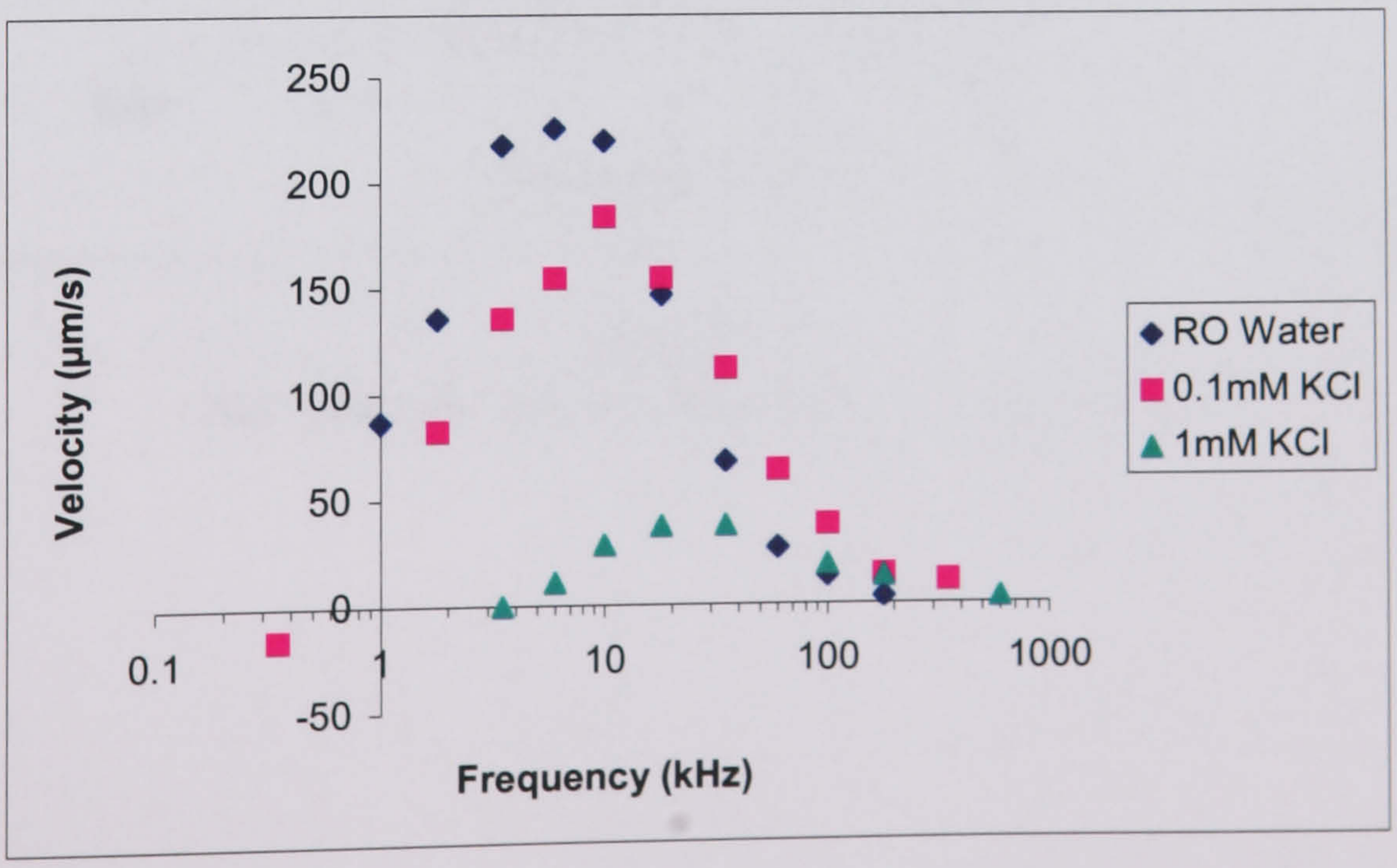

Figure 9-3

The variation of pumping velocity with fluid conductivity at 3.5V

9.3.3 Variation with voltage

The variation with voltage was measured across the frequency spectrum applying first a single signal in the manner indicated and then with an added high frequency signal on the other pair of previously earthed electrodes, in order to observe the device under the Brownian ratchet experimental conditions.

1 signal

The results of applying a single signal can be seen in Figure 9-4 with the power dependence of velocity on voltage illustrated in Figure 9-5. The error bars are large, reflecting the discrepancy which was observed in the overall velocity curves on repetition of experiments. This effect has also been noted by Brown *et al* [3] and attributed to the deposition of microspheres on the electrodes.

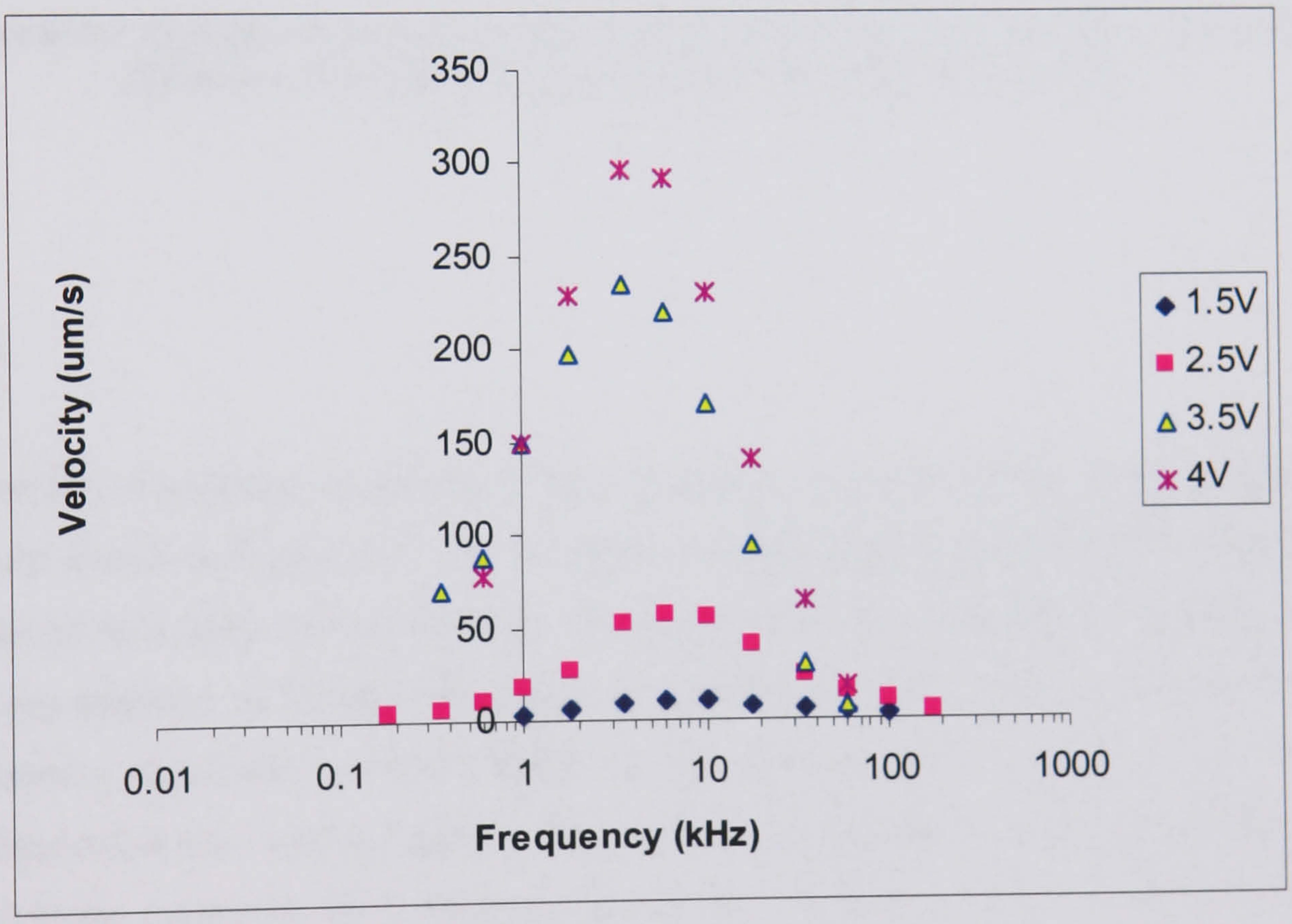

Figure 9-4
RO water, one signal on electrode 1, 2-4 earthed.

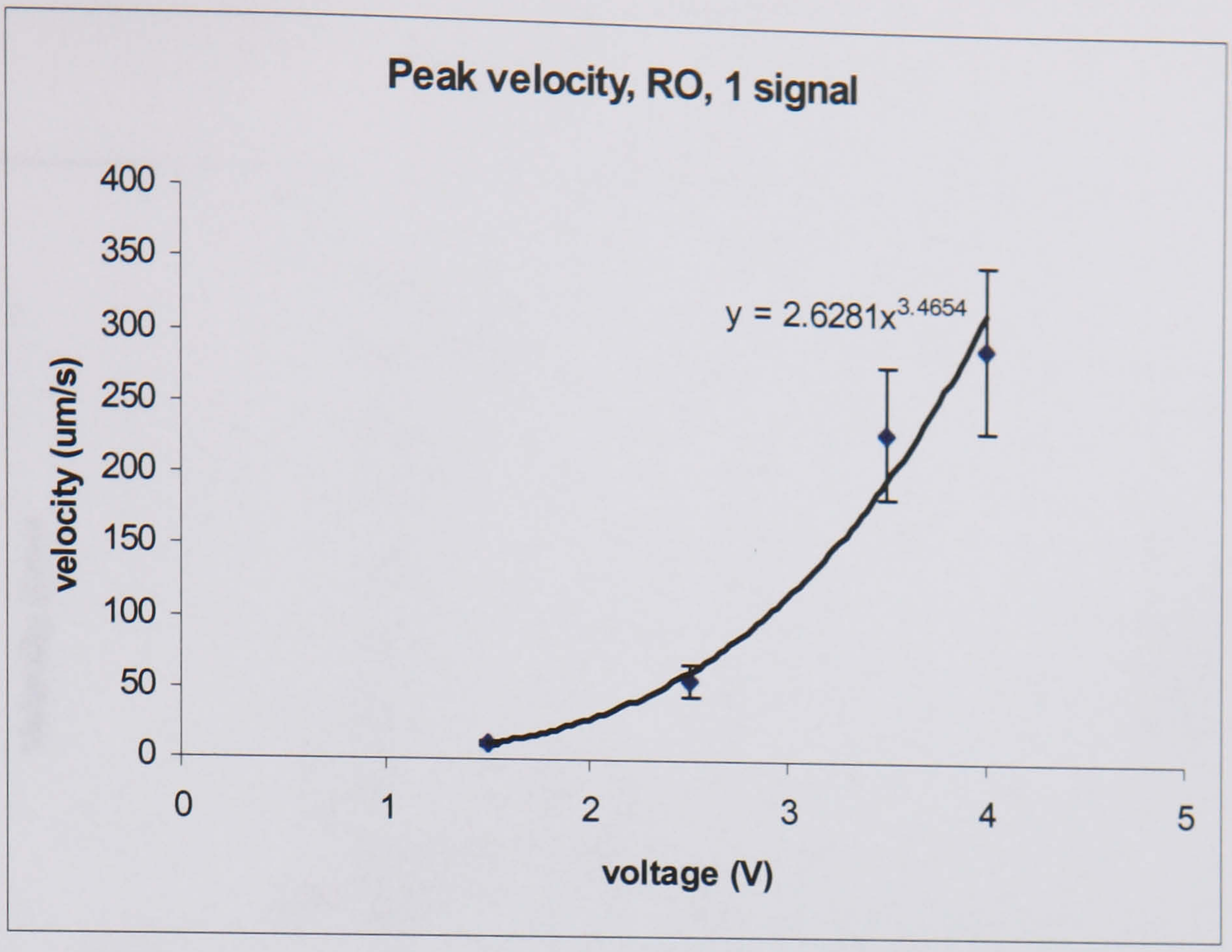

Figure 9-5

Dependence of peak velocity on applied voltage. The error bars are large, reflecting difference in magnitude of peaks between repeated data sets.

2 signals

The results of applying an additional high frequency signal (10MHz, 3.5V) to electrodes 3 and 4 are shown in Figure 9-6. The velocities are significantly higher with, in addition, a clear reversal of motion around 100kHz. The high frequency speeds peak at around 20µm/s but are very sensitive to voltage adjustment. A small increase in voltage around the applied value causes a significant velocity change. At 4V, for example, velocities around -40µm/s can be observed in this region. Figure 9-7 shows the peak velocity/voltage relationship.

The velocity curves on the 3 electrode device for 2 applied signals are shown in Figure 9-8 with the corresponding voltage dependence in Figure 9-9.

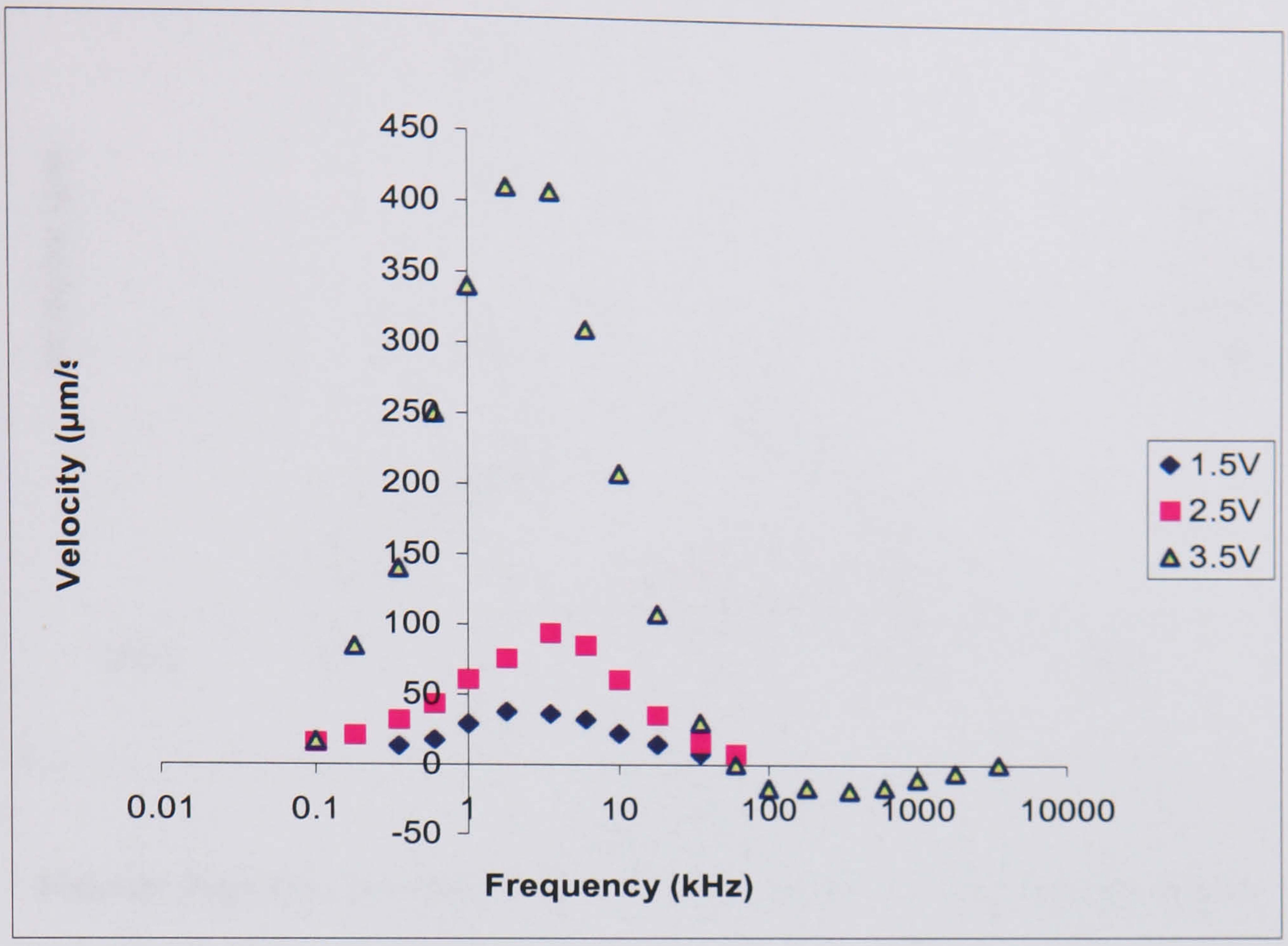

Figure 9-6

2 signals, RO water

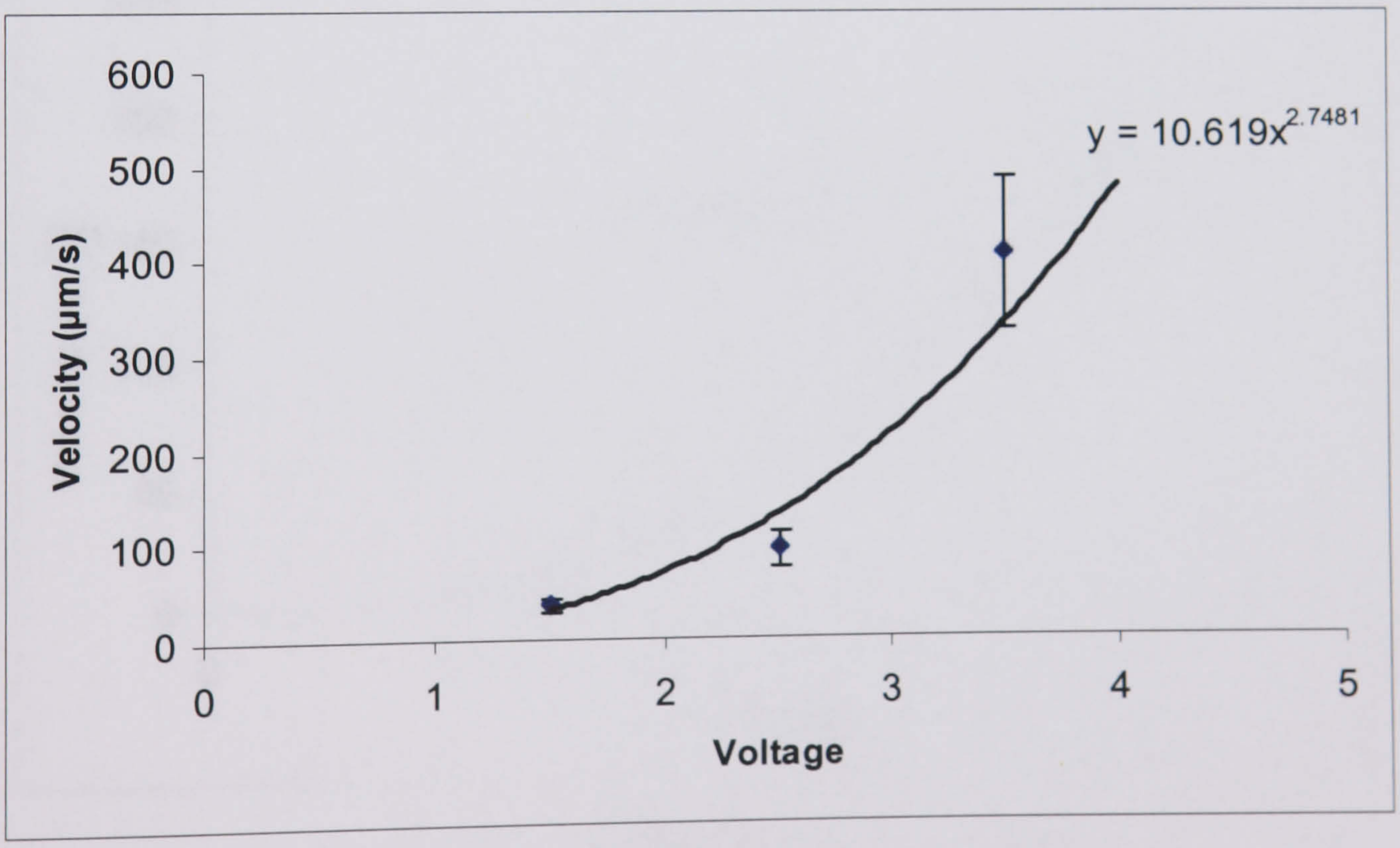

Figure 9-7

Dependence of velocity on voltage for two applied signals on the 4-electrode device.

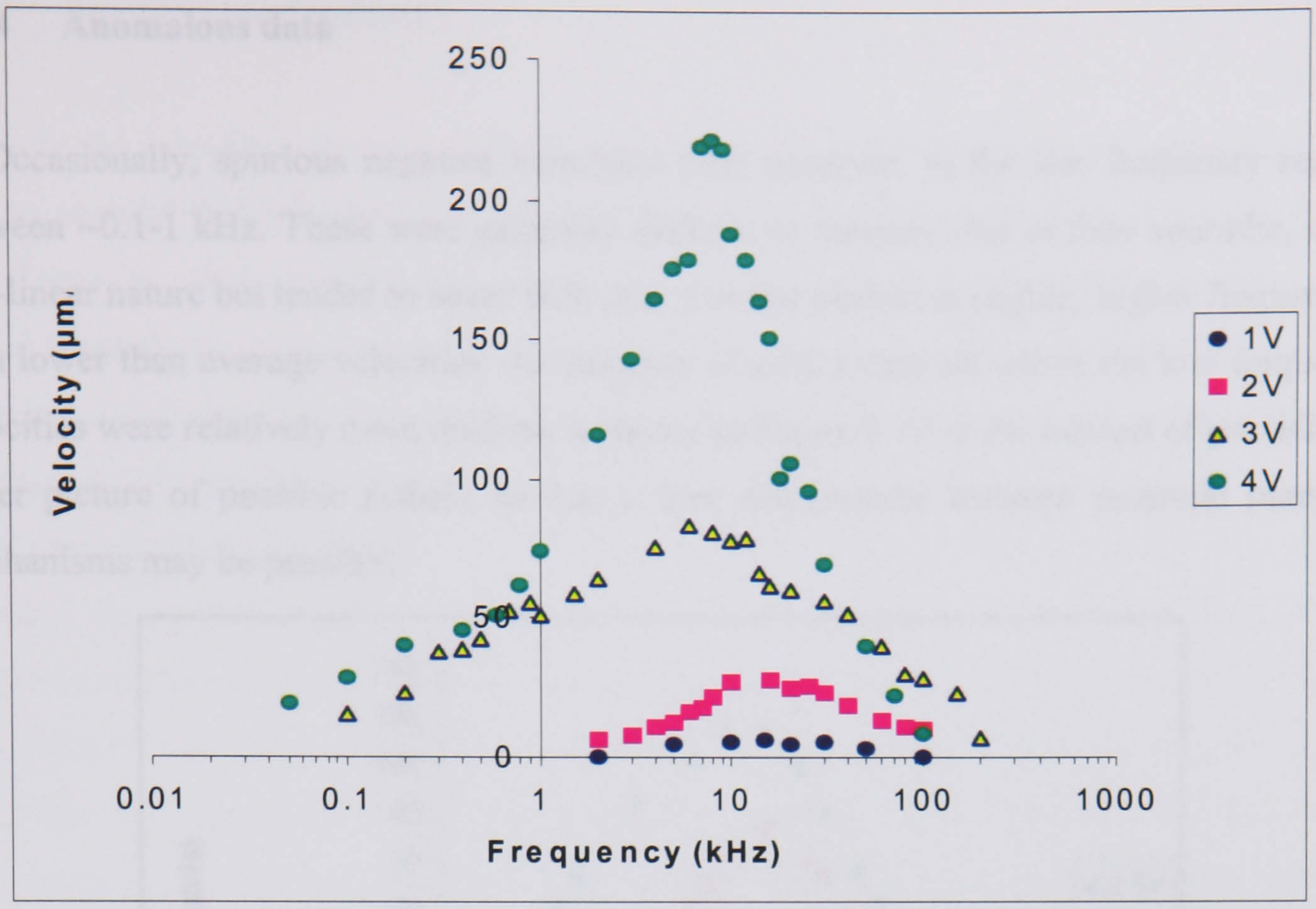

Figure 9-8

Velocity frequency distribution on the 3 electrode device with 2 applied signals.

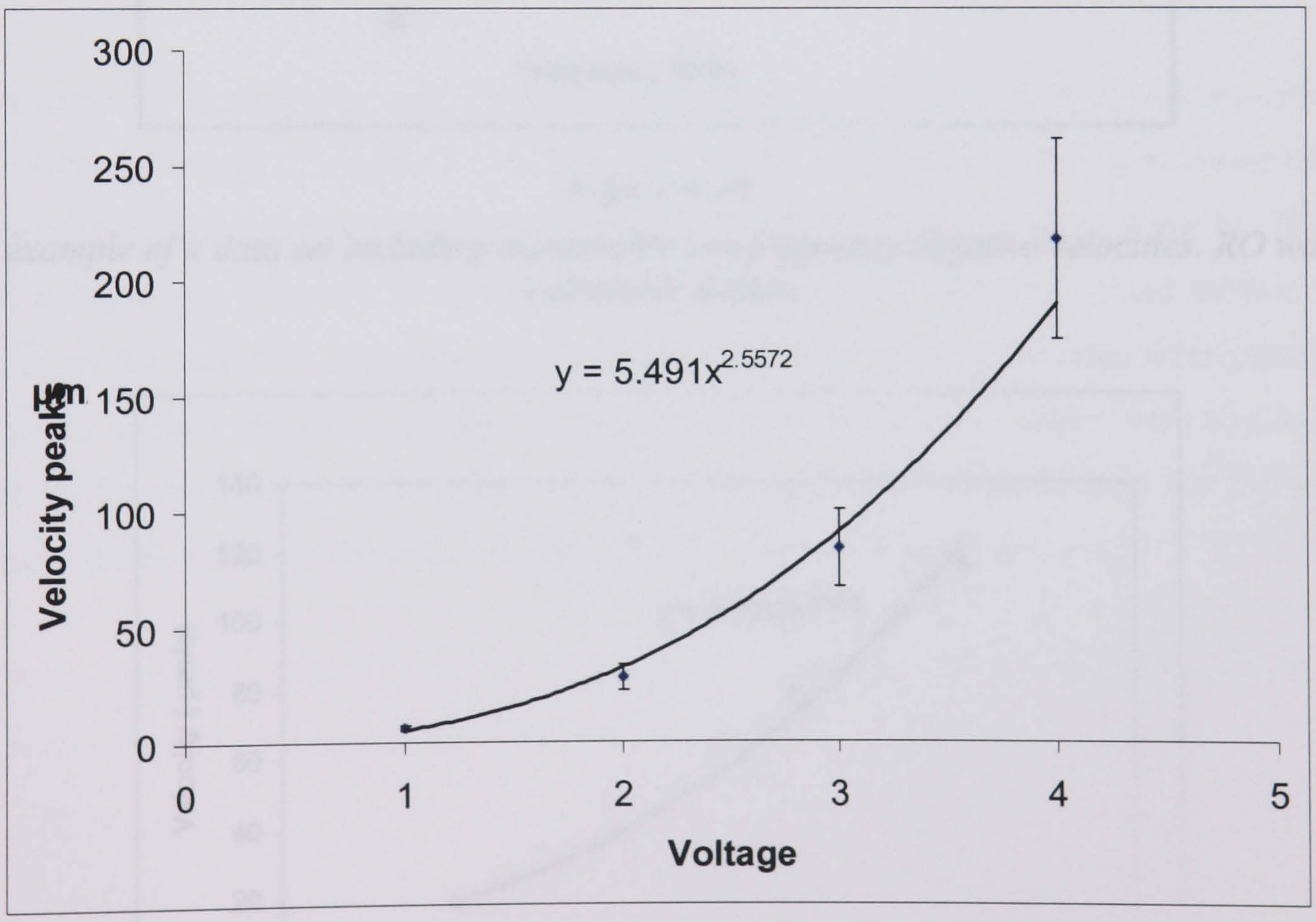

Figure 9-9

Velocity/voltage dependence on 3 electrode device

9.3.4 Anomalous data

Occasionally, spurious negative velocities were observed in the low frequency regime between ~0.1-1 kHz. These were generally difficult to measure due to their sporadic, often non-linear nature but tended to occur with data sets that peaked at slightly higher frequencies with lower than average velocities. An example of such a data set where the low frequency velocities were relatively more uniform is shown in Figure 9-10 in the interest of providing a wider picture of possible effects, so that a finer discernment between potential pumping mechanisms may be possible.

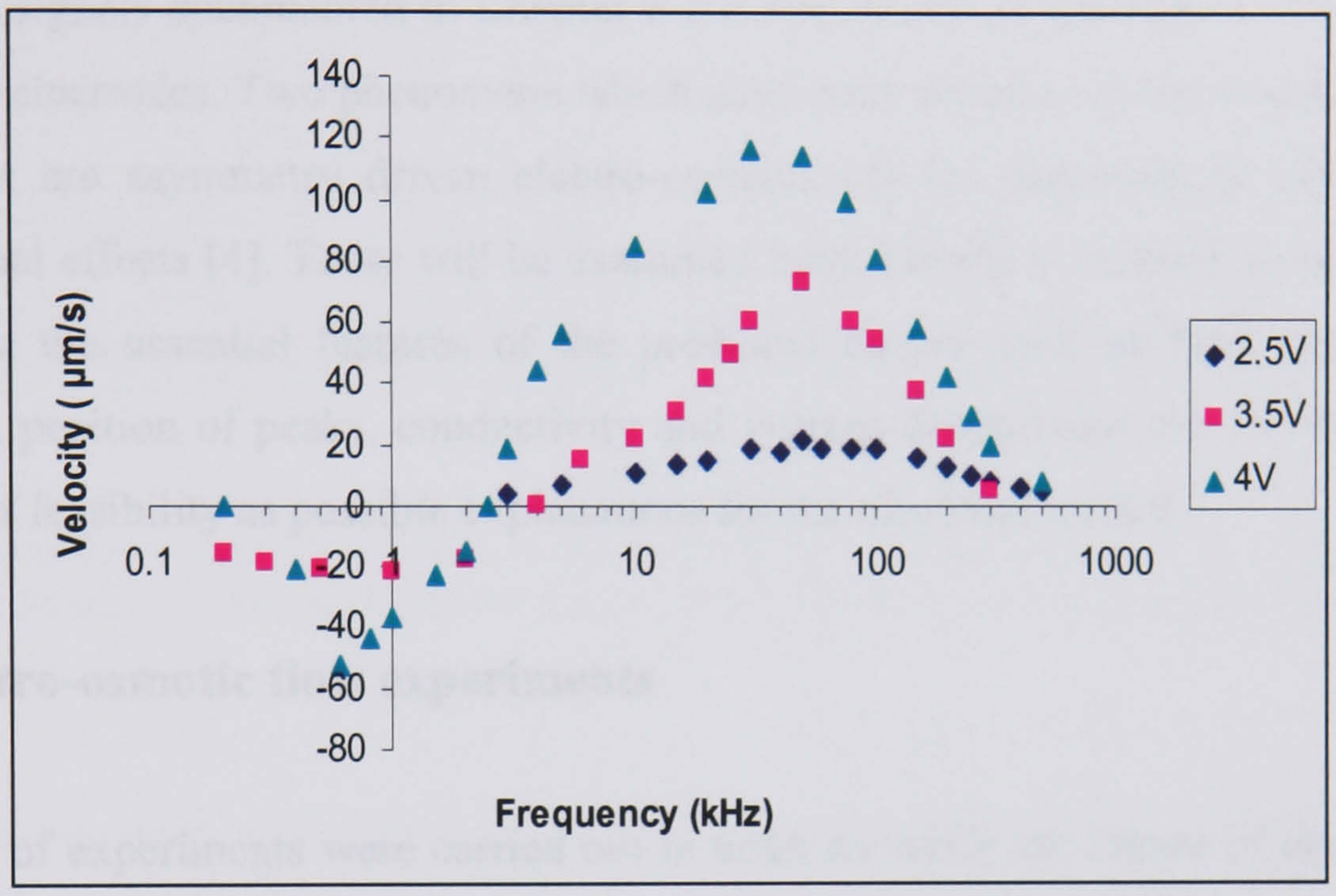

Figure 9-10

An example of a data set including measurable low-frequency negative velocities. RO water, 4 electrode device.

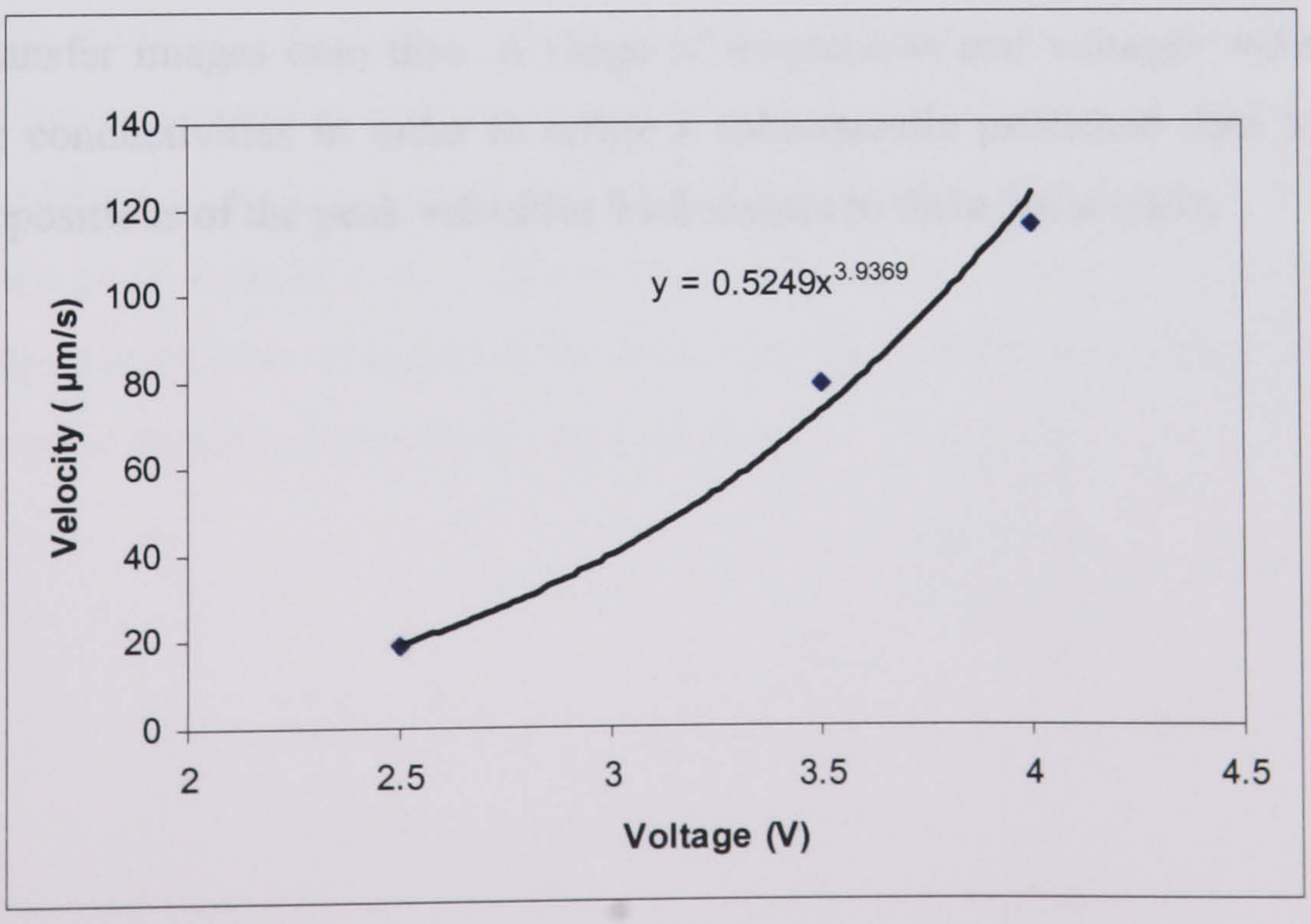

Figure 9-11

Velocity/voltage relationship in anomalous data set

9.3.5 Potential mechanisms

From the ostensible features of the velocity curves several possible pumping mechanisms can be postulated. Viscous drag resulting from the net asymmetric motion of the beads can be effectively ruled out since the pumping occurs also in the absence of the negative DEP signal when there is no asymmetric transport. Moreover, this would not explain the peaked velocity distribution or the reversal of direction at high voltages. A travelling wave mechanism can similarly be discounted on the grounds of functionality at a single frequency and is also unlikely to contribute in the case of 2 applied signals as the interference effects between the signals documented in Chapter 8 are insufficient to generate a consistent phase lag between electrodes. Two phenomena which have been reported in the literature to induce fluid motion are asymmetry driven electro-osmosis [3] (as described in Chapter 3) and electrothermal effects [4]. These will be examined more closely in relation to the data taking into account the essential features of the predicted curves such as their shape, velocity magnitudes, position of peaks, conductivity and voltage dependence etc. in order to assess their level of feasibility as possible explanations for the observed motion.

9.4 Electro-osmotic flow experiments

A series of experiments were carried out in order to verify the nature of electro-osmotic flow when a voltage is applied between a pair of parallel electrodes. The dimensions of the electrodes, which were fabricated using standard photolithography, were 2mm by 100μm with a 25μm gap in order to allow a sufficient distance for appraisal. Fluid motion was monitored by means of tracer particles – 557nm latex beads - using the same arrangement as before to transfer images onto disc. A range of frequencies and voltages were applied for three buffer conductivities in order to refine a subsequently published data set [5] which outlines the positions of the peak velocities with respect to these parameters.

9.4.1 Results

The effect of electro-osmotic flow on castellated electrodes is shown in Figure 9-12. Particles are pushed away from the electrode edges and collect in the middle of the electrodes.

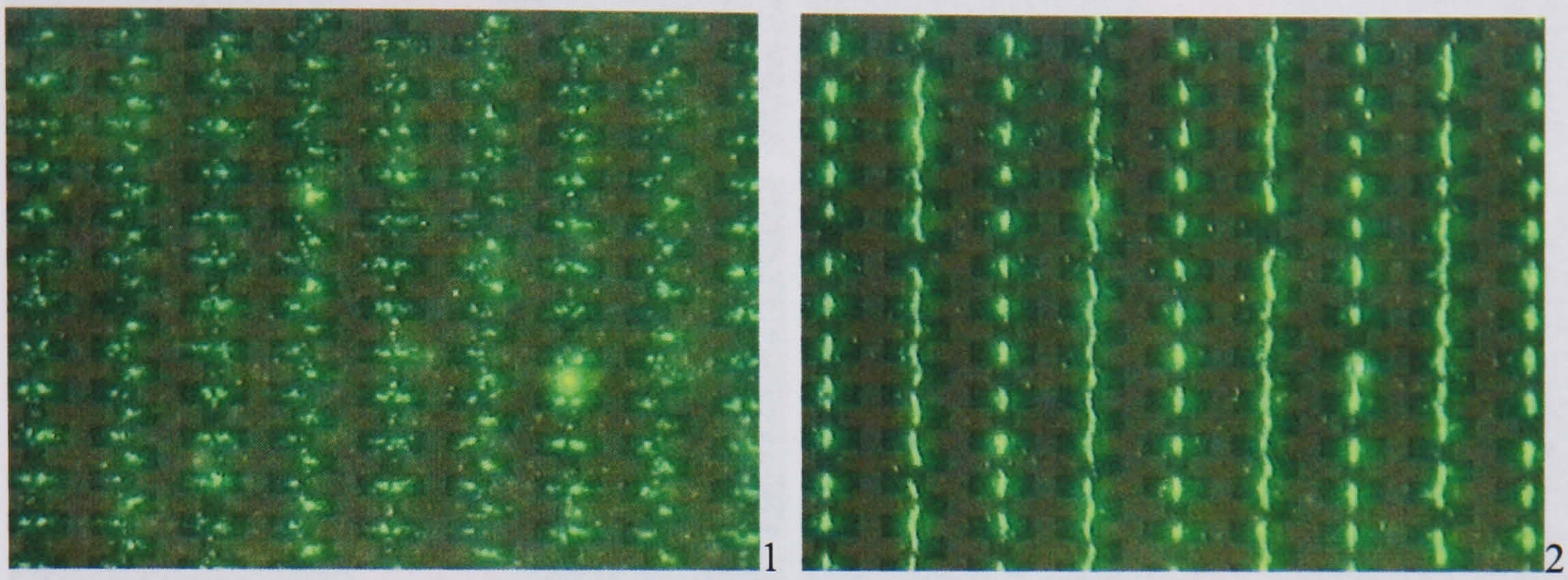

Figure 9-12

Electro-osmosis on castellated electrodes showing particles 1) being drawn into the centre of the electrodes on the application of a 3V, 10kHz signal, and 2) their final distribution.

The basic motion of the tracer particles on the parallel electrodes is shown in Figure 9-13.

Particles are initially drawn from above into the centre of the gap where they can be seen gradually coming into focus in consecutive video frames. They are then pushed across the electrodes in the manner theoretically described in Ch 3 with a peak velocity close to the electrode edge. Figure 9-15 and Figure 9-16 are typical examples of the type of motion observed. The result of this motion across the large electrodes is a re-circulation whereby particles are drawn upwards from the outer electrode edge and pulled back vertically into the gap. This fluid motion continues up to $\sim 10^5$Hz and for low conductivity peaks around 10^3Hz. The measured peak velocities as a function of voltage for 8.6mM KCl at 5µm over the electrode edge can be seen in Figure 9-14. The error bars correspond to the range in speeds observed over the data set measured for each voltage.

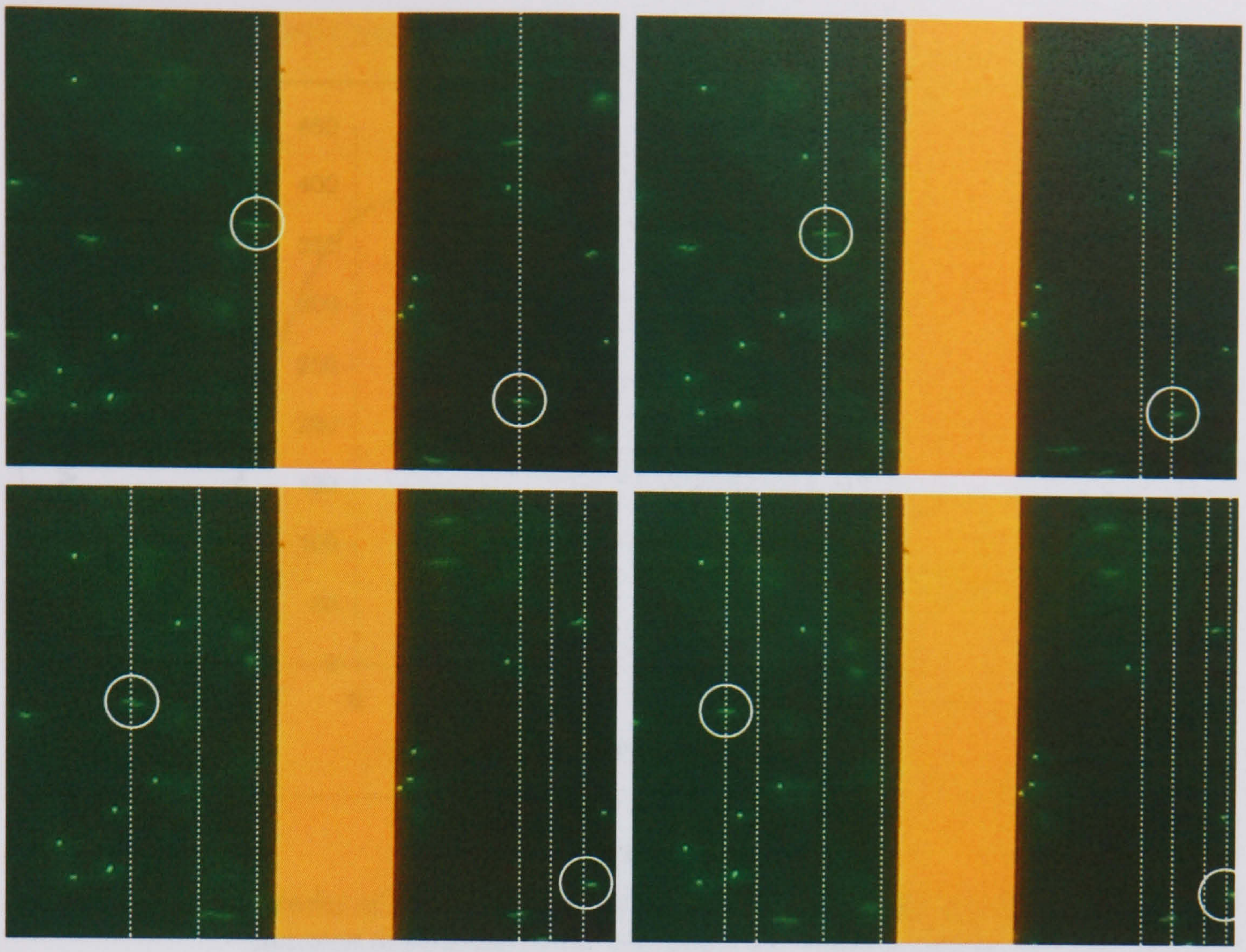

Figure 9-13

0.1s intervals showing particles being pushed away from the electrode gap with a peak velocity just beyond the electrode inner edge, slowing down towards the outside.

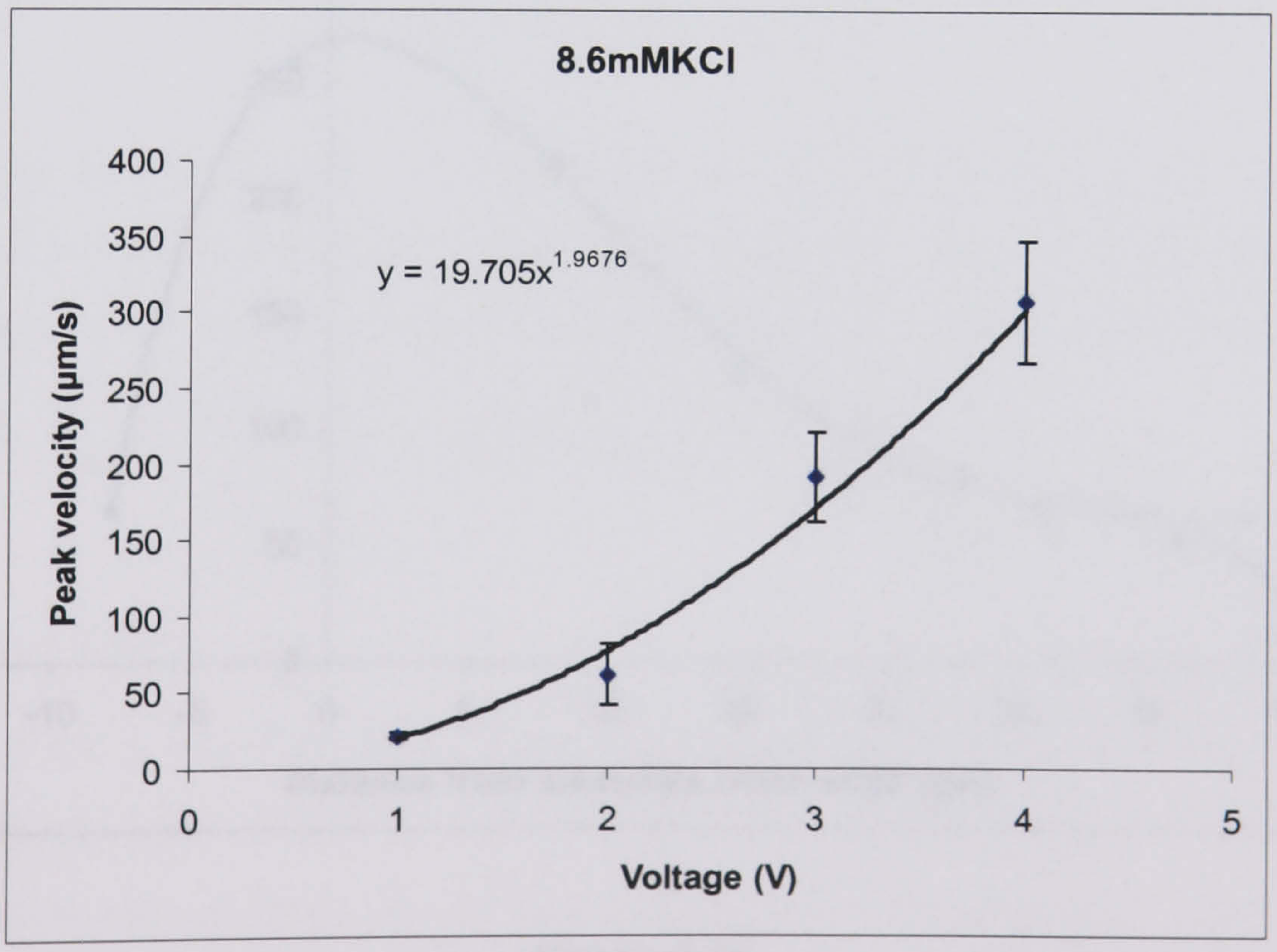

Figure 9-14

Peak velocity dependence on voltage for 8.6mM KC, showing very good agreement with the power 2 dependence indicated in [3] and [5]

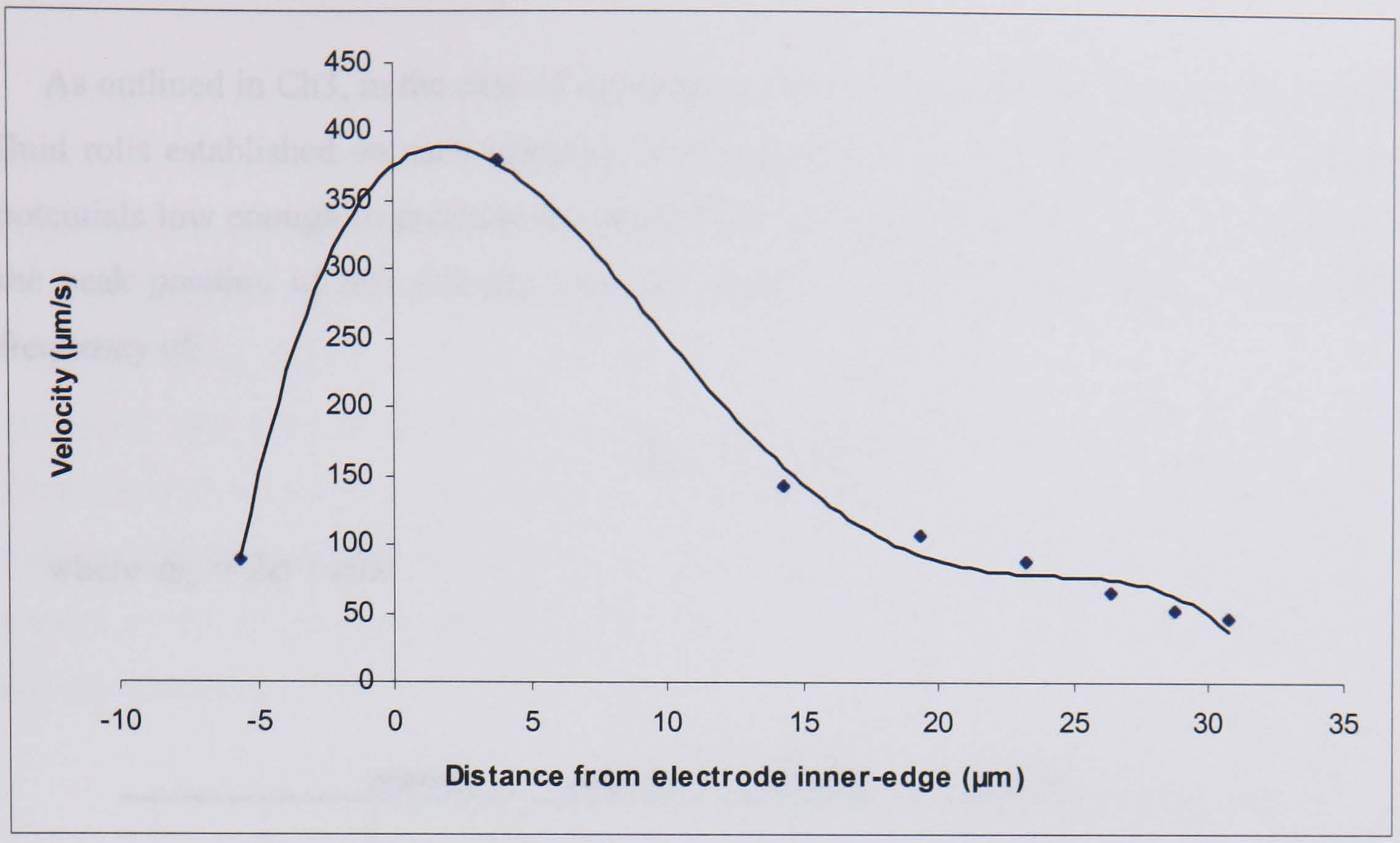

Figure 9-15

Motion across electrodes of electro-osmotically driven fluid. Velocity of tracer particles as a function of position on the electrode, 4V, 1kHz, 2.1mS/m

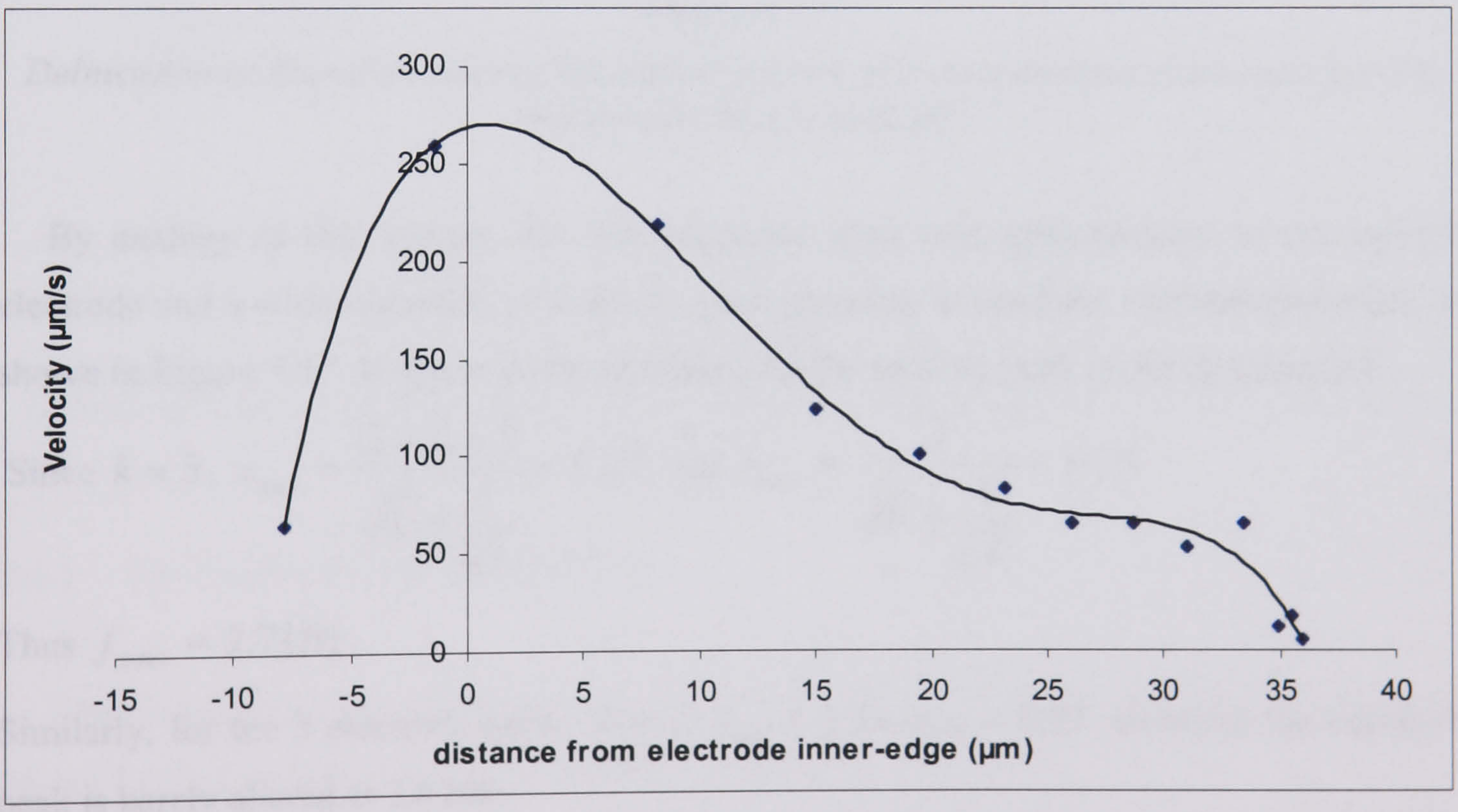

Figure 9-16

Observed fluid flow on parallel electrodes at 4V, 1kHz, 8.6mS/m

9.5 Electro-osmotic pumping

As outlined in Ch3, in the case of asymmetric electrode pairs there is an imbalance in the fluid rolls established on each electrode which results in net fluid propagation. At applied potentials low enough to preclude the electrolysis of water, [3] Brown *et al* have calculated the peak position of this velocity over the surface of the electrodes to be at an angular frequency of:

$$\omega_{\max} = \frac{\omega_0}{\sqrt{x_{\min} x_{\max}}}$$

where $\omega_0 = 2\sigma / \varepsilon\pi\kappa$.

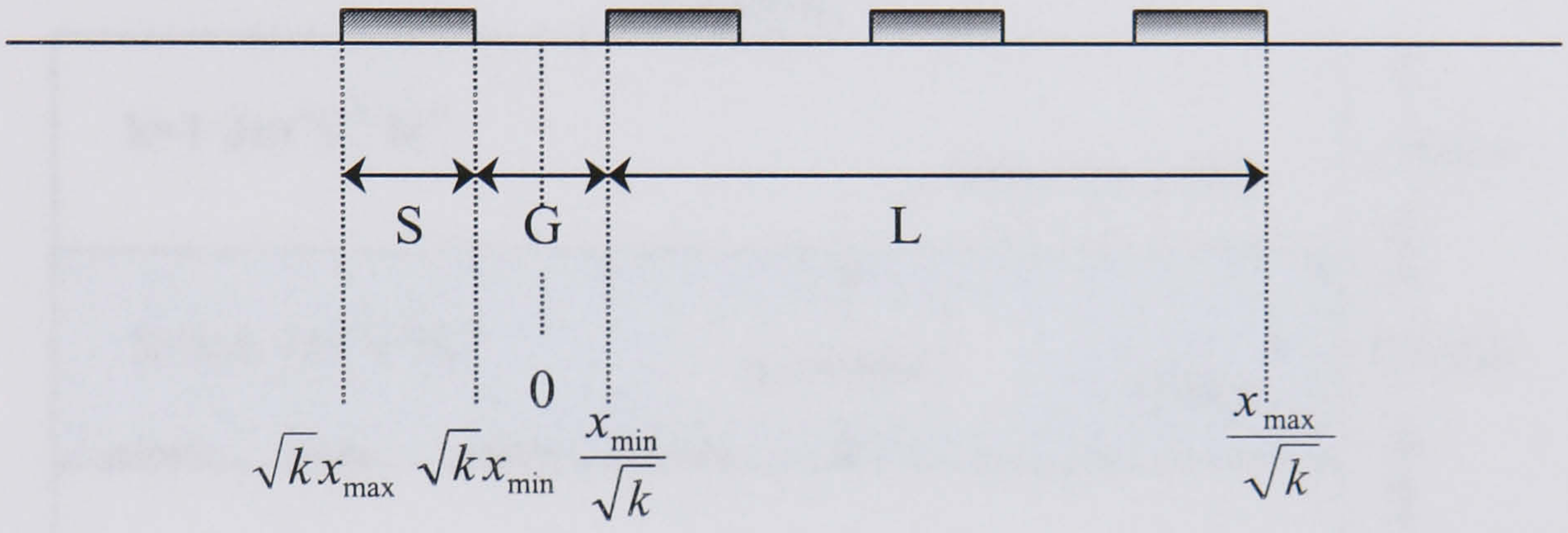

Figure 9-17

Delineation of Brownian ratchet electrodes in terms of a co-ordinate system analogous to that used by Brown et al [3]

By analogy to this system, the four electrode array was approximated to one narrow electrode and a wide electrode of width L, corresponding to the three earthed electrodes, as shown in Figure 9-17. In this way the frequency of the velocity peak could be estimated.

Since $k = 5$, $x_{\max} = \dfrac{G+L+S}{\sqrt{k}+\dfrac{1}{\sqrt{k}}} = 5.22$ and $x_{\min} = \dfrac{S}{\sqrt{k}+\dfrac{1}{\sqrt{k}}} = 0.75$

Thus $f_{peak} = 2.7kHz$.

Similarly, for the 3 electrode array, $k = 3$, $x_{\max} = 4.33$, $x_{\min} = 0.87$, therefore the expected peak is barely altered at 2.8 *kHz*.

According to this analysis, the position of the peak is unchanged by variation in the overall scale of the electrodes although size inversely affects the velocity magnitude.

9.6 Numerical simulation of electrothermal pumping

In order to theoretically assess the electrothermal flow resulting from this arrangement the solution for the electric field was used to obtain the thermal field so that the electric body force could be derived and substituted into the Navier-Stokes equation (3-4).

The electrical and corresponding thermal fields for the four electrode system were modelled using FlexPDE. The solution space is shown in Figure 9-18. Translational symmetry was assumed along the electrode array therefore periodic boundary conditions were used for all parts of the problem. The temperature boundary conditions were set at room temperature, 300K, on the upper and lower glass-air interfaces and the fluid velocity vectors at the water-glass interface were set at zero in accordance with an impenetrable viscous boundary.

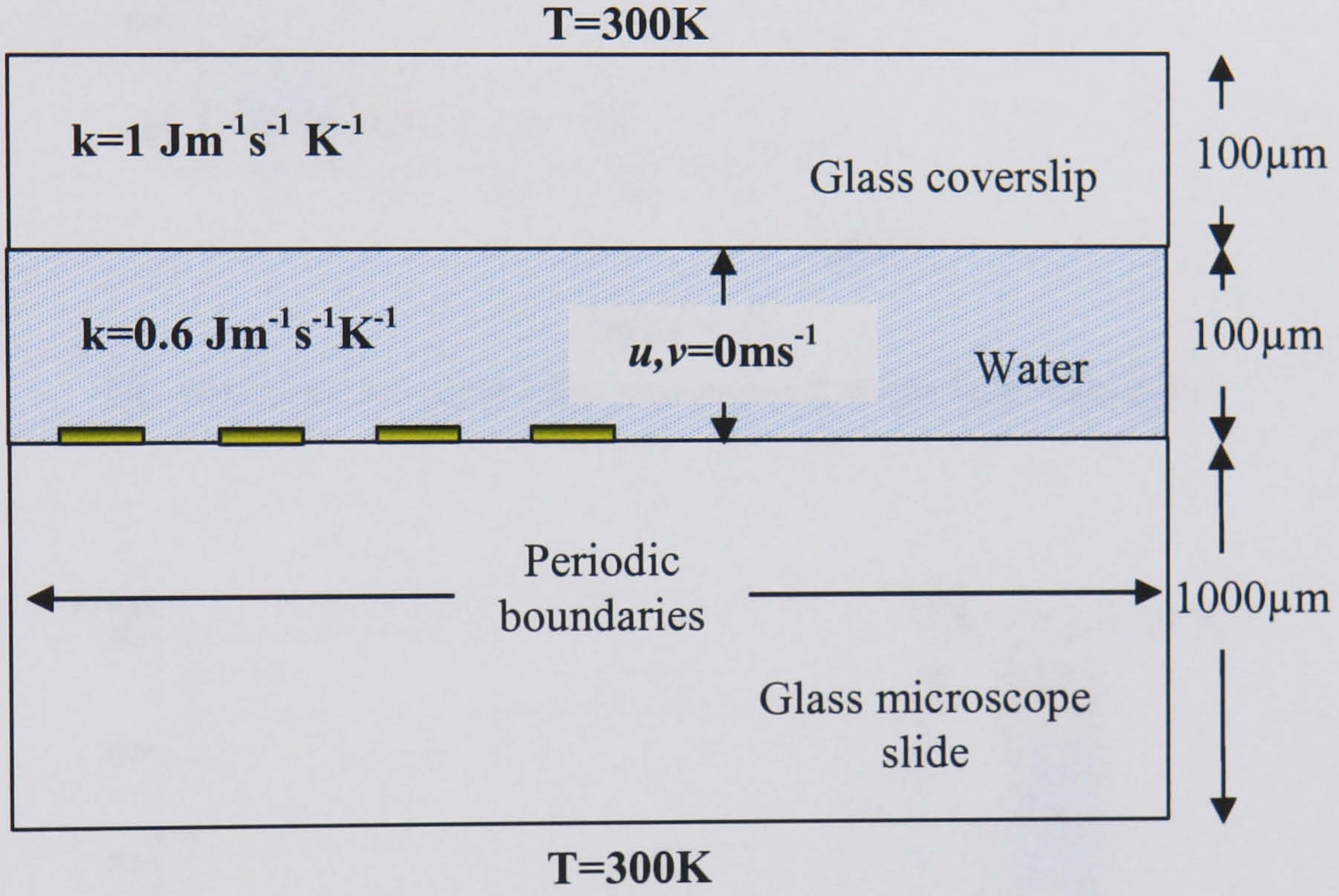

Figure 9-18

Outline of solution space and boundary conditions for the electrical, thermal and velocity calculations

9.6.1 Electrothermal field modelling

The electric field was calculated in the manner described in Chapter 6 and the steady state energy balance equation was used to obtain the thermal field i.e.:

$$k\nabla^2 T + \langle \sigma E^2 \rangle = 0 \tag{3-6}$$

where viscous dissipation and convection have been neglected for reasons outlined in Chapter 3. The electrodes, being very thin, were assumed to be transparent to the flux of heat and so the only heat source considered in this instance was that due to the electric field. The electrical potential, imported to the thermal calculation to produce the electric field source term, is shown in Figure 9-19 and the resulting thermal field in Figure 9-20.

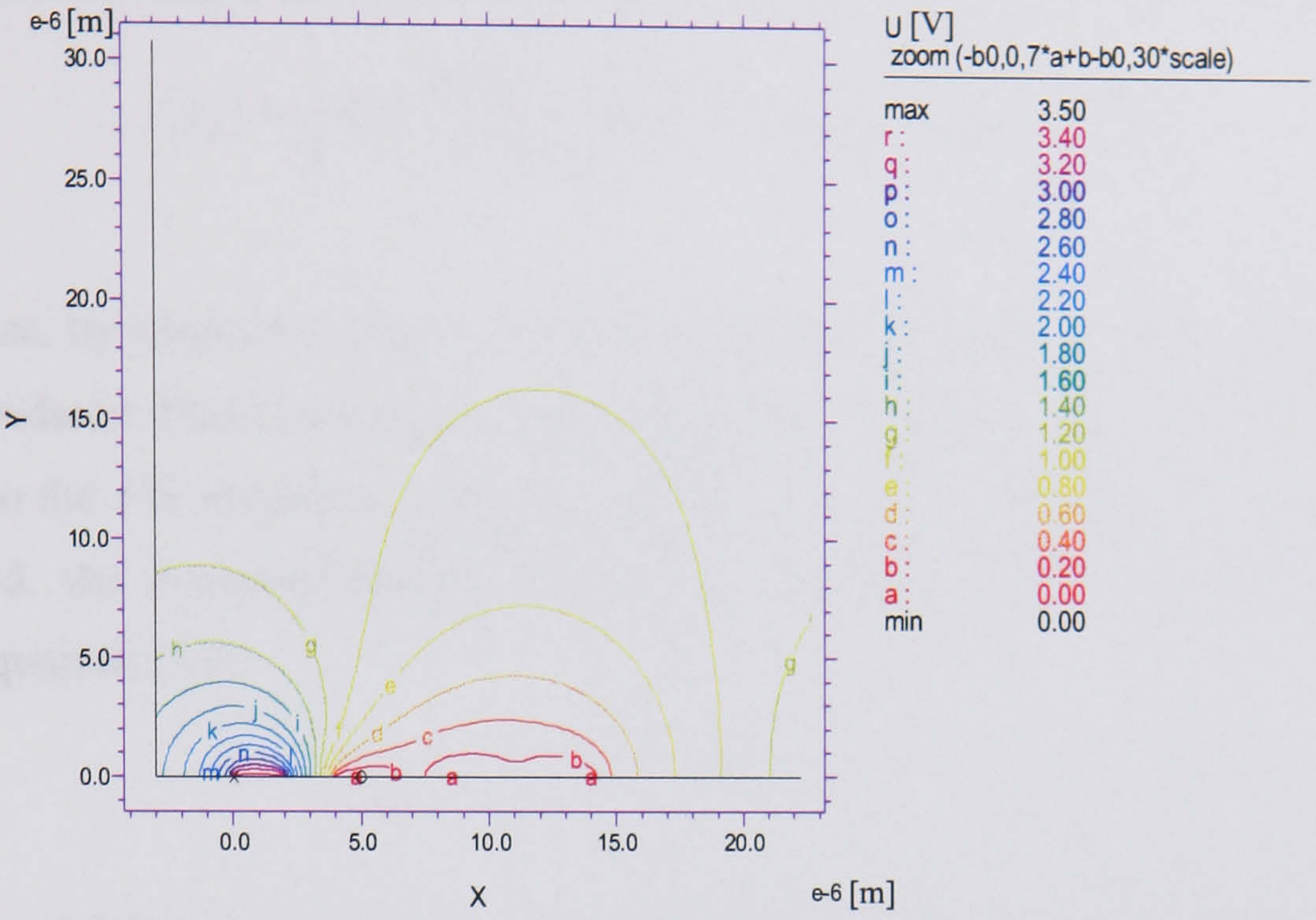

Figure 9-19

The electrical potential imported to the thermal field calculation.

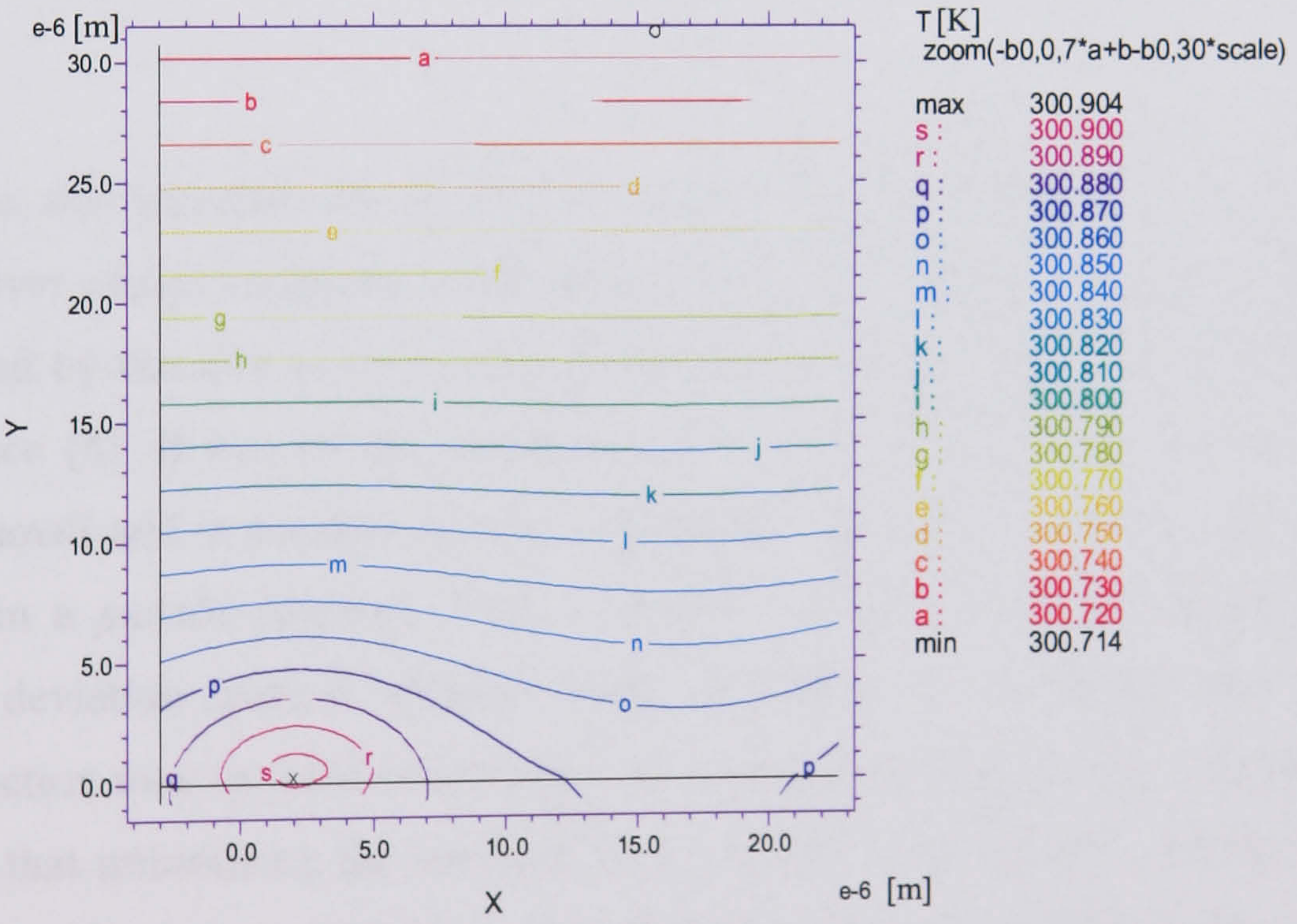

Figure 9-20

The thermal field as the result of Joule heating.

9.6.2 Simulated electrothermal flow pattern

In order to solve for the fluid motion using the Navier Stokes equation (3-4):

$$-\nabla p + \eta \nabla^2 \underline{u} + \rho\langle f_e \rangle = 0$$

the electric and thermal fields were used to calculate the force term, given by equation (3-13):

$$\langle f_e \rangle = \frac{1}{2}\mathrm{Re}\left(\frac{\sigma\varepsilon(\alpha-\beta)}{\sigma + i\omega\varepsilon}(\nabla T.E_0)E_0^* - \frac{1}{2}\varepsilon\alpha|E_0|^2 \nabla T \right)$$

In this case, by contrast to that of a travelling wave field, only the real part of the E-field need be considered. Fluid movement arises due to the asymmetry in the static thermal field - as opposed to the TW scenario, where translation of a symmetric field gives rise to pumping. As stipulated, the incompressibility of the fluid necessitates also the imposition of the continuity equation (3.5):

$$\nabla.\underline{u} = 0$$

Evidently, the Navier-Stokes and continuity equations alone are insufficient to solve for the velocity and pressure fields and so a third equation involving pressure must be derived. This was done by differentiating Navier-Stokes with respect to x then y and adding the two results. Using the continuity equation to eliminate terms this can be reduced to:

$$\nabla^2 p = 0 \qquad (9\text{-}1)$$

However, this increases the number of constraints on the final solution, which in a finite element solver causes heightened difficulty in obtaining convergence. This difficulty can be characterised by the size of the region of feasable solutions compared with the size of the sample space [6]. If two of the constraints are set exactly to zero, the feasible region is extremely small and in practice does not converge. Therefore, equations (3.5) and (9-1) are combined in a *penalty function*. This is simply a method of softening the constraint by penalising deviation from it without totally excluding all violations. Here, the simplest penalty function may be used which involves multiplying the continuity equation by a large number so that minimising the equation forces it very close to zero. Setting it equal to eq (9-1) imposes the same condition on this. Therefore the constraints on the system may be expressed as:

$$\nabla^2 p = L\left(\frac{\partial u_x}{\partial x} + \frac{\partial u_y}{\partial y} \right) \qquad (9\text{-}2)$$

where L is a large number - of the order 10^{15} for the optimum results.

The resulting flow profile is shown in Figure 9-21. As illustrated this does result in net motion of the fluid with a similar flow profile to that observed – but for the applied voltage and conductivity (3.5V, RO water) it appears, in magnitude, essentially negligible.

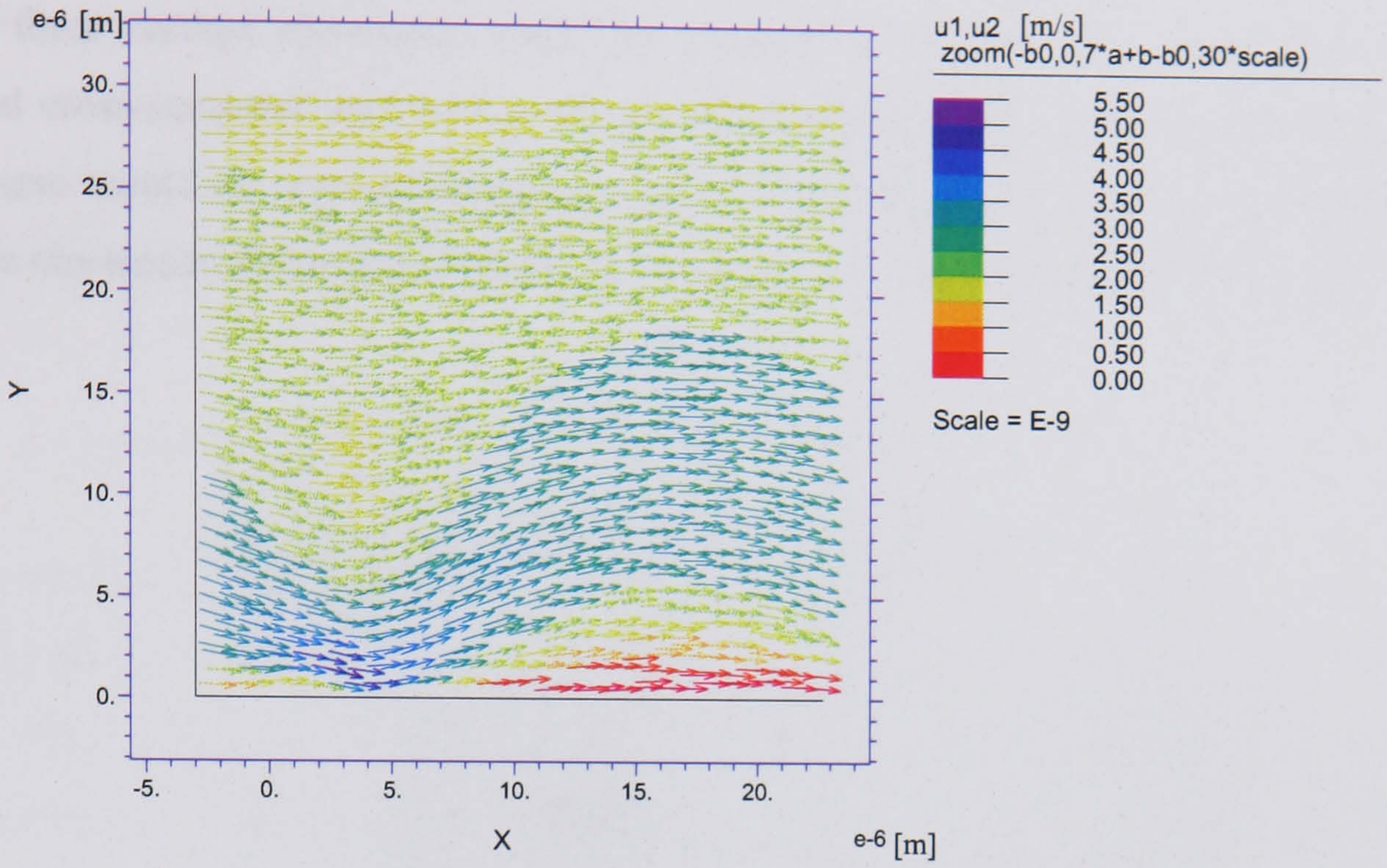

Figure 9-21

Electrothermal flow velocity profile in RO water, V=3.5, f=2.8kHz.

Heated electrodes

The case of an induced temperature rise on the electrodes as the result of the applied signal was also investigated. Electrothermal flow has been discussed in the context of heating from the fluorescent microscope lamp in, [4] where a temperature rise of 15K was measured on a pair of 0.5mm×2mm parallel electrodes with a 25 μm gap, causing fluid motion in combination with an applied AC signal.

It is proposed here that heating could occur if there was significant power dissipation in the electrodes due to current flow (proportionally greater in the electrode with the applied signal as an equal and opposite current will be distributed throughout the three earthed electrodes). As a first approximation, the electrodes have been assumed to have infinitely high conductance compared to the medium, so that no voltage drop was assumed along their length. However, at 2 μm width, they are extremely narrow, with a feature size considerably smaller than other devices of this type, therefore the potential difference across their length could be enough to generate a significant power output. Without precise measurements of this voltage drop and an adequate thermal map of the surrounding fluid, the degree of electrode heating can only be very crudely estimated. The following arguments are intended to show only that a significant temperature rise on the electrodes cannot, at this stage, be ruled out.

The resistance of a single electrode is readily calculable from $R = A / l\sigma$, where σ is the electrical conductivity, A is the cross sectional area of the electrode and l its length. Using the value of σ for gold, given by Table 9-1, this resistance is ~34 Ω. If the voltage drop across the bus-bars is considered negligible due to their much larger width, the parallel array of 100 such electrodes will have a combined resistance of 0.34 Ω. The resistance of the array of three earthed electrodes would be reduced by a factor of 3 accounting for their combined cross-sectional area and so the power dissipation and corresponding temperature rise in these would be correspondingly reduced. These can be assumed to be in series with the single electrodes and medium resistance/capacitance parallel combination (Figure 9-22).

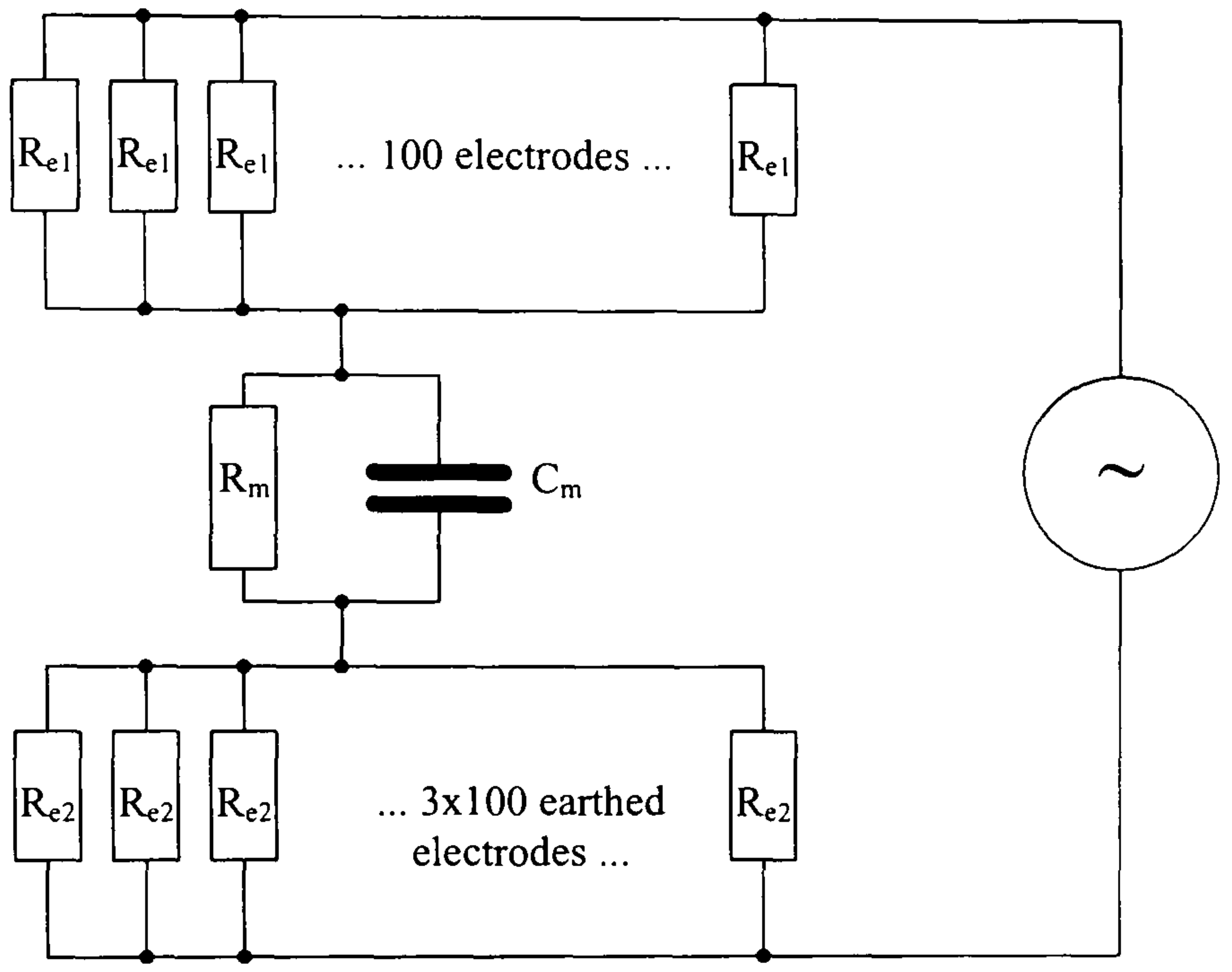

Figure 9-22

Equivalent circuit of device representing scenario with significant electrode resistances, R_{e1} for single electrodes, R_{e2} for 3 interconnected earthed electrodes. R_m and C_m are the effective fluid medium resistance and capacitance.

On the first electrode the resistance is such that a voltage drop along its length of 1mV would be compatible with a current of ~3mA. This translates into a power of $I^2R \approx 3\mu W$, which, considering that the thermal conductivity of the electrodes (Table 9-1) is several orders of magnitude greater than water, could be assumed to be distributed as heat much faster in the electrodes than it is dissipated in the medium. Thus, referring again to the data in Table 9-1, from simple heat capacity arguments, based on consideration of the mass, m, of metal in the bus-bar/electrode/bonding pad combination (~2×10^{-11}kg), it can be seen that if all the power went into heating the electrodes a temperature rise of several tens of degrees Kelvin per second i.e:

$$\frac{\Delta T}{t} = \frac{P}{cm} = \frac{3\times10^{-6}}{1280\times2\times10^{-11}} = 117\frac{K}{s}$$

is predicted. The temperature rise would, of course, peak some way below this since at a certain temperature the heat flow rate into the medium would be sufficient to establish an energy input-output balance even if thermal equilibrium with the fluid were not attained. This temperature should be comfortably below the boiling point of water, since bubble formation around the electrodes is not frequently observed – although sample drying is noticeably speeded up with an applied signal.

Electrical Conductivity (σ)	**Thermal Conductivity (k)**	**Density (ρ)**	**Specific Heat Capacity (c)**
$4.5\times10^{7}\ \Omega^{-1}\mathrm{m}^{-1}$	$318\ \mathrm{Jm^{-1}s^{-1}K^{-1}}$	$19.32\ \mathrm{gcm^{-3}}$	$1280\ \mathrm{Jkg^{-1}K^{-1}}$

Table 9-1

General properties of gold used to estimate temperature rise in electrodes

Possible temperature distributions on electrodes

In accordance with the above order of magnitude estimates of temperature as a result of current flow, three different thermal maps were considered, listed in Table 9-2, corresponding to the temperature definitions shown in Figure 9-23. In the first two cases, the highest temperature is applied on the first electrode In recognition of the fact that the current here is 3 times higher than on the earthed group, and therefore the power dissipated greater by a factor of 9. The second case corresponds to the possibility of an uneven distribution of current or significant heat flow across the first gap. The third temperature distribution is a limiting case assuming all electrodes reach thermal equilibrium - or indeed are heated by another external source such as the microscope light, as in the publication previously alluded to [4]. Essentially, however, these are introduced only as an academic exercise in order to investigate the type of thermal field that would give rise to velocities closer to those observed.

An example of thermal map 1, for T_{max}=30K, is shown in Figure 9-24 with the corresponding velocity profile in Figure 9-25. The results for T_{max} ranging from 10K-70K are shown in Figure 9-26 for all three temperature distributions.

As can be seen, the induced velocities are now of the order of microns/second, and therefore comparable to, if still considerably smaller than, those observed. In the case of a temperature rise only on the first electrode, corresponding to the largest thermal gradients, the highest velocities are reached.

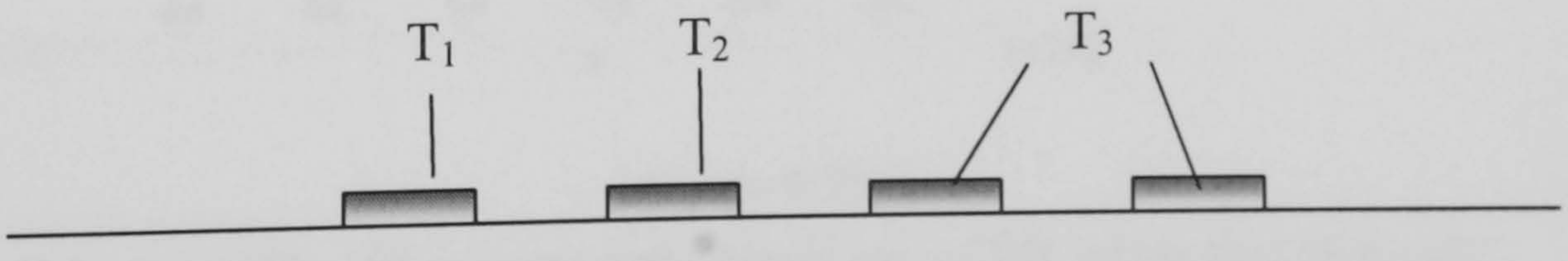

Figure 9-23

Temperature definitions as referred to in Table 9-2

Thermal map 1	Thermal map 2	Thermal map 3
$T_1=T_{max}$, $T_2=T_3=0$	$T_1=T_{max}$, $T_2=T_1/2$, $T3=0$	$T_1=T_2=T_3=T_{max}$

Table 9-2

Imposed temperature combinations on electrodes as defined in Figure 9-23

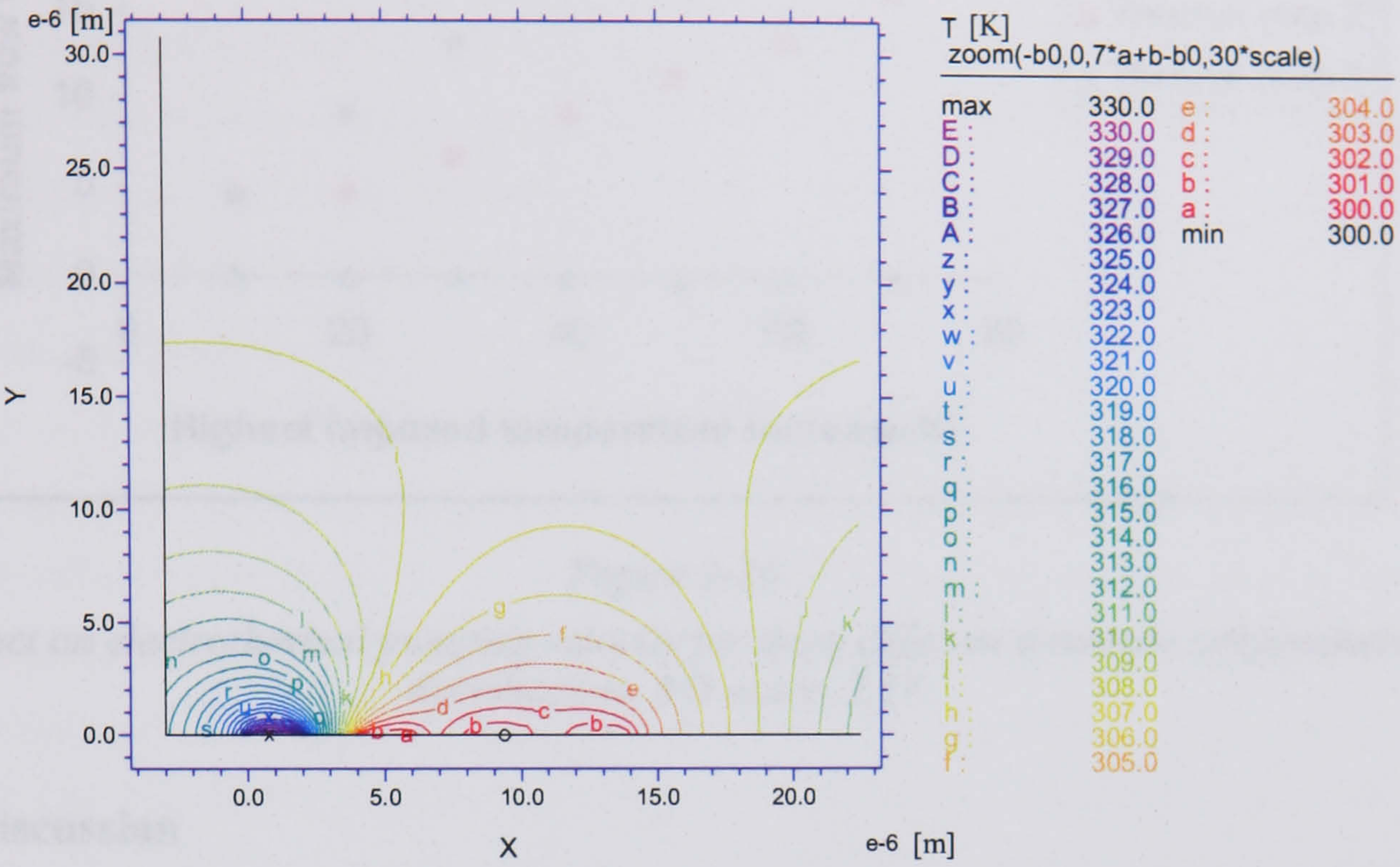

Figure 9-24

Thermal map associated with a temperature rise of 30K on the first electrode.

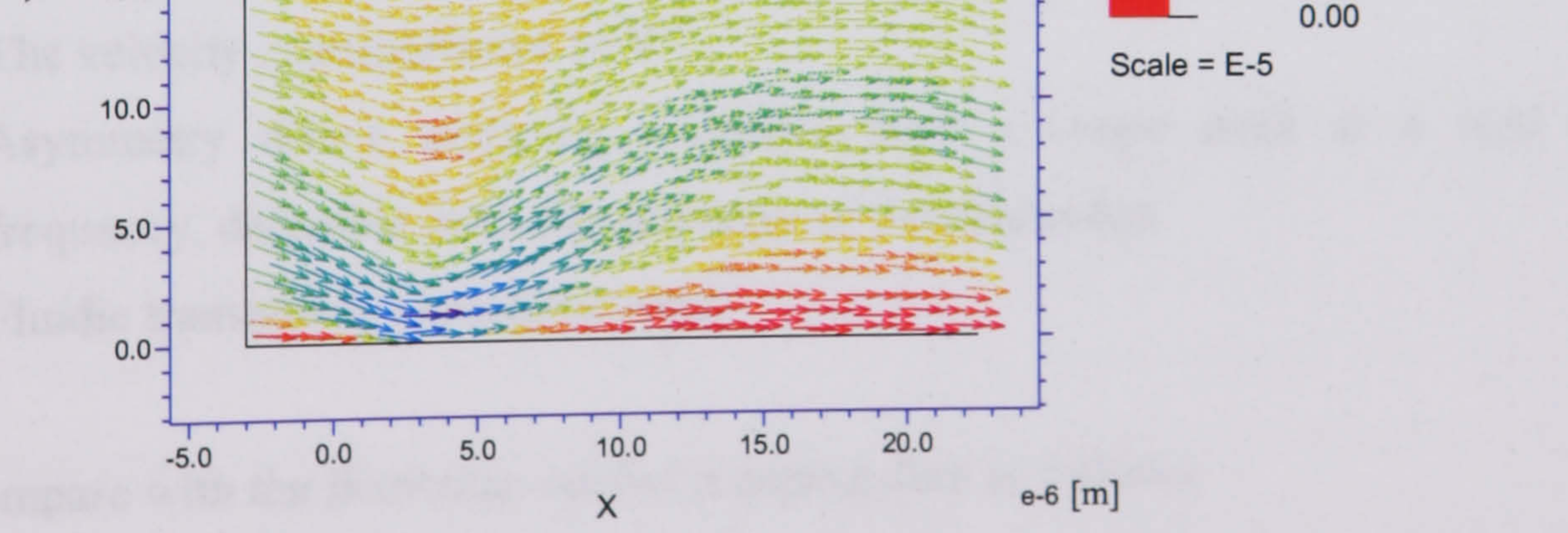

Figure 9-25

Velocity profile with imposed temperature rise of 30K on the first electrode.

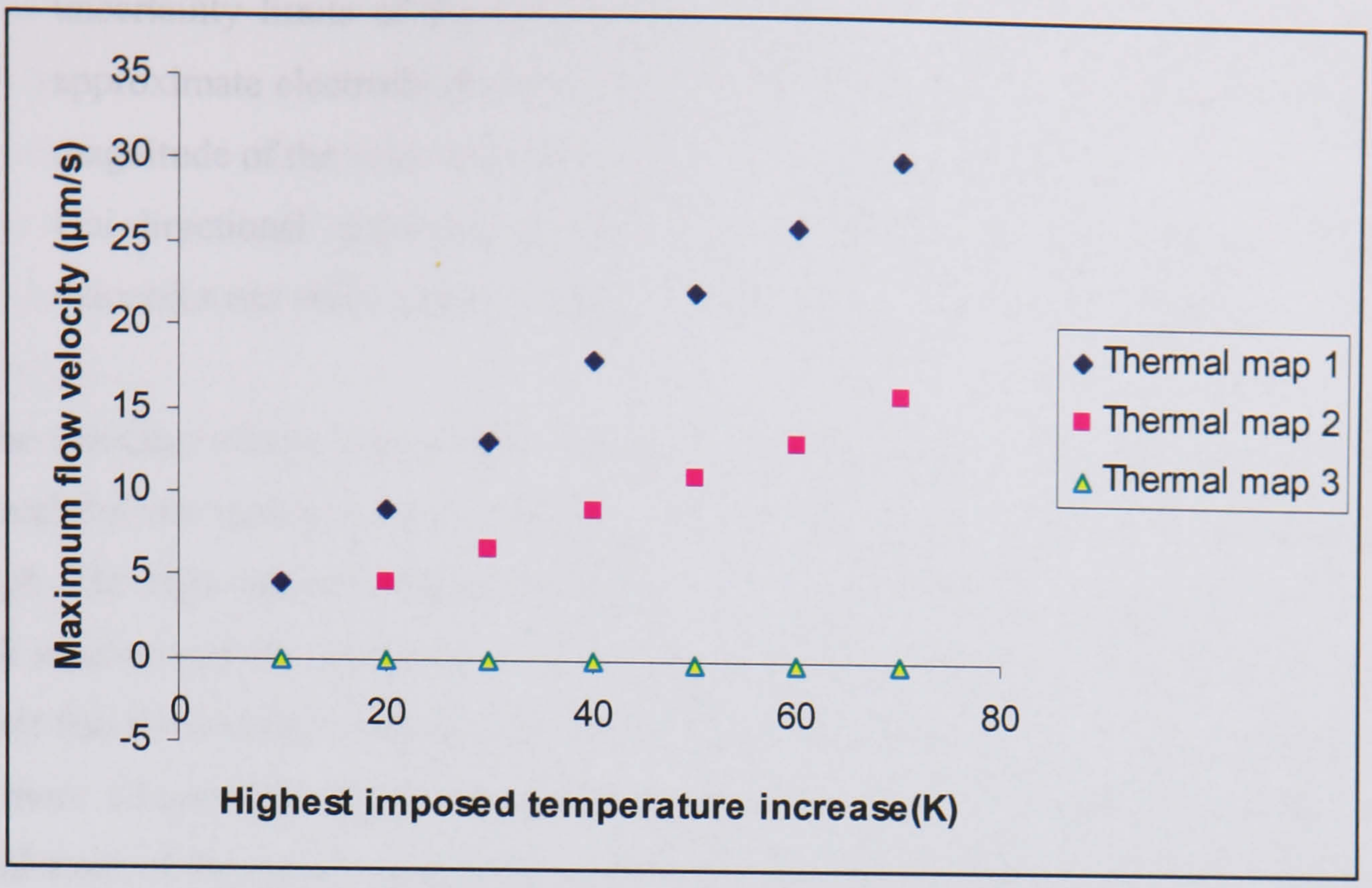

Figure 9-26

Effect on electrothermal pumping velocity for three different electrode temperature distributions. RO water, 3.5V.

9.7 Discussion

9.7.1 Compatibility with electro-osmosis

The correlation between the measured velocity curves on the Brownian ratchet electrodes and the predicted results of an electro-osmotic mechanism driven by the asymmetry of the system is apparent in various degrees. The essential features of electro-osmotic motion as derived from the experimental data on parallel electrodes [5] and the theoretical and experimental analysis of Brown *et al* are:

i) The velocity is inversely proportional to conductivity.
ii) The velocity is proportional to V^2.
iii) Asymmetry driven pumping velocities have a single peak at a well defined frequency, derivable from the geometry of the electrodes.
iv) Fluidic transport is monodirectional.

These compare with the Brownian ratchet pumping data as follows:

i) Inverse proportionality of velocity with salt concentration is manifest in Figure 9-3
ii) Indices of power dependence of velocity on applied voltage range from 2.56 to 3.94.
iii) The curves do manifest well defined peaks (3.5 and 1.8kHz on the 4-electrode device with one and two applied signals respectively) within the experimental

uncertainty limits of the value predicted by the treatment of Brown *et al* for the approximate electrode geometry and close to the observed electro-osmotic data. The magnitude of the velocity is higher than that observed by Brown.

iv) Uni-directional pumping is generally observed, although sporadic, negative velocities can occur at low frequencies and clear reverse motion at high.

The velocity-voltage relationship is largely ambiguous due to the high error range of the data and the low number of curve fitting points but the power indices do seem generally to be high. The high velocity magnitudes may be compatible with the use of RO water instead of salt solution and the smaller scale of the electrodes, if these factors are sufficient to cancel the fact that the increased capacitance of the Ti layer, on which an oxide forms, should lead to a more compressed double layer and therefore lower velocities. The variability of the overall scale of the curves on repetition of the experiments may also be linked to the relative instability of RO water conductivity. It has been suggested by Brown *et al* [3] that for field strengths of this magnitude some level of charge injection from the electrodes would have to be accounted for. No water insulation breakdown in the Brownian ratchet device was observed, but this does not preclude localised effects close to the electrodes which may diffuse into the bulk or result, in the absence of the attainment of equilibrium, in granular or stratified regions of locally varying conductivity. Brown *et al* have, in fact, deduced from impedance measurements that across the double layer formed on the electrodes the conductivity of their fluid is a factor of 14 times greater than that expected from a 10^{-4}M solution of $NaNO_3$ while κ is a factor of 7 smaller. This apparent compression of the double-layer can be attributed, possibly, to a high proportion of charge residing in a Stern layer, including, specifically, a large number of the small electrolysed water ions, H^+ and OH^-. It must be stressed, however, that this level of compression is not entirely physically viable as changes in the double-layer permittivity would also occur which would in turn affect the capacitance and hence the interpretation of the Debye length. It has also been pointed out that the larger conductivity could be related to the semi-circular field line approximation which may not be adequate near the electrode edges. Conduction between electrodes must also be considered, particularly in the Brownian ratchet device case where the field strengths are significantly higher. Instabilities could thus be generated leading to changes in the observed velocities or non-linear/chaotic motion. This may correspond to the sporadic motion occasionally observed at frequencies below 1kHz but does not elucidate why higher than average flow velocities should occur with the imposition of an additional, high frequency signal far outwith the electro-osmotic pumping range, since this should only increase the conductivity locally or globally as outlined, leading to a lowering of velocity.

A high frequency reversal of flow direction is also not predicted in the theoretical basis of asymmetry induced electro-osmotic pumping at its present level of development. Clearly the reversal of roll direction is unphysical in an electro-osmotic scenario, at least at frequencies lower than the charge relaxation frequency of the electrodes, therefore it is more meaningful to consider the origin of the net flow profile. This has only been qualitatively calculated in Brown's analysis by taking into account the distance above the electrodes over which the shear decays for each roll in order to establish which is dominant. For linear flow this has a characteristic distance, y_0, given by:

$$y_0 = \sqrt{\frac{\eta\tau}{\rho}}$$

where η and ρ are the viscosity and density of the medium and τ is the time over which the shear is applied to the fluid. If this time is taken to be that for the liquid to flow over the surface of the electrodes then considering the ratio of speeds between the small and large electrode, calculated to be k^3, the shear should penetrate k^2 times further over the large electrode. The net flow, then, should derive from the fact that the large rolls effectively merge in the bulk allowing free exchange of fluid between them. However, the validity of this approximation weakens as frequency increases since the velocity of large roll may become insignificant while that of the smaller roll is still considerable. How momentum and vorticity is dissipated by the separation into 3 of the large electrode, in the case of the Brownian ratchet is another factor which may reduce its dominance further. Small vortices may form above the connected electrodes, restricting the penetration of shear into the bulk, which could also be considered in terms of reducing the effective k factor. Discharging of the double layer due to ion movement in the small electrode would also be diminished at higher frequencies resulting in proportionally less velocity damping than would occur at low frequencies. Although still a small vortex, constrained by the physical size of the electrode, this could become dominant in determining the flow direction above a certain frequency.

9.7.2 Compatibility with electrothermal motion

The first observation is a negative one with respect to the applicability of this mechanism in that for the case of Joule heating the simulated flow rate is orders of magnitude too small. As outlined, however, Joule heating due to current flow in the fluid may not be the only heat source. Current flow in the electrodes, even on the scale of a few milliamps, is possibly enough to generate significant temperatures on the device. In this situation, the modelled flow rates are comparable to those observed experimentally, although still somewhat smaller.

However, the possibility, previously alluded to, of localised but substantial variations in conductivity and permittivity of the fluid may have a significant if as yet unquantifiable effect, particularly if the electrodes act as an additional heat source. If the pumping mechanism does have an electrothermal component then the observed velocities should be proportional to fluid conductivity and therefore these local, temperature induced variations may lead to an increased flow rate.

In the study carried out by Green *et al*, [7] with temperature increases of ~15K on the electrodes, electrothermally driven fluid rolls comparable to those formed by electro-osmosis have been observed. Small vortices close to the electrodes with a few particles entrained in rotational motion have been noted occasionally on the Brownian ratchet electrodes also. On this scale, with electrodes 250 times smaller than those used in the above study, the velocity of the rolls would be orders of magnitude higher. If these were due to electrothermal effects instead of electro-osmosis, they could feasibly produce a similar pumping mechanism with the penetration of this vorticity into the medium causing large scale fluid entrainment.

Apart from the unresolved scale issue, other essential features of electrothermal motion as outlined by Ramos *et al* [8] are worth considering in comparison with the data. The basic properties of the electrothermal vortices formed on two parallel electrodes are:

i) The velocity is essentially constant with frequency up to the point where the dielectric force begins to dominate over the Coulomb force (first and second terms respectively of (3-13)).

ii) The switch in dominance of these forces corresponds to a change in direction of the fluid rolls and occurs around the charge relaxation time.

iii) The maximum value of the dielectric force is smaller than the Coulomb force by a factor of approximately 10.

iv) The velocity in both cases is proportional to conductivity and the power relation with voltage has index 4.

These compare with the features of the data as follows:

i) Measured velocity not constant but with clearly discernable peak.

ii) Pumping generally falls off around the order of magnitude of the charge relaxation time ~100kHz for RO water.

iii) The ratio of speeds on either side of τ is ~10-20:1.

iv) The velocities have been observed to be generally higher for two signals. The velocity dependence on voltage is sometimes close to power index 4 but highly variable. The pattern on increasing the salt concentration of the medium as a whole, however, is a general decrease in pumping velocity.

These considerations also give some weight to the possibility of an electrothermal component to the flow. Although the first appears inconsistent, this does not preclude an electrothermal mechanism as there could be other perturbative flows present (see 9.7.3). As previously alluded to, heating induced increases in localised conductivity gradients may occur which would account for the higher velocities on the imposition of an additional high frequency, high voltage signal if the mechanism were electrothermal – i.e. with velocity proportional to conductivity.

The result that increasing the salt concentration of the medium as a whole causes a decrease in velocity (Figure 9-3) may have quite a different explanation in that the voltage applied to the device could be significantly lowered across the length of the electrodes in the presence of a fluid with uniformly higher conductivity. This drop could not be measured within the experimental set up due to the scale of the device, but with a micro-manipulable terminal voltmeter a more accurate assessment of the voltage across individual electrodes may be achieved. The voltage/velocity relationship is on average marginally closer to that expected from an electrothermal driving force although essentially inconclusive in differentiating between the two mechanisms.

9.7.3 A combination of mechanisms

The possibility exists that there is a combination of mechanisms in action and that the data curves may therefore be the result of a superposition of flows induced by both electrothermal and electro-osmotic forces. The observed peak, for example, could be the result of constant electrothermal motion being gradually reduced by an opposing electro-osmotic flow at lower frequencies. The fall off around 100kHz could be due to charge relaxation (this is higher with increased salt concentrations as expected) and the fact that a reversal of motion is not always measurable beyond this point could simply be attributed to the comparative scales of the Coulomb and dielectric forces. The lower frequency region where spurious negative velocities are sometimes observed may be the real electro-osmotic dominated region, where a smooth flow is not always established due to the potentially complex system of vortices formed on the electrode groups becoming unstable at high velocities. The magnitude of this flow can peak between 100Hz and 1kHz which is not incompatible with electro-osmotic data on parallel electrodes. This may correspond to data sets of generally lower than average velocities if the conductivity of the RO water in the sample was particularly low i.e. with minimal conductivity increases due to electrolysis etc – such that electrothermal motion, responsible for the higher frequency peaks, was less dominant with stronger electro-osmotic back flow. Moreover, if the application of two signals does indeed lead to local conductivity augmentation then the higher than average velocities measured in this case would be explainable as would the absence of negative velocities in the low frequency regime.

A summary of this hypothesis is illustrated in Figure 9-27 where potential regions of dominance of each force have been highlighted against a background schematic of a velocity curve with all of the experimentally observed features.

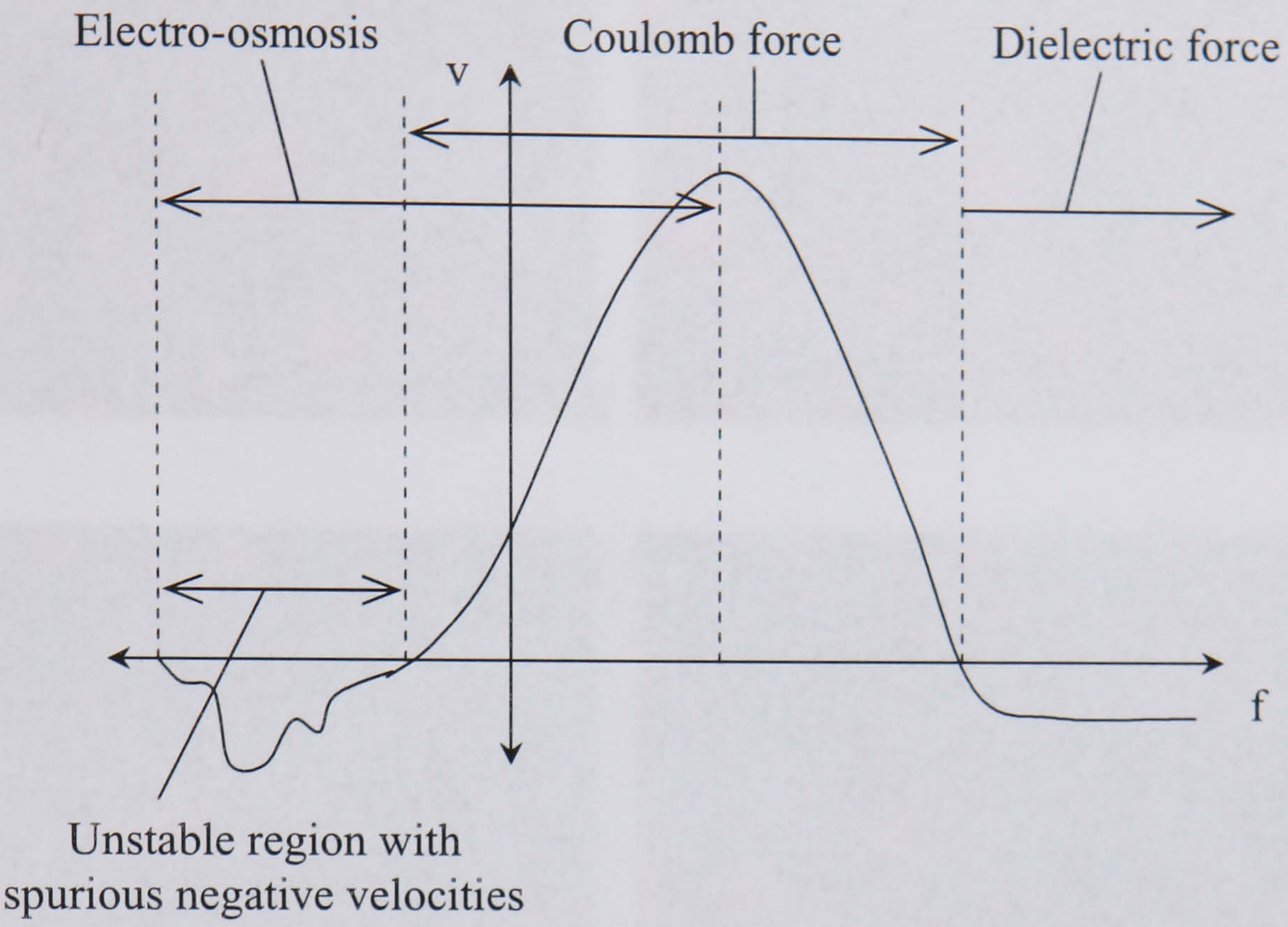

Figure 9-27

Potential regions of dominance of forces in a combined electrothermal/electro-osmotic model superimposed on a schematic data curve displaying the observed salient features.

9.8 Pumping - a gallery of possibilities

Some of the effects possible in fluid/particle manipulation are shown in Figure 9-28 - Figure 9-32. Red beads have been used to illustrate the flow trajectories while green beads highlight the electrodes, on/off cycles and give an indication of the frequency/voltage combinations used. In all cases an additional high frequency signal (10MHz, 4V) has been applied to smooth the motion and increase the number of flow possibilities.

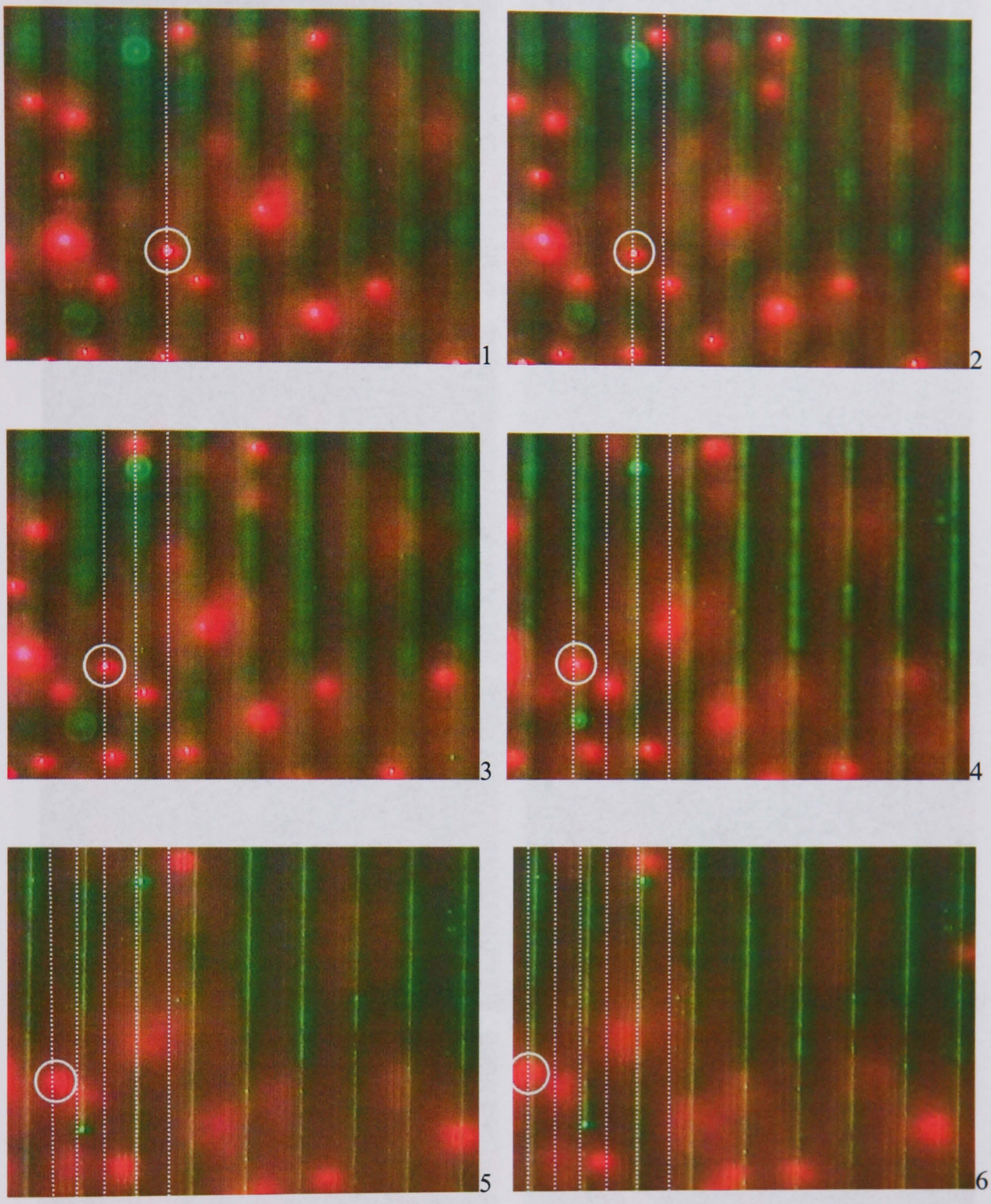

Figure 9-28

Transport of negatively dielectrophoretic red beads 30μm above electrodes. Frames shown at 2s intervals with focus moving from beads to electrodes. 800kHz, 3.5V.

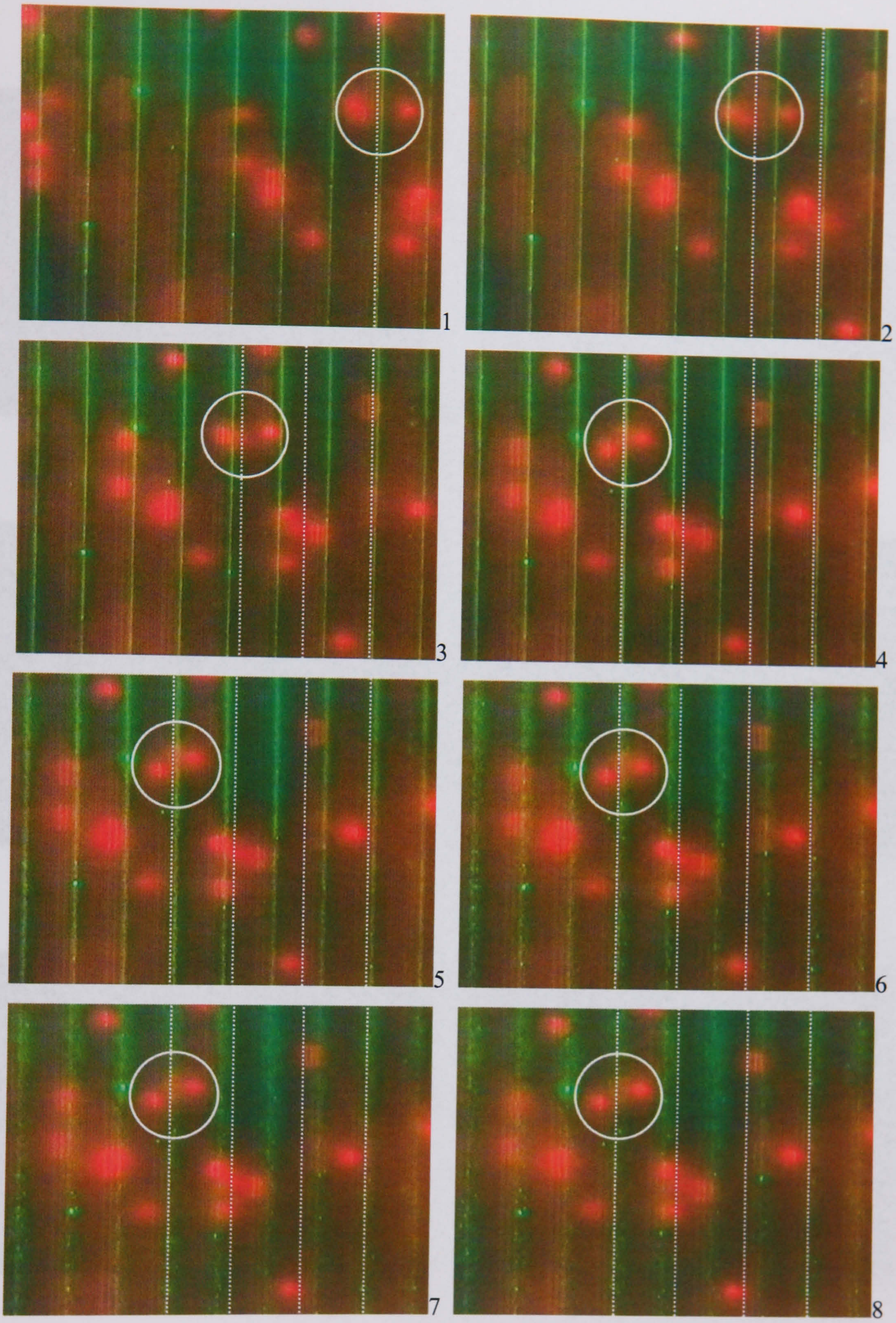

Figure 9-29

Frames 1-4 *at 3s intervals illustrating vector preserving transport of red beads during the on-cycle.* ***5-8*** *showing diffusion of green beads and stationary behaviour of red beads during off-cycle. 800MHz, 3.5V.*

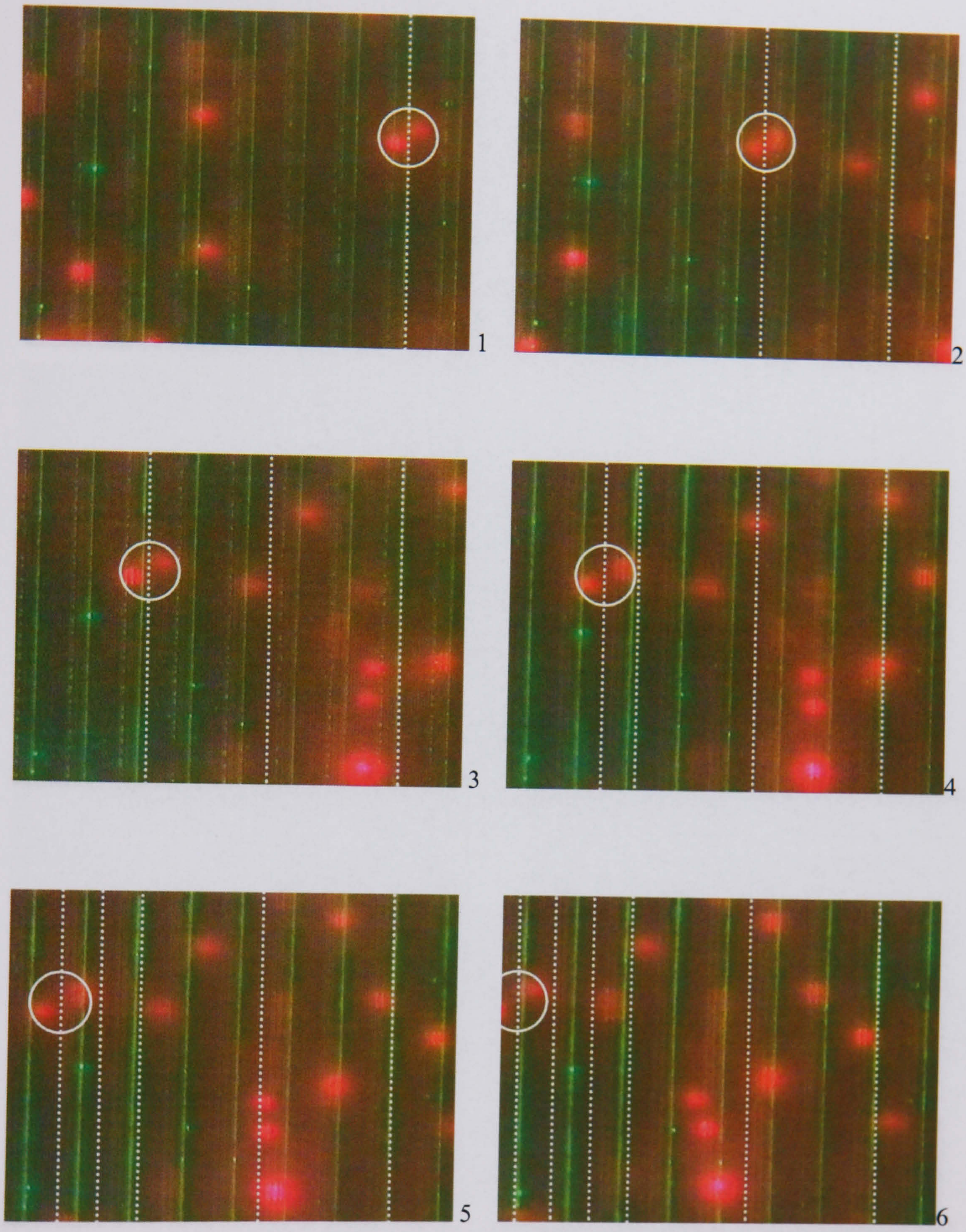

1 2 3 4 5 6

Figure 9-30

2s intervals depicting fast transport, voltage change 4V-2.5V and slow transport, monodirectional.

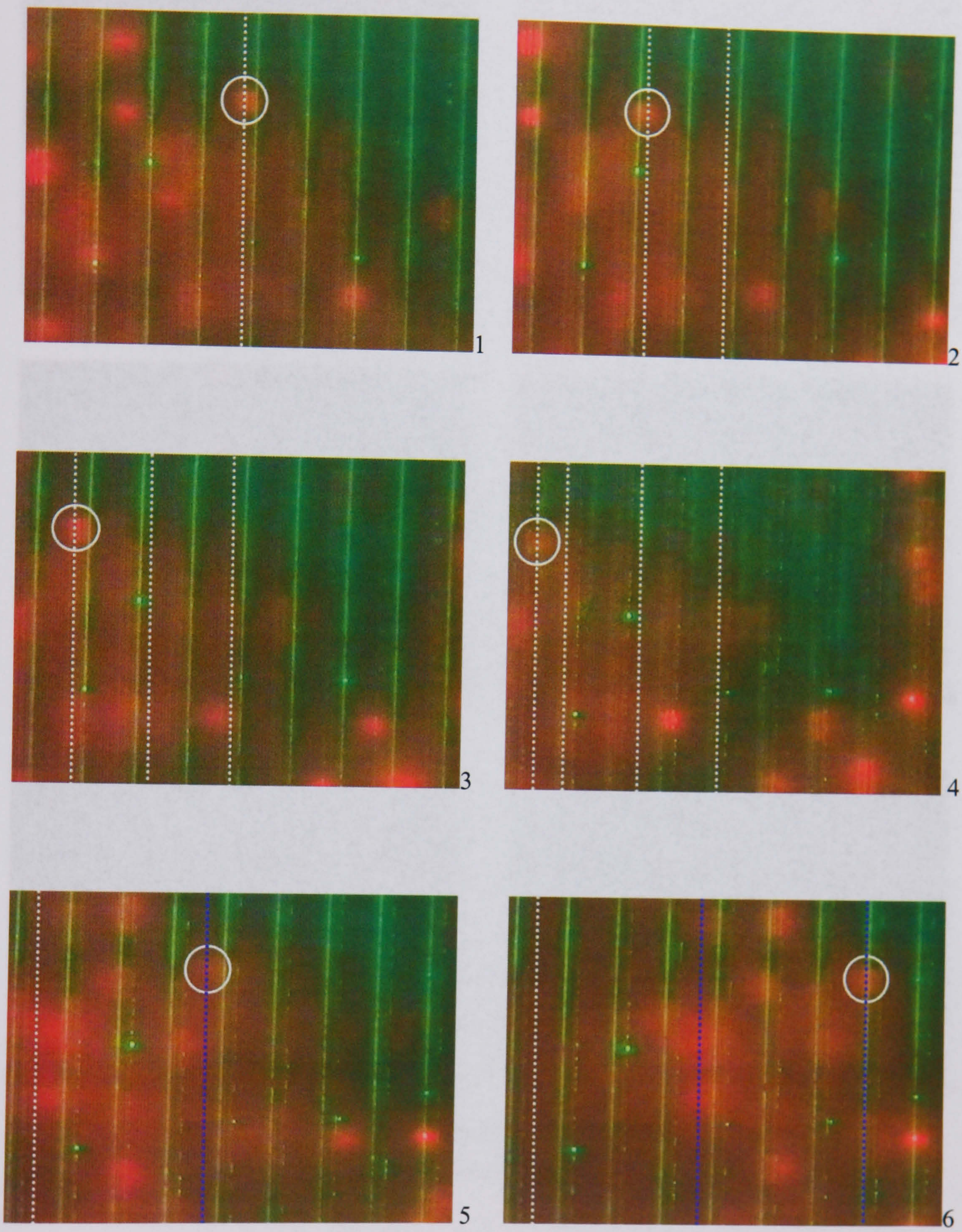

Figure 9-31

Sequence showing reversing motion and speed variation on switching the low and high frequency signals (800kHz, 3V; 10MHz, 4V). ***Frames 1-4****, 4s intervals;* ***5-6****, 2s intervals.*

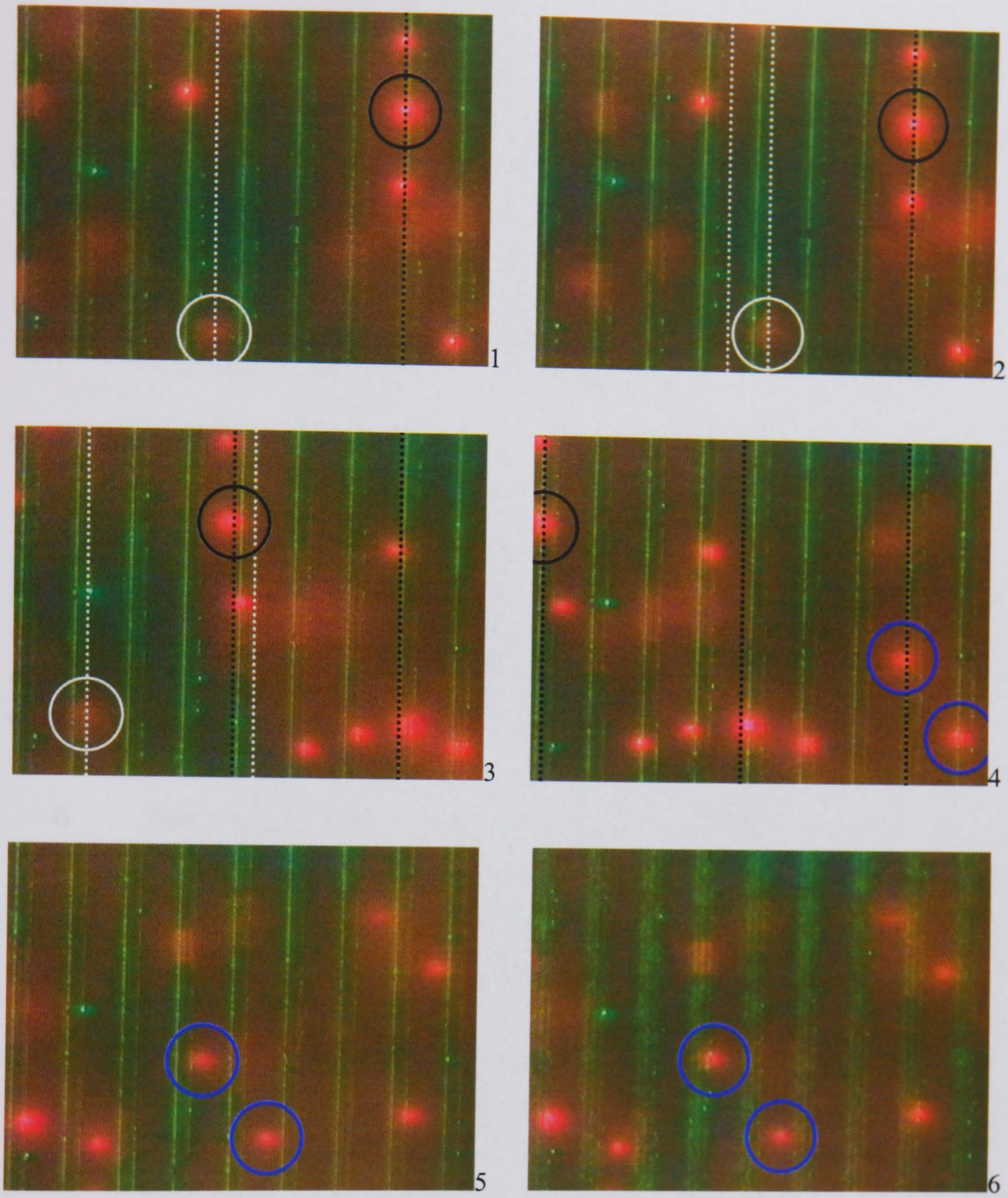

Figure 9-32
1.5s intervals.

Frames 1 and 2: *trapping of red beads combined with transport to right for beads outwith trap, 400kHz, 4V.*

Frames 3 and 4: *Frequency adjustment results in abrupt direction change and rapid motion to left of all red beads, 80kHz, 4V. Although now well below their DEP crossover frequency the flow is too strong for them to remain trapped.*

Frames 5 and 6: *No perturbation set up in system with completely stationary behaviour during off-cycle.*

9.9 Implications for Brownian ratchet functionality

The effect of fluid motion on the operation of the device as a Brownian ratchet is variable. If the positive DEP frequency is chosen in a frequency region of minimal fluid flow the collection will continue to occur only as a result of the asymmetric DEP force. It can also be chosen in a region where the flow acts in the same direction, enhancing apparent collection speed but possibly inhibiting trapping. If chosen in an opposing flow region, this would tend to de-functionalise the device. However, it is usually possible to choose the positive DEP frequency in a minimal flow region. This does restrict the available positive DEP voltage range but experiments have shown the device still to be highly tuneable.

9.10 Conclusion

The non-stochastic flow that has been observed on the Brownian ratchet device under certain conditions has been measured as a function of frequency, voltage, fluid conductivity and with one and two applied signals. On comparison of the velocity spectra with experimental and simulated results and theoretical considerations the conclusions reached on the basic driving mechanism of the flow are:

i) There is a high likelihood of an electro-osmotic component.

ii) The involvement of an electrothermal component is not supported by the scale of the flow simulations based on Joule heating from the electric field. Nonetheless, a net flow is predicted by this mechanism, similar in form if not in magnitude to that observed. The modelled velocities can be substantially increased, however, by considering the possibility of current flow in the electrodes as an additional heat source. Associated localised conductivity increases in the fluid may also enhance the flow rate. Theoretical considerations, moreover, suggest that the experimental velocity curves have some features in common with those expected from this mechanism.

iii) The velocity dependence on voltage is inconclusive in differentiating between the two mechanisms, perhaps because of data inadequacy or because there is more than one driving force in operation.

iv) Neither of the two mechanisms alone completely account for all of the observed flow patterns. A combination of the two, however, may provide an adequate framework.

As far as the functionality of the Brownian ratchet is concerned, the fluid flow need not terminally disrupt the system. The presence of solely stochastic transport would depend on an adequate calibration being made of the flow patterns in each sample in order to delineate frequency/voltage domains where non-stochastic flow is negligible. Considering the crossover data in Chapter 5 this should be within a feasible range for most of the entities measured in this thesis since the crossovers are generally significantly higher than the frequency regions where fluid flow is observed and therefore it should be possible to choose the low, positive DEP frequency in a stationary zone.

The potential for using this construction for microfluidic manipulation is large. A number of effects have been demonstrated which suggest that fine control of the magnitude and direction of the flow are possible combined with DEP trapping and levitation.

9.11 References

[1] L. Gorre-Talini, J. P. Spatz, and P. Silberzan, "Dielectrophoretic ratchets", *Chaos*, vol. 8, pp. 650-656, 1998.

[2] T. Schnelle, T. Muller, G. Gradl, S. G. Shirley, and G. Fuhr, "Dielectrophoretic manipulation of suspended submicron particles", *Electrophoresis*, vol. 21, pp. 66-73, 2000.

[3] A. B. D. Brown, C. G. Smith, and A. R. Rennie, "Pumping of water with ac electric fields applied to asymmetric pairs of microelectrodes", *Physical Review E*, vol. 63, 2000.

[4] N. G. Green, A. Ramos, A. Gonzalez, A. Castellanos, and H. Morgan, "Electrothermally induced fluid flow on microelectrodes", *Journal of Electrostatics*, vol. 53, pp. 71-87, 2001.

[5] N. G. Green, A. Ramos, A. Gonzalez, H. Morgan, and A. Castellanos, "Fluid flow induced by nonuniform ac electric fields in electrolytes on microelectrodes. I. Experimental measurements", *Physical Review E*, vol. 61, pp. 4011-4018, 2000.

[6] A. E. Smith and D. W. Coit, *Handbook of Evolutionary Computation*: Oxford University Press and Institute of Physics Publishing, 1995.

[7] N. G. Green, A. Ramos, A. Gonzalez, A. Castellanos, and H. Morgan, "Electric field induced fluid flow on microelectrodes: the effect of illumination", *Journal of Physics D-Applied Physics*, vol. 33, pp. L13-L17, 2000.

[8] A. Ramos, H. Morgan, N. G. Green, and A. Castellanos, "Ac electrokinetics: a review of forces in microelectrode structures", *Journal of Physics D-Applied Physics*, vol. 31, pp. 2338-2353, 1998.

10 Conclusion

10.1 DEP characterization

In this thesis the effect of biological surface modification on sub-micron colloids has been studied through DEP crossover measurements for the first time. The difference in the crossover response following the immobilization of various biological moieties has demonstrated the effect of covalent and absorptive coupling on the relaxation response of the colloids as well as producing evidence, in the case of secondary antibody coupling, of an immunological reaction and, with the secondary oligonucleotide layer, of biotin-avidin linkage. This crossover data has been well fitted with respect to a relaxation mechanism derived from the increasingly well accepted Gouy-Chapman-Graham-Stern double-layer model, by means of substitution of a structured surface conductance into the expression for a lossy, but classically non-dispersive, Debye particle. This model appears to more accurately fit the data than those attempted previously and has enabled predictions to be made of ζ-potential and conductance in the stagnant layer – following an increasing body of literature to suggest that charge transport behind the shear plane does indeed take place despite previous, long standing assumptions to the contrary. The absolute values of ζ-potential predictions, however, are not supported by those inferred through the Helmholtz-Smoluchowski relation from electrophoretic mobility data, even taking into account the Huckel correction for diffuse layer hindrance. This could be due in part to the experimental uncertainty inherent in crossover measurements, but also highlights the inconsistencies, well documented in the literature, between various methods of ζ-potential measurement - in particular, the frequently reported large scale underestimation of ζ-potential through electrophoretic means. The limitations of the predictive power of the model have also been discussed, and the conclusion reached that the method used, even with a mathematically minimised fitting routine, is only capable of generating fairly wide ranges for the parameters in question, becoming increasingly insensitive to changes in one parameter as the other is increased. This has led to very vague predictions of Stern-layer conductance in particular. This leaves room, however, for this parameter to be high enough to have significant effect on electrophoretic mobility which, as has been suggested in the literature, could give rise to the incongruent ζ-potential results. However, while the predicted absolute values of the ζ-potential are not in immediate agreement with the electrophoretic data, there is a good proportional correlation, suggesting that some calibration could be used to interpret crossover data, that would allow better predictions of absolute values. The DEP response of the beads on attachment of biological ligands has also enabled some speculation with reference to current literature on how the roughening of a surface with the introduction of additional charged or polarisable entities may influence the effective location of the slip plane and charge transport in the double layer. While this has been tackled in a mainly qualitative manner, it can be seen on increasing the effective diffuse layer viscosity in the modelled curves to account for protrusion of attached ligands well beyond the stagnant layer boundary that this could have some effect on the DEP response.

The main conclusion on the DEP characterisation experiments is that since there are observable differences before and after surface modification, considerable scope exists for the use of DEP as a tool in affinity separation.

10.2 Fractionation device development

Developmental work carried out on the design, modelling and fabrication of a fractionation device suitable for use with sub-micron particles has also been largely successful. While early work on the fabrication of a field flow fractionation device for use with submicron particles was hampered by technical difficulties, a Brownian ratchet design has proved much more practicable. A new electrode structure has been devised based on the simultaneous juxtaposition of positive and negative DEP and a microfluidic device constructed by adaptation of a method previously utilised on a larger scale. While it has not been possible, due to poor initial sample localisation, to observe on testing an ensemble particle drift by eye, stochastic transport rates have been inferred from the experimental observation of asymmetric collection and symmetric diffusion using various image processing techniques. Based on experimentally measured diffusion and collection rates, the predicted peak separation time of two populations of 216nm and 460nm beads has been shown to be 4 minutes, 50 seconds, which compares favourably with dielectrophoretic FFF so far carried out on larger particles. Potential separation on the basis of surface properties has also been illustrated, with the trapping of high crossover, uncoated beads while Brownian ratchet conditions are simultaneously upheld for a population of lower crossover, biotin modified beads.

10.3 Microfluidic pumping

The observation, under certain conditions, of non-stochastic, linear fluid pumping has also led to a series of investigations. A travelling wave mechanism having been ruled out due to insufficient signal phases, possible mechanisms for this transport have been reduced, effectively, to two – electro-osmotic and electrothermal. In terms of the expected flow rate, the former seems more applicable. According to the simulated flow from Joule heating, the effects from this mechanism alone are orders of magnitude too small to account for the experimental observations. The application of additional thermal gradients to the system, the main source of which could be resistive heating of the electrodes, leads to simulated flow magnitudes much closer to those observed. Comparison of other features of the measured flow patterns with theoretical, experimental and simulated results of the two investigated mechanisms suggests that a combination of both may be acting.

While the mechanism of the flow is not yet fully understood, however, a number of effects have been demonstrated which suggest that fine control of the magnitude and direction of the flow are possible. Thus combined with the additional possibilities of DEP trapping and levitation, the potential for using this construction for sub-micron particle manipulation and microfluidic control applications is large.

10.4 Fulfilment of aims

With reference to the stated aims, then, it has been concluded that:

1) i) Differentiation of submicron particles on the basis of surface properties is possible through DEP and therefore there exists a high potential for DEP based affinity separation techniques.

   ii) Some insight can be gained, dielectrophoretically, into charge transport in the double-layer with the surface immobilisation of biological ligands, since this introduces mechanical as well as electrical differences into the ion flow processes.

   iii) Adequate calibration is necessary for the conversion of DEP parameter predictions using the Gouy-Chapman-Graham-Stern model of the double layer into values reconcilable in the absolute sense with DC electrophoretic techniques.

2) i) On investigation of the methods of DEP fractionation, exploitation rather than suppression of the dissipative nature of sub-micron ensembles is an interesting and relatively unexplored line of pursuit.

   ii) The device constructed, using a new electrode structure to produce a highly tuneable DEP potential, behaves in the manner of a Brownian ratchet, and with adequate initial localisation of the sample and channel height optimisation, will be able to separate particles on the basis of their diffusion constants – or behave as a DEP trap/Brownian ratchet combination for the separation of particles on the basis of their crossovers, defined by size and/or surface properties.

   iii) The manipulation of particles is further enhanced by a highly controllable pumping mechanism produced by the asymmetry of the applied field, which could lead to interesting microfluidic applications as well as providing greater insight into electro-osmotic and electrothermal fluid flow induction.

10.5 Future Work

In summary and extrapolation of the suggestions made in the thesis, future development of the work undertaken here could be made in the following areas.

10.5.1 DEP characterisation

- Surface modification could be refined by taking into account antibody orientation in order to observe whether this improved significantly the measured crossover ranges of the double protein layer sample, or whether the experimental uncertainty is due mainly to other effects such as sample aggregation. This could be a useful indication of the sensitivity of DEP to this type of reaction.
- The DEP response of oligonucleotide sample with
    - different lengths
    - complementary binding

  could be measured with a view to comparing the DEP response with respect to surface roughening/steric hindrance and alteration of the electrical/dielectric properties of the attached moieties. This could enhance understanding of charge transport mechanisms in the double layer as well as assess the potential of DEP for use in DNA scavenging and sequence recognition.
- A more extensive experimental analysis of ζ-potential using non-electrophoretic means would be favourable for the establishment of a calibration of DEP crossover predictions with more generally accepted results. This could also provide insight into the differing response of AC measurement techniques as compared with more established means.
- Model utility and greater control over electrical surface properties could be improved by conducting DEP crossover measurements within various regions of highly controlled pH.

10.5.2 Brownian ratchet fabrication/utilization

Net stochastic transport in a Brownian ratchet device designed on this principle could be directly observed and measured with:

- better microfluidic control over sample introduction and
- the development of reliable fabrication techniques for the low channel height requirement.

This device could then be utilised to fractionate sub-micron colloids in a considerably more efficient manner than is theoretically possible with DEP-FFF, considering the problem of Brownian dissipation in the latter.

10.5.3 Fluid pumping

Better understanding of the pumping mechanism could be gained by:

- fabricating similar electrode structures with metals of different resistivity, combined with direct measurements of temperature and voltage gradients on the electrodes.
- Further theoretical exploration of the nature of electrothermal and electro-osmotic forces on asymmetric structures combined with more extensive flow pattern simulations

Also, with more experimental observation, integration of this highly versatile pump into microfluidic analysis systems in place of pressure gradients or high voltage electrophoresis could be established.

Publications and Presentations

[1] M. P. Hughes, M. F. Flynn, and H. Morgan, "Dielectrophoretic measurements of sub-micrometre latex particles following surface modification", *Institute of Physics Conference Series*, vol. 163, pp. 81-84, 1999.

[2] M. P. Hughes, M. F. Flynn, and H. Morgan, "The dielectrophoretic behaviour of latex spheres: Influence of surface conductance", *Journal of Colloid and nerface Science*, vol. 220, pp. 454-457, 1999.

[3] M. F. Flynn and H. Morgan, "DEP Brownian Ratchet manipulation of Surface Modified Colloids", *European Workshop on Electrokinetics and Electrohydrodynamics in Microsystems, poster presentation, Glasgow, Scotland*, 2001.

[4] M. F. Flynn and H. Morgan, "DEP Analysis of Oligonucleotide modified Latex Colloids", *6th Int. Conf. On dielectric and related phenomena, Spala, Poland*, 2000.

Prospective Publications

"DEP Brownian ratchet pumping through simultaneous application of positive and negative DEP"

"Asymmetric electric field driven fluid pumping"